UNIVERSIDAD AUTÓNOMA DE MADRID

Departamento de Química Orgánica

New Organic Semiconductors based on Triindole and other Cyclic Oligomers of Indole

Constanza A. Ruiz Domínguez

Director:

Dr. Berta Gómez-Lor Pérez

Madrid, 2016

ACKNOWLEDGMENTS

This thesis it has been made in the New Architectures in Materials Chemistry group at the Instituto de Ciencia de los Materiales de Madrid (ICMM). Here, I would like to thank of my thesis director Dr. Berta Gómez-Lor for being an out-standing advisor. Under her guidance I conduct independent research and understood how to purpose a well-documented research.

In this space I would like to thank the support of all the people which I could collaborate in the development of this thesis, and without this thesis would not have been possible. I'm especially thankful to Dr. Carmen Coya for the fabrication of OLED devices, and also to Dr. M. Carmen Ruiz Delgado for the theoretical measurements.

I like to extend my deepest appreciation and thankfulness to Prof. Antonio Facchetti for accepting my internship at his lab at Northwestern University (Chicago) that time was highly productive and rewarding.

Presentación

PRESENTACIÓN

El desarrollo de la electrónica orgánica ha traído consigo la generación de numerosos adelantos tecnológicos durante los últimos años. Este campo de investigación destaca por su multidisciplinariedad, implicando la combinación de conocimientos referentes al diseño y síntesis en química orgánica, al tratamiento y procesado de materiales, y al funcionamiento y diseño de dispositivos como OLEDs, OFETs y células fotovoltáicas. En este sentido, se pretende dar lugar a la generación de dispositivos ligeros y flexibles que no son accesibles con la electrónica convencional basada en el silicio. Por otra parte, esta nueva electrónica ofrece la oportunidad de la utilización de procesados basados en técnicas en disolución, de forma que su utilización permitirá abaratar los costes de producción a escala industrial.

Los grandes avances en esta área de la ciencia están relacionados con el desarrollo de moléculas que permiten el transporte eficiente de cargas eléctricas, que se cuantifica mediante el cálculo de la movilidad de cargas, μ. Este parámetro viene definido por la velocidad que adquieren los huecos o electrones bajo la aplicación de un campo eléctrico de acuerdo con la relación $v=\mu E$.

A partir del desarrollo de nuevos materiales semiconductores y la optimización de su procesado, ha sido posible conocer mejor los factores que afectan a la movilidad de cargas. Si bien se han desarrollado numerosos materiales que presentan altos valores de movilidad, la utilización de estos semiconductores a nivel industrial resulta aún complicada. Existe una clara necesidad de desarrollar candidatos eficientes que permitan combinar altos valores de movilidad con procesados escalables a nivel industrial.

Los materiales orgánicos presentan una amplia variedad de diseños y funcionalidades, pero curiosamente dentro del campo de los semiconductores orgánicos sólo una pequeña selección de ellos ha sido investigada. En este contexto, mi grupo de investigación ha introducido hace unos años la plataforma del triindol, esta molécula heptacíclica que tiene una gran tendencia a formar apilamientos columnares debido a su topología discótica (Figura 1). Esta plataforma ha demostrado ser una buena candidata para el transporte de carga, siendo destacable los altos valores obtenidos en cristales líquidos discóticos (2.8 $cm^2V^{-1}s^{-1}$), como resultado de la sinergia entre las propiedades intrínsecas de la plataforma con su organización supramolecular.

Con estos precedentes, el primer objetivo de esta tesis doctoral es la optimización de las propiedades electrónicas y de auto-organización de la plataforma del triindol, con

el fin de incorporarla en dispositivos electrónicos tipo OFETs y OLEDs (**capítulos 1**, **2** y **3**). Las propiedades de esta plataforma han sido moduladas en función de las características impuestas por las diferentes aplicaciones previstas.

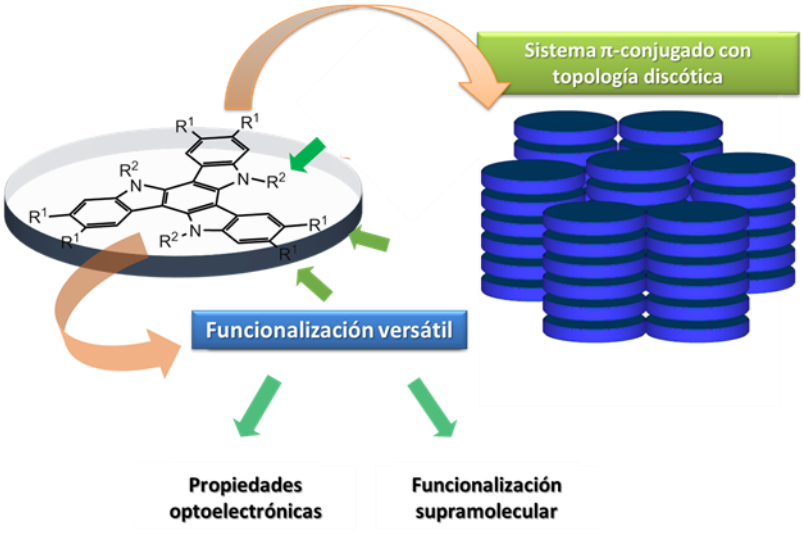

Figura 1: Esquema de la plataforma del triindol como un sistema π-conjugado con topología discótica, presentando dos posiciones fundamentales para su funcionalización.

Los sistemas aromáticos π-conjugados proporcionan gran cantidad de "electrones móviles" y sus propiedades electrónicas (luminiscencia, absorción, transporte de carga…) pueden ser moduladas fácilmente mediante la introducción de grupos funcionales. Es fundamental considerar que las propiedades de los materiales moleculares no se rigen únicamente por el comportamiento de las moléculas individuales, sino que la forma en la que se distribuyen en el espacio va a jugar un importante papel. Por este motivo el que el control de la organización de la estructura molecular es un importante reto en este campo de investigación.

Las estructuras cristalinas ofrecen una excelente oportunidad, para establecer claras relaciones estructura-propiedad y elucidar el mecanismo de transporte de carga en los materiales orgánicos. En el **capítulo 1** se realizará un estudio en el que procederemos a la variación sistemática del número de átomos de carbono que contiene la cadena anclada al nitrógeno, y estudiaremos cómo afecta este parámetro al empaquetamiento y a la morfología de los cristales resultantes. Se ha observado que las cadenas alquílicas tienen una gran influencia en la posición que ocupan unas moléculas con respecto a otras, dirigiendo la formación de diferentes empaquetamientos cristalinos y morfologías. Se ha podido así determinar la contribución de interacciones tipo CH-π en la generación de las diferentes superestructuras observadas (Figura 2).

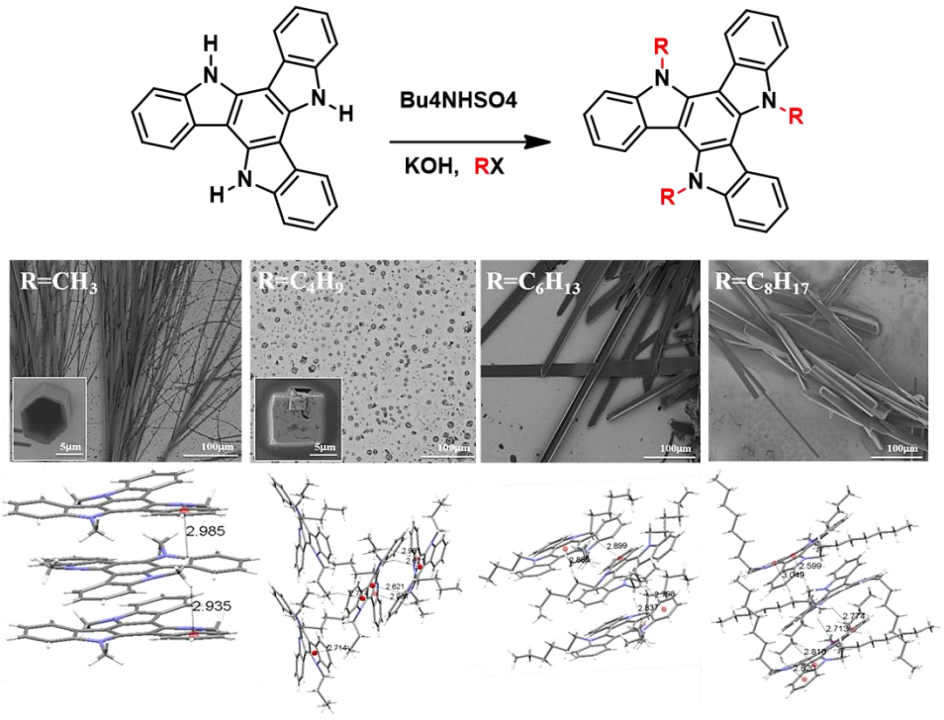

Figura 2: Esquema representativo de cómo afecta el tamaño de la cadena a al empaquetamiento molecular y a la morfología de los cristales resultantes.

Por otro lado, estos derivados se caracterizan por oxidarse fácilmente y de forma reversible, lo que les califica como prometedores candidatos para la inyección de huecos y el transporte de carga. En este contexto, al estudiar el empaquetamiento cristalino de los diferentes triindoles consideramos que el mejor candidato para ser incorporado en dispositivos tipo OFET era el *N*-trihexiltriindol. Este compuesto presentó un valor de movilidad de cargas de 1,42 x 10^{-2} $cm^2V^{-1}s^{-1}$.

Una vez hemos estudiado como se organizan las moléculas y las interacciones por las que se ve afectada la organización supramolecular, en el **capítulo 2** nos centraremos en el estudio de la funcionalización en la periferia de la plataforma del triindol, variando así sus propiedades ópticas con el fin de incorporarla en dispositivos tipo OLED.

En este trabajo, se muestra cómo la comunicación electrónica de los sustituyentes externos a la plataforma rica en electrones del triindol facilita la optimización de las propiedades ópticas de estos derivados. Los cambios en la naturaleza de los grupos periféricos se refleja claramente en sus espectros de absorción y emisión, que muestran desplazamientos batocrómicos significativos con el aumento del carácter aceptor. La dramática influencia que ofrecen los sustituyentes periféricos sobre las propiedades electrónicas de estos derivados, nos aporta asimismo una gran oportunidad para modular

sus niveles de energía. Teniendo en cuenta que los dispositivos electrónicos orgánicos se construyen generalmente usando arquitecturas con múltiples capas, esta posibilidad será fundamental para facilitar la inyección de carga y minimizar barreras de energía entre las diferentes capas. En esta tesis, presentamos las propiedades de emisión y de transporte de varios derivados del triindol en OLEDs procesados desde disolución.

Por otro lado, haciendo uso de la versatilidad sintética de esta plataforma se han sintetizado una serie de moroariltriindoles con el fin de estudiar el efecto que tiene la sustitución asimétrica en las propiedades electrónicas. Los resultados han mostrado como estos nuevos compuestos han presentado mejores rendimientos cuánticos, así como un aumento de la amplitud de los espectros de emisión en comparación con sus homólogos simétricos (Figura 3).

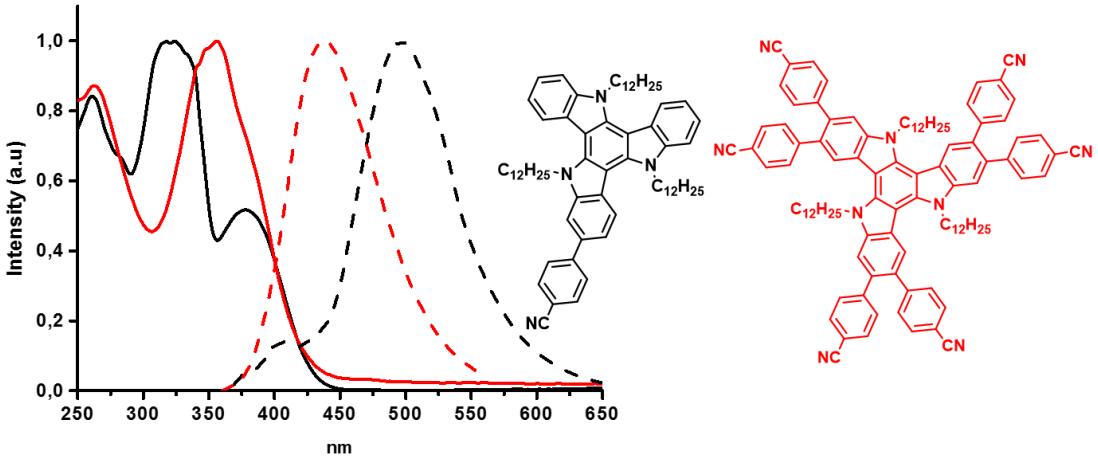

Figura 3: Espectro de absorción y emisión de triindoles mono y hexafuncionalizados.

En la búsqueda del balance entre buenos valores de movilidad, y procesados sencillos, los cristales líquidos discóticos resultan unos prometedores candidatos. En las mesofases columnares los núcleos aromáticos discóticos interactúan fuertemente de forma que se asegura una vía uniaxial de migración de portadores de carga, mientras que las cadenas alquílicas dan lugar a la generación de una zona aislante que rodea al núcleo. Al mismo tiempo que la naturaleza fluida de los cristales líquidos va a permitir la auto-reparación de los defectos del material y facilitará su procesado.

En el **capítulo 3** nos hemos centrado en la optimización de las propiedades de transporte de carga de cristales líquidos basados en la plataforma del triindol, con el

objetivo de aumentar la dimensionalidad del transporte de cargas y facilitar así su incorporación en dispositivos electrónicos.

Con el fin de disminuir esta dependencia de las propiedades eléctricas con la alineación (Figura 4), hemos seguido dos estrategias: la obtención de plataformas mesomorficas con una proporción mayor de la zona aromática con respecto a las cadenas aislantes que la rodean, y alternativamente hemos estudiado la síntesis de derivados con grupos periféricos capaces de establecer contactos con las moléculas vecinas.

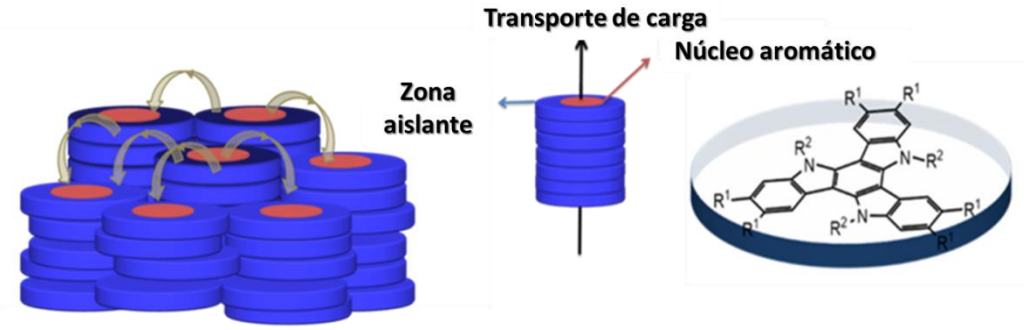

Figura 4: Esquema del aumento de la dimensionalidad del transporte de carga en cristales líquidos discóticos.

La disminución de la dependencia de la alineación se demostró al realizar medidas de transporte de cargas mediante la utilización de dos técnicas que requieren de diferentes alineamientos. Por un lado, determinamos la movilidad mediante *la técnica de Corriente Limitada por la Carga Espacial* (SCLC), técnica con una configuración tipo diodo (y que por tanto requiere una organización en el que el eje columnar se encuentra perpendicular al sustrato) y por otra mediante la construcción de un transistor de efecto campo (en donde el canal de conducción requiere una organización columnar paralela al sustrato). En ambos casos se pudo determinar la movilidad del transporte de carga, si bien los valores son mayores para los dispositivos tipo diodos. El hecho de poder determinar movilidades mediante la fabricación de transistores de efecto campo en este tipo de moléculas ya sugiere un aumento de la dimensionalidad del transporte de carga, puesto que los sistemas π-conjugados extendidos tienden a depositarse paralelos a la superficie del sustrato.

En un enfoque diferente en esta tesis exploramos la posibilidad de incorporar al triindol en el desarrollo de nuevos materiales electroactivos, tales como polímeros orgánicos microporosos.

Los polímeros aromáticos microporosos constituyen un nuevo tipo de materiales emergentes sintetizados a partir de monómeros π-conjugados, que presentan múltiples grupos reactivos para promover el acoplamiento molécula-molécula mediante enlaces π-conjugados. En este tipo de materiales, el enlace covalente de los componentes π-conjugados da lugar a capas bidimensionales, en donde el grado de conjugación lateral y el acoplamiento electrónico tendrá un importante efecto sobre el transporte de carga, mientras que su porosidad intrínseca ofrece la oportunidad para incorporar agentes químicos que permitan ajustar sus funcionalidades. Por otro lado, el carácter insoluble de estos polímeros microporosos limita el estudio de sus propiedades una vez ha sido sintetizado.

Con el objetivo de investigar las posibles aplicaciones de los triindoles en el desarrollo de este nuevos tipo materiales, en el **capítulo 4** hemos estudiado dos moléculas diméricas unidas entre sí a través de diferentes unidades puente (grupos *p*-fenileno o diacetileno, Figura 5). Estos dímeros han sido estudiados como sistemas modelo, con el fin de investigar la influencia de la unidad puente en sus propiedades electrónicas fundamentales.

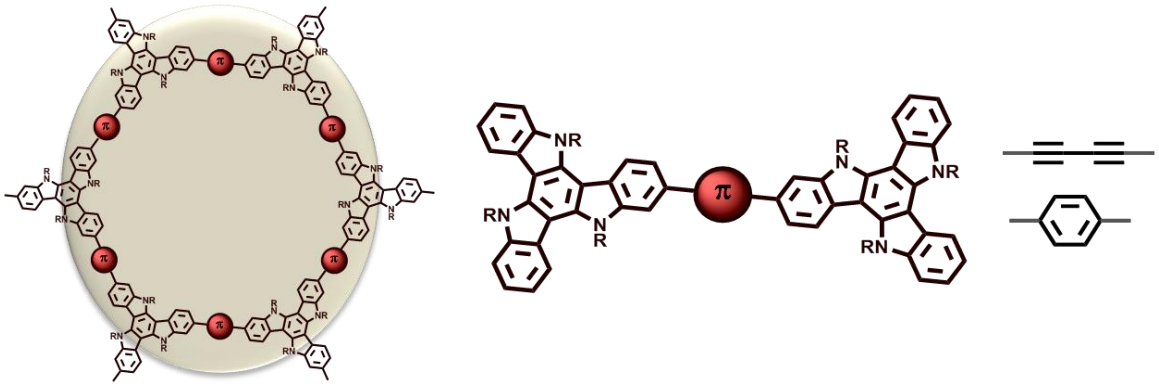

Figura 5: Diseño de síntesis de un posible polímero constituido por unidades de triindol unidas por puentes diacetileno o *p*-fenileno.

La combinación de estudios teóricos y experimentales de sus propiedades electrónicas, redox y foto-físicas que se realizaron sobre ambos dímeros, nos llevó a la conclusión de que el grupo diacetileno permite una mejor deslocalización de la carga. Este estudio permitirá el diseño futuro de nuevos polímeros microporosos basados en esta plataforma.

Finalmente, considerando las buenas propiedades semiconductoras obtenidas en los triindoles, en el transcurso de esta tesis doctoral se realizaron estudios sobre otros oligómeros cíclicos del indol, como son el triindol asimétrico y el tetraindol, apenas estudiados en este campo de investigación. En el **capítulo 5** de esta tesis recogemos los estudios teóricos y experimentales realizados sobre estas nuevas plataformas.

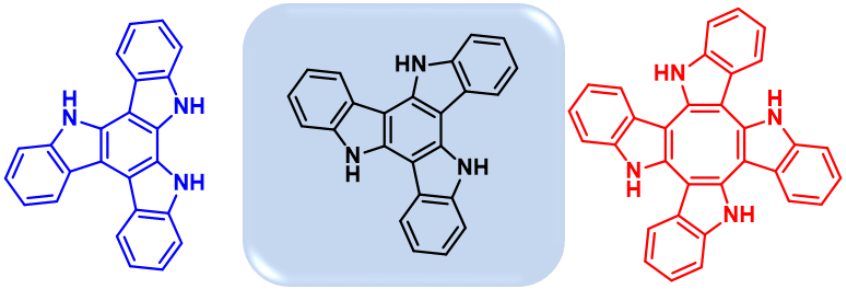

Figura 6: Esquema de las plataformas estudiadas en esta tesis doctoral.

En los estudios realizados sobre la plataforma asimétrica del triindol, se elaboró una comparativa entre sus propiedades y las del triindol simétrico. Observamos que la disminución de la simetría de la plataforma hace que haya un desplazamiento hacia el rojo del borde de absorción, así como un incremento de la emisión de fluorescencia y un aumento del rendimiento cuántico. Además, la voltametría cíclica y la espectroelectroquímica revelan la naturaleza reversible de los dos procesos de oxidación observables en los triindoles asimétricos alquilados, así como un aumento de la estabilidad de las especies oxidadas. Estudios teóricos indican la concordancia con los resultados experimentales y nos permiten una buena comprensión de las propiedades físico-químicas de

Por otro lado, en el capítulo 4 describimos además la síntesis del tetraindol, y de varios de sus derivados funcionalizados en las posiciones nitrogenadas. Este trabajo se llevó a cabo con el fin de diseñar sistemas 3D que nos permitiesen una mayor comunicación electrónica al aumentar el número de segmentos conjugados en diferentes direcciones, eliminando así los problemas que habíamos encontrado en estructuras columnares altamente anisotrópicas como la del triindol. Con el estudio de esta nueva plataforma se pretende trabajar con núcleos aromáticos de mayor tamaño, de forma demos lugar a un aumento de la dimensionalidad del transporte de carga.

Summary

SUMMARY

The field of organic electronics has progressed impressively, moving in only a few years from a basic research level to the development of devices already in the market. The great advances in this area have been closely related to the improvement of molecules that are able to transport charge efficiently, which is quantified by the charge carrier mobility μ, which reflects the speed of holes/electrons under an applied electric field according to the relation $v=\mu E$.

Continuous improvements in charge mobilities are being reported through the development of new semiconductors and optimization of materials processing, and this has been possible thanks to an increasingly better understanding of factors affecting charge mobility. While materials with high enough mobilities for current applications have been developed, progressing from laboratory into a reliable and large-area manufacturing process is proving challenging. There is a clear need of efficient candidates that meet the requirements necessary for the high throughput development of devices.

Organic materials present an unlimited variety in design and functionality, but curiously research on organic semiconductors has been performed on a narrow choice of molecules. In this context, our research group became interested on the electron-rich 10,15-dihydro-5*H*-diindolo[3,2-*a*:3',2'-*c*]carbazole (triindole) as a new organic semiconductor. Specially remarkably is the record hole mobility values (2.8 $cm^2V^{-1}S^{-1}$) determined on triindole-based semiconducting liquid crystals, as a result of the favourable synergy between the intrinsic properties of the platform and their supramolecular arrangement.

With these precedents, the first objective of thesis is to optimize the electronic and self-assembling properties of this high mobility semiconducting platform (**chapters 1**, **2** and **3**), towards its incorporation into electronic devices (OLEDs and OFETs) by taking advantage of the high chemical versatility of the triindole platform, with two different positions for structural modification (Figure 1). The properties of the molecular candidates have been modulated in accordance to the respective characteristics imposed by the different applications envisaged.

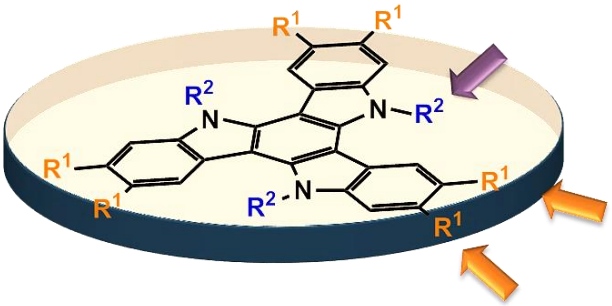

Figure 1: Chemical structure of triindole.

In order to investigate the structure-properties relationship and elucidate charge transport mechanism in organic materials, the organic single crystals offer an excellent opportunity. Here, the properties are not masked by grain-boundaries or other microstructure features that can severely localize and trap the charge carriers. Many efforts have been made to rationalize performance in terms of favorable crystallographic packing essential to improve the properties of the design of new promising materials.

In **chapter 1** we describe the study of a series of crystalline *N*-trialkyltriindoles functionalized with different length *N*-alkyl chains, in order to obtain a better understanding of the self-assembling behavior of this platform, and select the best candidate for their integration in devices.

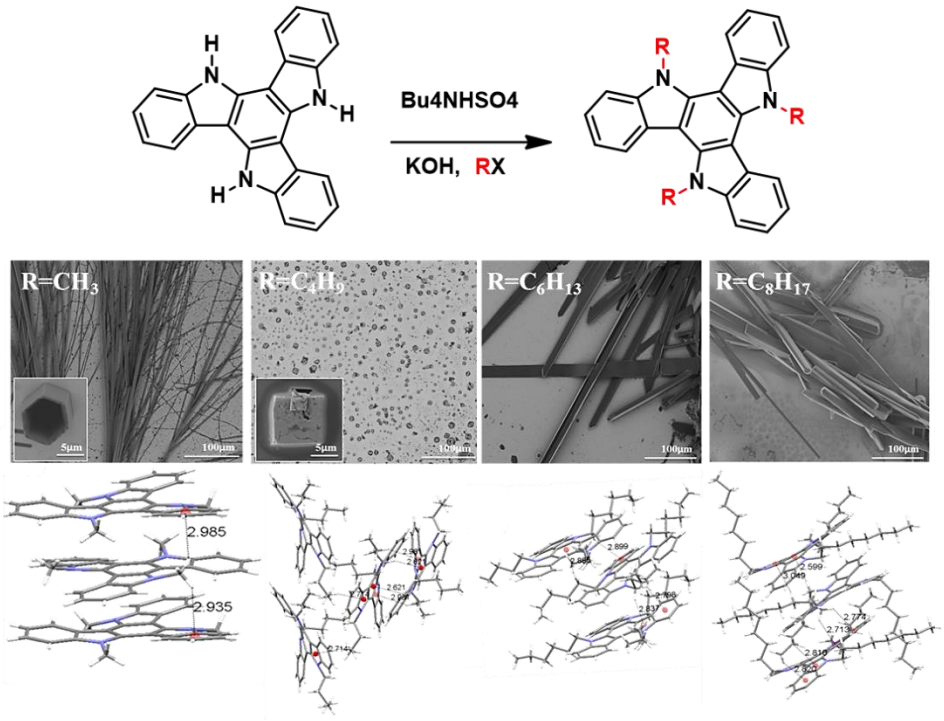

Figure 2: Scheme of how the intermolecular interactions and the crystallographic packing of *N*-trialkyltriindoles can be modulated.

It was found that the length of the alkyl chains does not affect significantly their electronic properties. However, it has a strong influence in the morphology and in the crystalline packing of these compounds (Figure 2). The contribution of several cooperative CH-π interactions to guide the self-assembly of this type of molecules have been clearly established.

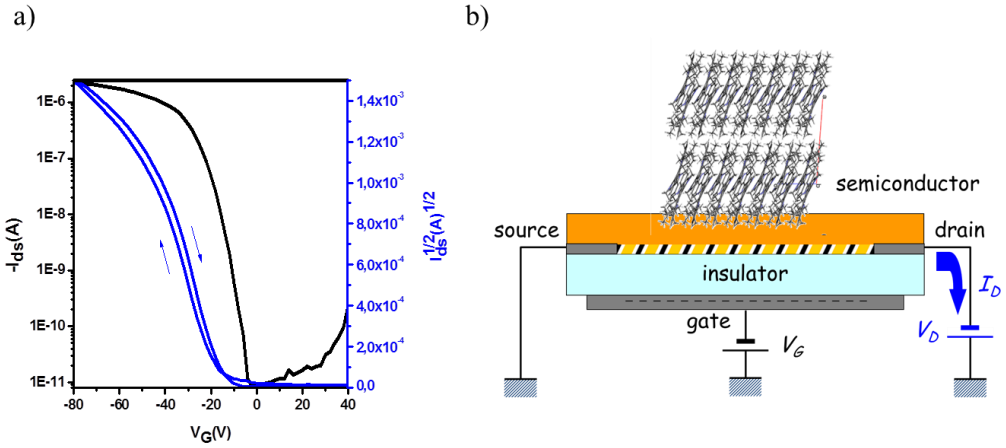

Figure 3: a) Transfer characteristics of *N*-hexyltriindole measured at a source-drain voltage of -80 V. Linear plot and square root plot of the drain current versus the gate voltage. b) Scheme of a field effect transistor, OFET.

All of these derivatives oxidizes readily and reversibly which qualify them as promising candidates for hole injection and transport. By studying the crystal packing of the different trialkylated triindoles we have selected the *N*-triahexyltriindole as the best candidate to be incorporated into OFETs. A mobility value, 1.42 x 10^{-2} $cm^2V^{-1}s^{-1}$ was obtained on standard bottom gate-top contact (Figure 3).

In **chapter 2** we focused on tuning the light-emitting properties and HOMO–LUMO levels of triindole, by functionalizing the periphery of this platform with the aim of incorporating them in OLEDs. In this work we have alkylated the nitrogen positions with three dodecyl chains, intended to induce solubility and introduced six peripheral bulky aryl groups that impede crystallization, and therefore facilitates the formation of homogeneous films necessary for good device performance.

In this chapter, we show how the electronic communication of the external substituents with the central electron-rich triindole facilitates the tuning of the optical properties of these derivatives. Changes in the nature of the peripheral groups, is clearly reflected in their absorption and emission spectra, which show significant bathochromic shifts as the acceptor character of the peripheral groups increases. The dramatic influence that peripheral substituents of triindoles exert on the electronic properties of these

derivatives offers also a great opportunity to modulate their energy levels by chemical functionalization (Figure 4). Considering that organic electronic devices are usually constructed using multilayer architectures, this possibility will be fundamental to facilitate charge injection from electrodes and minimize energy barriers between the different layers. In this thesis, we present the emission and transport properties of solution processed OLEDs based on three representative triindole derivatives.

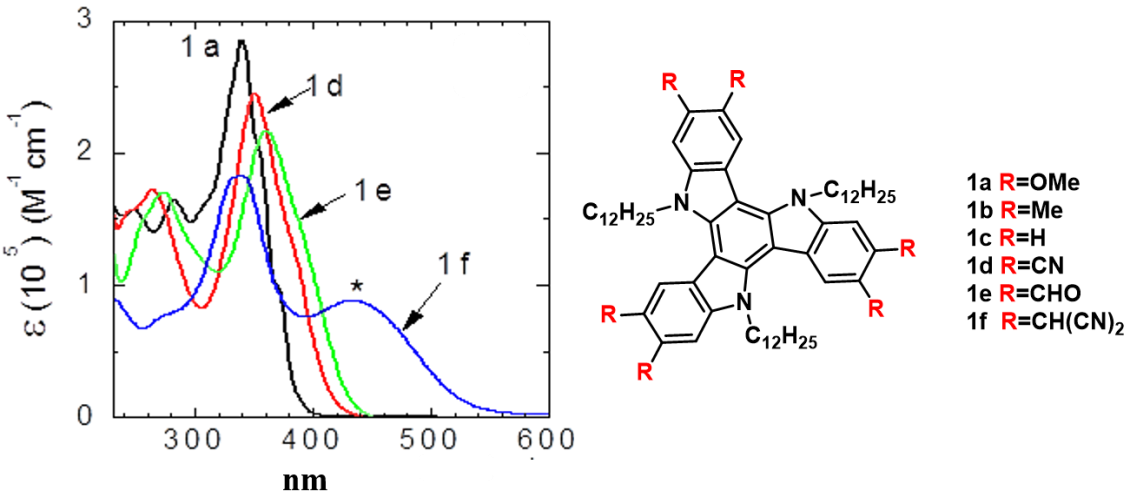

Figure 4: UV–vis spectra (molar absorption coefficients) of the derivatives triindoles.

On the other hand, and in order to broaden the synthetic versatility of this platform we have synthesized a series of monoaryltriindoles and study the effect that asymmetrical substitution has in the electronic properties of this semiconducting platform. Results show that asymmetrical derivatives offer significant advantages in terms of energy levels tailoring, and present higher quantum yields and increased range of emission spectra, when compared to their symmetrical counterparts (Figure 5).

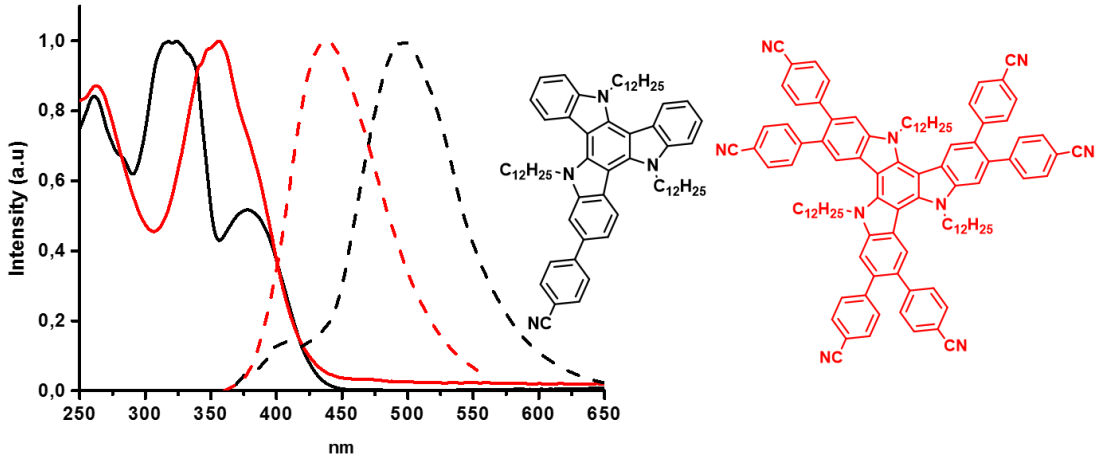

Figure 5: Absorption and emission spectra of mono- and hexa-functionalize triindoles.

In **chapter 3** we focused in the optimization of the charge transport properties of the triindole mesogens with the goal of incorporating them in Organic Field Effect transistors.

Discotic liquid crystals combine high mobility values with an easy processability, however the electrical performance in this type of materials is highly dependent on the degree of the columnar alignment, which represents an important drawback towards their incorporation in devices.

In order to decrease this dependence of the electrical properties on the alignment, we have followed two strategies: obtaining mesogens with a larger ratio of conducting part *versus* isolating cover and alternatively synthesizing new mesogens decorated with peripheral groups able to establish short contacts between neighbouring columns.

The increase of the conducting/isolating ratio will be attempted by decreasing the number of peripheral alkyl chains and enlarging the central conducting core. In this context, my research group has previously shown that in enlarged π-conjugated triindole–based aromatic cores, which can be easily obtained by oxidative cyclodehydrogention of hexaaryltriindoles, it is possible to induce mesomorphism, by attaching only three *N*-dodecyl chains (Figure 6).

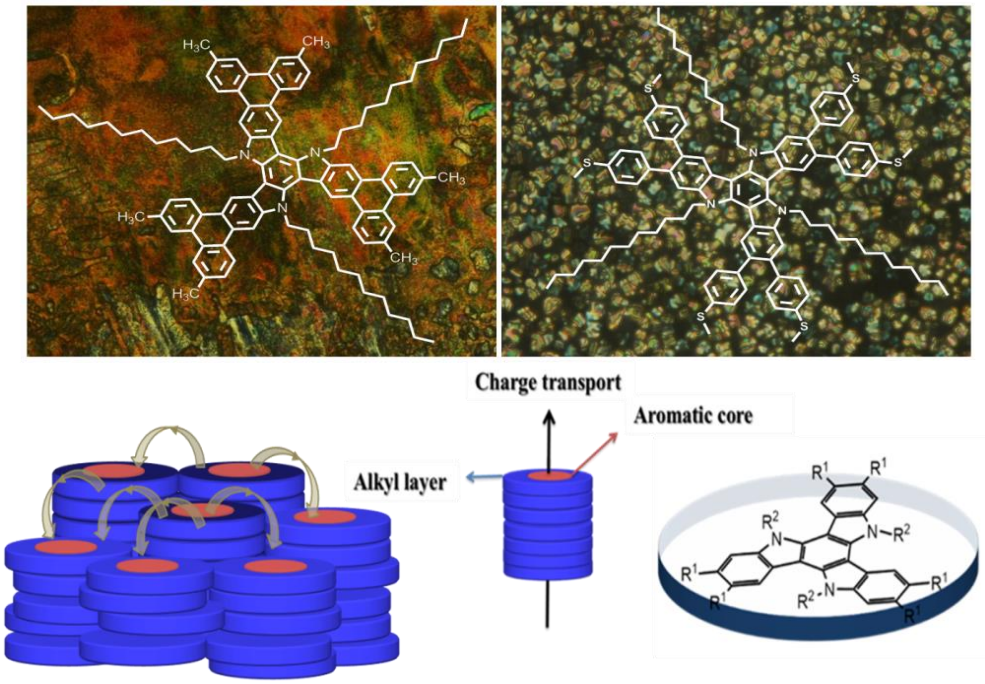

Figure 6: Microphotograh of the mesophases of the liquid crystal that we investigated (above) and a scheme of the modification of the aromatic core in discotic liquid crystal to increase the dimensionality of the charge transport.

In a second approach, to facilitate contacts between neighbouring columns, we have attached to the triindole platform, six peripheral groups able to establish intermolecular interactions. In particular we have synthesized a new triindole-based liquid crystal functionalized with six peripheral thiomethyl moieties (Figure 6). These moieties are able to establish S-S interaction, which have already shown beneficial to increase the contact between neighbouring columns in other semiconducting aromatic platforms.

The lower dependence of the electrical performance on the degree of columnar alignment of the charge transport properties, of these discotic liquid crystals, have been studied by comparing the mobility values obtained by applying two different methods with different alignment requirements: space-charge limited current (SCLC) measurements in a diode-like structure (which requires a conducting channel perpendicular to the surface) and field effect mobility measurements in thin film transistor devices (which requires a conducting channel parallel to the surface) (Figure 7). Although in both cases the mobility found on a diode type device is higher than that determined on thin-film transistors, the observation of field effect behaviour in a discotic liquid crystal processed by simple drop-casting suggest an increased dimensionality of charge transport, as π-conjugated molecules usually tend to deposit on surfaces with their aromatic cores parallel to the substrate planar.

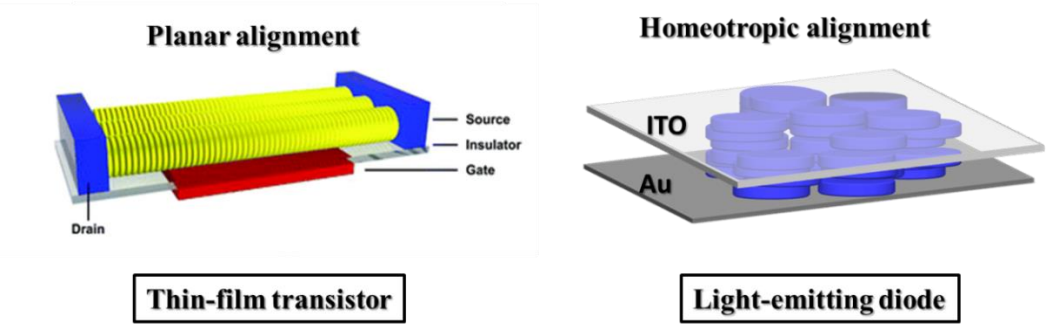

Figure 7: Scheme of the different alignment for the application devices.

In a different approach we explored the potential applications of triindole platforms in the development of new emergent electroactive materials, such as microporous organic polymers and covalent organic frameworks.

Aromatic microporous polymers constitute an emergent type of organic porous polymers synthesized from π-conjugated monomers with multiple reactive groups to promote molecule-molecule coupling via π-conjugated bonds. In this type of material, the covalent linkage of functional π-conjugated components gives rise to two-dimensional

(2D) layers, among which π-π stacking interactions can induce additional order while their intrinsic porosity offers significant opportunities to incorporate guests/chemicals to tune their functionalities. The insoluble character of covalent microporous polymers limits detailed postsynthetic studies to investigate how the structure will affect the desired properties, and thus the design of optimal polymeric materials on a molecular basis.

With the aim of investigating the potential applications of triindoles in the development of this type of new emergent electroactive materials in **chapter 4** we have studied two dimeric molecules bound together through different linkers (*p*-phenylene or diacetylene groups, Figure 8) as model systems, in order to investigate the influence of the π-bridge on their fundamental properties, such as the electronic, redox and photophysical properties.

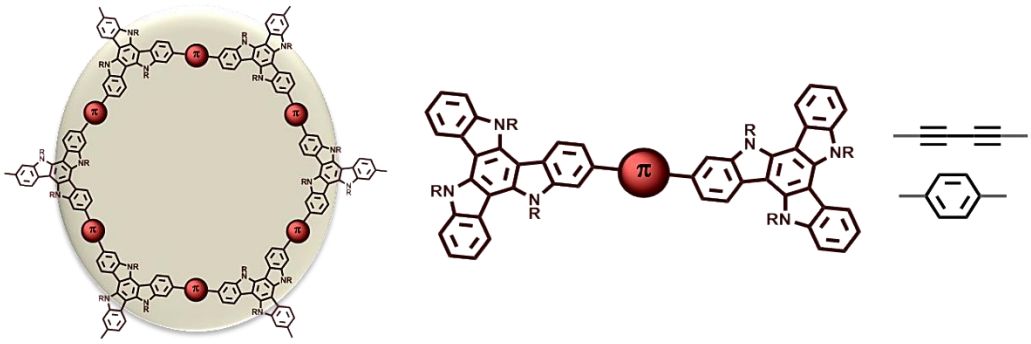

Figure 8: Dimeric material bounder by different linker.

Our results show us that while a *p*-phenylene bridge nearly isolates the two subunits of the dimers, a diacetylene bridge allows a high level of electronic connection between them (Figure 9). This conclusion renders the diacetylene moiety as the best linker in the synthesis of microporous polymeric material with opto-electronics applications.

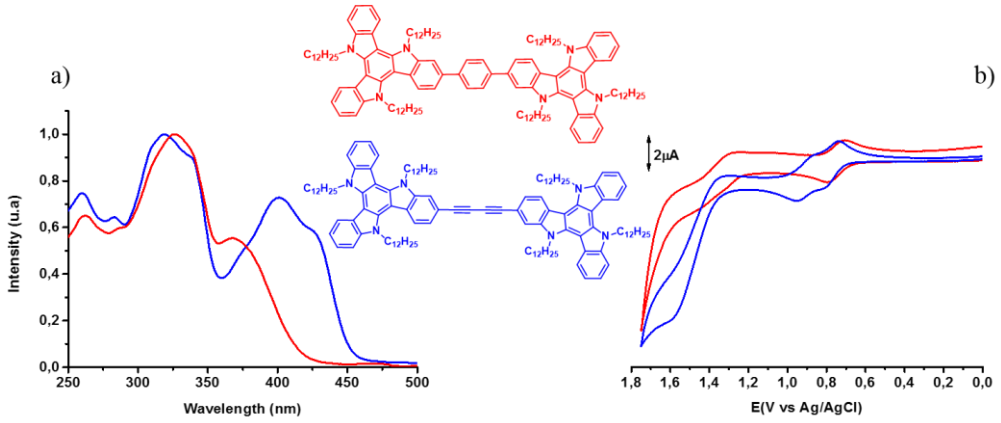

Figure 9: a) UV-vis spectra of the dimers in CH_2Cl_2, c = 5 x 10^{-6} M.; b) CV of dimers at c = 1 x 10^{-3} M recorded at a scan rate 100mV/s in CH_2Cl_2/0.1 M $TBAPF_6$ measured versus Ag/AgCl (3M NaCl).

Finally, considering the good semiconducting properties of this C_3-symmetric cyclotrimer of indole, we have made a study aimed to identify new semiconducting platforms based on this heterocyclic. In particular, in **chapter 5** we have investigated the electronic properties of an asymmetric cyclic dehydrotrimer of indole, as well as a highly strained saddle shaped tetramer of indole (tetraindole) towards their use in charge transport processes. To this purpose, we made a joint experimental and theoretical study that combines absorption and emission spectroscopies, cyclic voltammetry, and spectroelectrochemistry with DFT calculations.

First, we focused in a comparative study between this platform and its symmetrical counterpart. We have found that lowering the symmetry of the platform results in a slightly lower oxidation potential. Cyclic voltammetry and spectroelectrochemistry reveal the reversible nature of the two observable oxidation processes in the alkylated asymmetric triindoles together with an increase in the stability of their oxidized species. Remarkably, the asymmetric platform gives a red-shift of the absorption edge and a higher fluorescence quantum yield, when compared to the symmetrical one (Figure 10*)*.

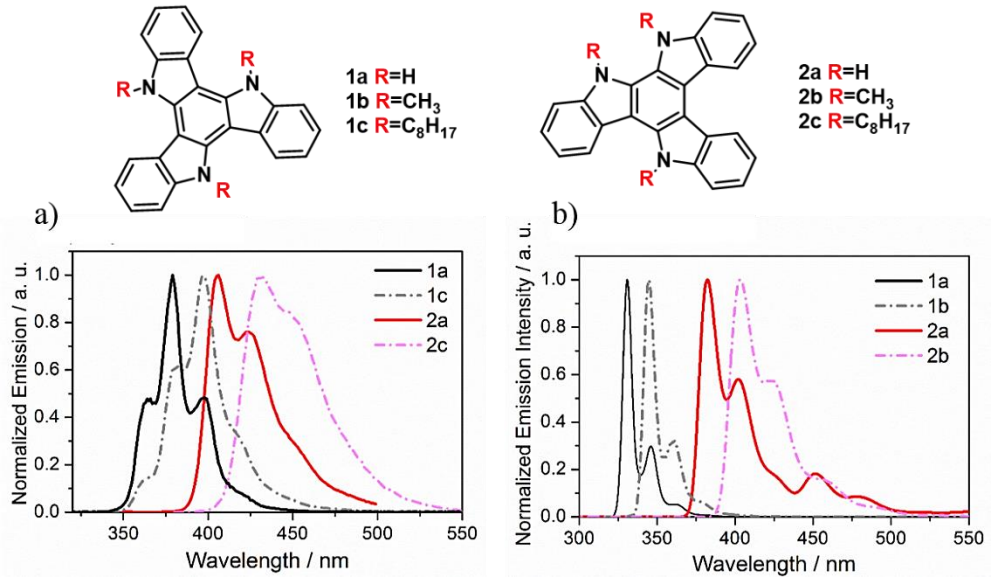

Figure 10 (a) Experimental emission spectra of the symmetric **1a**, **1c** and asymmetric **2a**, **2c** systems in CH_2Cl_2 solutions. (b) Vibronically resolved normalized emission of **1a**, **1b** and **2a**, **2b** systems. The methyl-susbtituted **1b** and **2b** are taken as models for the octyl-substituted **1c** and **2c** systems.

On the other hand, we present a similar study of a cyclic tetramer of indole with the aim of understanding the fundamental electronic properties of this three-dimensional platform and evaluate its potential in the construction of new semiconducting candidates.

Flat π-extended electroactive molecules, with inherent 2D character have a strong tendency to stack into columns forming one dimensional superstructure. However, due to their low dimensionality, these materials present anisotropic charge-transport properties which can pose specific problems for device fabrication and operation. The design of 3D electroactive systems allowing substantial electronic communication among conjugated segments in different directions may represent a potential answer to the problem of charge-transport anisotropy.

The result of this study suggests that cyclic tetraindole allows for a good electron delocalization in spite of its saddle-shaped structure, which can be attributed to a double hyperconjugative effect between the CC and π-orbitals across the twisted C-C bonds of the cyclooctatetraene. In this chapter, we explore the optical and electronic features of cyclic tetraindoles *N*-substituted with alkyl or alkyl aryl group, as a scaffold to arrange electroactive moieties in three dimensions with potential applications in the field of organic electronics.

In summary, our results reveal that asymmetric triindole, and their derivatives, have better photophysical properties than their symmetrical counterparts. On the other hand, we present tetraindole platform as a promising three-dimensional electroactive scaffold in the search of semiconducting systems with enhanced dimensionality of charge transport. We believe that this work may provide guidance for further development of these materials with improved potential for electronic applications.

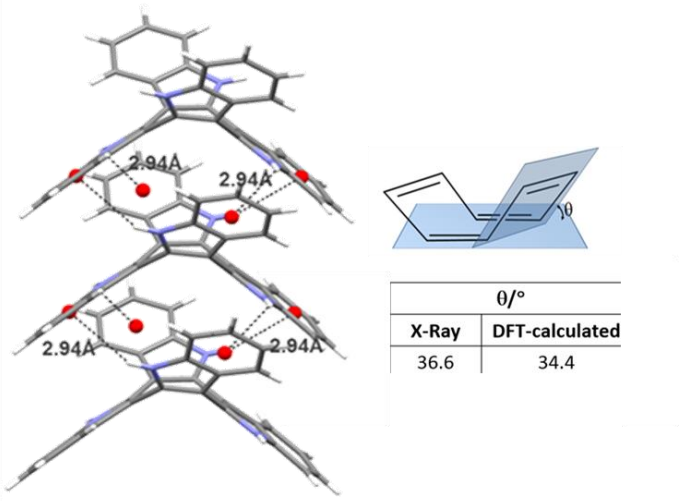

Figure 11: View of the packing of *N*-tetramethyltetraindole and the experimental and theoretical torsion angles.

In this context, my main contribution has been the synthesis of all the new molecules presented, study of their electronic and self-assembling properties, and the

fabrication of Organic Field Effect Transistors. The Field Effect Transistors were fabricated by myself during a stay in the Northwestern University, USA, in the group of Prof. A. Facchetti.

Index

INDEX

Introduction

INTRODUCTION

I.1. DEVELOPMENT OF ORGANIC ELECTRONICS

Organic materials have traditionally been considered as insulators of the electric current. However, this idea changed in 1948, when it was observed that some phthalocyanines crystals exhibited conductor behavior.[1]

Later, photoconductive and electroluminescence properties[2,3] were observed in organic crystals of naphthalene and anthracene. In 1954, Akamatu, Inokuchi and Matsunaga found that a perylene-bromine complex exhibited high paramagnetism and it was reasoned that this behavior was only possible if electrons could move freely in the solid. [4]

With these advances we arrive at 1973, when the first molecular material with metallic conductivity was discovered. The electron-acceptor complex between tetracyano-*p*-quinodimethane and donor tetrathiafulvalene, was a real revolution in this field.[5] These materials were capable of behaving like a metal in a wide range of temperatures.

Soon after, in 1977, the researchers Alan G. Heeger, Alan G. MacDiarmid and Hideki Shiakawa found that the conductivity of polyacetylene could be modulated from an insulating to a conducting behavior and the conductivity could increase, by more than seven orders of magnitude, by doping with electron withdrawing species such as I_2, Br_2 or Cl_2.[6,7] This research group obtained, because of this discovery, the Nobel Prize of Chemistry in 2000.[8]

The interest aroused by π-conjugated polymers, after the discovery that their electrical conductivity increases substantially upon chemical doping, paved the way to the emergence of the field of organic electronics. In only a few years, this area stimulated worldwide interest in the search for large area, flexible, lightweight and cost-effective optoelectronics. Conjugated polymers, usually amorphous materials can be easily

[1] Eley, D. D.; *Nature* **1948**, 162, 819.
[2] Bernanose, A.; *J. Appl. Phys*. **1955,** 6, S54.
[3] Kepler, R. G.; *Phys. Rev.* **1960**, 119, 1226.
[4] Akamatu, H.; Inokuchi, H.; Matsunaga, Y.; *Nature* **1954,** 173, 168-169.
[5] Ferraris, J.; Cowan, D. O.; Walatka, V. V.; Perlstein, J. H.; *J. Am. Chem. Soc.* **1973**, 95, 948.
[6] Shirakawa, H.; Louis, E. J.; MacDiarmid, A. G.; Chiang, C. K.; Heeger, A. J.; *J. Chem. Soc. Chem. Commun.* **1977**, 578.
[7] Shirakawa, J.; Louis, E. J.; Gau, S. C.; MacDiarmid, A. G.; *Phys. Rev. Lett.* **1978**, 40, 1472.
[8] http://www.nobelprize.org/nobel_prizes/chemistry/laureates/2000

processed from solution to yield homogeneous and uniform thin films, ideally suited for optoelectronics. Unfortunately, they pose problems of reproducibility due to variations in molecular weight, and polydispersity, from batch to batch. In spite of the great interest that arose this area, improving the charge transport behavior in polymeric materials was found to be a very difficult task due to the inherent intramolecular disorder of this material.

Low-molecular weight π-conjugated molecules have been identified as attractive targets to substitute the usual polymeric materials in electro-active devices. Although less appealing in terms of processability, they can be reproducibly prepared, functionalized and purified, owing to their monodisperse nature with well-defined chemical structure. In addition, perfectly ordered closely-packed molecules found in single crystals have demonstrated impressive transport properties with several examples already surpassing the performance of amorphous silicium.

I.2. CHARGE TRANSPORT IN ORGANIC ELECTRONICS

Organic electronics has progressed rapidly over the last few years,[9] with devices such as OLEDs already entering the market and the realization of efficient prototypes of organic photovoltaic cells or field-effect transistors. Interest in these devices has steadily increased in both academic and industrial institutions and many other applications are continuously being envisioned such as e-paper or radio frequency identification tags (Figure I.1). The main advantages of using organic materials relates to cost and processability.

Organic materials that are suitably modified are compatible with solution processing techniques, thereby eliminating the need for expensive lithography and vacuum deposition steps necessary for silicon-based materials. Low temperature solution processing also expands the repertoire of tolerant substrates and processing options, allowing flexible plastics, or fabrics to be used in conjunction with methods such as spin coating,[10] stamping,[11] or inkjet printing.[12]

[9] a) Organic Electronics: Materials, Manufacturing and Applications; Klauk, H., *Ed.; Wiley- VCH: Weinheim,* **2006**. b) Organic Electronics: More Materials and Applications; Klauk, H., *Ed.; Wiley- VCH: Weinheim,* **2012**.

[10] a) Garnier, F.; Hajlaoui, R.; Yassar, A.; Srivastava, P. *Science* **1994**, *265*, 1684.b) Sirringhaus, H.; Tessler, N.; Friend, R. H. *Science* **1998**, *280*, 1741

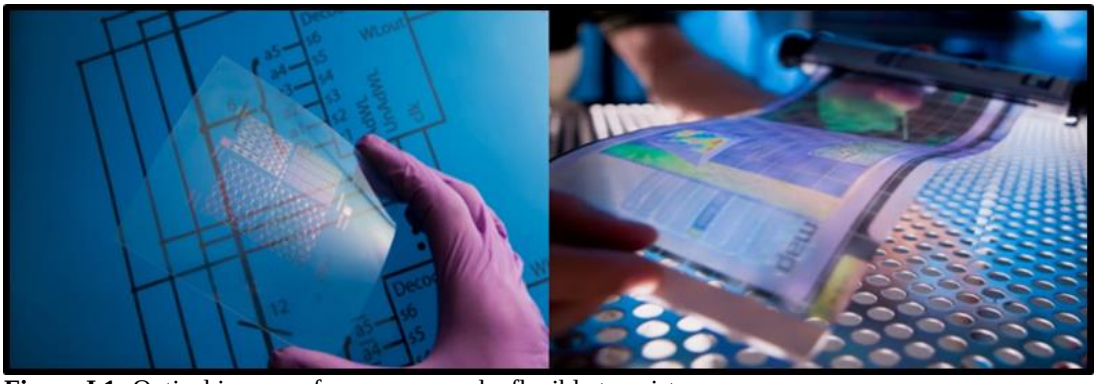

Figure I.1: Optical images of an e-paper and a flexible transistor.

All of these devices involve charge transport as the main process in their operation. The efficiency of charge transport [13] within the organic semiconducting materials, quantified by the charge carrier mobility, plays a key role in the performance of the devices. Charge carrier mobility μ reflects the speed of the holes/ electrons under an electric field according to the relation $v=\mu E$.

For example, in organic light-emitting diodes (OLEDs) good charge transport properties are required to reduce the impact of image effects upon charge injection, to confine light emission into the bulk of the organic layers, and to limit exciton-polaron quenching processes occurring at high polaron concentrations. In organic solar cells, high charge carrier mobilities are required to facilitate the dissociation of the generated electron–hole pairs in their hot state (i.e., prior to their full nuclear and electronic relaxation) and to limit the efficiency of recombination of the generated free carriers along the way to the electrodes. In organic field-effect transistors (OFETs), optimal mobility values are desirable to yield short switching times between on and off states and, by extension, to build organic-based electronic circuits with high-frequency operation.

Great advances in this area have been connected to the continuous increase in the charge mobility in the semiconducting materials, which has reached values already surpassing that of amorphous silicium currently employed in commercial flat-panel displays (~1 $cm^2V^{-1}s^{-1}$). While these mobility values are already acceptable for many of the intended applications, the use of organic molecules in the fabrication of devices still

---

[11] a) Rogers, J. A.; Bao, Z.; Meier, M.; Dodabalapur, A.; Schueller, O. J. A.; Whitesides, G. M. *Synth. Met.* **2000**, *115*, 5.b) Rogers, J. A.; Bao, Z.; Baldwin, K.; Dodabalapur, A.; Crone, B.; Raju, V. R.; Kuck, V.; Katz, H.; Amundson, K.; Ewing, J.; Drzaic, P. *Proc. Natl. Acad. Sci. U.S.A.* **2001**, *98*, 4835.

[12] a) Sirringhaus, H.; Kawase, T.; Friend, R. H.; Shimoda, T.; Inbasekaran, M.; Wu, W.; Woo, E. P. *Science* **2000**, *290*, 2123.b) Speakman, S. P.; Rozenburg, G. G.; Clay, K. J.; Milne, W. I.; Ille, A.; Gardner, I. A.; Bresler, E.; Steinke, J. H. G. *Org. Electron.* **2001**, *2*, 65.

[13] Coropceanu, V.; Cornil, J.; da Silva-Filho, D. A.; Olivier, Y.; Silbey, R.; Brédas, J. L. *Chem. Rev*. **2007**, 107, 926.

suffers from serious limitations mostly derived from problems of stability and processability. There is still a clear need of efficient candidates that meet the requirements necessary for the high throughput development of devices.

In classical inorganic semiconductors such as silicon, atoms are held together with strong covalent or ionic bonds forming a highly crystalline three-dimensional solid. Therefore, strong interactions of the overlapping atomic orbitals cause charge transport to occur in highly delocalized bands. Electrical conductivity in these systems will be determined by the susceptibility of electrons to excitation from the valence band to conduction band.

In contrast, organic semiconductors are composed by molecules usually containing a π-extended aromatic system with highly mobile delocalized electrons, whose electronic properties are determined by the highest occupied molecular orbital (HOMO) and the lowest unoccupied molecular orbital (LUMO). The energy of the HOMO and LUMO levels represent the ionization potential and electron affinity respectively, and therefore characterize the material ability to donate and accept electrons. In this sense, the HOMO level is to organic semiconductors what the valence band maximum is to inorganic semiconductors, and the same analogy exists between the LUMO level and the conduction band minimum (Figure I.2).

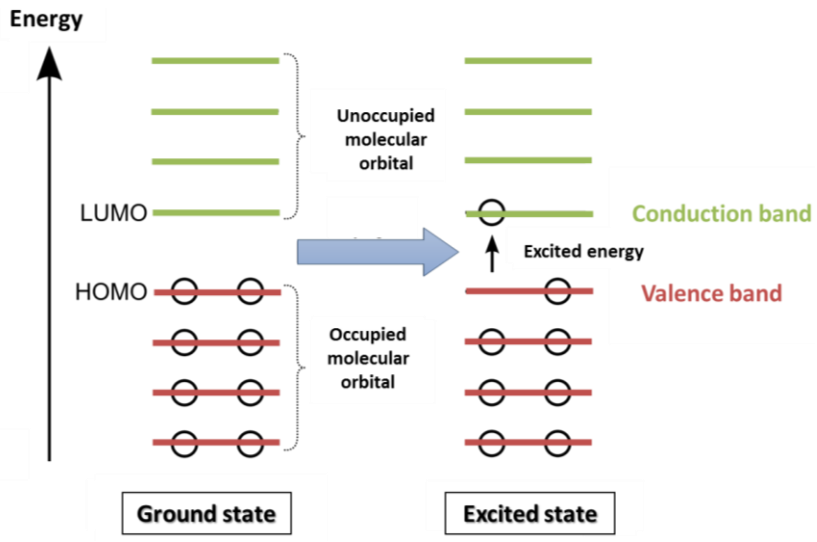

Figure I.2: Schematic representation of the HOMO and LUMO bands.

Organic semiconductors are commonly classified as either p-type (hole-conducting) or n-type (electron-conducting) depending on which type of charge carrier is more efficiently transported through the material. In theory, all organic semiconductors

should be able to conduct both, holes and electrons, but the differences in work function of the electrodes relative to the HOMO and LUMO energies of the material will determine the type of charge carriers that can be injected.[14] Nevertheless, there are far fewer accounts of n-type than p-type organic semiconductors primarily due to the inherent instability of organic anions in the presence of air and water, and problems with oxygen trapping within these materials. P-type organic semiconductors typically have HOMO levels between −4.9 and −5.5 eV, resulting in ohmic contact with high work-function metals such as gold (5.1 eV) and platinum (5.6 eV). N-type materials typically have LUMO levels between −3 and −4 eV, and should have better contact with low work-function metals such as calcium and lithium, but these metals are highly reactive and degrade rapidly with air exposure.

Transport models have been proposed to rely mostly on charge hopping which would operate in amorphous and polymeric materials, and on a band-like transport that would work in highly purified single crystals. In the charge hopping regime, polarons jump from one localized site to the next one, and can be thought of as an electron transfer between a charged and an adjacent neutral units (Figure I.3).

Figure I.3: Hopping model.

On the other hand, in an ideal system when conjugated organic molecules crystallize into an ordered lattice, the individual HOMO and LUMO energy levels would blend forming bands analogous to the conduction and valence bands in inorganic materials. This band-like transport would operate in defect-free single crystalline semiconductors (Figure I.4).

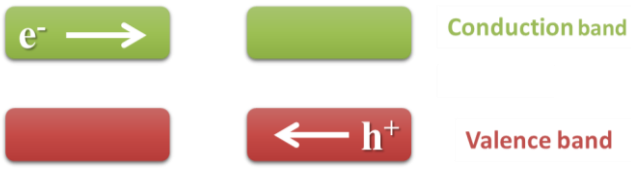

Figure I.4: Band transport model.

[14] a) Schmidt, R.; Ling, M. M.; Oh, J. H.; Winkler, M.; Könemann, M.; Bao, Z. N.; Würthner, F.; *Adv. Mater*. **2007**, 19, 3692. b) Schmidt, R.; Oh, J. H.; Sun, Y. S.; Deppish, M.; Krause, A. M.; Radacki, K.; Braunschweig, H.; Könemann, M.; Erk, P.; Bao, Z.; Wüthner, F.; *J. Am. Chem. Soc*. **2009**, 131, 6215. c) Salman, S.; Ruiz-Delgado, M. C.; Coropceanu, V.; Brédas, J. L.; *Chem. Mater*. **2009**, 21, 3593.

Nevertheless, single crystalline semiconductors are usually affected by dynamic disorder caused by nuclear motions while high mobility polymeric semiconductors present large crystalline domains, making neither an idealized band nor a hopping model applicable. [15] Models bridging between two limiting behaviors have been proposed, however at this stage the exact mechanisms of charge injection and transport in organic semiconductors are still heavily debated.

I.3. MODELING ELECTRICAL PROPERTIES

Independently of the type of model transport considered, the magnitude of the electronic coupling (transfer integral), that expresses the ease of migration charge between two adjacent molecules play a key role in the understanding of charge transport properties. This magnitude depends on the relative arrangement of neighboring molecules in the bulk material. In single crystals its value can be approximated as nearest-neighbor contributions, as the electronic couplings fall off rapidly with the distance.

In charge-carrier hopping processes, the transport mechanism between neighbouring molecules can be formulated as a hole (electron) transfer by the equation:

$$M + M^+ \rightarrow M^+ + M$$

where M and M^+ play the role of electron donor and electron acceptor molecules, respectively.

The charge-transfer rate, k_t, can be approximated by the Marcus electron-transfer theory [16] with the equation:

$$k_t = \frac{4\pi^2}{h}\frac{1}{\sqrt{4\pi K_B T}}t^2 \exp\left(-\frac{\lambda}{4K_B T}\right)$$

where h and K_B are Planck's and Boltzmann´s constants, T is the temperature, t is the electronic transfer integral between the donor and acceptor molecules, and λ is the reorganization energy for hole (electron) transfer between both molecules.

[15] McMahon, D. P.; Troisi, A. *Chem. Phys. Chem.* **2010**, 11, 2067.
[16] a) Marcus, R. A.; *Rev. Mod. Phys*. **1993**, 65, 599.b) da Silva-Filho, D. A.; Kim, E. -G.; Brédas, J. -L. *Adv. Mater*. **2005**, 17, 1073.

Therefore the transport process is determined by two important molecular parameters: the internal reorganization energy (λ), which needs to be small for an efficient charge transport and the intermolecular hole (electron) and transfer integral (t), which describes the strength of the electronic coupling between adjacent molecules.

The reorganization energy for hole transfer, λ, is the sum of two contributions, $\lambda_1 + \lambda_2$, that are defined as:

$$\lambda_1 = E_0(M^+) - E_0(M)$$

$$\lambda_2 = E_1(M) - E_1(M^+)$$

where $E_0(R)$ represents the ground-state energy for the nuclei configuration R in the neutral state, and $E_1(R)$ denotes the ground-state energy for configuration R in the charged state. M and M^+ refer here to the equilibrium molecular configurations for the neutral and charged states, respectively.

The hopping integral for intermolecular hole transfer, t, can be estimated from the energy splitting between the electronic level HOMO, e_H, and the HOMO-1, e_{H-1}, taken from the closed-shell configuration of the neutral state of a dimer M_2 by the relation:

$$t = \frac{e_H - e_{H-1}}{2}$$

The value of the transfer integral t depends strongly on the molecular configuration of the dimer.

By considering the expression for the diffusion coefficient associated to a one-dimensional jumping process:

$$D = k_t d_L^2$$

the hole (electron) mobility, μ, can then be obtained from the following expression :

$$\mu = e\, D/K_B\, T$$

where e is the electron charge.

I.4. METHODS FOR ESTIMATING HOMO AND LUMO LEVELS OF ORGANIC SEMICONDUCTORS

The hole or electron transport behavior of molecule-based systems is determined mostly by the intrinsic redox properties of their constituent electroactive molecules.

As previously mentioned for organic semiconductors, the HOMO level represents the energy required to extract an electron from a molecule, which is an oxidation process,

and the LUMO represents the energy necessary to inject an electron to a molecule, thus implying a reduction process. With this in mind, the energy of the frontier orbitals can be estimated by cyclic voltammetry (CV) by measuring the first redox potentials E_{red} and E_{ox} with respect to the ferrocene/ferrocenium redox couple and considering a value of - 4.8 eV for Fc with respect to zero vacuum level (Figure I.5).[17]

$$E\ (HOMO) = -\ [E_{ox} + 4.8]\ eV$$
$$E\ (LUMO) = -\ [E_{red} + 4.8]\ eV$$

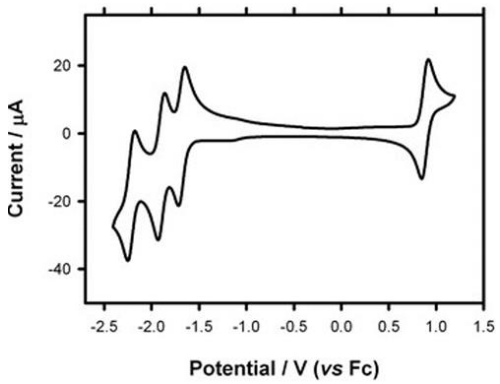

Figure I.5: CV of an organic molecule showing the oxidation and reduction process.

The energy difference between these two frontier orbitals, HOMO and LUMO, is known as the *bandgap* (E_g). This is a useful parameter to quantify the properties of organic semiconductors, and can be estimated by UV-Vis spectroscopy by assuming that the first electronic transition from the ground state S_0 to the first excited state S_1, corresponds to the promotion of an electron from the HOMO to the LUMO level of the excited material. This approach assigns the value of the HOMO-LUMO transition to the lowest energy transition up taking place upon absorption of a photon.

The longest absorption wavelength λ_{onset} is used to calculate the optical gap energy, E_g, according to the equation:

$$E_g = \frac{1240}{\lambda_{onset}(nm)}$$

By combining these two methods, we can estimate the value of the frontier levels for an organic semiconductor molecule.

[17]This estimate is calculated on the basis of a rather crude approximation neglecting solvent effects using the standard electrode potential (E^o) for the normal hydrogen electrode (NHE) at about -4,6 eV on the zero vacuum level scale and a value of 0.2 V *vs*. NHE.a) Liu, Y.; Liu, M. S.; Li, X.-C.; Jen, A. K. -Y.; *Chem. Matter*. **1998**, 10, 3301. b) A. J. Bard, L.R. Faulkner, Electrochemical Methods-Fundamentals and Applications, Wiley, New York, p 634. c) Pommerehne, J.; Vestwebwe, H.; Guss, W.; Mahrt, R. F.; Bässler, H.; Porsxh, M.; Daub, *J. Adv. Mater*. **1995**, 7, 551.

I.5. EXPERIMENTAL MEASUREMENTS OF CARRIER MOBILITIES

There is a rich variety of methods which can be used to measure charge mobility in molecular semiconductors[18] including time-of-flight (TOF), time-resolved microwave conductivity (TRMC), space charge limited current (SCLC), the hall effect or field-effect transistor (FET) measurements. However, comparison among mobility values obtained from different experimental measurements should be made with care since they depend strongly upon the measurement technique employed. In SCLC devices, charge transport is typically measured perpendicular to the substrate, while OFET devices measure mobility parallel to the substrate.

On the other hand field effect transistor measurements probes the mobility at high charge carrier densities, while space charge limited current measurements technique requires a strict condition of an ohmic contact at one of the electrode/organic interfaces, (otherwise the extracted mobility is physically meaningless and will be underestimated), and time-resolved microwave conductivity probes the most mobile fraction of charges and therefore it usually overestimates the mobility values. All these differences accounts for many of the disagreements found in the literature.

In this thesis we have extracted mobility values of the new materials synthesized by using both SCLC and OFETS. Therefore these methods will be explained with more detail.

- **SCLC measurement**

In such measurements, substances are confined between two electrodes, with one of them injecting charges of a given sign (ohmic contact) while the other one should be non-injecting for charges of the opposite sign, show Figure I.6. This method is based on the assumption that the injection contact is ohmic and therefore it requires a good alignment between the energy levels of the materials and the electrode.

The choice of the electrodes is generally made in such a way that only electrons or holes are injected at low voltage. In the absence of traps and at low electric fields, the current density *J* scales quadratically with applied bias *V*. Such behavior is characteristic

[18] Karl, N. *Synth. Met.* **2003**, 133, 649.

of a space-charge limited current (SCLC); it corresponds to the current obtained when the number of injected charges reaches a maximum because their electrostatic potential prevents the injection of additional charges.[19] In that instance, the current depends only on the carrier mobility, assuming contacts to be ohmic and the material to be trap free.[20] In this regime, when neglecting diffusion contributions, the *J-V* characteristics can be expressed as the Mott-Gurney equation:

$$J = \frac{9}{8} \epsilon_o \epsilon_r \, \mu \frac{V^2}{L^3}$$

where ϵ_r denotes the dielectric constant of the medium and L is the device thickness. Note that a field-dependence of the mobility has to be considered at high electric fields. The *J-V* curves become more complex in the presence of traps. They first exhibit a linear regime, where transport is injection-limited, followed by a sudden increase for an intermediate range of applied biases. Finally, the V^2 dependence of the trap-free SCLC regime is reached (Figure I.6). The extent of the intermediate region is governed by the spatial and energetic distribution of trap states,[21] which is generally modeled by a Gaussian[22] or exponential distribution.[23] Since all the other parameters in the equation are measurable, charge mobility can be easily obtained.

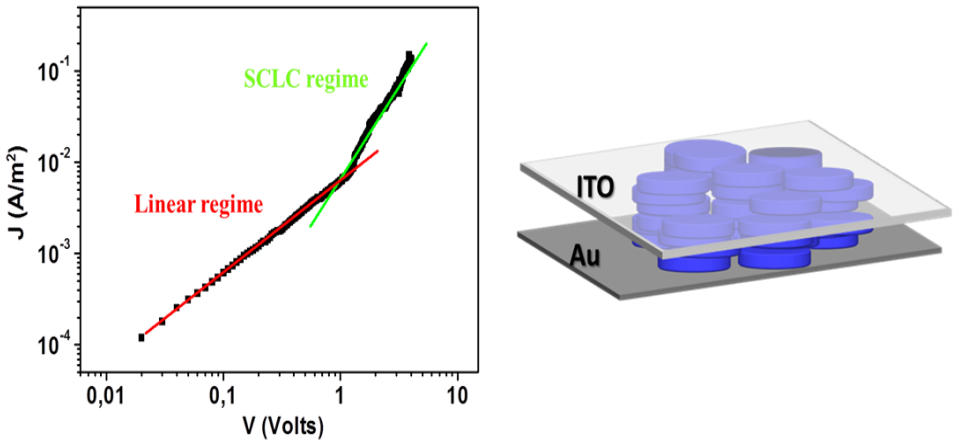

Figure I.6: Current/Applied voltage curve. In order to appreciate the quality of the data, two continuous lines with slopes 1 and 2 have been included, representing ideal linear and quadratic regimes of the current as a function of applied voltage.

[19] Blom, P. W. M.; de Jong, M. J. M.; Vleggaar, J. J. M. *Appl. Phys. Lett.* **1996**, *68*, 3308.
[20] Fichou, D. *Handbook of Oligo- and Polythiophenes*; Wiley-VCH: Weinheim: New York, **1999**.
[21] Podzorov, V.; Sysoev, S. E.; Loginova, E.; Pudalov, V. M.; Gershenson, M. E. *Appl. Phys. Lett.* **2003**, *83*, 3504.
[22] Bassler, H. *Phys. Status Solidi B* **1993**, *175*, 15.
[23] Horowitz, G.; Hajlaoui, M. E.; Hajlaoui, R. *J. Appl. Phys.* **2000**, *87*, 4456.

The SCLC technique is sensitive not only to the charge injection effectiveness at the electrodes but also to orientation order defects, for this reason it should be considered as a lower limit for the charge–carrier mobility.

- **Field-Effect Transistor Configuration**

A field-effect transistor (organic or inorganic) requires the following components (shown in Figure I.7): a thin semiconducting layer, which is separated from a gate electrode by the insulating gate dielectric and source and drain electrodes of width *W* (channel width) separated by a distance *L* (channel length) that are in contact with the semiconducting layer. The semiconducting layer in the case of an organic FET is usually vacuum sublimed, spin-coated, or drop-cast depending on the semiconductor. The gate electrode can be a metal or a conducting polymer, but very often, highly doped silicon serves as substrate and gate electrode at once (oxidation of the silicon surface forms an insulating SiO_2 layer, usually with thicknesses of ~100-300 nm).

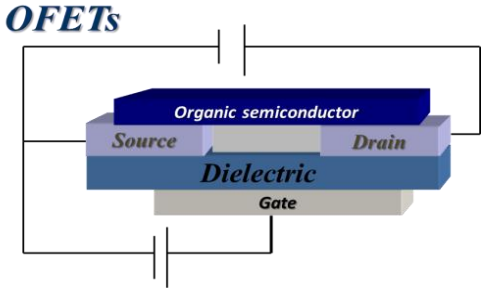

Figure I.7. Structure of OFET device.

Devices can be constructed in either top or bottom contact geometry, each with their own advantages. In top contact geometry (Figure I.8), the organic film is deposited on a uniform dielectric surface, and then the source and drain electrodes are deposited on top by metal evaporation through a shadow mask. In this device geometry, contact resistance is usually minimal due to intimate contact between the semiconductor and the electrodes, and the charge mobilities tend to be higher.

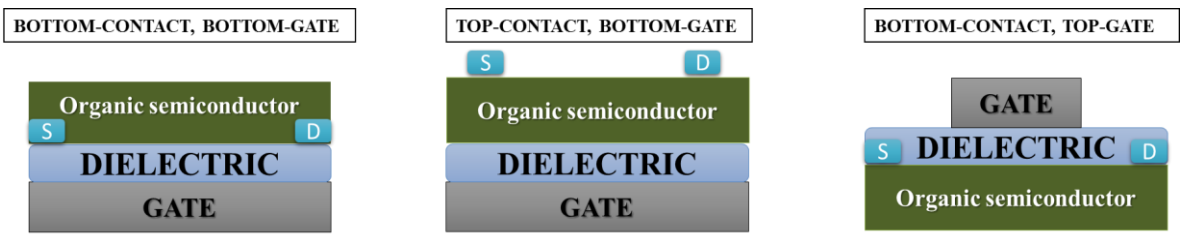

Figure I.8. Three popular organic-transistor geometries. From left to right: bottom contacts, bottom gate; top contacts, bottom gate; t bottom contacts, top gate. S: source; D: drain.

The role of the source and drain electrodes is to inject and retrieve charge carriers to and from the semiconductor. The organic semiconductors should be a near-zero current between the source and drain when there is no voltage applied to the gate electrode. Applying a voltage between the source and the gate results in charging the capacitor, which in turn modulates the current between the source and drain.

The origin of the gate-induced charging (also known as the "field effect") is clarified in the simplified electronic energy level diagrams shown in Figure I.9. This field causes a shift in the HOMO and LUMO energy levels in the organic semiconductor. Depending on the work function of the electrodes relative to the HOMO/LUMO levels, electrons will either flow out of the HOMO into the electrodes (leaving behind holes) or flow from the electrodes into the LUMO, forming a conducting channel between the source and drain. Current can then be driven through the device by applying a voltage between the source and drain. The quality of the interface between the dielectric and the semiconductor is a crucial parameter, because it has been shown that the majority of charge carriers are generated in the first one to two monolayers of semiconductor nearest to the dielectric surface.[24]

When the gate voltage V_G goes beyond a given threshold V_T, an equal amount of charge, but opposite in sign, appears at both sides of the dielectric, which results in the formation of the conducting channel. The sign of the gate voltage is opposite to that of the charges in the conducting channel, that is, positive for an n-channel and negative for a p-channel. The advent of a threshold voltage has several origins. One of them is the presence of shallow traps in the semiconductor that need to be filled before mobile charge can be induced in the channel.[25] Another one is a result of charged states or dipoles at the dielectric surface: depending on the sign of these charges, accumulation of charges in the channel may be already present when $V_G=0$ (negative threshold), or an additional gate voltage is necessary to induce the formation of the channel (positive threshold).[26]

[24] a) Dinelli, F.; Murgia, M.; Levy, P.; Cavallini, M.; Biscarini, F.; De Leeuw, D. M. *Phys. Re*v. *Lett.* **2004**, 92, 116802.b) Dodabalapur, A.; Torsi, L.; Katz, H. E. *Science* **1995**, 268, 270.
[25] Horowitz, G.; Hajlaoui, R.; Bouchriha, H.; Bourguiga, R.; Hajlaoui, M.; *Adv. Mater*. **1998**, 10, 923.
[26] Pernstich, K. P.; Haas, S.; Oberhoff, D.; Goldmann, C.; Gundlach, D. J.; Batlogg, B.; Rashid, A. N.; Schitter, G.; *J. Appl. Phys*. **2004**, 96, 6431.

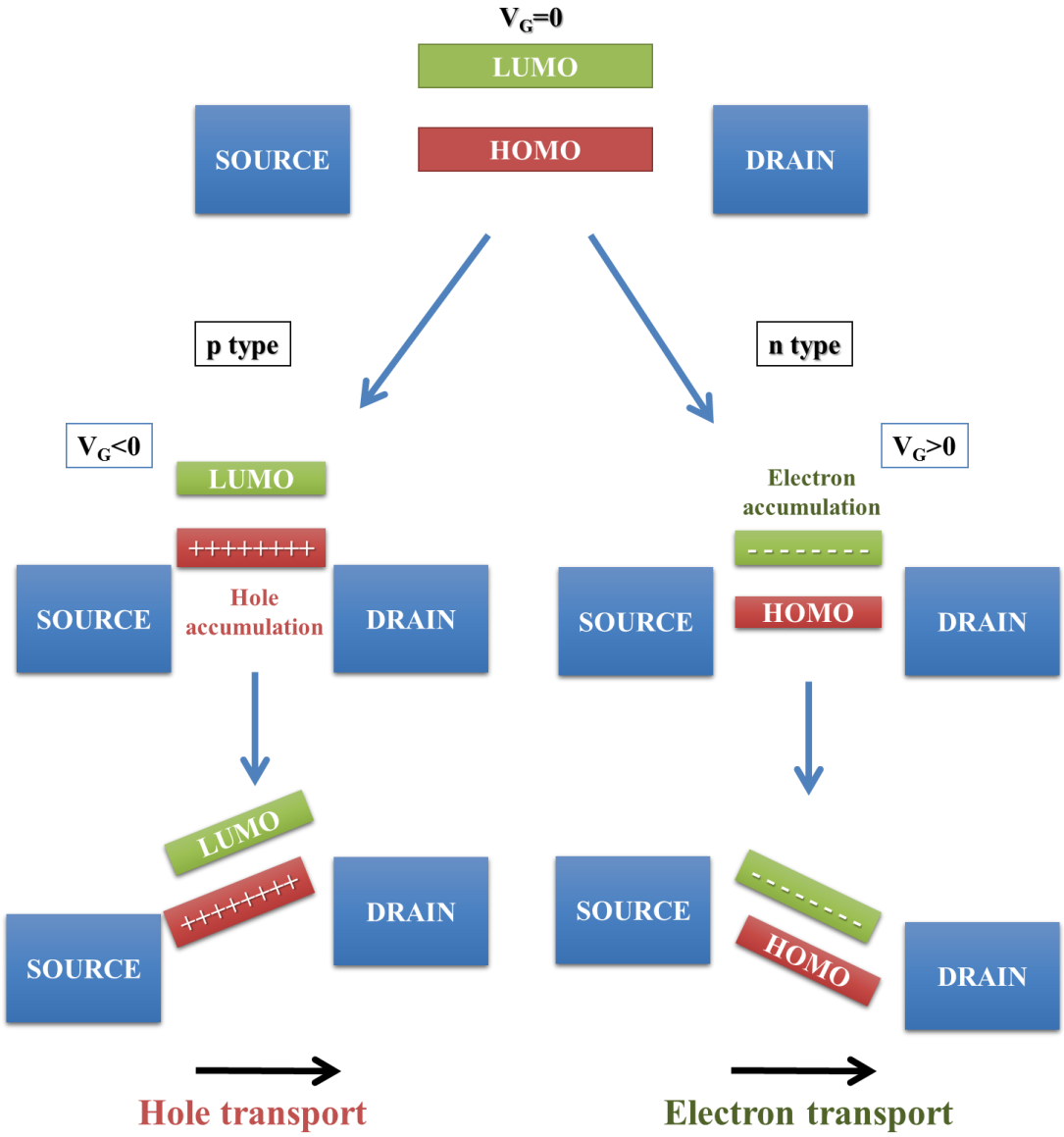

Figure I.9. Idealized energy level diagram of an OFET at V_G = 0 and V_D = 0. Demonstrate the principle of field effect transistor operation for the case of electron and hole accumulation transport.

As long as $V_D > V_G$, a charge is present all along the channel and the drain current I_D grows linearly with V_D. When the drain current increases up to $V_G - V_T$, the potential at a point of the channel close to the drain electrode falls to zero, and so does the charge in the channel, which means that the channel is pinched off. At this point, the drain current saturates. A further increase of V_D induces a slight extension of the region void of charges around the drain, but no significant increase of the current. Equations (1) and (2) give the drain current in the linear and saturation regimes, respectively:

$$I_D = \frac{W}{2L} C_i \mu (V_G - V_{TH}) V_D \qquad V_D < V_G - V_T \qquad (1)$$

$$I_D = \frac{W}{2L} C_i \mu (V_G - V_{TH})^2 \qquad V_D > V_G - V_T \qquad (2)$$

Equations (1) and (2) are the premise of the two most popular methods for mobility extraction. The principle of the method can be illustrated by rewriting Equation (2) as:

$$\sqrt{I_D} = \sqrt{\frac{W}{2L}} C_i \mu (V_G - V_T) \qquad (3)$$

Equation (3) predicts that plotting the square root of the saturation current against gate voltage would result in a straight line. The mobility is obtained from the slope of the line, while the threshold voltage corresponds to the extrapolation of the line to zero current. The charge mobility is the average drift velocity per unit electric field and can be calculated in the saturation regime using equation 3, where W = channel width, L =channel length, C_i = capacitance of the insulator, μ = field-effect mobility, V_G = gate voltage, and V_T = threshold voltage.

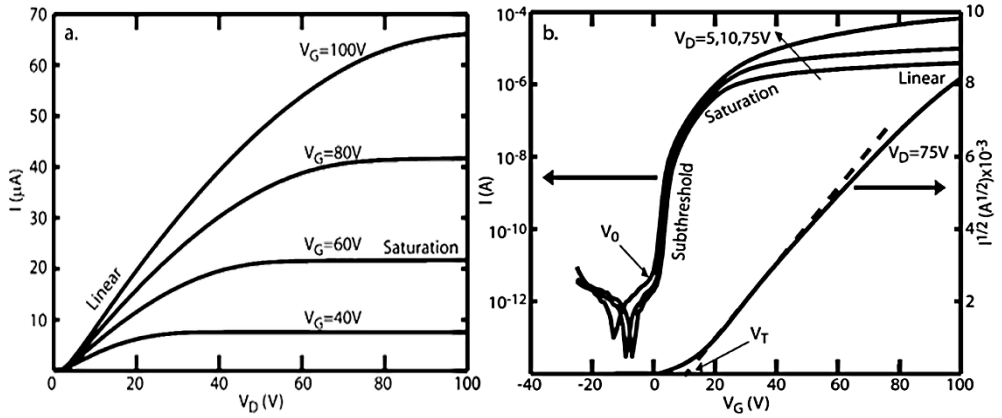

Figure I.10: a) Example I_D-V_D curves for OFET for various values of V_G. b) Example I_D-V_G curves plotted on semilogarithmic axes for the same device for various values of V_D. The $I_{1/2}$ vs V_G curve for V_D = 75 V is shown on the right hand axis.

OFETs are typically characterized in one of two ways, either by holding V_G constant and sweeping V_D (commonly referred to as I_D-V_D or output curves; see Figure I.10a) or by holding V_D constant and sweeping V_G (commonly referred to as I_D-V_G or transfer curves; see Figure I.10b). If contact effects and trapping are not too problematic, these traces can be modeled quantitatively using *I-V* relationships derived from Ohm's law.

The most critical properties of an organic semiconductor are the charge mobility, μ, and I_{on}/I_{off} ratio that can be defined as the ratio of current flow between the source and drain when there is no gate bias and the current flow at maximum gate bias. However,

this value is highly dependent on the voltages used, the device geometry, and the dielectric material.

I.6. ORGANIC SEMICONDUCTORS AND SUPRAMOLECULAR ORDER

As previously mentioned, the electronic coupling and the transfer integral are highly sensitive to the relative positions of interacting units and therefore the efficiency of charge transport is closely related to the extent of molecular order in the bulk material. But supramolecular organization may compromise the processability of organic semiconductors. Thus, while perfectly ordered, closely-packed molecules found in single crystals have demonstrated impressive high mobilities, these materials are fragile and brittle and difficult to process. In contrast, amorphous and solution processable polymeric semiconductors meet the manufacturing requirements for low-cost electronics, but in these materials mobilities are low due to their inherent disorder. In that context, an intermediate situation can be found in liquid crystals, soft and self-organized states of matter, characterized by a dynamism that facilitates processing of the materials, while maintaining a significant supramolecular order.

At this stage, it is clear that supramolecular order, processing and performance are directly influenced by each other. Nowadays, the critical trade-off between performance and processability has not yet been successfully accomplished, however continuous improvements in charge mobilities are being reported through the development of new semiconductors and optimization of materials processing.

In this section the advantages and drawbacks of the different types of materials, classified according to their supramolecular order are presented with the final goal to lead to a better understanding of the factors which affect the mobility.

- **Crystalline semiconductors**

Highest mobilities so far have been found on ordered crystalline materials with molecular packing and crystallinity having a critical influence in their performance. A clear example is found in pentacene **1** (Figure I.11), the prototype of high mobility system

that presents mobilities over 1 $cm^2V^{-1}s^{-1}$ when measurements are performed on well-oriented crystalline films[27] but is practically insulating in amorphous films.[28]

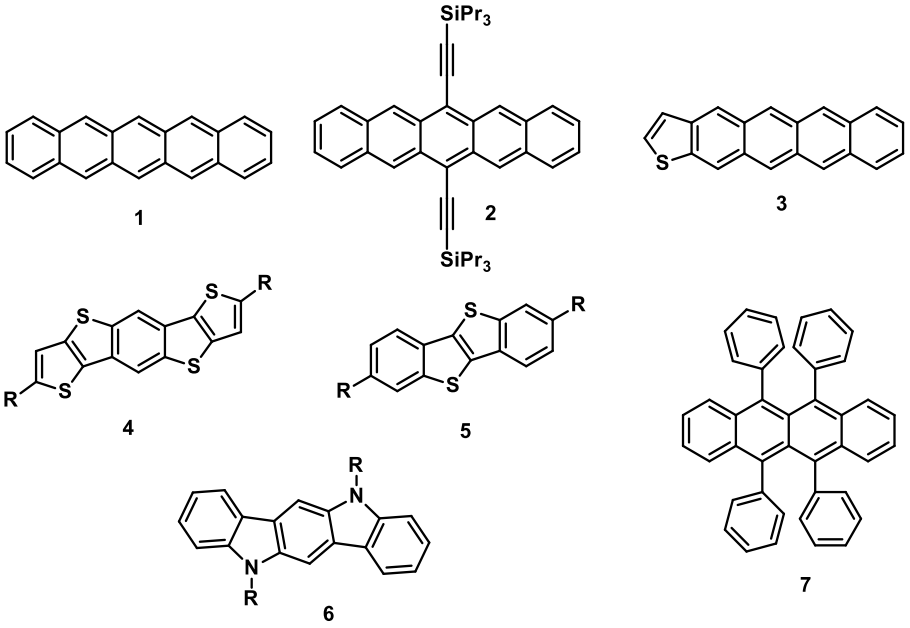

Figure I.11. Chemical structure of different acenes and heteroacenes.

In spite of being probably the most studied organic semiconductor, pentacene has major drawbacks that prevent its practical applications, such as instability in air and low solubility in organic solvents. This is a common problem found in organic semiconductors that, on the other hand, tend to self-organize into well-ordered polycrystalline thin films upon thermal vacuum evaporation. Thin film devices based on crystalline materials are mostly prepared by vaporization of the semiconductors and condensation onto the desired substrate. Molecular ordering, crystallinity degree, grain size, film morphology or orientation of crystalline domains are critical to determine mobility and have to be tuned by optimizing different parameters such as the deposition rate, substrate temperature, etc. In addition, the need of an evaporation step eliminates much of the advantages of organic electronics that promise the fabrication of devices by using simple printing techniques.

Many efforts in the field have been focused on finding organic semiconductors with better solubility and higher stability. A particularly successful example, is

[27] Podzorov, V.; Menard, E.; Borissov, A.; Kiryukhin, V.; Rogers, J. A.; Gershenson, M. E.; *Phys. Rev. Lett*. **2004**, 93, 086602.
[28] Dimitrakopoulos, C. D.; Malenfant, P. R. L.; *Adv. Mater*. **2002**, 14, 99.

triisopropylsilylethynyl pentacene (TIPS) **2** (Figure I.11) developed by Anthony *et al.*[29] In addition to providing a high degree of solubility in common organic solvents, the functionalization of pentacene at the central ring protects the molecules from oxidation and is beneficial for the molecular packing in the solid state by forcing molecules in a stacked arrangement favoring π-π interactions.

The search of organic semiconductors with superior properties has also involved skeletal modification of acenes. For example, the replacement of the benzene rings of pentacene by thiophene rings **3**-**5** enhances the air stability which has been ascribed to the lowering of the HOMO level.[30] Benzene rings of pentacene have also been replaced by pyrrole rings like in indolocarbazole **6**. The advantage of this approach is the chemical versatility that offers the presence of Nitrogen atoms in the aromatic core to further tune electronic properties, solubility or crystalline packing through *N*-functionalization.[31]

Among heteroacenes, special attention must be paid to diacene-fused [1]benzothieno[3,2-*b*]-thiophenes **5** first introduced by Takimiya *et al.*[32] Attachment of long alkyl chains in positions 2 and 7, led to soluble compounds that show good air stability. In these materials, more polarizable sulfur promote enhanced intermolecular overlap and electronic dimensionality, resulting in mobilities over 1 $cm^2V^{-1}s^{-1}$ by simple spin coating and annealing.[33] This value could subsequently be considerably enhanced in different derivatives by optimization of processing conditions, confirming the benefits of this structural motif in the construction of high mobility semiconductors.

The availability of soluble semiconductors allows the use of solution processes that involves coating of a solution of the semiconductor on a substrate (by spin-coating, drop casting, printing…) followed by evaporation of the solvent, while molecules initially independently dispersed in the solvent self-organize in crystalline domains. Like evaporation techniques, solution processes usually leads to polycrystalline thin films, with microstructure characteristics that has to be carefully tuned for each device by varying parameters such as concentration, solvent, temperature or evaporation rate.

---

[29] Anthony, J. E.; Brooks, J. S.; Eaton, D. L.; Parkin, S. R. *J. Am. Chem. Soc.* **2001**, 123, 9482.
[30] a) Gao, P.; Beckmann, D.; Tsao, H. N.; Feng, X.; Enkelmann, V.; Baumgarten, M.; Pisula, W; Müllen, K. *Adv. Mater*. **2009**, 21, 213. b) Tang, M. L.; Okamoto, T.; Bao, Z. *J. Am. Chem. Soc*. **2006**, 128, 16002.
[31] Boudreault, P. -L. T.; Wakim, S.; Blouin, N.; Simard, M.; Tessier, C.; Tao, Y.; Leclerc, *J. Am. Chem. Soc*. **2007**, 129, 9125.
[32] Takimiya, K.; Sakamoto, H. K.; Izawa, T.; Otsubo, T.; Kunugi, Y. *J. Am. Chem. Soc*. **2006**, 128, 12604.
[33] Ebata, H.; Izawa, T.; Miyazaki, E.; Takimiya, K.; Ikeda, M.; Kuwabara, H.; Yui, T. *J. Am. Chem. Soc.* **2007**, 129, 15732.

Molecular disorder and barrier-like grain-boundaries in both solution and vapor processed polycrystalline thin films can localize and trap the charge carriers[34] and are major obstacles to achieve high charge carrier mobilities. These problems are not present in single crystals characterized by an enhanced extent of molecular ordering. In particular, rubrene **7** single crystals showed mobilities above 20 $cm^2V^{-1}s^{-1}$.[35] Charge transport in rubrene has been found to be highly anisotropic. By identification of crystal axes, it has been possible to assess that highest mobility occurs along the direction of strongest electronic coupling in which molecules organize in a shifted coaxial arrangement.[36]

After pioneer work in the study of the mobility anisotropy found on rubrene, many single crystalline semiconductors have been investigated in order to rationalize performance in terms of favorable crystallographic packing essential to design new promising materials.[37, 38] Recently, it has been reported 2,6-diphenylanthracene may show mobility values up to 34 $cm^2 V^{-1} s^{-1}$ depending on the direction of measurements. Remarkably this material also exhibits high emission fluorescence. This observation hold a great promise in the search of semiconductors for optoelectronics as the dense packing necessary to achieve efficient transport usually produce flueorescec aggregation induced quenching.[39]

Face-to-face π-stacking motifs (Figure I.12a) are proposed to be more efficient for charge transport than commonly found edge-to face herringbone packing structures (Figure I.12b) as a result of enhanced π-π overlap and in consequence an increased electronic coupling between neighboring molecules within the stacks. Brick-wall (Figure I.12c) arrangements are also very promising to achieve high mobility structures by increasing the dimensionality of charge transport and rendering the systems less sensitive to charge-traps.[40]

[34] Kaake, L. G.; Barbara, P. F.; Zhu, X.-Y. *J. Phys. Chem. Lett*. **2010**, 1, 628.
[35] Sundar, V. C.; Zaumseil, J.; Podzorov, J. V.; Menard, E.; Willett, R. L.; Someya, T.; Gershenson, M. E.; Rogers, J. A. *Science* **2004**, 303, 1644.
[36] da Silva-Filho, D. A.; Kim, E. -G.; Brédas, J. -L. *Adv. Mater*. **2005**, 17, 1073.
[37] Mas-Torrent, M.; Masirek, S.; Hadley, P.; Crivillers, N.; Oxtoby, N. S.; Reuter, P.; Veciana, J.; Rovira, C.; Tracz, A.; *Organic Electronics* **2008**, 9, 143.
[38] Brillante, A.; Bilotti, I.; Guido Della Valle, R.; Venuti, E.; Milita, S.; Dionigi, C.; Borgatti, F.; Lazar, A. N.; Biscarini, F.; Mas-Torrent, M.; Oxtoby, N. S.; Crivillers, N.; Veciana, J.; Rovira, C.; Leugfgen, M.; Schmidt, G.; Molenkamp, L. W.; *CrystEngComm* **2008**, 1899.
[39] Liu, J.; Zhang, H.; Dong, H.; Meng, L.; Jiang, L.; Jiang, L.; Wang, Y.; Yu, J.; Sun, Y.; Hu, W.; Heeger, A.; *Nature Communications* **2015**, 6, 10032.
[40] Mas-Torrent, M.; Rovira, C.; *Chem. Rev.* **2011**, 111, 4833.

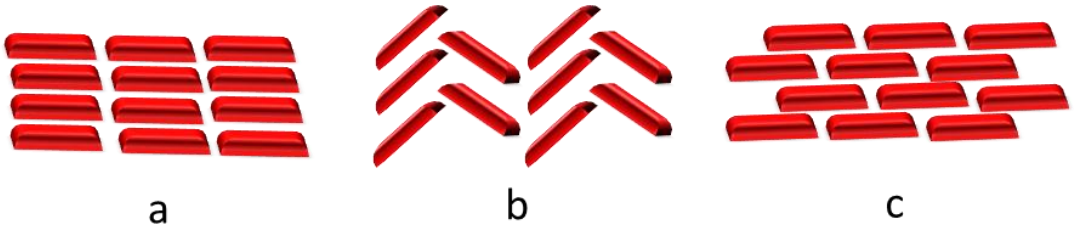

Figure I.12. Schematic illustration of common crystal packing motifs: a) cofacial, b) herringbone, c) "brick-wall".

Joined efforts, involving a tight cooperation between synthetic chemists, theoreticians, and experimental physicists has offered an increasing understanding of the most important parameters for charge transport by providing justification of experimentally observed semiconducting performance. Recently, it has been shown that theoretical predictions on non-yet-synthesized materials can be also successfully used to identify novel semiconductors. For example, an *in silico* screening led to the selection of the optimal candidate **8** (Figure I.13) among different potential derivatives of dinaphtho[2,3-*b*:2′,3′-*f*]thieno[3,2-*b*]thiophene. [41] Synthesis and characterization confirmed **8** as a new high-performance organic semiconductor presenting a mobility higher than 10 $cm^2V^{-1}s^{-1}$.

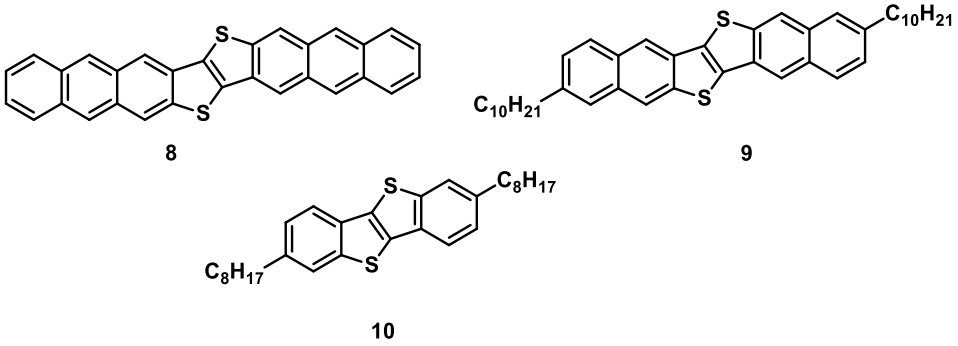

Figure I.13. Chemical structure of high mobility diacene-fused thieno[3,2-*b*]-thiophenes.

While many recent efforts have resulted in new methods for patterning organic single crystalline semiconductors, that have enabled for example direct deposition of large arrays of organic single crystals onto prefabricated transistor source–drain electrodes,[42] fabrication of devices from single crystals often requires manual selection and placing of individual crystals. For that reason, single crystals have not been traditionally meant to be incorporated in commercial devices, but to serve as model

[41] Sokolov, A. N.; Atahan-Evrenk, S.; Mondal, R.; Akkerman, H. B.; Sánchez-Carrera, R. S.; Granados-Focil, S.; Schrier, J.; Mannsfeld, S. C. B.; Zoombelt, A. P.; Bao, Z.; *Nat. Commun.* **2011**, 2, 437.
[42] Liu, S.; Wang, W. M.; Briseno, A. L.; Mannsfeld, S. C. B.; Bao, Z.; *Adv. Mater.* **2009**, 21, 1217.

systems and to provide a well-defined structure, in which the intrinsic electronic properties can be measured. This situation has changed dramatically over the last year with the development of solution processing techniques intended to obtain single crystalline thin films with enhanced molecular ordering that have led to impressive mobility values. For example, by directing the gradual shift of the liquid–atmosphere boundary upon evaporating a solution of **9** (Figure I.13) a single crystalline domain could be obtained with a benchmark mobility of 10 $cm^2V^{-1}s^{-1}$.[43]

On another recent example, triisopropyl pentacene **2** have been processed by a mechanical shearing technique that resulted in a strained lattice and consequently an increased mobility (4.6 $cm^2V^{-1}s^{-1}$ for strained versus 0.8 $cm^2V^{-1}s^{-1}$ for unstrained films).[44] During processing, a shearing plate drags the solution across a heated substrate while keeping the bulk of the solution between the plate and the substrate, with only the evaporation front exposed. Triisopropyl pentacene domains with lengths of up to one centimeter are observed with the long axis parallel to the shearing direction.

Hasegawa *et al.* have reported a method directed to combine the best of the single crystal electronic properties and the ease of the thin film fabrication by inkjet printing technologies.[45] By mixing fine droplets of a solution of the active semiconducting component and an antisolvent within a confined area, uniform single crystalline films of **10** have been successfully printed (Figure I.14). The gradual growth of the single crystalline film has been possible because of the fluidic nature of the microliquid droplet in which laminar flow dominates over turbulent flow. Thin films transistors prepared by using this technique present average carrier mobility as high as 16.4 $cm^2V^{-1}s^{-1}$. Important sample-to-sample deviations are however found indicating that optimization of this method is still necessary.

[43] Nakayama, K.; Hirose, Y.; Soeda, J.; Yoshizumi, M.; Uemura, T.; Uno, M.; Li, W.; Kang, M. J.; Yamagishi, M.; Okada, Y.; *Adv. Mater*. **2011**, 23, 1626.
[44] Gir, G.; Verploegen, E.; Mannsfeld, S. C. B.; Atahan-Evrenk, S.; Kim, D. H.; Lee, S. Y.; Becerril, H. A.; Aspuru-Guzik, A.; Toney, M. F.; Bao, Z.; *Nature* **2011**, 480, 504.
[45] Minemawari, H.; Yamada, T.; Matsui, H.; Tsutsumi, J.; Haas, S.; Chiba, R.; Kumai, R.; Hasegawa, T.; *Nature* **2011**, 475, 364.

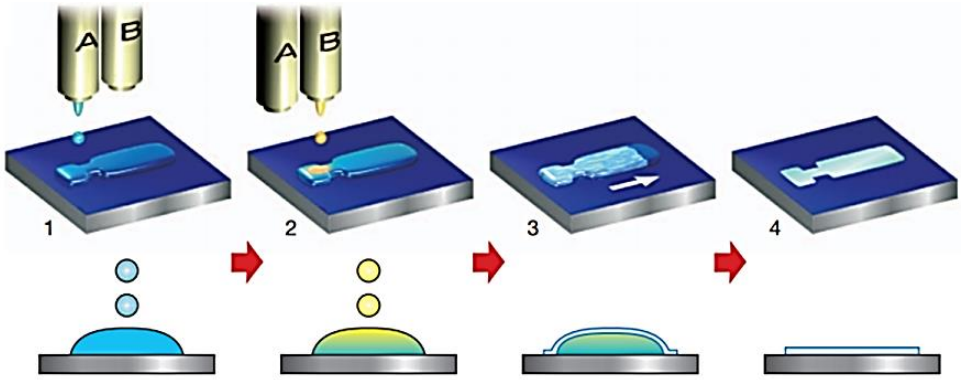

Figure I.14. Inkjet printing of organic single-crystal thin films. Antisolvent ink (A) is first inkjet-printed (step 1), and then solution ink (B) is overprinted sequentially to form intermixed droplets confined to a predefined area (step 2). Semiconducting thin films grow at liquid–air interfaces of the droplet (step 3), before the solvent fully evaporates (step 4).

All these results hold great promise in the search of high mobility solution-processed devices. However preparation of single crystalline thin films requires careful control of different nucleation parameters highly sensitive to subtle variations and the generality of these processing methodologies has to be demonstrated

- **Liquid crystals**

In an effort to prepare monodomain films, the soft and self-organizing nature of liquid crystals have been envisaged as highly promising for easy-to-process high mobility semiconductors. Liquid crystals can be easily aligned and solution/melt processed and more importantly they have the ability to self-repair defects that act as traps for charge carriers.

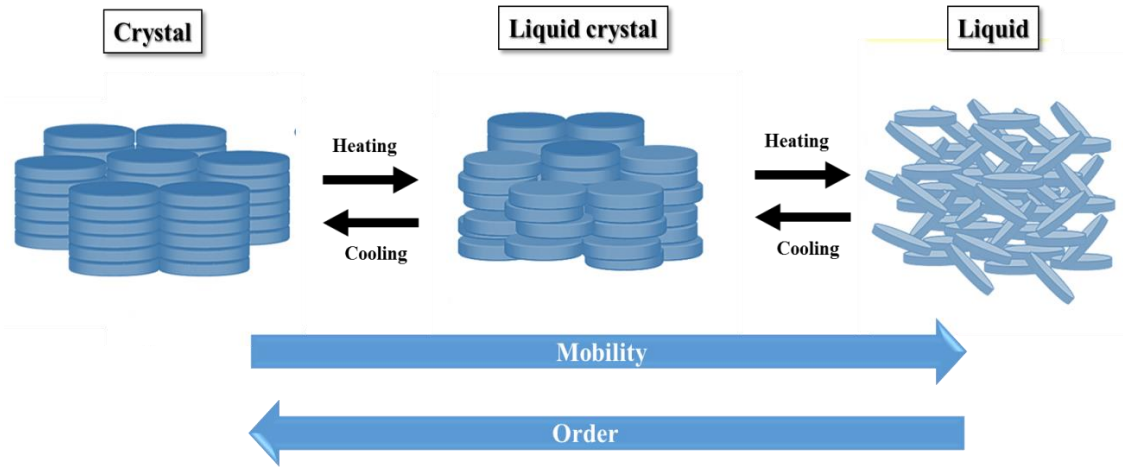

Figure I.15. Schematic representation of thermal properties in discotic liquid crystal.

Liquid crystalline mesophases are thermodynamically stable phases, with a degree of order intermediate between the isotropic melt and crystalline solids that can be induced in some shape-anisotropic molecules by the action of temperature or solvents (Figure I.15). In particular, discotic liquid crystals, usually composed by a rigid inner aromatic disk-like core (Figure I.16) surrounded by a number of flexible chains linked to it, have been found promising materials for organic electronics. In the columnar mesophases characteristic of this type of materials, the disk-like molecules stack on top of one another forming highly ordered columnar superstructures along which the π-orbital overlap between adjacent molecules favors the one-dimensional migration of charge carriers.

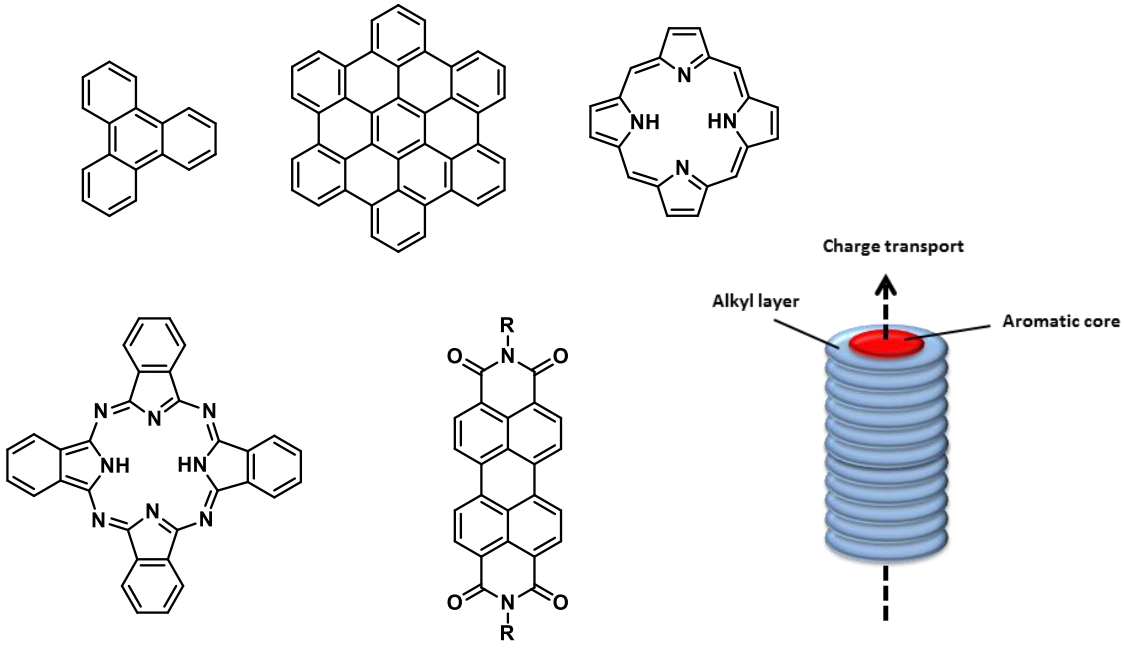

Figure I.16. Aromatic cores of widely studied discotic and schematic representation of charge migration pathway in discotic liquid crystals.

Early studies aimed to determine the semiconducting properties of discotic liquid crystals were performed on hexakis (hexylthio)triphenylene **11** (Figure I.17) that presented a hole mobility to 0.1 $cm^2V^{-1}s^{-1}$ in a three-dimensional helical columnar phase.[46] This high value motivated an enormous activity in the field directed to understanding and optimizing charge transport in discotic mesophases. The core, size, nature of chains or connecting groups between the aromatic core and the flexible peripheral chains have been systematically varied in an attempt to establish clear design principles for high performance semiconductors.

[46]Adam, D.; Schuhmacher, P.; Simmerer, J.; Häussling, L.; Siemensmeyer, K.; Etzbachi, K. H.; Ringsdorf, H.; Haarer, D.; *Nature* **1994**, 371, 141.

One of the factors that affect more the mobility is the size of the central core as it has a strong influence in the overlapping π-orbital area. Large polycyclic aromatic cores have emerged as promising high mobility liquid crystals like hexabenzocoronene **12** (Figure I.17) which presents a mobility of 0.3 $cm^2V^{-1}s^{-1}$ in the liquid crystalline phases that increases to 1.1 $cm^2V^{-1}s^{-1}$ upon crystallization.[47] The relative local molecular orientation and intermolecular separation of neighboring aromatic cores within the stacks, also have an important influence in the transfer integral and hence in the charge transport as has been extensively discussed at both experimental and theoretical level.[48]

In spite of the promising initial results obtained on triphenylene and the large activity in this area surpassing the limit 1 $cm^2V^{-1}s^{-1}$ in the mesophases for hole semiconductors have been shown to be a difficult task. Higher mobilities could be found however for n-type semiconducting discotic liquid crystals. Marder *et al.* found that 3,4,9,10-perylenediimide **13** (Figure I.17) displays a charge-carrier mobility of 1.3 $cm^2V^{-1}s^{-1}$ in its disordered columnar hexagonal phase at room temperature.[49] Even higher values (6 $cm^2V^{-1}s^{-1}$) were found for closely related columnar discotic 2,3:8,9-tetracarboxydiimide substituted with perfluorooctyl chains **14** (Figure I.17).[50] In spite of this impressive high mobility authors do not anticipate potential applications for this compound due to its extreme instability.

The reason for the difficulties in obtaining high mobilities in liquid crystals can be found in the fluctuation of the molecules within the stacks that confers liquid crystals their interesting self-healing properties but that is also responsible of a certain intrastack dynamism, reducing carrier mobility in the bulk.[51]The preferred strategy for improving mobility in discotic mesophases has been the enhancement of the intermolecular order within the stacks by locking translation and rotation by bulky groups or introducing groups able to establish strongly directional interactions.

---

[47] van de Craats, A. M.; Warman, J. M.; Fechtenkötter, A.; Brand, J. D.; Harbison, M. A.; Müllen, K.*; Adv. Mater*. **1999**, 11, 1469.

[48] a) Cornil, J.; Lemaur, V.; Calbert, J.-P.; Brédas, J.-L.; *Adv. Mater*. **2002**, 14, 726. b) Feng., X.; Marcon, V.; Pisula, W.; Hansen, M. R.; Kirkpatrick, J.; Grozema, F.; Andrienko, D.; Kremer, K.; Müllen, K.; *Nat. Mater*. **2009**, 8, 421.

[49] An, Z.; Yu, J.; Jones, S. C.; Barlow, S.; Yoo, S.; Domercq, B.; Prins, P.; Siebbeles, L. D. A.; Kippelen, B.; Marder, S. R.; *Adv. Mater.* **2005**, 17, 2580.

[50] An, Z.; Yu, J.; Domercq, B.; Jones, S. C.; Barlow, S.; Kippelen, B.; Marder, S. R.; *J. Mater. Chem*. **2009**, 19, 6688.

[51] Haverkate, L. A.; Zbiri, M.; Johnson, M. R.; Deme, B.; Mulder, F. M.; Kearley, G. J.; *J. Phys. Chem. B* **2011**, 115, 13809.

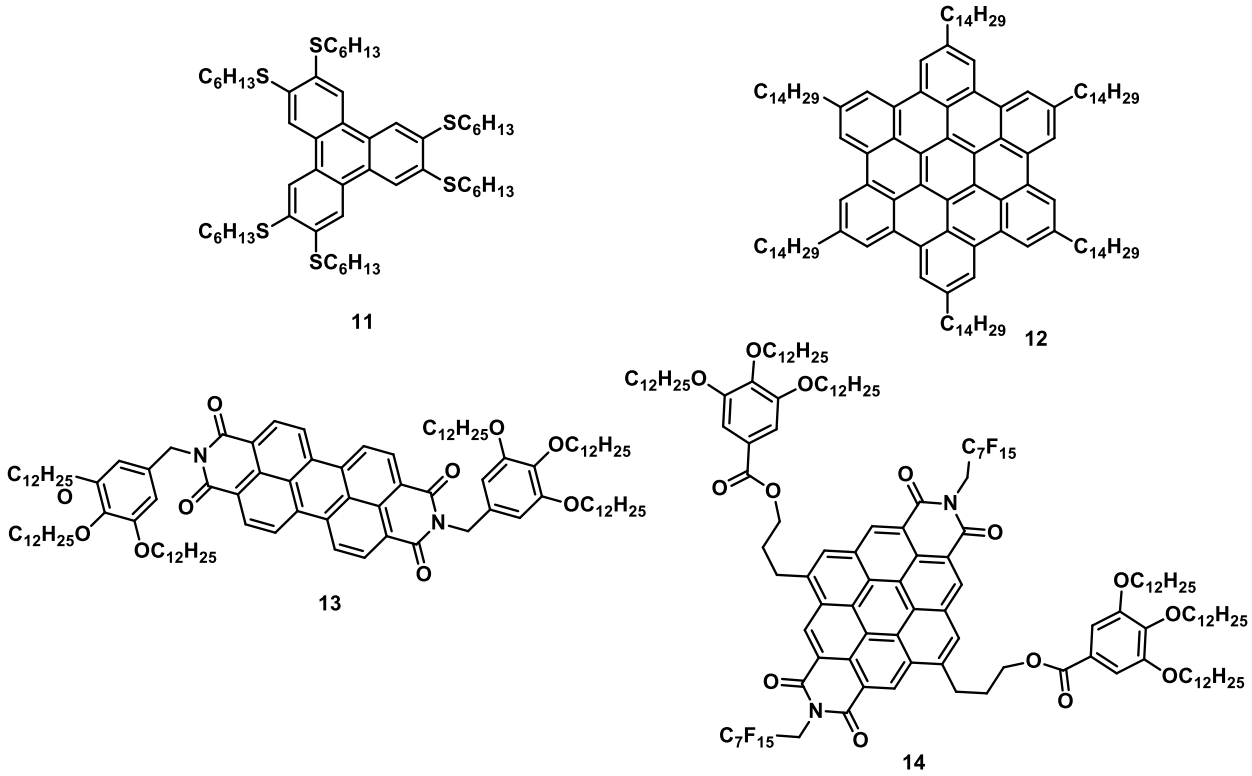

Figure I.17. Chemical structure of discotic liquid crystalline semiconductors.

Our research group has introduced heptacyclic 10,15-dihydro-5H-diindolo[3,2-*a*:3',2'-*c*]carbazole (triindole), as a new central core for the construction of discotic liquids. Attaching peripheral flexible alkyl chains to the triindole platform gives rise to columnar mesophases that are strongly affected by the nature of the spacers used to link the chains to the central core.

Thus direct attachment of six decyl chains **15** (Figure I.18) resulted in columnar hexagonal mesophases with no stacking periodicity. Despite the intracolumnar disorder, **15** has been found to exhibit a high hole mobility μ = 0.05 $cm^2V^{-1}s^{-1}$ in the mesophase.[52] Alkyne linkers has proved to efficiently increase the supramolecular order in the discotic mesophases, while maintaining a reasonable distance between molecules in the stack, resulting in the discotic liquid crystalline material **16** with very high hole mobility (μ ~1.4 $cm^2V^{-1}s^{-1}$).[53] On the other hand, distancing the peripheral alkyl chains by bulky phenyl moieties (compound **17**) can efficiently interlock the molecules within the columns yielding highly ordered mesophases. However, the high steric demand induced by these

[52] Talarico, M.; Termine, R.; García-Frutos, E. M.; Omenat, A.; Serrano, J. L.; Gómez-Lor, B.; Golemme, A.; *Chem. Mater.* **2008**, 20, 6589.
[53] García-Frutos, E. M.; Pandey, U. K.; Termine, R.; Omenat, A.; Barberá, J.; Serrano, J. L.; Golemme, A.; Gómez-Lor, B.; *Angew. Chem. Int. Ed*. **2011**, 50, 7399.

connecting groups resulted in large stacking distances (c = 4.4 Å), which translates in a significant lowering of the mobility.

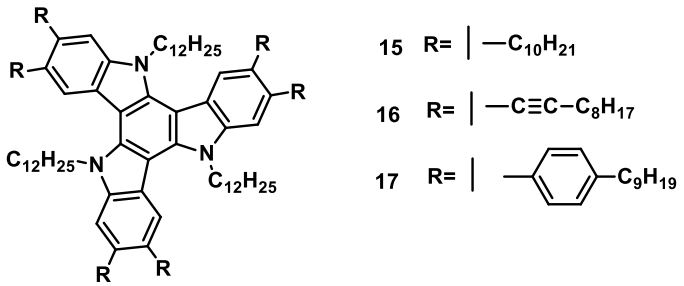

Figure I.18: Chemical structure of discotic liquid crystalline semiconductors based on triindole platform.

We have found that the phase behavior of hexaphenyltriindoles can be further tuned by changing the substitution pattern on the nitrogens. In particular 12 and 8 carbon atoms give rise to a ordered columnar mesophases in broad temperature range: both derivatives behaves very similar in terms of stacking distances and transition temperatures, but further reducing the length of the alkyl chains to 4 carbon atoms precludes mesomorphism. However, reducing even more the length of the attached chains to *N*-CH_3 result again in mesomorphic behavior. Interestingly in this case we observe a striking shortening of the intrastack distance, providing the highest hole mobility discotic liquid crystalline semiconductor reported to date (up to 2.8 $cm^2V^{-1}s^{-1}$).[54]

On the other hand, starting from the adequate hexathiophene or hexaaryl-triindoles via oxidative cyclodehydrogenation it is possible to obtain significantly π-extended cores like **18**[55] or **19**[56] (Figure I.19). Interestingly attaching only three alkyl chains to the triphenylene fused triindole, result in mesomorphic behaviour in a broad range of temperatures.

[54] Benito-Hernández, A.; Pandey, U. K.; Cavero, E.; Termine, R.; García-Frutos, E. M.; Serrano, J.L.; Golemne, A.; Gómez-Lor, B.; *Chem. Mater*. **2013**, 25, 117.
[55] García-Frutos, E. M.; Omenat, A.; Barberá, J.; Serrano, J. L.; Gómez-Lor, B.; *J. Mater. Chem*. **2011**, 21, 6831.
[56] Luo, J.; Zhao, B.; Shao, J.; Lim, K. A.; Chan, H. S. O.; Chi, C.; *J. Mater. Chem.* **2009**, 19, 8327.

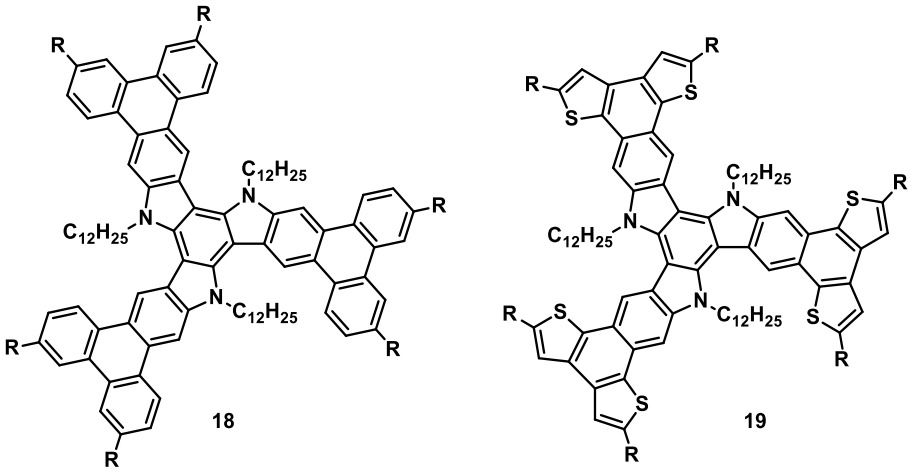

Figure I.19: Chemical structure of discotic liquid crystalline semiconductors based on extended triindole platform.

Due to their characteristic structure (active conducting core, surrounded by an isolating cover) conduction in these materials is highly anisotropic, and contacts among aromatic units of different columns are hampered by the mantle of soft alkylic chains. A precise control of the aromatic cores on the substrate, is therefore imperative to obtain optimal charge transport in the desired direction since orientation of the molecules will determine the direction of charge migration.

Disk-shaped molecules can be forced to orientate with columns parallel to the substrate (planar uniaxial alignment), as required for FETs or with columnar axis perpendicular to the substrate (homeotropic alignment) as needed for OLEDs or solar cells (Figure I.20). Unfortunately, increasing the intercolumnar order drives to enhanced mobilities but significantly lowers the viscosity of the mesophases making it more difficult to align the material. Orientation has been successfully achieved in many cases by different physical methods, but solutions found to this problem vary from material to material. At this stage, the controlled alignment of columns represents a major challenge for the practical application of high mobility discotic liquid crystals.

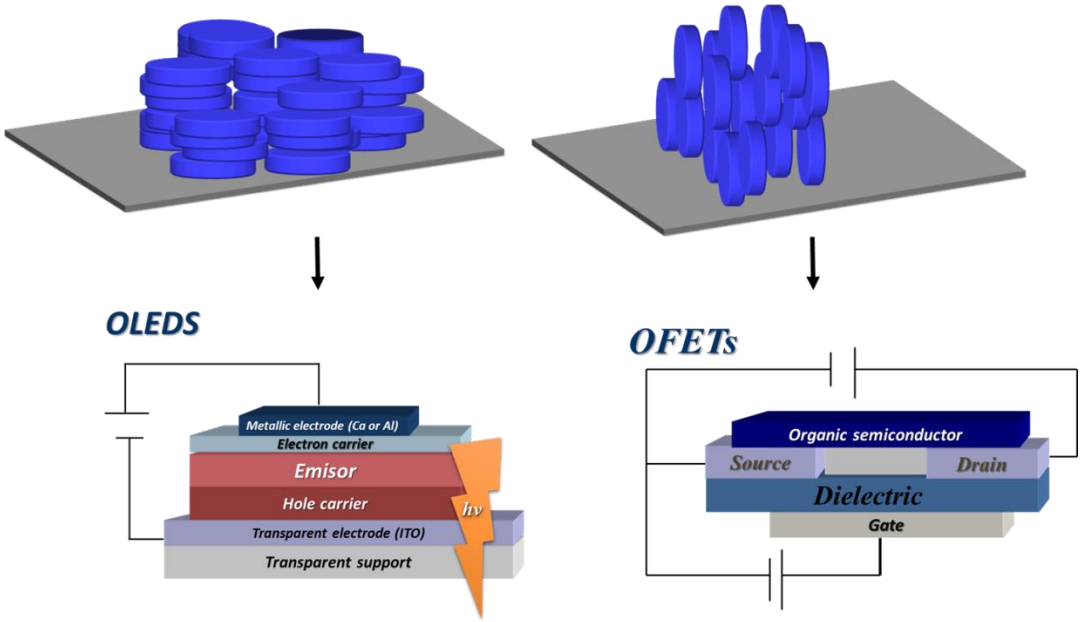

Figure I.20: Scheme of the different alignment required for the devices applications.

It has been recently shown that different extended columnar assembles of π-conjugated molecules bearing amide-appended chains can be aligned by the action of an electric field. The mechanism operating is proposed to involve unidirectional orientation of the amide linkers causing a macroscopic dipole which can be oriented antiparallel to the applied electric field. An unprecedented long-range homeotropic columnar orientation could be achieved even in a 500µm-thick film.[57] While this behavior has been previously observed in other discotic liquid crystals,[58] the generality of the observation presented in this recent work holds a great promise for overcoming the problems of alignment on discotic liquid crystals necessary to develop practical applications of these materials.

- **Polymeric materials**

Soluble polymeric semiconductors provide the desired ready processability needed for fast inkjet printing processes and roll to roll techniques required for the massive production of low cost electronics. However, mobility values in polymeric semiconductors have traditionally remained behind crystalline semiconductors due to their inherent disorder.

[57] Miyajima, D.; Araoka, F.; Takezoe, H.; Kim, J.; Kato, K.; Takata, M.; Aida, T.; *Angew. Chem. Int. Ed*, **2011**, 50, 7865.
[58] Bushey, M. L.; Nguyen, T. -Q.; Nuckolls, C.; *J. Am. Chem. Soc*. **2003**, 125, 8264.

As for conducting polymers we focus our attention on polythiophenes **20** (Figure I.21) as representative, most widely studied class of compounds. Polythiophenes usually form amorphous films with mobilities below 10^{-3} $cm^2V^{-1}s^{-1}$ resulting from the absence of long-range structural order. Higher mobilities (around 0.1 $cm^2V^{-1}s^{-1}$) have been found on regioregular poly(3-alkylthiophenes) **21** (Figure I.21),[59] the most studied polymeric semiconductors. In these materials, the strong interaction between regularly oriented alkyl side chains leads to a two dimensional lamellar structure in which the thienyl moieties are held in a close distance in a coplanar fashion (Figure I.21). Mobility varies as a function of the degree of regiogularity, molecular weight and deposition conditions and is highly dependent on the orientation of the ordered lamellar domains.

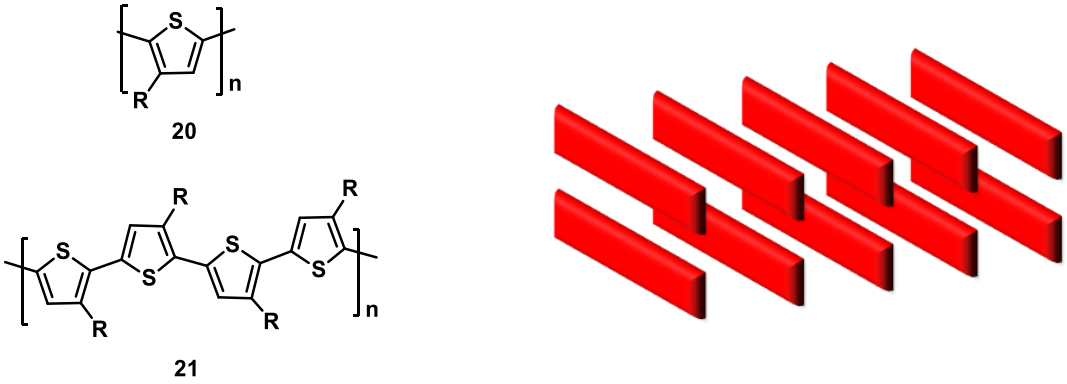

Figure I.21. Chemical structure of polythiophenes and schematic representation of ordered lamellar domains.

Attempts to increase the crystallinity have been performed by introducing more rigid units like thieno[3,2-*b*]thiophene moieies into the polythiophene backbone in order to reduce the conformational freedom. Upon annealing at the liquid crystalline phase and subsequent cooling, copolymer **22** (Figure I.22) crystallizes forming highly ordered domains that render mobility values as high as 0.7 $cm^2V^{-1}s^{-1}$.[60]

Design strategies to improve charge carrier mobility of polythiophenes include the incorporation of electron deficient aromatic rings into the backbone. Attaching electron withdrawing moieties lowers HOMO level which improves the air stability of these polymers (an important drawback of polythiophenes). It has been also reasoned that donor-acceptor interactions may help to closely pack the polymer chains resulting in

[59] Sirringhaus, H.; Brown, P. J.; Friend, R. H.; Nielsen, M. M.; Bechgaard, K.; Langeveld-Voss, B. M. W.; Spiering, A. J. H.; Janssen, R. A. J.; Meijer, E. W.; Herwig, P.; *Nature* **1999**, 401, 685.
[60] McCulloch, I.; Heeney, M.; Bailey, C.; Genevicius, K.; MacDonald, I.; Shkunov, M.; Sparrowe, D.; Tierney, S.; Wagner, R.; Zhang, W.; *Nat. Mater.* **2006**, 5, 328.

enhanced mobilities. Mobilities up to 0.79 $cm^2V^{-1}s^{-1}$ has been found in air-stable isoindigo-based conjugated polymer **23** (Figure I.22). [61]

This strategy has been extensively exploited using different donor and acceptor moieties such as copolymers **24** and **25** (Figure I.22) reaching mobility values around 1 $cm^2V^{-1}s^{-1}$.[62] Following this concept Müllen *et al.* have recently reported a polymeric semiconductor **26** (Figure I.22) that consists of the alternating arrangement of cyclopentadithiophene as a donor and a benzothiadiazole as an acceptor unit. The planar conjugated backbone ensures a close π-stacking of neighboring polymer chains. In this particular case long range macroscopic order and hole mobility increases with the number average molecular weight, (M_n) leading to a mobility value of 3.3 $cm^2V^{-1}s^{-1}$ for the highest M_n(35 $Kgmol^{-1}$).[63]

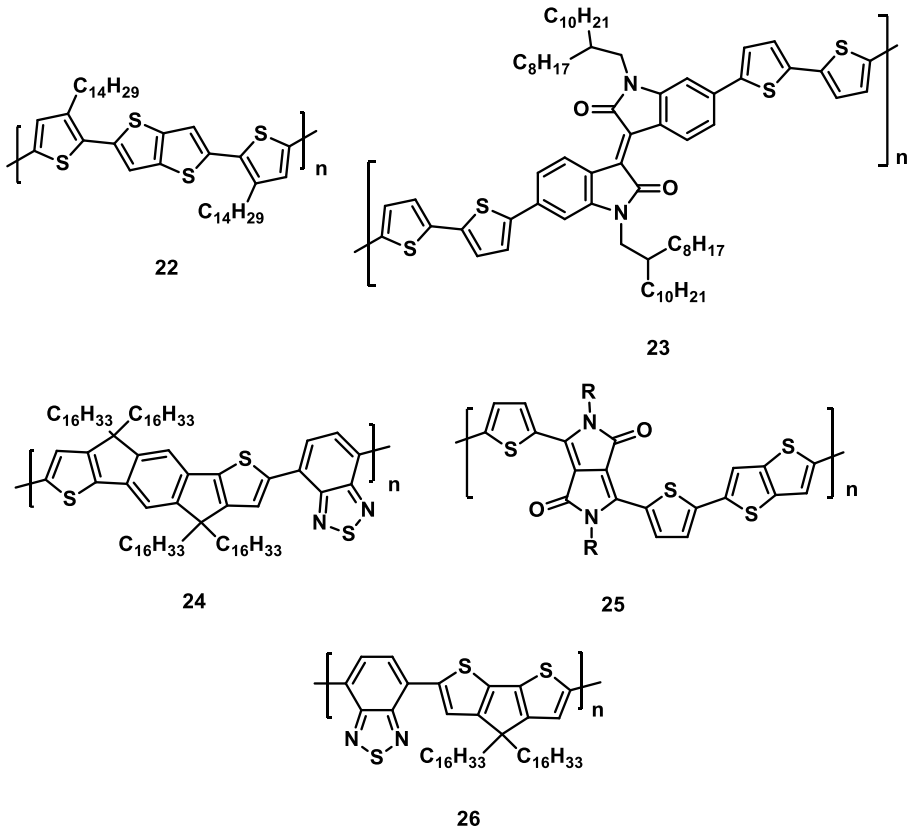

Figure I.22. High mobility polymeric semiconductors.

[61] Lei, T.; Cao, Y.; Fan, Y.; Liu, C.-J.; Yuan, S.-C.; Pei, J.; *J. Am. Chem. Soc.* **2011**, 133, 6099.
[62] a) Zhang, W.; Smith, J.; Watkins, S. E.; Gysel, R.; McGehee, M.; Salleo, A.; Kirkpatrick, J.; Ashraf, S.; Anthopoulos, T.; Heeney, M.; *J. Am. Chem. Soc.* **2010**, 132, 11437−11439. b) Li, Y.; Singh, S. P.; Sonar, P. A.; *Adv. Mater.* **2010**, 22, 4862.
[63] Tsao, H. N.; Cho, D. M.; Park, I.; Hansen, M. R.; Mavrinskiy, A.; Yoon, D. Y.; Graf, R.; Pisula, W.; Spiess, H. W.; Müllen, K. U.; *J. Am. Chem. Soc*. **2011**, 133, 2605.

Polymers are very appealing in terms of processability but they pose problems of reproducibility due to variations in molecular weight, and polydispersity, from batch to batch. In addition as it has been shown, that crystallinity is a key factor also in polymeric materials and in best examples anisotropic transport is observed, requiring a precise control of the material organization and alignment to achieve optimal mobilities and complicating device fabrication. In spite of this drawback, orientational alignment of polymer chains may provide a more robust approach towards large-area electronics than the deposition of highly crystalline film. Recently it has been shown that by combining pre-aggregating solvents and by adopting a room temperature wired bar-coating technique, it is possible to enable the directional self-assembling of a model electron-transporting polymer exhibiting large transport anisotropy and a mobility up to $6.4\ cm^2\ V^{-1}\ s^{-1}$.[64]

Very little explored in this area are aromatic porous polymers. Conjugated microporous polymers (CMPs) first introduced by Cooper *et al*.[65] constitute an emergent type of organic porous polymers consisting in a porous network synthesized from π-conjugated monomers with multiple reactive groups to promote molecule-molecule coupling via a π-conjugated bonds. Like conventional lineal polymeric materials the synthesis of these networks is dominated by kinetically controlled reactions, which irreversibly form covalent bonds and therefore they usually show no long-range molecular order. Closely related, Covalent Organic Frameworks (COFs), first developed by O. Yaghi,[66] are crystalline materials synthesized using reversible reactions to link the multifunctional π-conjugated monomers. Bridging bonds, which formed following the dynamic covalent chemistry covalent, can be formed, broken, and reformed with "error checking" and "proof-reading" characteristics. As a result, the most thermodynamically stable polymer skeleton is formed and polymerization occurs alongside the crystallization process. In conclusion, it is possible to obtain periodic structures within a 2D sheet and columnar alignment in the 3D, combine both the long-range order feature of molecular crystals and the extended conjugation as in conjugated polymers.

These two type of porous materials have emerged a new platform for the molecular design of electronic and optoelectronic materials. The different geometries of

[64] Bucella, S. G.; Luzio, A.; Gann, E.; Thomsen, L.; McNeill, C. R.; Pace, G.; Perinot, A.; Chen, Z.; Facchetti, A.; Caironi, M.*; Nature Communications* **2015**, 6, 8394.
[65] Jiang, J. X.; Su, F. B.; Trewin, A.; Wood, C. D.; Campbell, N. L.; Niu, H. J.; Dickinson, C.; Ganin, A. Y.; Rosseinsky, M. J.; Khimyak, Y. Z.; Cooper, A. I.; *Angew. Chem., Int. Ed.* **2007**, 46, 8574.
[66]. Côté, A. P.; Benin, A. I.; Ockwig, N. W.; O'Keeffe, M.; Matzger, A. J.; Yaghi, O. M.; *Science* **2005**, 310, 1166.

the building blocks, reactive groups and π-linkers provides an enormous flexibility of design in this type of materials. On the other hand, their intrinsic porosity offers huge opportunities to incorporate guests/chemicals within the channels and tune their properties and functionalities.

The potential offered by the porous nature of these materials is clearly exemplified in TTF- COF[67] (Figure I.23). This well-defined 2D framework contains TTF units highly aligned and stacked and open nanochannels which allow the incorporation of molecular dopants as a charge-transfer partner. The combination of these structural features allows the generation of mixed-valence TTF stacks, and result in tuneable electrical conductivity. Exposure of the thin film to I_2 vapour in a closed chamber results in significant increase of electrical conductivity that reaches a maximum of 0.28 Sm^{-1} (an increase of up to three orders of magnitude relative to the pristine material).

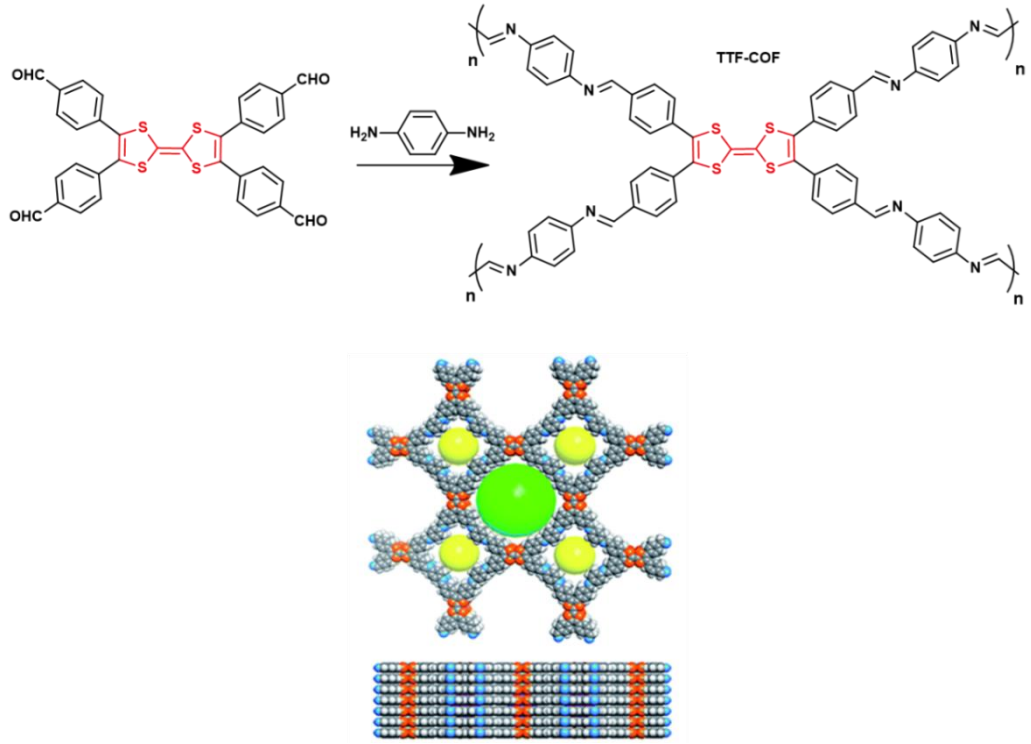

Figure I.23. General scheme for the synthesis of TTF- COF (above) and ilustration of the calculated top and side view packing.

Porous materials containing π-electron rich or deficient units, such as thiophene,[68] pyrene,[69] phthalocyanine[70] and benzothiadiazole[71] have been prepared, some of which are

[67]Cai, S.-L.; Zhang, Y.-B.; Pun , A.B.; He, B.; Yang, J.; Toma, F. M.; Sharp, I.D.; Yaghi, O. M.; Fan, J.; Zheng, S.-R.; Zhang, W.-G.; Liu, Y.; *Chem. Sci*. **2014**, 5, 4693.
[68] Dogru, M.; Handloser, M.; Auras, F.; Kunz, T.; Medina, D.; Hartschuh, A.; Knochel, P.;Bein, T.; *Angew. Chem., Int. Ed.* **2013**, 52, 2920.
[69] Wan, S.; Guo, J.; Kim, J.; Ihee, H.; Jiang, D.; *Angew. Chem., Int. Ed*. **2008**, 47, 8826.

shown to have high charge carrier mobilities as measured by electrodeless microwave conductivity measurements.

Despite the high charge-carrier mobility exhibited by many of these materials the lack of solution processability of this powdery materials impedes their integration into large-area, flexible devices. To solve this problem many attempts are being pursued to generate thin films of these type of materials. Growth of crystalline thin films directly on substrates may be an interesting solution to this problem.[72] Recently showed the formation of thin films (thicknesses ~2–200 nm) of an imine-based two-dimensional covalent organic framework at the solution air-interface (Figure I.24). Films can be transferred to any desired substrate by lifting from underneath, enabling their use as the semiconducting active layer in field-effect transistors. Although mobility is low ($3x10^{-6}$ $cm^2V^{-1}s^{-1}$), this example represent the first use of a covalent organic framework as semiconducting layer in a field effect transistor.[73]

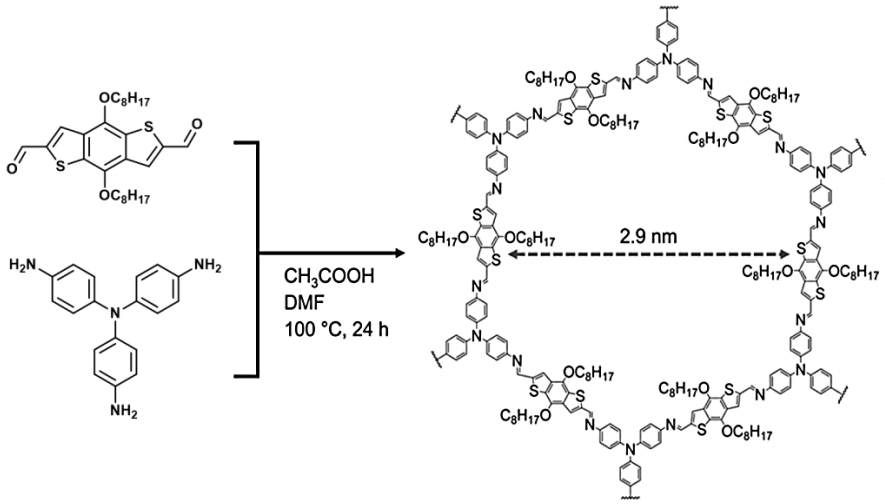

Figure I.24. General scheme for the synthesis of TTF-COF.

I.7. TRIINDOLE AS A NEW SEMICONDUCTING PLATFORM

As has been highlighted along this introduction it is clear that the critical trade-off between performance and processability has not yet been successfully accomplished.

[70] Ding, X.; Guo, J.; Feng, X.; Honsho, Y.; Guo, J.; Seki, S.; Maitarad, P.; Saeki, A.; Nagase, S.; Jiang, D.; *Angew. Chem., Int. Ed.* **2011**, 50, 1289.
[71] Feng, X.; Chen, L.; Honsho, Y.; Saengsawang, O.; Liu, L.; Wang, L.; Saeki, A.; Irle, S.; Seki, S.; Dong, Y.; Jiang, D.; *Adv. Mater*. **2012**, 24, 3026.
[72] Medina, D. D.; Werner, V.; Auras, F.; Tautz, R.; Dogru, M.; Schuster, J.; Linke, S.; Döblinger, M.; Feldmann, J.; Knochel, P.; Bein, T.; *ACS Nano* **2014**, 8, 4, 4042.
[73] Feldblyum, J. I.; McCreery, C. H.; Andrews, S. C.; Kurosawa, T.; Santos, E. J. G.; Duong, V.; Fang, L.; Ayzner, A. L.; Bao, Z.; *Chem. Commun*. **2015**, 51, 13894.

Organic materials present an unlimited variety in design and functionality, but, curiously, research on organic semiconductors has been performed on a narrow choice of molecules. There is a clear need of new versatile candidates that are easy to functionalize (therefore offering flexible tailoring possibilities) in order to develop new materials with the molecular and supramolecular complexity necessary to fulfill the different device requirements.

In this context our research group became interested on the electron-rich 10,15-dihydro-5*H*-diindolo[3,2-*a*:3',2'-*c*]carbazole (triindole) as a new organic semiconductor. The presence of delocalized π-electrons in this platform provides the interesting electronic properties, while its discotic topology induces highly ordered organizations, due to stacking paving the way for a favorable overlap of π-orbitals and consequently to an increased charge-carrier mobility. In addition, the platform of triindole presents two different types of positions that can be functionalized independently, offering varied possibilities for tuning their electronic properties as well as their morphology through chemical functionalization. The three *N*-positions can be easily functionalized taking advantage of the typical reactivity of azoles, while starting from known hexabromine triindol, the exploitation of cross-coupling methodologies opens flexible strategies to various peripheral functionalization (Figure I.25).

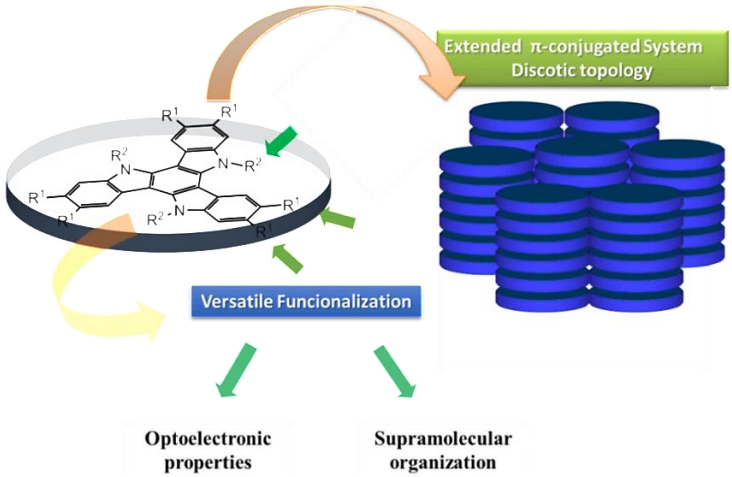

Figure I.25: Scheme of the discotic topology, and a representation of the two different types of positions that can be functionalized on the triindole platform.

When this thesis was started, our research group had already stated the importance of this platform in the search of easy-to-process high hole mobility semiconducting materials (See Section I.6). Specially remarkably is the record hole mobility values (2.8 $cm^2V^{-1}S^{-1}$)[57] determined on triindole-based semiconducting liquid crystals, which provide

an active conducting core surrounded by an isolating cover, as a result of the favourable synergy between the intrinsic properties of the platform and their supramolecular arrangement. Unfortunately, as it is common in discotic mesogens the high dependence of their electrical performance of these materials on the degree of columnar alignment represents an important drawback towards device application.

With these precedents, the main goal of this thesis is to optimize the electronic and self-assembling properties of this high mobility semiconducting platform, towards their incorporation in devices by taking advantage of its extraordinary chemical versatility. The properties of the molecular candidates will be modulated in accordance to the respective characteristics imposed by the different applications envisaged. In particular, we explore the possibility of integration of active layers based on triindole in organic electronic devices by means of the fabrication and characterization of Organic Light Emitting Diodes and Organic Field Effect Transistors. Towards this goal, the specific contribution of this thesis has been the synthesis of rationally designed candidates, study of their electronic and self-assembling properties, and the fabrication of Organic Field Effect Transistors.

Additionally, with the aim of investigating the potential applications of this platforms in the development of new emergent electroactive materials, such as microporous organic polymers and covalent organic frameworks materials, we have synthesized new model triindole trimers and studied the effect that π-spacers exerts on their fundamental properties, such as the electronic, redox and photophysical properties.

Finally, considering the good semiconducting properties of this C_3-symmetric cyclotrimer of indole, we have made a study aimed to identify new semiconducting platforms based on this heterocyclic. In particular, we have investigated the electronic properties of the asymmetric cyclic dehydrotrimer of indole, as well as a highly strained saddle shaped tetramer of indole (tetraindole) towards their use in charge transport processes.

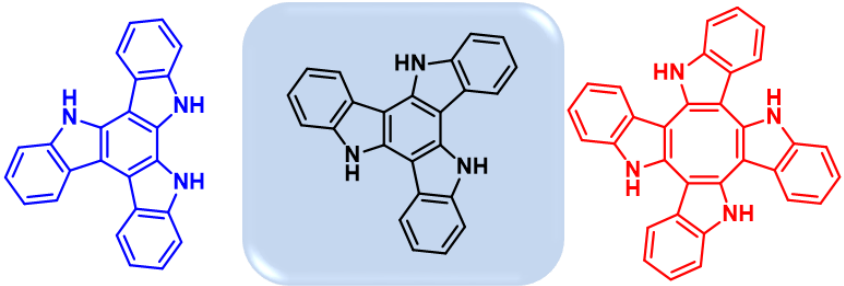

Figure I.26: Scheme of the platforms that we studied in this thesis.

In this context, my main contribution has been the synthesis of all the new molecules presented, study of their electronic and self-assembling properties, and the fabrication of Organic Field Effect Transistors. The Field Effect Transistors were fabricated by myself during a stay in the Northwestern University, USA, in the group of Prof. A. Facchetti.

I.8. BACKGROUND SYNTHESIS OF TRIINDOLE AND OTHER INDOLES DERIVATIVES

The first reference found on the synthesis of the triindole platform dates from 1964. *N*-trimethyltriindole was obtained by Müller in a low yield heating 3-chloro-N-methylindole with aqueous sodium hydroxide in an autoclave at 180-200ºC [74]

In 1980, Bergman *et al.* observed that the during the copper activated promoted coupling of indoles to form 2,2-biindolyls, this symmetric cyclic trimer of indole was obtained as a side product in a reasonable yield.[75] Simultaneously the same group, reported an alternative synthesis of this compound, which consisted in the condensation of 2-methylindole and 2-methyloxindole mediated by $POCl_2$ at 100ºC, followed by a DDQ induced cyclization (Scheme I.1)[76].

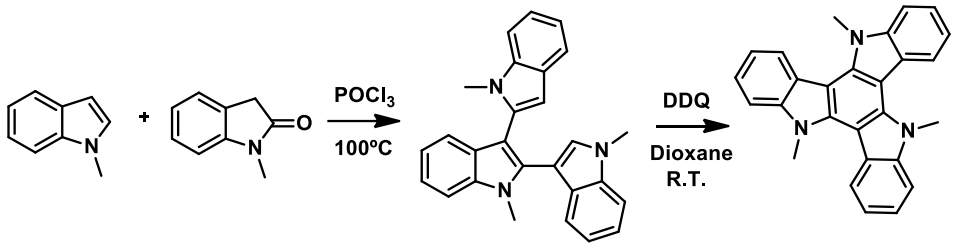

Scheme I.1: Synthesis described by Bergman *et al.*

Nowadays, triindole is obtained in a one-pot procedure, starting from 2-oxiindol following a slight variation of the synthesis described by Bergman *et al.* [76]The symmetric cyclotrimerization of 2-oxiindol in $POCl_2$ at 100ºC, leads to the unsubstituted triindole core, in 48% yield (Scheme I.2) [77,78] together with other open oligomers and cyclic tetraindole as secondary products. The formation of the cyclic tetramer can be favored by diluting the reaction mixture with chlorobenzene or $POCl_3$, although it is always obtained

[74] Müller, H.; Diss. Heidelberg, **1964**.
[75] Bergman, J.; Eklund, N.; *Tetrahedron*, **1980**, 36, 1439.
[76] Bergman, J.; Eklund, N.; *Tetrahedron*, **1980**, 36, 1445.
[77] Hiyoshi, H.; Kumagai, H.; Ooi, H. *Pat. Appl. Publ.* **2005** ,WO2005077956.
[78] Franceschin, M.; Ginnari-Satriani, L.; Alvino, A.; Ortaggi, G.; Bianco, A. *Eur. J. Org. Chem.* **2010**, 134.

as a minor product together with the trimeric compound which complicates its purification.[79] Otherwise, its synthesis through a multistep procedure has been also reported.[80] In the development of this thesis we also have found that by performing the cyclotetramerization reaction in an autoclave, we can favor the tetramerization *vs* the trimerization rendering a much more easy to purify compound.

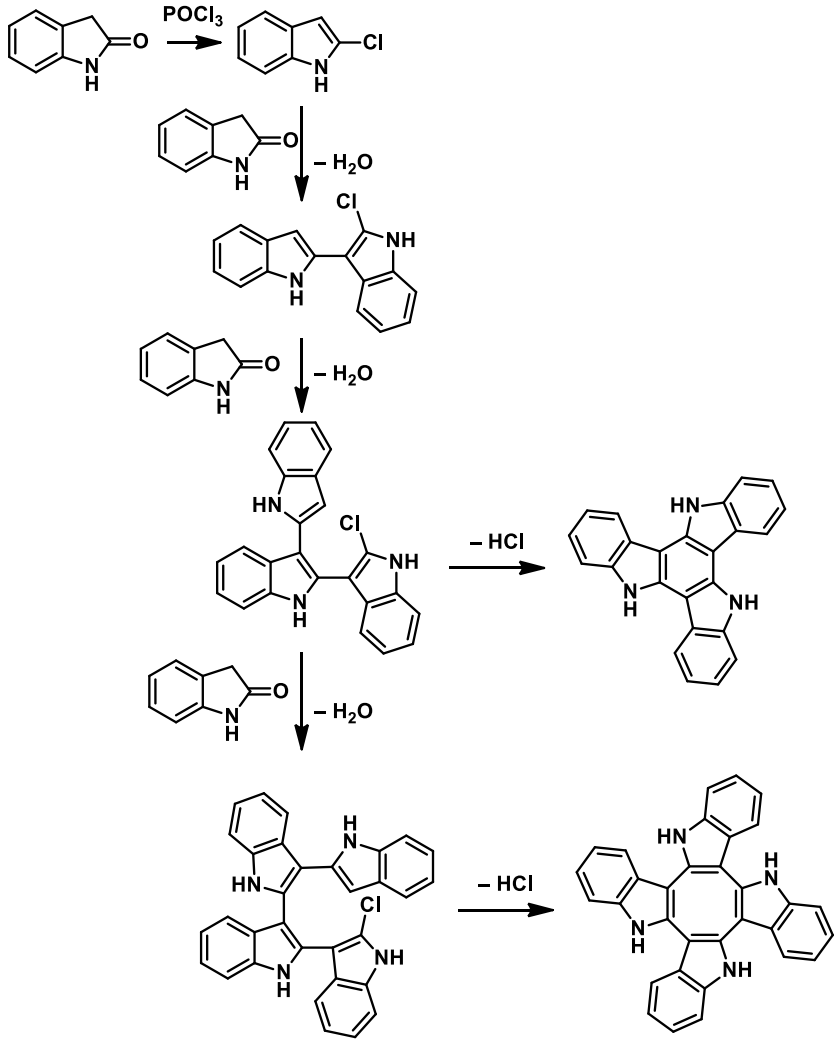

Scheme I.2: Synthesis for triindole and tetraindole.

Alternatively, triindole can be obtained by reductive dehalogenation of hexabromotriindole mediated by ammonium formiate and catalyzed by Pd/C [81](Scheme I.3) which can be readily obtained by treating indole with three equivalent of bromine. Although in principle, one equivalent of bromide should be sufficient to complete the cyclotrimerization, under these conditions only the 2,3-dimer isolated, whereas three

[79] Wang, F.; Li, X. C.; Lai, W. Y.; Chen, Y.; Huang, W.; Wudl, F. *Org. Lett*. **2014**, 16, 2942.
[80] Talaz, O.; Saracoglu, N.; *Tetrahedron* **2010**, 66, 1902.
[81] Gomez-Lor, B.; Echavarren, A. M.; *Org. Lett*. **2004**, 6, 2993.

equivalents were necessary to obtain the brominated symmetric indole trimers (Scheme I.3).[82]

The interest of this approach derives from the low solubility of hexabromine triindole in common organic solvents, which allows the easy purification of this compound by simple filtration of the reaction mixture. In addition, the presence of six bromines in strategic position allows further functionalization of this platform in its periphery.

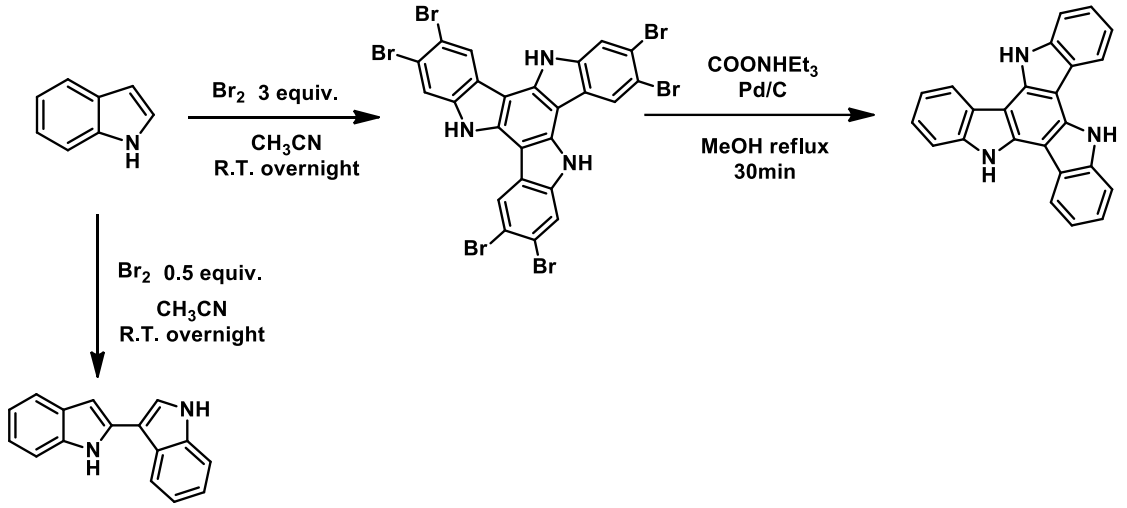

Scheme 1.3. Different routes of synthesis for triindole and tetraindole, a) reaction of indole with 3 eq. Br_2 in CH_3CN, and b) cyclocondesation of 2-oxiindole with $POCl_3$.

In contrast to the well-documented C_3-symmetric dehydrotrimer of indole, the asymmetric analogue is much less explored. The first report of the synthesis of this molecule can be found in 1981, when Itaika *et al.* described its synthesis by the reaction of indoles with titanium, (III)-hydrogen peroxide system under acid conditions.[83] Differently substituted cyclic asymmetric trimers have subsequently been obtained during the electropolymerization of functionalized indoles.[84,85,86,87,88] Its formation has been explained by considering the greatest electron spin density distribution in indole monomer, dimer, and linear trimer radical cations.[89,90]

[82] Robertson, N.; Parson, S.; MacLean, E. J.; Coxall, R. A.; Mount, A.R.; *J. Mater. Chem.*, **2000**, 10, 2043.
[83] Kaneko, T.; Matsuo, M.; Iitaka, Y.; *Chem. Phar. Bull*. **1981**, 29, 12, 3499.
[84] Bocchi, V.; Colombo, A.; Porzio, W.; *Synth. Met.* **1996**, 80, 309.
[85] Jennings, P.; Jones, A. C.; Mount, A. R.; Thomson, A. D.; *J. Chem. Soc., Faraday Trans*. **1997**, 93, 3791.
[86] Mackintosh, J. G.; Mount, A. R.; *J. Chem. Soc., Faraday Trans*. **1994**, 90, 1121−1125.
[87] Mackintosh, J. G.; Wright, S. J.; Langridge-Smith, P. R. R.; Mount, A. R..; *J. Chem. Soc., Faraday Trans.* **1996**, 92, 4109.
[88] Mount, A. R.; Thomson, A. D.; *J. Chem. Soc., Faraday Trans*. **1998**, 94, 553.
[89] Henry, J. B.; Mount, A. R.; *J. Phys. Chem. A*, **2009**, 113, 13023.
[90] Kettle, L. J.; Bates, S. P.; Mount, A. R.; *Phys. Chem. Chem. Phys.* **2000**, 2, 195.

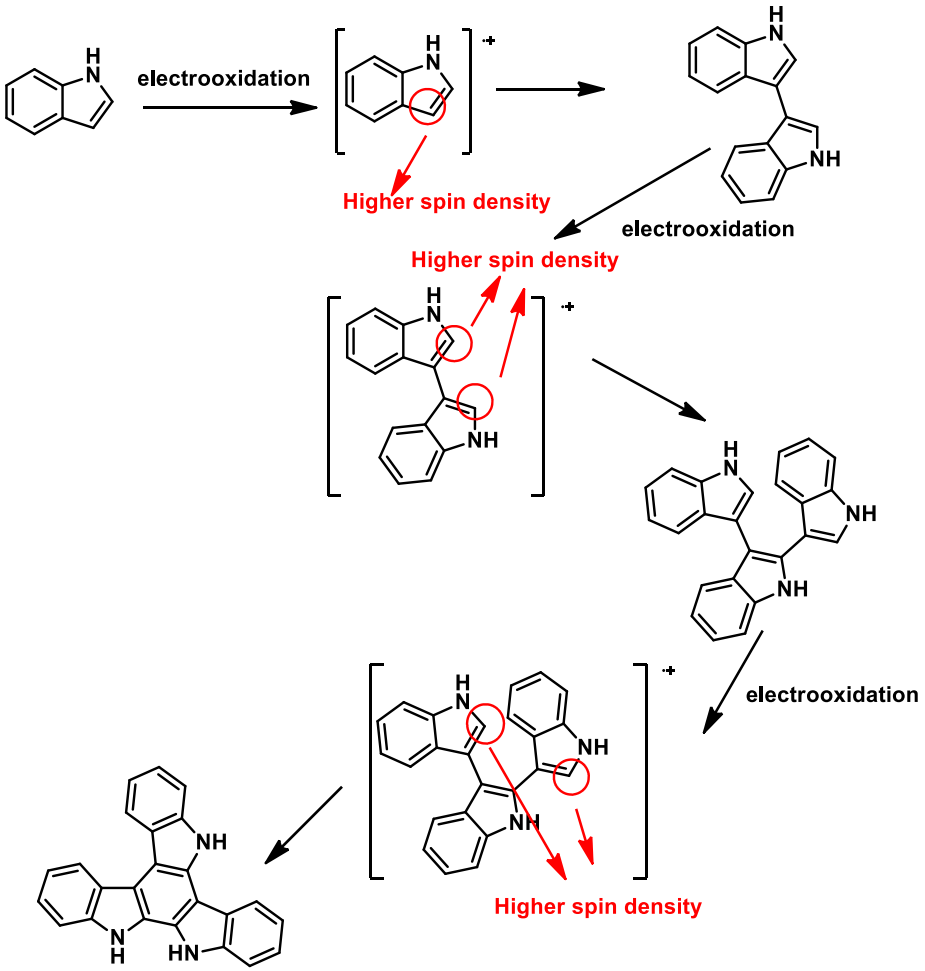

Scheme I.4. Electropolymerization of indoles to form asymmetric triindole.

Alternatively, preparative synthesis of this scaffold by reaction of indole with nitrosobenzene[91] has also been reported (Scheme I.5).

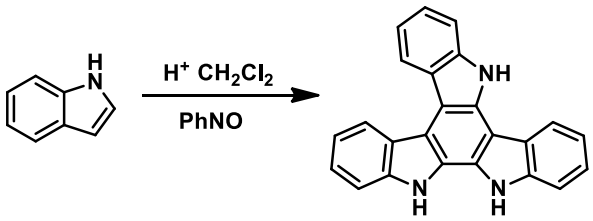

Scheme I.5. Synthesis of asymmetric triindole.

Recently, Norvaisa and co-workers published a synthetic method for asymmetric triindol (Scheme I.6).[92] Acetic acid catalyzed condensation reaction between 5-bromo-*N*-ethylisatin and 5- bromo-*N*-ethylindole afforded the condensation product in good yield. Subsequent reductive rearrangement at room temperature in the presence of lithium

[91] Greci, L.; Tommasi, G.; Petrucci, R.; Marrosu, G.; Trazza, A.; Sgarabotto, P.; Righi, L.; Alberti, A.; *J. Chem. Soc., Faraday Trans*. 2, **2000**, 2337.
[92] Reghu, R. R.; Volyniuk, D.; Kostiv, N.; Norvaisa, K.; *Dyes and Pigments* **2016,** 125, 159.

aluminum hydride yielded trimer. For the preparation of cycle-trimer, a DDQ-induced cyclization reaction was performed. Interestingly the synthesis of this tribromoderivative opens new opportunities for the functionalization of this platform in its periphery.

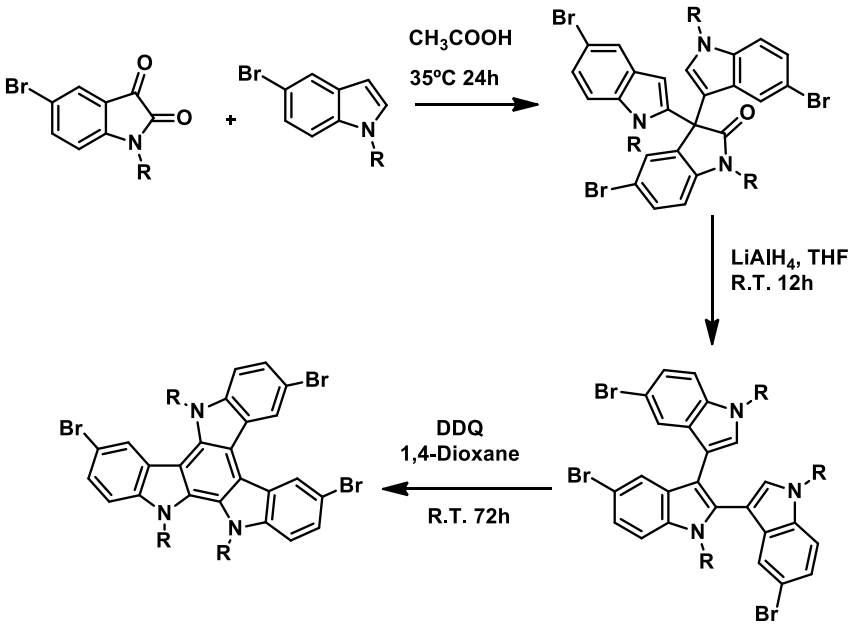

Scheme 1.6. Synthesis of asymmetric triindole describe by Norvaisa and co-workers.

I.9. APPLICATIONS IN ELECTRONIC DEVICES

As previously mentioned triindole platform is highly stable and has intrinsic physical favorable properties such as attractive redox, and linear and nonlinear optical properties. Despite the fact that this C_3-symmetrical scaffold has only recently been investigated, due to this favorable properties, it has already been investigated in the development of organic light emitting diodes and solar cells.

- **Organic light emitting diodes, OLEDs**

Several solution-processed devices OLEDs incorporating dendrimers hyperbranched polymers, or oligomers based on a triindole core and bearing polyfluorenes branches, have been fabricated.[93,94] (Figure I.27a). These devices exhibit efficient blue electroluminescence (EL) and demonstrate striking color stability, almost

[93] Lai, W. Y.; He, Q. Y.; Zhu, R.; Chem, Q. Q.; Huang, W.; *Adv. Funct. Mater*. **2008**, 18, 265.
[94] Levermore, P. A.; Xia, R.; Lai, W.; Huang, X. H.; Bradley, D. D. C.; *J. Phys. D. Appl. Phys*. **2007**, 40, 1896.

unchanged with increasing driving voltage showing remarkably better results than devices based on linear oligofluorene or polyfluorene counterparts. These results proved that the oligomers based in triindole core with linked star-shaped architecture are extremely promising for efficient and stable blue EL.

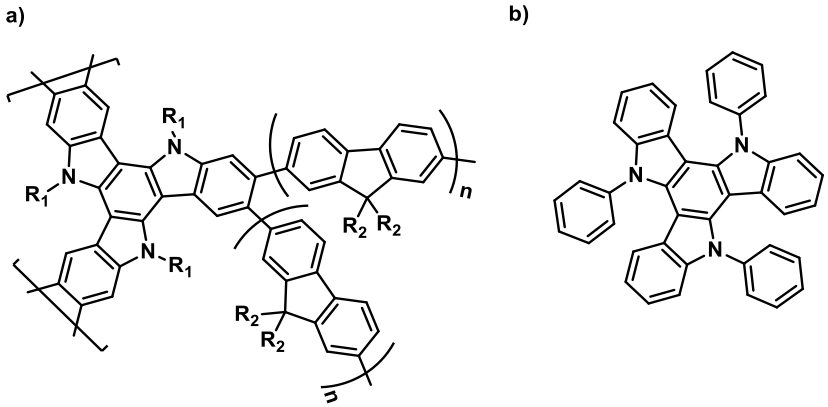

Figure I.27: a) Oligofluorene/triindole hybrid; b) 5,10,15-triphenyl-5H-diindolo[3,2-a:3 ,2 -c]carbazole

Recently, 5,10,15-triphenyl-5*H*-diindolo[3,2-a:3 ,2 -c]carbazole has been reported for organic light-emitting device applications (Figure I.27b). Particularly this small molecule has been successfully integrated as active layer in fluorescent blue emitting OLEDs and phosphorescent green OLEDs.[95]

In the context of this thesis, we have developed a series of hexafunctionalized trindoles with tunable light-emitting properties (Figure I.28). Single-layer solution processed OLEDs have been fabricated based on these compounds and characterized with the aim to investigate the influence of the functionalization periphery species on the optoelectronic properties of the platform.

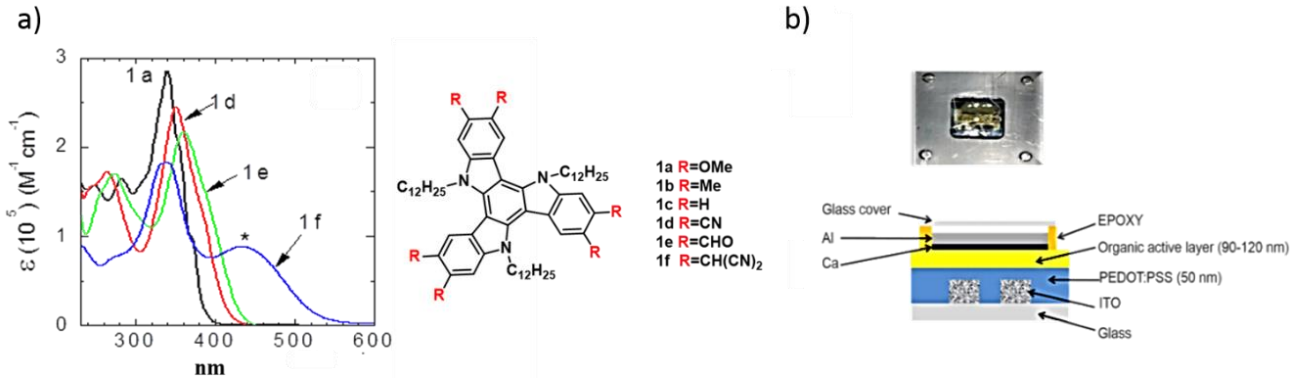

Figure I.28: a) Absorption spectra of hexa-functionalize triindoles; b) OLED design for the synthetized molecules.

[95] Huh, D. H.; Kim, G. M.; Kim, G. H.; Kulshreshtha, C.; Kwon, J.H.; *Synthetic Metals* **2013**, 180, 79-84.

- **Field effect transistor, OFETs**

In spite of the high mobility values exhibited by this platform in discotic mesophases it has been very scarcely implemented in Organic Field Effect Transistors.

The first triindole based OFET was reported in 2012 by Roberson and co-workers [96] (Figure I. 29a), who fabricated a solution processed OFET incorporating a thin film of a tribrominated *N*-trioctyltriindole derivative obtaining a discouraging hole mobility value of $1.42x10^{-6}$ $cm^2V^{-1}s^{-1}$.

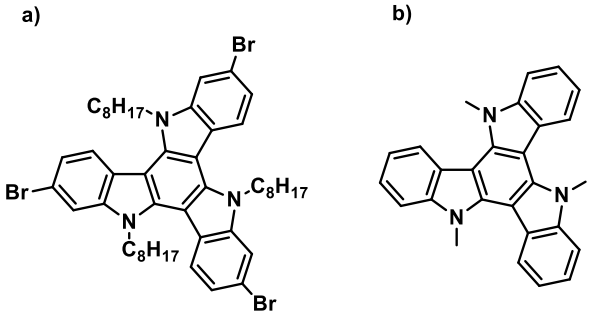

Figure I.29: Triindole derivatives incorporated in Field Effect Transistors. a) Tribrominated *N*-trioctyltriindole . b) *N*-trimethyltriindole.

Recently, Velasco *et al*. have reported the fabrication of an OFET by vapor deposition of a crystalline layer of *N*-trimethyltriindole (Figure I.29b) which showed a mobility value $3x10^{-2}$ $cm^2V^{-1}s^{-1}$ (Figure I.30) [97] It should be noted that our group has previously found a hole mobility 0.4 $cm^2V^{-1}s^{-1}$ for single crystals of this molecule by using the SCLC technique.[98] The absence of grain boundaries that characterize single crystalline materials probably accounts for these differences.

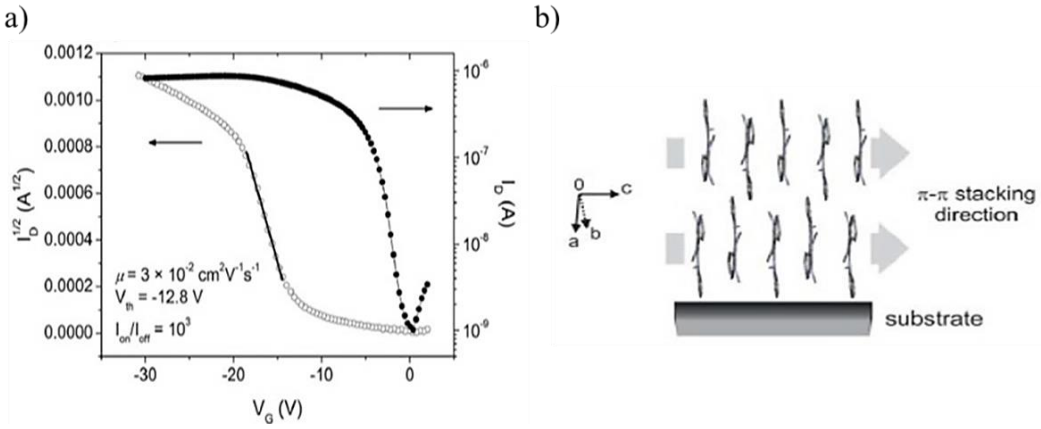

Figure I.30: a) Transfer characteristics of N-trimethylltriindole measured at a source-drain voltage of -20 V. b) Supramolecular organization onto the substrate of OFET.

[96] Valentine, R. A.; Whyte, A.; Awaga, K.; Robertson, N.; *Tetrahedron Letters* **2012**, 53, 657.
[97] Reig, M.; Puigdollers, J.; Velasco, D.; *J. Mater. Chem. C.*, **2015**, 3, 506.
[98] García-Frutos, E. M.; Gutierrez-Puebla, E.; Monge, M. A.; Ramírez, R.; de Andrés, P.; de Andrés, A.; Ramírez, R.; Gómez-Lor, B.; *Org. Electr.***2009**,10, 643.

In this thesis, by studying the crystal packing of the different trialkylated triindoles we have selected the N-triahexyltriindole as the best candidate to be incorporated into OFETS. A mobility value, 1.42 x 10^{-2} $cm^2V^{-1}s^{-1}$ was obtained on standard bottom gate-top contact.

On the other hand, trying to found a balance between mobility and processability, in this thesis we developed discotic liquid crystals that have a lower dependence of columnar alignment with the charge transport properties. The mobility values of these compounds were obtained by applying two different methods with different alignment requirements: space-charge limited current measurements and field effect mobility measurement, and found that on a diode type device is higher than that determined on thin-film transistors. Furthermore, the observation of field effect behavior in a discotic liquid crystal processed by simple drop-casing suggests an increased dimensionality of charge transport.

- **Organic solar cells**

The optical and electronic properties of these molecules make them suitable as a hole extracting/electron blocking layer, i.e. transparency in the visible region and high hole carrier mobility. Taking advantage of this properties, Shelton and co-workers reported the use of two solution-processable triindoles (triindole and *N*-trimethyltriindole) as hole selective materials in organic solar cells (Figure I.31).[99]

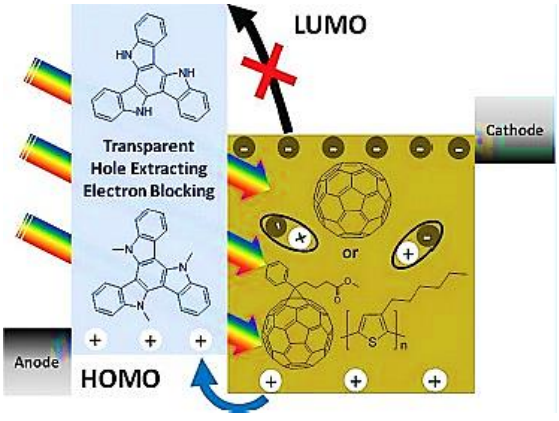

Figure I.31: Scheme of the solar cell fabricated with triindoles.

[99] Shelton, S. W.; Chen, T. L.; Barclay D. E.; Ma, B.; *ACS Appl. Mater. Interfaces* **2012**, 4, 2534.

On the other hand, triindoles have also been utilized to design new organic dyes for dye-sensitized solar cells. A series of triindoles functionalized Bodipy which showed large absorption coefficients and fluorescence quantum yields as well as interesting electrochemical properties were synthetized (Figure I.32). The blue dyes of this series exhibited also interesting photovoltaic effect in bulk heterojunction solar cells.[100]

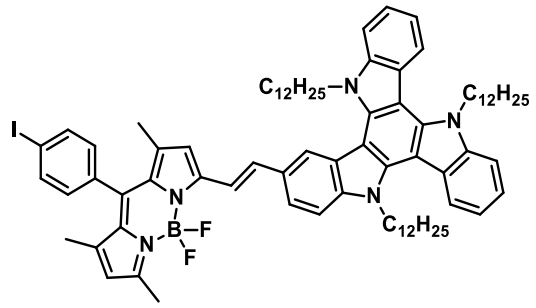

Figure I.32: Triindole functionalized Bodipy.

Bura and co-workers have designed new series of donor-π-acceptor dyes using triindole moieties as donors (Figure I.33). The photoelectronic properties of these dyes can be tuned by changing π-conjugated linkers. The best performance was found with thiophene as the conjugated linker and cyanoacrylic acid as the acceptor which showed a power conversion efficiency up to 6.10% . [101]

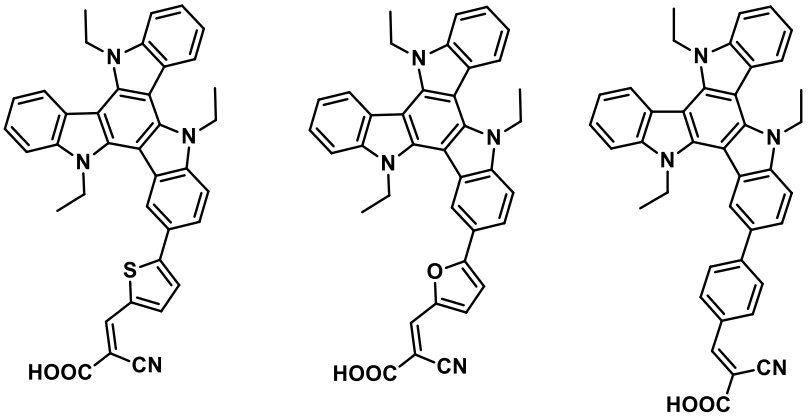

Figure I.33. Structure of the triindole based dyes.

Additionally a remarkable power conversion efficiency (over 18%) has been recently reported in a solar cell by using 5,10,15-trihexyl- 3,8,13-tris(4-methoxyphenyl)-10,15-dihydro-5H-diindolo[3,2-a:3′,2′-c]carbazole with a composite perovskite absorber

[100] Bura, T.; Leclerc, N.; Fall, S.; Lévêque, P.; Heiser, T.; Ziessel, R.; *Org. Lett*. **2011**, 13, 22, 6030.
[101] Qian, X.; Zhu, Y. Z.; Song, J.; Gao, X. P.; Zheng, J. Y.; *Org. Lett*., **2013**, 15, 6034.

(Figure I.34). This result qualifies triindoles as promising hole transporting materials for the fabrication of highly efficient perovskite solar cells.[102]

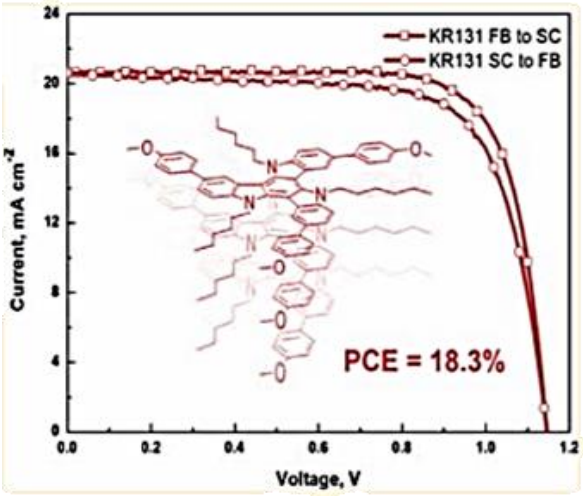

Figure I.34. *J*−*V* curves of best performing photovoltaic solar cells.

[102] Rakstys, K.; Abate, A.; Ibrahim Dar, M.; Gao, P.; Jankauskas, V.; Jacopin, G.; Kamarauskas, E.; Kazim, S.; Ahmad, S.; Grätzel, M.; Nazeeruddin, M.K.; *J. Am. Chem. Soc.* **2015**, 137, 16172−16178.

Objectives

OBJECTIVES

The main objective of this thesis aims to tailor the electronic and self-assembling properties of triindol platform, towards its incorporation into electronic devices (OLEDs and OFETs) by taking advantage of its high chemical versatility with two different positions for structural modification. The properties of the molecular candidates will be modulated in accordance to the respective characteristics imposed by the different applications envisaged.

In addition, with the aim of guiding the design of triindole-based emergent materials such as microporous organic polymers and covalent organic frameworks materials we will develop different dimeric models to study the effect that π-spacers has on the electron transfer abilities between different triindole units.

Finally, considering the good semiconducting properties of this C_3-symmetric cyclotrimer of indole, an exploratory study aimed to identify new semiconducting platforms based on this heterocyclic will be performed.

The specific objectives of this thesis are:

- Study a series of crystalline *N*-trialkyltriindoles functionalized with different length *N*-alkyl chains, in order to obtain a better understanding of the self-assembling behavior of this platform, and select the best candidate for their integration in devices.

- Optimization of the optical properties of the triindol platform by functionalizing its periphery, and selection of the best candidates for their integration in organic light emitting diodes.

- Optimization of the charge transport properties of triindole mesogens with the goal of incorporating them in Organic Field Effect transistors by obtaining mesogens with a larger ratio of conducting part *versus* isolating cover, and alternatively by synthesizing new mesogens decorated with peripheral groups able to establish short contacts between neighbouring columns.

- Investigate the potential applications of triindoles in the development of new emergent electroactive materials, such as microporous organic polymers, by the study of different dimeric molecules as model systems.

- Development of new cyclic oligomers of triindoles and study of their electronic properties in the search of new semiconducting platforms.

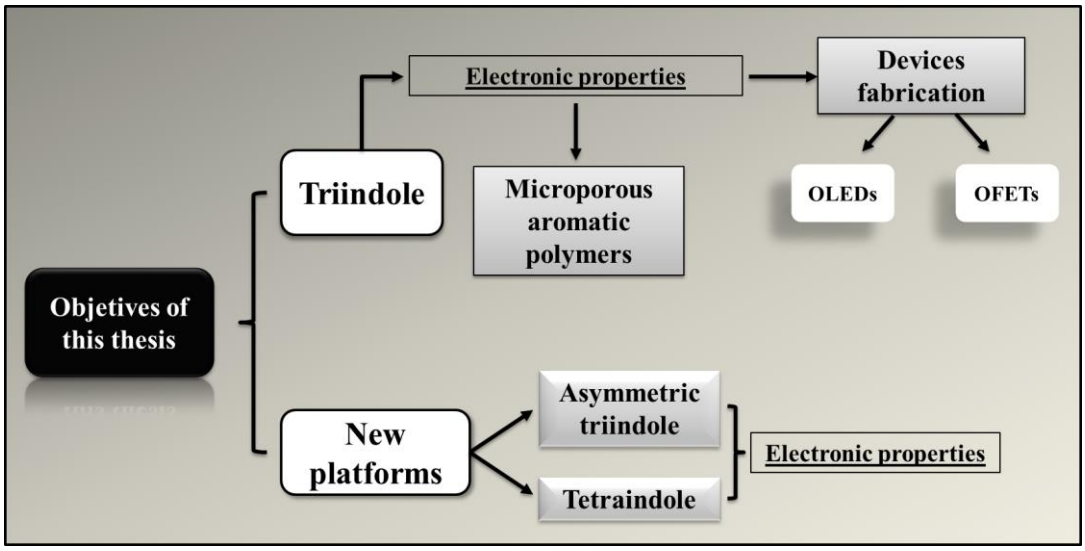

Chapter 1. *N*-Trialkylated Triindoles

1. CHAPTER 1. *N*-TRIALKYLATED TRIINDOLES

1.1. SUMMARY

Organic single crystals offer an excellent opportunity to investigate structure-properties relationships and to elucidate charge transport mechanism in organic materials. Here, the properties are not masked by grain-boundaries or other microstructure features that can severely localize and trap the charge carriers. Many efforts have been made to rationalize performance in terms of favorable crystallographic packing essential to improve the properties of the design of new promising materials.

In this chapter we show how through an adequate functionalization, the intermolecular interactions and the crystallographic packing of *N*-trialkyltriindoles can be modulated, and how these parameters may affect to the electronic properties of the platform. To achieve this goal, we have studied a series of crystalline *N*-trialkyltriindoles in which the number of carbon atoms of the alkyl chains attached to the nitrogen was systematically varied.

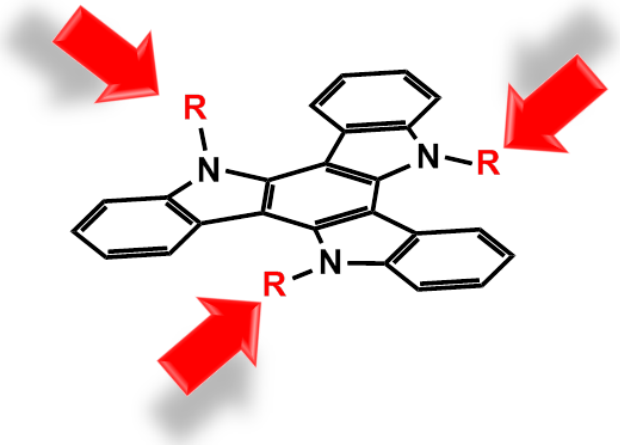

It was found that the length of the alkyl chains does not affect significantly their electronic properties however it has a strong influence in the morphology and in the crystalline packing of these compounds. As has been determined by single crystal analysis behind the different crystalline habits and macroscopic morphologies observed, is the way in which molecules pack in the crystals and interacts with their nearest neighbours. The contribution of several cooperative CH-π interactions to guide the self-assembly of this type of molecules have been clearly established.

All of these derivatives oxidizes readily and reversibly which qualify them as promising candidates for hole injection and transport. By studying the crystal packing of the different trialkylated triindoles we have selected the *N*-trihexyltriindole as the best candidate to be incorporated into OFETS. A mobility value, 1.42 x 10^{-2} $cm^2V^{-1}s^{-1}$ was obtained on a standard bottom gate-top contact configuration.

1.2. THE ROLE OF CH-π INTERACTIONS IN THE CRYSTAL MORPHOLOGY AND PACKING OF *N*-TRIALKYLATED TRIINDOLES.

Constanza Ruiz, Ángela Benito-Hernández, Enrique Gutiérrez-Puebla, Ángeles Monge-Bravo, and Berta Gómez-Lor*

Instituto de Ciencia de Materiales de Madrid, CSIC, C/ Sor Juana Inés de la Cruz 3, 28049 Madrid, Spain.

Crystal Growth & Design 2016, cg-2016-00144v

1.2.1. ABSTRACT

The self-assembling trends of a series of *N*-trialkyltriindoles in which the number of carbon atoms of the alkyl chains attached to the nitrogens was systematically varied have been investigated in the crystalline state. We have found that the length of the *N*-alkyl chains significantly impact on the position adopted in the crystal by each molecular component with respect to its neighbors and strongly influences the final morphology of the crystals which predominantly prefer to grow into one-dimensional shapes. Single crystal analysis demonstrate that this habit is determined by the highly anisotropic supramolecular bonding in the crystal packing and allows us to recognize the contribution of several cooperative CH-π interactions to guide the self-assembly of this type of molecules. The results of this study represent a step forward towards the rational control of the supramolecular arrangement of this high performance semiconducting platform.

1.2.2. INTRODUCTION

The use of molecule-based semiconductors in the construction of electronic devices has expanded impressively in the last few years. Organic semiconductors arose great expectations in the development of low-cost, flexible and large-area devices [1,2] but also offer the possibility of fine tuning key properties through a convenient molecular design. Extended aromatic systems provide a high amount of ¨mobile¨ π-electrons and their electronic properties (luminescence, absorption, energy band gaps, charge transport…) can be readily modulated by introduction of functional groups in defined

[1] a) *Organic Electronics: Materials, Manufacturing and Applications*; Klauk, H., Ed.; Wiley- VCH: Weinheim, **2006**. b) *Organic Electronics: More Materials and Applications*; Klauk, H., Ed.; Wiley- VCH: Weinheim, **2012**.

[2] Special issue on π-functional materials for organic electronics: *Chem. Mater.* **2011**, 23, 309.

positions of the molecules.[2] However fundamental properties of molecular materials are not only governed by those of individual molecules but also by the way they are spatially ordered in the bulk.[3, 4,5] Controlling the organization of the molecular building blocks at the nanometer level is therefore a main challenge in the field.

One-dimensional microstructures of π-extended molecules are gaining increasing attention in the development of next generation of organic devices. In these anisotropic structures, π-electron rich aromatic rings are usually arranged in stacks or slipped stacks providing an efficient pathway for charge migration owing to increased overlap between the electronic wavefunctions of neighboring molecules. As a result 1D supramolecular structures have been extensively used as n or p-channel in field effect transistor devices.[6]

In order to be able to control the supramolecular organization of a particular building unit in a predefined manner, it is necessary to have a perfect knowledge of the non-covalent interactions acting among the molecules. This is usually a challenging task as intermolecular interactions involving π-conjugated systems are weak in nature and act in a cooperative way but often in opposite directions complicating their understanding.[7] Single crystal analysis provides invaluable information on the nature of intermolecular interactions among neighboring units and offers an excellent opportunity to investigate molecular arrangement dependent properties.

The presence of long alkyl side chains is a common structural feature to influence in the self-assembly of π-extended aromatics without significantly affecting the electronic properties of individual molecules: they increase the molecular solubility facilitating their processability and may induce their arrangement in highly anisotropic columnar

[3] Liu, Z.; Zhang, G.; Zhang, D.; *Chem. Eur. J.* **2016**, *22*, 462.

[4] Modulation of optical properties of π-conjugated materials through a supramolecular approach: a) Varughese, S.; *J. Mater. Chem. C* **2014**, *2*, 3499-3516. b) Varughese, S.; Das, S.; *J. Phys. Chem. Lett*. **2011**, 2, 863. c) Grepioni, F; D'Agostino, S.; Braga, D.; Bertocco, A.; Catalano, L.; Ventura, B. *J. Mater. Chem. C* **2015**, *3*, 9425. d) Nagarajan, K.; Rajagopal, S. K.; Hariharan M.; *CrystEngComm* **2014**, *16*, 8946.

[5] Modulation of semiconducting properties of π-conjugated materials through a supramolecular approach: a) Mas-Torrent, M.; Rovira C.; *Chem. Rev.* **2011**, *111*, 4833. b) Mei, J.; Diao, Y.; Appleton, A. L.; Fang, L.; Bao, Z.; *J. Am. Chem. Soc.* **2011**, *133*, 6724. c) Wang, C.; Dong, H.; Hu, W.; Liu, Y.; Zhu D.; *Chem. Rev*. **2012**, *112*, 2208. d) Ruiz, C.; García-Frutos, E.; Hennrich, G.; Gómez-Lor, B.; *J. Phys. Chem. Lett.* **2012**, *3*, 1428.

[6] For some relevant reviews on one-dimensional materials able to transport charge carriers see: a) Briseno, A.L.; Mannsfeld S.C.B.; Jenekhe, S. A.; Bao, Z.; Xia, Y.; *Materials Today* **2008**, *11*, 38. b) Li, R.; Wu, H.; Liu, Y.; Zhu, D. *Acc. Chem. Res.* **2010**, *43*, 529-540; c) Oh, J. H:, Lee, H. W.; Mannsfeld, S.; Stoltenberg, R.M.; Jung, E.; Jin, Y.W.; Kim, J.M.; Yoo, J. -B.; Bao, Z.; *Proc. Mat. Acad. Sci.* **2009**, 106, 6065. d) Hasegawa, M.; Iyoda, M.; *Chem. Soc. Rev.* **2010**, *39*, 2420.

[7] a) *The Importance of π-Interactions in Crystal Engineering: Frontiers in Crystal Engineering*; Tiekink, E R.T., Zukerman-Schpector, J. Eds.; John Wiley & Sons, Ltd, Chichester, UK. b) Salonen, L.M.; Ellermann, M.; Diederich, F.; *Angew. Chem. Int. Ed.* **2011**, *50*, 4808. c) Wheeler, S.E.; Bloom, J. W. G.; *J. Phys. Chem. A*, **2014**, *118*, 6133. d) Desiraju, G. R.; *J. Am. Chem. Soc.* **2013**, *135*, 9952.

mesophases.[8] The one– dimensional supramolecular organization found in columnar liquid crystals has aroused much interest in the search of efficient charge transporting systems.[9] In this context we became interested on electron-rich 10,15-dihydro-5*H*-diindolo[3,2-*a*:3',2'-*c*]carbazole (triindole) **1a** as new high performance π-extended semiconducting mesogen [10, 11, 12]Attachment of six long peripheral alkyl chains through bulky phenyl linkers to this disk-shape molecule, give rise to a columnar mesomorphism whose phase behavior can be further tuned by changing the substitution pattern on the nitrogen.[12] For example *N*-alkylation of this mesogen with 12, 8 or 6 carbon atoms chains give rise to hexagonal columnar mesophases in a broad temperature range. Curiously further reducing the length of the alkyl chains to 4 carbon atoms precludes mesomorphism, rendering a compound that melts into the isotropic liquid nearly at room temperature while reducing even more the length of the attached chains to three methyl groups result again in mesomorphic behavior. Interestingly in this case we observe a striking shortening of the intrastack distance, providing the highest hole mobility discotic liquid crystalline semiconductor reported to date.[12]

In this manuscript we investigate the crystal structure of laterally unsubstituted parent *N*-trialkylated single crystalline triindoles finding that the size of the alkyl chains has also an important effect on the crystal packing and on their tendency to self-assemble into 1D-arrangements. Interesting parallelism can be driven between liquid crystals and non-mesogenic crystalline analogues as again only the butyl groups prevent the one-dimensional assembly of these molecules. In this particular case CH-π interactions have been identified as responsible of driving the different supramolecular organizations. It should be noted that although this type of interactions are individually quite weak, their effects are additive and therefore their influence can be really powerful.[13]

---

[8] *Chemistry of Discotic Liquid Crystals: From Monomers to Polymers;* Kumar, S. Ed.; CRC Press, Taylor & Francis: Boca Raton, **2011**.

[9] a) Pisula, W.; Zorn, M.; Chang, J. Y.; Müllen, Zentel, K. R.Macromol.; *Rapid Commun.* **2009**, 30, 1179. b) Kaafarani, B. R.; *Chem. Mater*. **2011**, *23*, 378; c) Sergeyev, S.; Pisula, W.; Geerts Y. H.; *Chem. Soc. Rev*. **2007**, *36*, 1902 d) Wöhrle, T.; Wurzbach, I.; Kirres, J.; Kostidou, A.; Kapernaum, N.; Litterscheidt, J.; Haenle, J. C.; Staffeld, P.; Baro, A.; Giesselmann, F.; Laschat s.; *Chem. Reviews* **2016** DOI: 10.1021/acs.chemrev.5b00190.

[10] Talarico, M.; Termine, R.; García-Frutos, E. M.; Omenat, A.; Serrano, J. L.; Gómez-Lor, B.; Golemme, A.; *Chem. Mater*. **2008**, 20, 6589.

[11] García-Frutos, E. M.; Pandey, U. K.; Termine, R.; Omenat, A.; Barberá, J.; Serrano, J. L.; Golemme, A.; Gómez-Lor, B.; *Angew. Chem. Int. Ed.* **2011**, 50, 7399.

[12] Benito-Hernández, A.; Pandey, U. K.; Cavero, E.; Termine, R.; García-Frutos, E. M.; Serrano, J. L.; Golemme, A.; Gómez-Lor, B.; *Chem. Mater*. **2012**, 25, 117.

[13] a) The CH/π interaction. Evidence, Nature and Consequences, Nishio, M., Hirota, Y., Umezawa, Ed.; Wiley-VCH, New York, **1998**. b) Nishio, M. *CrystEngComm*. **2004**, 6, 130.

1.2.3. MATERIALS AND METHODS

SEM Characterization. Scanning electron microscopy (SEM) images were obtained on a Nova NanoSEM 230 FEI field-emission scanning electron microscope with a vCD detector operating at low pressure with an accelerating voltage of 5 kV.

X-ray structure. A colorless crystal of **1c** showing well defined faces were mounted on a Bruker Smart CCD diffractometer equipped with a normal focus, 2.4 kW sealed-tube X-ray source (MoKα radiation, λ=0.71067 Å) operating at 50 kV and 30 mA. Data were collected over a hemisphere of the reciprocal space by a combination of three exposure sets. Each exposure of 10 s covered 0.3º in ω over the range 2.5º <θ <28º. The first 100 frames were recollected at the end of the data collection to monitor crystal decay.

A colorless crystal of **1d** showing well defined faces was mounted on a Bruker four circle kappa-diffractometer equipped with a Cu INCOATED microsource, operated at 30 W power (45 kV, 0.60 mA) to generate CuKα radiation (λ = 1.54178 Å), and a Bruker VANTEC 500 area detector (microgap technology). Diffraction data were collected exploring over a hemisphere of the reciprocal space in a combination of φ and ω scans to reach a resolution of 0.86 Å, using a Bruker APEX2[14] software suite (each exposure of 40 s covered 1o in ω or φ).

Unit cell dimensions were determined for least-squares fit of reflections with I > 20σ.

A semi-empirical absorption and scale correction based on equivalent reflection was carried out using SADABS APEX[14]. The structures were solved by direct methods. The final cycles of refinement were carried out by full-matrix least-squares analyses with anisotropic thermal parameters of all non-hydrogen atoms. The hydrogen atoms were fixed at their calculated positions using distances and angle constraints. All calculations were performed using SMART[15] and APEX2[14] software for data collection and for data reduction; SHELXS[16] and SHELXL[17] to resolve and refine the structures using Olex2 GUI[18].

[14] APEX2; Bruker-AXS: Madison, WI, **2006**.
[15] Software for the SMART system, V.5.04, Bruker-Siemens Analytical X-ray Instruments, Inc., Madison, WI, USA, **1998**.
[16] Sheldrick, G. M.; *Acta Cryst.* **2008**, A64, 112.

CCDC 1021612 and CCDC 1446933, contain the supplementary crystallographic data for **1c** and **1d** respectively. These data can be obtained free of charge at www.ccdc.cam.ac.uk/conts/retrieving.html [or from the Cambridge Crystallographic Data Centre, 12, Union Road, Cambridge CB2 1EZ, UK; fax: +44-1223/336-033; e-mail: deposit@ccdc.cam.ac.uk].

1.2.4. RESULTS AND DISCUSSION

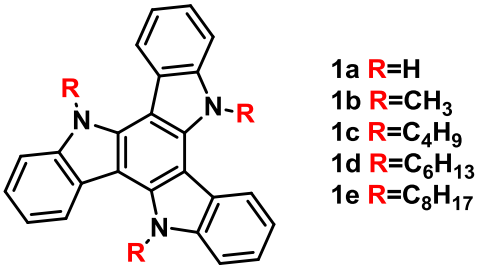

Figure 1. Chemical structure of the triindoles **1a**-**1e** under study.

Compounds **1b**-**1e** can be readily obtained by alkylation of triindole **1a** in the presence of a charge transfer catalyst as it has been previously reported. [19,20,21,22]The length of the alkyl chains do not affect significantly their electronic properties (see SI), all of these derivatives oxidizes readily and reversibly which qualify them as promising candidates for hole injection and transport. However they influence strongly on how these molecules- which have a strong tendency to crystallize- interact with each other. The self-assembly tendencies of these molecules was initially investigated by scanning electron microscopy. Dip-coating of a substrate in a CH_2Cl_2:CH_3CN (1:1) solution of **1b** render highly aligned microwires that can reach a length up to some centimeters long and only a few micrometers of diameter (Figure 1a). As can be observed in the inset of Figure 1a, the wires show a perfect hexagonal cross-section. The formation of crystals of **1c**-**1e** can be readily accomplished by aging a CH_2Cl_2:CH_3CN (1:1) solution of each compound for a

[17] Sheldrick, G. M.; *Acta Cryst.* **2015**, C71, 3.
[18] Dolomanov, O. V., Bourhis, L. J., Gildea, R.J, Howard, J. A. K. & Puschmann, H.; *J. Appl. Cryst.* **2009**, 42, 339.
[19] García-Frutos, E. M.; Gutierrez-Puebla, E.; Monge, M. A.; Ramírez, R.; Andrés, P. d.; Andrés, A. D.; Ramírez, R.; Gómez-Lor, B. *Org. Electron.* **2009**, 10, 643.
[20] Yuan, M. -S.; Li, T. -B.; Wang, W. -J.; Du, Z. -T.; Wang, J. -R.; Fang, Q.; *Spectrochim. Acta Mol. Biomol. Spectrosc.* **2012**, *96*, 1020.
[21] Lai, W. -Y.; He, Q. -Y.; Zhu, R.; Chen, Q. -Q. Huang W.; *Adv. Funct. Mater.* **2008**, *18*, 265.
[22] Gallego-Gómez, F.; García-Frutos, E. M.; Villalvilla, J. M.; Quintana, J. A.; Gutierrez-Puebla, E.; Monge, A.; Díaz-García, M. A.; Gómez-Lor, B.; *Adv. Funct. Mater*. **2011**, *21*, 738.

few minutes until a turbidity is clearly observed. The resulting aggregates were deposited on a silicon substrate and visualized by Field Emission Scanning Electron Microscopy (FE-SEM). As can be observed in the Figure 1, all the aggregates have perfectly delimited facets indicative of their crystalline character. X-Ray Powder diffraction experiments of the aggregates show in all cases sharp diffraction peaks confirming that these supramolecular assemblies are crystalline (see Figures S3-S6). The images show that size of the alkyl chains has a dramatic influence in the crystal habit of these compounds: thus while most of these derivatives show a preference to grow into anisotropic shapes forming long crystalline wires (**1b**), microbelts (**1d**) or rods (**1e)**, the tributyl derivative (**1c**) grow as cubes. This trend is reminiscent of the mesomorphic behaviour observed in previously reported liquid crystalline triindoles in which only the tributyl chains prevent the one dimensional self-assembly[12]. Comparative studies between liquid crystals and non-mesogenic crystalline analogues have been previously found useful to shed light on the organizational preferences of mesogens and on the intermolecular forces that gives rise to mesomorphism. [23,24,25]

[23] Wu, D.; Pisula, W.; Enkelmann, V.; Feng, X.; *J. Am. Chem. Soc.* **2009**, 131, 9620.
[24] Nguyen, H. L.; Horton, P. N.; Hursthouse, M. B.; Legon, A. C.; Bruce, D. W.; *J. Am. Chem. Soc.* **2004**, *126*, 16.
[25] Dai, C.; Nguyen, P.; Marder, T. B.; Scott, A. J.; Clegg, W.; Viney, C.; *Chem. Commun*. **1999**, 2493.

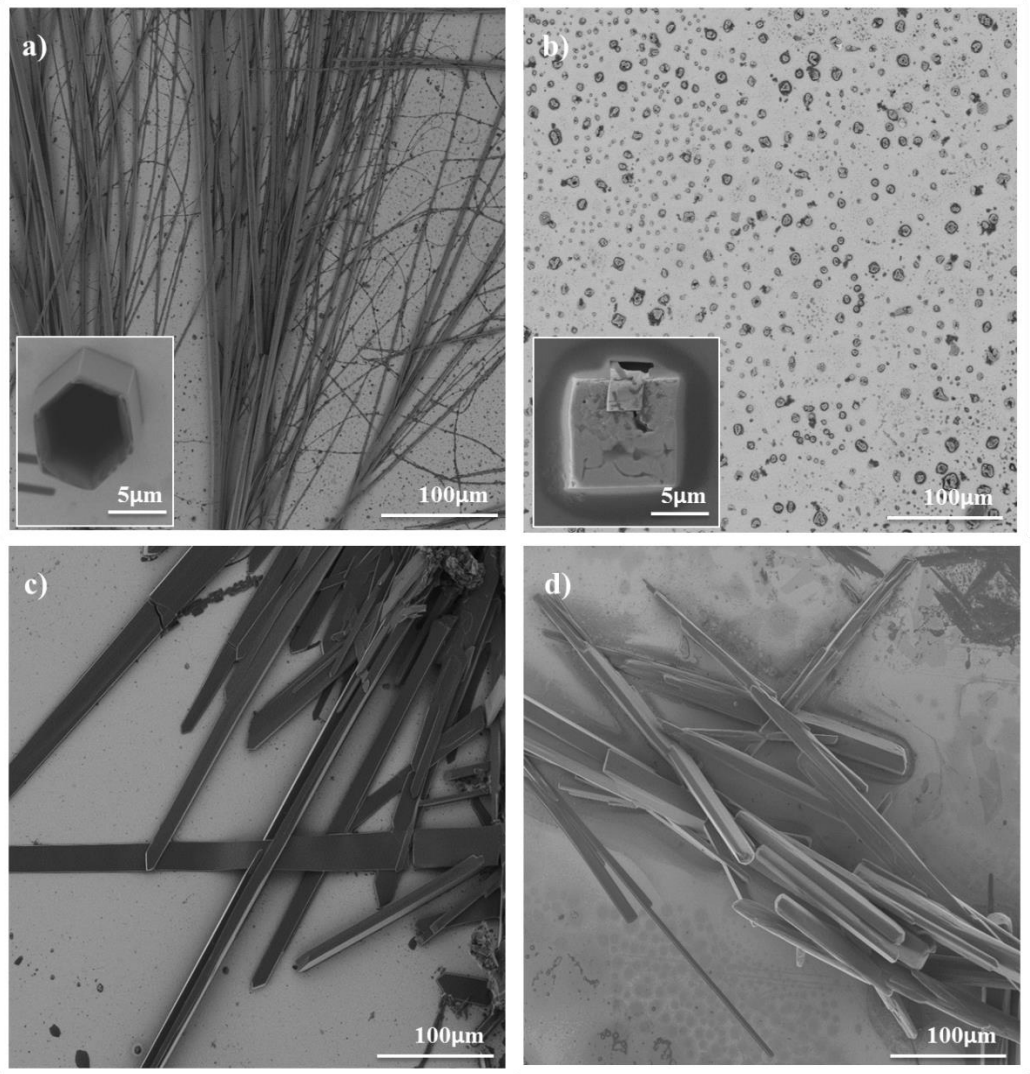

Figure 2. a) Images of the crystalline structures of **1b** (inset: view of the cross section) formed by dip-coating a silicon substrate on a concentrated 1:1 CH_2Cl_2:CH_3CN solution; b) c) and d) Images of the crystalline structures of **1c** (two different amplifications), **1d** and **1e** obtained by ageing a 1:1 CH_2Cl_2:CH_3CN solution of the corresponding compound and deposition of the crystalline material formed on silicon substrate.

In order to gain insight into the origin of these different crystalline habits and macroscopic morphologies, we have obtained crystals with sufficient size for X-ray single crystal analysis of **1c** and **1d** by slow evaporation of 1:1 CH_2Cl_2:CH_3CN solutions of the corresponding compounds and analysed how molecules pack in the crystals. The crystal structures of **1b**[19] and **1e**[22] have been previously reported by us. Simulated powder diffraction patterns of the bulk crystals of **1b**-**1d** match well with those obtained for the aggregates deposited on substrates confirming that they correspond to the same crystal phase. An analysis of the crystal packing shows that compounds **1b**, **1d** and **1e** crystallize as columnar assemblies, favoring the one-dimensional macroscopic growth; in contrast

the tributyl derivative **1c** crystallizes as dimers that pack in a herringbone-like array resulting in no preferred growth direction. To understand the origin of these different packing tendencies we have traced how molecules interact with each other by establishing close contacts in the structures.

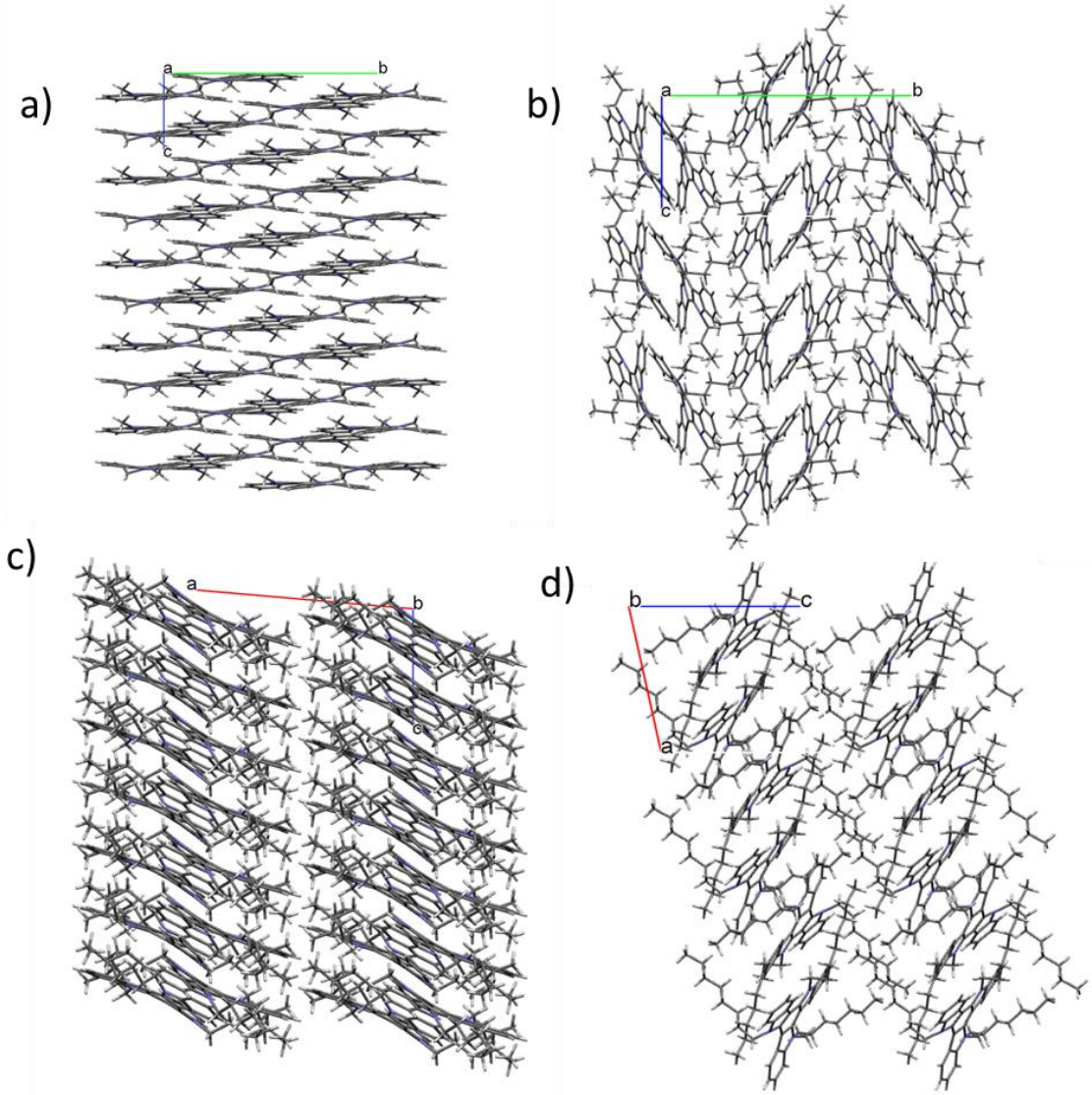

Figure 3. Different crystal packing shown by a) **1b** view along a, b) **1c** view along a, c) **1d** view along b and d) **1e** view along b .

Compound **1b** crystallizes in the $R\bar{3}$ space group with the hexagonal lattice parameters of a = 21.477(6) Å and c= 7.210(3) Å. In the crystals, molecules pack forming stacks along the crystallographic c-axis (Figure 1) which is coincident with the longest dimension of the crystal. The molecules are oriented face-to-face in an alternate arrangement; one molecule rotated 60 degrees with respect to the next molecular unit, being the central aromatic rings perfectly superimposable. Due to this rotation each

methyl group is involved in CH-π interactions with the aromatic rings that lie above and below it. Figure 3a depicts the unique interactions of **1b** (contact distances between the hydrogen of the methyl group and the centroid of the external ring: 2.935 Å and 2.985Å). As the molecule has C_3 symmetry with the centroid of the central aromatic ring situated in the threefold axis, all the methyl groups in the crystal are involved in CH-π interactions stabilizing the columnar arrangement. This network of interactions explains the high tendency of these molecules to crystallize in long wires. It has long been accepted that the growth rate of a facet is directly related to its attachment energy, which is considered as the energy necessary to split a slide of a facet. In this case cooperative interactions can be observed along the [001] direction crossing the most energetic plane.[26] No interaction can be observed which would justify the growth direction of other facets of the crystal.

Compounds **1d** and **1e** crystallize in the P-1 and P2(1)/c space group respectively. Both compounds crystallize also into columns that grow along a preferred direction. In this case molecules are not parallel but tilted with respect to the column axis (which coincide with the *c* and *a* axis respectively) and translated with respect to their neighbors in the column. An analysis of the close contacts in the crystal suggests that again multiple CH-π interactions are responsible of the packing and final morphology of the crystals as intermolecular interactions are only detected along the column while no interaction between the different stacks can be traced.

By elongating the chain, we increase the number of potential CH-π donors resulting in the observed columnar slipped arrangement. In the crystals of these two compounds, several CH hydrogen atoms of one alkyl chain of each molecular component are interacting with different 5 and 6 membered rings of the heptacyclic platform located below it, while several CH hydrogen atoms of other alkyl chain is involved in different CH-π interactions with the molecule placed above it (Figure 3b and 3c). Thus in the crystals of compound **1e**, each molecule is showing contact distances of 2.820 Å, 2.810 Å, 2.713 Å and 2.774Å with the molecule above and 2.599 Å and 3.049 Å with its next neighbor below, while compound **1d** each molecule show short contacts of 2.885Å and 2.899 Å with the molecule above and 2.837 Å and 2.796Å with its next neighbor below.

[26] a) Bacchi, A.; Cantoni, G.; Cremona, D.; Pelagatti, P.; Ugozzoli, F.; *Angew. Chem. Int. Ed.* **2011**, *50*, 3198. b) Massaro, F. R.; Moret, M.; Bruno; M.; Aquilano, D.; *Cryst. Growth Des.* **2013**, *13*, 1334. c) Hartman, P; Bennema, P.; *J. Cryst. Growth* **1980**, *49*, 145.

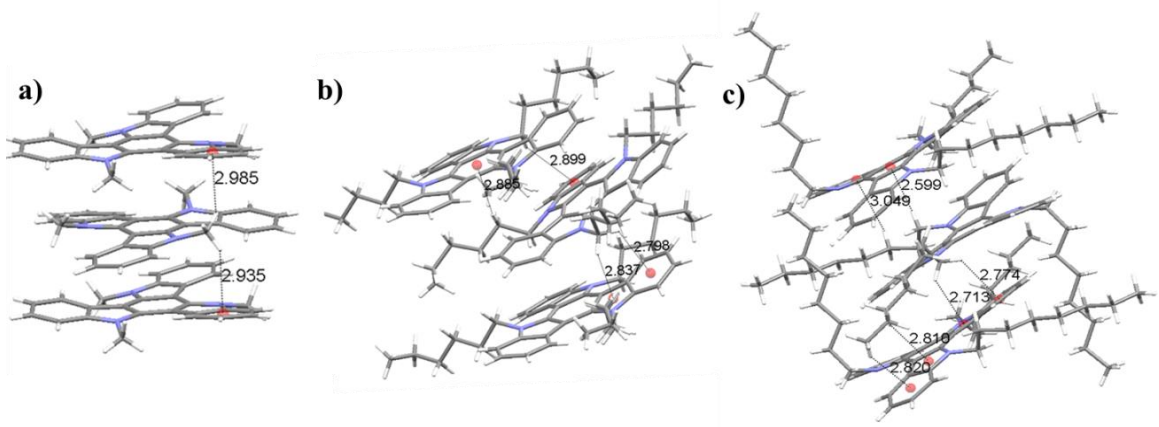

Figure 4. Depiction of the intermolecular CH-π interactions that stabilizes the arrangement into columns of (a) **1b**, (b) **1d** and (c) **1e**. Only unique interactions are shown, but the packing is stabilized by a number of additional interactions related by crystal symmetry. (Ring centroids are represented as red balls).

Table 1. Selected crystallographic data of **1b-1d**.

Parameters	**1b**	**1c**	**1d**	**1e**
Formula	$C_{27}H_{21}N_3$	$C_{36}H_{39}N_3$	$C_{42}H_{51}N_3$	$C_{48}H_{63}N_3$
Crystal System	Hexagonal	Monoclinic	Monoclinic	Triclinic
Space group	$R\bar{3}$	P2(1)/c	P2(1)/c	P-1
***a* (Å)**	21.477(6)	13.1045(14)	15.3638(19)	12.181(2)
***b* (Å)**	21.477(6)	21.445(2)	26.471(3)	12.617(3)
***c* (Å)**	7.210(3)	10.3406(11)	8.4581(8)	14.509(3)
***α* (deg)**	90.00	90.00	90.00	70.355(3)
***β* (deg)**	90.00	90.654(2)	94.961(7)	74.237(3)
***γ* (deg)**	120.00	90.00	90.00	77.492(3)
Volume (Å^3)	2879.9(17)	2905.8(5)	3427.0(7)	2001.7(7)
Z	6	4	4	2
ranges of *h,k,l*	$-21 \le h \le 9$ $-19 \le k \le 21$ $-6 \le l \le 7$	$-17 \le h \le 17$ $-27 \le k \le 27$ $-13 \le l \le 13$	$17 \le h \le 17$ $-29 \le k \le 29$ $-3 \le l \le 7$	$-16 \le h \le 16$ $-17 \le k \le 16$ $-19 \le l \le 19$
ranges of *θ*	$1.90 \le \theta \le$ 20.79	$2.45 \le \theta \le$ 28.00	$2.89 \le \theta \le$ 61.60	$1.73 \le \theta \le$ 29.04
Reflns total	656	5569	4731	7839
Reflns gt	452	2953	3015	4288
R factor all	0.1308	0.2420	0.2819	0.1450
R factor gt	0.0864	0.1192	0.0840	0.0762

Compound **1c** crystallize in space group P2(1)/c with the unit cell dimensions of *a* =13.1045(14) **Å**, *b* = 21.445(2) **Å**, *c* =10.3406(11) **Å**, *α* =90.00º, *β* =90.654(2)º, *γ* =90.00º.

In contrast to the other three derivatives this compound grows as cube-like crystalline prisms. Molecules arrange in the crystal as dimers that pack in a herringbone-like array. The different packing tendency exhibited by **1c**, can be also ascribed to the cooperation of a number of CH-π interactions. An analysis of the close contacts in its crystal packing evidences that each molecule is interacting with the other component of the dimer (contact distances: 2.621 Å and 2.981 Å) but is also with molecules of two adjacent dimers (contact distances: 2.714 Å) placed in planes above and below. These results in a 3D network of interactions which would explain the different morphologies observed (Figure 4).

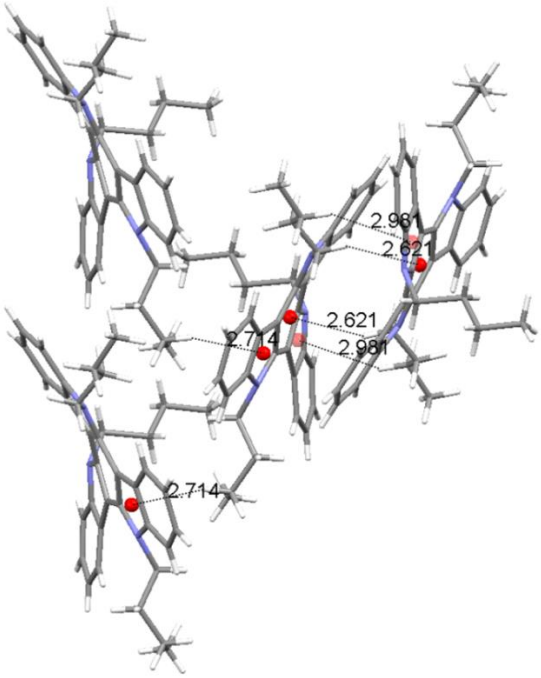

Figure 5. Depiction of the intermolecular CH-π interactions established between the molecules of **1c** within the dimers and among neighboring dimers (ring centroids are represented as red balls).

1.2.5. CONCLUSIONS

In conclusion, the relationship between the length of the *N*-alkyl chains and organization preferences of a series of *N*-trialkyl triindoles has been investigated. We have found that the size of the alkyl chains attached to the three nitrogens of this semiconducting platform, has a strong influence in the morphology of laterally

unsubstituted crystalline *N*-trialkyl triindoles. A study of the crystalline packing of compounds **1b**-**1e**, allowed us to demonstrate that behind the different crystalline habits and macroscopic morphologies observed is the way in which molecules pack in the crystals and interacts with their nearest neighbors allowing us to establish interesting parallelism with triindole based liquid crystalline mesophases. The results of this study suggest that the influence of the length of the *N*-alkyl chains in the one dimensional assembly of triindoles is non-innocent and point towards cooperative CH-π interactions in the origin of the different superstructures observed. The recognition of such interactions is a prerequisite for obtaining well defined arrangements, relevant for their electronic applications.

1.3. ELECTRONIC APPLICATIONS OF *N*-ALKYL TRINDOLS

Our research group has previously found that single crystals of *N*-trimethyltriindole exhibits high hole mobilities values (up to μ = 0,4 $cm^2V^{-1}s^{-1}$) as determined by SCLC. This compound combines intrinsic electron donor properties with a highly ordered columnar packing that paves the way for increased charge carrier mobility due to favorable intermolecular π-orbitals overlap.[27] Recently, this compound could be incorporated as a vaporized thin film in a field effect transistor, showing a mobility value around $3x10^{-2}$ $cm^2V^{-1}s^{-1}$.[28]

With these precedents in mind and by studying the crystal packing of the different trialkylated triindoles we have selected the *N*-trihexyltriindole as the best candidate to be incorporated into field effect transistor. This molecule has a columnar organization whose distances between neighboring molecules are even lower than those found in *N*-trimethyltriindole, as shown in the previous section.

In order to estimate the charge carrier mobilities of this compound, in this work, field effect transistors with a vacuum-deposited active layer in a standard bottom gate-top contact were fabricated. First, the gate/dielectric substrates (Si/300 nm SiO_2) were cleaned in an ultrasonic bath with acetone, hexane and ethanol previous to drying under a flow of nitrogen. Next, the surface was functionalized with a self-assembled monolayer of hexamethyldisilazane (HMDS) to minimize interfacial trapping sites[29]. Then, thin films of *N*-trihexyltriindole were prepared by slow sublimation in vacuum condition. Finally, 30 nm gold source and drain electrodes were thermal evaporated through a shadow mask. Devices were tested under vacuum by using an Agilent B1500 semiconductor parameter analyzer and a customized vacuum probe station.

Simulated powder diffraction patterns of the bulk crystals of *N*-trihexyltriindole match well with those obtained for the thin film deposited on substrates, as determined by grazing incidence X-ray diffraction (GIXRD), which indicates that both correspond to the same crystalline phase. As shown in Figure 1.1, only the peak indexed as (*100*) can be observed in the thin film, which indicates a highly aligned crystalline film with the columns parallel to the surface.

[27] García-Frutos, E. M.; Gutierrez-Puebla, E.; Monge, M. A.; Ramírez, R.; de Andrés, P.; de Andrés, A.; Ramírez, R.; Gómez-Lor, B.; *Org. Electr.* **2009**, 10, 643–652.
[28] Reig, M.; Puigdollers, J.; Velasco, D.; *J. Mater. Chem. C.* **2015**, 3, 506.
[29] Yoon, M. -H.; Kim, C.; Facchetti, A.; Marks, T.J.; *J. Am. Chem. Soc*. **2006**, 128, 12851.

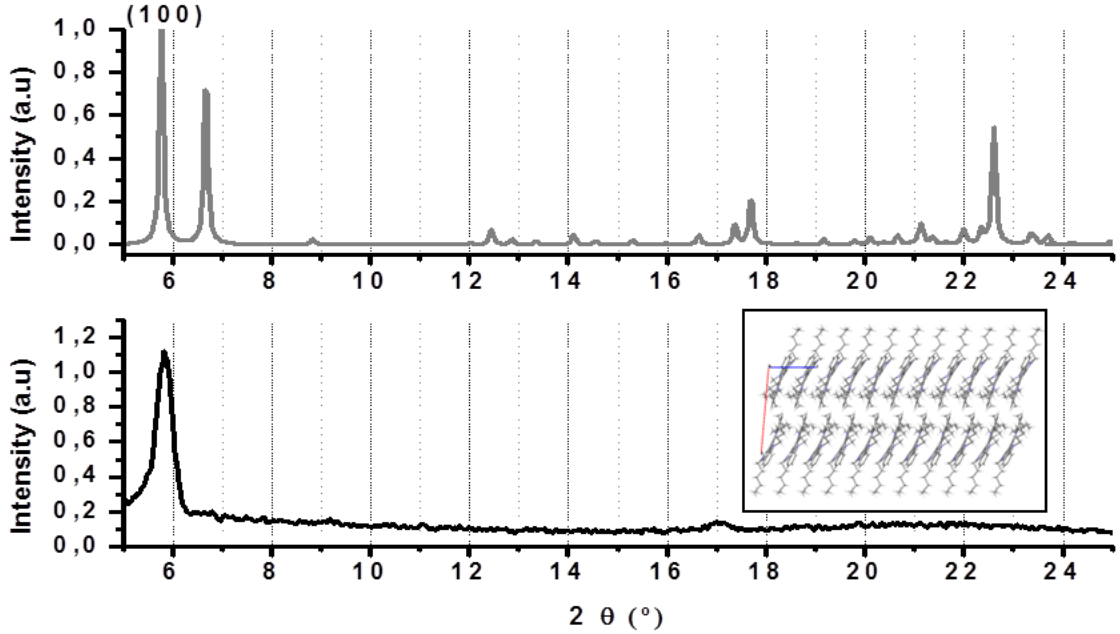

Figure 1.1: Powder X-ray diffractograms obtained from the single crystal data (above) and the experimental GIXRD of *N*-trihexyltriindole deposited by slow sublimation in vacuum condition (below). The inset images show the molecular packing in the thin films, with the plane (100) that indicate the orientation of the molecules parallel to the substrate.

Figure 1.2a shows the transfer characteristics of *N*-hexyltriindole measured at a fixed source-drain voltage of -80 V. Charge transport evaluation was carried out *via* analysis of the OFET current-voltage response in the saturation regime with the hypothesis of conventional transistors theory, following eqn:

$$I_D = \frac{WC_{ox}\mu}{2L}(V_G - V_{th})^2$$

Where W and L are the channel width and length, respectively, C_{ox} is the capacitance per unit area of the dielectric layer, μ is the hole mobility and V_{th} is the threshold voltage. A mobility of 1.42 x 10^{-2} $cm^2V^{-1}s^{-1}$with a threshold voltage close to -12 V could be determined with this technique.

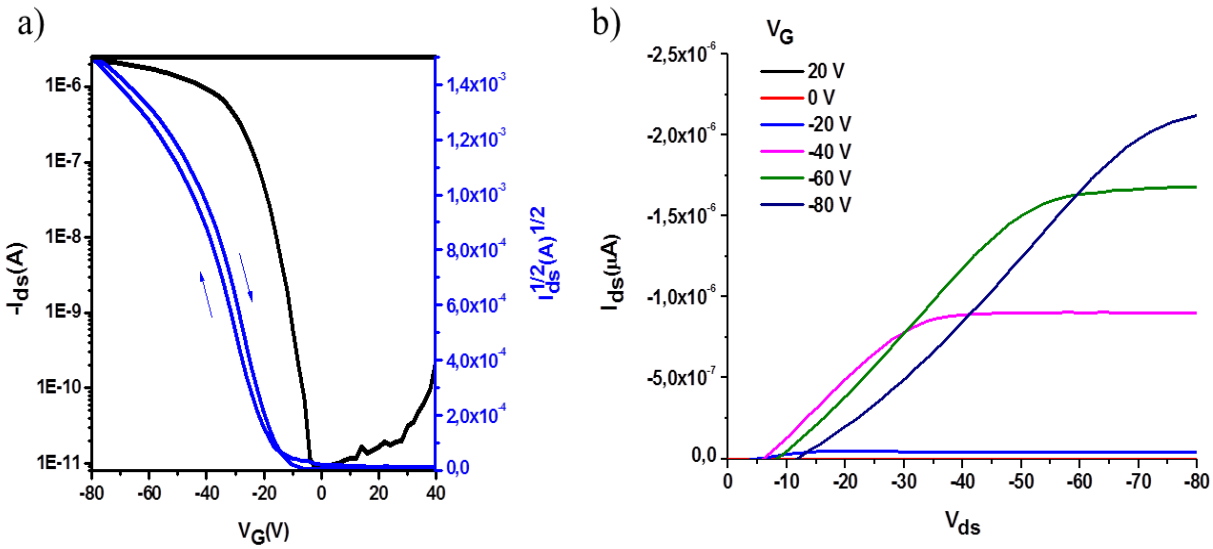

Figure 1.2. a) Transfer characteristics of *N*-hexyltriindole measured at a source-drain voltage of -80 V. b) Out-put curves of *N*-hexyltriindole measured at gate voltages from 0 to -80 V in intervals of 20 V.

Figure 1.2b represents the output curves of *N*-trihexyltriindole measured at gate voltages from 0 to -80 V in intervals of 20 V. It seems that the contact resistance of the device is not at a fixed state. One possibility is that when the V_G is lower, the contact resistance of the device is lower, which result in higher current in output curve when the V_{ds} is around -10 V ~-30 V. This problem needs further study.

In conclusion, in this work we present how through an adequate functionalization we can modulate both the intermolecular interactions and the crystallographic packing of this aromatic platform towards its incorporation in OFEts. The application of *N*-trihexyltriindole into OFET devices, confirm triindole-based molecules as promising hole transport materials.

Chapter 2. Modulation of optical properties

2. CHAPTER 2. MODULATION OF OPTICAL PROPERTIES

2.1. SUMMARY

The target of this work is the tuning of the light-emitting properties and HOMO–LUMO levels of the triindole platform, by changing the nature of the functionalization in the periphery with the aim of incorporating them in OLEDs. Device fabrication and electrical measurements on three representative triindole derivatives have been performed in collaboration with Dr. Carmen Coya and her team at the Rey Juan Carlos University in Madrid.

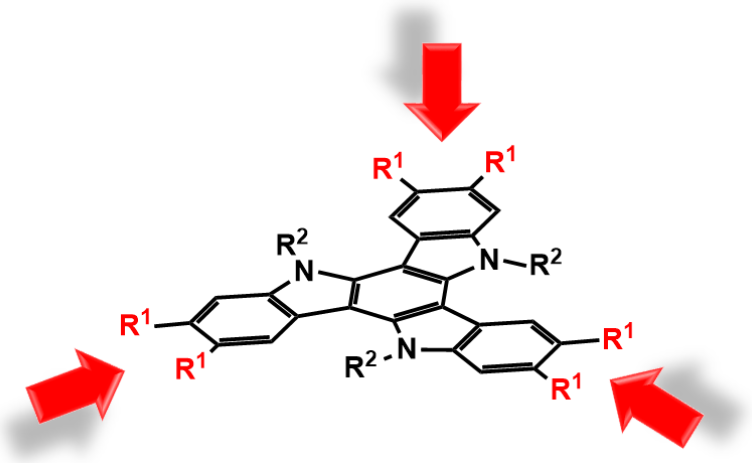

Taking advantage the chemical versatility of this platform we have alkylated the nitrogen positions with three dodecyl chains intended to induce solubility, and introduced six peripheral bulky aryl groups that impede crystallization and therefore facilitates the formation of homogeneous films necessary for good device performance. Peripheral substitution is easily achieved starting from known hexabromine triindol by means of six-fold Suzuki cross coupling with different boronic acids in the key step.

In this work, we show how the electronic communication of the external substituents with the central electron-rich triindole facilitates the tuning of the light-emitting properties and HOMO–LUMO levels. The electrochemical influence of the six peripheral groups has been studied by cyclic voltammetry, which shows that the oxidazibility of these molecules varies in agreement with the nature of the peripheral substituents. Thus, attaching electrondonating groups results in an increase of the electron density in the π system and in consequence in a shift of the oxidation potentials to lower

values. In contrast, upon attaching peripheral electron-withdrawing groups the oxidation potentials shifts anodically as increasing the acceptor character of the substituents. The modulation of the properties, by changing the nature of the peripheral groups, is also clearly reflected in their absorption and emission spectra, that show significant bathochromic shifts as the acceptor character of the peripheral groups increases. The dramatic influence that peripheral substituents exert on the electronic properties of these derivatives offers a great opportunity to modulate their energy levels by chemical functionalization. Considering that organic electronic devices are usually constructed using multilayer architectures this possibility will be fundamental to facilitate charge injection from electrodes and minimize energy barriers between the different layers.

On the other hand, and in order to broaden the synthetic versatility of this heptacyclic aromatic molecule, we have synthesized a series of monoaryltriindoles and study the effect that asymmetrical substitution has in the electronic properties of this semiconducting platform. Results show that asymmetrical derivatives offer significant advantages in terms of energy levels tailoring, and present higher quantum yields and increased range of emission spectra, when compared to their symmetrical counterparts.

2.2. STAR-SHAPED HEXAARYLTRIINDOLES SMALL MOLECULES: TUNING MOLECULAR PROPERTIES TOWARDS SOLUTION PROCESSED ORGANIC LIGHT EMITTING DEVICES

Carmen Coya [a,*], Constanza Ruiz [b], Ángel Luis Álvarez [a], Susana Álvarez-García [a,c], Eva M. García-Frutos [b], Berta Gómez-Lor [b,*], Alicia de Andrés [b,*]

a. Escuela Superior de Ciencias Experimentales y Tecnología, Electronic Technology Department, Universidad Rey Juan Carlos, 28933 Madrid, Spain
b. Instituto de Ciencia de Materiales de Madrid, Cantoblanco, 28049 Madrid, Spain
c. Instituto Química-Física Rocasolano, CSIC, C/Serrano 119, 28006 Madrid, Spain

Organic Electronics 13 (2012) 2138–2148

2.2.1. ABSTRACT

We present a series of differently substituted star-shaped hexaaryltriindoles with tunable light-emitting properties. The deep blue emission is unchanged by donor peripheral substituents while an increasing acceptor character produces a reduction of the optical gap, an increased Stokes shift and eventually leads to the appearance of a new electronic level and to the simultaneous deep blue (413 nm) and green (552 nm) emission in solution. Quenching by concentration increases with the acceptor character but is lower as the tendency of these compounds to aggregate is stronger. Solution processed thin films present optical and morphological qualities adequate for device fabrication and similar electronic structure compared to solutions with an emission range from 423 nm (blue) up to 657 nm (red), demonstrating the possibility of tuning the energy levels by chemical functionalization.

We have fabricated and characterized single-layer solution processed organic light emitting diodes (OLED) to investigate the influence on transport and emission properties of the substituting species. We analyzed the I–V response using a single-carrier numerical model that includes injection barriers and non-uniform electric-field across the layer. As a result, we obtained the electric field dependence of the mobility for each device. Best results are obtained on the most electron rich derivative functionalized with six donor methoxy groups. This material shows the highest emission efficiency in solid state, due to aggregation-induced enhancement, and better transport properties with the highest mobility and a very low turn-on voltage of 2.8 V. The solution processed OLED devices

produce stable deep blue (CIE coordinates (0.16, 0.16)) to white (CIE coordinates (0.33, 0.3)) emission with similar luminous efficiencies.

2.2.2. INTRODUCTION

In recent years an intense research effort has facilitated that a new generation of devices based on organic materials enters the market. Organic semiconductors offer great expectations in the development of low-cost, flexible and large area devices (properties difficult to achieve with conventional electronics) but also the possibility of fine tuning key properties (luminescence, absorption, energy band gaps, and charge transport) through a convenient molecular design.

A wide variety of polymers and small molecule organic semiconductors have been developed and investigated in devices such as organic thin-film transistors (OTFTs), organic photovoltaic cells (OPVs), and organic light-emitting diodes (OLEDs).

Amenability to solution or wet processing, is an inevitable prerequisite for large area, low cost mass production, and must be taken into consideration when designing molecules for organic active layers[1]. Conjugated polymers, usually amorphous materials can be easily processed from solution to yield homogeneous and uniform thin films, ideally suited for optoelectronics. However, small molecule semiconductors offer intrinsic advantages over polymeric materials in terms of ease of synthesis and purification. Owing to their mono disperse nature with well-defined chemical structure, they can be reproducibly prepared, functionalized and purified and batch-to batch variations common in polymeric materials are not a problem. These considerations make small molecules ideal candidates for structure-properties studies.

Incorporation of flexible alkyl chains is a useful strategy for enhancing the solubility of small molecules, facilitating wet processing. On the other hand, incorporation of bulky substituents able to promote various conformers, have successfully prevented easy packing of the molecules and hence ready crystallization resulting in excellent film forming abilities and morphological stability in properly designed molecules. We have recently became interested in new organic semiconductor, the electron-rich 10, 15- dihydro-5H-diindolo[3,2-a:3’,2’-c]carbazole (triindole).

[1] Duan, L.; Hou, L.; Lee, T. W; Qiao, J.; Zhang, D.; Dong, G.; Wang, L.; Qiu, Y. J.; *J. Mater. Chem.* **2010**, 20, 6392.

Triindole-based single crystalline[2] or liquid crystalline materials have been found to exhibit high hole mobilities [3, 4] since they combine the good hole transport properties of carbazoles with a high tendency to form columnar supramolecular arrangements owing to their disk-like extended π-surface. Devices, such as OFETs[5] and OLEDs [6] have been fabricated using triindole-based semiconductors.

In addition, this platform provides two different locations for structural modification, essential to tailor electronic and self-assembling properties. Nitrogen can be easily N-substituted, while starting from known hexabromine triindol, the exploitation of cross-coupling methodologies opens flexible strategies to various functionalizations.

Taking advantage of this chemical versatility we have introduced in this platform flexible N-alkyl chains intended to induce solubility (long alkylic chains) and peripheral bulky aryl groups that impede crystallization [7] to render a family of star-shaped hexaaryl triindoles that can be easily processed from solution to give good film-forming properties. A study of the electronic character of the peripheral substituents on the self-association behavior in these series indicates that the electron-donating character of the terminal substituents facilitates self-association while electron withdrawing groups inhibit aggregation in agreement with important contributions of solvophobic and CH-π interactions in the self-assembly process. In fact attaching six strong donor methoxy groups result in a material that is liquid crystals in a broad range of temperature[8].

In this work, we show how the electronic communication of the external substituents with the central electron-rich triindole facilitates the tuning of the light-emitting properties and HOMO–LUMO levels. We study these small molecular materials in amorphous thin film morphology and we report emission and transport properties of solution processed OLEDs based on three representative triindole derivatives. The fabricated OLEDs have simple structure: glass/ indium-tin oxide (ITO)/ poly(3,4 ethylenedioxythiophene)- poly(styrenesulfonate) (PEDOT:PSS)/active layer/Ca/Al. The

[2] García-Frutos, E. M.; Gutierrez-Puebla, E; Monge, M. A.; Ramírez, R.; de Andrés, P.; de Andrés, A.; Ramírez, R.; Gómez-Lor, B.; *Org. Electron.* **2009**,10, 643.
[3] Talarico, M.; Termine, R.; García-Frutos, E. M.; Omenat, A.; Serrano, J. L.; Gómez-Lor, B.; Golemme, A.; *Chem. Mater.* **2008**, 20, 6589.
[4] García-Frutos, E. M.; Pandey, U. K.; Termine, R.; Omenat, A.; Barberá, J.; Serrano, J. L.; Golemme, A.; Gómez-Lor, B.; *Angew Chem. Int. Ed. Engl*. **2011**, 50, 7399.
[5] Valentine, R. A.; Whyte, A.; Awaga, K.; Robertson, N.; *Tetrahedron Lett*. **2012**, 53, 657.
[6] Lai, W. Y.; He, Q.Y.; Zhu, R.; Chen, Q. Q.; Huang, W.; *Adv. Funct. Mater*. **2008**, 18, 265.
[7] García-Frutos, E. M.; Hennrich, G.; Gutierrez, E.; Monge, A.; Gómez- Lor, B.; *J. Org. Chem.* **2010**, 75, 1070.
[8] García-Frutos, E. M.; Omenat, A.; Barberá, J.; Serrano, J. L.; Gómez-Lor, B.; *J. Mater. Chem*. **2011**, 21, 6831.

devices allow us to study the current–voltage (I–V) response using a numerical model that includes field dependent carrier mobility under a single carrier approach. The mobility dependence with electric field and the electroluminescence (EL) performance is discussed.

2.2.3. EXPERIMENTAL

Synthesis and characterization of 2,3,7,8,12,13-Hexakis- (p-formylphenyl)-5,10,15-tris-(dodecyl)-10,15-dihydro-5Hdiindolo[3,2-a:30,20-c]carbazole (1e). A mixture of N-dodecylhexabromotriindole [9] (100 mg, 0.075 mmol), $Pd(PPh_3)_4$ (43 mg, 0.037 mmol), 4-formylphenyl boronic acid (136 mg, 0.907 mmol) in 0.5 mL of 2 M aqueous K_2CO_3 and 4 mL of THF was degassed. The mixture was heated at 90 ºC for 4 days under nitrogen. The orange suspension was partitioned between H_2O and CH_2Cl_2, and the organic phase dried ($MgSO_4$). The solvent was evaporated and the residue was precipitated with acetone and acetonitrile to give **1e** as a yellow solid (78 mg, 70%): mp:173–176 ºC, ^{1}H NMR (200 MHz, $CDCl_3$) d 10.02 (s, 6H), 8.37 (s, 3H), 7.82 (d, J = 8.0, 12H), 7.68 (s, 3H), 7.46 (d, J = 8.0, 12H), 4.99 (m, 6H), 2.10 (m, 6H), 1.05 (m, 54H), 0.85 (t, J = 6.7, 9H); ^{13}C NMR (50 MHz, $CDCl_3$) d 191.8, 191.7, 148.7, 148.10, 140.8, 140.0, 134.8, 134.6, 134.4, 132.0, 131.0, 130.8, 129.6, 123.6, 123.2, 112.2, 103.2, 47.4, 31.8, 30.3, 29.6, 29.5, 29.4, 29.3, 26.7, 22.6, 14.1; UV (CH2Cl2, 25_C) kmax (loge) 361 (4.99); MALDITOF MS m/z 1475 (M+); HRMS (MALDI-TOF) calcd. For $C_{102}H_{111}N_3O_6$: 1473.84674, found: 1473.84387.

Synthesis and characterization of 2,3,7,8,12,13-Hexakis- (p-dicyanomethyl)-5,10,15-tris-(dodecyl)-10,15-dihydro-5Hdiindolo[3,2-a:30,20-c]carbazole (1f). To a mixture of **1e** (100 mg, 0.067 mmol), malononitrile (53.5 mg, 0.435 mmol), pyridine (0.13 mL, 1.62 mmol) and CH_2Cl_2 (20 mL), titanium (IV) chloride (0.11 mL, 0.81 mmol) was added. The mixture reaction mixture was stirred overnight at room temperature. The suspension was partitioned between H_2O and CH_2Cl_2, and the organic phase dried ($MgSO_4$). The solvent was evaporated and the residue was washed with MeOH to yield **1f** as a red solid (87 mg, 74%): ^{1}H NMR (200 MHz, $CDCl_3$) d 8.35 (s, 6H),7.89 (d, J = 7.5H, 12H,), 7.69 (s, 3H), 7.48 (s, 3H), 7.46 (d, J = 7.5H, 12H), 5.00 (m, 6H), 2,08 (m, 6H), 1,21(m, 54H)., ^{13}C NMR (50 MHz, $CDCl_3$) d 158.9, 153.6, 148.8, 148.1, 141.0, 140.3,

[9] García-Frutos, E. M.; Gómez-Lor, B.; *J. Am. Chem. Soc.* **2008**,190, 9173.

134.3,131.38, 130.8, 129.5, 129.2, 123.9, 123.6, 113.7, 112.8, 112.5, 103.3, 82.5, 82.3,47.4, 31.9, 29.6, 29.3, 26.7, 22.6, 14.1, UV (CH_2Cl_2, 25ºC) kmax (log e) 230 (5.25), 338 (5.55), 434 (5.24); MALDI-TOF MS m/z 1763 (M+); HRMS (MALDI-TOF) calcd. for $C_{102}H_{111}N_3O_6$: 1762.9173, found: 1762.9134.

- **Optical measurements**

Optical absorption and photoluminescence (PL) spectra of the material in solution and in thin films on quartz substrates have been measured at room temperature. The absorption spectra were recorded with a Varian spectrophotometer model Cary 4000. PL was excited with the 365 nm line of a Hg lamp, and analyzed with a Jobin-Yvon HR 460 monochromator coupled to a N_2 cooled charge coupled device. All the emission spectra have been corrected by the spectral response of the experimental setup. Emission lifetimes were recorder at room temperature exciting with an OPO laser from EKSPLA and an ultra-rapid intensified charge coupled device from Stanford Computer Optics. Spectral radiance and luminance from diodes was recorded with a Konica-Minolta CS-2000 spectroradiometer, in the same excitation conditions (duty cycle) as those used to measure J–V characteristics (duty cycle of 0.2%) using aTTi40 MHz arbitrary waveform generator and a TREK-601C amplifier.

- **Device fabrication**

The structure of the devices are ITO/PEDOT: PSS (50 nm)/ Active layer/Cathode. Pre-patterned ITO glass plates with four circular diodes (1mm and 1.5mm radii) were extensively cleaned, using chemical and UV–ozone methods, just before the deposition of the organic layers. PEDOT: PSS (483095 from Aldrich) was deposited at 2000 rpm by spin-coating and then cured on a hot plate at 110 ºC for 10–15 min. The active layers were deposited by spin coating from chloroform solutions and cured at 50ºC for 30 min on a hot plate. Precursor solutions (10mg/mL) were kept in an ultrasonic bath for 10min and filtered through a 0.2 µm polytetrafluoroethylene (PTFE) syringe filter, prior to be spin coated. We have found that heating the sample just below the solvent boiling point results in an improved film uniformity (highly reflecting surfaces)[10]. The thickness of the layers was measured using an Alpha step 200 profilomenter (Tenkor Instruments). The

[10] Coya, C.; de Andrés, A.; Gómez, R.; Seoane, C.; Segura, J. L.; *J. Lumin*. **2008**, 128,761.

cathode was thermally evaporated in an atmosphere of 8 $x10^{-6}$ Torr on top of the organic layer surface and finally, the structure was encapsulated using a glass cover attached by a bead of epoxy adhesive [EPO-TEK(302-3M)]. All the process was carried out in an inert atmosphere glovebox (<0.1 ppm O_2 and H_2O).

- **Electrical measurements**

The device current–voltage characteristics were measured using a semiconductor parameter analyzer Agilent 4155C and a SMU pulse generator Agilent 41501B. A pulse train was used as input signal. The duty cycle was set to be 0.2%, thus having a pulse width of 0.5 ms for a period of 100 ms. Refresh time between two consecutive pulses ensures long time operation without significant device degradation.

Furthermore, the I–V curve stability was achieved by gradually increasing the pulse amplitude up to the point where reproducible measurements were observed. The voltage range was maintained below the onset for the electroluminescence (EL).

2.2.4. RESULTS AND DISCUSSION

- **Synthesis**

The synthesis of the hexaaryl triindoles **1a**–**1d** Fig. 1 has been previously reported and was achieved using six fold Suzuki coupling of known N-dodecylhexabromotriindole with commercially available boronic acids substituted in para with groups of different electronic character [7]. Using the same cross-coupling conditions **1e** was readily achieved by reaction of N-dodecylhexabromotriindole with (4-formylphenyl) boronic acid. Knoevenagel reaction of **1e** with malononitrile in the presence of $TiCl_4$ gave rise to compound **1f** as a deep red material in good yield.

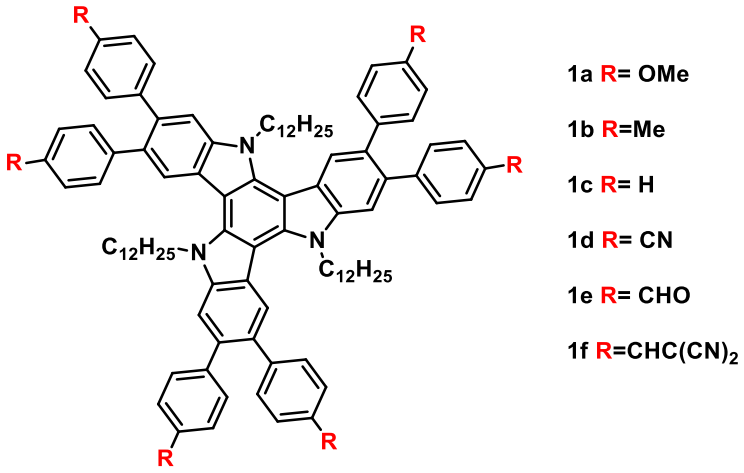

Figure 1. Peripheral functionalization of triindoles.

- **Characterization of the electronic properties of solutions and thin films**

The influence of the six peripheral groups, in the electronic properties of this family of compounds has been studied by cyclic voltammetry (Supporting information).

All the compounds can be easily oxidized to stable radical cations and higher cationic charged species. The oxidazibility of these molecules varies in agreement with the nature of the peripheral substituents. Thus, attaching electrondonating groups results in an increase of the electron density in the π system and in consequence in a shift of the oxidation potentials to lower values. In contrast, upon attaching peripheral electron-withdrawing groups the oxidation potentials shifts anodically as increasing the acceptor character of the substituents. Compound **1f** show also a quasi-reversible reduction wave in the accessible potential window of the solvent (CH_2Cl_2).

The HOMO energy values for these derivatives (Table 1) have been estimated from the first oxidation potential values with respect to ferrocene value of -4.8 eV with respect to zero vacuum level. This value is obtained from the calculated value of -4.6 eV for the standard electrode potential (E^o) using a normal hydrogen electrode (NHE) on the zero vacuum level and the value of 0.2 V for Fc vs. NHE.

The influence of the peripheral groups on the electronic properties of the differently substituted hexaaryltriindoles is also clearly reflected in their absorption and emission spectra. Fig. 2(a) and (b) compare the absorption and the emission spectra obtained at 365 nm excitation of **1a**, **1d**, **1e** and **1f**. Compounds **1a**, **1b** and **1c** present almost identical absorption and emission spectra (shapes and intensities) while **1d** and **1e**

show significant bathochromic shifts as the acceptor character of the peripheral groups increases.

The emission of compound **1f** is very weak (note the factor x20 in Fig. 2(b)) and presents two well separated peaks at 413 and 552 nm (3.0 and 2.25 eV). The molar absorption coefficients are in the order of 105 ($M^{-1}cm^{-1}$) as it corresponds to π–π*transitions[11]. In Fig. 2(c) and (d) we compare the absorption spectra and their second derivatives for **1a** and **1f** compounds in solution and as thin films.

Table 1. Values of HOMO, lowest transition and absorption onset E_g^{onset} (from absorbance) and main photoluminescence energies (E_{PL}) of compounds **1a**–**1f** in solution and in thin films. All data are in eV.

R	Solutions HOMO	Lowest trans.	E_g^{onset}	E_{PL}	Film Lowest trans.	E_g^{onset}	E_{PL}
1a	-5.07	3.17	3.00	3.08, 2.98	3.03	2.64	2.91
1b	-5.12	3.16	3.01	3.08, 2.98	3.07	2.66	2.91
1c	-5.12	3.17	3.03	3.08,2.98	3.09	2.66	2.93
1d	-5.28	3.21	2.66	2.63	3.16	2.50	2.65
1e	-5.32	3.15	2.55	2.32	3.07	2.50	2.56
1f	-5.28	2.80	2.10	3.00, 2.25	2.66	1.96	1.89

Second derivatives of absorbance are useful to evidence the different components of the spectra[12] (minima correspond to absorption maxima and therefore to electronic transitions). In Fig. 2(c), the vertical dashed lines correspond to transitions of **1a** in solution. The five transitions (dashed vertical lines) of lower energy are equidistant in energy (around 151 meV = 1220 cm^{-1}) and correspond to transitions from the ground state (HOMO) to different vibrational states of the first excited state (LUMO) labeled with (0–i) with i = 0 to 4. The lowest transition (0–0) occurs at 3.17 eV while the main absorption peak is at 3.63 eV. This shift (0.46 eV) reveals that the atomic configuration of the excited state is different from that corresponding to the ground state of the molecule. The observation of the vibrational levels allows identifying the 0–0 transition.

The absorption onset (departure from zero in the second derivatives of the absorption spectra) is often used to define the optical gap (3 eV, in this compound) since

[11] Bernard Valeur, Molecular Fluorescence: *Principles an Application*, Wiley-VCH, **2001**.

[12] The second derivative procedure searches for local minima within a smoothed second derivative data stream. These local minima often reveal hidden peaks. This procedure is often used in commercial software for spectroscopy and chromatography analysis.

it is the minimum energy where an optical absorption occurs and corresponds to the transition between the upper and lower edges of the HOMO and LUMO bands, respectively. Since HOMO and LUMO are bands whose width is related to homogeneous but also to inhomogeneous broadening which has different origins as different environments, stacking, inter-molecular coupling, defects, etc., the gap calculated from the absorption onset is not an intrinsic parameter. On the contrary, the energies of the absorption peaks are closer to an intrinsic description of the electronic structure. Strictly speaking, the LUMO should be obtained using the (0–0) transition. Table 1 collects the observed ‘‘lowest transition’’ values, that correspond to the (0–0) transition in **1a** to **1c**, and that we used to obtain an estimation of the LUMO levels shown in Fig. 3(b). Table 1 also collects the optical gap, E_g^{onset}, corresponding to the absorption onset.

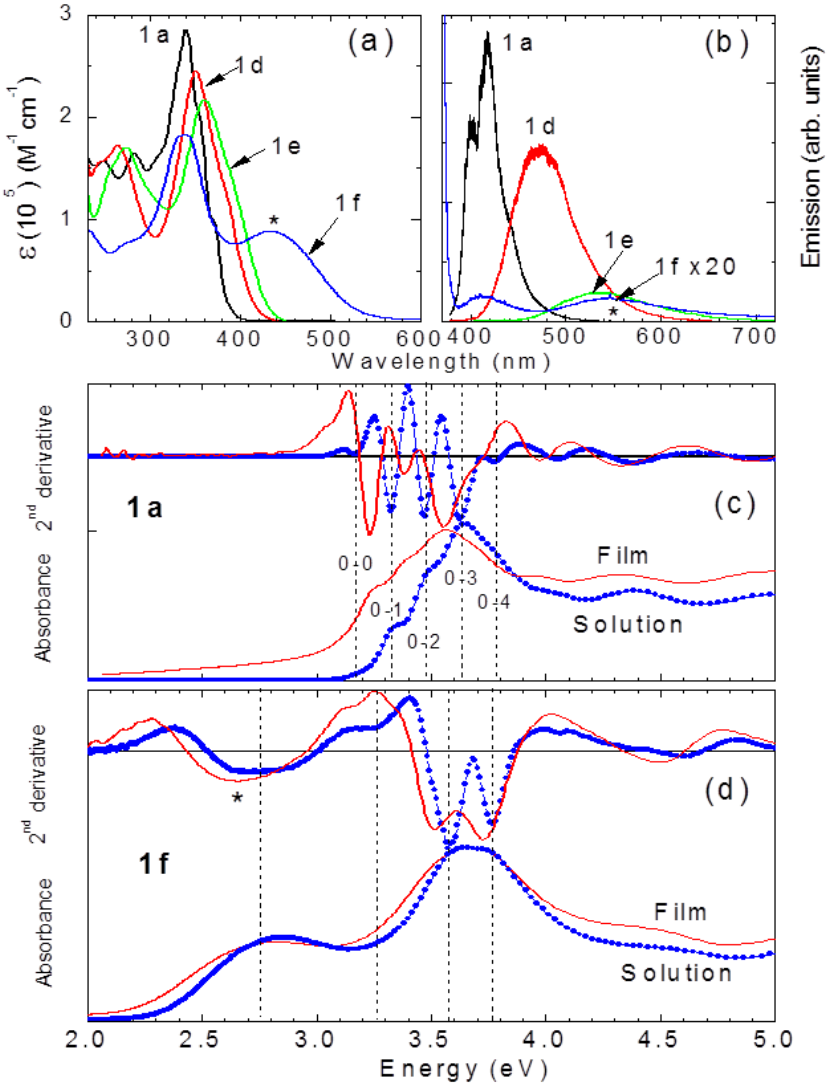

Figure 2. (a) UV–vis spectra (molar absorption coefficients) and (b) photoluminescence spectra (excitation at 365 nm) in CH_2Cl_2 of **1a**, **1d**, **1e** and **1f** (c = 10^{-5} M). (c) and (d) Comparison between absorption spectra and the second derivatives of **1a** (c) and **1f** (d) in solution and in thin film, respectively.

The energy of the main peak (stars) as well as that of the lowest detected transition for the different compounds (rhombi) are plotted in Fig. 3(a). The figure evidences that the energy of the main peak is almost unvaried except for **1d** and **1e** where the coupling to the acceptor groups produces a lowering of the main peak energy and the loss of the vibronic structure. As a result the gap is shifted to lower energies. But only the $CHC(CN)_2$ groups, found in **1f**, which combine a strong acceptor character with an increase of the conjugation, lowers the gap down to about 2.1 eV by means of a new transition (at 2.8 eV, indicated with an asterisk in Fig. 2(a) and a circle in Fig. 3(a)). This new electronic state is most probably related to the electronic density transferred from the core to the peripheral groups giving rise to an octupolar character of the molecule. The progressive loss of the vibrational structure in **1d** and **1e** compounds prevents identifying the (0–0) transition so that the lowest observed transition in these compounds are most probably related to the (0–1) transition.

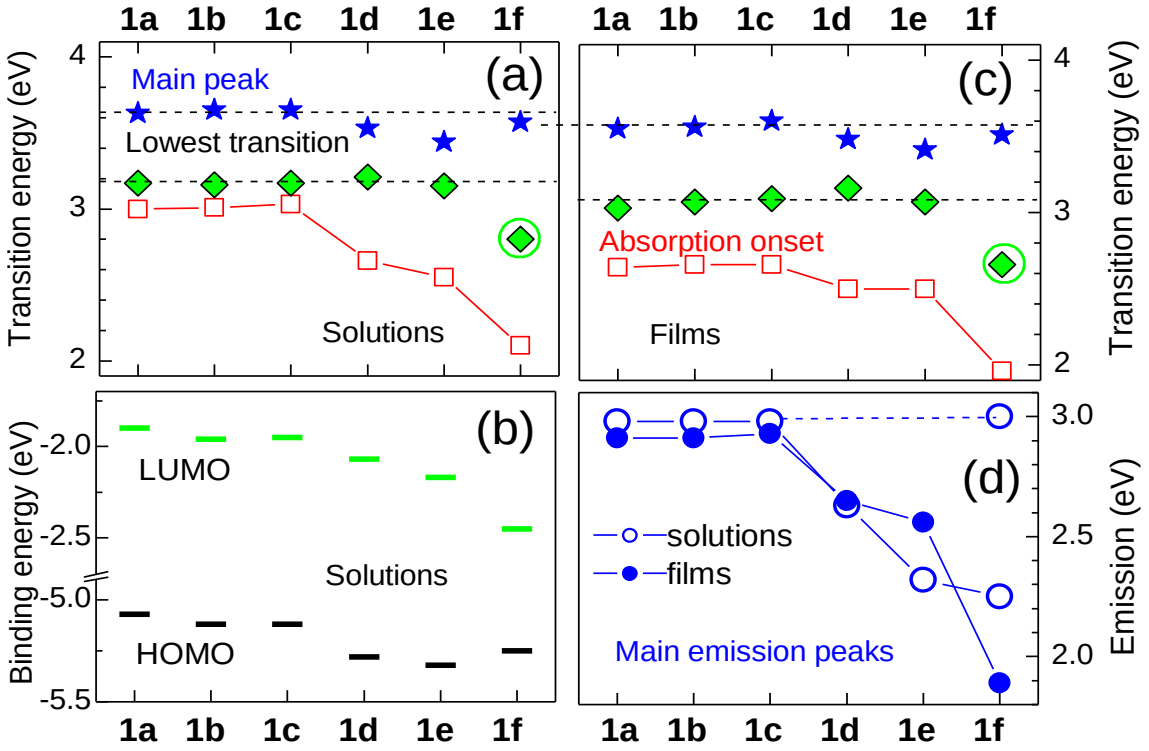

Figure 3. Summary of relevant electronic transitions from absorption spectra in solution (a) and thin films (c), stars: main absorption peak, rhombi: lowest observed transition, open squares: absorption onset. (b) HOMO, from cyclic voltammetry, and LUMO, from the lowest detected transitions, for solutions. (d) Main emission energies in solutions and in thin films for all samples.

The dramatic influence that peripheral substituents of triindoles exert on the electronic properties of these derivatives offers a great opportunity to modulate their optical gap, again demonstrating the possibility of tuning the energy levels of these

derivatives by chemical functionalization. Considering that organic electronic devices are usually constructed using multilayer architectures this possibility will be fundamental to facilitate charge injection from electrodes and minimize energy barriers between the different layers.

The emission spectra of **1a**, **1b** and **1c** compounds in solution are almost identical with two peaks at 403 and 418 nm (3.08 and 2.97 eV). In Fig. 2(b), the photoluminescence spectrum of **1a** is shown as well as those corresponding to **1d**, **1e** and **1f**. The emission spectra are consistent with the changes in the electronic structure, previously deduced from the absorption data, related to the different character of the peripheral groups. Time resolved spectroscopy experiments performed for **1a** solution showed a lifetime of 3.0 ns for the 10^{-5} M solution which is consistent with fluorescence relaxation from singlet excited state (see Supplementary Information). The red shift of the emission peaks of solutions of **1d** and **1e** increases as the acceptor character of the peripheral groups increases (Fig. 3(d) and Table 1). **1f** emission in solution exhibits two distinct emission lines at 413 and 551 nm (3.0 and 2.25 eV, respectively). The highest energy peak, which coincides with that observed for **1a**–**1c**, corresponds to the relaxation from the excited state corresponding to the ‘‘main peak’’ in Fig. 3(a) while the lower energy one (2.25 eV) is the relaxation from the electronic level related to the charge transferred to the peripheral groups.

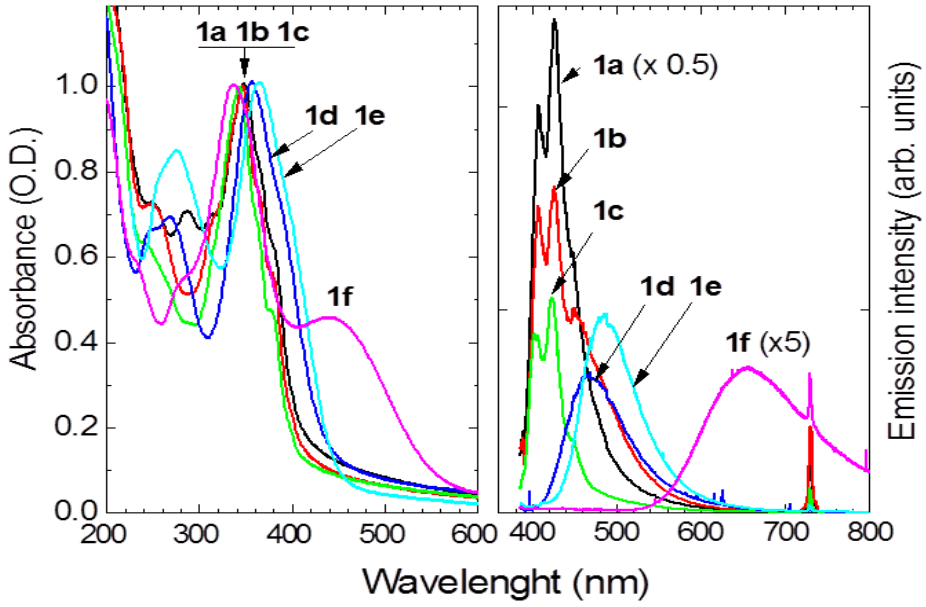

Figure. 4. Optical absorption spectra normalized to 1 at the main peak around 340 nm (left) and emission under 365 nm excitation (right) of **1a**– **1f** thin films. The emission intensities of the films have been corrected by the factor that normalizes their absorption to 1. Note that **1a** film emission intensity is divided by 2 and that of **1f** is multiplied by 5. (The narrow peak at 730 nm = 2 x 365 nm corresponds to the lamp).

In order to select the best candidates for practical applications we have studied the film-forming properties of the new derivatives synthesized. Films of triindole derivatives were prepared by spin coating from 1 wt.% dichloromethane or chlorobenzene as precursor solutions on quartz. The obtained films were highly transparent and uniform to the eye and the optical microscope images reveal no inhomogeneities. Films thickness ranges from 20 to 100 nm.

The optical absorption spectra of the films, collected in Fig. 4(a), demonstrate their high optical quality and show almost identical features compared to the corresponding solution spectra with some differences in the peak energies (Table 1). The vibronic fine structure is also observed in thin films from **1a** to **1c** compounds maintaining the coupling of the excited state to the 150 meV vibration (see 2nd derivative in Fig. 2(c)). The main absorption peaks correspond, as in the solutions, to the (0–3) transitions.

Figs. 3b and c collect the energies of relevant electronic transitions from absorption and emission spectra of the thin films. A systematic shift to lower energies, in the range of 50–100 meV, is observed for the absorption bands of thin films compared to their dilute forms (Figs. 2 and 3). The lowering of the transition energies may be explained by the renormalization of the energy levels due to the close packing of the molecules. This energy shift is the only detected effect on the electronic structure related to the aggregation of the molecules in the thin films electronic transitions. The main emission of the thin films (Fig. 4(b)) ranges from the deep blue of the **1a**–**1c** compounds (426 nm) to the red for **1f** (656 nm). It is therefore possible to tune the emission in the whole visible range by chemical functionalization.

It is well known that whereas many organic molecules emit strongly in solution, they become weak fluorophores when increasing the concentration or when forming thin films due to non-radiative relaxation processes as energy transfer between neighboring molecules. This is a common problem found when looking for molecules that have to be incorporated in devices. However, in conveniently functionalized molecules emission may be enhanced when increasing the concentration owing to the restriction of intramolecular rotation processes upon aggregation or from the inhibition of geometry relaxation of the vertical excited state to a non-emitting state[13].

[13] Bian, Z.; Shakouri, A.; *Appl. Phys. Lett.* **2006**, 88, 012102.

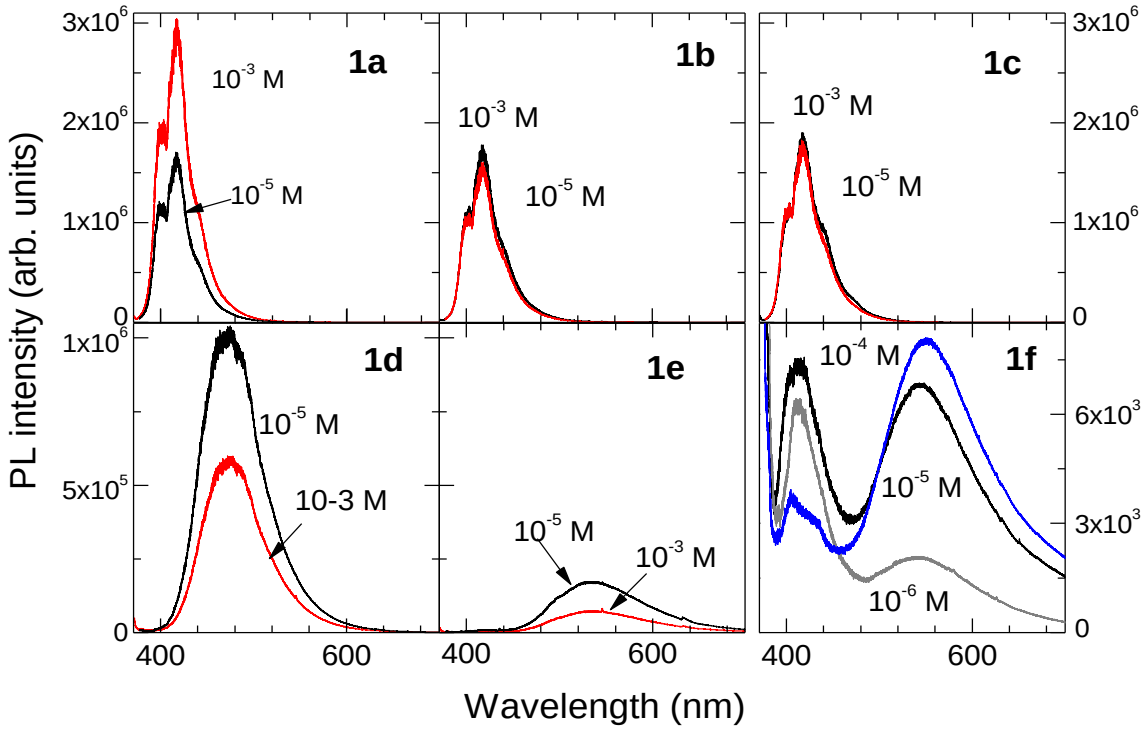
PL intensity (arb. units)
Wavelength (nm)
1a
1b
1c
1d
1e
1f
10-3 M
10-5 M
10-4 M
10-6 M
10-3 M
10-5 M
10-5 M
10-3 M
10-5 M
10-3 M
10-5 M
10-6

corresponding to the **1c** (**1b**) film while in solution their efficiencies are almost identical. It should be noted that this material has a strong tendency to self-assembly. In fact upon heating it enters a columnar hexagonal mesophase at 45 ºC that extend in a broad range of temperatures[3]. Another interesting observation is the increase of the red emission efficiency of **1f** thin film compared to its solution (observe the factors applied to the spectra for the solution (x20) and for the film (x5) in Figs. 2 and 4, respectively). In this case the behavior of the two emission bands upon the solution concentration is different. While the 413 nm peak is rapidly quenched following the tendency of the whole series (in fact this emission is not observed in the film) the orange emission is not quenched. Moreover, this orange emission is significantly shifted to the red from the solution to the film (from 551 to 655 nm) probably indicating a different configuration of the peripheral groups in the solid state.

- **Fabrication and characterization of organic light emitting diodes**

In order to analyze the semiconducting properties of these materials, solution-processed organic light emitting diodes (OLEDs) based on **1a**, **1d** and **1e** have been fabricated as described in the experimental section. These compounds have been selected considering their electronic properties, specifically their markedly different HOMO levels, band gaps and peak emissions (Table 1), as well as by their observed good film-forming properties. The structure of the fabricated OLED consists of: ITO (140 nm)/PEDOT: PSS (50 nm)/active layer/Ca/Al (200 nm). The thicknesses of the active layers are 85 nm, 110 nm and 116 nm for **1a**, **1d** and **1e**, respectively.

In Fig. 6 the energy level structure for materials **1a**, **1d** and **1e**, together with the work functions of anode and cathode, are shown. In this plot, we have used the HOMO levels of the solutions and the LUMO level energies calculated using the thin film absorption bandgaps, E_g^{onset} (Table 1)[14]. The work function for PEDOT:PSS thin films has been reported to range from 4.8 to 5.1 eV[15], depending on the PSS content in the top surface upon the addition of high-boiling solvents.

The electroluminescence (EL) spectra recorded from **1a**, **1d** and **1e**-based devices and their evolution with the driving current are plotted in Fig. 7. **1a**-based OLED exhibits

[14] For charge injection the relevant energy is the lower edge of the LUMO band which is obtained using the absorption onset.

[15] Nardes, A. M.; Kemerink, M.; de Kok, M. M.; Vinken, E.; Maturova, K.; Janssen, R. A. J.; *Org. Electron.* **2008**, 9, 727.

a deep blue emission, CIE coordinates (0.16, 0.16), with the maximum at 427 nm, and well resolved bands at 408 and 439 nm, similar to the thin film PL (Fig. 4). **1d** and **1e**-based OLED present broad emissions with white (CIE coordinates of (0.33, 0.3)) and whitish green colour (CIE coordinates of (0.56, 0.3)), respectively. The radiance, at 10 mA, is 0.14, 0.03 and 0.015 Wsr^{-1} m^{-2} for **1a**, **1e** and **1d** respectively. The inferior EL performance of **1d** and **1e**-based OLEDs is consistent with their lower PL efficiencies. Nevertheless, the recorded luminance for **1a**, **1e** and **1d** are similar for the three devices (9, 11.2 and 3.6 Cd m^{-2} respectively) because of the low efficiency of human eye response to the deep blue emission of **1a** (0.03 at 427 nm).

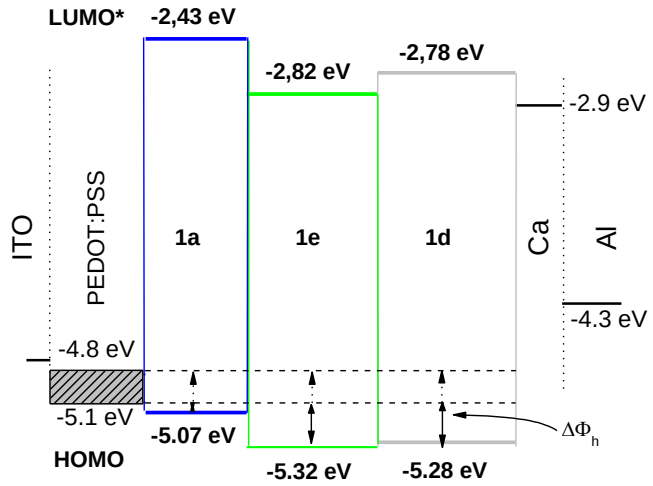

Figure 6. Structure of solution processed OLEDs and energy levels of the electrodes and the materials. We use HOMO for solutions and LUMO levels are obtained from onset absorption energies of thin films.

In devices **1a** and **1e** a very stable emission with increasing voltage is observed (see normalized spectra in Fig. 7 inset). However, in **1d**-based device, with very poor emissive efficiency the noticeable broadening of EL spectra compared to PL is attributed to a degradation which might be associated with an overheating by non radiative relaxation of injected carriers.

In Fig. 8, the experimental I–V responses (open symbols) of **1a**, **1d** and **1e**-based diodes are shown up to currents slightly above the onset for EL. We emphasize that minimizing turn-on voltages, V_T, and driving currents is an important issue in the organic electronics industry. In the present case, **1a**-based device exhibits a quite low threshold voltage (around 2.8 V) together with low driving currents. On the other hand, **1d** and **1e**-based devices show both higher turn-on voltages (V_T > 11 V) and driving currents, while their EL efficiencies are smaller.

The observed EL performance of the three devices maybe qualitatively explained in terms of energy level alignment, electrical character (p or n) of the materials, and charge transport through the device. Using directly the HOMO and LUMO energies of isolated materials to determine the energy level alignment at interfaces is an assumption that may fail at organic-organic or metal–organic junctions, but it provides a reasonable approach for the energy barriers encountered by carriers during transport. On the other hand, in order to estimate the relevance of a barrier, one should keep in mind that for the usual low carrier mobilities in OLED active layers, it has been proven that an injection barrier below 0.3 eV does not limit current significantly[16] since transport turns to be bulk-limited instead of injection-limited. Our experience confirms this statement.

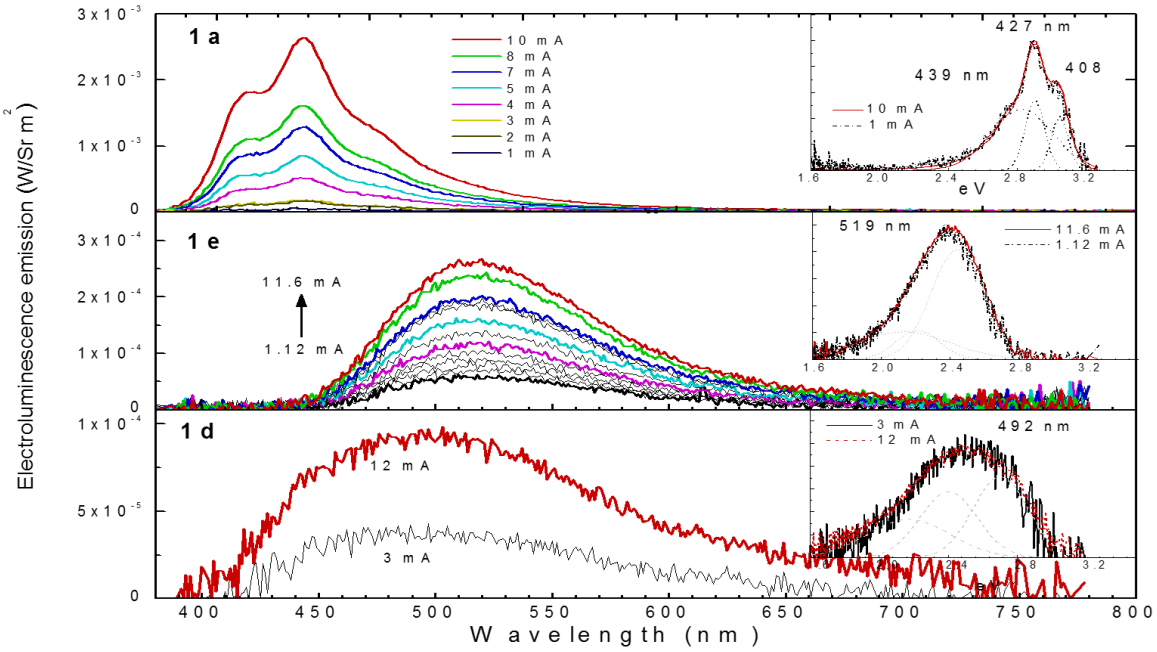

Figure 7. EL spectral radiance for **1a**, **1d** and **1e** based OLEDs and their evolution with the driving current. The inset shows the normalized EL spectra for the maximum and minimum driving current fitted to a combination of Gaussian functions.

In Fig. 6, the alignment between PEDOT:PSS and **1a** levels suggests a negligible barrier for hole injection. According to this view, below V_T, conduction should be carried out by holes. For **1d** and **1e** materials, the energy level alignment is quite different presenting a noticeable increment of the barrier for hole injection together with a lowering of the electron injection barrier, (0.12 eV and 0.08 eV, respectively) and hence presumably an electron-driving conduction. Nevertheless electron mobility is usually

[16] Arkhipov, V. I.; von Seggern, H.; Emelianova, E. V.; *Appl. Phys. Lett.* **2003**, 83, 5074.

lower than hole mobility in p-type materials. This could explain the higher threshold voltage and the poor EL performance of **1d** and **1e**-based OLEDs.

To get quantitative insight on the transport and EL mechanisms in the devices we have used a conduction model for voltages below the onset for EL, V_T, where single carrier transport is assumed [17, 18] in order to fit the experimental I–V curves (Fig. 8) of **1a**, **1d** and **1e**-based diodes (open symbols). This model takes into account injection barriers, non-uniform electric-field across the layer thickness and field-dependent carrier mobility.

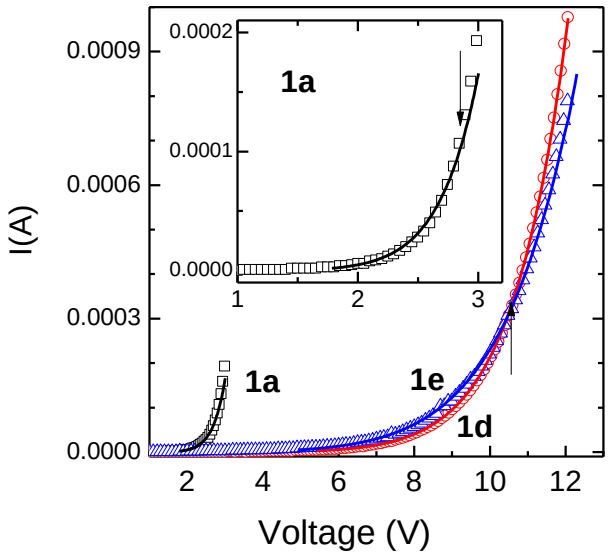

Figure 8. Recorded I–V curves (open symbols) of diodes. The arrows mark the EL onset. Solid lines represent the fit using the model explained in the text. The inset shows an expansion of **1a** results.

Active layer thickness is a relevant input of the model because it strongly affects the diodes threshold voltage not only in those of bulk-limited conduction but also in those of injection-limited conduction. In the latter case this is due to the influence of the layer thickness on the interface field which drives the injection process[19]. It is therefore of major concern obtaining the electric field variation across the layer thickness *E(x)*. Moreover, in disordered organic materials carrier transport is usually accomplished by hopping between localized states and the mobility is a field-dependent function that can be approached to the expression [20, 21]:

[17] Alvarez, A. L.; Romero, B.; Arredondo, B.; Quintana, X.; Mallavia, R.; Oton, J. M.; *Int. J. Numer Model Electron. Networks Devices Fields* **2010**, 23, 332.
[18] Coya, C.; Alvarez, A. L.; Yoon, W. S.; Park, S. Y.; *J. Appl. Phys.* **2011**, 109, 094507.
[19] Arkhipov, V. I.; Emelianova, E. V.; Tak, Y. H.; Bassler, H.; *J. Appl. Phys.* **1998**, 84, 848.
[20] Bässler, H.; *Phys. Status. Solidi. B* **1993**, 13, 175.
[21] Baranosvski, S.; *Charge transport in disordered solids with application in electronics*, in: S. Baranovski, O. Rubel (Eds.), Wiley, New York, **2006** (Chapter 6).

$$\mu(E) = \mu_{oexp(K\sqrt{E})} \qquad (1)$$

where E is the internal electric field, μ_0 is the so-called mobility at zero field [22] (i.e. at E not sufficiently high to enhance the conduction by reducing the effective barrier for trapped carriers) and k is a phenomenological factor related to the lowering of the effective trap depth or Frenkel effect [22].The expression for the drift current density J_b Eq. (2), which includes the mobility Eq. (1), the one-dimensional Poisson Eq. (3) and the integral expression of voltage Eq. (4), are the fundamental equations of the model:

$$J_b = e\mu_o \exp\left(K\sqrt{E}\right)[p_n]E(x) = e\mu_o^* \exp(K\sqrt{E}\,[p]E(x)) \qquad (2)$$

$$\frac{dE(x)}{dx} = \frac{e[p]}{\varepsilon\varepsilon_o} \qquad (3)$$

$$V_b = \int_0^L E(x)dx \qquad (4)$$

where e the elementary charge, ε_o the vacuum permittivity, ε the material dielectric constant, L is the active layer thickness, V_b the external bias voltage and $[p]$ is the total carrier density. Finally $[p_n] = \theta[p]$ is the actual density of carriers contributing to transport. In disordered materials, only a small fraction, $\theta << 1$, of the injected carriers, those with energies close to the so-called transport level, contribute to the transport [23]. Since the determination of this parameter is usually difficult, from here on we use the effective mobility $\mu^*(E) = \mu(E)\theta$ and will extract the effective parameter $\mu_0^*(E) = \mu_0\,\theta$.

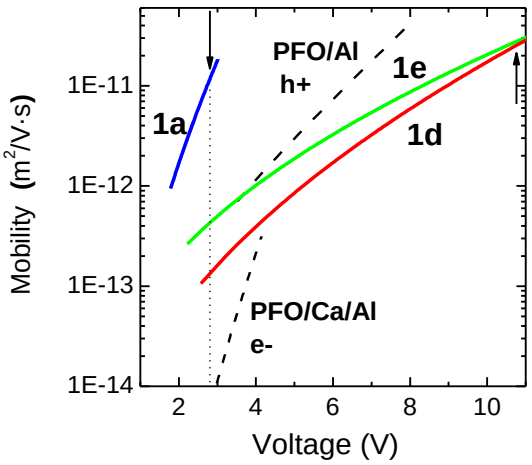

Figure 9. Carrier mobility (μ^*)-applied voltage relationship derived from the model for **1a**, **1d** and **1e** based OLEDs (continuous lines) and for both PFO devices (dashed lines). The arrows mark the EL onsets.

[22] Murgatroyd, P. N.; *J. Phys. D: Appl. Phys*. 3, **1970**, 151.
[23] Arkhipov, V.I.; Emelianova, E.V.; Bässler, H.; *Philos. Mag. B.* **2001**, 81, 985.

Integrating Eq. (3) using Eq. (2) it is possible to obtain the electric field dependence across the active layer $E(x, L, J_b)$. Further details of these calculations have been reported elsewhere [17, 18]. A second integration of the electric field using Eq. (4) provides the electrical response of the diode $V_b(E_0, E_L, J_b)$ where E_0 and E_L are the values of the electric field at both interfaces: $E_0 = E(x = 0)$, $E_L = E(x = L)$. The determination of E_0 is obtained numerically via the continuity equation for the current density across the device: $J_{inj}(E_0) = J_b$, where J_{inj} is the injection current which is generally dependent on the electric field at the interface (E_0). In this work we have assumed the injection mechanism proposed by Arkhipov [19], in which the injection of carriers from the Fermi level of the electrode to the conduction level in the organic is not accomplished by conventional tunneling, but by incoherent hopping between localized states with an injection barrier Φ. The describe model has been used to fit the experimental *I–V* curves using a standard quasi-Newton algorithm, where μ_0^*, κ and Φ (in eV) are the output parameters.

The fits, shown as continuous lines in Fig. 8, reproduce very well the experimental data below the threshold voltage, V_T, in all cases while, in those devices with better EL performance (**1a** and **1e**) the agreement gets worse beyond the EL onset. This is attributed to the additional enhancement of conductivity associated with exciton recombination, which is a physical mechanism not included in the model. However, for the **1d**-based device, where the EL mediated carrier recombination is quite inefficient (with the worst EL performance), the model still fits nicely beyond this onset.

In order to validate the model and compare the output parameters (κ, μ^* and Φ) to those of a commercial compound, we have fabricated OLEDs using blue emitting polyfluorene (PFO) with a multilayer structure identical to previous ones, being L_{PFO} = 85 nm. The PFO HOMO and LUMO levels were elsewhere determined by cyclo-voltammetry to be at -5.6 eV and -2.43 eV, respectively [24]. To promote an electron-based conduction, a Ca layer was inserted between PFO and Al at the cathode, whereas the removal of this layer should promote a hole-based conduction (as expected from the Al work function at -4.3 eV). The devices without Ca do not exhibit EL up to 12–15 V, and transport is expected to be driven by holes injected across a noticeable barrier. In the devices with Ca, the onset for EL drops significantly down to 3 V, and electron-driven conduction is assumed. Despite the low threshold voltage, the electron mobility resulting

[24] Mallavia, R.; Montilla, F.; Pastor, I.; Velasquez, P.; Arredondo, B.; Alvarez, A. L.; Mateo, C. R.; *Macromolecules* **2005**,38, 3185.

from the model is much lower than that for holes, as shown in Fig. 9. This is consistent with an electron-driven transport in a non-favorable p-type material as this type of polyfluorene [24]. We remark that hole mobility has been extracted in the presence of an injection barrier Φ = 0.51 eV, in reasonable agreement with the energy level scheme.

Table 2. Fitting parameters μ_0^*, κ and Φ obtained for the active layer of each device. Average mobilities, μ^*, at the EL onset of **1a** based device (2.8 V). Results obtained for both holes (h^+) and electrons (e^-) from a commercial blue-emitting polyfluorene (PFO) based OLED are included for comparison.

	1a- h^+	**1e-**e^-	**1d-**e^-	**PFO-**h^+	**PFO-**e^-
μ_0* (×10^{-9}) [m^2/Vs]	5.2x10^{-2}	20.8	2.0	1.51x10^{-2}	1.91x10^{-7}
k (×10^{-3}) [V/m]$^{-1/2}$	2.84	1.02	1.33	1.49	3.84
Φ [eV]	< 0.3	< 0.3	0.38	0.51	< 0.3
μ*(at 2.8V) (×10^{-11}) [m^2/Vs]	1.1	4.4x10^{-2}	1.3 x10^{-2}	3.7x10^{-2}	9 x10^{-4}

Table 2 summarizes the obtained fitting parameters, μ_0^*, κ and Φ for **1a**, **1d** and **1e** based devices and for both PFO OLEDs. Since the electric field E(x) is not uniform, $\mu^*[E(x)]$ has been numerically averaged across the whole layer. The resulting average carrier mobility vs. applied voltage $\mu^*(V_b)$ is plotted in Fig. 9. We can observe that the carrier mobility in **1a** device (Fig. 9) is much higher in its operating range than that for devices **1d** and **1e** (Table 2 collects the average mobilities at 2.8 V for the all devices).

The present model for charge transport across this OLED structure has allowed us to obtain both electron and hole mobilities for these derivatives by fitting the *I–V* curves at low voltages ($<V_T$) where the transport is dominated by one carrier type. As explained previously, the alignment of the level energies of the successive layers favors hole conduction for **1a** and PFO/Al devices while mainly electron conduction occurs in **1d**, **1e** and PFO without Al. The results indicate that hole mobility is more than two orders of magnitude higher compared to electron mobility, which is consistent with p-type materials. This factor is also observed comparing hole and electron mobilities in PFO (Fig. 9 and Table 2). Finally, we emphasize that hole-mobility of the solution processed **1a**-based device results significantly higher than that of PFO/Al. Regarding OLED performance, it is clear that increasing the luminance would require the optimization of the electron injection in **1a**-based device and of hole injection in **1d** and **1e** devices.

Nevertheless, we can conclude that these solution processed devices exhibited encouraging level of performance in terms of transport.

2.2.5. CONCLUSIONS

We have introduced peripheral groups in the electronrich 10,15-dihydro-5H-diindolo[3,2-a:30,20-c]carbazole (triindole) platform that render solution processable and good film-forming compounds. The influence of the different peripheral groups on the electronic properties of solutions and films is evidenced in the tuning of the HOMO, LUMO, gap and emission energies which are discussed and correlated to the electronic communication of the external substituents with the central electron-rich triindole. The resulting films are amorphous, highly homogeneous and stable for months therefore suitable for device fabrication. The thin films emission ranges from deep blue (423 nm) to red (657 nm).

Single layer organic light emitting diodes (OLED) have been fabricated by solution processing methods with the structure: ITO/PEDOT:PSS/active layer/Ca/Al. Three compounds with different HOMO–LUMO alignment to the electrode work functions and different emission wavelengths were used to investigate the influence on transport and emission properties of the substituting species. A numerical model for conductivity that includes injection barriers and non-uniform electric-field across the layer as well as field dependent mobility has been used to analyze the OLEDs *I–V* response and to compare the results to devices fabricated with commercial PFO. Best results are obtained on the most electron rich derivative functionalized with six donor methoxy groups. This material shows the highest emission efficiency in solid state, due to aggregation-induced enhancement, and favors carrier transport with the highest mobility in the whole operating voltage range. We demonstrated encouraging performance in terms of very low turn on voltage (2.8 V) and carrier mobility of a solution processed deep blue emitting molecular based OLED.

2.3. MONO-FUNCTIONALIZATION ON THE TRIINDOLE PLATFORM

In the previous section we demonstrated the possibility of integrating triindole-based material into color tunable OLEDs. However, the efficiency of these devices has to be improved if we expect them to be competitive.

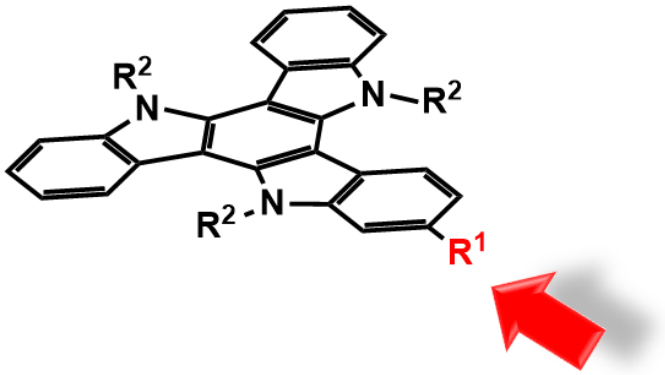

In order to achieve this goal, in this section we study the effect that asymmetric substitution of the platform, have in its final properties by performing a comparative study between a series of monoaryltriindoles and their symmetrical counterparts (Figure 2.1).

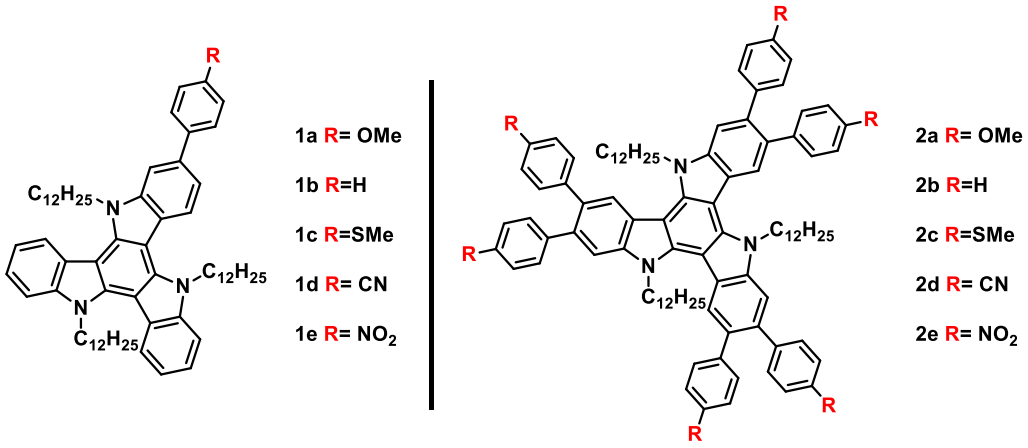

Figure 2.1. Peripheral mono- and hexa-functionalization of triindoles.

The synthesis of the new triindole derivatives has been performed starting from *N*-tridodecyltriindole, by bromination with 1 equivalent of n-bromosuccinimide (NBS) under high-dilution conditions followed by palladium-catalyzed Suzuki cross-coupling reaction with the corresponding boronic acid (Scheme 2.1).

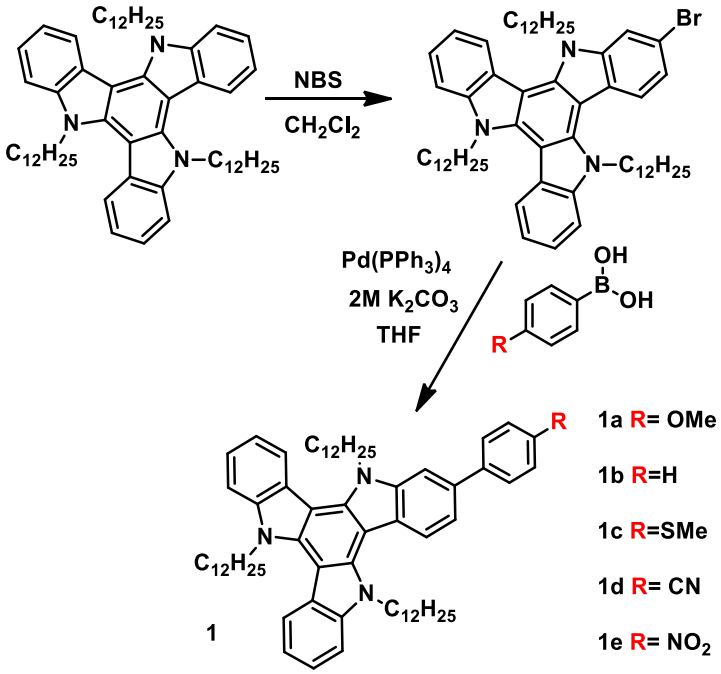

Scheme 2.1. Synthesis of the mono-substituent derivatives.

The influence of the peripheral groups, in the electronic properties of this family of compounds, has been initially studied by cyclic voltammetry. As can be observed in Figure 2.2 all of these compounds exhibit a first oxidation reversible process which in contrast to the hexasubstituted derivatives (in which an anodic shift is observed as the acceptor character of the peripheral substituent is increased), are not affected by the electronic nature of the substituents. This implies the low influence that the peripheral groups have on the HOMO levels of these derivatives, which match very well with Au work function (Φ_{Au} = 5.1 eV). Thus low barriers are expected for hole injection from gold electrodes with these new family of compounds.

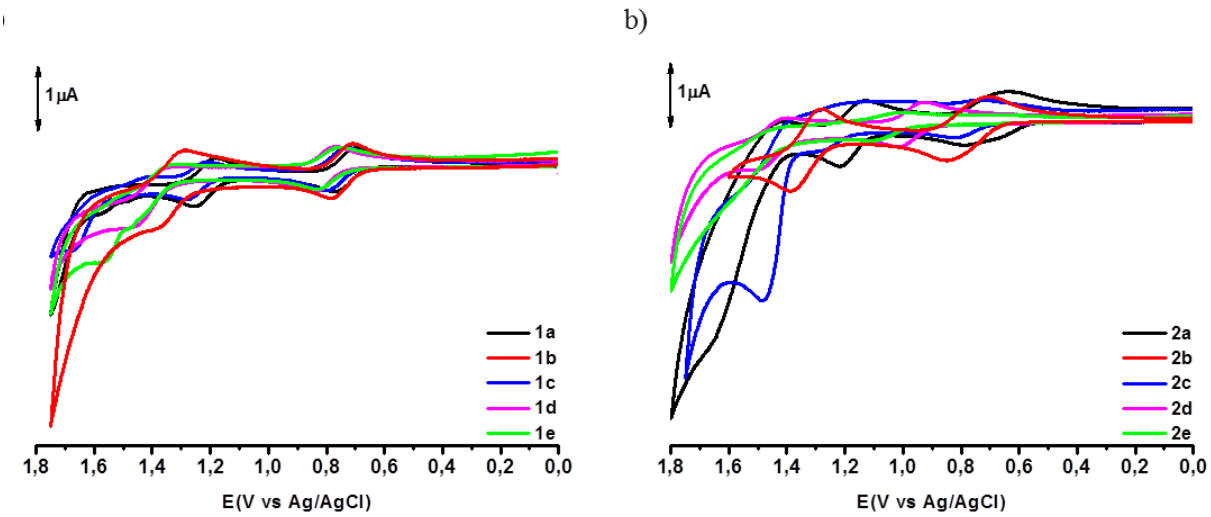

Figure 2.2: CV at c = 1 x 10^{-3} M recorded at a scan rate 100mV/s in CH_2Cl_2/0.1 M $TBAPF_6$ measured versus Ag/AgCl (3M NaCl) for a) one- peripheral group and for) hexa- peripheral group.

In contrast, the influence of the peripheral group in UV-vis spectra of these monosubstituted derivatives is more pronounced than in the hexasubstituted ones. As depicted in Figure 2.3 a significant bathochromic shifts of the maximum absorption and absorption edge occurs upon increasing the acceptor character of the substituents, with all that implies in term of HOMO-LUMO gap tuning.

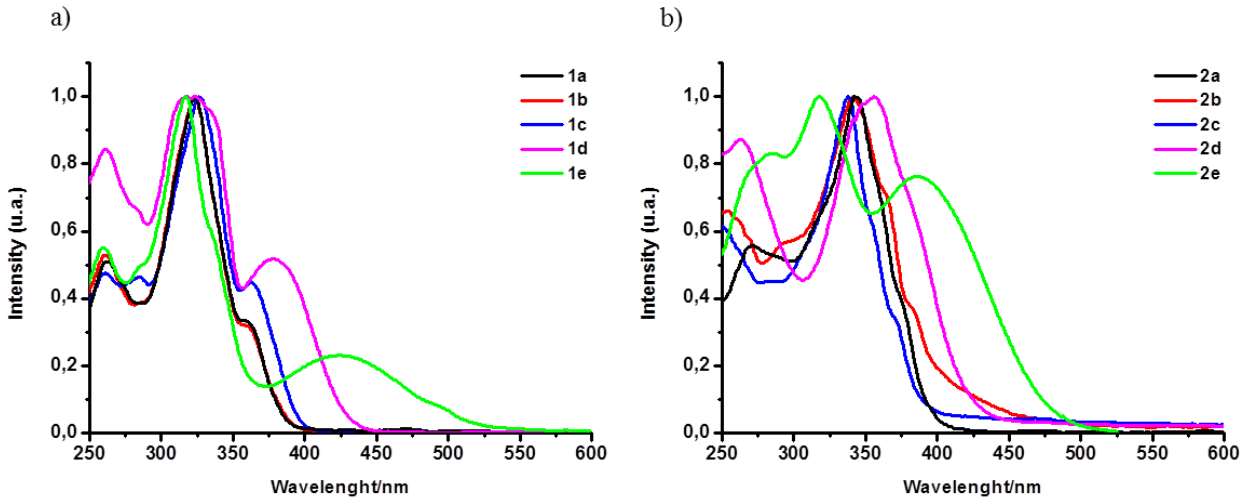

Figure 2.3. UV-vis spectra of compounds mono and hexa- substituent in CH_2Cl_2, c = 5 x 10^{-6} M.

As summarized in the Figure 2.4, mono-substitution allows us to change the LUMO level without affecting the favorable HOMO value, in contrast to the hexa-substituted derivatives in which both levels change simultaneously.

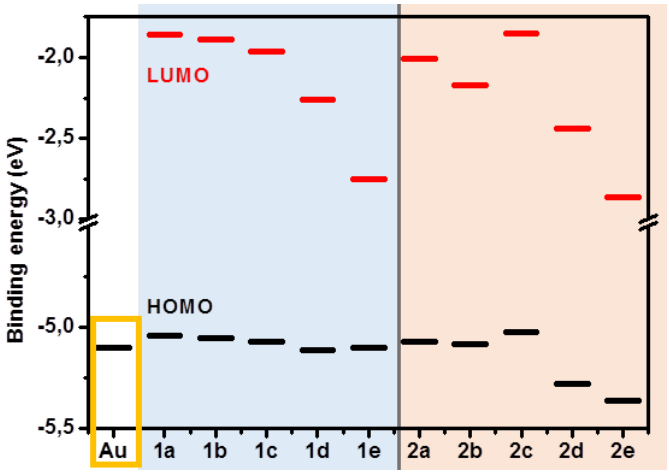

Figure 2.4: Summary of the HOMO-LUMO level of both families of compounds in a comparative with the Au work function.

Interesting differences can be also observed when comparing the emission properties of these two series of compounds. The emission spectra of the hexa-substituted triindoles (Figure 2.5) show that substitution with electrondonating groups does not affect emission properties, while substitution with electronacceptor groups induces a significant bathochromic shift. Although similar trends are observed in the mono-substituted series of triindoles, a higher range of emission color which expands from blue to green (411 to 496nm) and an enhancement in the fluorescence quantum yield is clearly observed (see Table 2.1).

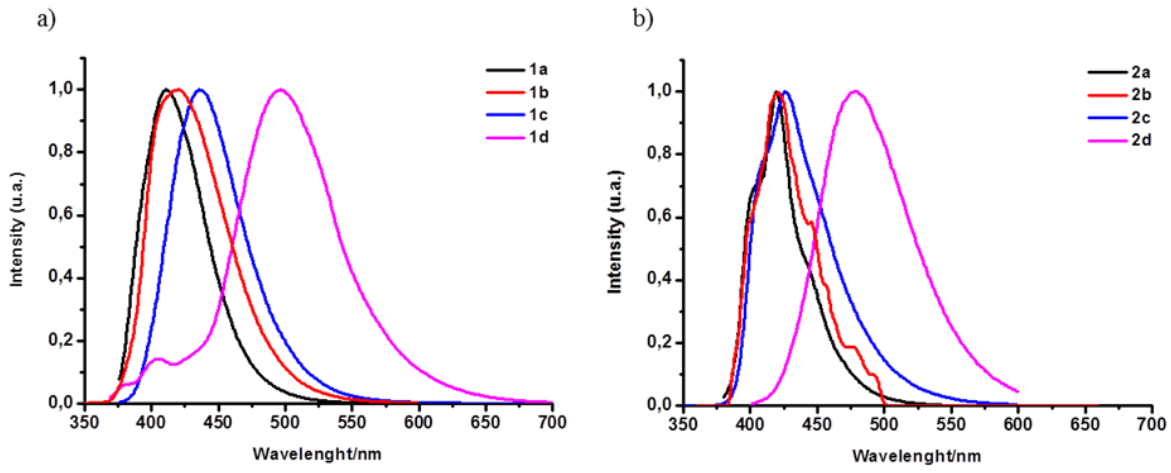

Figure 2.5: Spectral emission in CH_2Cl_2, c = 5 x 10^{-6} M for a) mono-substituted and b) hexa-substituted triindole series. Attachemnt nitrophenyl group quenches fluorescence in both cases.

It should be noted that, in both cases the nitrophenyl group gives a very weak fluorescence.

Table 2.1: The values of the maximum wavelength of the emission spectra, the Stockes shift and the fluorescence quantum yield for the mono and hexa-substituted compounds.

	λ_{em}(nm)	Stokes shift nm)	Φ[a] (%)		λ_{em}(nm)	Stokes shift (nm)	Φ[a] (%)
1a	411	89	0,35	**2a**	419	76	0,33
1b	421	96	0,50	**2b**	419	77	0,29
1c	437	112	0,40	**2c**	425	89	0,20
1d	496	173	0,54	**2d**	479	123	0,35
1e	---	---	---	**2e**	---	---	---

[a] The quantum yield were calculated using quinine sulfate 0,5M in H_2SO_4 like standard parameter.[i]

In conclusion, in this section we show that asymmetrical derivatives offer significant advantages when compared to their symmetrical counterparts towards their incorporation in light emitting device.

The comparative study of these two families of compounds shows us that monofuctionalization allows the tuning of the LUMO level without affecting the beneficial HOMO level, at the same time that we obtained an improve of the quantum yield and an increase the range of the emission spectra. These excellent results lead us to consider the possibility of incorporating the new mono-functionalized derivatives in the manufacture of light-emitting diodes.

[i] The fluorescence quantum yield (Φ) is the ratio of photons absorbed to photons emitted through fluorescence. In other words, the quantum yield gives the probability of the excited state being deactivated by fluorescence rather than by another, non-radiative mechanism.

The quantum yield was calculated by the application of:

$$\Phi = \Phi_{Reference}\ x\ \frac{Abs_{Reference}}{Abs_{Compound}}\ x\ \frac{Area_{Compound}}{Area_{Reference}}\ x\ \frac{n^2_{Compound}}{n^2_{Reference}}$$

where *Abs* is the absorbance at the maximum excitation ($\lambda_{exc} \approx \lambda_{abs}$), *Area* represents the integrated area of emission peak, and *n* is the refractive index of the solvent for the compound and for the reference ($n_{H_2SO_4 1N} = 1{,}333$, $n_{CH_2Cl_2} = 1{,}398$).

Chapter 3. Charge transport properties on triindole platform

CHAPTER 3. CHARGE TRANSPORT PROPERTIES ON TRIINDOLE PLATFORM

3.1. SUMMARY

In this chapter we focus in the optimization of the electrical properties of the triindol platform, trying to obtain materials that combine high mobility values with an easy processability. To achieve this goal we take advantage of the high tendency of these materials to self-assembly into columnar mesophases.

Although discotic liquid crystals are very appealing in terms of processability and semiconducting properties, the high dependence of the electrical performance on the degree of columnar alignment represents an important drawback towards their incorporation in devices. Due to their inherent structure, characterized by an active conducting core, surrounded by an isolating cover, transport in liquid crystal is highly anisotropic as contacts among aromatic units of different columns are hampered by the mantle of soft alkyl chains making mobility values highly dependent of the ordering of the columns on the substrate.

In order to tackle with this problem, in this chapter we attempt to obtain molecular candidates which present increased dimensionality of charge transport (Figure 3.1). This objective is approached by obtaining mesogens with a larger ratio of conducting part versus isolating cover, and alternatively by synthesizing new mesogens decorated with peripheral groups able to establish short contacts between neighboring columns.

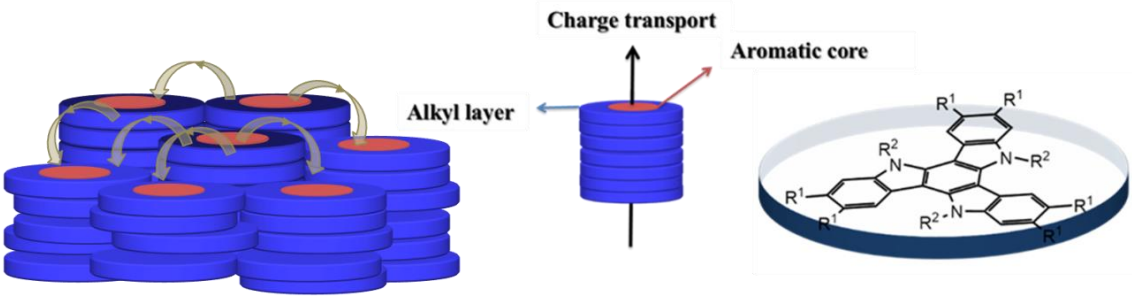

Figure 3.1: Scheme of the modification of the aromatic core in discotic liquid crystal to increase the dimensionality of the charge transport.

The increase of the conducting/isolating ratio will be attempted by decreasing the number of peripheral alkyl chains and enlarging the central conducting core. My research group has previously shown that in enlarged π-conjugated triindole–based aromatic cores, which can be easily obtained by oxidative cyclodehydrogention of hexaaryltriindoles, it is possible to induce mesomorphism, by attaching only three *N*-dodecyl chains.

In a second approach to facilitate contacts between neighboring columns, we have attached to the triindole platform, six peripheral groups able to establish intermolecular interactions In particular we have synthesized a new triindole-based liquid crystal functionalized with six peripheral thiomethyl moieties. These moieties are able of establishing S-S interaction which have already shown beneficial to increase the contact between neighboring columns in other semiconducting aromatic platforms.[1] In addition, thioalkyl groups have been long considered to obtain high mobility discotic mesophases. [2]

The lower dependence of the electrical performance of these discotic liquid crystals on the degree of columnar alignment has been studied by comparing the mobility values obtained by applying two different methods with different alignment requirements: space-charge limited current (SCLC) measurements in a diode-like structure (which requires a conducting channel perpendicular to the surface) and field effect mobility measurements in thin film transistor devices (which requires a conducting channel parallel to the surface). Although in both cases the mobility found on a diode type device is higher than that determined on thin-film transistors, the observation of field effect behavior in a discotic liquid crystal processed by simple drop-casing suggest an increased dimensionality of charge transport. The differences obtained can be understood by the high tendency of π-conjugated molecules to deposit on surfaces with their aromatic cores parallel to the substrate.

In this chapter the measurements of space charge limited current have been made in collaboration with Prof. Attilio Golemme (University of Calabria), while the field effect transistor measurement have been made by myself during my research stay in the Northwestern University with Prof. Antonio Facchetti.

---

[1] a) Kimoto, T.; Tanaka, K.; Kawahata, M.; Yamaguchi, K.; Otsubo, S.; Sakai, Y.; Ono, Y.; Ohno, A.; Kobayashi, K.; *J. Org. Chem*. **2011**, 76, 5018. b) Kobayashi, K.; Shimaoka, R.; Kawahata, M.; Yamanaka, M.; Yamaguchi, K.; *Org. Lett*. **2006**, 8, 11.

[2] Adam, D.; Schuhmacher, P.; Simmerer, J.; Haussling, L.; Siemensmeyer, K.; Etzbachi, K. H.; Ringsdorf, H.; Haarer, D.; *Nature*, **1994**, 371, 141–143. b) Ohta, K.; Hatsusaka, K.; Sugibayashi, M.; Ariyoshi, M.; Ban, K.; Maeda, F.; Naito, R.; Nishizawa, K.; van de Craats, A. M.; Warman, J. M.; *Mol. Cryst. Liq. Cryst.*, **2003**, 397, 25.

3.2. OFET *VS* SCLC MOBILITY OF A SEMICONDUCTING π-EXTENDED DISCOTIC LIQUID-CRYSTALLINE TRIINDOLES

Constanza Ruiz[1,2], Upendra K. Pandey[3], Roberto Termine[3], Eva María García-Frutos,[1] Guzmán López-Espejo,[4] Rocío Ponce Ortiz,[4] Wei Huang,[2] Tobin J. Marks[2], Antonio Facchetti,[2] M. Carmen Ruiz Delgado,[4] Attilio Golemme,[3] Berta Gómez-Lor[1]

[1] Instituto de Ciencia de Materiales de Madrid, CSIC, Cantoblanco, 28049, Madrid (Spain)

[2] Department of Chemistry and the Materials Research Center, the Argonne-Northwestern Solar Energy Research Center, Northwestern University, 2145 Sheridan Road, Evanston, Illinois 60208, United States

[3] LASCAMM CR-INSTM, CNR-NANOTEC Lab LiCryL, Dipartimento di Fisica, Università della Calabria, 87036 Rende (Italy)

[4] Department of Physical Chemistry, University of Málaga, 29071, Málaga (Spain).

3.2.1. INTRODUCTION

The field of organic electronics has evolved impressively in the last few years and the first generation of devices based in this technology has already reached the market.[3, 4] Advances achieved in this field have been associated to the development of organic semiconductors able to transport charge carriers with high mobility. However, finding organic semiconductors with the right balance between mobility and processability is still a major necessity in the area. In this context, discotic liquid crystals constituted by an aromatic central core surrounded by flexible alkyl tails are among the most promising candidates.[5, 6] In the columnar mesophases induced by discotic mesogens the aromatic cores are strongly interacting ensuring an uniaxial pathway for efficient charge carrier migration, while the soft and self-repairing nature of these materials facilitates their easy processing and the realization of defect free domains over large areas.[7, 8, 9, 10] Due to their characteristic structure (active conducting core, surrounded by an isolating cover) charge transport in discotic liquid crystals is highly anisotropic and a precise control of

[3] *Organic Electronics: Materials, Manufacturing and Applications*; Klauk, H., Ed.; Wiley- VCH: Weinheim, **2006**.
[4] *Organic Electronics: More Materials and Applications*; Klauk, H., Ed.; Wiley- VCH: Weinheim, **2012**
[5] *Chemistry of Discotic Liquid Crystals: From Monomers to Polymers* (Ed. S. Kumar), CRC Press, Taylor & Francis: Boca Raton, **2011**.
[6] Laschat, S.; Baro, A.; Steinke, N.; Giesselmann, F.; Hagele, C.; Scalia, G.; Judele, R.; Kapatsina, E.; Sauer, S.; Schreivogel, A. *Angew. Chem. Int. Ed*.**2007**, 46, 4832.
[7] Sergeyev, S. Pisula, W.; Geerts, Y. H. *Chem. Soc. Rev*.**2007**, 36, 1902.
[8] Pisula, W.; Zorn, M.; Chang, J. Y.; Müllen, H.; Zentel, R. *Macromol. Rapid Commun*.**2009**, 30, 1179.
[9] O´Neill, M.; Kelly, S. M.; *Adv. Mater*.**2011**, 23, 566.
[10] Kaafarani, B. R.; *Chem. Mater*.**2011**, *23*, 378.

orientation of the columnar axis on the substrate is therefore imperative to obtain optimal charge transport.[11, 12]

This high dependence of the electrical performance on the degree of columnar alignment represents an important drawback towards device application of discotic mesogens by simple solution-processing techniques. Although the uniform macroscopic orientation of columns on different substrates has been successfully achieved through varied strategies such as the application of electric[13, 14] or magnetic fields[11, 15], use of surface modifiers[16, 17], and confinement effects[18, 19] among others, to date solutions vary from material to material and are complicated by the fact that each type of device has different geometry requirements. Planar alignment of columns (conducting channel parallel to the dielectric substrate) is needed in thin-film transistors, whereas homeotropic alignment of columns (conducting channel perpendicular to electrodes) is required in photovoltaic cells or light-emitting diodes.[7,8] At this stage, the controlled alignment of columns represents a major challenge for the practical application of discotic liquid crystals.

Heptacyclic 10,15-dihydro-5*H*-diindolo[3,2-*a*:3',2'-*c*]carbazole (triindole) has been widely studied as a π-conjugated platform in the construction of high mobility semiconducting liquid crystals.[20, 21, 22, 23] Especially remarkable is the record hole mobility values determined on hexaphenyltriindole columnar mesophases (up to 2.8$cm^2V^{-1}s^{-1}$)[21] as

[11] Eccher, J.; Zajaczkowski, W.; Faria, G. C.; Bock, H.; von Seggern, H.; Pisula, W.; Bechtold, I. H.; *ACS Appl. Mater. Interfaces* **2015**, 7, 16374.
[12] Shklyarevskiy, I.O.; Jonkheijm, P.; Stutzmann, N.; Wasserberg, D.; Wondergem, H. J.; Christianen, P. C. M.; Schenning,A. P. H. J.; de Leeuw, D. M.; Tomovic, Z.; Wu, J.; Müllen, K.; Maan, J. C.; *J. Am. Chem. Soc.*, **2005**, 127, 16233.
[13] Miyajima, D.; Araoka, F.; Takezoe, H.; Kim, J.; Kato, K.; Takata, M.; Aida, T.; *Angew. Chem. Int. Ed*., **2011**, 50, 7865.
[14] Hu, N.; Shao, R.; Shen, Y.; Chen, D.; Clark, N. A.; Walba, D. M.; *Adv. Mater.*, **2014**, *26*, 2066.
[15] Kim, H. -S.; Choi, S. -M.; Lee, J. -H.; Busch, P.; Koza, S. J.; Verploegen, E. A.; Pate, B. D.; *Adv. Mater.* **2008**, *20*, 1105.
[16] Bramble, J. P.; Tate, D. J.; Revill, D. J.; Sheikh, K. H.; Henderson, J. R.; Liu, F.; Zeng, X.; Ungar, G.; Bushby, R. J.; Evans, S. D.; *Adv. Funct. Mater.* **2010**, *20*, 914.
[17] Kajitani, T.; Suna, Y.; Kosaka, A.; Osawa, T.; Fujikawa, S.; Takata, M.; Fukushima, T.; Aida, T.; *J. Am. Chem. Soc.* **2013**, *135*, 14564.
[18] Mouthuy, P. -O.; Melinte, S.; Geerts, Y. H.; Jonas, A. M.; *Nano Lett.* **2007**, 7, 2627.
[19] Cattle, J.; Bao, P.; Bramble, J. P.; Bushby, R. J.; Evans, S. D. Lydon, J. E.; Tate, D. J.; *Adv. Funct. Mater.* **2013**, *23*, 5997.
[20] García-Frutos, E. M.; Pandey, U. K.; Termine, R.; Omenat, A.; Barberá, J.; Serrano, J. L.; Golemme, A.; Gómez-Lor, B.; *Angew. Chem. Int. Ed*. **2011**, *50*, 7399.
[21] Benito-Hernández, A.; Pandey, U. K.; Cavero, E.; Termine, R.; García-Frutos, E. M.; Serrano, J. L.; Golemme, A.; Gómez-Lor, B.;*Chem. Mater.***2013**, *25*, 117.
[22] Zhao, B.; Liu, B.; Png, R. Q.; Zhang, K.; Lim, K.A.; Luo, J.; Shao, J.; Ho, P.K.H.; Chi, C.; Wu, J.; *Chem. Mater*. **2010**, *22*, 435.
[23] Talarico, M.; Termine, R.; García-Frutos, E. M.; Omenat, A.; Serrano, J. L.; Gómez-Lor, B.; Golemme, A.; *Chem. Mater.* **2008**, 20, 6589.

a result of the favorable synergy between the intrinsic properties of the platform and the high degree of supramolecular order triggered by bulky phenyl moieties that efficiently interlock the molecules within the columns. Interestingly, three-fold oxidative cyclodehydrogenation of hexaphenyltriindole render the significantly enlarged aromatic core **1**, with structural characteristics of both triphenylene moieties and triindole. In this π-extended discotic core the attachment of only three flexible alkyl chains to the nitrogen atoms is sufficient to induce mesomorphism. [24] Thus compound **1** (Figure 1) functionalized with six peripheral methyl groups and three long flexible dodecyl chains attached to the nitrogens shows an ordered mesophase in a broad range of temperature. In this compound, the ratio of conducting versus isolating fraction is considerably enhanced comparing to triindole liquid crystals not only by enlarging the size of the central core, but also by reducing the amount of isolating peripheral chains.

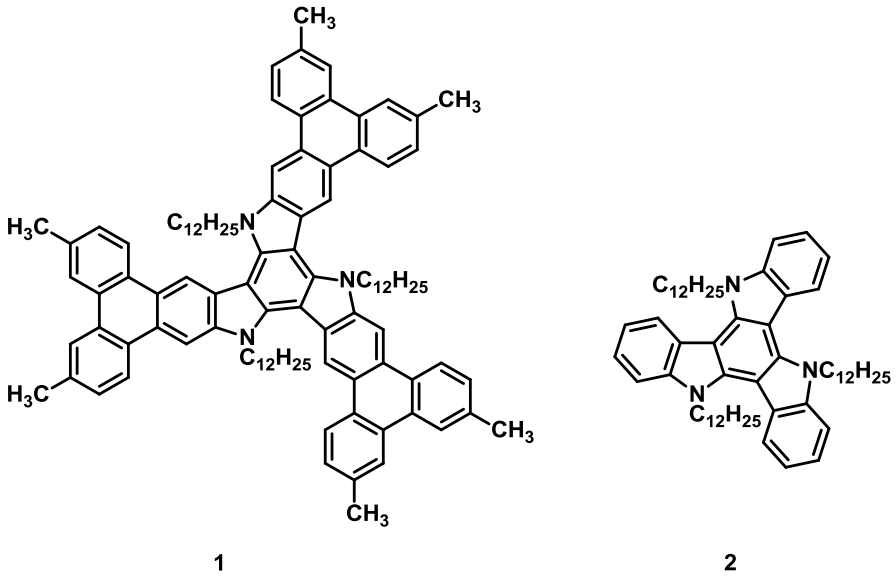

Figure 1: Structure of triphenylene-fused triindole **1** and triindole **2** cores under study.

In this manuscript we investigate the semiconducting properties of this aromatic platform with the aim of lowering the dependence of alignment, usually found on discotic liquid crystals and necessary towards their easy incorporation in devices. We have investigated the electrical properties of compound **1** by applying two complementary methods: space-charge limited current (SCLC) measurements in a diode-like structure[25, 26, 27, 28] and field effect mobility measurements in a thin-film transistor device[29, 30] which

[24] García-Frutos, E. M.; Omenat, A.; Barberá, J.; Serrano, J. L.; Gómez-Lor, B.; *J. Mater. Chem.* **2011**, 21, 6831.
[25] Rose, A. *Phys. Rev*. **1955**, 97, 1538.
[26] Blom, P. W. M.; de Jong, M. J. M.; van Munster, M. G. *Phys. Rev. B* **1997**, 55, R656.

could be easily prepared by melt or solution processing respectively. The mobility values obtained by the two methods differ by 3 orders of magnitude which can be ascribed to the different alignment requirements for both techniques. In spite of the differences exhibited in mobility values obtained by the two methods, the acceptable performance found on **1**-based $OFET_S$ fabricated by simple drop-casting processing of such an enlarged aromatic core is remarkable and suggest the facilitated hopping between neighboring columns owing to the large conducting/isolating ratio found in this discotic platform.

3.3.2. EXPERIMENTAL SECTION

- **Raman measurements**

Microscope Raman scattering spectra with excitation at λ = 785 nm were performed on Laser-Raman spectrophotometer (NRS-5100 JASCO). The operating power for the exciting laser radiation was kept to 12.2 mW in all experiments. Samples were analysed as bulk or thin films by averaging 50 scans with 10 s of integration time. The thin films samples prepared by spin-coating or drop-casting solutions were deposited on Au or SiO_2 surfaces.

- **Space Charge Limited Current (SCLC) measurements**

In order to prepare cells for mobility measurements in **1**, lithographically patterned (several 1 mm wide stripes on each substrate) ITO coated glasses (UNAXIS, 110 nm ITO thickness) were cleaned by successive ultra-sonication using lightly soapy water, distilled water, acetone and isopropyl alcohol. The cleaned glasses were then transferred to a vacuum oven for overnight drying at 90 °C and immediately transferred inside a glove box with a nitrogen atmosphere (O_2< 0.1 ppm, H_2O < 0.1 ppm) where cells were prepared by squeezing the melt at 150 °C between two substrates with patterned electrodes, gold on one side and ITO on the other side. Gold electrodes were prepared previously by thermal evaporation of gold on glass substrates cleaned as described above. Samples were

[27] Reynaert, J.; Arkhipov, V. I.; Borghs, G.; Heremans, P.; *Appl. Phys. Lett*. **2004**, 85, 603.
[28] Blom, P. W. M.; Tanase, C.; de Leeuw, D. M.; Coehoorn, R.; *Appl. Phys. Lett*. **2005**, 86, 092105.
[29] Newman, C. R.; Frisbie, C. D.; da Silva,D. A.; Brédas, J. L.; Ewback, P. C.; Mann, K. R. *Chem. Mater*. **2004**, 16, 4436.
[30] Braga, D.; Horowitz, C.; *Adv. Mater*. **2009**, 21, 1473.

then allowed to slowly cool to room temperature before being sealed using epoxy glue and taken out of the glove box for thickness and SCLC measurements. The thickness (22 micrometers) was obtained from the interference maxima and minima in the near-IR region when the light intensity transmitted by the samples was recorded by an AGILENT 8453 UV-Vis spectrometer.

- **Field-effect transistor fabrication**

The characterization of organic field effect transistors was carried out in order to determine field effect charge carrier mobilities (μ_{FET}). In this work, transistors with bottom gate, top contact configuration were used. First, the gate/dielectric substrates (Si/300 nm SiO_2) were cleaned in an ultrasonic bath with acetone, hexane and ethanol previous to drying under a flow of nitrogen. Next, the surface was functionalized with a self-assembled monolayer of hexamethyldisilazane (HMDS) to minimize interfacial trapping sites[31, 32]. Then, thin films of compound **1** were made by drop-casting (40µL of a 5mg/ml in chloroform solution) under nitrogen atmosphere. At last, 30 nm gold source and drain electrodes were thermal evaporated through a shadow mask. Devices were tested under vacuum by using an Agilent B1500 semiconductor parameter analyzer and a customized vacuum probe station.

- **Computational details**

The theoretical study was carried out in the frame of density functional theory (DFT) using the B3LYP functional[33, 34] and the 6-31G** basis set[35, 36] as implemented in the Gaussian 09 program.[37] The geometry optimizations of triphenylene-fused triindole **1** and related triindole **2** were performed considering C_3 symmetry constraints. Note that the long dodecyl side chains on the nitrogens of the compounds subjected to the experimental study were replaced with methyl groups in order to reduce the computational cost. Based on the resulting ground-state geometries, harmonic vibrational frequencies were

[31] Yoon, M-H.; Kim, C.; Facchetti, A.; Marks, T. J.; *J. Am. Chem. Soc*. **2006**, 128, 12851.
[32] Usta, H.; Lu, G.; Facchetti, A.; Marks, T. J.; *J. Am. Chem. Soc.* **2006**, 128, 28, 9034.
[33] Becke, A. D.; *J. Chem. Phys.* **1993**, 98, 5648.
[34] Lee, C. T.; Yang, W. T.; Parr, R. G.; *Phys. Rev. B* **1988**, *37*, 785.
[35] Harihara, P. C.; Pople, J. A.; *Theor. Chim. Acta* **1973**, *28*, 213.
[36] Hehre, W. J.; Ditchfield, R.; Pople, J. A.; *J. Chem. Phys*. **1972**, *56*, 2257.
[37] Frisch, M. J.; Gaussian 09, revision C.01; Wallingford, CT, **2009**.

calculated analytically at the same theoretical level. The reorganization energies were calculated directly from the relevant points on the potential energy surfaces using the standard procedure detailed in the literature.[38]

The transfer integrals of two adjacent molecules were calculated at the B3LYP/6-31G(d,p) level, according to the approach described by Valeev *et al.* [39] with the corresponding matrix elements evaluated with Gaussian 09. Note that the coupling values depend on the functional used and generally increase with the increasing percentage of Hartree-Fock exchange in the functional.[40]

3.2.3. RESULTS AND DISCUSSION

The synthesis and mesomorphic properties of compound **1** has been previously reported by our group.[24] This compound shows an ordered columnar hexagonal mesophases which extends from 26 ºC to 226 ºC. A lattice constants of *a*= 24.2 Å has been determined by X-ray diffraction together with a clear 001 diffuse reflection corresponding to the regular stacking of the molecules of 3.85 A within the columnar mesophases.[24]

We have performed a Raman spectroscopy comparative study on **1** and the parent *N*-dodecyltriindole **2** in order to investigate the influence of the external triphenylene groups on the π-conjugation. As seen in Figure 2, the Raman band associated to a C-C stretching mode (*i.e.*, mode 8a of benzene[16]) localized on the external benzene rings shifts towards higher wavenumbers upon increasing the molecular core (i.e., 1605 cm^{-1} in **2** and 1614 cm^{-1} in **1**), whereas the same C-C stretching mode located in the innermost benzene ring shifts towards lower frequencies (i.e., 1567 cm^{-1} in **2** and 1562 cm^{-1} in **1**). Thus, the insertion of external triphenylene groups results in much softer π-conjugated triindole core; note that the frequency downshift of the C-C stretching vibrations is associated with an overall relaxation of the structure upon elongation of the core. On the other hand, the I_{1605}/I_{1567} intensity ratio increases upon enlarging the core of the platform which is also in line with a more efficient π-conjugation in the extended platform **1** when compared to related triindole **2**. The good agreement found between the theoretical and the experimental Raman spectrum supports our discussion (see Supporting Information).

[38] Brédas, J. L.; Beljonne, D.; Coropceanu, V.; Cornil, J.; *Chem. Rev*. **2004**, 104, 4971.
[39] Valeev, E. F.; Coropceanu, V; da Silva, D. A., Salman, S., Bredas J. L.; *J. Am. Chem. Soc*. **2006**, 128, 9882.
[40] Sini, G., Sears, J. S., Bredas, J. L.*; J. Chem. Theory Comput*. **2011**, 7, 602.

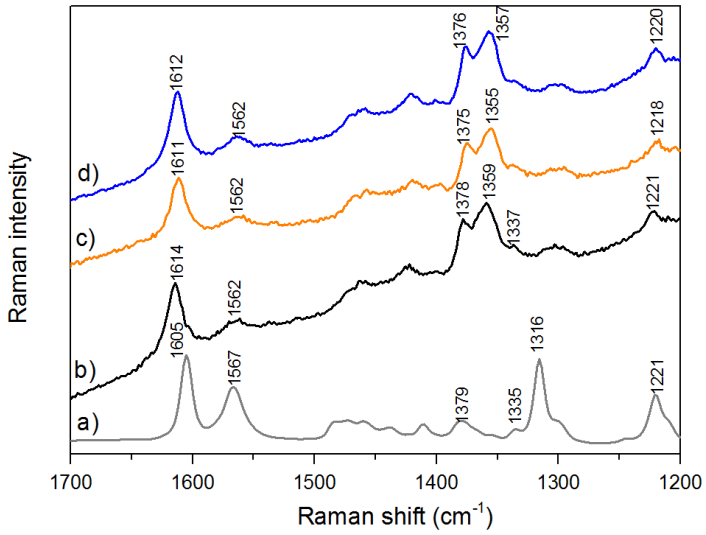

Figure 2. Raman spectra of *N*-dodecyl triindole **2** as a bulk a). Raman spectra of π-extended triindole **1** as a bulk b), as a drop-casted thin film on gold c) and on SiO_2 d) surfaces.

The extended triindole platform shows a high tendency to self-assemble in solution as determined by a ^{1}H-NMR study at variable temperature. In chloroform solution, ^{1}H-NMR spectra of compound **1** are concentration dependent, with several aromatic proton signals of the core moving up field with increasing concentration (see Figure 3).This effect has been well documented as symptomatic of aromatic interactions and reflects the magnetic anisotropy that an aromatic system exerts on a proton in its close vicinity. Study of self-aggregation by NMR gives a lot of information on the geometry of aggregates. In this particular case, the central triindole protons and the protons labeled as *a* and *b* in the triphenylene unit are the most affected, while those placed in the fiord region (labeled as *d*) remain nearly constant. A clear pronounced up field effect is also observed for the *α-CH*$_2$ (labeled as *m*) proton signals of the *N*-dodecyl chains. The different extent of shielding effects observed in the different proton signals suggests an alternated arrangement in which each molecule is rotated by 60º with respect to the next molecular unit. Such arrangement would place *Hc* and *Hc´* protons out of the shielding cone of the aromatic system, thus explaining their poor shifting.

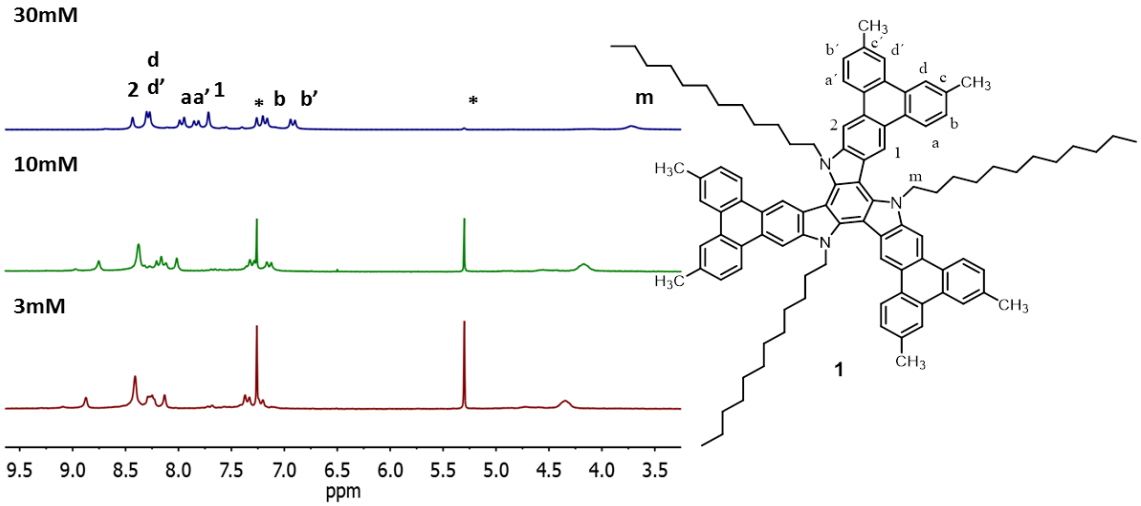

Figure 3.Variation of the aromatic and methylenic ^{1}H-NMR signals of compound **2a** upon varying the concentration.

Charge mobility measurements were performed initially by the Space Charge Limited Current (SCLC) method on samples sandwiched between two electrodes. This method has been widely used to obtain values of mobility of different triindole-based derivatives[21-23] and other discotic mesogens.[41, 42] It should be noted that this technique measures bulk mobility and is very sensitive to structural defects of the macroscopic alignment (as it requires a conduction channel perpendicular to the electrodes) and to the charge injection effectiveness at the electrodes. Therefore the measured values of mobility can be considered as a lower limit.

In a current/voltage measurement, at low fields the observed current is ohmic, depending linearly on the field, while at higher fields the number of injected charges starts to be non-negligible and a space-charge field is present, with the current following the Mott-Gurney equation:

$$J = \frac{9}{8}\varepsilon_0\varepsilon_r\mu\frac{V^2}{d^3} \qquad (1)$$

where J is the measured current density, μ is the charge mobility, ε_0 is the free space permittivity, ε_r is the relative dielectric constant of the material, V is the applied voltage and d is the thickness of the compound layer in the device. From the equation, since the relative dielectric constant ε_r and the sample thickness can be easily measured, it is possible to obtain the mobility. By using this method, in order to extract meaningful information from experiments, materials have to be sandwiched between two electrodes

[41] Cour, I.; Pan, Z.; Lebruin, L. T.; Case, M.A.; Furis, M.; Headrick, R. L.; *Org. Electr.* **2012**, *13*, 419.
[42] An, Z.; Yu, J.; Domercq, B.; Jones, S. C.; Barlow, S.; Kippelen, B.; Marder, S. R.; *J. Mater. Chem.* **2009**, *19*, 6688.

which are chosen in such a way that an ohmic contact is obtained either with the HOMO level of the molecular semiconductor or with its LUMO level. In the first case hole mobility can be measured, while electron mobility is extracted in the second case.

Gold was used as the positive electrode because its work function W(Au) = -5.1 eV.[43, 44] matches the HOMO value of **1** (-5.12 eV), ensuring the efficient hole injection necessary in order to avoid major underestimations of mobility values.

As a counter-electrode we used ITO because its work function W(ITO) ~ -4.6 eV is much lower than the estimated LUMO energy of **1** and because, being transparent, allows to check the orientation of the liquid crystal by Optical Microscopy. In this particular case, Polarizing Optical Microscopy indicates that the sample is partially aligned. Figure 4 shows a typical J/V curve, acquired by connecting the positive pole to the Au electrode and the negative pole to the ITO. As it can be observed, the shift from the ohmic to the SCLC regime is quite clear.[45] Different samples showed similar behavior and the average value of mobility is 0.65 ± 0.15 $cm^2V^{-1}s^{-1}$.

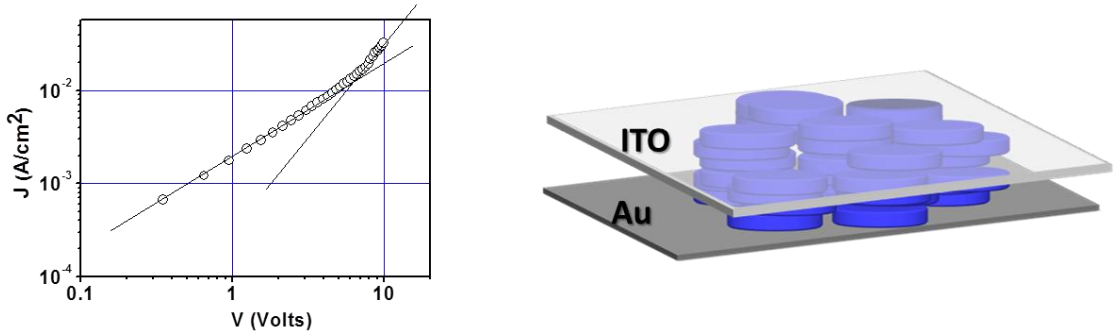

Figure 4. Current/Applied voltage curve for a sample of **1** with a 22 µm thickness. In order to appreciate the quality of the data, two continuous lines with slopes 1 and 2 have been included, representing ideal linear and quadratic regimes of the current as a function of applied voltage.

Alternatively we have determined the charge mobility of this semiconducting mesogen in a field effect transistor device. In this technique charge transport highly relies on the first few layers of molecules and its performance depends strongly on the molecular orientation of the semiconductor at the dielectric-semiconductor interface. Thin-film transistors were fabricated in a bottom gate, top contact configuration by drop-casting a chloroform solution of **1** on HMDS-functionalized Si/SiO_2 substrate, followed by evaporation of gold electrodes through a shadow mask. Figure 5 shows the transfer characteristics of **1** measured at a fixed source-drain voltage of -80 V. Charge transport

[43] Chen, S.-H.; *J. Appl. Phys.***2005**, 97, 073713.
[44] Sharma, A.; Kippelen, B.; Hotchkiss, P. J.; Marder, S. R. *Appl. Phys. Lett*. **2008**, 93, 163308.
[45] Mott, N. F.; Gurney, D.; *Electronic Processes in Ionic Crystals*; Academic Press: New York, **1970**.

evaluation was carried out *via* analysis of the OFET current-voltage response in the saturation regime with the hypothesis of conventional transistors theory, following eqn:

$$I_D = \frac{WC_{ox}\mu}{2L}(V_G - V_{th})^2 \qquad (2)$$

where *W* and *L* are the channel width and length, respectively, C_{ox} is the capacitance per unit area of the dielectric layer, μ is the hole mobility and V_{th} is the threshold voltage. Figure 5b represents the output curves of **1** measured at gate voltages from 0 to -80 V in intervals of 20 V. A mobility of $1.01x10^{-4}$ $cm^2V^{-1}s^{-1}$ with a threshold voltage close to -2 V could be determined wit this technique.

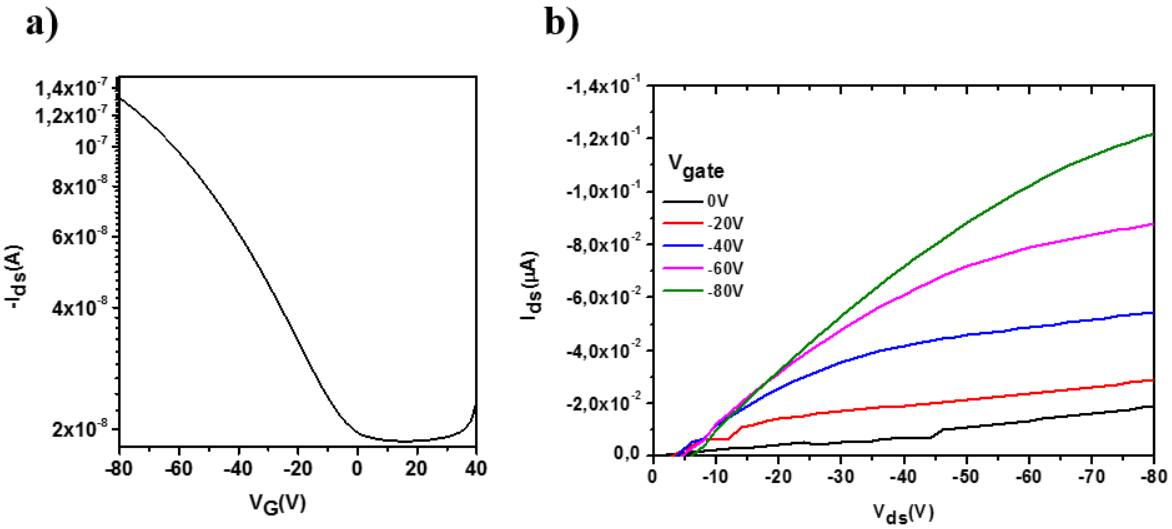

Figure 5.a) Transfer characteristics of **2a** measured at a source-drain voltage of -80V. Linear plot of the drain current versus the gate voltage. b) Characteristic transistor curves of **2a** measured at gate voltages from 0 to -80V in intervals of 20V.

Note that due to the uniaxial conduction found in discotic liquid crystals it is common to observe differences of up to more than 5 orders of magnitude when comparing measurements of mobility along different directions, performed by a different or even by the same technique.[46, 47] In order to shed light on the origin of the lower OFET charge mobility when compared to the SCLC mobility, we established the molecular orientation at the bottom interfaces of thin films of compound 2 by Surface Enhanced Raman Scattering (SERS). SERS is a very useful technique for the characterization of molecular features near the surface providing valuable information of the interfacial layer in thin films[48] as it allows for greatly enhanced Raman scattering from molecules that

[46] Eccher, J.; Faria, G. C.; Bock, H.; von Seggern, H.; Bechtold, I. H.; *ACS Appl. Mater. Interf.* **2013**, 5, 11935.
[47] Deibel, C.; Janssen, D.; Heremans, P.; de Cupere, V.; Geerts, Y.; Benkhedir, M. L.; Adriaaenssens, G.; *J. Org. Electr*. **2006**, 7, 495.
[48] Xu, J.; Diao, Y.; Zhou, D.; Mao, Y.; Giri, G.; Chen, W.; Liu, N.; Mannsfeld, S. C. B.; Xue, G.; Bao, Z.; *J. Mater. Chem. C*, **2014**, 2, 2985.

have been adsorbed onto specially prepared metal surfaces.[49] This surface enhancement (*i.e.*, the surface signal overwhelms the bulk signal) is a combination of a local enhancement of the electromagnetic field and contributions from chemical interactions between the molecules and the metal surface. We carried out Raman measurements on drop-casted and spin-coated film of triindole **1** prepared on gold and SiO_2 surfaces. Neither, Raman enhancement of selected peaks nor appearance of new peaks is observed when comparing the spectra of films on SiO_2 and on gold surfaces (see Figure 2). Similar results are found for the films prepared by either drop-casting or spin-coating. Note that normal modes involving vibrations associated with a component of the polarizability tensor which is normal to the surface should be selectively enhanced due to the SERS effect. In the case of an "edge-on orientation", these normal modes would be the ones associated with a component of the polarizability tensor along the molecular axis, such as the ones recorded at 1614 and 1562 cm^{-1}. However, no changes in Raman intensity are recorded for films deposited on both substrates (SiO_2 and gold), thus suggesting that compound **1** takes a "face-on" orientation with respect to the substrate, which would hamper transport parallel to the dielectric as required in OFETs. This is consistent with the decrease in the mobilities values obtained when comparing the thin-film transistor devices and SCLC measurements in a diode-like structure where, on the contrary, the charge-transport occurs through cofacially overlapped molecules.

In order to analyze in more detail the charge-transport parameters impacting charge mobility at the molecular level we have made use of DFT calculations. The charge-transport properties of a particular system is connected to the interplay between charge localization effect due to electron-phonon coupling and a charge delocalization effect due to the electronic coupling. The reorganization energy, λ, measures the strength of the so-called local electron-phonon coupling;[50] the smaller λ, the larger the expected charge mobility. Here we focus on the intramolecular reorganization energy associated with hole transfer (λ_h) that reflects the geometric changes needed to accommodate charge.

[49] López-Tocón, I.; Otero, J. C.; Arenas, J. F.; Garcia-Ramos, J. V.; Sánchez-Cortes S.; *Anal. Chem*. **2011**, *83*, 2518.
[50] Coropceanu, V.; Cornil, J.; da Silva, D. A.; Olivier, Y.; Silbey, R.; Bredas, J. L.; *Chem. Rev*. **2007**, 107, 926.

As seen in Figure 6a, enlarging the size of the central core by attaching external triphenylene groups results in smaller λ_h values (*i.e.*, λ_h decrease by 84 meV[51] when comparing **1** and **2** as expected with increasingly larger conjugated backbones). This is in consonance with the small participation of the external triphenylene groups in the geometrical relaxation upon oxidation which is in line with their minimal contribution to the HOMO wave functions (*i.e.*, for both extended **1** and related triindole **2,** HOMO wave functions are mainly localized in the central triindole core, see Figure 6b). It is interesting to note that the calculated λ_h values in triphenylene-extended triindoles (i.e., 147 meV in **1**) is even smaller than that calculated for benchmarking hole-transport materials such as rubrene (159 meV).[52]

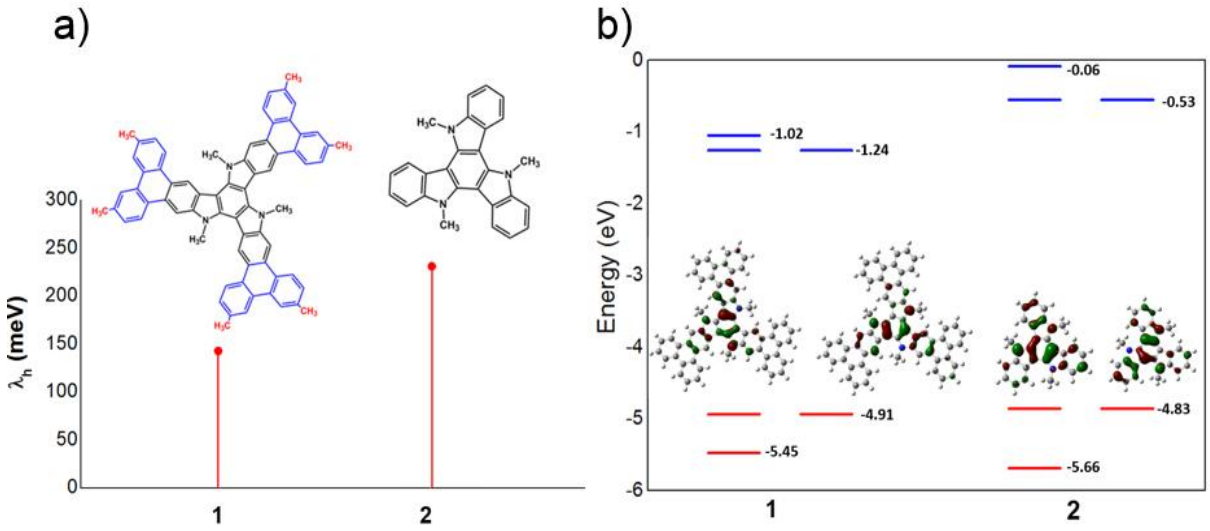

Figure 6. a) DFT-calculated reorganization energy values for holes (λ_h) for triphenylene-extended triindole **1** and related triindole **2**at the B3LYP/6-31G** level. b) B3LYP/6-31G** molecular orbital energies and topologies for both derivatives.

The electronic coupling is defined by the transfer integral. A cofacial dimer in a staggered fashion, with a rotation angle of 60º between the disks and an intermolecular distance of 3.8Å is considered here for the calculation of the transfer integral (see Figure 7). We have chosen this geometry for the adjacent molecules considering the high tendency of these molecules to aggregate in solution adopting an alternated arrangement in which each molecule is rotated by 60º with respect to the next molecular unit[53] and the

[51] Ruiz, C.; García-Frutos, E. M.; da Silva Filho, D. A.; López Navarrete, J. T.; Ruiz Delgado, M. C.; Gómez-Lor, B.; *J. Phys. Chem. C*, **2014**, *118*, 5470.
[52] da Silva D. A.; Kim E. G.; Bredas, J. L.; *Adv. Mater*. **2005**, 17, 1072.
[53] Similar alternated stacking has been observed in aggregates of different triindole derivatives both in solution and in the solid state. See for example: a) García-Frutos, E. M.; Hennrich, G.; Gutierrez, E.;

intrastack periodic distance of ~3.8 Å which has been determined experimentally by XRD for these mesophases. The calculated hole transfer integral for this dimer is found to be -52 meV. Therefore, the HOMO electronic coupling remains moderate for staggered dimers (60º rotated) highlighting the crucial role played by wave function overlap in the central core of the triindole platforms. Note that slightly larger values are obtained for an equivalent dimer made of two triindole molecules. The calculated reorganization energy in the π-extended model is much larger than the electronic coupling, this result suggests that charge localization takes place and transport is expected to occur via a charge-hopping mechanism. In this case, the hopping rate can be estimated in the context of the semi-classical Marcus theory as[54]

$$k_{ET} = t^2 \sqrt{\frac{\pi}{\hbar^2 k_B T \lambda}} exp\left(-\frac{\lambda}{4k_B T}\right) \qquad (3)$$

where λ is the reorganization energy, *t* the transfer integral, k_B the Boltzman constant, *T* the temperature and *ħ* the Planck constant.

At high temperature, the mobility can be expressed as[55]

$$\mu = \frac{qd^2}{k_B T} k_{ET} \qquad (4)$$

where d is the intermolecular distance between the molecules.

Rough estimates of the transfer rates and mobilities can be made by injecting in eqs. 3 and 4 the calculated charge transport parameters for the π-extended aromatic compound **1**. As we can see in Figure 4, the intrisic hole mobility calculated for compound **1** (0.80 $cm^2V^{-1}s^{-1}$) is in very good agreement with the experimental value obtained by SCLC measurements (0.65 $cm^2V^{-1}s^{-1}$).

Monge, A.; Gómez-Lor, B.; *J. Org. Chem.* **2010**, *75*, 1070. b) García-Frutos, E. M.; Gutierrez-Puebla, E.; Monge, M. A.; Ramírez, R; de Andrés, P.; de Andrés, A.; Ramírez, R.; Gómez-Lor, B.; *Org. Electr.***2009**, *10*, 643.

[54] Marcus, R. A.; *Reviews of Modern Physics* **1993**, *65*, 599.

[55] Pope, M.; Swenberg, C. E.; *Electronic Processes in Organic Crystals and Polymers*; 2nd ed.; Oxford University Press: New York, **1999**.

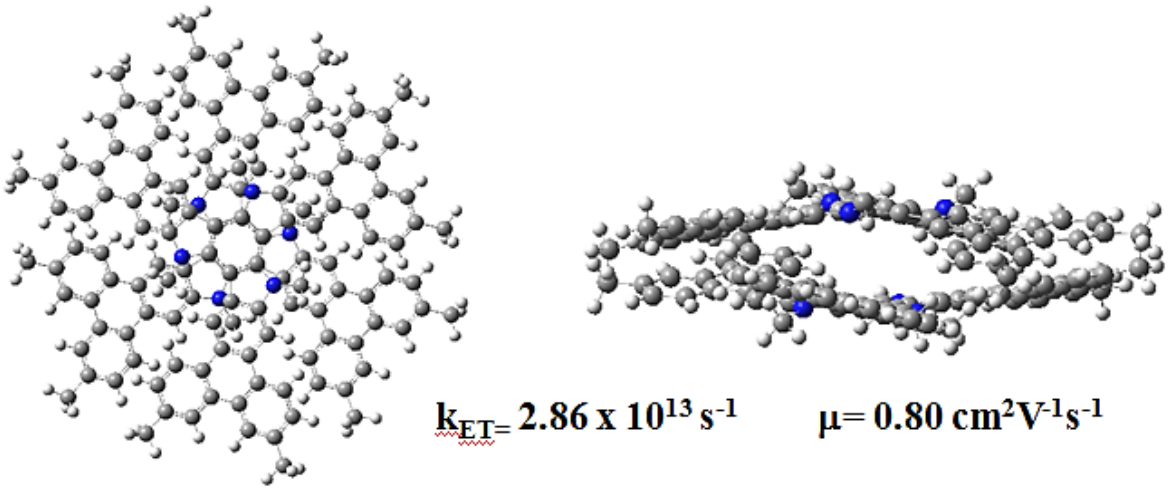

Figure7. Top and lateral views of a cofacial dimer of **2** in a staggered fashion, with a rotation angle of 60º between the disks and an intermolecular distance of 3.8 Å. The transfer rates (k_{ET}) and mobilities (μ) calculated for the model dimer are also shown.

3.2.4. CONCLUSION

In conclusion we have studied the electrical properties of a discotic liquid crystal based on a π-extended aromatic platform that contains structural characteristics of both triphenylene and triindole by applying two different methods: space-charge limited current (SCLC) measurements in a diode-like structure and field effect mobility measurements in a thin film transistor device. The mobility found on a diode type device is higher than that determined on thin film transistors, which can be understood by the high tendency of large π-conjugated molecules to deposit on surfaces with their extended core parallel to the substrate as demonstrated by SERS. However, the observation of field effect behavior in a discotic liquid crystal processed by simple drop-casting suggests an increased dimensionality of charge transport by facilitating hopping between neighboring columns as a result of the large conducting/isolating ratio found in this discotic platform. The hole-mobility of this material theoretically predicted via a charge-hopping mechanism is in very good agreement with the experimental values determined at the space-charge limited current (SCLC) regime.

3.3. LOWER DEPENDENCE OF THE ALIGNMENT ON THE ELECTRONIC PROPERTIES OF DISCOTIC LIQUID CRYSTAL

In this section, a different attempt designed to decrease the high dependence of semiconducting triindole-based liquid crystals towards alignments, is presented. In this approach we have attached to the triindole platform six peripheral groups able to establish intermolecular interactions in order to facilitate contacts between neighbouring columns.

As shown in chapter 1, the heptacyclic platform of triindole is highly prone to establish CH-π interactions, a type of interactions that are favored by increasing the electron density in the π-acceptor system. The importance of CH-π interactions in driving the self-assembly of triindole-based materials have already been previously noted by my research group, which has shown that by attaching six peripheral electron-donor substituents in triindole-based materials it is possible to induce aggregation in solution and mesomorphism.[56, 57] With these previous results in mind, in this chapter we investigate the influence of six *p*-thiomethylphenyl substituents in the self-assembling behavior of triindoles. Although according to the Hammett substituent constants, the thiomethyl groups are neither electron-donors nor electron-acceptors, when situated in *para*-positions they are able to add significant electron density to the π-system due to resonance effects. On the other hand, thiomethyl groups are prone to establish S-S interactions which have already been shown favorable to increase contact between neighboring columns in other semiconducting aromatic platforms.[58]

In an attempt to obtain single crystalline and possibly liquid crystalline bulk materials which allow us to state the influence of these moieties in the self-assembly of triindoles (Scheme 3.1), we have synthesized two derivatives with different functionalization in the nitrogens, **1a** (which bearins three methyl groups) and **1b** (which bears three dodecyl groups).

[56] García-Frutos, E. M.; Hennrich, G.; Gutierrez, E.; Monge, A.; Gómez-Lor, B.; *J. Org. Chem.*, **2010**, 75, 1070.
[57] García-Frutos, E. M.; Omenat, A.; Barberá, J.; Serrano, J. L.; Goméz-Lor, B.; *J. Mater. Chem*., **2011**, 21, 6831.
[58] a) Kimoto, T.; Tanaka, K.; Kawahata, M.; Yamaguchi, K.; Otsubo, S.; Sakai, Y.; Ono,Y.; Ohno, A.; Kobayashi, K.; *J. Org. Chem*. **2011**, 76, 5018. b) Kobayashi, K.; Shimaoka, R.; Kawahata, M.; Yamanaka, M.; Yamaguchi, K.; *Org. Lett*. **2006**, 8, 11.

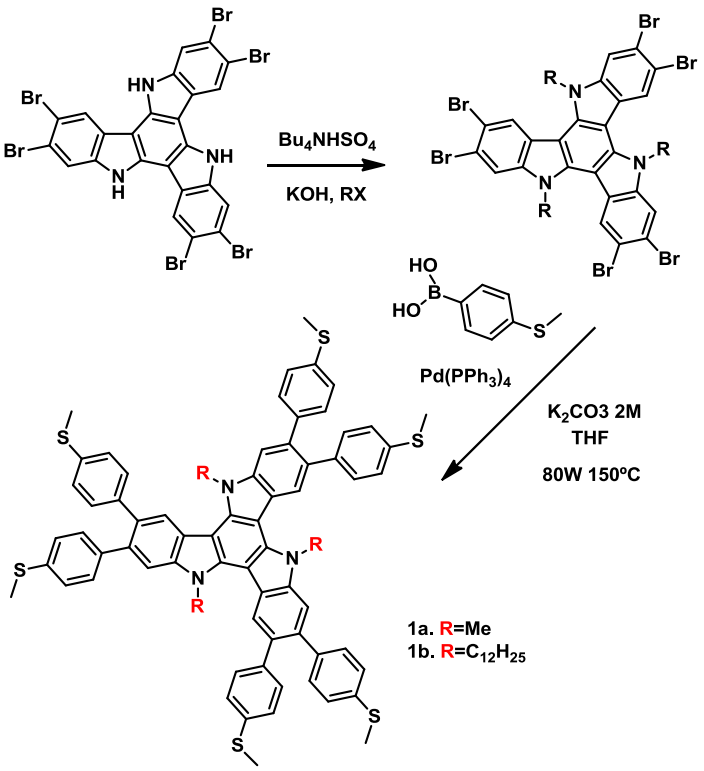

Scheme 3.1: Synthesis of compounds **1a** and **1b**.

Compound **1a** is obtained as a microcrystalline powder, however all attempts to grow crystals with sufficient size for X-ray single crystal analysis failed, probably due to its poor solubilitiy. In order to gain insight into the organization of the molecules in the crystal we have obtained its X-ray powder diffractogram. As shown in Figure 3.2a the diffractogram of **1a** is characterized by four strong Bragg reflections at low angle at 2θ = 4.63º, 7.94º, 9.16º and 12.10º (d= 19.06 Å, 11.12 Å, 9.64 Å and 7.31 Å) which correspond to a reciprocal spacing ratio of 1:√3:2:√7, indicative of a columnar hexagonal organization. This organization is reminiscent of the one observed for laterally unsubstituted parent *N*-trimethyltriindole.

As shown in chapter 1, *N*-trimethyltriindole adopt a columnar hexagonal organization forming stacks along the crystallographic *c*-axis which is the longest dimension in the crystal (Figure 3.2b). This organization has been reasoned considering the contribution of a number of cooperative CH-π interactions in stabilizing the columnar arrangement. As the molecule has C_3 symmetry with the centroid of the central aromatic ring situated in the threefold axis, all the methyl groups would be in involved in such interactions.

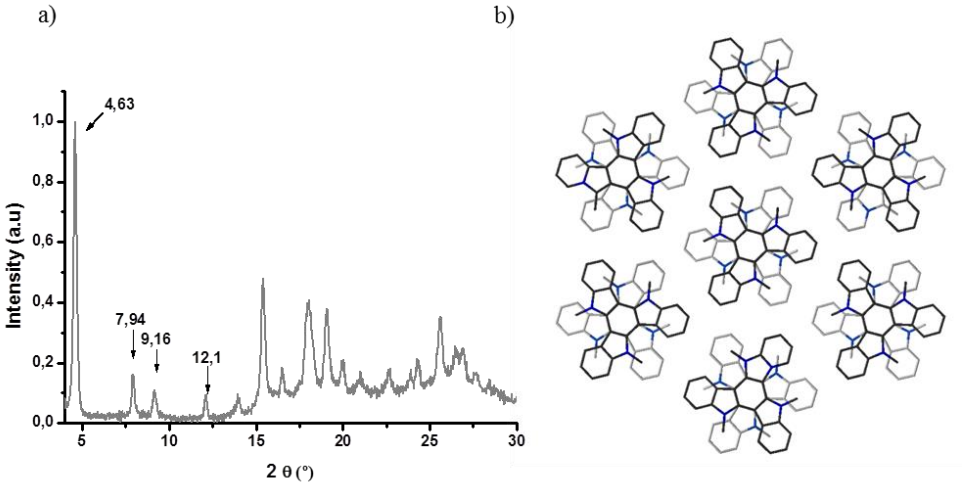

Figure 3.2: a) Powder X-ray diffraction of the *N*-methyl phenyltiomethyl triindole. b) Hexagonal packing of the *N*-methyltriindole.

We have obtained SEM images of the crystallites of **1a** deposited on a silicon substrate and compared them with those obtained for parent trimethyltrindole. As can be observed in Figure 3.3, although both crystalline materials have a hexagonal cross section (see inset amplification), their final morphology differs strongly: *N*-trimethyltriindole crystallize as wires, while **1a** grow as hexagonal platelets.

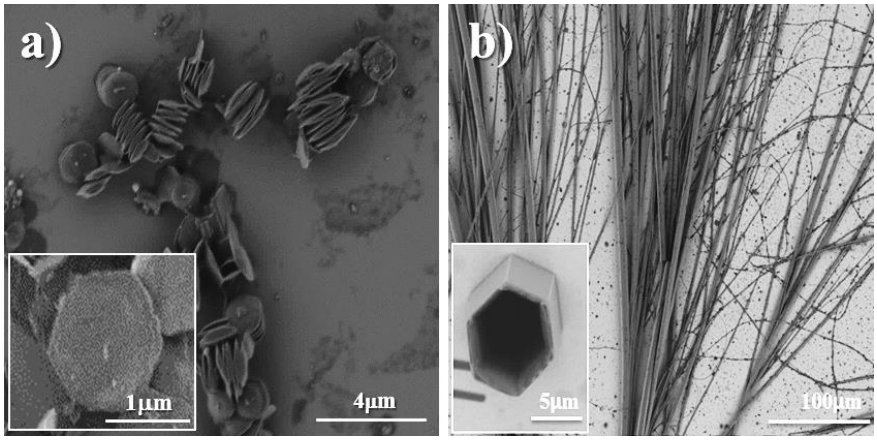

Figure 3.3: Images of Field Emission Electron Microscopy (FE-SEM) of the crystalline structures of a) **1a** and b) *N*-methyl triindole deposited by dip-coating on a silicon substrate

Considering that the growth rate of a facet is directly related to its attachment energy (the energy necessary to split a slide of a facet), the different morphology observed in these two derivatives is indicative of important lateral interactions between the columns in **1a** which would favour the growth of the crystals along the diameter of the column. In contrast *N*-trimethyltriindole shows interactions only along the [001] direction

while no interaction can be found between columns which would justify the growth of other facets of the crystal.

In contrast to **1a**, compound **1b** is highly soluble in common organic solvents. Thin films of this compound were fabricated by drop casting a chloroform solution of **1b** and studied by powder X-ray diffraction. As we can see in the Figure 3.4, the diffractogram is dominated by an intense peak at low angles 2θ = 3.82º (24.9 Å), a broad halo at high angles (which probably correspond to the three disordered *N*-alkyl chains) and a weak and poorly defined peak at 19.49º (4.54 Å) which can be assigned to a intracolumnar periodic distance of 2θ = 4.54 Å. Such X-ray patterns would be in agreement with a columnar mesophase however the total absence of fluidity of this material suggests it to be a poorly organized crystalline phase.

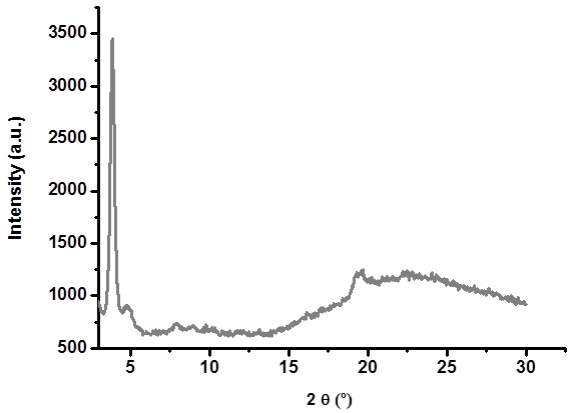

Figure 3.4: Powder X-ray diffractograms of a film of **1b** deposited by drop-casting a chloroform solution on the substrate

The thermal properties of **1b** were studied in collaboration with the group of Prof. J. L Serrano at the University of Zaragoza. This compound form a mesophase that extends from 59.3ºC- 160.7ºC in spite of being endowed with only three long alkyl chains. The mesophase has been assigned (by means of DSC, polarized optical microscopy and X-ray diffraction at different temperatures), as an ordered columnar hexagonal mesophase with a lattice constant *a* = 24.9 Å and periodic intracolumnar distance of 4.3 Å.

- **Mobilities measurements**

In order to confirm that we could increase the dimensionality of the charge transport by the incorporation of six peripheral thiomethyl groups, we have made an

analogous study to that performed in section 3.2, which consists in comparing the mobility values obtained by applying two different methods with different alignment requirements: space-charge limited current (SCLC) measurements in a diode-like structure (which requires a conducting channel perpendicular to the surface) and field effect mobility measurements in thin film transistor devices (which requires a conducting channel paralel to the surface).

Samples for SCLC measurements were performed by squeezing a sample of the compound previously heated, between one gold and one ITO electrode and then let the material to cool down to room temperature rendering a film of ≈ 2.4 μm. The use of gold as positive electrode ensures the efficient hole injection as its work function is W(Au) = -5.1 eV which matches well with the HOMO value of **1b** (-5.02 eV) which is necessary in order to avoid major underestimations of mobility values.

As a counter-electrode we used ITO because its work function W(ITO) ~ -4.6 eV is much lower than the estimated LUMO energy of **1b** (-2.01 eV) and because it is transparent and therefore allows checking the orientation of the liquid crystal by Optical Microscopy.

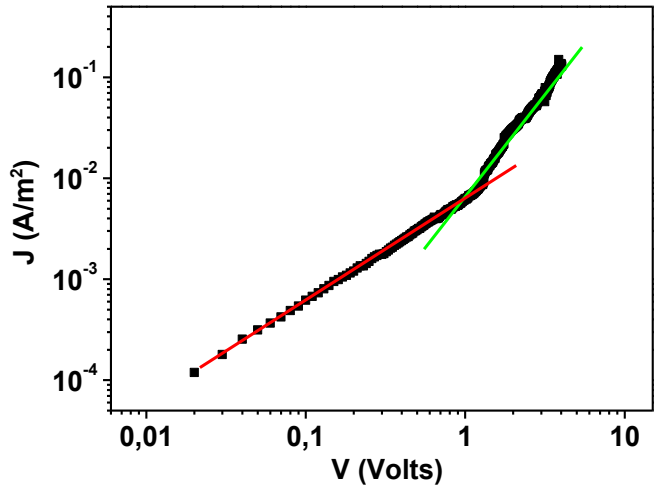

Figure 3.5: Current/Applied voltage curve for a sample of **1** with a 2,4 µm thickness. In order to appreciate the quality of the data, two continuous lines with slopes 1 and 2 have been included, representing ideal linear and quadratic regimes of the current as a function of applied voltage.

Figure 3.5 shows a typical J/V curve, acquired by connecting the positive pole to the Au electrode and the negative pole to the ITO. As can be observed the shift from the ohmic to the SCLC regime is quite clear. Different samples showed similar behavior and the average value of mobility is 3.26 x 10^{-2} $cm^2V^{-1}s^{-1}$. This value represent a significant enhancement when compared with values previously obtained in the group for closely

related hexaphenylnonyltriindole ($\mu \sim 6$ x10^{-4} cm^2 V^{-1} s^{-1}) for **1b** by this same technique.[59] These measurements have been obtained in collaboration with Prof. A. Golemme (University of Calabria).

Alternatively we have determined the mobility values of this semiconducting mesogen in a field effect transistor device. Thin-film transistors were fabricated in a bottom gate, top contact configuration by drop-casting a chloroform solution of **1b** on HMDS-functionalized Si/SiO_2 substrate, followed by evaporation of gold electrodes through a shadow mask. Figure 3.6b shows the transfer characteristics of **1b** measured at a fixed source-drain voltage of -80 V. Figure 3.6a represents the output curves of **1b** measured at gate voltages from 0 to -80 V in intervals of 20 V. A mobility of 3,01 *x* 10^{-4} $cm^2V^{-1}s^{-1}$ with a threshold voltage close to -5 V could be determined wit this technique.

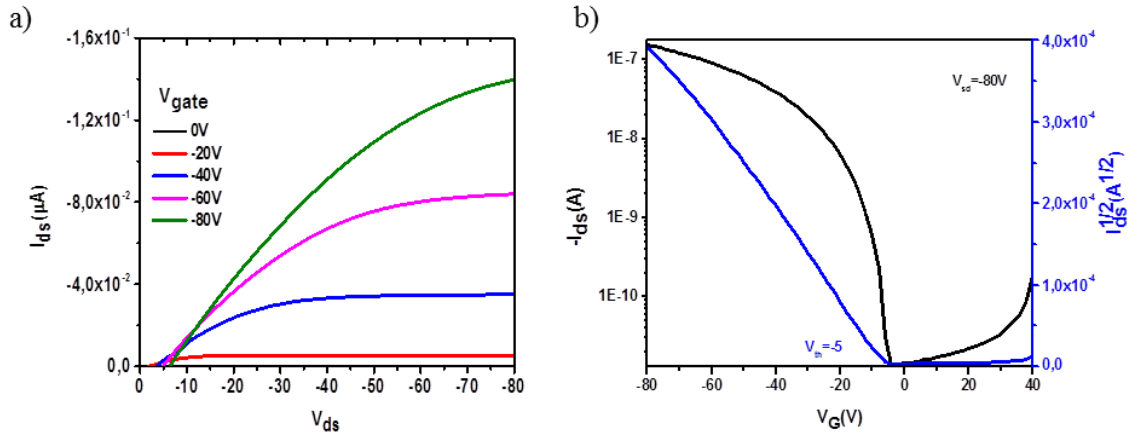

Figure 3.6. a) Characteristic transistor curves of **1** measured at gate voltages from 0 to -80V in intervals of 20V.b) Transfer characteristics of **1** measured at a source-drain voltage of -80V.

The good coincidence between both measurements (the mobility found on a field effect transistor is only 2 orders of magnitude lower than the mobility than the one determined by SCLC), highlights the low dependence of the charge transport properties from alignment which suggest that the thiomethyl groups favor the intercolumnar contacts.

In summary, in this thesis we synthetized a new triindole-based liquid crystal with only three flexible alkyl chain, that allow us an increase of the dimensionality of charge transport, as reflected by the possibility of measuring the mobility by two different techniques with opposite alignment requirements. Although, mobility found on a field effect transistor is only 2 orders of magnitude lower than the mobility than we determined

[59] García-Frutos, E. M.; Pandey,U. K.; Termine, R.; Omenat, A.; Barberá, J.; Serrano, J. L.; Golemme, A.; Gómez-Lor, B.; *Angew. Chem. Int. Ed*. **2011**, 50, 7399.

by SCLC, the observation of field effect behavior in a discotic liquid crystal processed by simple drop-casing suggest an increased dimensionality of charge transport by facilitating hopping between neighboring columns as a result of the large conducting/isolating ratio found in this discotic platform.

Even though unequivocal evidences of the participation of the thiomethyl groups in favoring contacts between columns could not be obtained, an study of the morphology of hexagonal microcrystals of the trimethylated analogue, which prefer to grow in the direction perpendicular to the columnar axis, suggest the existence of strong intercolumnar interactions which would be responsible of the higher attachment energy of these facets.

Chapter 4. Triindole in the generation of microporous aromatic polymers

4. CHAPTER 4. TRIINDOLE IN THE GENERATION OF MICROPOROUS AROMATIC POLYMERS.

4.1. SUMMARY

With the aim of exploring the potential applications of triindole platforms in the development of new emergent electroactive materials, such as microporous organic polymers and covalent organic frameworks, in this chapter we have synthesized two dimeric molecules bound together through different linkers (*p*-phenylene or diacetylene groups), as model systems to investigate the influence of the π-bridge on their fundamental properties, such as the electronic, redox and photophysical properties.

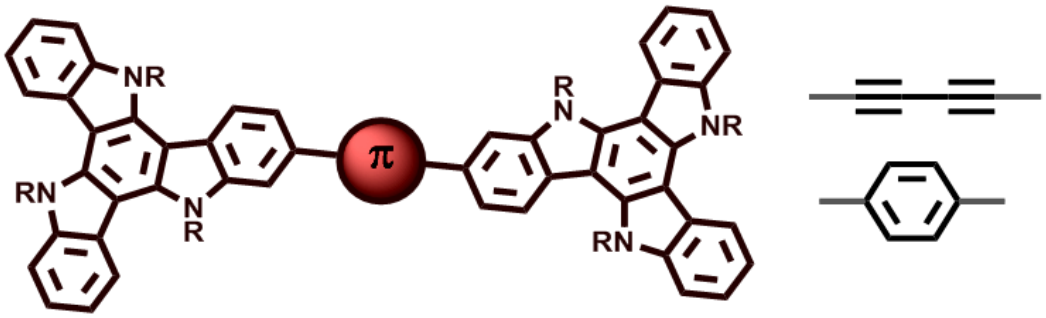

Aromatic microporous polymers constitute an emergent type of organic porous polymers synthesized from π-conjugated monomers with multiple reactive groups to promote molecule-molecule coupling via a π-conjugated bonds. In this type of material, the covalent linkage of functional π-conjugated components gives rise to two-dimensional (2D) layers, among which π -π stacking interactions can induce additional order while their intrinsic porosity offers significant opportunities to incorporate guests/chemicals to tune their functionalities. However, the insoluble character of covalent microporous polymers limits detailed postsynthetic studies to investigate how the structure will affect the desired properties, and thus the design of optimal polymeric materials on a molecular basis. Models as those presented in this chapter with well-defined chemical structures may represent invaluable models to establish clear structure-property relationships, avoiding insolubility, irreproducibility issues, and variations drawbacks in polymeric materials.

Our results show us that while a *p*-phenylene bridge nearly isolates the two subunits of the dimers, a diacetylene bridge allows a high level of electronic connection between them. This conclusion render the diacetylene moiety as the best linker in the synthesis of microporous polymeric material with opto-electronics applications.

This work combine experimental studies of the electronical and photo-physical properties of these new molecules with theoretical studies that have been made in collaboration with Dr. M. Carmen Ruiz Delgado of the University of Málaga.

4.2. TRIINDOLE-BRIDGE-TRIINDOLE DIMERS AS MODELS FOR TWO DIMENSIONALMICROPOROUS POLYMERS

Constanza Ruiz,† Juan T. López Navarrete,‡ M. Carmen Ruiz Delgado,*,‡ and Berta Gómez-Lor*,†

†Instituto de Ciencia de Materiales de Madrid, CSIC, Cantoblanco 28049, Madrid, Spain

‡Department of Physical Chemistry, University of Málaga, 29071 Málaga, Spain

Org. Lett., 2015, 17 (9), pp 2258–2261

4.2.1. ABSTRACT

New dimers with two triindole subunits bound together through different linkers (*p*-phenylene or diacetylene groups) have been synthesized and studied as model systems to determine the differences in the electron transfer ability of the two bridging units. Our results show that whereas a *p*-phenylene bridge nearly isolates the two subunits of the dimers a diacetylene bridge allows a high level of electronic connection between them.

4.2.2. INTRODUCTION

During the past decade, heptacyclic 10,15-dihydro-5*H*-diindolo[3,2-a:3′,2′-c]carbazole (triindole) has been extensively studied as a new π-conjugated platform in the construction of dendrimers and self-assembling materials for optoelectronics due to its strong light emission[1] and efficient charge transport properties.[2],[3] Especially remarkable is the record hole mobility values determined on triindole-based semiconducting liquid crystals as a result of the favorable synergy between the intrinsic properties of the platform and its supramolecular arrangement.[3] This molecule has also recently been explored as the functional component in a microporous chemosensing polymer.[4]

[1] Lai, W. Y.; He, Q. Y.; Zhu, R.; Chen, Q. Q.; Huang, W.; *Adv. Funct. Mater.* **2008**, *18*, 265-276. (b) Levermore, P. A.; Xia, R.; Lai, W.; Wang, X. H.; Huang, W.; Bradley, D. D. C.; *J. Phys. D: Appl. Phys.***2007**, *40*, 1896.

[2] a) García-Frutos, E. M.; Gutierrez-Puebla, E.; Monge, M. A.; Ramírez, R.; Andrés, P. d.; Andrés, A. d.; Gómez-Lor, B.; *Org. Electr.* **2009**, *10*, 643. b) Reig, M.; Puigdollers, J.; Velasco, D.; *J. Mater. Chem.C* **2015**, *3*, 506.

[3] a) Ye, Q.; Chang, J.; Shao, J.; Chi, C.; *J. Mater. Chem.* **2012**, *22*, 13180. b) Benito-Hernández, A.; Pandey, U. K.; Cavero, E.; Termine, R.; García-Frutos, E. M.; Serrano, J. L.; Golemme, A.; Gómez-Lor, B.; *Chem. of Mater.* **2013**, *25*, 117. c) García-Frutos, E. M.; Pandey, U. K.; Termine, R.; Omenat, A.; Barberá, J.; Serrano, J. L.; Golemme, A.; Gómez-Lor, B.; *Angew. Chem. Int. Ed.* **2011**, *50*, 7399.

[4] Liu, X.; Xu, Y.; Jiang, D.; *J. Am. Chem. Soc.***2012**, *134*, 8738.

Covalent microporous polymers constituted by π-conjugated building units have emerged as a new kind of organic material for electronic applications.[5] In this type of material, the covalent linkage of functional π-conjugated components gives rise to two-dimensional (2D) layers, among which π -π stacking interactions can induce additional order while their intrinsic porosity offers significant opportunities to incorporate guests/chemicals to tune their functionalities. Potential applications have been demonstrated, such as light harvesting,[6] luminescence,[7] sensing,[4] photochemical water splitting,[8] and charge transport.[9] For optoelectronic applications, it is highly desirable that the π-conjugation spans the 2D sheets; however, in covalent microporous polymers, electronic conjugation is often limited to the constituent building π-functional units. The degree of lateral conjugation and electronic coupling is highly dependent upon the nature of the bridge that connects the individual interacting components and has a profound effect on the behavior of excitons and charge carriers. In spite of the impressive progress that this field has experienced during the past few years, the insoluble character of covalent microporous polymers limits detailed postsynthetic studies to investigate how the structure will affect the desired properties and thus the design of optimal polymeric materials on a molecular basis. Note that examples of soluble conjugated microporous polymers reported to date are quite scarce.[10] Discrete low molecular weight oligomers with well-defined chemical structures may represent invaluable models to establish clear structure−property relationships, therefore avoiding insolubility, irreproducibility issues, and variations from batch-to-batch, which are common drawbacks in polymeric materials.

To facilitate the design of new triindole-based polymeric materials on a molecular basis and establish clear guidelines to fine-tune parameters, such as energy gap, light absorption, and light emitting properties, we have synthesized two new dimers in which the two triindole molecules are linked by *p*-phenylene or diacetylene bridges. The present work aims to investigate the influence of the π-bridge in the electronic communication

[5] a) Xu, Y.; Jin, S.; Xu, H.; Nagai, A.; Jiang, D. *Chem. Soc. Rev.* **2013**, *42*, 8012. b) Thomas, H. *Angew. Chem. Int. Ed.* **2010**, *49*, 8328.

[6] Chen, L.; Honsho, Y.; Seki, S.; Jiang, D.; *J. Am. Chem. Soc.* **2010**, *132*, 6742.

[7] a) Jiang, J. X.; Trewin, A.; Adams, D. J.; Cooper, A. I.; *Chem. Sci.*, **2011**, *2*, 1777. (b) Xu, Y.; Chen, L.; Guo, Z.; Nagai, A.; Jiang, D.; *J. Am. Chem. Soc.* **2011**, *133*, 17622.

[8] Ding, H.; Li, Y.; Hu, H.; Sun, Y.; Wang, J.; Wang, C.; Wang, C.; Zhang, G.; Wang, B.; Xu, W.; Zhang, D.; *Chem. Eur. J.* **2014**, *20*, 14614. (c) Bildirir, H.; Paraknowitsch, J. P.; Thomas, A.; *Chem. Eur. J.* **2014**, *20*, 9543.

[9] Bura, T.; Leclerc, N.; Fall, S.; Lévêque, P.; Heiser, T.; Ziessel, R. *Org. Lett.* **2011**, *13*, 6030.

[10] The regioselectivity of the reaction can be understood considering the radical character of the aromatic bromination exerted by NBS. The 2-position bears significant higher electron density than the 3-position, as has been previously determined by a Mulliken population analysis of the electron spin distribution of the triindole radical cation. See reference 2a.

between the two triindole groups. To this end, we performed a detailed study of the electronic and photophysical properties of the new dimers and their monomeric analogues using absorption, emission, and Raman spectroscopies, cyclic voltammetry, and DFT calculations.

The synthesis of the two dimeric molecules has been performed starting from 2-monobromo-N-dodecyltriindole. This molecule has been obtained by bromination of *N*-dodecyltriindole **1** with 1 equiv of NBS under high-dilution conditions. Under these conditions, compound **2** is obtained along with some dibrominated derivatives. It should be noted that this molecule has been previously wrongly assigned as 3-monobromotriindole.[11] The unambiguous characterization of this molecule has been performed by MS, ^{1}H and ^{13}CNMR, as well as HMBC and HMQC 2D experiments (see Supporting Information).[12] Compound **6**, with two triindole units separated by a phenylene linker, was obtained by a palladium-catalyzed Suzuki cross-coupling reaction between 2 equiv of 2-bromotriindole **2** and 1 equiv of benzene 1,4- diboronic acid. Separately, compound **7** was obtained by Glaser homocoupling of 1-ethynyltrindol **5** (obtained by Sonogashira coupling of the monobrominated precursor with TMS acetylene to render **4**, followed by deprotection with NaOH).

[11] Ruiz Delgado, M. C.; Casado, J.; Hernández, V.; López Navarrete, J. T.; Fuhrmann, G.; Bäuerle, P.; *J. Phys. Chem B.* **2004**, *108*, 3158.
[12] Wilson, E. B.; Decius, J. C.; Cross, P. C.; *Molecular Vibrations. The Theory of Infrared and Raman Vibrational Spectra*; McGraw-Hill: New. York, Toronto, London, **1955**.

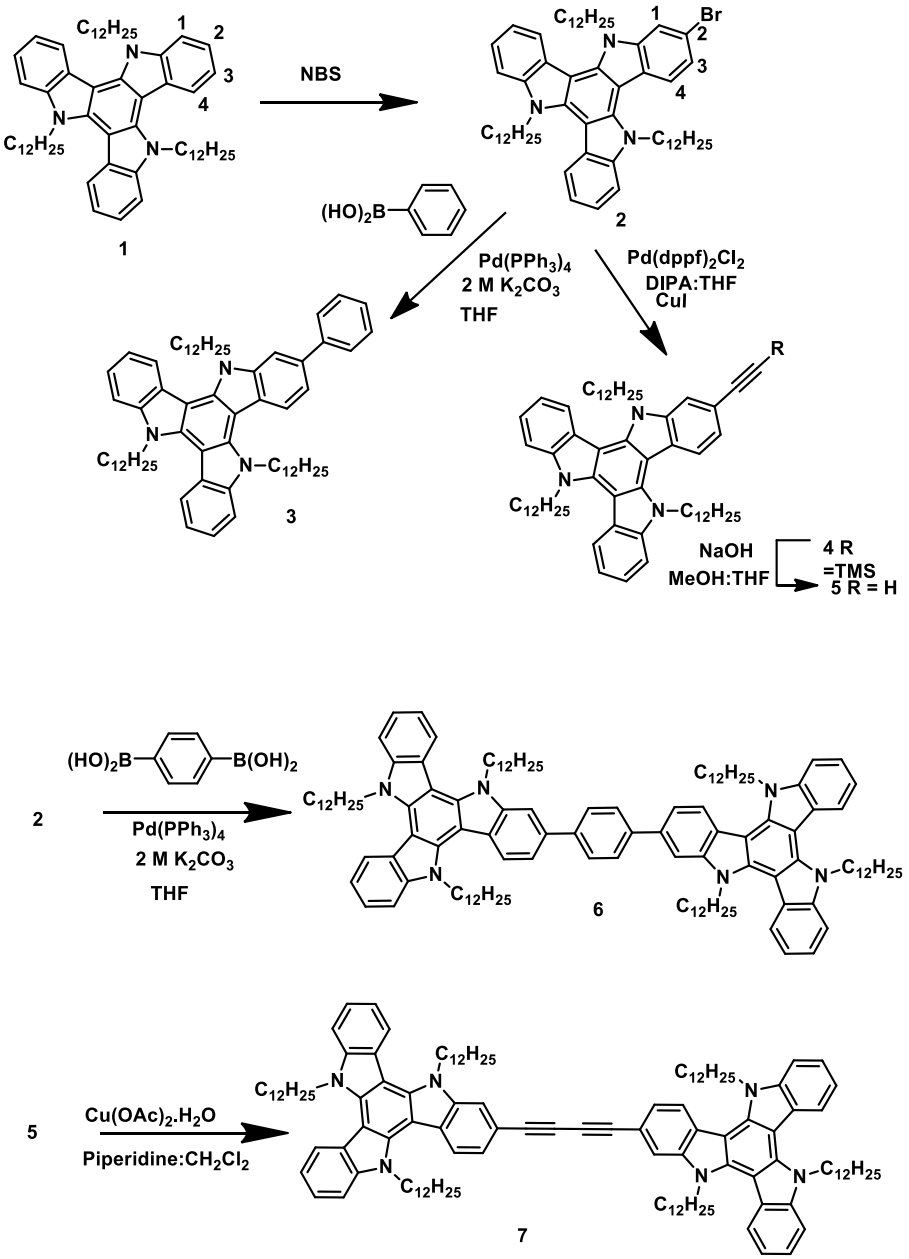

Scheme 1. Synthesis of dimeric molecules **6** and **7** and their monomer analogues **3** and **5**, respectively.

As shown in Figure 1 and Table 1, the electronic absorption maxima and the absorption edge of **3** and **5** monomers are slightly red-shifted when compared to the unsubstituted triindole **1** with both ethynyl and phenyl substituents exerting a very similar effect. This HOMO−LUMO gap decrease is associated with stabilization of the LUMO upon insertion of the ethynyl or phenyl groups, while the HOMO energies are slightly affected; note that the LUMOs of **3** and **5** are more localized at the external ethynyl or phenyl groups, whereas their HOMOs are delocalized over the entire molecular π-frameworks (see Figure S1, Supporting Information). However, when going from the

monomers to the dimers, the overall shapes of the electronic spectra change with the appearance of a new band at a longer wavelength and a significant red-shift of the absorption edge with this effect being more significant in the diacetylene-bridged triindole dimer **7** (see Figure 1). Time dependent DFT vertical excitation energies are in agreement with the experimental data and predict that this band is associated with a HOMO → LUMO one-electron excitation (see Table 1 and Figure S2, Supporting Information). As evidenced by the frontier molecular orbitals of dimers **6** and **7** shown in Figure 2, the lowest-energy electronic transition has a certain charge-transfer character (i.e., the HOMOs are delocalized over the entire molecular π-frameworks whereas the LUMOs are more localized at the central spacer) thus resulting in a HOMO − LUMO decrease. This effect is more pronounced in **7** due to the electron-accepting character and cylindrical symmetry of the diacetylenic spacer, which allows for better extension of π-conjugation.[13] In fact, the rotation around the triindole moieties and the central spacer has been explored by DFT calculations (see Figure S3, Supporting Information), and a rather flat torsional potential is found for the diacetylenic-bridged dimer **7** with a very small energy difference (0.32 kcal/mol) between the perpendicular conformation and the most stable trans coplanar conformer. The coexistence of these two conformers at room temperature has also been confirmed by temperature-dependent absorption spectra measurements (see Supporting Information). However, the most stable conformation of dimer **6** corresponds to a moderately distorted configuration, where the central phenyl ring is rotated by 36° with respect to the triindole moieties, which is thus less favorable toward π-electron delocalization than that of the diacetylenic spacer.

[13] Ruiz, C.; García-Frutos, E. M.; da Silva Filho, D. A.; López Navarrete, J. T.; Ruiz Delgado, M. C.; Gómez-Lor B. *J. Phys. Chem C.* **2014**, *118*, 5470.

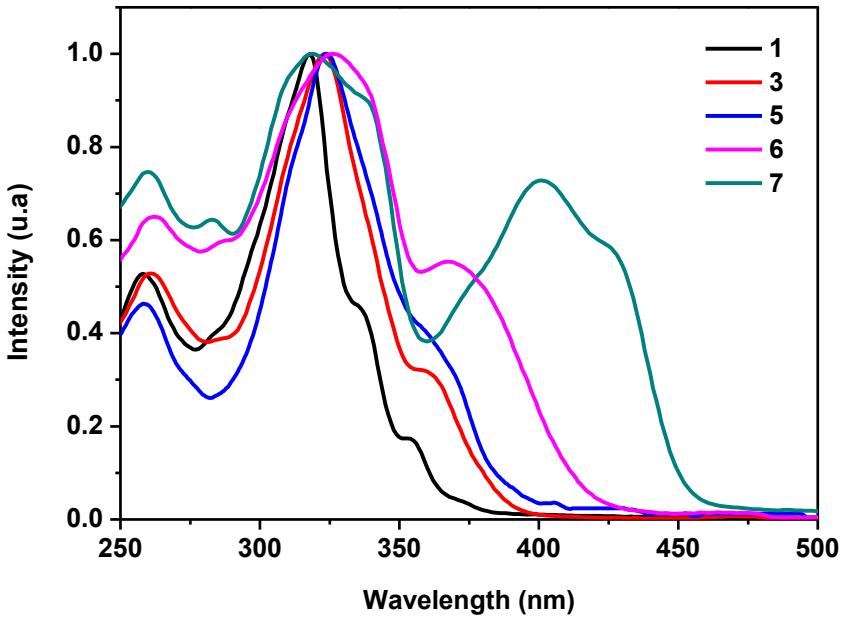

Figure 1. Experimental UV-vis spectra of unsubstituted **1**, monomers **3, 5** and dimers **6**, **7** in CH_2Cl_2, *c* = 5 x 10^{-6} M.

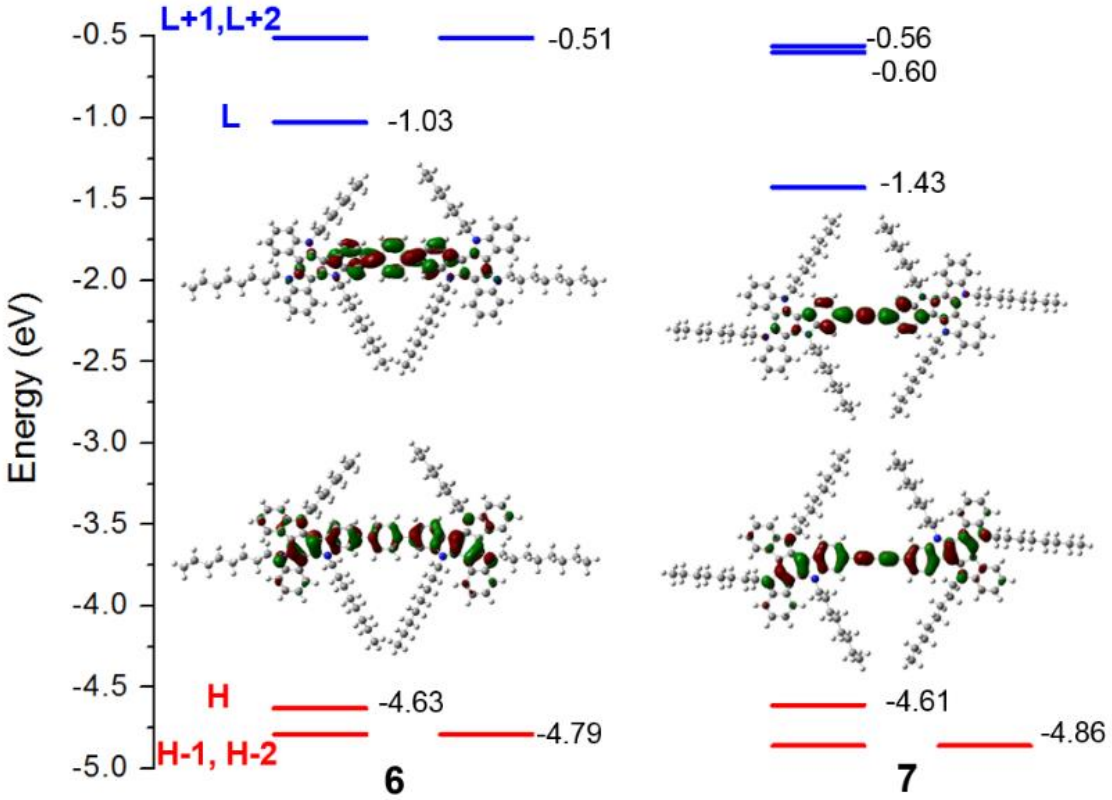

Figure 2. DFT-calculated molecular orbital energies (B3LYP/6-31G** level) for dimers **6** and **7**. The topologies of the frontier molecular orbitals are also shown.

Table 1. Optical and Fluorescence Properties.

	HOMO[a](eV)	LUMO[a](eV)	$\lambda_{(abs)}$[b](nm)	$\lambda_{(abs,\ calc)}$[b](nm)	$\lambda_{(em)}$(nm)	Φ_{PL}(%)
1	-5,05	-1,78	318[4,19]	312 (*f=0.46)*	397	0,23
3	-5,05	-1,93	320,[5.10]	353 (*f=0.30)*	421	0,50
5	-5,13	-1,97	322,[4.90]	352 (*f=0.21)*	427	0,47
6	-5,06	-2,07	326,[5.01]	390 (*f=0.1.66)*	447	0,48
7	-5,08	-2,39	318,[5.23]	444 (*f=2.38)*	468	0,42

[a]The HOMO energy values for **1** to **7** were estimated from the first oxidation potential with respect ferrocene/ferrocenium redox couple. The LUMO energy values were estimated by substracting the energy of the optical band gap *obtained* by UV-vis to the HOMO values. [b]Absorbance (log ε) values are given in parentheses. [c]Absorption maxima calculated at the B3LYP/6-31G** level within the TD-DFT approach. Oscillator strengths (f) are given in parentheses. [d]Fluorescence quantum yields are relative to quinine hemisulfate.

Next, the effective π-conjugation of the triindole dimers are investigated by Raman spectroscopy. As seen in Figure 3, the strongest Raman band of triindole molecules is measured at ∼1605 cm^{-1} and arises from a CC stretching mode (i.e., mode 8a of benzene[14]) involving the external benzene rings, whereas the Raman band at ∼1567 cm^{-1} is due to the same CC stretching mode but located in the innermost benzene ring. Compared to unsubstituted triindole **1**, this doublet band increases in intensity in the monomers and dimers with respect to the rest of the bands recorded below 1500 cm^{-1}. A frequency downshift of this doublet and an increase in the I_{1605}/I_{1567} intensity ratio is also found in the following order: unsubstituted **1** < monofunctionalized monomers **3** and **5** < dimers **6** and **7**. This indicates more efficient π-conjugation in the dimers, which is in consonance with their larger geometrical relaxation when compared to the monomers (see Figure S4, Supporting Information). In diacetylenic-bridged dimer **7**, the most intense Raman band measured at 2210 cm^{-1} is described as fully in-phase C≡C stretching vibrations and evidences the strong participation of the diacetylenic bridge in the overall π- conjugation. The increase of the intensity of this band with respect to that associated with the central benzene rings (1605 cm^{-1}) in dimer **7** compared to monomer **5** is indicative that π- conjugation takes place more efficiently in the central part of the molecules and decreases toward the ends. The good agreement found between the theoretical and experimental Raman spectra gives support to the reliability of the

[14] Sun, Y. M.; Ma, Y. Q.; Liu, Y. Q.; Lin, Y. Y.; Wang, Z. Y.; Wang, Y.; Di, C. A.; Xiao, K.; Chen, X. M.; Qiu, W. F.; Zhang, B.; Yu, G.; Hu, W. P.; Zhu, D. B.1, *Adv. Funct. Mater*. **2006**, *16*, 426.

structural information derived from this discussion (see Figure S5, Supporting Information).

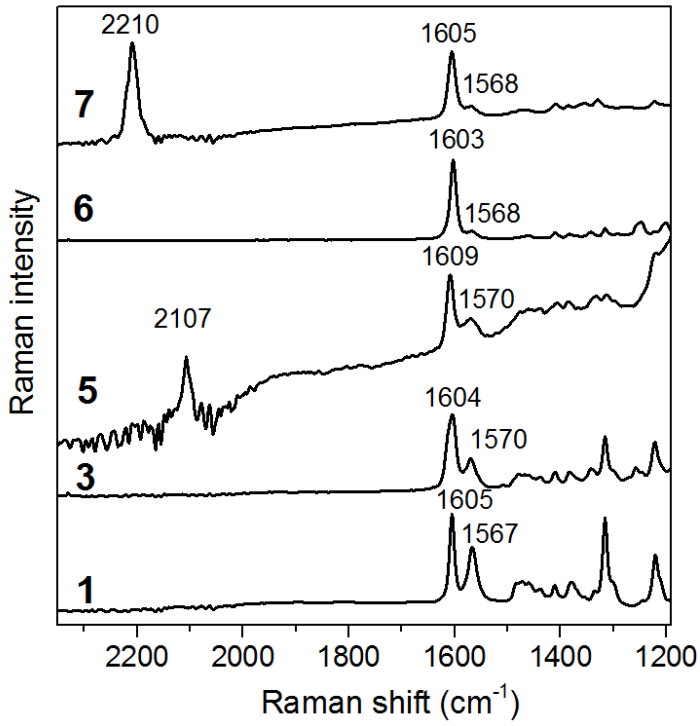

Figure 3. Experimental Raman spectra of unsubstituted 1, monomers **3**, **5** and dimers **6**, **7**.

Cyclic voltammetry analysis of these electron-rich triindole platforms shows that all compounds exhibit a first oxidation reversible process, which is associated with the easy generation of a cation radical as well as the formation of higher cationic charged species (see Figure 4 for **6** and **7** dimers and the Supporting Information for the rest of the compounds). For the monomeric species, the first oxidation potential is found to slightly shift anodically on going from **3** to **5** as a consequence of the electron-withdrawing effect of the ethynyl group; this is in consonance with the small HOMO stabilization calculated for **5** (Table 1 displays the estimated HOMO levels from the first oxidation waves). For the dimers, the values of the first oxidation process are very similar and are in agreement with the low influence that the two different spacers have on the HOMO levels. However, whereas the cyclic voltammogram of dimer **6** is identical to that of its phenyltriindole monomer analogue **3**, indicating that the two triindole units are electronically isolated, the first oxidation wave of dimer **7** is split into two overlapping waves (Figure 4). This is evidence that, in the diacetylene-bridged system, the two triindole moieties are

electronically coupled, allowing for their subsequent oxidation. This is consistent with the DFT calculations that show a larger charge delocalization in radical cation **7** than in **6**, and therefore better electronic conjugation across the diacetylenic group than over the phenyl spacer (see Figure S6, Supporting Information).

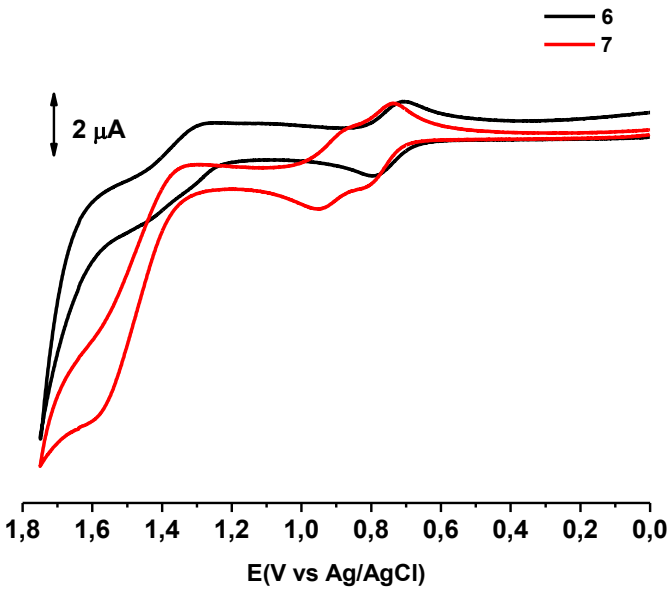

Figure 4. CV of dimers **6**, **7** at c = 1 x 10^{-3} M recorded at a scan rate 100mV/s in CH_2Cl_2/0.1 M $TBAPF_6$ measured versus Ag/AgCl (3M NaCl).

The easy one-electron reversible oxidation of the triindole dimers together with their moderate predicted values of hole intramolecular reorganization energy (λ_h) would render them as potential hole-transport material candidates, as previously found in unsubstituted triindoles.[15] Note that λ_h values of 149 and 163 meV are obtained for dimers **6** and **7**, respectively, which are on the same order as those calculated for many other organic systems considered to be good hole-transport materials (i.e., 306 meV was obtained for phenyl-susbtituted dithienoacene for which hole field-effect mobilities as high as 0.31 $cm^2\ V^{-1}\ s^{-1}$ were reported[16]).

An examination of the fluorescence properties (see Table 1) shows two clear effects: (i) a red-shift of the emission maxima is found when going from unsubstituted **1** to monofunctionalized monomers **3** and **5** and dimers **6** and **7** with this being more pronounced in the acetylenic-substituted systems compared to the phenyl-substituted analogues, and (ii) an increase in the fluorescence quantum yield is found upon insertion of the linkers with the four derivatives (**3**, **5**, **6**, and **7**) showing similar values.

4.2.3. CONCLUSIONS

In summary, we have presented the first systematic investigation focusing on the effects that π-spacers in triindole dimers exert on their fundamental properties, such as electronic, redox, and photophysical properties. Our study demonstrates that the optoelectronic properties of the triindole dimers are strongly influenced by the nature of the π-linkers; the diacetylenic bridges allows for better electronic delocalization. We hope that this study can not only advance useful structure−property relationships of conjugated triindole dimers but also guide the design of new polymeric microporous materials based on this interesting platform.

Chapter 5. New semiconducting platforms

5. CHAPTER 5. NEW SEMICONDUCTING PLATFORMS

5.1. SUMMARY

Considering the good semiconducting properties of the C_3-symmetric cyclotrimer of indole, we decided to study the properties of two analogous oligomer compounds: asymmetric triindole and tetraindole, and their derivatives. We expect that these new compounds maintain the favorable redox behavior responsible of their intrinsic semiconducting properties while these new shapes provide the opportunity to improve the contact between the neighboring units. In this chapter, we use a joint experimental and theoretical approach that combines absorption and emission spectroscopies, cyclic voltammetry, and spectroelectrochemistry with DFT calculations, to get a deep understanding of their fundamental electronic properties.

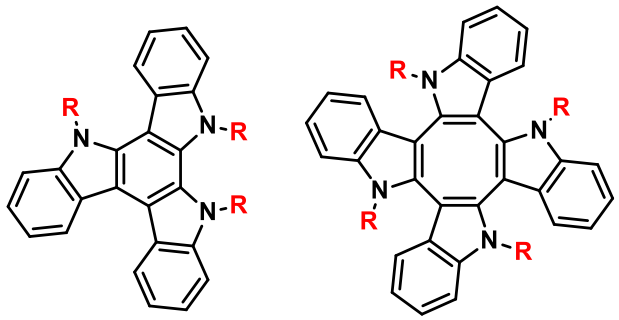

asymmetric triindole tetraindole

First, we focused in a comparative study between this platform and its symmetrical counterpart. We have found that lowering the symmetry of the platform results in a slightly lower oxidation potential. Cyclic voltammetry and spectroelectrochemistry reveal the reversible nature of the two observable oxidation processes in the alkylated asymmetric triindoles together with an increase in the stability of their oxidized species. Remarkably, the asymmetric platform gives a red-shift of the absorption edge and a higher fluorescence quantum yield, when compared to the symmetrical one.

On the other hand, we present similar study of a cyclic tetramer of indole with the aim of understanding the fundamental electronic properties of this three-dimensional platform and evaluate its potential in the construction of new semiconducting candidates.

Flat π-extended electroactive molecules, with inherent 2D character have a strong tendency to stack into columns forming one dimensional superstructure. However, due to their low dimensionality, these materials present anisotropic charge-transport properties which can pose specific problems for device fabrication and operation. The design of 3D electroactive systems allowing substantial electronic communication among conjugated segments in different directions may represent a potential answer to the problem of charge-transport anisotropy.

The result of this study suggests that cyclic tetraindole allows for a good electron delocalization in spite of its saddle-shaped structure, which can be attributed to a double hyperconjugative effect between the CC and π-orbitals across the twisted C-C bonds of the cyclooctatetraene. In this chapter, we explore the optical and electronic features of cyclic tetraindoles *N*-substituted with alkyl or alkyl aryl group, as a scaffold to arrange electroactive moieties in three dimensions with potential applications in the field of organic electronics.

In summary, in this study we investigated the electronic properties of two new cyclic oligomers of triindole showing their potential in organic electronic. Our results reveal that asymmetric triindole, and their derivatives, improve the photophysical properties. At the same time, we demonstrated that increased of the dimensionality of charge transport might be possible by the design of 3D electroactive systems, like tetraindole platform. We believe that this work may provide guidance for further development of these materials with improved potential for electronic applications.

5.2. SYMMETRY LOWERING IN TRIINDOLES: IMPACT ON THE ELECTRONIC AND PHOTOPHYSICAL PROPERTIES

Constanza Ruiz,[†] Eva M. García-Frutos,[†] Demetrio A. da Silva Filho,[‡] Juan T. López Navarrete,[*,§] M. Carmen Ruiz Delgado,[*,§] and Berta Gómez-Lor[*,†]

[†]Instituto de Ciencia de Materiales de Madrid, CSIC, Cantoblanco 28049, Madrid, Spain

[‡]Institute of Physics, University of Brasilia, Brasilia 70.919-970, Brazil

[§]Department of Physical Chemistry, University of Málaga, 29071 Málaga, Spain

5.2.1. ABSTRACT

The electronic and photophysical properties of 6,11-dihydro-5Hdiindolo[2,3-a:2′,3′-c]carbazole, an asymmetric cyclic dehydrotrimer of indole, have been explored and compared to its symmetric analogue, 10,15-dihydro-5Hdiindolo[3,2-a:3′,2′-c]carbazole (triindole), a well-known high hole mobility semiconductor. To this purpose, we use a joint experimental and theoretical approach that combines absorption and emission spectroscopies, cyclic voltammetry, and spectroelectrochemistry with DFT calculations. Lowering the symmetry of the triindole platform causes a red-shift of the absorption edge and emission maxima and improved the fluorescence quantum yield. Cyclic voltammetry and spectroelectrochemistry reveal the reversible nature of the two observable oxidation processes in the alkylated asymmetric triindoles together with an increase in the stability of their oxidized species. On the other hand, the insertion of alkyl groups on the nitrogen atoms results in a further fluorescence enhancement although larger reorganization energies are found. DFT and time-dependent (TD-DFT) calculations successfully support the experimental data and aid in the understanding of the tuning of the physicochemical properties of the triindole platform upon symmetry lowering toward their incorporation in electronic devices.

5.2.2. INTRODUCTION

The interest aroused by π-conjugated polymers after the discovery that their electrical conductivity increases substantially upon electrochemical doping paved the way to the emergence of the field of organic electronics. In only a few years, this area stimulated worldwide interest in the search for large area, flexible, lightweight, and cost-

effective optoelectronics. Conjugated polymers, usually amorphous materials, can be easily processed from solution to yield homogeneous and uniform thin films ideally suited for optoelectronics.[1,2,3,4,5] Unfortunately, they pose problems of reproducibility due to variations in molecular weight, and polydispersity, from batch to batch. Low-molecular-weight π-conjugated oligomers have been identified as attractive targets to substitute the usual polymeric materials in electroactive devices. Although less appealing in terms of processability, they can be reproducibly prepared, functionalized, and purified, owing to their monodisperse nature with well-defined chemical structure.

In this context, we and others became interested in a C3- symmetric dehydrotrimer of indole (triindole) readily available by cyclocondensation of either indolin-2-one[6] or indole itself through halogenation[7] followed by reductive dehydrohalogenation. [8] This novel molecule is highly stable and has intrinsic physical favorable properties such as attractive redox and linear and nonlinear optical properties. Despite the fact that this novel C3-symmetric scaffold has only recently been investigated, it has already found applications in the development of bulk heterojunction solar cells,[9] organic light-emitting diodes,[10,11,12] and field effect transistors,[13] and it has been utilized as a central core in semiconducting discotic liquid crystals[14] showing record hole mobilities.[15,16,17]

In contrast to the well-documented C3-symmetric dehydrotrimer of indole, its asymmetric analogue is much less explored.[18] Different substituted cyclic asymmetric trimers have been obtained during the electropolymerization of functionalized

[1] Beaujuge, P. M.; Reynolds, J. R.; *Color. Chem. Rev*. **2010**, 110, 268.
[2] Burroughes, J. H.; Bradley, D. D. C.; Brown, A. R.; Marks, R. N.; Mackay, K.; Friend, R. H.; Burns, P. L.; Holmes, A. B.; *Nature* **1990**, 347, 539.
[3] Facchetti. A.; *Chem. Mater*. **2011**, 23, 733.
[4] Guenes, S.; Neugebauer, H.; Sariciftci, N. S.; *Chem. Rev*. **2007**, 107, 1324.
[5] Gustafsson, G.; Cao, Y.; Treacy, G. M.; Klavetter, F.; Colaneri, N.; Heeger, A. J.; *Nature* **1992**, 357, 477.
[6] Franceschin, M.; Ginnari-Satriani, L.; Alvino, A.; Ortaggi, G.;Bianco, A.; *Eur. J. Org. Chem*. **2010**, 134.
[7] Robertson, N.; Parsons, S.; MacLean, E. J.; Coxall, R. A.; Mount, R. A.; *J. Mater. Chem*. **2000**, 10, 2043.
[8] Gómez-Lor, B.; Echavarren, A. M. *Org. Lett*. **2004**, 6, 2993.
[9] Bura, T.; Leclerc, N.; Fall, S.; Lévêque, P.; Heiser, T.; Ziessel, R.; *Org. Lett*. **2011**, 13, 6030.
[10] Coya, C.; Ruiz, C.; Álvarez, Á. L.; Álvarez-García, S.; García- Frutos, E. M.; Gómez-Lor, B.; de Andrés, A.; *Org. Electron.* **2012,** 13, 2138.
[11] Lai, W. Y.; He, Q. Y.; Zhu, R.; Chen, Q. Q.; Huang, W.; *Adv. Funct. Mater*. **2008**, 18, 265.
[12] Levermore, P. A.; Xia, R.; Lai, W.; Wang, X. H.; Huang, W.; Bradley, D. D. C. J.*; Phys. D: Appl. Phys*. **2007**, 40, 1896.
[13] Valentine, R. A.; Whyte, A.; Awaga, K.; Robertson, N.; *Tetrahedron Lett.* **2012**, 53, 657.
[14] Gomez-Lor, B.; Alonso, B.; Omenat, A.; Serrano, J. L.; *Chem. Commun*. **2006**, 5012.
[15] Benito-Hernández, A.; Pandey, U. K.; Cavero, E.; Termine, R.; García-Frutos, E. M.; Serrano, J. L.; Golemme, A.; Gómez-Lor, B.; *Chem. Mater*. **2013**, 25, 117.
[16] García-Frutos, E. M.; Pandey, U. K.; Termine, R.; Omenat, A.; Barberá, J.; Serrano, J. L.; Golemme, A.; Gómez-Lor, B.; *Angew. Chem., Int. Ed*. **2011**, 50, 7399.
[17] Ye, Q.; Chang, J.; Shao, J.; Chi, C. J.*; Mater. Chem*. **2012**, 22, 13180.
[18] Kaneko, T.; Matsuo, M.; Iitaka, Y.; **1979**, 12, 471.

indoles.[19,20,21,22,23]In fact, it has been proposed that polyiindole is composed by linked redox-active asymmetric trimers initially formed upon electrooxidation and coupling. [20−23] Its formation has been explained by considering the greatest electron spin density distribution in indole monomer, dimer, and linear trimer radical cations.[24,25] Preparative synthesis of this scaffold by reaction of indole with nitrosobenzene[26] has also been reported; however, a deep study of its electronic properties is still lacking.

In the present study, we explore the electronic and photophysical properties of the asymmetric dehydrotrimer of indole in comparison with its symmetric analogue by using absorption and emission spectroscopies, cyclic voltammetry, and spectroelectrochemistry. The electronic structure differences between the symmetric and asymmetric platforms are investigated with the help of DFT and time-dependent (TD-DFT) calculations of the ground states (S_0), singlet excited states, and charged states. As it has been previously observed that insertion of alkyl groups on the nitrogen atoms benefits the redox and thermal stability of symmetric triindoles, [14−16] the influence of *N*-alkylation on the electronic properties of these compounds is also studied. This work aims to deepen the understanding of the structure−property relationships of triindoles and provide guidance for further development of these materials aiming potential applications in organic electronics. The results presented reveal that molecular engineering of this conjugated core via varying the symmetry as well as *N*-alkyl functionalization can be used to effectively tune their physicochemical (i.e., photophysical and electrochemical) properties.

[19] Bocchi, V.; Colombo, A.; Porzio, W. *Synth. Met.* **1996**, 80, 309.
[20] Jennings, P.; Jones, A. C.; Mount, A. R.; Thomson, A. D. *J. Chem. Soc., Faraday Trans*. **1997**, 93, 3791.
[21] Mackintosh, J. G.; Mount, A. R. *J. Chem. Soc., Faraday Trans*. **1994**, 90, 1121.
[22] Mackintosh, J. G.; Wright, S. J.; Langridge-Smith, P. R. R.; Mount, A. R.,*J. Chem. Soc., Faraday Trans.* **1996**, 92, 4109.
[23] Mount, A. R.; Thomson, A. D. *J. Chem. Soc., Faraday Trans*. **1998**, 94, 553.
[24] Henry, J. B.; Mount, A. R., *J. Phys. Chem. A*, **2009**, 113, 13023.
[25] Kettle, L. J.; Bates, S. P.; Mount, A. R., *Phys. Chem. Chem. Phys.* **2000**, 2, 195.
[26] Greci, L.; Tommasi, G.; Petrucci, R.; Marrosu, G.; Trazza, A.; Sgarabotto, P.; Righi, L.; Alberti, A., *J. Chem. Soc., Faraday Trans*. 2, **2000**, 2337.

5.2.3. EXPERIMENTAL SECTION

- **Materials Synthesis**

The synthesis of unsubstituted **1a** and **2a** can be easily performed in just one step starting from indolin-2-one and indole, respectively, following previously reported procedures.[6, 25] Simple alkylation under basic conditions and in the presence of a phase transfer catalyst can be easily achieved in quantitative yields allowing for the functionalization of the three indolic *NH* centers with alkyl groups (Scheme 1). Alkylated **1b**, [27] **1c**, [28] and **2b** [29] have been previously described; **2c** (see Supporting Information) is a new compound.

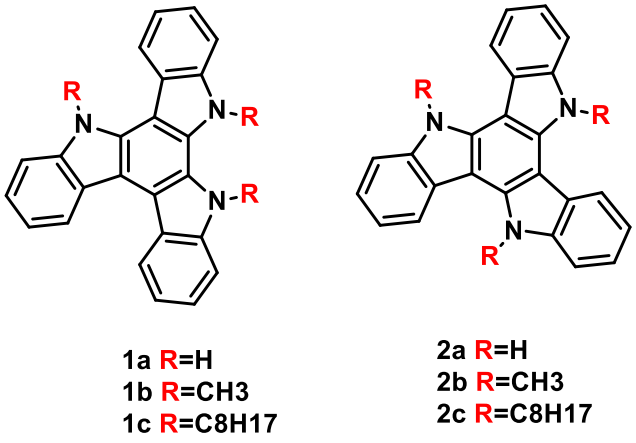

Scheme 1. Chemical structure of symmetric **1a-1c** and asymmetric **2a-2c** triindoles.

- **Linear Spectroscopy**

UV−vis studies were carried out on a PerkinElmer Lambda XLS+ spectrometer. Fluorescence spectra were recorded on an Aminco SLM 8000 spectrophotometer.

- **Electrochemistry and Spectroelectrochemistry**

Cyclic voltammetry (CV) experiments were performed on a Bioanalytical Systems Inc. (BASI) Epsilon electrochemical workstation in a three-electrode cell at room

[27] García-Frutos, E. M.; Gutierrez-Puebla, E.; Monge, M. A.; Ramírez, R.; de Andrés, P.; de Andrés, A.; Ramírez, R.; Gómez-Lor, B.; *Org. Electron*. **2009**, 10, 643.
[28] Gallego-Gómez, F.; García-Frutos, E. M.; Villalvilla, J. M.; Quintana, J. A.; Gutierrez-Puebla, E.; Monge, A.; Díaz-García, M. A.; Gómez-Lor, B.; *Adv. Funct. Mater*. **2011**, 21, 738.
[29] Bergman, J.; Eklund, N.; *Tetrahedron* **1980**, 36, 1445.

temperature under a nitrogen atmosphere. Electrochemical measurements were carried out in acetonitrile solution (c = 1 × 10^{-3} M) containing 0.1 M tetra-n-butylammonium hexafluorophosphate ($TBAPF_6$) of supporting electrolyte at a scan rate 100 mV/s. A three electrode setup was used including a platinum working electrode, a Ag/AgCl (3 M NaCl) reference electrode, and a platinum wire auxiliary electrode. Ferrocene was used as an internal standard, and all potentials were referenced to the ferrocene/ferrocenium redox couple. Spectroelectrochemical experiments were performed using a BASI spectroelectrochemical cell kit, including a thin-layer quartz cuvette, a platinum minigrid working electrode, a platinum wire counter electrode, and a Ag/AgCl (3 M NaCl) reference electrode. The measurements were carried out in acetonitrile solution (c = 1 × 10^{-4} M) containing 0.1 M of supporting electrolyte tetra-nbutylammonium hexafluorophosphate ($TBAPF_6$). The voltage was held at different potential values during the measurements while the absorption spectra were monitored on a PerkinElmer Lambda XLS+ spectrometer.

- **Computational Details.**

The molecular geometries of the neutral and radical-ion states were calculated at the density functional theory (DFT) level using the B3LYP functional [30, 31] and the 6-31G(d,p)[32,33] basis set, as implemented in the Gaussian 09 program.[34] The ionization energies (IEs) were calculated directly from the relevant points on the potential energy surfaces using the standard procedure detailed in the literature.[35] Specifically, vertical IEs were evaluated as the difference between the energy of the cation at the neutral geometry and that of the neutral species at the neutral geometry. Vertical one-electron excitations were computed using the time-dependent DFT (TD-DFT) method.[36, 37] Absorption spectra were simulated through convolution of the vertical transition energies and oscillator strengths with Gaussian functions characterized by a full width at halfmaximum (fwhm) of 0.3 eV.

[30] Becke, A. D.; *J.Chem. Phys*. **1993**, 98, 5648.
[31] Lee, C. T.; Yang, W. T.; Parr, R. G.; *Phys. Rev. B* **1988**, 37, 785.
[32] Harihara, P. C.; Pople, J. A.; *Theor. Chim. Acta* **1973**, 28, 213.
[33] Hehre, W. J.; Ditchfield, R.; Pople, J. A. J.; *Chem. Phys.* **1972**, 56, 2257.
[34] Frisch, M. J.; et al. Gaussian 09, revision C.01; Wallingford, CT, **2009**.
[35] Bredas, J. L.; Beljonne, D.; Coropceanu, V.; Cornil, J.; *Chem. Rev*. **2004**, 104, 4971.
[36] Gross, E. K. U.; Kohn, W. In Advances in Quantum Chemistry; Per-Olov, L., Ed.; Academic Press: New York, **1990**; Vol. 21, pp 255.
[37] Runge, E.; Gross, E. K. U.; *Phys. Rev. Lett*. **1984**, 52, 997.

The geometries of the first excited state (S_1) were optimized by the TD-DFT method. An algorithm included in this version of Gaussian 09[34] was used to generate a vibronically resolved absorption spectrum and emission to allow for a direct comparison with the experimental data.[38, 39]

5.2.4. RESULT AND DISCUSSION

- **Absorption Spectra and Orbital Topologies**

Figure 1 displays the UV−vis absorption spectra of symmetric **1a**, **1c** and asymmetric **2a**, **2c** compounds (the spectra of **1b** and **2b** are shown in Figure S1). An examination of the electronic absorption spectra shows two clear effects: (*i*) lowering the symmetry of the platform leads to a more complex spectrum and considerably red-shifts the absorption edge (i.e., 375 nm in 1c and 430 nm in **2c**),[40] and (*ii*) when going from the unsubstituted 1a, **2a** to the octyl-substituted **1c**, **2c** systems, the overall shapes of the spectra remain unchanged but the position of their maxima and absorption edge are red-shifted by about 10−20nm. However, completely superimposable absorption spectra are obtained when the octyl chains are replaced by the much shorter methyl groups (see Figure S1); this suggests that the geometrical effect (i.e., distortions from planarity upon Nalkyl substitution) seems to have a stronger impact than the larger inductive effect of the long alkyl chains.

As shown in Figure 1, the time-dependent DFT (TD-DFT) vertical excitation energies reproduce quite nicely (*i*) the higher complexity of the UV−vis spectra when the C3-symmetry is broken (i.e., a large number of transitions with moderate intensity are predicted for **2a**, **2c** in comparison to **1a**, **1c**) and (*ii*) the red-shift of the absorption spectra when going from the symmetric to the asymmetric systems and upon *N*-alkylation. For example, in the symmetric systems, the strongest band at 306 (317) nm in 1a (**1c**) corresponds to the degenerate $S_0 \rightarrow S_3/S_0 \rightarrow S_4$ electronic transitions calculated at 296 (312)nm, which is assigned to a combination of HOMO−1 → LUMO, HOMO → LUMO+1, HOMO−1 → LUMO+1, and HOMO → LUMO one-electron excitations. Note

[38] Barone, V.; Bloino, J.; Biczysko, M.; Santoro, F. Fully.; *J. Chem. Theory Comput.* **2009**, 5, 540.
[39] Bloino, J.; Biczysko, M.; Crescenzi, O.; Barone, V., *J. Chem. Phys*. **2008**, 128, 244105.
[40] Please note that the absorption maximum is slightly blueshifting by about 10 nm upon symmetry lowering; however, our TDDFT calculations confirm that this band is associated to electronic transitions between excited states that have different nature in the symmetric and asymmetric systems. Therefore, the evolution of the absorption maximum upon symmetry lowering cannot be directly correlated.

that in the symmetric systems the $S_0 \rightarrow S_1$ transition is forbidden by symmetry with respect to dipole−dipole selection rules.[41] However, the $S_0 \rightarrow S_1$ transition becomes allowed in the asymmetric compounds; as seen in Figure 1, this band is calculated at 372 nm (f = 0.13) in **2a** and 382 nm (f = 0.14) in **2c**, and it is associated with a HOMO → LUMO transition.

Figure 2 shows the DFT//B3LYP/6-31G** frontier molecular orbitals of symmetric **1a**, **1c** and asymmetric **2a**, **2c**. Because of its C3-symmetric structure, the HOMO and LUMO orbitals of **1a** and **1c** are doubly degenerated, whereas an energy gap of 0.25 (0.24) eV between HOMO and HOMO−1 and 0.78 (0.73) eV between LUMO and LUMO+1 is observed in the asymmetric **2a** (**2c**) analogues. In going from the symmetric to the asymmetric systems, LUMO is largely stabilized (by ~0.50 eV) and HOMO is moderately destabilized (by ~0.12 eV), thus decreasing the HOMO− LUMO gap. Upon *N*-alkylation, HOMO and LUMO are moderately destabilized with this effect being more pronounced for HOMO due to the inductive effect of the alkyl groups, thus resulting in a HOMO−LUMO gap decrease. These data are in good accordance with the experimental red-shift of the absorption edge when lowering the symmetry of the molecule and upon *N*-alkylation, which is found to be more pronounced in the former than in the latter case in accordance with the DFT calculations.

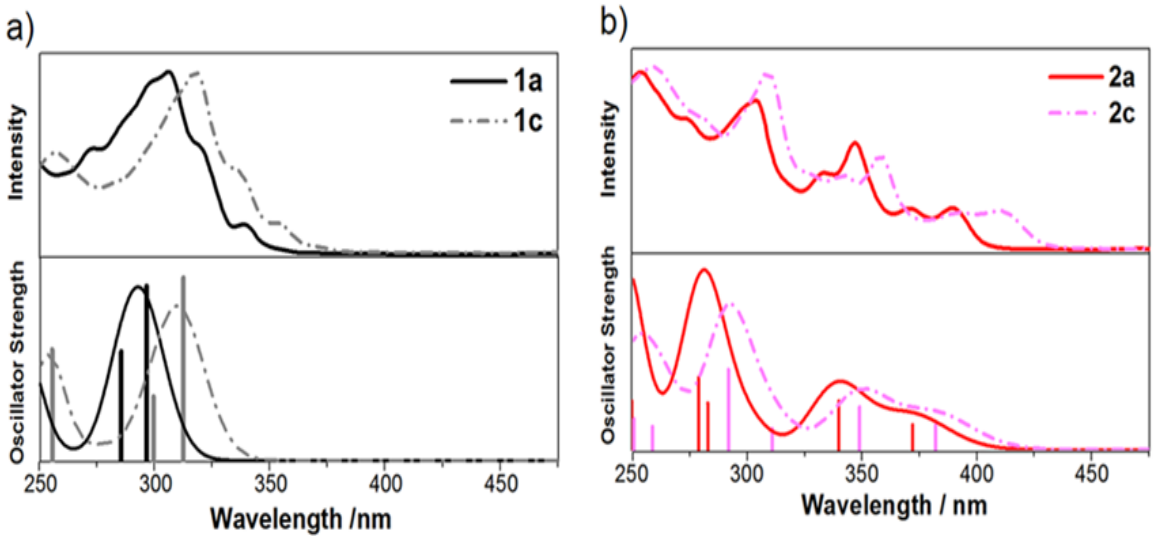

Figure 1. (a) Top: Experimental UV-Vis absorption spectra of **1a** and **1c** in CH_2Cl_2, c = 5 × 10^{-6} M. Bottom: Simulated absorption spectra of **1a** and **1c** together with the TD-DFT//B3LYP/6-31G** excitations (wavelength vs. oscillator strength) shown as vertical bars. (b) Top: Experimental UV-Vis absorption

[41] The discrepancy between the experimental and theoretical part of the spectrum in the region of 350 nm for the symmetric **1a** and **1c** systems can be related to the distortions from the C3 geometry in solution that can contribute to the actication of the $S_0 \rightarrow S_1$ transition.

spectra of **2a** and **2c** in CH_2Cl_2, c = 5 × 10^{-6} M. Bottom: Simulated absorption spectra of **2a** and **2c** together with the TD-DFT//B3LYP/6-31G** excitations (wavelength vs. oscillator strength) shown as vertical bars.

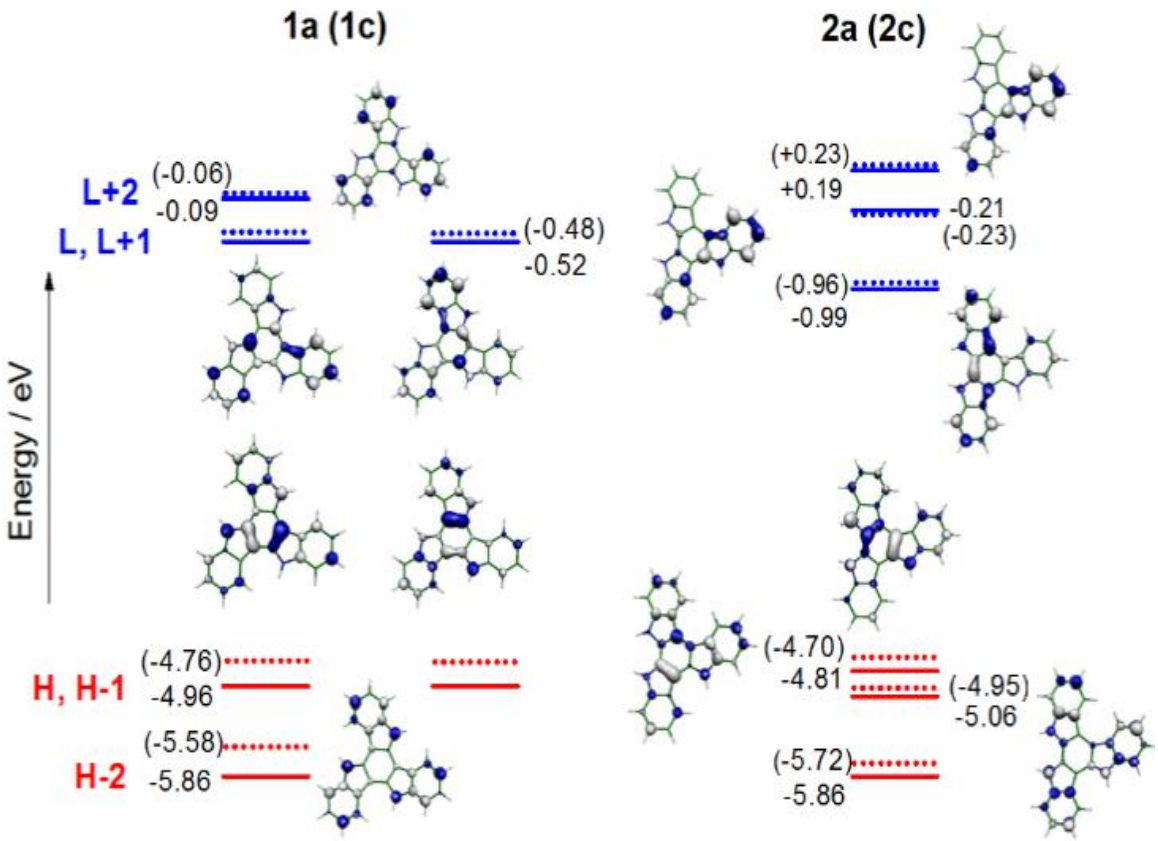

Figure 2. DFT//B3LYP/6-31G** molecular orbital energies for **1a**, **2a** (solid lines) and **1c, 2c** (dotted lines, with the values shown in parentheses). The molecular orbital topologies for **1a** and **2a** are also shown (see the Supporting Information for the molecular orbital topologies of **1c** and **2c**).

- **Cyclic Voltammetry and UV/vis−NIR Spectroelectrochemistry**

As determined by cyclic voltammetry, all six compounds exhibit a first oxidation reversible process as well as the formation of higher cationic charged species in the accessible potential window of the solvent. The first oxidation process which is associated with the easy generation of a cation radical in these electron-rich platforms allow us to estimate the value of the HOMO levels of these compounds (see Table 1, Figure 3, and Figure S2). The first oxidation potential shifts slightly anodically as decreasing the symmetry of the system. This trend is well captured by the DFT-calculated ionization energies (IE) as smaller IE values are found upon lowering the symmetry (i.e., 6.27/6.15, 6.09/5.99, and 5.94/5.91 eV for **1a**/ **2a**, **1b**/ **2b**, and **1c**/ **2c** couples) and is consistent with the HOMO destabilization obtained when the symmetry is lowered (see Table 1). Conversely, the oxidation potentials are barely affected upon *N*-alkylation; this

is not in consonance with the somewhat small destabilization of the calculated HOMO values upon *N*-alkylation. This disagreement, in turn, can be attributed to the fact that our calculations are in gas phase and do not account for geometrical distortions that are expected to occur in solution. It is interesting to note that the estimated HOMO levels from the first oxidation potentials of all the systems under study are adequate for the easy hole injection from gold electrode (Au work function 5.1 eV).

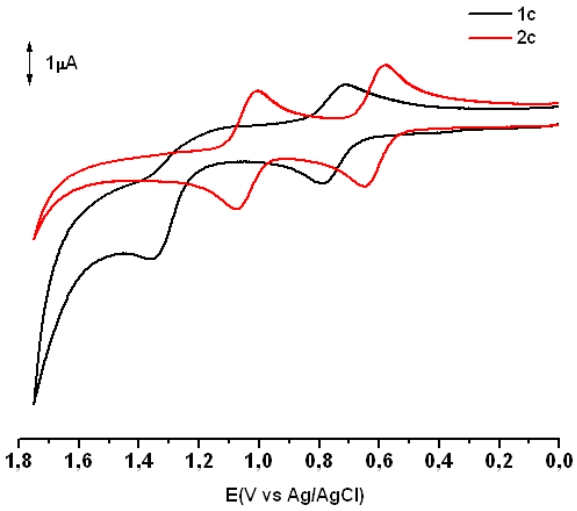

Figure 3. Cyclic voltammogram of **1c** and **2c** at c = $1x10^{-3}$ M recorded in CH_3CN/ 0.1M tetra-*n*-butylammonium hexafluorophosphate ($TBAPF_6$) at a scan rate 100mV/s using a Pt working electrode, a Ag/AgCl (3M NaCl) reference electrode and a Pt wire auxiliary electrode.

Table 1. Formal oxidation potentials, HOMO energies estimated from cyclic voltammetry data, HOMO energies calculated (DFT//B3LYP/6-31G** theoretical data), and DFT-calculated vertical (IEv) ionization energies.

Compound	E°´ (V)	$HOMO_{exp}$(eV)	$HOMO_{calc}$ (eV)	IEv (eV)
1a	0.69	-5.07	-4.96	6.27
1b	0.73	-5.10	-4.83	6.09
1c	0.75	-5.11	-4.76	5.94
2a	0.56	-4.94	-4.81	6.15
2b	0.56	-4.94	-4.71	5.99
2c	0.60	-4.97	-4.70	5.91

[a]The HOMO energy values for **1a-c** and **2a-c** were estimated from the first oxidation potential with respect ferrocene/ferrocenium redox couple[42] and considering a value of - 4.8 eV for Fc with respect to zero vacuum level. This value is obtained from the calculated value of - 4.6 eV for the standard electrode potential (E) using a normal hydrogen electrode (NHE) on the zero vacuum level and the value of 0.2 V for Fc vs. NHE.[43, 44]

[42] Gritzner, G.; Kuta, J. Recommendations on Reporting Electrode-Potentials in Nonaqueous Solvents (Recommendations 1983). *Pure Appl. Chem*. **1984**, 56, 461.
[43] Bard, A. J.; Faulkner, L. R. Electrochemical Methods: Fundamentals and Applications; Wiley: New York, **2001**.
[44] Trassati, S. The Absolute Electrode Potential: An Explanatory Note. *Pure Appl. Chem*. **1986**, 58, 955.

The influence of the platform symmetry on the electronic structure of the different oxidized species had been investigated by means of chemical oxidation, spectroelectrochemistry, and DFT calculations. Figure 4 shows the electronic spectra recorded during the electrochemical oxidation of **1c** and **2c** in CH_3CN. Upon oxidation at 0.90−0.80 V, the absorption of the neutral species disappears and a dominant broad band appears at 720 nm that can be ascribed to the formation of the radical cation species (Figure 4). This first process is found to be completely reversible for both systems as confirmed by back reduction that recovers the neutral parent systems (Figures S3 and S5). TD-DFT calculations for the radical cation species allow the assignment of this experimental band to a HOMO−2 → SOMO transition predicted at 670 (715) nm for $1c^{\bullet+}$ ($2c^{\bullet+}$); the molecular orbital topologies are shown in the Figure S8. As observed in Figure 4, further increase of the potential up to 1.6−1.4 V drives to the disappearance of the band at 720 nm together with the emergence of new bands at 410 nm in **1c** and 480 nm in **2c**, presumably corresponding to the formation of the corresponding dications. Back-reduction from this second oxidation process leads to the recovery of the neutra compounds only in the case of **2c**, highlighting the higher stability of the cation in the asymmetric platform. Similar spectral changes evolution has been observed for the UV/vis− NIR spectra recorded upon in situ chemical doping with $NOSbF_6$ (see Figures S4 and S6). The blue-shift of the dication bands with respect to those of the parent radical cation is very well captured by TD-DFT calculations that predict a vertical transition at 568 (602) nm for the dication of **1c** (**2c**). Note that a similar electronic spectral evolution upon oxidation has been predicted for the methyl-substituted **1b** and **2b** compounds (Figure S9 and Table S2).

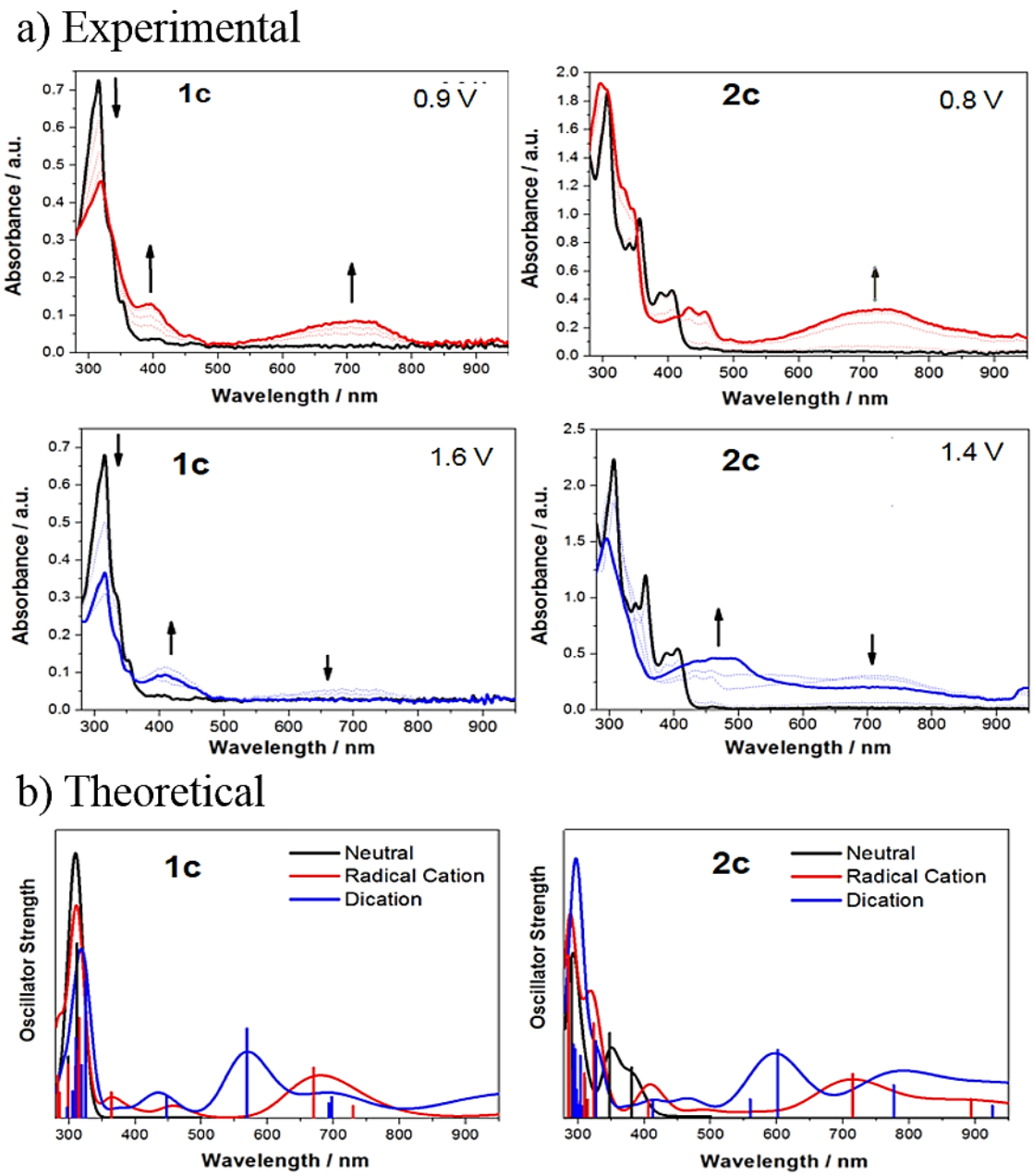

Figure 4. (a) UV/Vis-NIR spectra of **1c** and **2c** obtained at different time intervals after applying a potential of 0.90-0.80 V (top) and 1.6-1.4 V (bottom) in CH_3CN. (b) Simulated absorption spectra predicted for the neutral, radical cation and dication of **1c** and **2c** together with the TD-DFT//B3LYP/6-31G** excitations (wavelength versus oscillator strength) shown as vertical bars.

The easy one-electron reversible oxidations of these derivatives render them potential candidates as hole-transport materials. In fact, symmetric triindole have been found to be a high hole mobility semiconductor in both its crystalline[27] and liquid-crystalline state.[15, 16] We now turn to a discussion of the intramolecular reorganization energies λ associated with hole transfer (λ_h), a molecular parameter which considers the structural reorganization needed to accommodate charge as a prerequisite for efficient transport. As see in Figure 5, larger λ_h values are found when the symmetry is lowered; this is in line with the larger geometrical relaxation found upon oxidation in the asymmetric platform, which mainly involves the central benzene ring and the C−N bonds connected to it, especially those facing in the same side (see the Supporting Information). However, it is important to note that the λ_h values for the asymmetric molecules (in the range of 282−420 meV) are in the same order than those calculated for many other organic systems considered as good hole-transport materials. For instance, values of 281 and 306 meV were obtained for phenyl-substituted tetrathienoacene (DP-TTA) and dithienoacene (DP-DTT) for which hole field-effect mobilities as high as 0.28[45] and 0.31[46] $cm^2/(V \cdot s)$, respectively, were reported.

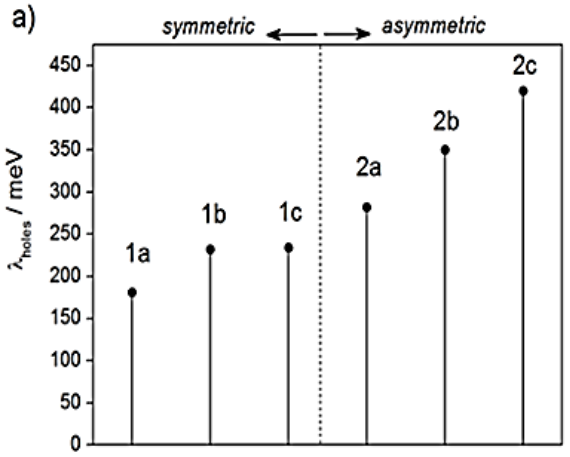

b)

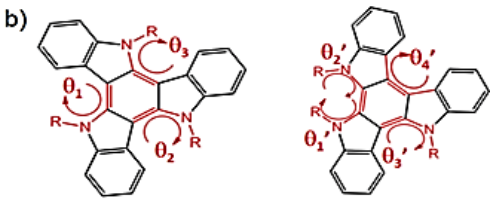

Symmetric Systems			
Compound	$\Delta\theta_1$	$\Delta\theta_2$	$\Delta\theta_3$
1a	0	0	0
1b	7	7	1
1c	8	8	1

Asymmetric Systems				
Compound	$\Delta\theta_1$'	$\Delta\theta_2$'	$\Delta\theta_3$'	$\Delta\theta_4$'
2a	14	18	3	2
2b	10	15	7	4
2c	7	23	7	7

Figure 5. (a) DFT-calculated reorganization energy values for holes (λ_h) for the symmetric and asymmetric triindole derivatives at the B3LYP/6-31G** level. (b) DFT-calculated dihedral changes (in absolute values) upon oxidation when going from the neutral to the cation states.

[45] Youn, J.; Huang, P.-Y.; Huang, Y.-W.; Chen, M.-C.; Lin, Y.-J.; Huang, H.; Ortiz, R. P.; Stern, C.; Chung, M.-C.; Feng, C.-Y.; Chen, L.-H.; Facchetti, A.; Marks, T. J.; *Adv. Funct. Mater.* **2012**, 22, 48.
[46] Sun, Y. M.; Ma, Y. Q.; Liu, Y. Q.; Lin, Y. Y.; Wang, Z. Y.; Wang, Y.; Di, C. A.; Xiao, K.; Chen, X. M.; Qiu, W. F.; Zhang, B.; Yu, G.; Hu, W. P.; Zhu, D. B.; *Adv. Funct. Mater.* **2006**, 16, 426.

On the other hand, *N*-alkylation increases the λ_h values (i.e., by 138 meV upon insertion of octyl groups from **2a** to **2c**). This is attributed to the larger distortions found upon oxidation when the nitrogen atoms are substituted with alkyl groups, especially in the case of the asymmetric platforms (see Figure 5b). In fact, the larger DFT dihedral changes are found in **2c** that exhibits the highest λ_h value (420 meV) within the series while the totally planar symmetric **1a** system displays the lowest λ_h value (181 meV).

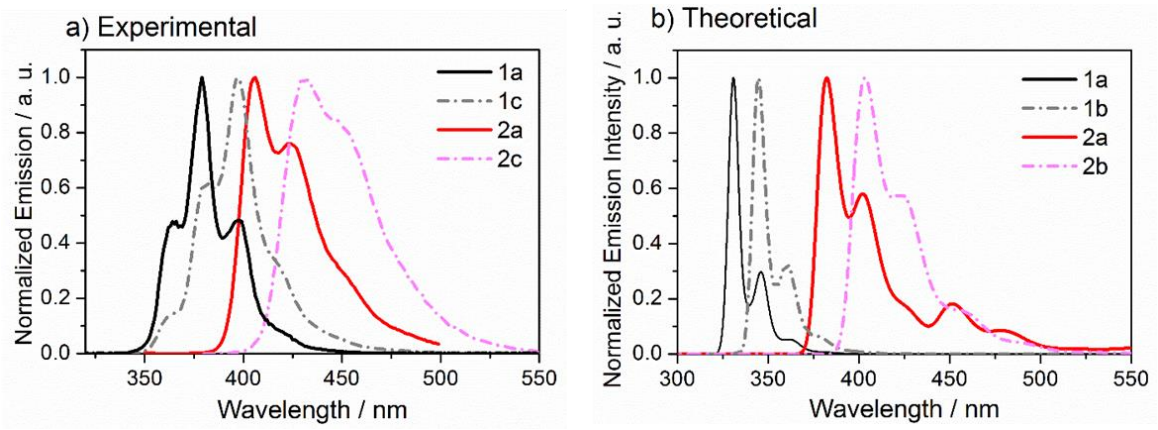

Figure 6. (a) Experimental emission spectra of the symmetric **1a**, **1c** and asymmetric **2a**, **2c** systems in CH_2Cl_2 solutions. (b) Vibronically resolved normalized emission of **1a**, **1b** and **2a**, **2b** systems. The methyl-susbtituted **1b** and **2b** are taken as models for the octyl-substituted **1c** and **2c** systems.

Table 2. Fluorescence quantum yields of **1a** (λ_{exc}=305 nm), **1c** (λ_{exc}=317 nm), **2a** (λ_{exc}=347 nm) and **2c** (λ_{exc}=357 nm) in CH_2Cl_2, c= 5x10^{-6} M.

Compound	$\lambda_{max,em}$/nm	Φ_f
1a	379	0.03
2a	405	0.42
1c	397	0.35
2c	431	0.75

- **Fluorescence Spectra**

The fluorescent properties of the C3-symmetric derivatives vary significantly when compared to their asymmetric analogues. Lowering the symmetry of the aromatic platform produces a red-shift of the emission maximum by about 30 nm and greatly enhances the quantum yield efficiency (see Figure 6 and Table 2).

The theoretical emission spectra of **1a** and **2a** including the vibronic progression for the $S_1 \rightarrow S_0$ transition reproduces quite well those experimentally observed (see Figure 6b). By comparing the shape of the emission spectra of **1a** and **2a** (or **1c** and **2c**), it

is clear that the asymmetric derivative displays a larger electron−phonon coupling than its symmetric analogue; this is in consonance with the large relaxation energy of the $S_1 \rightarrow S_0$ transition obtained for the asymmetric platforms (see Table S2). By looking at the Huang−Rhys factors (dimensionless electron−vibration coupling constant) that provides a measure of the amount of energy contributed by a given mode to the overall relaxation energy (see Tables S3−S6), we observe that the vibronic progression in 1a is mainly determined by the presence of two normal modes at 632 and 1330 cm^{-1}, while that in the less symmetric **2a** is mainly determined by the presence of several low-frequency modes associated with out-of-plane vibrations (an illustration of the main normal modes are displayed in the Supporting Information). On the other hand, *N*-alkylation results in a broader vibronic progression; this is associated with the larger contributions of the out-of-plane normal modes in the most distorted alkyl-substituted systems, in consonance with the larger distortion from coplanarity observed upon *N*-alkyl substitution (see Tables S4−S6).

Figure 7 displays the TD-DFT energies for the low-lying excitations together with the structural changes along the $S_1 \rightarrow S_0$ transition in **1b** and **2b** systems taken as model systems (the calculated bond length changes are displayed in the Supporting Information). The increase in the fluorescence efficiency in the asymmetric derivatives can be related to (*i*) the fact that the $S_0 \rightarrow S_1$ transition becomes allowed in the asymmetric systems while it is forbidden in the symmetric derivatives, and (*ii*) the larger structural changes upon $S_1 \rightarrow S_0$ transition observed in the asymmetric platforms in comparison to the symmetric derivatives which results in a less favorable coupling between the S_0 and S_1 states and thus favoring the fluorescence.

Interestingly, *N*-alkylation leads to stronger emission in both types of derivatives (see Table 1). This can be explained by the loss of planarity caused by the introduction of alkyl chains that could have a double effect: (1) increase of geometrical changes upon going from S_1 to S_0, thus reducing the coupling between the S_0 and S_1 states, and (2) mitigation of n−π* character contributions imparted by the lone electron pairs of the nitrogen atoms, which is known to quench fluorescence emission.[47, 48, 49]

[47] Chang, J. H.; Choi, Y. M.; Shin, Y. K. A.; *Bull. Korean Chem. Soc.* **2001**, 22, 527.
[48] Juarez, R.; Moreno Oliva, M.; Ramos, M.; Segura, J. L.; Aleman, C.; Rodriguez-Ropero, F.; Curco, D.; Montilla, F.; Coropceanu, V.; Bredas, J. L.; Qi, Y.; Kahn, A.; Ruiz Delgado, M. C.; Casado, J.; Lopez Navarrete, J. T.; *Chem.-Eur. J.* **2011**, 17, 10312.
[49] Mrozek, J.; Rzeska, A.; Guzow, K.; Karolczak, J.; Wiczk, W.; *Biophys. Chem*. **2004**, 111, 105.

5.2.5. CONCLUSION

The optical and electronic features of the asymmetric triindole platform have been investigated by using a combined experimental and theoretical approach that links electronic spectroscopies (i.e., absorption, emission, spectroelectrochemistry) with DFT calculations. A comparison with the properties of the C3-symmetric triindole homologue is proposed. Lowering the symmetry of the platform results in (*i*) slightly lower oxidation potential and red-shift of the absorption edge in agreement with the observed HOMO destabilization and LUMO stabilization; (*ii*) higher fluorescence quantum yield, which is related with the large geometrical differences between the S_0 and S_1 states and the allowed character of the $S_0 \rightarrow S_1$ transition; (*iii*) a broadening of the vibrational emission features that are mainly determined by the strong coupling with the low-frequency modes; (*iv*) more stable cation and dication species as observed by inspection of the electronic absorption spectra evolution upon oxidation in combination with TD-DFT calculations; and (*v*) larger intramolecular reorganization energies for hole transfer, which is consistent with the observed significant geometrical relaxations upon oxidation.

The insertion of alkyl groups on the nitrogen atoms is found to further increase the fluorescence efficiencies and reorganization energies, especially in the asymmetric systems. This is explained in connection with the larger structural changes (distortions from coplanarity) observed upon *N*-alkylation when going from the S_1 excited states to the S_0 ground states and upon oxidation, respectively.

In summary, this detailed structure−property study reveals that the photophysical and electronic properties of triindoles can significantly be tuned via lowering the symmetry of the conjugated platform as well as *N*-alkyl functionalization. These intramolecular features together with the intermolecular effects are critical for their performance in organic electronics. Further studies of the symmetry lowering influence on the morphologies and charge-transport properties are currently under investigation. We believe that this work may provide guidance for further development of these materials with improved potential for electronic applications.

5.3. SADDLE-SHAPED INDOLE CYCLIC TETRAMERS: 3D ELECTROACTIVE MOLECULES

Constanza Ruiz,[a] Ángeles Monge,[a] Enrique Gutiérrez-Puebla,[a] Ibon Alkorta,[b] José Elguero[b] Juan T. López Navarrete,[c] M. Carmen Ruiz Delgado*[c] and Berta Gómez-Lor*[a]

[a] Instituto de Ciencia de Materiales de Madrid, CSIC Cantoblanco, 28049 Madrid (Spain) Fax: (+34) 91-3349031 E-mail: bgl@icmm.csic.es

[c] Instituto de Química Médica, CSIC Juan de la Cierva 3, E-28006 Madrid (Spain)

[c] Department of Physical Chemistry, University of Málaga, 29071-Málaga, Spain

Chemistry - A European Journal. The submission number is chem.201600932

5.3.1. ABSTRACT

In this manuscript we present a joint theoretical and experimental study of a cyclic tetramer of indole with the aim of understanding the fundamental electronic properties of this three-dimensional (3D) platform and evaluate its potential in the construction of new semiconducting candidates. To this end, we combine absorption and emission spectroscopies, cyclic voltammetry, and spectroelectrochemistry with DFT calculations. Our results suggest that this platform can be easily and reversibly oxidized showing a HOMO level that matches very well with the work function of gold, therefore charge injection from this electrode is expected to occur without significant barriers. Interestingly, cyclic tetraindole allows for a good electron delocalization in spite of its saddle-shaped structure. The steric constrain introduced by N-substitution significantly inhibits ring inversion of the central cyclooctatetraene (COT) while it only barely affects its optical and electrochemical properties which show a slightly higher oxidation potential and blue-shift of the absorption edge upon alkylation.

5.3.2. INTRODUCTION

Flat π-extended electroactive molecules, with inherent 2D character have a strong tendency to stack into columns forming one dimensional superstructures. Such superstructures have been long considered to be among the best candidates to achieve high mobility semiconductors[50]. However due to their low dimensionality, these materials present anisotropic charge-transport properties which can pose specific problems for

[50] Zang¸ L.; Che, Y.; Moore, J. S.; *Acc. Chem. Res*. **2008**, 41, 1596.

device fabrication and operation. The design of 3D electroactive systems allowing substantial electronic communication among conjugated segments in different directions may represent a potential answer to the problem of charge-transport anisotropy.[51] In this context several electroactive molecules containing silicon[52] or sp^3 carbon nodes[53] for connecting conjugated systems, have been reported. In these materials the central node interrupts electronic delocalization a factor that can be unfavorable for charge transport. Other approaches directed to obtain electroactive molecules with 3D architectures have made use of tetraphenyladamantane cores,[54] twisted bithiophenes,[55] or spirofluorenes[56] as connecting cores.

We have been long involved on the study a C_3-symmetrical cyclic dehydrotrimer of indole (triindole) a flat disk-like electroactive molecule, which can be easily obtained by $POCl_3$ mediated cyclocondensation of 2-indolinone.[57] This molecule has been extensively investigated in the area of organic electronics and has been successfully integrated as active layer in OLEDs,[58] solar cells[59] and OFEts.[60] Interestingly very high hole-mobility values have been obtained in triindole-based discotic liquid crystals which provide an active conducting core, surrounded by an isolating cover.[61,62] Unfortunately, as it is common in discotic mesogens, the high dependence of their electrical performance on the degree of columnar alignment represents an important drawback towards device application.

In this manuscript we propose the use of a highly strained saddle shape tetramer of indole (tetraindole) as a 3D rigid scaffold to obtain electroactive molecules with increased dimensionality. This tetramer, constituted by four indole molecules fused via a

[51] Roncali, J.; Leriche, P.; Cravino, A.; *Adv. Mater*. **2007**, *19*, 2045. b) Skabara, P.J.; Arlin, J.B.; Geerts, Y. H.; *Adv. Mater*. **2013**, 25, 1948.
[52] Roquet, S.; de Bettignies, R.; Leriche, P.; Cravino, A.; Roncali, J.; *J. Mater. Chem*. **2006**, 16, 3040.
[53] Chen, W.; Yang, X. Long, G.; Wan, X.; Chen, Y.; Zhang, Q.; *J. Mater. Chem. C*, **2015**, 18, 4698.
[54]Wang, S.; Oldham, W. -J.; Hudack, Jr., R. -A.; Bazan, Jr., G.; *J. Am. Chem. Soc*. **2000**, 122, 5695.
[55]Karpe, S.; Cravino, A.; Frère, P.; Allain, M.; Mabon, G.; Roncali, J.; *Adv. Funct. Mater*. **2007**, 17, 1163.
[56] Wu, C. -C.; Liu, T. -L.; Hung, W. -Y.; Lin, Y. -T.; Wong, K. -T.; Chen, R. -T.; Chien, Y. -M.; Chien, Y.-Y.; *J. Am. Chem. Soc*. **2003**, 125, 3710.
[57] Franceschin, M.; Ginnari-Satriani, L.; Alvino, A.; Ortaggi, G.; Bianco, A.; *Eur. J. Org. Chem*. **2010**, 134.
[58] a) Lai, W. Y.; He, Q. Y.; Zhu, R.; Chem, Q. Q.; Huang, W.; *Adv. Funct. Mater*. **2008**, *18*, 265. b) Coya, C.; Ruiz, C.; Luis-Álvarez, L.; Álvarez-García, S.; García-Frutos, E.; Gómez-Lor, B.; Andrés, A.; *Org. Electr*. **2012**, 13, 2138.
[59] a) Rakstys, K.; Abate, A.; Ibrahim Dar, M; Gao, P.; Jankauskas, V.; Jacopin, G.; Kamarauskas, E.; Kazim, S.; Ahmad, S.; Grätzel, M.; Nazeeruddin, M. K.; *J. Am. Chem. Soc.* **2015**, 137, 16172. b) Shelton, S. W.; Chen, T. L.; Barclay, D. E.; Ma, B.; *ACS Appl. Mater. Interfaces* **2012**, 4, 2534.
[60] Reig, M.; Puigdollers, J.; Velasco, D.; *J. Mater. Chem. C.*, **2015**, 3, 506.
[61] Benito-Hernández, A.; Pandey, U.K.; Cavero, E.; Termine, R.; García-Frutos, E.M.; Serrano, J. L.; Golemme, A.; Gómez-Lor, B.; *Chem. Mater*. **2013**, *25*, 117.
[62] García-Frutos, E. M.; Pandey, U. K.; Termine, R.; Omenat, A.; Barberá, J.; Serrano, J. L.; Golemme, A.; Gómez-Lor, B.; *Angew. Chem. Int. Ed. Engl*. **2011**, *50*, 7399.

cyclotetraene (COT) core, is usually obtained as a side product during the synthesis of planar triindole by $POCl_3$ promoted cyclocondensation of 2-indolinone.[63,64] However in contrast to its trimeric counterpart, its electronic properties have been barely investigated probably due to difficulties to obtain it in large scale and pure form. Only recently this molecule has aroused interest in the synthesis on non-linear optical chromophores and electron donor moieties in D-π-A dyes for solar cells.[65,66] Although the formation of tetraindole can be favored by diluting the reaction mixture with chlorobenzene or $POCl_3$ although it is always obtained as a minor product together with the trimeric compound which complicates its purification.[67,68] Alternatively its synthesis through a multistep procedure has been also reported.[69] We have found that by performing the cyclotetramerization reaction in an autoclave we can favor the tetramerization *vs.* the trimerization rendering a much more easy to purify compound.

While fluxional dynamism characteristic of flexible cyclooctatetraenes has been long exploited in the development of molecule-based devices, such as electromechanical actuators[70] thermochromic [71] or environmental-dependent luminescent materials[72] the absence of flipping in rigid sterically hindered cyclooctatetraenes has been previously used to obtain molecular tweezers, optically active ligands[73] or chiral receptors[74] as high inversion barriers prevent racemization processes. In this manuscript we want instead to bring the attention to the potential of highly strained cyclooctatetraene as a scaffold to arrange electroactive moieties in three dimensions with potential applications in the field of organic electronics. It should be noted that while cyclooctatetraene planarization render it the prototype of 4n π antiaromatic system and twisting precludes effective π

[63] The obtention of tetramers as side products in acid mediated trimerization of ketones has been reported for other moieties, see for example: a) Boorum, M. M.; Vasilév, Y. V.; Drewello, T.; Scott, L.T.; *Science*, **2001**, *294*, 828. b) Bergman, J.; Egestad, B.; *Tetrahedron Lett*. **1978**, 19, 3143.
[64] From all the possible coupling schemes for the polymerization of indole compound **2** and **3** have been predicted as the most stable cyclized oligomers: M. Yurtsever, E. Yurtsever, *Polymer* **2002**, 43, 6019.
[65] Qian, X.; Gao, H. –H.; Zhu, Y. –Z.; Pan, B.; Zheng, J. –Y.; *Dyes Pigm*. **2015**, 121, 152.
[66] Wang, L.; Fang, Q.; Lu, Q.; Zhang, S. –J.; Jin, Y. Y., Liu, Z. –Q.; *Org. Lett*. **2015**, 17, 4164.
[67] Wang, F.; Li, X. C.; Lai, W. Y.; Chen, Y.; Huang, W.; Wudl, F.; *Org. Lett*. **2014**, 16, 2942.
[68] Hiyhoshi, H.; Sonoda, T.; Mataka, S.; *Heterocyles* **2006**, 68, 763.
[69] Talaz, O.; Saracoglu N.; *Tetrahedron* **2010**, 66, 1902.
[70] Marsela, M. J.; Rodney, J. R.; Estassi, S.; Wang, L. –S.; *J. Am. Chem. Soc*. **2002**, 124, 12507.
[71] Nishiuchi, T.; Kuwatani, Y.; Nishinaga, T.; Iyoda, M.; *Chem. Eur. J.* **2009**, 15, 6838.
[72] a) Nishiuchi, T.; Tanaka, K.; Kuwatani, Y.; Sung, J.; Nishinaga, T.; Kim, D.; Iyoda, M.; *Chem. Eur. J.* **2013**, 19, 4110. b) Yuan, C.; Saito, S.; Camacho, C.; Irle, S.; Hisaki, I.; Yamaguchi, S.; *J. Am. Chem. Soc.* **2013**, 135, 8842.
[73] a) Rajca, A. Rajca, S.; *Angew. Chem. Int. Ed*. **2010**, *49*, 672. b) Wender, P.; Christy, J. P.; Lesser, A. B.; Gieseler, M. T.; *Angew. Chem. Int. Ed*. **2009**, 48, 7687.
[74] a) Cheng, C.; Cai, Z.; Peng, X. –S.; Wong, N. H. C.; *J. Org. Chem*. **2013**, 78, 8562. b) Cui, J. –F.; Chen, C.; Cai, Z.-W.; Hang, J.-W.; Wong, H. N. C.; *Helv Chim. Acta*, **2012**, 95, 2604.

conjugation, it has been recently recognized that strong stabilizing electron delocalization effects operates in tub-shaped cyclooctatetraenes, such as "two-fold" (double) hyperconjugative interactions across the twisted C–C bonds.[75]

Here, we perform a joint experimental and experimental study which combines absorption spectroscopy, cyclic voltammetry, and spectroelectrochemistry with DFT calculations, in order to understand the fundamental optical and electronic properties of the cyclic tetraindole platform (1a in Scheme 1) and explore its potential in the development of new 3D semiconducting systems. The modulation of the photophysical and electrochemical properties of these cyclic tetramers upon *N*-alkylation (*i.e.*, methyl groups in **1b** or alkyl aryl groups in **1c**-**1d**, see Scheme 1) as well as a comparison with its trimeric counterpart, the high performance semiconductor triindole (**2** in Scheme 1), will be also presented. Interestingly, the X-ray crystal structures of tetraindole derivatives **1a** and **1c** are also successfully reported.

5.3.3. RESULT AND DISCUSSION

Compound **1a** was obtained by treating 2-indolinone with $POCl_3$ in an autoclave at 150ºC. Under these conditions **1a** is obtained together with a large amount of insoluble oligomers. Although the reaction yield is not improved compared to those based on classical heating, the absence of competing triindole **2** significantly facilitates the preparation of this material in pure form.[76] Akylation of this tetramer was achieved readily by treatment of **1a** with the corresponding alkyl halides in the presence of KOH as base and tetrabutylammonium hydrogensulfate as solid-liquid phase transfer catalyst in refluxing acetone in good yield.

[75] a) Wu, J. I.; Fernández, I.; Mo, Y.; Schleyer, P. v. R.; *J. Chem. Theory Comput*. **2012**, 8, 1280. b) Wu, J. I.; Schleyer, P. v. R.; *Pure Appl. Chem*. **2013**, 85, 921.

[76] At this stage it is not clear the reason for the preferred formation of the tetramer vs. the trimeric species. Probably it is just more stable under this harsh condition.

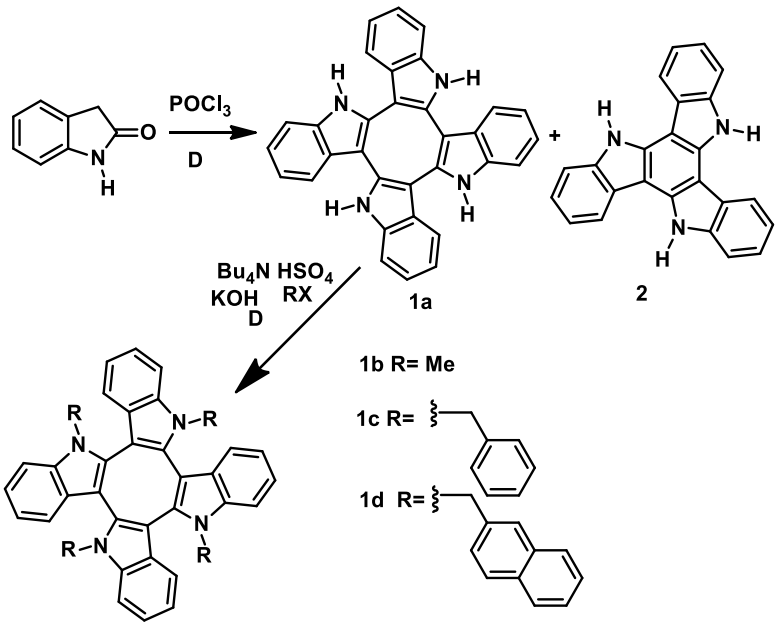

Scheme 1. Synthesis of cyclic tetraindoles **1a**−**1d** and its cyclic trimer triindole counterpart **2**.

Single crystal of **1a** suitable for crystallographic analysis was obtained by slow solvent evaporation from hexane: EtOAc. **1a** crystallize in the tetragonal system, in the I-4 spatial group. X-ray diffraction analysis confirm the saddle shape adopted by these molecules in which two opposite pairs of indole moieties are oriented above or below the average plane of the central eight membered ring presenting a bent angle of 36.6° showing a tub-to-tub inversion barrier of 123 kJ·mol^{-1} as has been calculated by DFT.

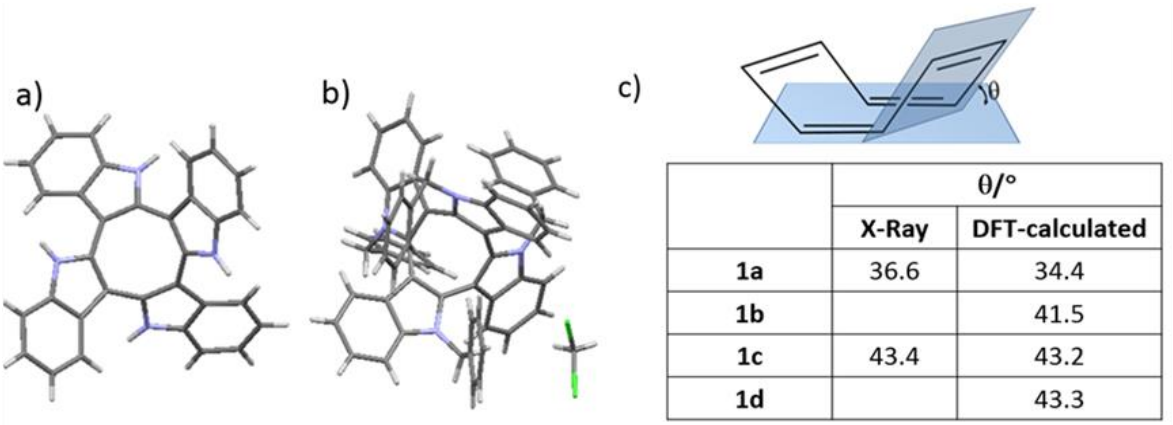

	θ/°	
	X-Ray	DFT-calculated
1a	36.6	34.4
1b		41.5
1c	43.4	43.2
1d		43.3

Figure 1. Crystal Structure of **1a** and **1c**, and comparisom of the theoretical and calculated bent angles.

The molecules crystallize forming columns that extend along the crystallographic *c* axis. Along the columns molecules are perfectly superimposed, stabilizing this arrangement by NH-π interactions that involve all the indole rings of the molecules. Indole rings situated below the average plane of the central eight membered rings are

interacting with those situated in the upper wings of the neighboring molecule and vice versa.[77]

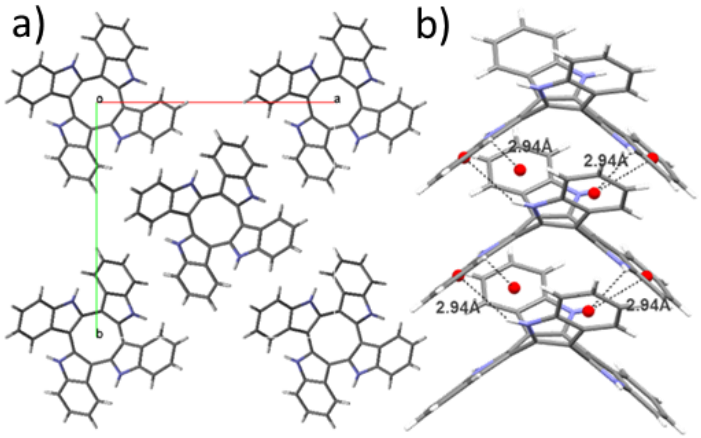

Figure 2. a) View of the packing of **1a** along the crystallographic *c* axis. b) Depiction of the intermolecular NH-π interactions that stabilizes the arrangement into columns of **1a**.

Single crystals of **1c** were obtained by slow solvent evaporation from CH_2Cl_2. Compound **1c** crystallizes in the tetragonal system, spatial group $P4_122$ with one CH_2Cl_2 molecule in the asymmetric unit. This compound crystallize forming orthogonal columns that extend along the perpendicular *a* and *b* axis. In contrast to the packing shown by **1a**, in this case no interaction are observed within the stacks. However each molecule is interacting with neighboring molecules of situated adjacent orthogonal columns through CH-π interactions resulting in a compact network that extends along the *a* and *b* axis. This arrangement leads to the formation of longitudinal channels along the c-axis which can be used to accommodate guest in these structures. The steric constrained introduced by alkylation is reflected in an enhanced bend angle that increases to 43.42°.

[77] While this manuscript was on the preparation the structure of compound **1a** was reported. See Reference 66.

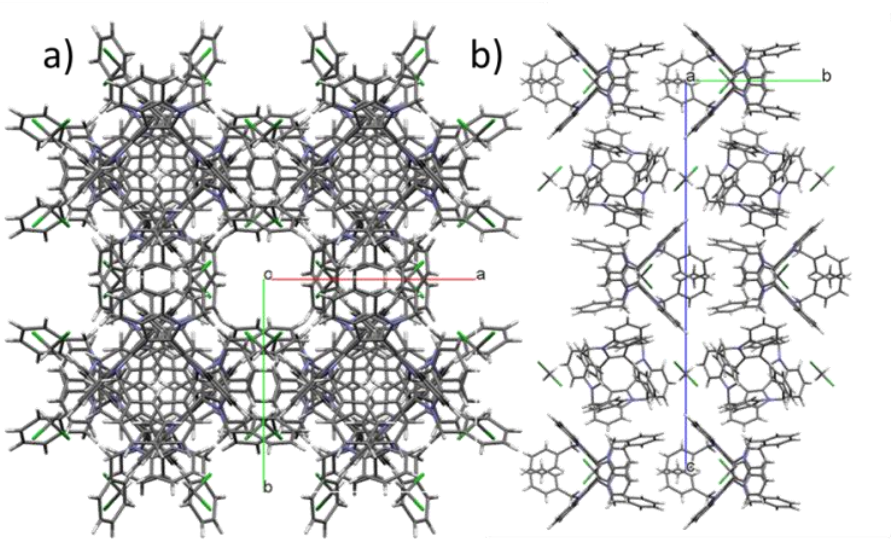

Figure 3. a) View of the packing of **1c** along the crystallographic c axis. b) View of the packing of **1c** along the crystallographic *a* axis. The stacks are aligned along the mutually orthogonal axis.

Alkylation have been found to significantly inhibit ring inversion of the central COT ring, the estimated energy barrier increasing from 123 kJ·mol^{-1} up to 280 kJ·mol^{-1} upon methylation of **1a** to afford **1b** and up to 269 kJ·mol^{-1} upon benzylation to afford **1c**. We have calculated barriers for other compounds containing a cyclooctatetraene ring (see Supporting Information) obtaining correct values when experimental barriers were known. It is interesting to note that the ring inversion barrier of COT is strongly modulated by changing ring annulation on COT. (See table S1).

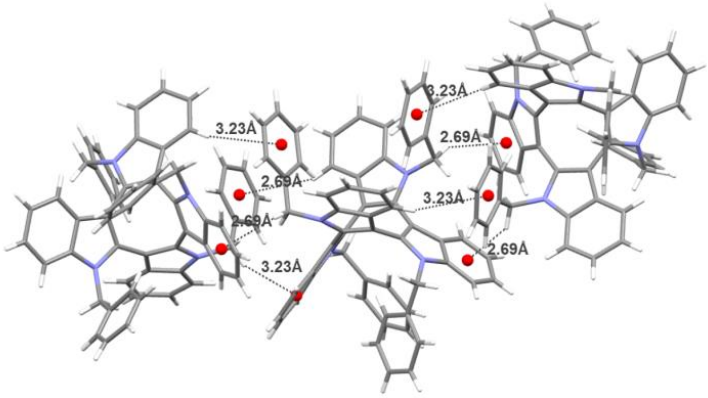

Figure 4. Depiction of the cooperative CH-π interactions among the perpendicular columns of **1c**.

Compounds **1a-1d** show one single set of signals, the chemical shifts of the indole moieties being slightly up field shifted when compared with those of the triindole counterparts. Unequivocal assignment of the signals is performed on the basis of HMBC, HMQC and NOESY experiments. Methylene hydrogen atoms of **1c** and **1d** appear as AX systems with a coupling constant of J = 16.2 Hz highlighting the rigidity of this framework which is confirmed by performing NMR experiments at variable temperature.

The absence of changes in the NMR signals upon heating indicates that neither COT inversion nor aryl rotation is taking place. Also notable is the significant influence observed in the chemical shifts mostly in the signals of the non-equivalent methylene protons when they are exposed to different solvent environments. The aromatic protons of the benzyl group are strongly magnetically shielded as they lie under the concave surface protons (see Supporting information).

The molecular geometries for the neutral state of **1a**-**1d** were optimized at the DFT level under S_4 symmetry. The agreement between the computed and experimental geometry of **1a** and **1c** is very good (see Table SI). Moderately large twisting of the saddle-shaped tetraindole core is obtained upon nitrogen substitution with methyl groups (**1b**) or methyl aryl groups (**1c** and **1d**) when compared to unsubstituted tetraindole **1a**, see Figure 1. Regarding the geometrical relaxation observed in the cyclic tetraindoles, it is interesting to highlight that the fusion of four indoles to the central COT ring results in a decreased degree of C-C bond-length alternation when compared to that in unsubstituted COT unit; for instance, C-C/C=C bond lengths in unsubstituted COT are 1.472/1.341 Å *vs.* 1.455/1.390 Å in **1a**. However, the bond length alternation pattern found for the phenyl rings of the indole moieties is very similar to that obtained for its indole cyclotrimer counterpart (see Figure S1).

We now used Raman spectroscopy in order to gain further insights into the structural and electronic properties of the cyclic tetraindoles. As seen in Figure 5a, the Raman spectra of the cyclic tetraindoles **1a**-**1d** are dominated by three strong Raman bands in the 1500-1700 cm^{-1} region. The band around 1620 cm^{-1} corresponds to a C-C stretching mode (*i.e.*, mode 8a of benzene)[78] involving the external benzene rings, whereas the bands at 1600 (1570) cm^{-1} corresponds to symmetric (antisymmetric) C=C stretching modes localized in the central COT ring. These assignments are supported by the vibrational eigenvectors (see Figure S5). The good agreement between the experimental and theoretical Raman spectra of the cyclic tetraindoles confirms the good validity of our DFT approach (see Figure 7b). It is interesting to note that the C=C stretching modes associated to the COT ring (at 1651 and 1635 cm^{-1} in unsubstituted COT)[79] downshifts upon the fusion of four indoles (at around 1600 and 1570 cm^{-1} in **1a**-**1d**). This is in agreement with the decreased in bond length alternation of the central COT

[78] Wilson, E. B.; Decius, J. C.; Cross, P. C.; *Molecular Vibrations. The Theory of Infrared and Raman Vibrational Spectra*; McGraw-Hill: New York, Toronto, London, **1955**.
[79] a) Zhou, X.; Liu, R.; Pulay, P.; *Spectrochim. Acta* **1993**, 49A, 953. b) Lippincott, E. R.; Lord, R.C.; McDonald, R. S.; *J. Am. Chem. Soc.* **1951**, 73, 3370.

ring when compared to the cyclic tetraindoles as discussed above. Interestingly, *N*-substitution produces moderate changes in the relative position (slight frequency upshift) of the main Raman bands. This suggests that the geometrical effect (*i.e.*, *N*-substituted **1b-1d** display larger twisted structures than unsubstituted **1a**) seems to have a stronger impact than the larger inductive effect of the long alkyl aryl groups.

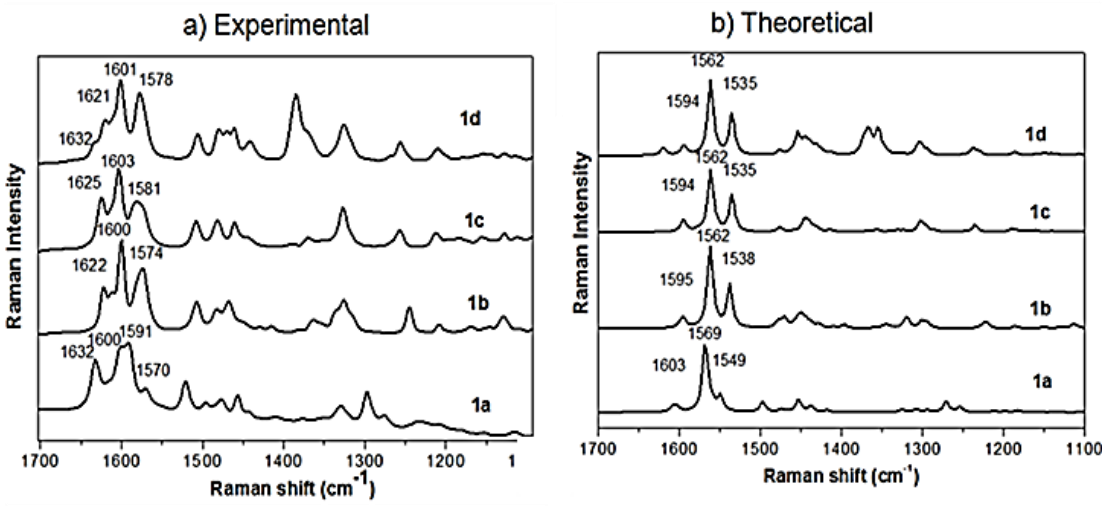

Figure 5. Comparison between the experimental (a) and theoretical (b) Raman spectra of cyclic tetraindoles 1a-1d.

Furthermore, to complement the Raman analysis the nucleus-independent chemical shift (NICS) have been calculated (details of NICS calculations are provided in the SI). NICS methodology is one of the most widely employed indicators of aromaticity and is defined as the negative of the magnetic shielding at some selected point in space, *i.e.*, at a ring center.[80, 81] Significant negative values imply aromaticity (diatropic ring current) and positive values correspond to antiaromaticity (paratropic ring current). The NICS value of the central COT ring in **1a** is estimated to be +3.98 ppm while for an unsubstituted COT ring this value is +5.34 ppm (see Figure S5); this indicates a smaller degree of antiaromatic character upon fusion of the indole units which is in consonance with lower bond length alternation and lower Raman frequencies in cyclic tetraindoles. The NICS values for the external benzenoid groups of **1a** exhibits negative values (–8.98 ppm) revealing the aromatic character; interestingly, these values are very similar to those

[80] a) Schleyer, P. v. R.; Maerker, C.; Dransfeld, A.; Jiao, H.; van Eikema Hommes, N. J. R.; *J. Am. Chem. Soc*. **1996**, 118, 6317. b) Zywietz, T. K.; Schleyer, P. v. R.; Meijere, A.; *J. Org. Chem.* **1998**, 63, 3417.
[81] NICS values have been calculated using the GIAO method (K. Wolinski, J. F. Hilton, P. Pulay, *J. Am. Chem. Soc.* **1990**, 112, 8251) at the 6-311++G(2df,p) level. These data are considered only at the six (eight)-member ring centers which are determined by the nonweighted mean of the heavy atom coordinates.

obtained for triindole, thus suggesting similar electron delocalization in both cyclic trimer and tetramer systems. These results support the good electronic delocalization that is taking place in cyclic tetraindoles despite their twisted structures that would be expected to decrease the π-conjugation. This can be attributed to a double hyperconjugative effect between the CC and π orbitals across the twisted C-C bonds of the COT unit[75] which could enhance the electron delocalization in the cyclic tetraindole cores.

Next, in order to estimate the electron donor character of these cyclic tetramers we have investigated their electrochemical properties by cyclic voltammetry. These molecules oxidize readily. In anhydrous dichloromethane the cyclic voltammograms of these tetramer exhibited two subsequent reversible oxidation waves with half-wave potentials at 0.54 and 0.87 mV for **1a** and 0.72 and 1.09 mV for **1b** , 0.81 and 1.19 mV for **1c** and 0.86 and 1.25 mV for **1d** (see Figure 6). From the first oxidation process it is possible to estimate the HOMO level that is found to be very close to the work function of gold, and therefore hole injection from this electrode is expected to occur without significant barrier (see Table S2). As can be observed the first oxidation potential moderately shifts positively upon *N*-substitution (*i.e.*, 0.54 V in unsubstituted **1a** and 0.86 V in aryl-substituted **1d**). This experimental trend is well reproduced by the DFT calculations, which predicts larger ionization energies and stabilized HOMO levels (see Figure 7 and Table S2) upon *N*-substitution. Interestingly, the inclusion of an additional indole unit in the S_4-symmetric derivatives results in lower first oxidation potentials and then more easily oxidized systems when compared to the C_3-symmetric indole cyclotrimers (*i.e.*, 0.54 V in **1a** and 0.69 V in triindole analogue, see Table S2) [82]; this is in consonance with the HOMO destabilization in going from triindole to cyclic tetraindoles (*i.e.*, –4.96 eV in **2** and -4.60 eV in **1a**).

[82] Ruiz, C.; García-Frutos, E. M.; Da Silva Filho, D. A.; López Navarrete, J. T.; Ruiz Delgado, M. C.; Gómez-Lor, B.; *J. Phys. Chem. C* **2014**, 118, 5470.

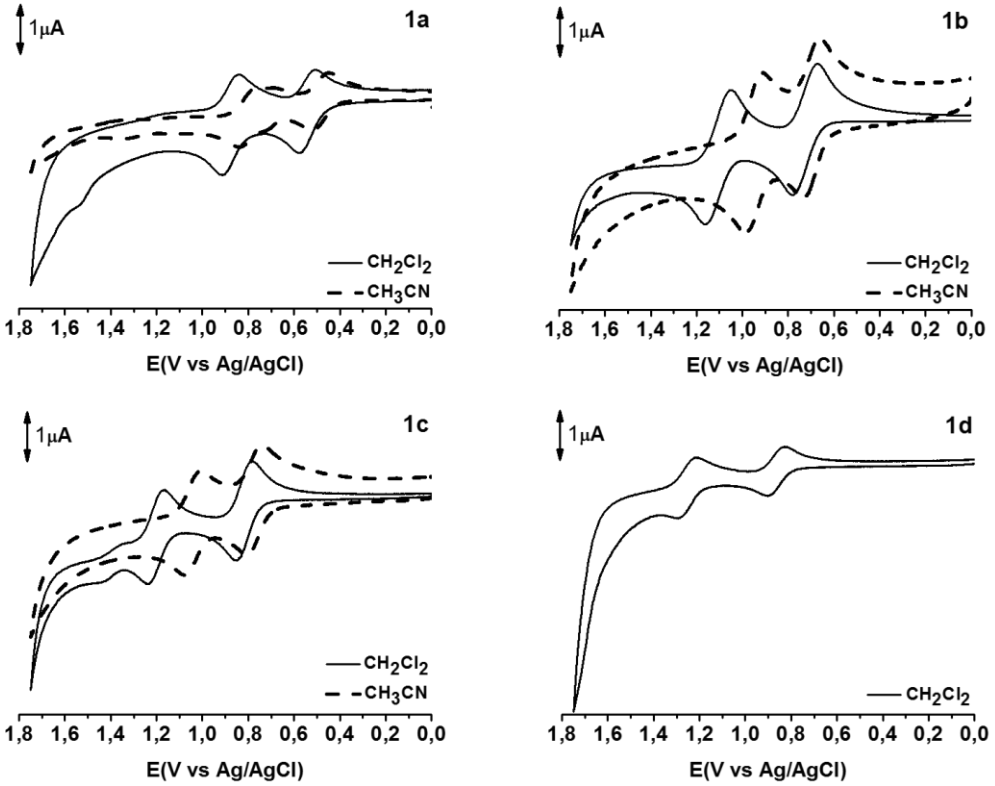

Figure 6. Cyclic voltammograms of **1a**–**1d** in $1x10^{-3}$ M solutions of CH2Cl2 (continuous line) and acetonitrile (dotted line) recorded at a scan rate 100mV/s using 0.1M tetra-n-butylammonium hexafluorophosphate (TBAPF6) as supporting electrolyte, a Pt working electrode, a Ag/AgCl (3M NaCl) reference electrode and a Pt wire auxiliary electrode.

Interestingly, we have found that the redox processes of the cyclic tetraindoles are strongly influenced by the nature of the solvent being highly facilitated in CH_3CN *vs.* CH_2Cl_2 (see Figure 6). For instance, the second oxidation process is shifted anodically by 0.15 (0.08) for **1c** (**1b**) when the experiment is performed in CH_3CN. The stabilization of charged species gained in polar solvents point towards a more localized charge in the cyclic tetraindole species, and therefore a higher sensitivity to solvation in comparison with their trimer triindole analogues. This is in consonance with DFT-calculations that predicts large localization of the charge in the oxidized tetraindoles when compared to triindole derivatives (see Figure S2). For instance, 20% (18%) of the positive charge is located in the central COT ring in the radical (dication) states of tetramer **1a** while in the central phenyl ring of triindole radical (dication) the charge decreases to 15% (13%). In the same context, for cyclic tetraindoles the most significant geometrical changes upon ionization are localized in the central COT ring whereas in the case of triindoles

significant bond length changes are also observed over the external phenyl rings (see Figure S3).

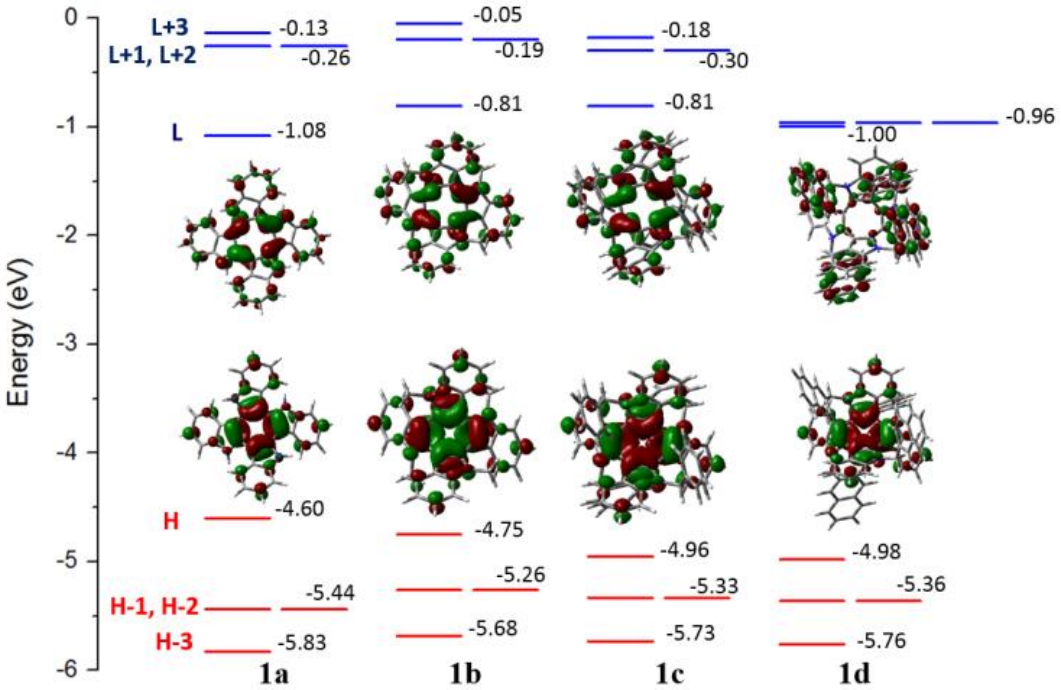

Figure 7. DFT-calculated molecular orbital energies (B3LYP/6-31G** level) for cyclic tetraindoles **1a-1d**. The molecular orbital topologies of the HOMO and LUMO orbitals are also shown.

The easy one-electron reversible oxidations of these derivatives render them potential candidates as hole-transport materials as occur with the triindole derivatives for which hole mobilities as high as 2.7 $cm^2/V^{-1}\cdot s^{-1}$ were reported.[61] To evaluate that possibility we investigated the intramolecular reorganization energies λ associated with hole transfer (λ_h), a molecular parameter which considers the structural reorganization needed to accommodate charge as a prerequisite for efficient transport. The λ_h values for the unsubstituted **1a** and methyl substituted **1b** systems are 332 and 389 meV, respectively. These values are in the same order than those calculated for many other organic systems considered as good hole-transport materials (*i.e.*, values of 306 meV were obtained for dithienoacene for which hole field-effect mobilities of 0.31 $cm^2/V^{-1}\cdot s^{-1}$ were reported).[83]

The absorption spectra of cyclic tetraindoles **1a-1d** are characterized by a band at 290-320 nm, see Figure 8. *N*-substitution with methyl groups remains unchanged the position of the maxima but moderately blue-shits the absorption edge, whereas substitution with bulky alkyl aryl groups blue-shifts both the maxima and absorption edge.

[83] Sun, Y. M.; Ma,Y. Q.; Liu, Y. Q.; Lin, Y. Y.; Wang, Y. Z.; Wang, Y.; Di, C. A.; Xiao, K.; Chen, X. M.; Qiu, W. F.; Zhang, B.; Yu, G.; Hu, W. P.; Zhu, D. B.; *Adv. Funct. Mater*. **2006**, 16, 426.

This is in consonance with the largest HOMO-LUMO gap predicted by DFT calculations upon *N*-alkylation as result of the HOMO (LUMO) stabilization (destabilization), see Figure 6.

TD-DFT calculations nicely predicts the experimentally observed blue-shift upon *N*-substitution (see Figure 8b). The strongest band at ≈ 300 nm in cyclic tetraindoles corresponds to the degenerate electronic transitions (*i.e.*, $S_0 \rightarrow S_5/S_0 \rightarrow S_6$ in **1a**); note that the $S_0 \rightarrow S_1$ transition is forbidden because of the S_4-symmetry of these systems. For instance, this band is calculated at 310 nm for **1a**, which is assigned to a combination of HOMO−2 → LUMO, HOMO → LUMO+2, HOMO−1 → LUMO, and HOMO→ LUMO+1 one-electron excitations (see Figure S4).

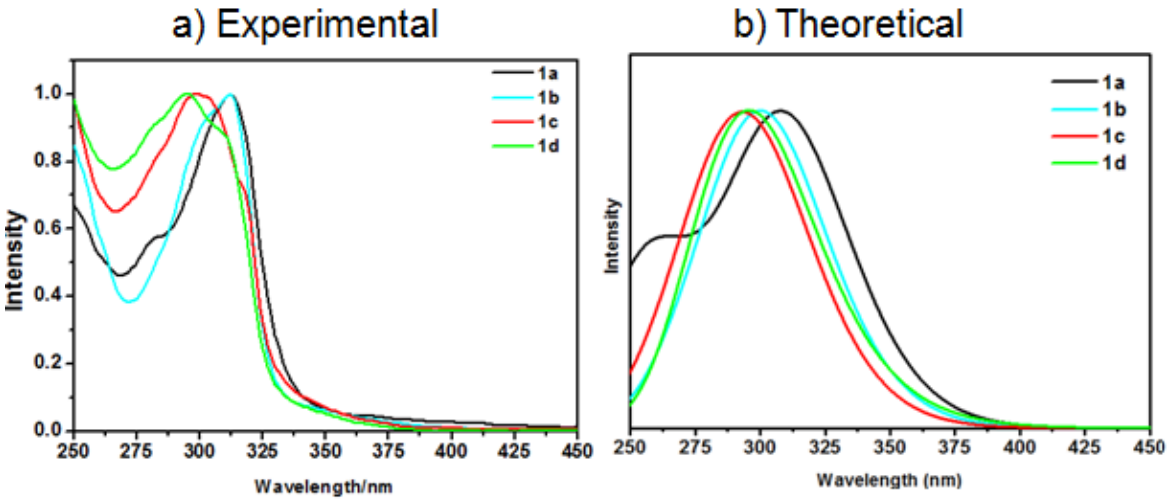

Figure 8. (a) Experimental UV/Vis spectra of **1a**–**1d** in 10^{-5}M CH_2Cl_2 solutions and (b) the corresponding simulated absorption spectra as determined with TD-DFT at the B3LYP76-31G** level.

In order to gain insight into the electronic structure of the oxidized species we perform spectroelectrochemical measurements by sequentially increasing the potential in order to stepwise oxidize them. Figure 7 shows the electronic spectra of **1a-1d** recorded during electrochemical oxidation. The electronic spectrum of the first oxidized species shows a dominant broad band around 700 nm which can be ascribed to the formation of a radical cation species. When the potential was increased up to 1000 mV and 1500 mV respectively, the broad bands increase in intensity and a new band around 400 nm emerges. These processes are reversible as confirmed by back-reduction which provides the starting neutral derivatives (see SI). The blue-shifting of the absorption band in going from the radical cation to the dication species is very well captured by TD-DFT calculations (see Figure S5).

It is interesting to note that cyclic tetraindoles show a very similar spectral evolution upon oxidation when compared to the cyclic triindole counterparts with a slight blue-shifting of the absorption maxima. For instance, the band ascribed to the radical cation (dication) appears at 690 (440)nm in triindole **2** and at 600 (408)nm in tetraindole **1a**. This is in consonance with the larger charge localization found for both oxidized species in cyclic tetraindoles when compared to triindole (see figure S2-S3). Note also that the saddle-shaped (twisted) structure of tetraindoles is still maintained upon oxidation (*i.e.*, DFT-calculations predict that the bend angle slightly decreases from 34.3° to 32.0° and 30.8° in **1a** when going from the neutral, to the cation radical and dication species) whereas the oxidized triindole derivatives exhibit nearly planar conjugated cores.

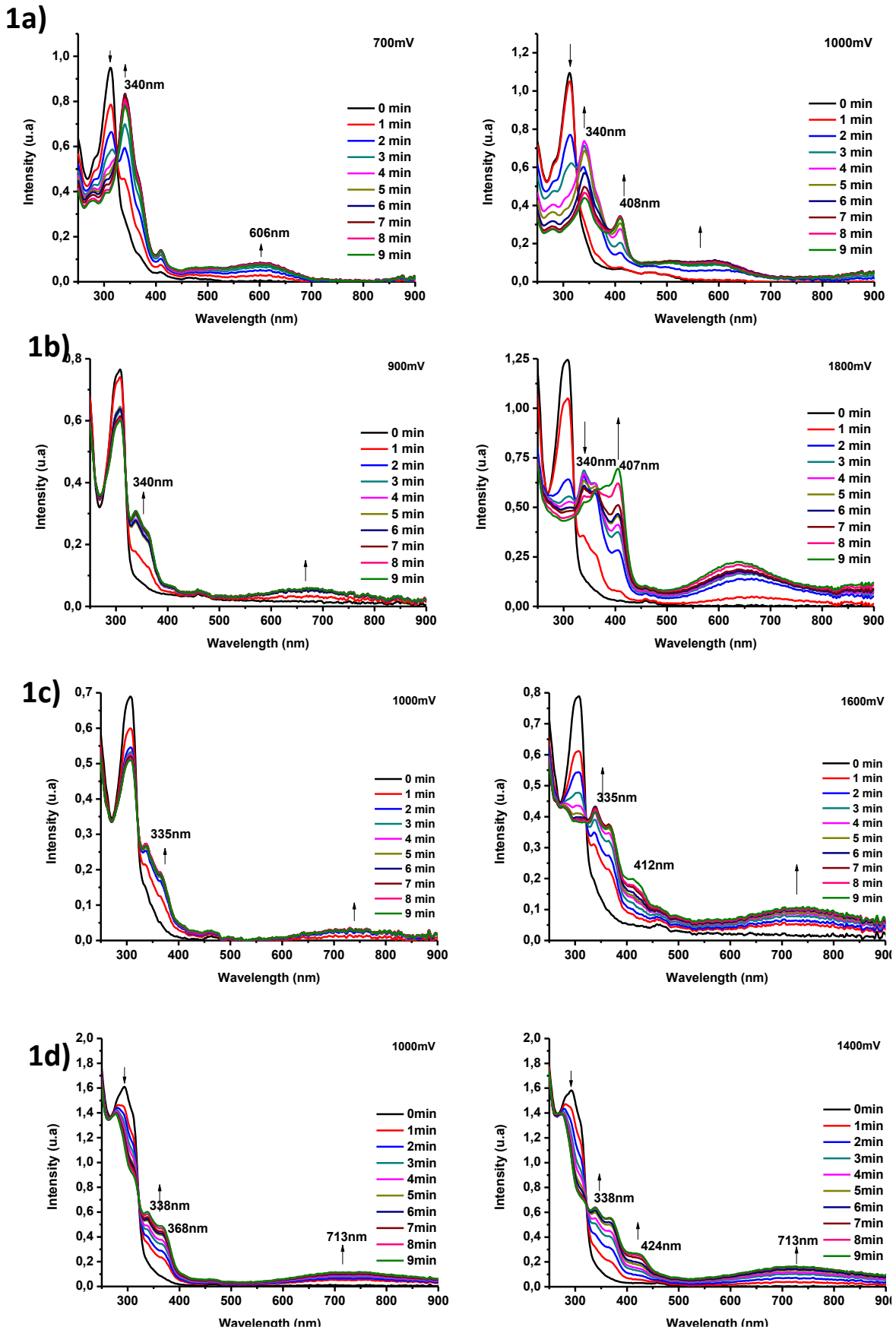

Figure 9. UV/Vis-NIR spectra of **1a**–**1d** obtained at different time intervals after applying a potential of 0.7-1.0 V (left) and 1.0-1.4 V (right) in CH_2Cl_2.

5.3.4. CONCLUSIONS

Here we explore the optical and electronic features of cyclic tetraindoles *N*-substituted with alkyl or alkyl aryl groups as interesting electroactive platforms with 3D architectures. The X-Ray crystal structures confirms their saddle-shaped structures which present moderately large tub-to-tub inversion barrier when compared to unsubstituted cyclooctatetraene (COT) rings. Interestingly, the steric constrain introduced by *N*-substitution results in more twisted structures and significantly inhibit ring inversion of the central COT unit but affect only slightly the optical and electrochemical properties. Raman spectroscopy suggests that cyclic tetraindoles allow for a good electron delocalization despite their twisted structures. The electronic absorption spectra evolution upon oxidation together with the DFT calculations evidences the formation of stable cation and dication species in cyclic tetramers with charge defects more localized in the central COT ring. In summary, we present cyclic tetraindole as an interesting electroactive scaffold to connect in three dimension functional moieties with potential applications in the field of organic materials.

5.3.5. EXPERIMENTAL SECTION

Experimental Details Routine ^{1}H and ^{13}C NMR spectra were recorded on Bruker AMX 300 and Bruker AC-200 spectrometers. Solvents were purified and dried using standard procedures. Chromatography purifications were carried out using flash grade silica gel with distilled solvents. All reactions were carried out under Ar.

5,10,15,20-tetrahydrocycloocta[1,2-b:3,4-b':5,6-b'':7,8-b''']tetraindole,1a. A mixture of 2-Oxindole (2g, 15mmol) in 4 mL of toluene was stirred and 1mL of $POCl_3$ (10.71mmol) was slowly added. Then the mixture was heated at 150ºC in an autoclave overnight. To removal $POCl_3$ ice was added, and the mixture was neutralized with concentrated KOH to pH =7–8. The mixture was diluted with EtOAc, washed with water and then the organic phase dried ($MgSO_4$). The solvent was evaporated and the residue was purified by chromatography with EtOAc/hexane (1:3) to give a yellow solid crystalline **1a** (330mg, 19%). ^{1}H NMR (500 MHz, $C_2D_2Cl_4$) δ 8.75 (s, 4H), 7.68 (d, *J* = 7.7 Hz, 4H), 7.45 (d, *J* = 7.9 Hz, 4H), 7.17 (dt, *J* = 21.4, 7.2 Hz, 8H). 13C NMR (50 MHz, $C_2D_2Cl_4$) δ 137.2, 135.4, 127.5, 122.4, 121.3, 118.7, 111.2, 106,3. UV (CH_2Cl_2, 25 ºC)

λ_{max} (log ε) 312 (4.40); MALDI-TOF MS m/z 460.2 (M+); HRMS (MALDI-TOF) calcd for $C_{32}H_{20}N_4$: 460.1682, found: 460.1701.

5,10,15,20-tetramethyl-5,10,15,20-tetrahydrocycloocta[1,2-b:3,4-b':5,6-b'':7,8-b''']tetraindole, 1b. A mixture of **1a** (40mg, 0.087 mmol), KOH (146mg, 2.1 mmol) and $[CH_3(CH_2)_3]_4N(HSO_4)]$ (5 mg, 0.03mmol) was heated to reflux in acetone (10mL). Metilsulfate (0,05ml, 0.522mmol) was added and the mixture was stirred for 12 h. The mixture was cooled to room temperature and the solvent was evaporated. The mixture was diluted with CH_2Cl_2, washed with water, and dried ($MgSO_4$); the solvent was then evaported. The residue was triturated with CH_3CN to give a white solid **1b** (25mg, 54%). ^{1}H NMR (200 MHz, $CDCl_3$) δ 7.41 (dd, *J* = 6.9 Hz, 8H), 7.34 – 7.08 (m, 8H), 3.69 (s, 12H). ^{13}C NMR (50 MHz, $CDCl_3$) δ 138.6, 138.4, 127.7, 121.7, 120.3, 119.1, 109.9, 106.1, 31.7. UV (CH_2Cl_2, 25 ºC) λ_{max} (log ε) 312 (4.98); MALDI-TOF MS m/z 516.3(M+); HRMS (MALDI-TOF) calcd for $C_{36}H_{28}N_4$: 516.2308, found: 516.2323

5,10,15,20-tetrabenzyl-5,10,15,20-tetrahydrocycloocta[1,2-b:3,4-b':5,6-b'':7,8-b''']tetraindole, 1c. A mixture of **1a** (100 mg, 0.22 mmol), KOH (316 mg, 5.64 mmol) and $[CH_3(CH_2)_3]_4N(HSO_4)]$ (12 mg, 0.07 mmol) was heated to reflux in acetone (10 mL). Benzyl bromide (233 mL, 1.9 mmol) was added and the mixture was stirred for 12 h. The mixture was cooled to room temperature and the solvent was evaporated. The mixture was diluted with CH_2Cl_2, washed with water, and dried ($MgSO_4$); the solvent was then evaporated. The residue was triturated with CH_3CN to give a white solid **1c** (108mg, 60%). ^{1}H NMR (300 MHz, $C_2D_2Cl_4$) δ 7.24 (dd, *J* = 12.0, 7.9 Hz, 8H), 7.05 (dt, *J* = 14.7, 7.0 Hz, 8H), 6.72 (t, *J* = 7.4 Hz, 4H), 6.61 (d, *J* = 7.5 Hz, 8H), 6.38 (t, *J* = 7.7 Hz, 8H), 5.45 (d, *J* = 16.2 Hz, 4H), 5.21 (d, *J* = 16.1 Hz, 4H). ^{13}C NMR (50 MHz, $C_2D_2Cl_4$) δ 139.2, 137.6, 129.5, 128.4, 128.2, 127.1, 126.2, 122.2, 120.9, 119.2, 111.0, 107.6, 48.4. UV (CH_2Cl_2, 25 ºC) λ_{max} (log ε) 300 (3.88); MALDI-TOF MS m/z 820.4 (M+); HRMS (MALDI-TOF) calcd for $C_{60}H_{44}N_4$: 820.3560 found: 820.3579

5,10,15,20-tetrakis(naphthalen-2-ylmethyl)-5,10,15,20-tetrahydrocycloocta[1,2-b:3,4-b':5,6-b'':7,8-b''']tetraindole, 1d. A mixture of **1a** (45 mg, 0.10 mmol), KOH (146 mg, 2.6 mmol) and $[CH_3(CH_2)_3]_4N(HSO_4)]$ (5.6 mg, 0.03 mmol) was heated to reflux in acetone (2 mL). 2-(Bromomethyl)naphthalene (217 mg, 0.98 mmol) was added and the mixture was stirred for 12 h. The mixture was cooled to room temperature and the solvent was evaporated. The mixture was diluted with CH_2Cl_2, washed with water, and dried ($MgSO_4$); the solvent was then evaporated. The residue was triturated with CH_3CN to give a white solid **1d** (17mg, 41%). ^{1}H NMR (200 MHz, $CDCl_3$) δ 7.38 (d, *J* = 8.1 Hz,

4H), 7.30 (d, *J* = 6.1 Hz, 4H), 7.26 (d, 4H), 7.15 (t, *J* = 7.3 Hz, 4H), 7.08 (d, *J* = 6.3 Hz, 4H), 7.02 (s, 4H), 6.93 (d, 8H), 6.88 (t, *J* = 7.5 Hz, 4H), 6.76 (t, *J* = 7.5 Hz, 4H), 6.23 (d, *J* = 8.2 Hz, 4H), 5.77 (d, *J* = 16.3 Hz, 4H), 5.48 (d, *J* = 16.3 Hz, 4H). ^{13}C NMR (50 MHz, $CDCl_3$) δ 139.4, 137.6, 135.1, 133.1, 132.3, 128.3, 128.2, 127.5, 127.1, 125.7, 125.2, 125.5, 124.5, 122.2, 121.2, 119.0, 111.1, 107.5, 48.6. UV (CH2Cl2, 25 ºC) λ_{max} (log ε) 295 (4.12); MALDI-TOF MS m/z 1020.5 (M+); HRMS (MALDI-TOF) calcd for $C_{76}H_{52}N_4$: 1020.4186 found: 1020.4176

X-ray structure determinations. Colorless crystal of **1c** showing well defined faces were mounted Bruker four circle kappa-diffractometer equipped with a Cu INCOATED microsource, operated at 30 W power (45 kV, 0.60 mA) to generate CuKα radiation (λ = 1.54178 Å), and a Bruker VANTEC 500 area detector (microgap technology). Diffraction data were collected exploring over a hemisphere of the reciprocal space in a combination of φ and ω scans to reach a resolution of 0.86 Å, using a Bruker APEXII[84] software suite. The structure was solved by the Multan and Fourier methods. Crystal dimensions 0.20 *x* 0.20 *x* 0.20 mm^3, unit cell dimensions **a** = 12.3240(5) , **b** = 12.3240(5), **c** = 35.3681(19) Å, monoclinic, *P*4$_1$22 space group, **β** = 98.253 (1)° , **V**= 9144.9(3) Å3, **Z** = 8, $\rho_{\mathbf{calcd}}$ 1.12 Mg/m3. The structure was refined anisotropically R1(F) = 0.0768 for observed data (I>2σ(I)), R1(F) = 0.0893 for all data; GOF(F2) = 1.005.

Most of the calculations were carried out with APEXII[84] software for data collection and reduction, and OLEX2[85] for structure solution and refinements. CCDC 1455532 contain the supplementary crystallographic data for **1c** respectively. These data can be obtained free of charge via www.ccdc.cam.ac.uk/conts/retrieving.html (or from the Cambridge Crystallographic Data Centre, 12 Union Road, Cambridge CB21EZ, UK; (fax: (+44) 1223-336-033; or e-mail: deposit@ccdc.cam.ac.uk). P41 Some solvent molecules **1c** could not be modelled properly and have been disregarded. The Olex2 [86] program was used to calculate the solvent disorder area and remove its contribution to the overall intensity data.

Computational details. The molecular geometries of neutral, radical-cation and dication states of tetraindoles **1a-1d** were calculated at the Density Functional Theory

[84] APEX2; Bruker-AXS: Madison, WI, **2006**.
[85] Software for the SMART system, V.5.04, Bruker-Siemens Analytical X-ray Instruments, Inc., Madison, WI, USA, **1998**.
[86] Dolomanov, O.V.; Bourhis, L.J.; Gildea, R.J.;Howard, J.A.K.; Puschmann, H.; *J. Appl. Cryst.* **2009**, 42, 339.

(DFT) level using the hybrid, generalized gradient approximation (GGA) functional B3LYP[87,88] and a 6-31G** basis[89,90,91] set, as implemented in the GAUSSIAN09 program.[92] For comparison purposes the molecular geometries of triindole and unsubstituted cyclooctatraene (COT) were calculated at the same level. For the neutral state of tetraindoles (triindole) S_4 (C_3) symmetry constraints were imposed during the optimization process. On the resulting ground-state optimized geometries, harmonic frequencies calculations were performed to ensure we are in a global minimum. Vertical electronic excitation energies were computed by using the time-dependent DFT (TD-DFT) approach on the previously optimized molecular geometries. Absorption spectra were simulated through convolution of the vertical transition energies and oscillator strengths with Gaussian functions characterized by a half width at half-maximum (fwhm) of 0.3 eV. Molecular orbital contours were plotted using GausView 5.0. The reorganization energies associated with hole transfer were calculated directly from the relevant points on the potential energy surfaces using the standard procedure detailed in the literature.[93] Using the B3LYP/6-31G** optimized structures, NICS[94] values were calculated at the B3LYP/6-11++G(2d,f) level using the GIAO[95] (gauge-independent atomic orbital) method. Inversion barriers were calculated at the B3LYP/6-31+G** computational level within the Gaussian-09 package. Frequencies calculations have been carried out to confirm that the structures obtained correspond to energetic minima or true transition state.

[87] Becke, A.D.; *J. Chem. Phys.* **1993**, 98, 5648.
[88] Lee, C.T.; Yang, W.T.; Parr, R.G.; *Phys. Rev. B* **1988**, 37, 785.
[89] Hariharan, P.C.; Pople, J.A.; *Theor. Chim. Acta* **1973**, 28, 213.
[90] Hehre, W.J.; Ditchfield, R.; Pople, J.A.; *J. Chem. Phys.* **1972**, 56, 2257.
[91] Francl, M.M.; Pietro, W.J.;. Hehre, W.J.; Binkley, J.S.; Gordon, M.S.; Defrees, D.J.; Pople, J.A.; *J. Chem. Phys.* **1982**, 77, 3654.
[92] Frisch, M.J.; Trucks, G.W.; Schlegel, H.B.; Scuseria,G.E.; Robb,M.A.; Cheeseman,J.R.; Scalmani, G.; Barone, V.; Mennucci, B.; Petersson, G.A.; Nakatsuji, H.; Caricato, M.; Li, X.; Hratchian, H.P.; Izmaylov, A.F.; Bloino, J.; Zheng, G.; Sonnenberg, J.L.; Hada, M.; Ehara, M.; Toyota, K.; Fukuda, R.; Hasegawa, J.; Ishida, M.; Nakajima, T.; Honda, Y.; Kitao, O.; Nakai, H.; Vreven, T.; Montgomery,J.A.; Peralta, Jr. J.E.; Ogliaro, F.;Bearpark, M.; Heyd, J.J.; Brothers, E.; Kudin, K.N.; Staroverov, V.N.; Kobayashi, R.; Normand, J.; Raghavachari, K.; Rendell, A.; Burant, J.C.; Iyengar, S.S:; Tomasi, J.; Cossi, M.; Rega, N.; Millam, J.M.; Klene, M.; Knox, J.E.; Cross, J.B.; Bakken, V.; Adamo, C.; Jaramillo, J.; Gomperts, R.; Stratmann, R.E.; Yazyev, O.; Austin, A.J.; Cammi, R.; Pomelli, C.; Ochterski, J.W.; Martin, R.L.; Morokuma, K.;. Zakrzewski, V.G.; Voth, G.A.; Salvador, P.; Dannenberg, J.J.; Dapprich, S.; Daniels, A.D.; Farkas, Ö.; Foresman, J.B.; Ortiz, J.V.; Cioslowski J.;. Fox, D.J.; Gaussian 09, Revision D.01, Gaussian, Inc., Wallingford CT, **2009**.
[93] Bredas, J.L.; Beljonne, D.; Coropceanu, V.; Cornil, J.; *Chem. Rev.* **2004**, 104, 4971.
[94] Schleyer, P. v. R.; Maerker, C.; Dransfeld, A.; Jiao, H.; Hommes, N. J. R. v. E.; *J. Am. Chem. Soc.* **1996**, 118, 6317.
[95] Wolinski, K.; Hilton, J.F.; Pulay,P.; *J. Am. Chem. Soc.* **1990**, 112, 8251.

Conclusion

CONCLUSION

The following conclusion can be extracted from this thesis:

1. We have studied a series of crystalline *N*-trialkyltriindoles in which the number of carbon atoms of the alkyl chains attached to the nitrogen was systematically varied. We found that the length of the alkyl chains does not affect significantly their electronic properties, despite of having a strong influence in the morphology and in the crystalline packing of these compounds.

A study of the crystalline packing of compounds allowed us to demonstrate that behind the different crystalline habits and macroscopic morphologies observed how molecules pack in the crystals and interacts with their nearest neighbors. The contribution of several cooperative CH-π interactions to guide the self-assembly of this type of molecules have been clearly established. Studying the crystal packing of the different trialkylated triindoles we have selected the *N*-trihexyltriindole as the best candidate to be incorporated into OFETS. A mobility value, $1.42\ x\ 10^{-2}\ cm^2V^{-1}s^{-1}$ was obtained on a standard bottom gate-top contact configuration.

2. We studied how electronic communication of the external substituents with the central triindole platform facilitates the tuning of the light-emitting properties and HOMO–LUMO levels. We fabricated OLEDs devices with these derivatives from solution techniques.

Moreover, we have synthesized a series of monoaryltriindoles and studied the effect that asymmetrical substitution has in the electronic properties of this semiconducting platform. Results show that asymmetrical derivatives offer significant advantages in terms of energy levels tailoring, and present higher quantum yields and increased range of emission spectra when they are compared to their symmetrical counterparts.

3. We found that we could increase the dimension of charge transport in discotic liquid crystal, increasing the conducting/isolating ratio, with an enlarged π-conjugated triindole based aromatic core, and, with the incorporation of peripheral groups able to establish intermolecular interactions. In this particular case, we

have synthesized a new triindole-based liquid crystal functionalized with six peripheral thiomethyl moieties. These moieties are able of establishing S-S interaction which has already shown their benefits to increase the contact between neighboring columns in other semiconducting aromatic platforms. We studied the lower dependence of the electrical performance of these discotic liquid crystals by comparing the mobility values obtained by: space-charge limited current and field effect mobility measurements in thin film transistor devices. In both cases, the mobility founded on a diode type device is higher than that determined on thin-film transistors. The observation of field effect behavior in a discotic liquid crystal processed by simple drop-casing suggests an increased dimensionality of charge transport. The differences obtained can be understood by the high tendency of π-conjugated molecules to deposit on surfaces with their aromatic cores parallel to the substrate.

4. We explored the potential applications of triindole platforms in the development of new emergent electroactive materials, such as microporous organic polymers and covalent organic frameworks. We have synthesized two dimeric molecules bound together through different linkers (*p*-phenylene or diacetylene groups), as model systems to investigate the influence of the π-bridge on their fundamental properties, such as the electronic, redox and photophysical properties. Our results show us that while a *p*-phenylene bridge nearly isolates the two subunits of the dimers, a diacetylene bridge allows a high level of electronic connection between them. This conclusion renders the diacetylene moiety as the best linker in the synthesis of microporous polymeric material with opto-electronics applications.

5. We studied the properties of two analogous oligomer compounds: asymmetric triindole and tetraindole, and their derivatives. On one hand, we found that asymmetric triindole, and their derivatives, improve the photophysical properties than their symmetrical counterparts. And in the other hand, we present tetraindole platform as a promising three-dimensional electroactive scaffold in the search of semiconducting systems with enhanced dimensionality of charge transport. We believe that this work may provide guidance for further development of these materials with improved potential for electronic applications.

CONCLUSIONES

Las siguientes conclusiones han sido extraídas de esta tesis doctoral:

1. Hemos realizado un estudio de una serie de *N*-trialquiltriindoles cristalinos en donde el número de átomos de carbono en las cadenas alquílicas unidas al nitrógeno ha sido variado sistemáticamente. Hemos encontrado que el tamaño de la cadena no afecta de forma significativa a sus propiedades electrónicas, sin embargo sí que tiene una enorme influencia en sus propiedades morfológicas y en el empaquetamiento cristalino de estos compuestos.

Este estudio nos permite demostrar que detrás de los diferentes hábitos cristalinos y morfologías observadas, está el efecto de cómo las moléculas interactúan con las moléculas vecinas más cercanas. Se ha podido así determinar la contribución de interacciones tipo CH-π en la generación de las diferentes superestructuras observadas. Mediante un estudio del empaquetamiento cristalino de los diferentes triindoles, se *N*-trihexiltriindol como el mejor candidato para ser incorporado en dispositivos tipo OFET. Este compuesto presentó un valor de movilidad de cargas de $1{,}42 \; x \; 10^{-2}$ $cm^2V^{-1}s^{-1}$.

2. Se ha estudiado cómo la comunicación electrónica de los sustituyentes externos a la plataforma central del triindole facilita la optimización de las propiedades de emisión y la variación de los niveles HOMO-LUMO de la plataforma. Llegándose a la fabricación de OLEDs procesados desde disolución con diferentes derivados del triindol.

Así mismo, se han sintetizado una serie de moroariltriindoles con el fin de estudiar el efecto que tiene la sustitución asimétrica en las propiedades electrónicas, demostrándose que estos nuevos compuestos presentan mejores rendimientos cuánticos, así como un aumento en el rango de emisión en comparación con sus homólogos simétricos.

3. Se ha encontrado que podemos aumentar la dimensionalidad del transporte de carga en cristales líquidos discóticos, basados en la plataforma del triindol, mediante dos estrategias alternativa. Por un lado a partir del aumento la contribución de la parte conductora de la molécula con respecto de la parte

aislante, y por otro a partir de la incorporación de grupos periféricos capaces de establecer interacciones intermoleculares con las moléculas vecinas. En ambos casos se pudo determinar la eficiencia de la movilidad del transporte de carga mediante la utilización de técnicas que requerían alineamientos opuestos. Si bien los valores obtenidos para dispositivos tipo diodos fueron mayores que los obtenidos en dispositivos tipo transistor, el hecho de poder determinar movilidades mediante la fabricación de transistores de efecto campo en este tipo de moléculas ya sugiere un aumento de la dimensionalidad del transporte de carga.

4. Se ha realizado la síntesis de dos dímeros del triindol unidos por diferentes unidades puente (*p*-fenileno o grupos diacetileno) con el fin de tomarlos como modelos para explorar la posibilidad de incorporar al triindol como plataforma en el desarrollo de polímeros orgánicos microporosos. La combinación de estudios teóricos y experimentales de sus propiedades electrónicas, redox y foto-físicas que se realizaron sobre ambos dímeros, nos llevó a la conclusión de que el grupo diacetileno permite una mejor comunicación electrónica entre las unidades de triindol. Este estudio permitirá el diseño futuro de nuevos polímeros microporosos basados en esta plataforma.

5. Se realizaron estudios sobre otros oligómeros cíclicos del indol, como son el triindol asimétrico y el tetraindol, y sus derivados. Por un lado encontramos que el triindol asimétrico mejora las propiedades fotofísicas con respecto a su homologo simétrico. Y por otro lado presentamos a la plataforma de tetraindol como un sistema tridimensional que se presenta como un candidato prometedor para el aumento de la dimensionalidad del transporte de carga. Creemos que este trabajo puede resultar una guía para el desarrollo de estos materiales y su aplicación en dispositivos electrónicos.

Supporting Information

SUPPORTING INFORMATION

S.1. SECTION 1.2. *"THE ROLE OF CH-π INTERACTIONS IN THE CRYSTAL MORPHOLOGY AND PACKING OF N-TRIALKYLATED TRIINDOLES."*

Constanza Ruiz,† Ángela Benito-Hernández,† Enrique Gutiérrez-Puebla,† Ángeles Monge-Bravo,† and Berta Gómez-Lor*,†

*E-mail: bgl@icmm.csic.es

S.1.1. Experimental section

Absortion spectra. UV−vis studies were carried out on a PerkinElmer Lambda XLS+ spectrometer. Fluorescence spectra were recorded on an Aminco SLM 8000 spectrophotometer.

Cyclic Voltammetry Measurements. Cyclic voltammetry (CV) experiments were performed on a Bioanalytical Systems Inc. (BASI) Epsilon electrochemical workstation in a three-electrode cell at room temperature under a nitrogen atmosphere. Electrochemical measurements were carried out in acetonitrile solution ($c = 1 \times 10^{-3}$ M) containing 0.1 M tetra-n-butylammonium hexafluorophosphate ($TBAPF_6$) of supporting electrolyte at a scan rate 100 mV/s. A three electrode setup was used including a platinum working electrode, a Ag/AgCl (3 M NaCl) reference electrode, and a platinum wire auxiliary electrode. Ferrocene was used as an internal standard, and all potentials were referenced to the ferrocene/ferrocenium redox couple.

Powder X Ray diffraction. X-ray powder diffraction were performed by a Bruker D8 diffractometer with a Sol-X energy dispersive detector, working at 40 kV and 30 mA and employing CuKα (λ = 1.5418 Å) filtered radiation. The diffractograms were registered with a step size of 0.02º and exposure time of 0.5 s per step and a 2θ range of 5-30º.

S.1.2. Electronic Properties

All four derivatives present nearly identical absorption spectra and cyclic voltammograms. From the first oxidation process we can estimate a HOMO level -5,08 eV and from the optical gap we estimate an HOMO-LUMO gap of 3,36 eV which render a

LUMO level of -1,72 eV. The value of the HOMO and LUMO energy levels of these compounds are adequate for the use as p-type semiconductors in organic electronic devices.

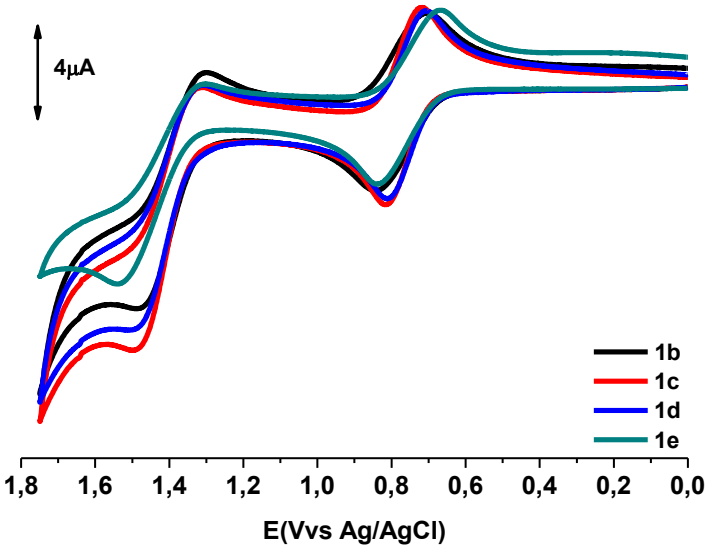

Figure S1. Cyclic voltammograms of **1b**, **1c**, **1d** and **1e** at c = $1x10^{-3}$ $molL^{-1}$ recorded in CH_2Cl_2/ 0.1M tetra-n-butylammonium hexafluorophosphate ($TBAPF_6$) measured versus Ag/AgCl (3M NaCl) and containing ferrocene as internal standard. Measurements were performed at a scan rate 100mV/s using a Pt working electrode and a Pt wire auxiliary electrode.

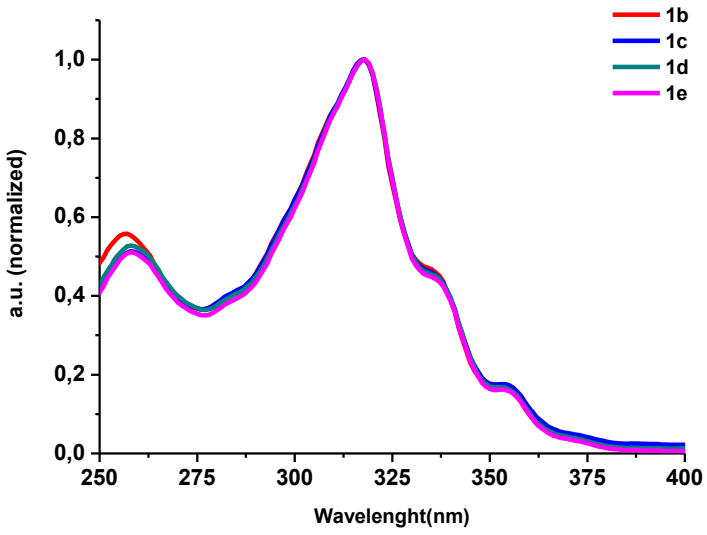

Figure S2. Experimental UV-Vis spectra of **1a**, **1b**, **1c**, **1d** and **1e**c = $1x10^{-6}$ $molL^{-1}$ recorded in CH_2Cl_2.

S.1.3. Powder X-ray diffraction

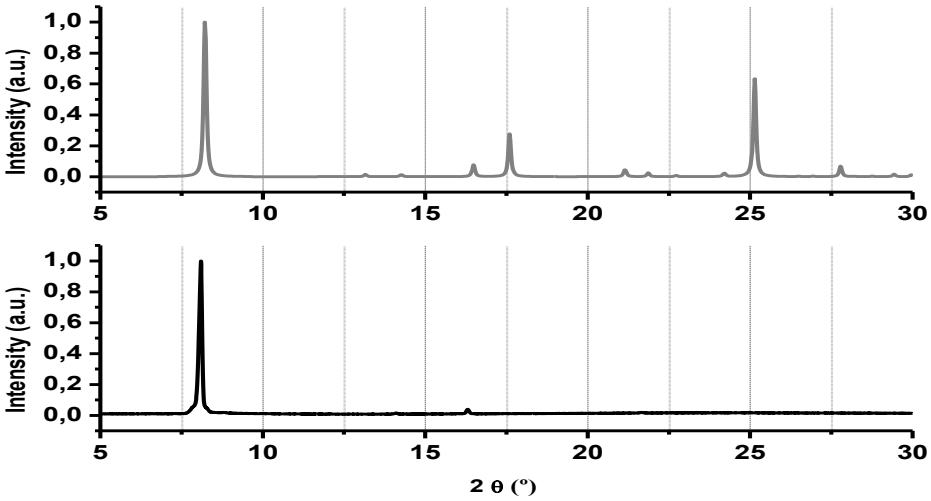

Figure S3. Powder X-ray diffractograms obtained from the single crystal data (above) and the experimental Powder X-ray diffractograms of the aggregates of **1b** deposited by drop-casting on the substrate (below).

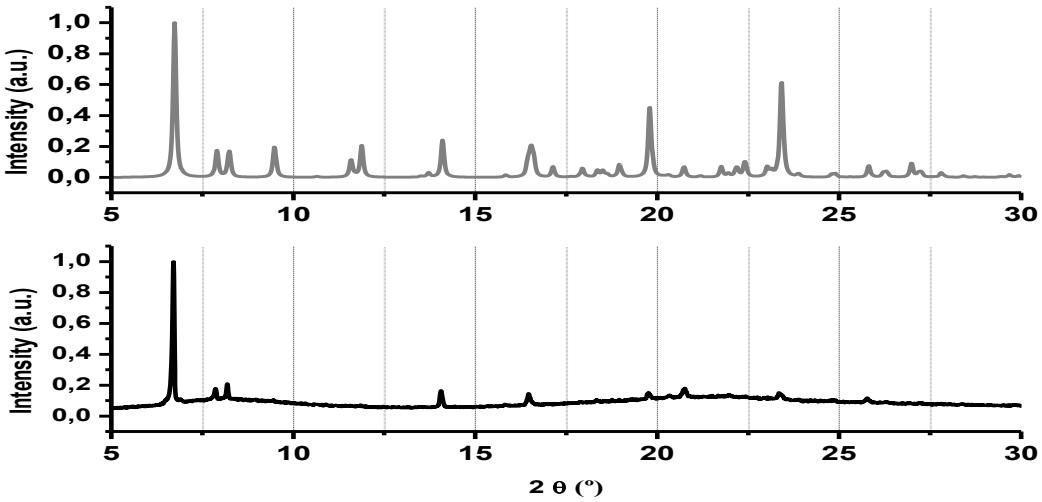

Figure S4. Powder X-ray diffractograms obtained from the single crystal data (above) and the experimental Powder X-ray diffractograms of the aggregates of **1c** deposited by drop-casting on the substrate (below).

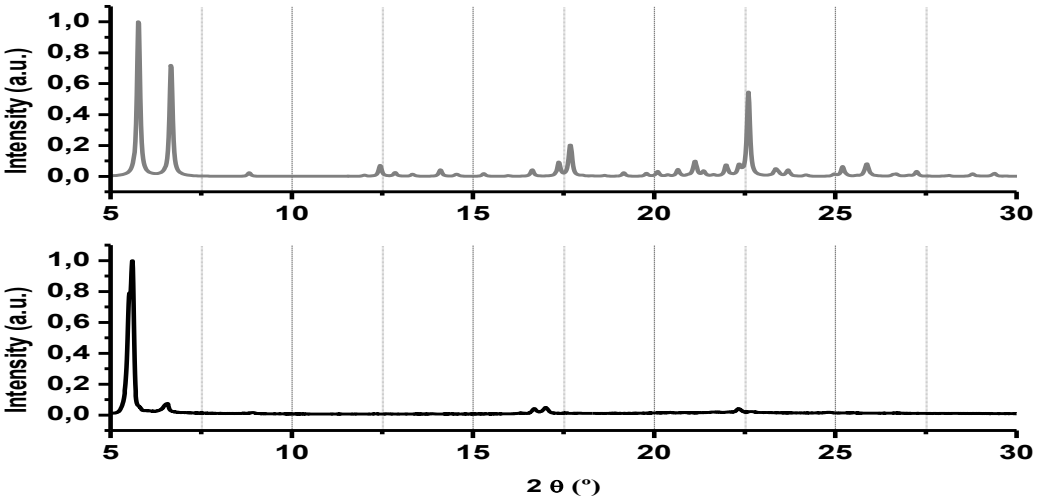

Figure S5. Powder X-ray diffractograms obtained from the single crystal data (above) and the experimental Powder X-ray diffractograms of the aggregates of **1d** deposited by drop-casting on the substrate (below).

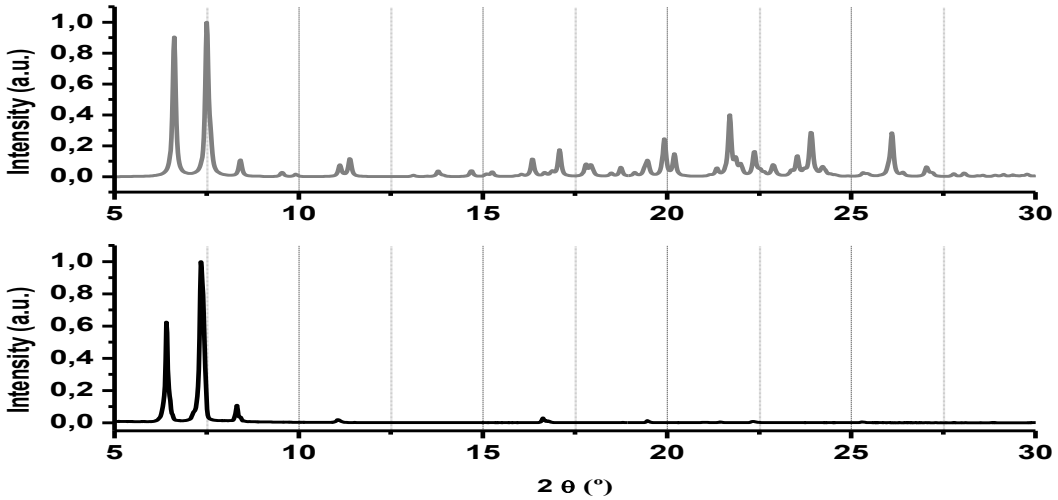

Figure S6. Powder X-ray diffractograms obtained from the single crystal data (above) and the experimental Powder X-ray diffractograms of the aggregates of **1e** deposited by drop-casting on the substrate (below).

S.1.4. X-Ray structure determinations

	1c	1d
Empirical formula	$C_{36}H_{39}N_3$	$C_{42}H_{51}N_3$
Formula weight	513.70	597.85
Temperature, K	296	296
Wavelength, Å	0.71073	1.54178
Crystal system	Monoclinic	Monoclinic
Space group	P2(1)/c	P2(1)/c
Unit cell dimensions	a = 13.1045(14) Å α= 90° b = 21.445(2) Å β= 90.654(2)° c = 10.3406(11) Å γ = 90°	a = 15.3638(19) Å α= 90° b = 26.471(3) Å β= 94.961(7)° c = 8.4581(8) Å γ= 90°
Volume, Å^3	2905.8(5)	3427.0(7)
Z	4	4
Density (calculated), Mg/m^3	1.174	1.159
Absorption coefficient, mm^{-1}	0.068	0.505
F(000)	1104	1296.0
Crystal size, mm^3	0.40 x 0.10 x 0.06	0.8 × 0.08 × 0.08
Theta range for data collection	2.45 to 28.00°	5.774 to 123.206º
Index ranges	$-17 \le h \le 17$, $-27 \le k \le 27$, $-13 \le l \le 13$	$-17 \le h \le 17$, $-29 \le k \le 29$, $-3 \le l \le 7$
Reflections collected	16156	15392
Independent reflections	5569 [$R_{(int)}$ = 0.0695]	4731 [$R_{(int)}$ = 0.0334]
Goodness-of-fit on F^2	1.186	1.043
Data / restraints / parameters	5569/2/356	4731/4/409
Final R indices [I>2sigma(I)]	R1 = 0.1180, wR2 = 0.1824	R1 = 0.0838, wR2 = 0.2419
R indices (all data)	R1 = 0.2602, wR2 = 0.2282	R1 = 0.1191, wR2 = 0.2787
Largest diff. peak and hole	0.317 and -0.219 e.Å^{-3}	0.45/-0.33 e.Å^{-3}

Table S1 Crystal data and structure refinement for **1c** and **1d**.

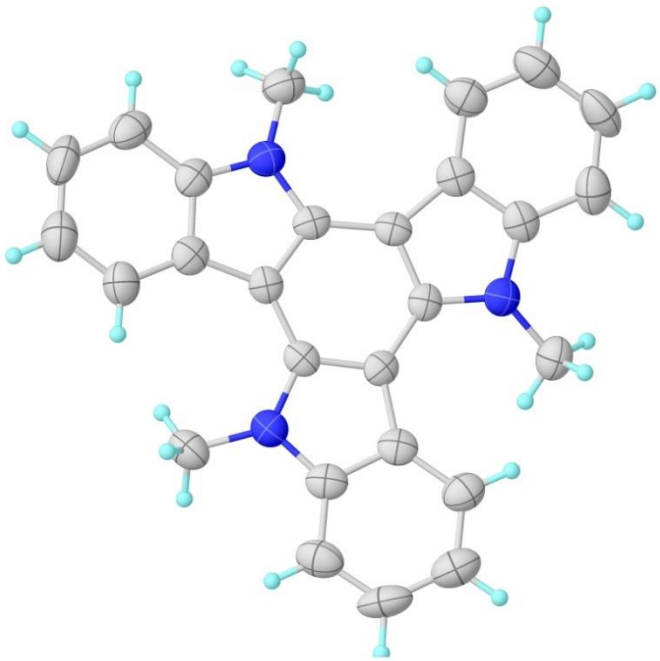

Figure S7: Representations of **1b**. Atoms: C in grey; O in dark blue; H in cyan.

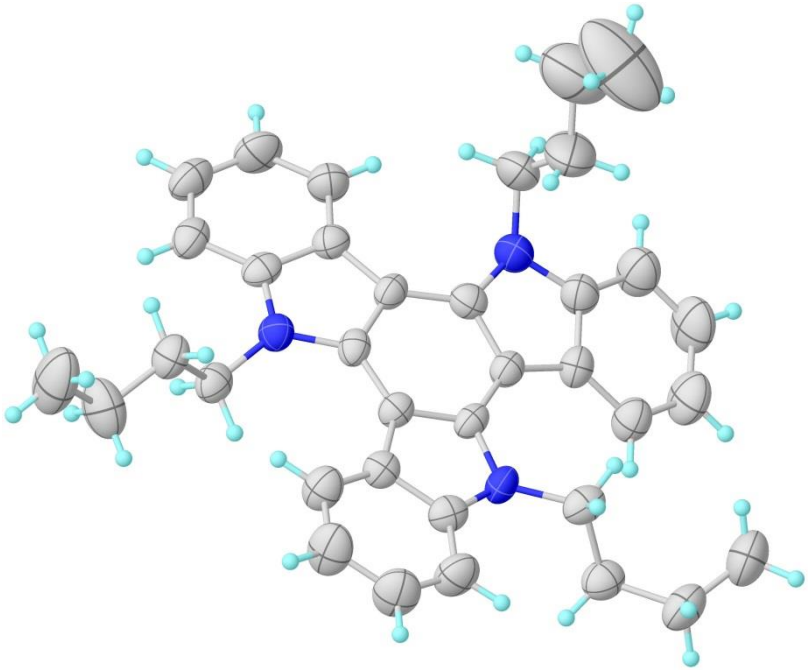

Figure S8: Representations of **1c**. Atoms: C in grey; O in dark blue; H in cyan.

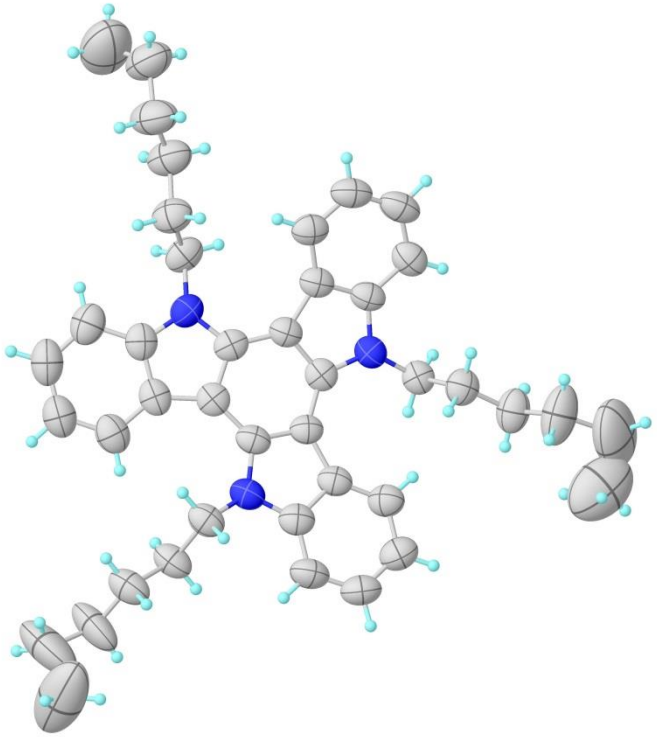

Figure S9: Representations of **1d**. Atoms: C in grey; O in dark blue; H in cyan.

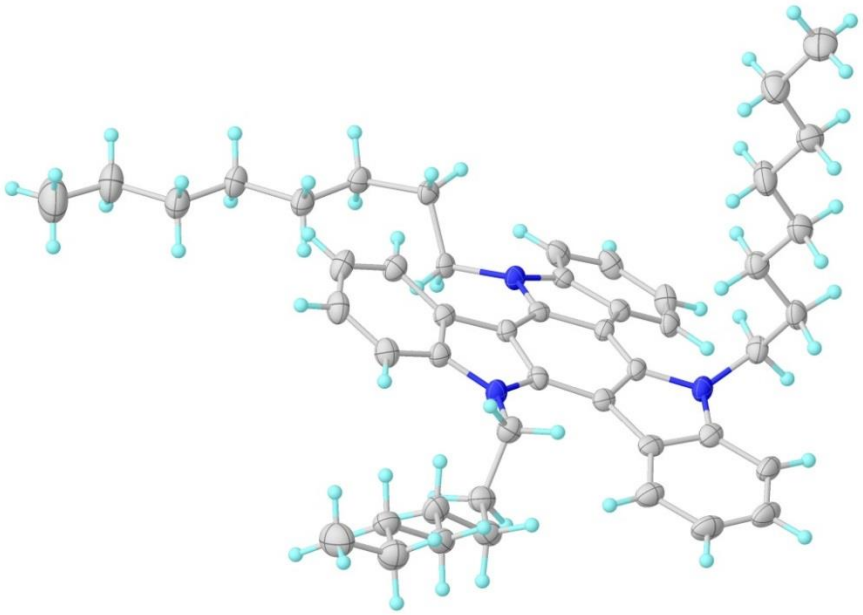

Figure S10: Representations of **1e**. Atoms: C in grey; O in dark blue; H in cyan.

S.2. SECTION 2.2. *"STAR-SHAPED HEXAARYLTRIINDOLES SMALL MOLECULES: TUNING MOLECULAR PROPERTIES TOWARDS SOLUTION PROCESSED ORGANIC LIGHT EMITTING DEVICES."*

Carmen Coya[*1], Constanza Ruiz[2], Ángel Luis Álvarez[1], Susana Álvarez-García[2,3], Eva M. García-Frutos[2], Berta Gómez-Lor[*2] and Alicia de Andrés[*2]

S.2.1. Cyclic Voltammetry Measurements

Cyclic voltammetric (CV) experiments were performed on an Epsilon Electrochemical Analyzer in a three electrode cell (Pt working electrode) at room temperature, under nitrogen atmosphere. Electrochemical measurements were performed in a milimolar CH_2Cl_2 solution containing 0.1 M of recrystallized supporting electrolyte tetra-*n*-butylammonium hexafluorophosphate ($TBAPF_6$). Potentials were measured against Ag/AgCl as reference electrode. A large area coiled Pt wire was used as a counter electrode. At this conditions a first reversible oxidation step sensitive to the peripheral substitution in all the series

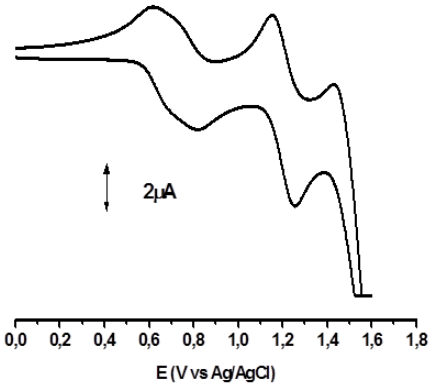

Figure S1. Cyclic voltammogram of **1a.**

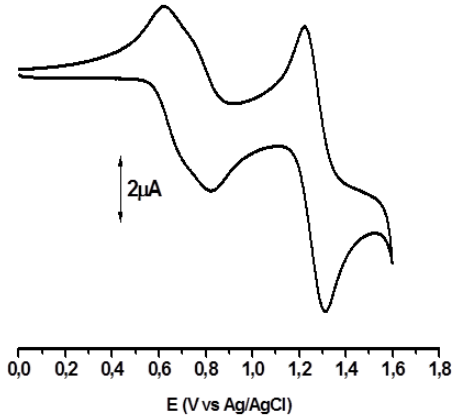

Figure S2. Cyclic voltammogram of **1b.**

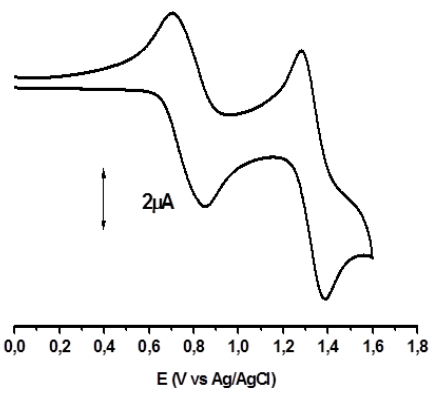

Figure S3. Cyclic voltammogram of **1c.**

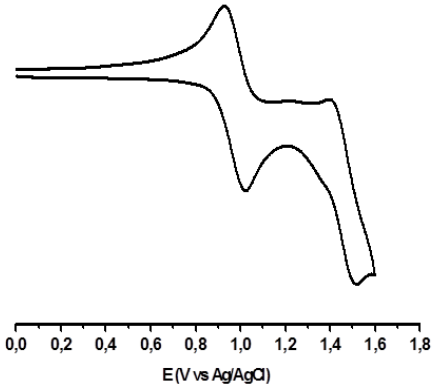

Figure S4. Cyclic voltammogram of **1d.**

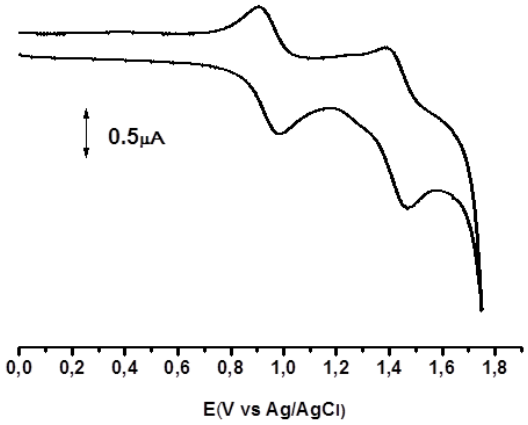

Figure S5. Cyclic voltammogram of **1e.**

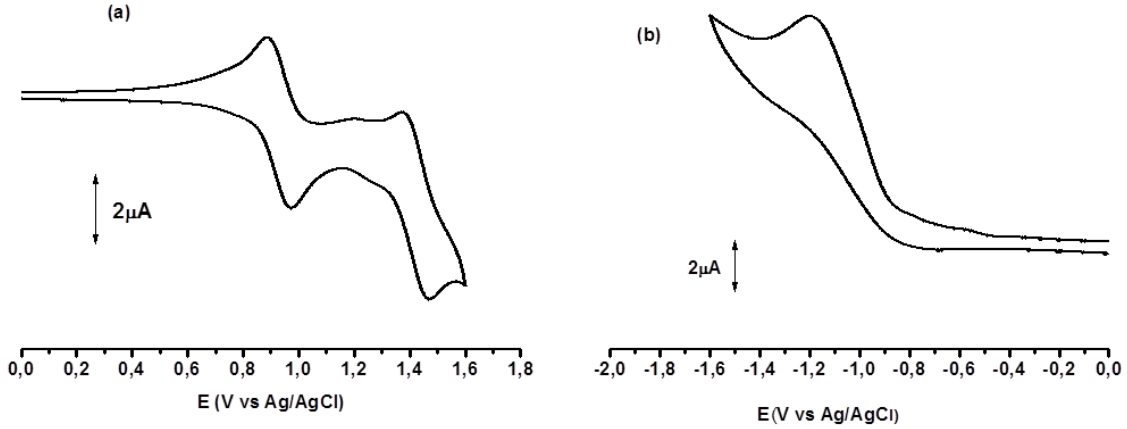

Figure S6. Cyclic voltammogram oxidation (a) and reduction (b) of **1f.**

S.3. SECTION 2.3. MONO-FUNCTIONALIZATION ON THE TRIINDOLE PLATFORM.

S.3.1. Experimental section

The synthesis of compound **2-bromo- 5,10,15- tridodecyl-10,15- dihydro- 5H-diindolo [3,2-a:3',2'-c] carbazole** and **5,10,15-tridodecyl-2-phenyl-10,15-dihydro-5H-diindolo[3,2-a:3',2'-c]carbazole** will be described in detail in **Chapter 4.**

5,10,15-tridodecyl-2,3,7,8,12,13-hexakis(4-(methylthio)phenyl)-10,15-dihydro-5H-diindolo[3,2-a:3',2'-c]carbazole compound will be described in **Chapter 3**, and the rest of the hexa-substituted derivatives have been previously described.

5,10,15-tridodecyl-3-(4-methoxyphenyl)-10,15-dihydro-5H-diindolo[3,2-a:3',2'-c]carbazole (1a). A mixture of **2-bromo- 5,10,15- tridodecyl-10,15- dihydro- 5H-diindolo [3,2-a:3',2'-c] carbazole** (100 mg, 0.108mmol), $Pd(PPh_3)_4$ (35.6mg, 0.048 mmol), 4-methoxyphenylboronic acid (24.9mg, 0.164 mmol) in 0.5 mL of 2M aqueous K_2CO_3 and 3 mL of THF was degassed. The solution was irradiated with Anton Paar microwave irradiator (CEM) at 150ºC (80W) for 180 min. The mixture was diluted with CH_2Cl_2, washed with water, and dried ($MgSO_4$); the solvent was then evaporated and the residue was purified by chromatography with CH_2Cl_2 /hexane (1:3) to give a white solid **1a** (51mg, 48%).^{1}H NMR (200 MHz, $CDCl_3$) δ 8.30 (d, *J* = 7.9 Hz, 3H), 7.81 – 7.26 (m, 10H), 7.07 (d, *J* = 8.6 Hz, 2H), 4.93 (dq, *J* = 8.4, 4.4, 4.0 Hz, 6H), 3.90 (d, *J* = 2.7 Hz, 3H), 2.13 – 1.89 (m, 6H), 1.49 – 0.94 (m, 54H), 1.06 – 0.68 (m, 9H).^{13}C NMR (50 MHz, $CDCl_3$) δ159.1, 141.9, 141.2, 135.8, 134.8, 128.6, 123.6, 122.9, 121.7, 119.8, 119.1, 14.5, 110.6, 108.7, 103.4, 55.6, 47.2, 32.1, 29.7, 29.5, 26.8, 22.9, 14.3.UV (CH_2Cl_2, 25 ºC) λ_{max} (log ε) 323 (5.03). MALDI-TOF MS m/z 955.8 (M+); HRMS (MALDI-TOF) calcd for $C_{66}H_{93}N_3O_1$: 955.7313, found: 955.7319.

^{1}H NMR (200MHz, $CDCl_3$) **1a**:

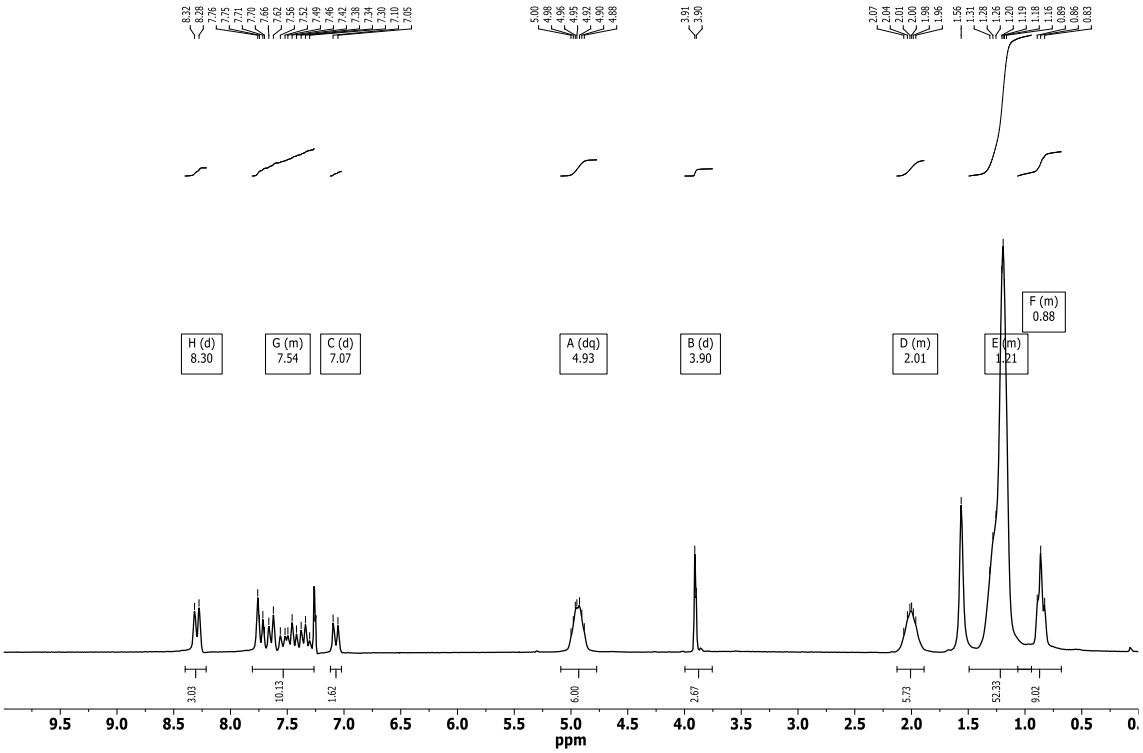

^{13}C NMR (50MHz, $CDCl_3$) **1a**:

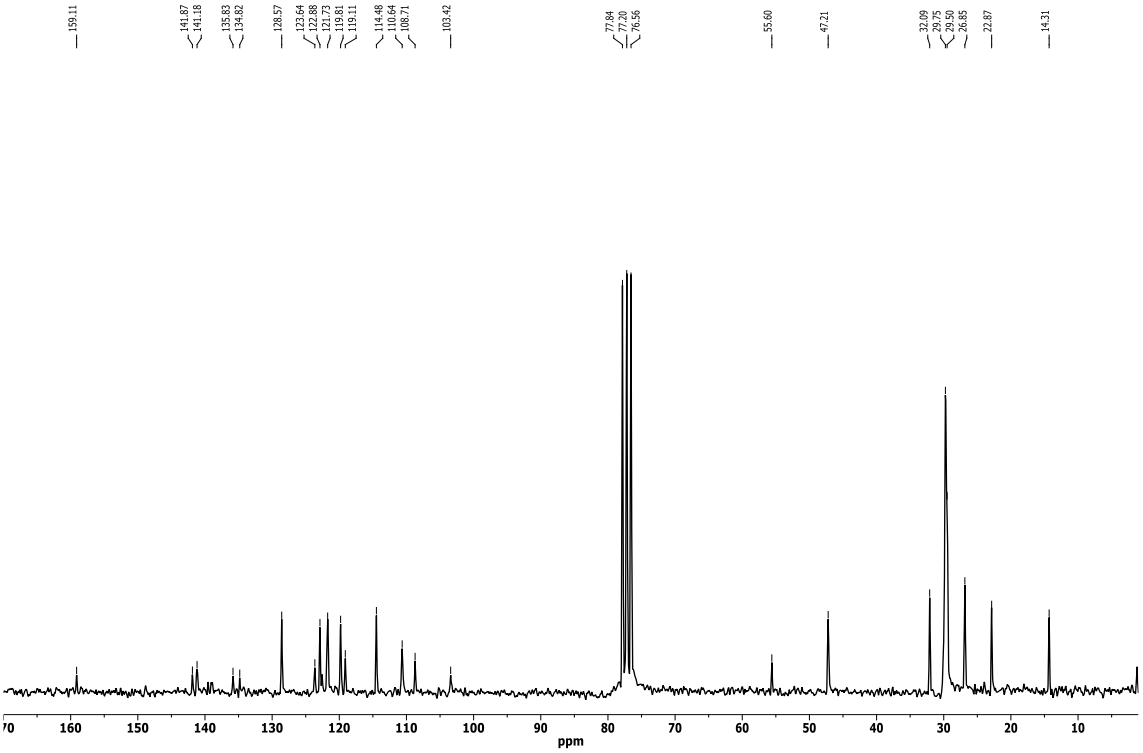

5,10,15-tridodecyl-2-(4-(methylthio)phenyl)-10,15-dihydro-5H-diindolo[3,2-a:3',2'-c]carbazole (1c). A mixture of **2-bromo- 5,10,15- tridodecyl-10,15- dihydro- 5H-diindolo [3,2-a:3',2'-c] carbazole** (100 mg, 0.108 mmol), $Pd(PPh_3)_4$ (35.6 mg, 0.048 mmol), 4-(methylthio)phenylboronic acid (27.2 mg, 0.164 mmol) in 0.5 mL of 2M aqueous K_2CO_3 and 3 mL of THF was degassed. The solution was irradiated with Anton Paar microwave irradiator (CEM) at 150ºC (80W) for 180 min. The mixture was diluted with CH_2Cl_2, washed with water, and dried ($MgSO_4$); the solvent was then evaporated and the residue was purified by chromatography with CH_2Cl_2 /hexane (1:3) to give a white solid **1c** (46mg, 40%).^{1}H RMN (200 MHz, $CDCl_3$) δ 8.45 – 8.24 (m, 3H), 7.87 – 7.57 (m, 5H), 7.41 (dq, *J* = 22.4, 8.3, 7.4 Hz, 7H), 4.92 (t, *J* = 8.0 Hz, 6H), 2.58 (s, 1H), 2.14 – 1.85 (m, 6H), 1.23 (t, *J* = 11.2 Hz, 56H), 0.87 (t, *J* = 6.4 Hz, 9H).^{13}C RMN (50 MHz, $CDCl_3$) δ141.9, 141.2, 139.7, 139.1, 137.2, 35.4, 127.9, 127.5, 123.7, 122.9, 121.7, 119.8, 119.1, 110.7, 108.8, 103.4, 47.2, 32.1, 29.7, 29.5, 26.9, 22.9, 16.3, 14.3. UV (CH_2Cl_2, 25 ºC) λ_{max} (log ε) 325 (4.36). MALDI-TOF MS m/z 971.7 (M^+); HRMS (MALDI-TOF) calcd for $C_{67}H_{93}N_3S$: 971.7085, found: 971.7066

^{1}H NMR (200MHz, $CDCl_3$) **1c**:

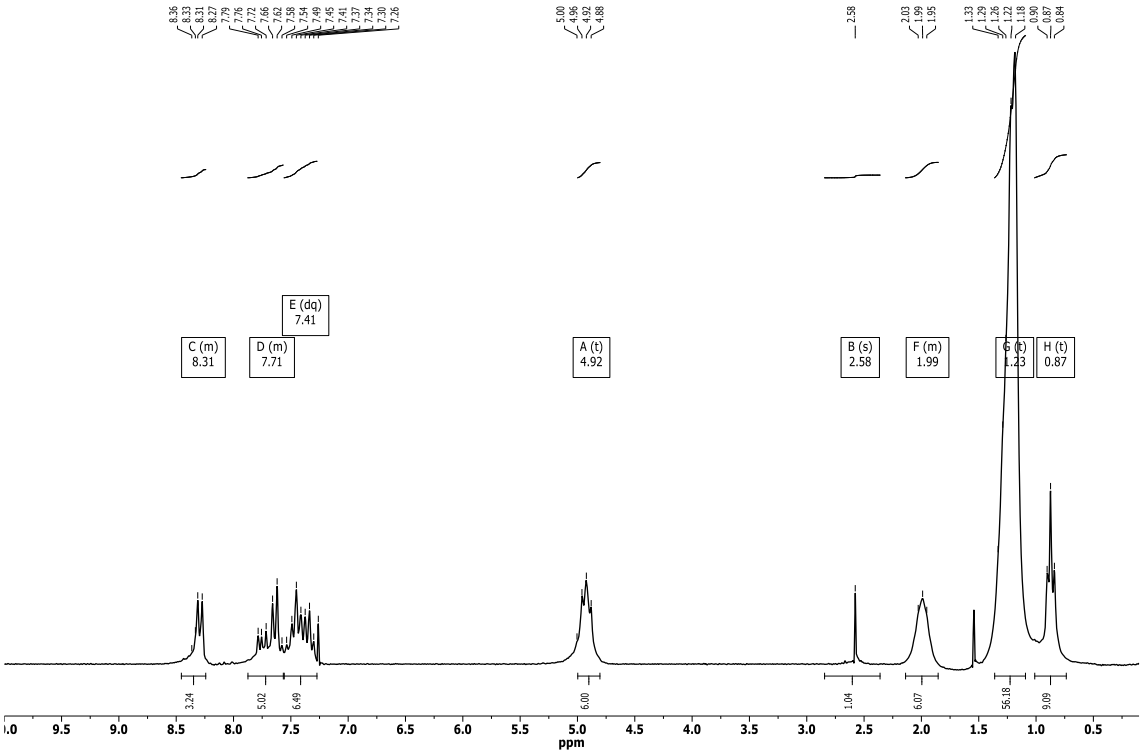

^{13}C NMR (50MHz, $CDCl_3$) **1c**:

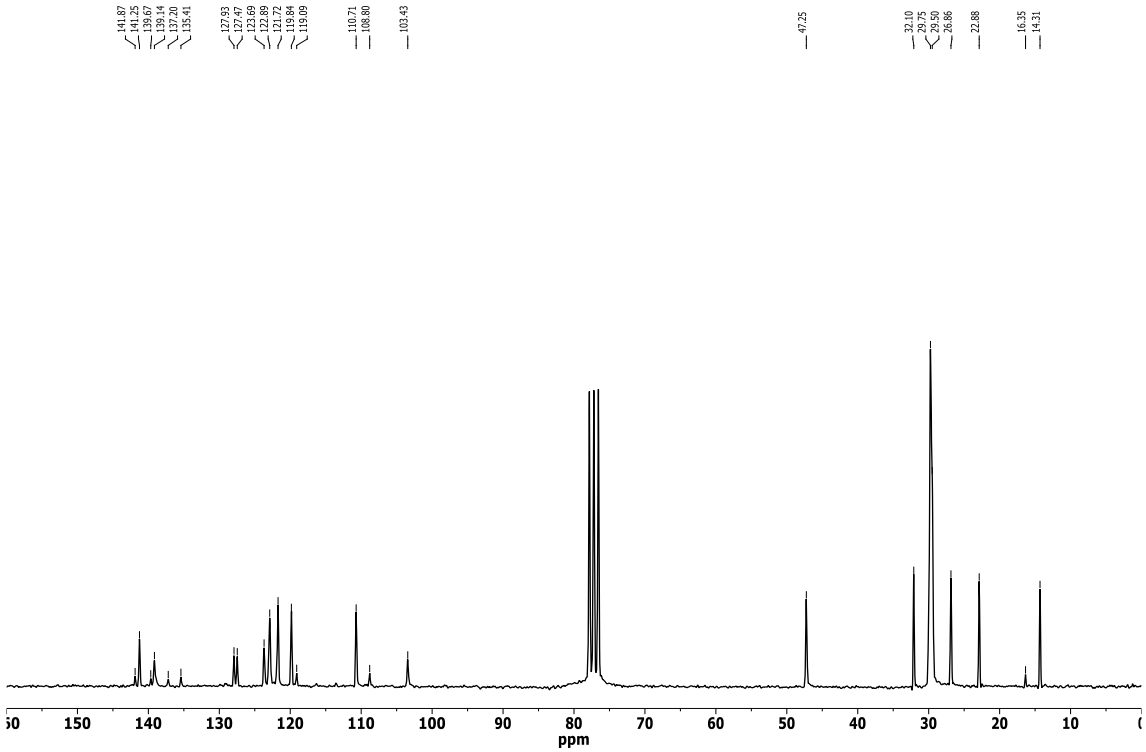

4-(5,10,15-tridodecyl-10,15-dihydro-5H-diindolo[3,2-a:3',2'-c]carbazol-2-yl)benzonitrile (1d). A mixture of **2-bromo- 5,10,15- tridodecyl-10,15- dihydro- 5H-diindolo [3,2-a:3',2'-c] carbazole** (100 mg, 0.108 mmol), $Pd(PPh_3)_4$ (35.6mg, 0.048 mmol), 4-cyanophenylboronic acid (22.4 mg, 0.164 mmol) in 0.5 mL of 2M aqueous K_2CO_3 and 3 mL of THF was degassed. The solution was irradiated with Anton Paar microwave irradiator (CEM) at 150ºC (80W) for 180 min. The mixture was diluted with CH_2Cl_2, washed with water, and dried ($MgSO_4$); the solvent was then evaporated and the residue was purified by chromatography with CH_2Cl_2 /hexane (1:3) to give a yellow solid **1d** (55mg, 54%). ^{1}H NMR (200 MHz, $CDCl_3$) δ 8.31 (t, *J* = 8.1 Hz, 3H), 7.89 (d, *J* = 8.2 Hz, 2H), 7.85 – 7.71 (m, 3H), 7.71 – 7.30 (m, 7H), 4.94 (q, *J* = 8.9, 8.4 Hz, 6H), 1.99 (d, *J* = 9.5 Hz, 6H), 1.21 (dt, *J* = 13.5, 6.9 Hz, 54H), 0.86 (t, *J* = 6.4 Hz, 9H). ^{13}C NMR (50 MHz, $CDCl_3$) δ 146.7, 141.7, 141.2, 140.0, 139.5, 138.9, 133.6, 132.8, 128.0, 124.2, 123.6, 123.1, 122.1, 121.7, 120.0, 119.2, 110.8, 110.4, 109.2, 103.4, 47.2, 32.1, 29.8, 26.8, 22.9, 14.3. UV (CH_2Cl_2, 25 ºC) λ_{max} (log ε) 323 (4.82). MALDI-TOF MS m/z 950,7 (M^+); HRMS (MALDI-TOF) calcd for $C_{67}H_{90}N_4$: 950,7160, found: 950,7141.

^{1}H NMR (200MHz, $CDCl_3$) **1d**:

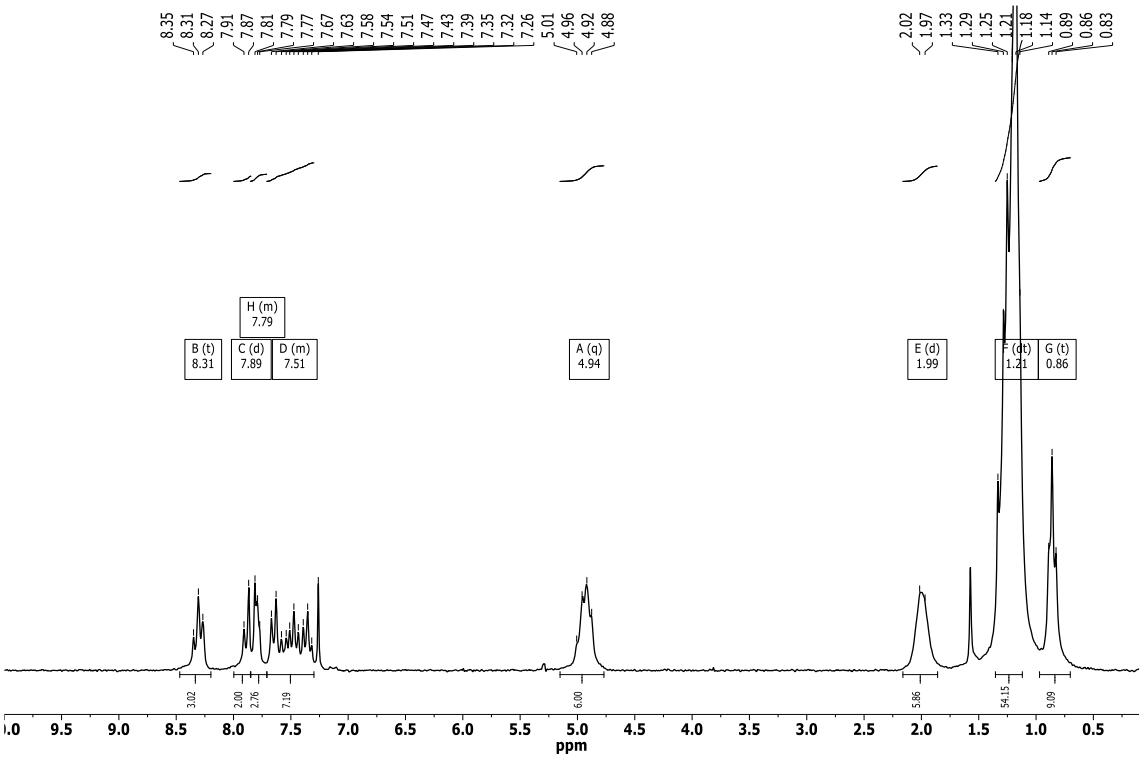

^{13}C NMR (50MHz, $CDCl_3$) **1d**:

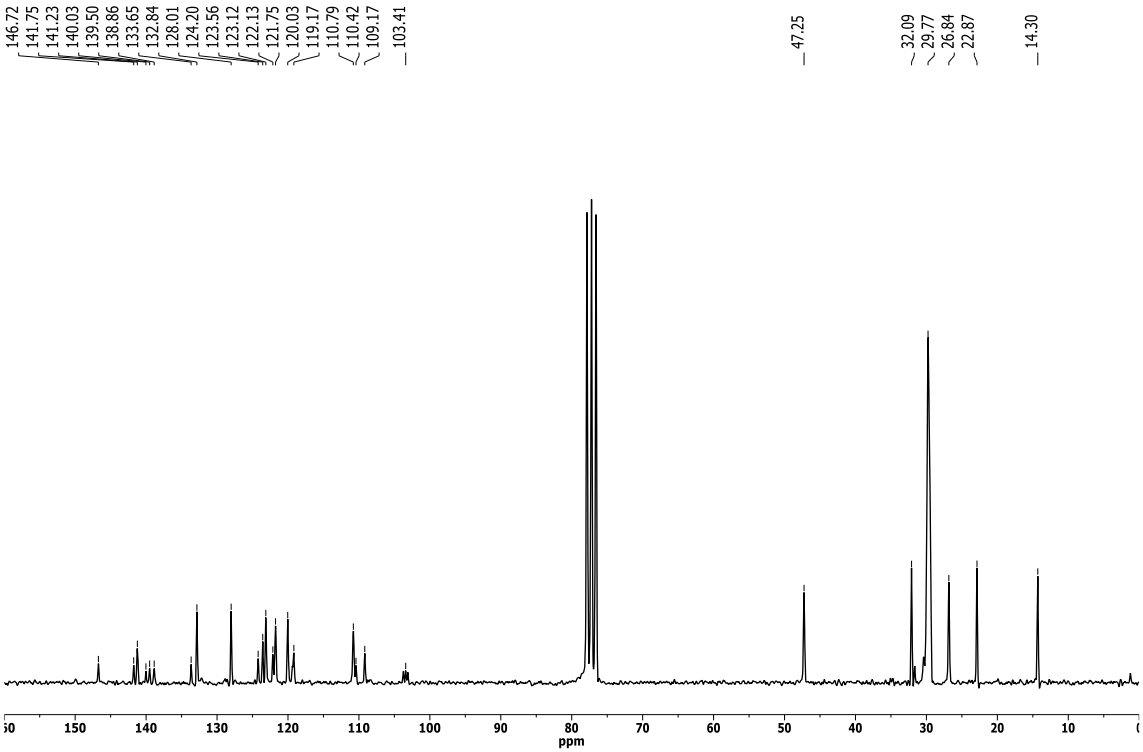

5,10,15-tridodecyl-2-(4-nitrophenyl)-10,15-dihydro-5H-diindolo[3,2-a:3',2'-c]carbazole (1e). A mixture of **2-bromo- 5,10,15- tridodecyl-10,15- dihydro- 5H-diindolo [3,2-a:3',2'-c] carbazole** (100 mg, 0.108 mmol), $Pd(PPh_3)_4$ (35.6mg, 0.048 mmol), 4-nitrophenylboronic acid (46.7 mg, 0.164 mmol) in 0.5 mL of 2M aqueous K_2CO_3 and 3 mL of THF was degassed. The solution was irradiated with Anton Paar microwave irradiator (CEM) at 150ºC (80W) for 180 min. The mixture was diluted with CH_2Cl_2, washed with water, and dried ($MgSO_4$); the solvent was then evaporated and the residue was purified by chromatography with CH_2Cl_2 /hexane (1:3) to give an orange solid **1e** (70mg, 67%).^{1}H NMR (200 MHz, $CDCl_3$) δ 8.58 – 8.17 (m, 5H), 8.06 – 7.74 (m, 3H), 7.72 – 7.56 (m, 3H), 7.42 (dt, *J* = 23.2, 7.1 Hz, 4H), 4.95 (qd, *J* = 10.4, 9.0, 4.0 Hz, 6H), 2.14 – 1.86 (m, 6H), 1.53 – 1.08 (m, 53H), 0.86 (td, *J* = 6.8, 2.3 Hz, 9H). ^{13}C NMR (50 MHz, $CDCl_3$) δ148.6, 146.8, 141.6, 141.2, 140.1, 139.5, 138.8, 133.1, 127.9, 124.4, 123.5, 123.1,122.1, 121.8, 120.0, 129.3, 101.7, 109.3, 103.3, 47.2, 32.1, 30.0, 29.9, 29.8, 29.7, 29.5, 29.4, 26.8, 22.8, 14.3. UV (CH_2Cl_2, 25 ºC) λ_{max} (log ε) 319 (4.42), 424 (5.30). MALDI-TOF MS m/z 970.7 (M^+); HRMS (MALDI-TOF) calcd for $C_{66}H_{90}N_4O_2$: 970.7058, found: 970.7052.

^{1}H NMR (200MHz, $CDCl_3$) **1e**:

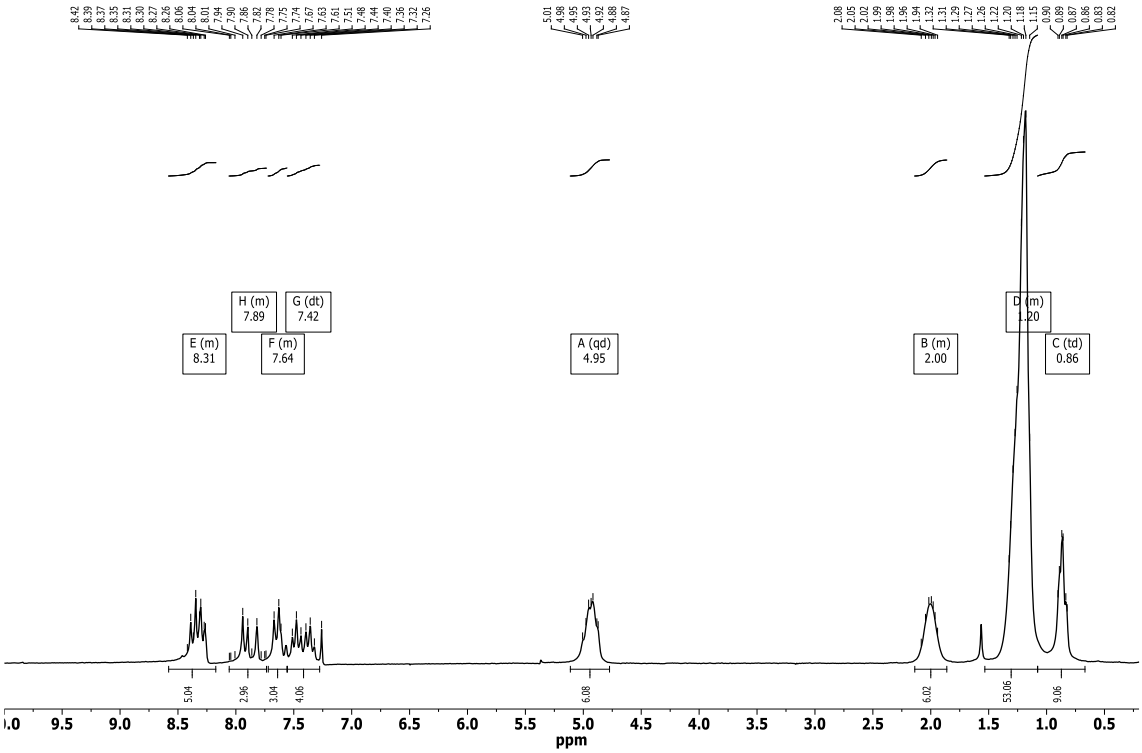

^{13}C NMR (200MHz, $CDCl_3$) **1e**:

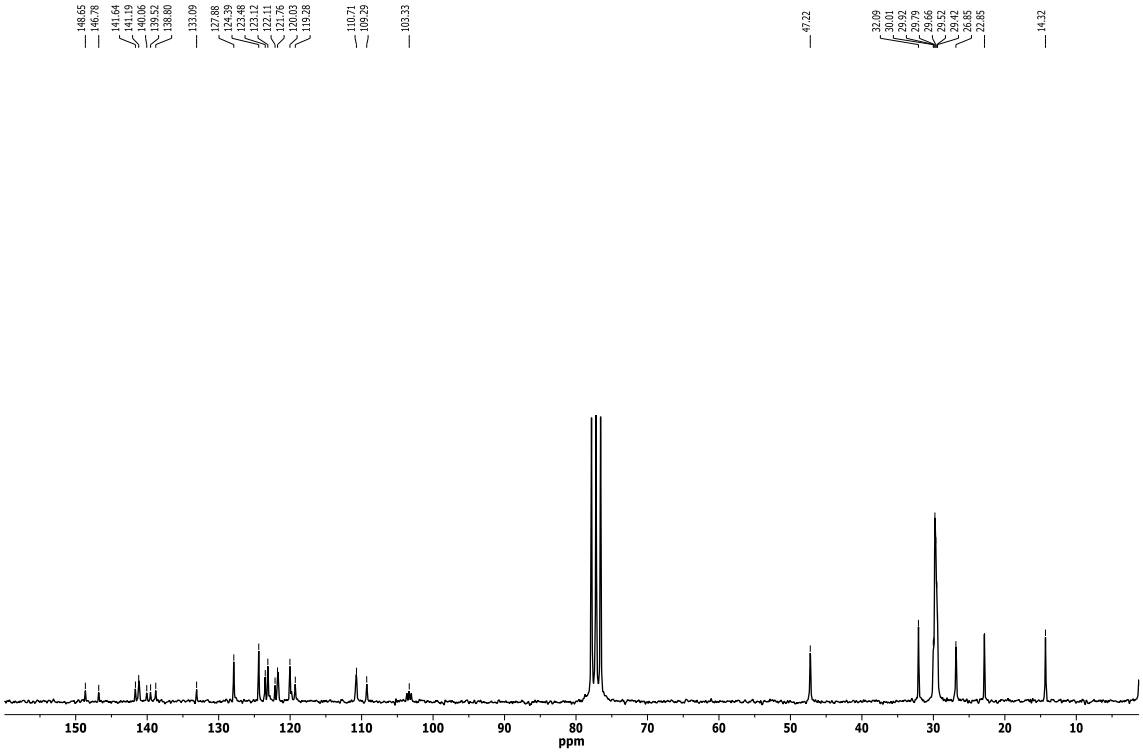

S.3.2. Electronic Properties

Table 2.1. Values of HOMO-LUMO of compounds. All data are in eV.

	HOMO[a]	LUMO[a]		HOMO[a]	LUMO[a]
1a	-5.04	-1.86	**2a**	-5.07	-2.01
1b	-5.05	-1.89	**2b**	-5.08	-2.17
1c	-5.07	-1.96	**2c**	-5.02	-1.85
1d	-5.11	-2.26	**2d**	-5.28	-2.44
1e	-5.10	-2.75	**2e**	-5.36	-2.86

[a.] The HOMO energy values were estimated from the first oxidation potential with respect ferrocene/ferrocenium redox couple. The LUMO energy values were estimated by substracting the energy of the optical band gap obtained by UV-vis to the HOMO values.

Table 2.2: The values of the maximum wavelength of the absorption spectra and the bandgap energy for the mono and hexa-substituted compounds.

	λ_{abs} (nm)	E_{gap} (eV)		λ_{abs} (nm)	E_{gap} (eV)
1a	322	3.18	**2a**	343	3.06
1b	322	3.18	**2b**	342	2.91
1c	325	3.11	**2c**	336	3.17
1d	323; 378	2.85	**2d**	356	2.84
1e	317; 424	2.35	**2e**	317; 386	2.50

S.4. SECTION 3.3. LOWER DEPENDANCE OF THE ALIGNMENT ON THE ELECTRONIC PROPERTIES OF DISCOTIC LIQUID CRYSTAL

S.4.1. Experimental section

5,10,15-trimethyl-2,3,7,8,12,13-hexakis(4-(methylthio)phenyl)-10,15-dihydro-5H-diindolo[3,2-a:3',2'-c]carbazole. A mixture of **5,10,15-trimethyl-10,15-dihydro-5H-diindolo[3,2-a:3',2'-c]carbazole** (100 mg, 0.116 mmol), $Pd(PPh_3)_4$ (38.2 mg, 0.052 mmol), 4-(methylthio)phenylboronic acid (234 mg, 1.39 mmol) in 0.5 mL of 2M aqueous K_2CO_3 and 6 mL of THF was degassed. The solution was irradiated with Anton Paar microwave irradiator (CEM) at 150ºC (80 W) for 180 min. The mixture was diluted with CH_2Cl_2, washed with water, and dried ($MgSO_4$); the solvent was then evaporated and the residue was purified by chromatography with CH_2Cl_2 to give a white solid **1a** (52 mg, 40 %).^{1}H NMR (200 MHz,$C_2Cl_4D_2$) δ 8.39 (s, 3H), 7.47 (s, 3H), 7.33 – 6.95 (m, 24H), 4.41 (s, 6H), 2.44 (s, 18H). ^{13}C NMR (50 MHz, $C_2Cl_4D_2$) 142.7, 141.0, 140.3, 137.7, 137.3, 137.0, 133.7, 132.5, 127.4, 127.3, 125.4, 123.4, 113.0, 37.8, 17.1 UV ($C_2Cl_4H_2$, 25 ºC) λ_{max} (log ε) 340 (6.23). MALDI-TOF MS m/z 1119.3 (M^+); HRMS (MALDI-TOF) calcd for $C_{69}H_{57}N_3S_6$: 1119.2871, found: 1119.2862.

^{1}H NMR (200 MHz,$C_2Cl_4D_2$) **1a**:

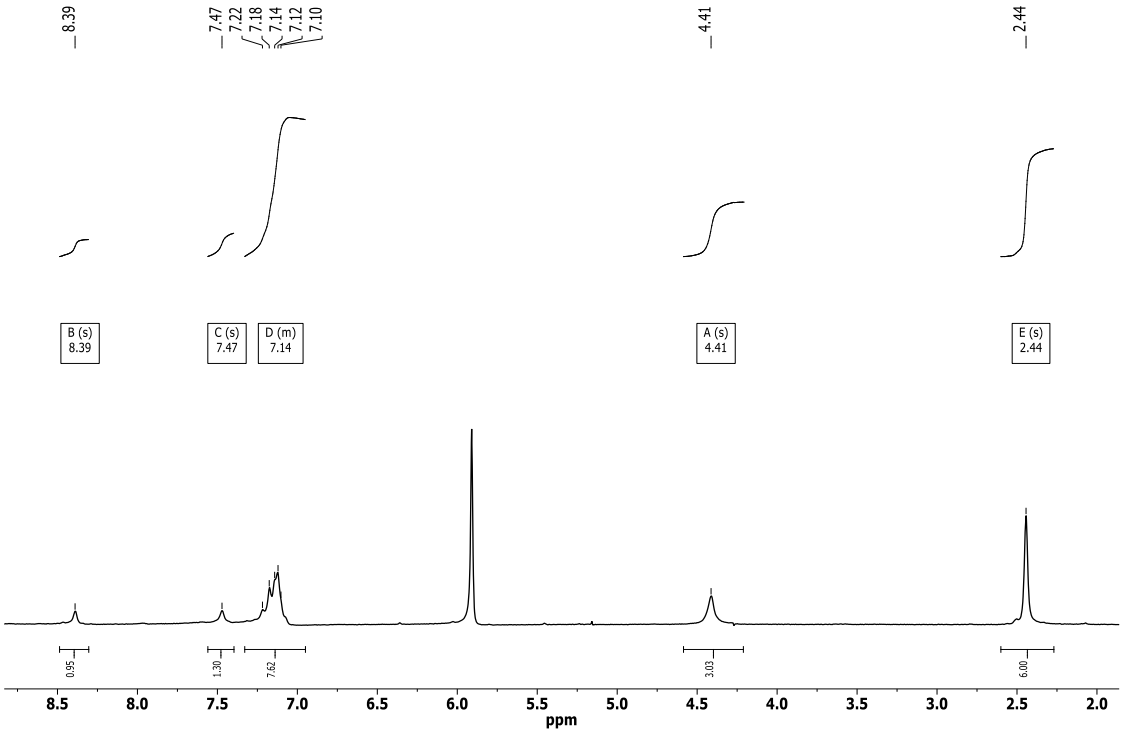

^{13}C NMR (50 MHz, $C_2Cl_4D_2$) **1a**:

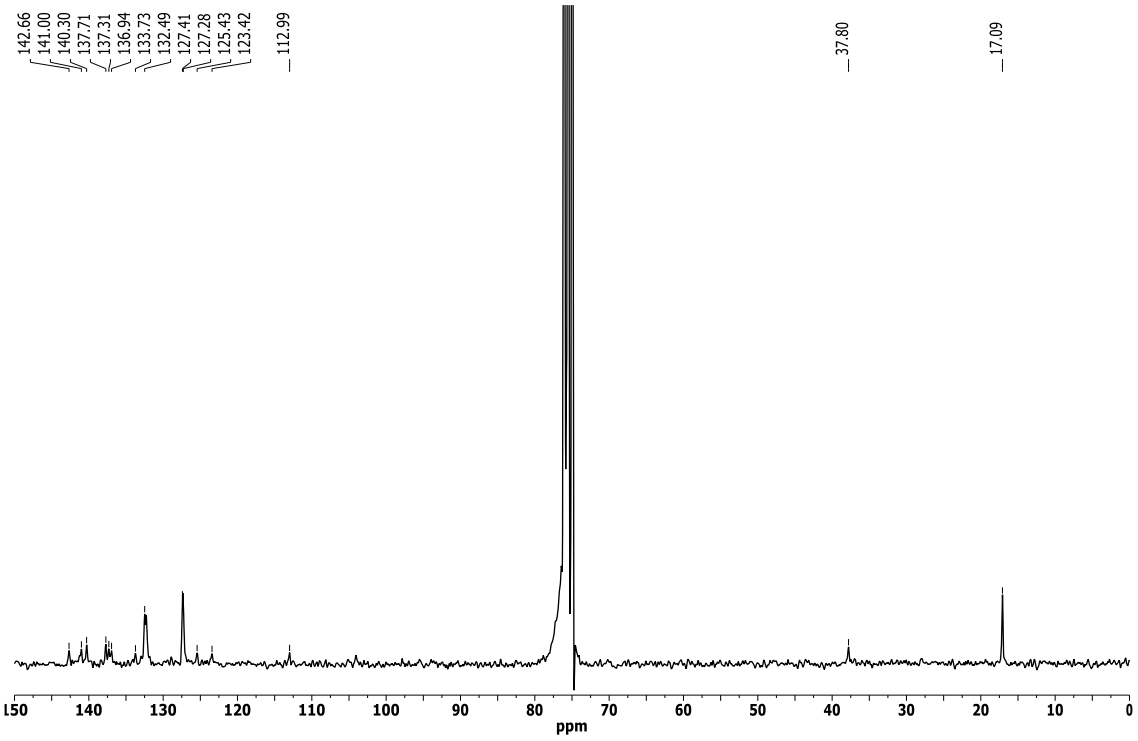

5,10,15-tridodecyl-2,3,7,8,12,13-hexakis(4-(methylthio)phenyl)-10,15-dihydro-5H-diindolo[3,2-a:3',2'-c]carbazole. A mixture of **5,10,15-tridodecyl-10,15-dihydro-5H-diindolo[3,2-a:3',2'-c]carbazole** (100 mg, 0.076 mmol), $Pd(PPh_3)_4$ (21.9mg, 0.030 mmol), 4-(methylthio)phenylboronic acid (152 mg, 0.906 mmol) in 0.5 mL of 2M aqueous K_2CO_3 and 6 mL of THF was degassed. The solution was irradiated with Anton Paar microwave irradiator (CEM) at 150ºC (80 W) for 180 min. The mixture was diluted with CH_2Cl_2, washed with water, and dried ($MgSO_4$); the solvent was then evaporated and the residue was purified by chromatography with CH_2Cl_2 /hexane (1:3) to give a white solid **1b** (67mg, 56%).^{1}H NMR (200 MHz,$CDCl_3$) δ 8.29 (s, 3H), 7.59 (s, 3H), 7.27 (d, J = 4.4 Hz, 24H), 4.83 (s, 6H), 2.60 (s, 18H), 2.09 (s, 6H), 1.40 – 1.08 (m, 54H), 1.07 – 0.82 (m, 9H). ^{13}C NMR (50 MHz, $CDCl_3$) 140.6, 139.8, 139.3, 136.7, 136.3, 135.4, 132.6, 131.0, 126.2, 123.7, 122.8, 111.9, 103.0, 47.2, 32.2, 30.7, 30.0, 29.9, 29.7, 27.1, 23.0, 16.0, 14.5. UV (CH_2Cl_2, 25 ºC) λ_{max} (log ε) 341 (6.03). MALDI-TOF MS m/z 1582.8 (M^+); HRMS (MALDI-TOF) calcd for $C_{102}H_{123}N_3S_6$: 1582.8067, found: 1582.8054.

^{1}H NMR (200 MHz,$CDCl_3$) **1b**:

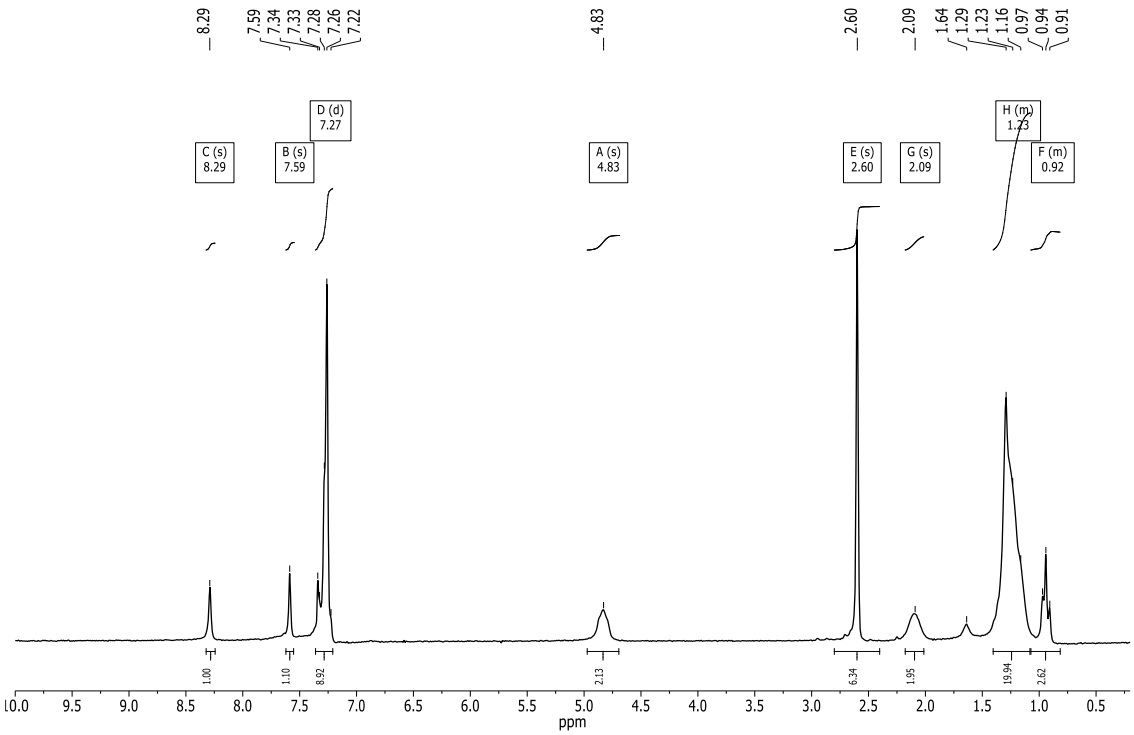

^{13}C NMR (50 MHz, $CDCl_3$) **1b**:

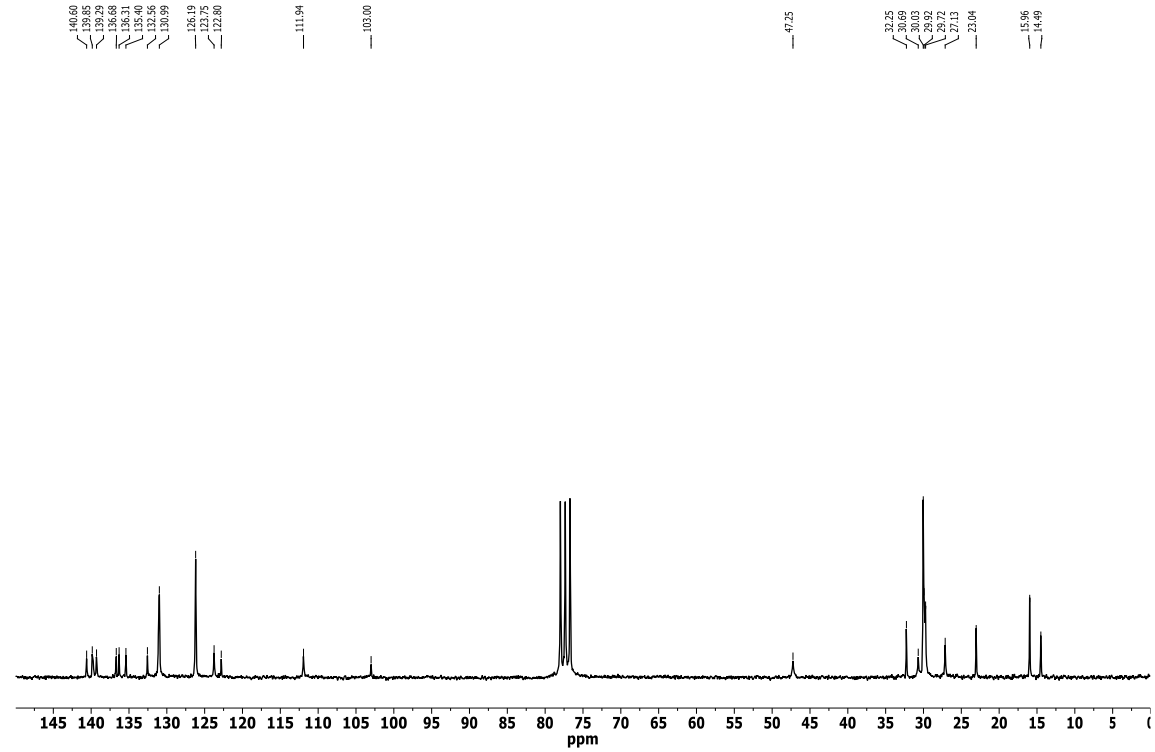

S.5. SECTION 4.2. *"TRIINDOLE-BRIDGE-TRIINDOLE DIMERS AS MODELS FOR TWO DIMENSIONAL MICROPOROUS POLYMERS."*

Constanza Ruiz, Juan T. López Navarrete, M. Carmen Ruiz Delgado* and Berta Gómez-Lor*
*E-mail: carmenrd@uma.es; bgl@icmm.csic.es

S.5.1. Synthesis and Characterization of compounds 2-7

2-bromo- 5,10,15- tridodecyl-10,15- dihydro- 5H- diindolo [3,2-a:3',2'-c] carbazole (2). 5,10,15- tridodecyl- 10,15- dihydro- 5H- diindolo [3,2-a:3',2'-c] carbazole, compound **1**, (150mg, 0.18mmol) in 40ml of CH_2Cl_2 was stirred and cooled at 0ºC with an ice bath. Then at this temperature N-bromosuccinimide (38.44mg, 0.22mmol) in 1ml of dimethylformamide was slowly added. Then dimethylformamide was evaporated under vacuum chamber. The mixture was extracted with CH_2Cl_2, washed with water, and then the organic phase dried ($MgSO_4$). The solvent was evaporated and the residue was purified by chromatography with hexane/toluene (95:5) to give a white solid **1** (97,1mg, 58%). ^{1}H NMR (200 MHz, $CDCl_3$) δ 8.26 (dd, J = 7.0 Hz, 2H), 8.10 (d, J = 8.3 Hz, 1H), 7.74 (s, 1H), 7.64 (d, J = 7.8 Hz, 2H), 7.40 (m, J = 16.7, 8.2 Hz, 5H), 4.87 (m, 6H), 1.96 (m, 6H), 1.20 (m, J = 9.0 Hz, 54H), 0.87 (m, 9H). ^{13}C NMR (50 MHz, $CDCl_3$) δ 142.1, 141.2, 139.3, 139.7, 123.6, 123.1, 122.7, 121.8, 121.9, 120.0, 116.3, 113.6, 110.8, 103.7, 103.3, 103.0, 47.2, 32.1, 29.9, 29.8, 29.6, 26.8, 22.9, 14.3. UV (CH_2Cl_2, 25 ºC) λ_{max} (log ε) 318 (4.20). MALDI-TOF MS m/z 929.7 (M^+); HRMS (MALDI-TOF) calcd for $C_{60}H_{88}Br_1N_3$: 929.5966, found: 929.5995.

5,10,15-tridodecyl-2-phenyl-10,15-dihydro-5H-diindolo[3,2-a:3',2'-c]carbazole (3). A mixture of **2** (50 mg, 0.055 mmol), $Pd(PPh_3)_4$ (18.1mg, 0.02 mmol), phenylboronic acid (13.4mg, 0.11 mmol) in 0.5 mL of 2M aqueous K_2CO_3 and 3 mL of THF was degassed. The solution was irradiated with Anton Paar microwave irradiator (CEM) at 150ºC (80W) for 180 min. The mixture was diluted with CH_2Cl_2, washed with water, and dried ($MgSO_4$); the solvent was then evaported and the residue was purified by chromatography with CH_2Cl_2 /hexane (1:3) to give a yellow solid **1b** (17mg, 33%). ^{1}H NMR (200 MHz, $CDCl_3$) δ 8.30 (d, J = 7.2 Hz, 2H), 7.83 (d, 2H), 7.66 – 7.31 (m, 12H), 4.93 (m, 6H), 2.00 (m, 6H), 1.23 (m, J = 12.2 Hz, 54H), 0.87 (m, 9H). ^{13}C NMR (50 MHz, $CDCl_3$) δ 142.3, 141.8, 141.3, 139.7, 139.2, 139.0, 136.2, 129.1, 127.7, 127.4, 127.1, 123.7,

122.9, 121.7, 119.9, 119.4, 110.8, 109.2, 103.5, 103.2, 47.3, 32.1, 30.1, 30.0, 29.8, 29.7, 29.6, 29.4, 26.9, 22.9, 14.3. UV (CH_2Cl_2, 25 ºC) λ_{max} (log ε) 320 (5.10). MALDI-TOF MS m/z 925.7 (M^+); HRMS (MALDI-TOF) calcd for $C_{66}H_{91}N_3$: 925.7208, found: 925.7192.

5,10,15- tridodecyl-2- ((trimethylsilyl)ethynyl)- 10,15- dihydro- 5H-diindolo [3,2-a:3',2'-c] carbazole (4). A mixture of **2** (100mg, 0.11 mmol), CuI (3.8mg, 0.022mmol) and $Pd(dppf)_2Cl_2$ (40.2mg, 0.055mmol). in 9ml of a 2:1 mixture DIPA:THF was degassed, and then, ethynyl trimethylsilane (0.07ml, 0.55mmol) was added. The solution was heated 110ºC for 12 h. Then the mixture was diluted with CH_2Cl_2, washed with water, and dried ($MgSO_4$); the solvent was then evaported and the residue was purified by chromatography with CH_2Cl_2 /hexane (1:3) to give a brown solid **2a** (74.0mg, 73%)**.** ^{1}H NMR (200 MHz, $CDCl_3$) δ 8.25 (d, *J* = 7.5 Hz, 2H), 8.14 (d, *J* = 8.4 Hz, 1H), 7.70 (s, *J* = 6.2 Hz, 1H), 7.61 (d, *J* = 8.0 Hz, 2H), 7.43 (m, *J* = 6.6 Hz, 3H), 7.32 (t, *J* = 7.4 Hz, 2H), 4.79 (m, *J* = 20.9 Hz, 6H), 1.94 (t, 6H), 1.25 – 1.15 (m, 54H), 0.86 (m, *J* = 6.3 Hz, 9H), 0.33 (s, 9H). ^{13}C NMR (50 MHz, $CDCl_3$) δ 141.2, 140.6, 139.9, 139.5, 138.8,124.0, 123.6, 123.0, 121.8, 121.3, 120.0, 116.8, 114.1, 110.8, 107.1, 103.6, 103.3, 93.4, 47.2, 32.1, 29.8, 29.5, 26.8, 22.9, 14.3, 0.41. UV (CH_2Cl_2, 25 ºC) λ_{max} (log ε) 327 (4.70). MALDI-TOF MS m/z 945.8 (M^+); HRMS (MALDI-TOF) calcd for $C_{65}H_{95}N_3Si$: 945.72900, found: 945.7299.

5,10,15-tridodecyl-2-ethynyl-10,15-dihydro-5H-diindolo[3,2-a:3',2'-c]carbazole (5). A mixture of compound **4** (100mg, 0.11mmol) and NaOH (66mg, 3.45mmol) was stirred for 12h at room temperature in 8 ml of a 1:1 mixture of THF:MeOH. Then the mixture was diluted with CH_2Cl_2, washed with water, and dried ($MgSO_4$); the solvent was then evaporated and the residue was purified by chromatography with CH_2Cl_2 /hexane (1:3) to give a brown solid **2b** (70.3mg, 73%) .^{1}H NMR (200 MHz, $CDCl_3$) δ 8.27 (d, *J* = 5.5 Hz, 2H), 8.18 (d, *J* = 8.4 Hz, 1H), 7.76 (s, 1H), 7.63 (d, *J* = 7.9 Hz, 2H), 7.46 (t, *J* = 7.2 Hz, 3H), 7.34 (t, *J* = 7.4 Hz, 2H), 4.88 (t, *J* = 5.3 Hz, 6H), 3.19 (s, 1H), 1.97 (m, 6H), 1.20 (d, *J* = 9.0 Hz, 54H), 0.87 (t, *J* = 6.0 Hz, 9H). ^{13}C NMR (50 MHz, $CDCl_3$) δ 141.1, 140.5, 139.9, 139.4, 138.8, 124.0, 123.8, 123.5, 123.0, 121.8, 121.3, 120.0, 115.7, 114.3, 110.8, 103.6, 103.2, 85.5, 47.2, 32.1, 30.0, 29.9, 29.8, 29.7, 29.6, 29.4, 26.8, 22.9, 14.3.UV (CH_2Cl_2, 25 ºC) λ_{max} (log ε) 322 (4.90). MALDI-TOF MS m/z 874.37 (M^+); HRMS (MALDI-TOF) calcd for $C_{62}H_{87}N_3$: 873.6895, found: 873.6891.

1,4-bis(5,10,15-tridodecyl-10,15-dihydro-5H-diindolo[3,2-a:3',2'-c]carbazol-2-yl)benzene (6). A mixture of **1** (50 mg, 0.055 mmol), $Pd(PPh_3)_4$ (8.89mg, 0.012 mmol), benzene-1,4-diboronic acid (4.50mg, 0.027 mmol) in 0.5 mL of 2M aqueous K_2CO_3 and 3 mL of THF was degassed. The solution was irradiated with Anton Paar microwave irradiator (CEM) at 150ºC (80W) for 180 min. The mixture was diluted with CH_2Cl_2, washed with water, and dried ($MgSO_4$); the solvent was then evaported and the residue was purified by chromatography with CH_2Cl_2 /hexane (1:3) to give a yellow pale solid **1b** (13mg, 27%). ^{1}H NMR (200 MHz, $CDCl_3$) δ 8.41 – 8.28 (m, 5H), 7.95 (d, *J* = 10.3 Hz, 5H), 7.75 – 7.62 (m, 6H), 7.41 (dt, *J* = 14.7, 7.1 Hz, 10H), 4.98 (t, 12H), 2.02 (m, 12H), 1.23 (m, *J* = 8.2 Hz, 108H), 0.85 (m,18H). ^{13}C NMR (50 MHz, $CDCl_3$) δ141.9, 141.2, 139.9, 139.2, 138.9, 135.6, 129.0, 128.0, 127.7, 127.2, 123.7, 122.9, 121.8, 119.9, 119.3, 110.7, 109.0, 103.5, 47.2, 32.1, 29.8, 29.5, 26.9, 22.9, 14.3. UV (CH_2Cl_2, 25 ºC) λ_{max} (log ε) 326 (5.01). MALDI-TOF MS m/z 1774.3 (M^+); HRMS (MALDI-TOF) calcd for $C_{126}H_{176}N_6$: 1774.3984, found: 1774.3971.

1,4-bis(5,10,15-tridodecyl-10,15-dihydro-5H-diindolo[3,2-a:3',2'-c]carbazol-2-yl)buta-1,3-diyne (7). A mixture of **2b** (100mg, 0.11mmol) and $Cu_2(OAc)_4 \cdot H_2O$ (16.4mg, 0.082mmol) in 10ml of a 1:1 mixture of Piperidine: CH_2Cl_2 was stirred for 12h at room temperature. Then the mixture was diluted with CH_2Cl_2, washed with water, and dried ($MgSO_4$); the solvent was then evaported and the residue was purified by chromatography with CH_2Cl_2 /Hexane (1:3) to give a yellow solid **3**(57.8mg, 60%). ^{1}H NMR (200 MHz, $CDCl_3$) δ 8.41 – 8.29 (m, 5H), 7.95 (d, *J* = 10.3 Hz, 4H), 7.72 – 7.63 (m, 5H), 7.52 – 7.34 (m, 8H), 4.98 (s, 12H), 2.02 (s, 12H), 1.23 (d, *J* = 8.2 Hz, 108H), 0.85 (s, 18H).^{13}C NMR (50 MHz, $CDCl_3$) δ 141.2, 140.6, 140.1, 139.6, 138.8, 124.2, 123.5, 123.1, 121.7, 121.4, 120.0, 115.5, 114.7, 110.8, 103.7, 103.4, 103.2, 83.7, 74.1, 47.2, 32.1, 29.8, 29.6, 29.4, 26.8, 22.9, 14.3. UV (CH_2Cl_2, 25 ºC) λ_{max} (log ε) 318 (5.23), 400 (5.10). MALDI-TOF MS m/z 1746.4 (M^+); HRMS (MALDI-TOF) calcd for $C_{124}H_{172}N_6$: 1746.3655, found: 1746.3671.

S.5.2. Elucidation of the regiochemistry in compound 2

The characteristic lowest field signals of the spectra usually corresponding to the protons H4, H9 and H14 are all doublet, contrary to what would be expected if substitution occurred in the 3 position.

^{1}H NMR spectrum of compound **2**.

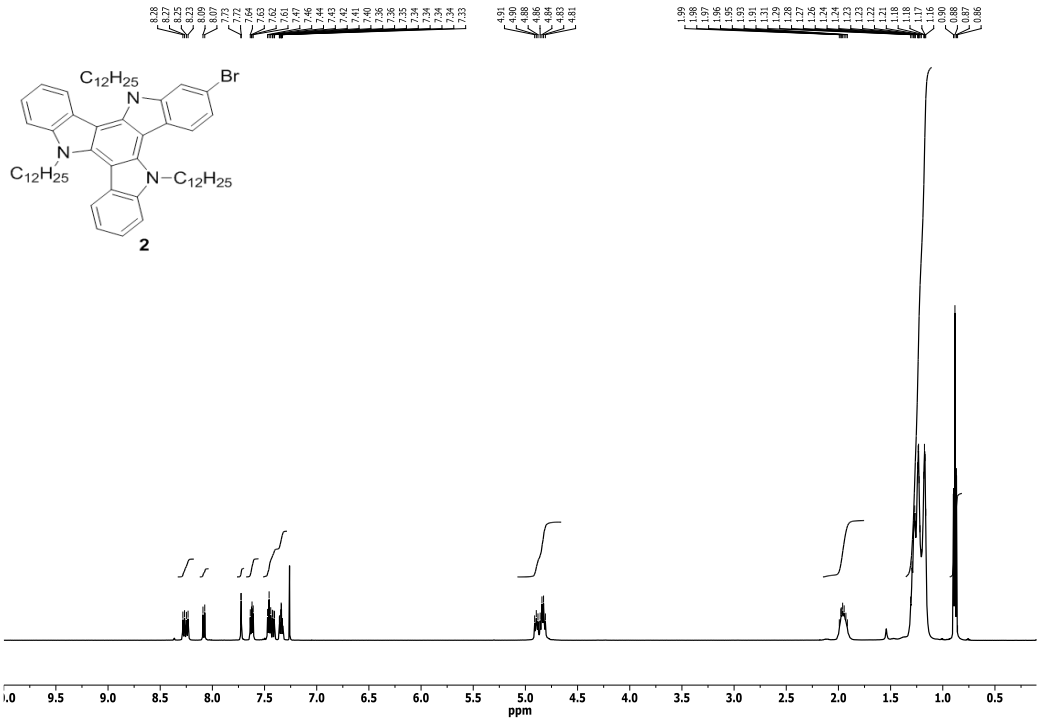

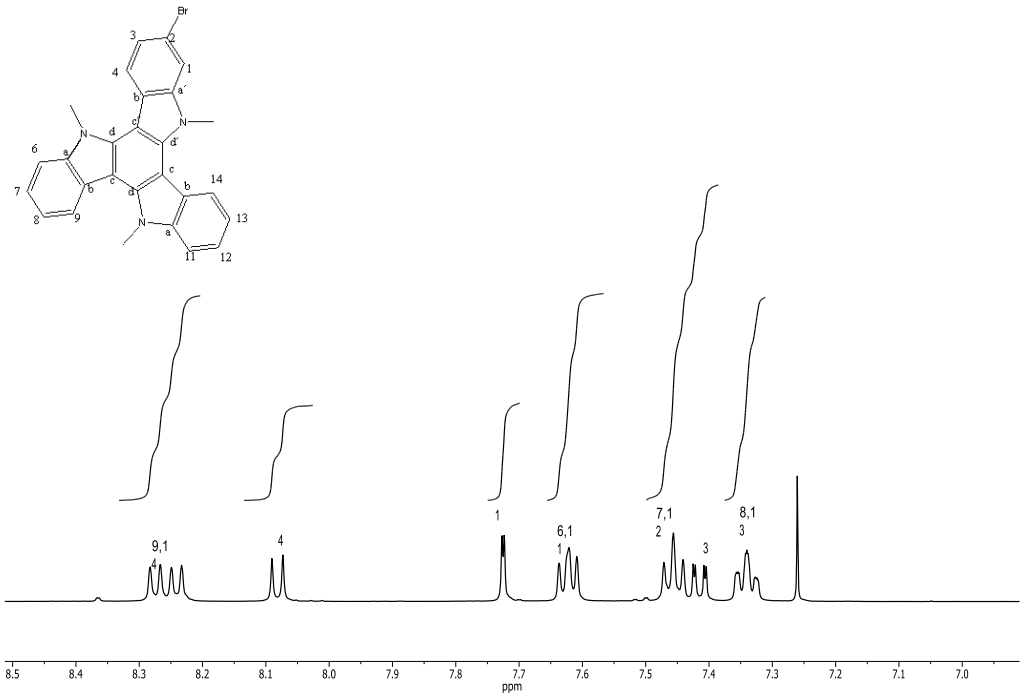

^{13}C NMR spectrum of compound **2**.

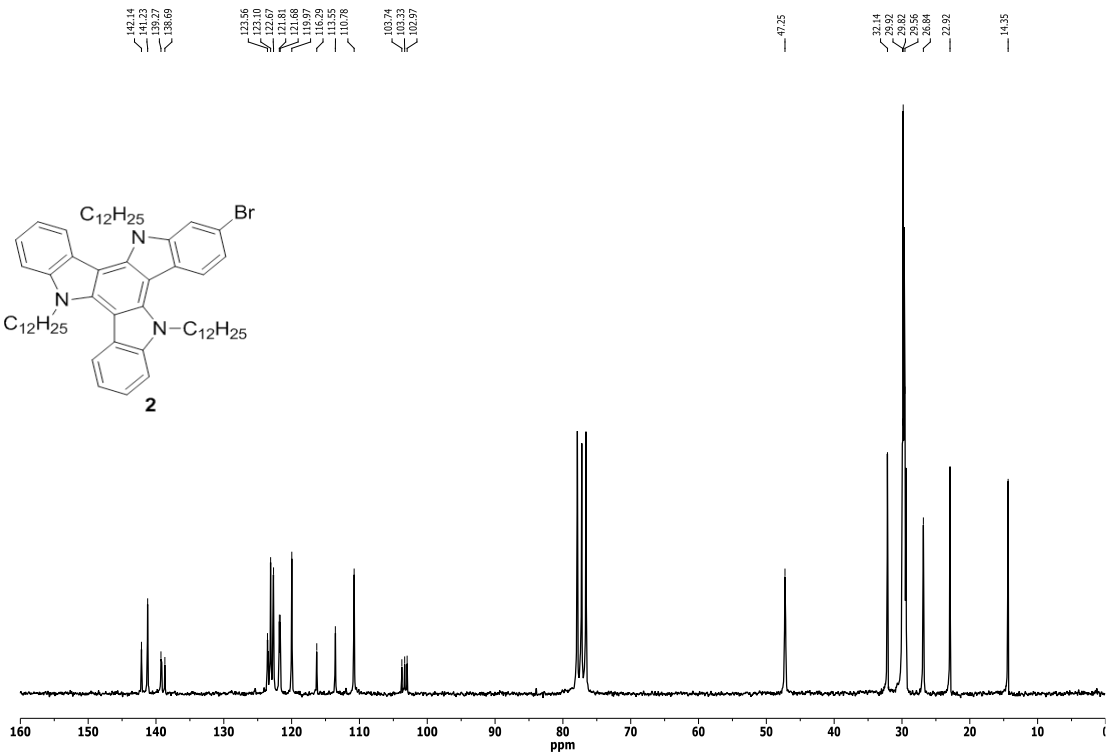
142.14
141.23
139.27
138.69
123.56
123.10
122.67
121.81
121.68
119.97
116.29
113.55
110.78
103.74
103.33
102.97
47.25
32.14
29.92
29.82
29.56
26.84
22.92
14.35
C12H25
Br
N
N
C12H25
N–C12H25
2
160
150
140
130
120
110
100
90
80
70
60
50
40
30
20
10
ppm

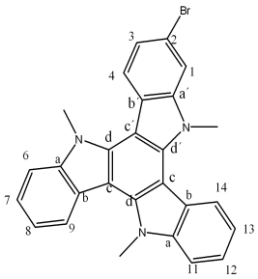
Br
N
N
N

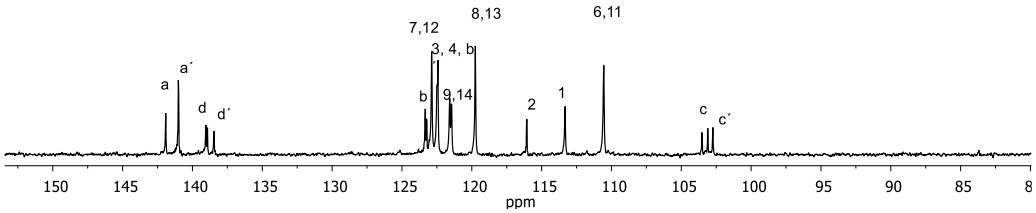
7,12
8,13
6,11
3, 4, b
a
a´
d
d´
b
9,14
2
1
c
c´
150
145
140
135
130
125
120
115
110
105
100
95
90
85
ppm

- <u>Aromatic region of the ^{1}H-^{13}C-HMBC spectrum of the compound 2</u>

The long range correlation cross peak between the three lowest field doublets and the highest field quaternary carbon signal (corresponding to carbon in ortho to the nitrogen in the inner aromatic ring) unequivocally allow us to identify these three signals as they are the only separated at the necessary distance (3 or less bonds).

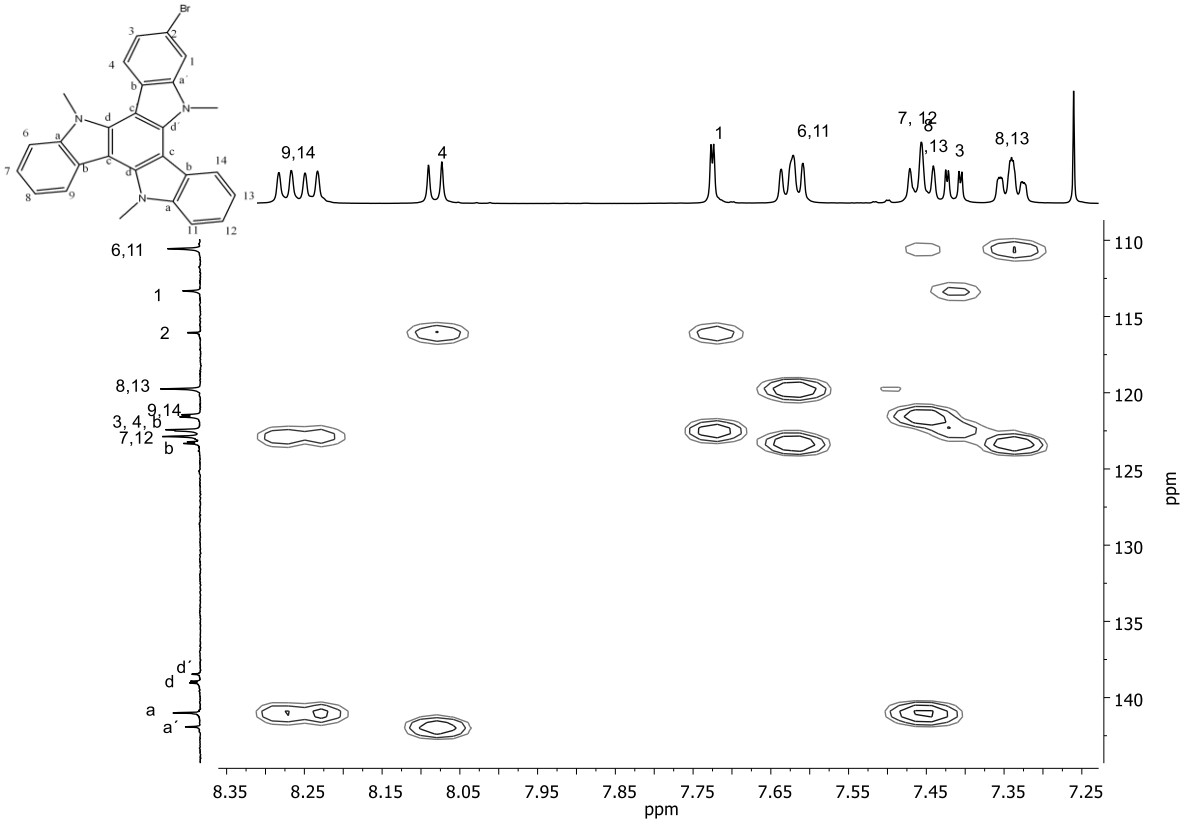

- Aromatic region of the ^{1}H-^{13}C-HMQC spectrum of compound 2

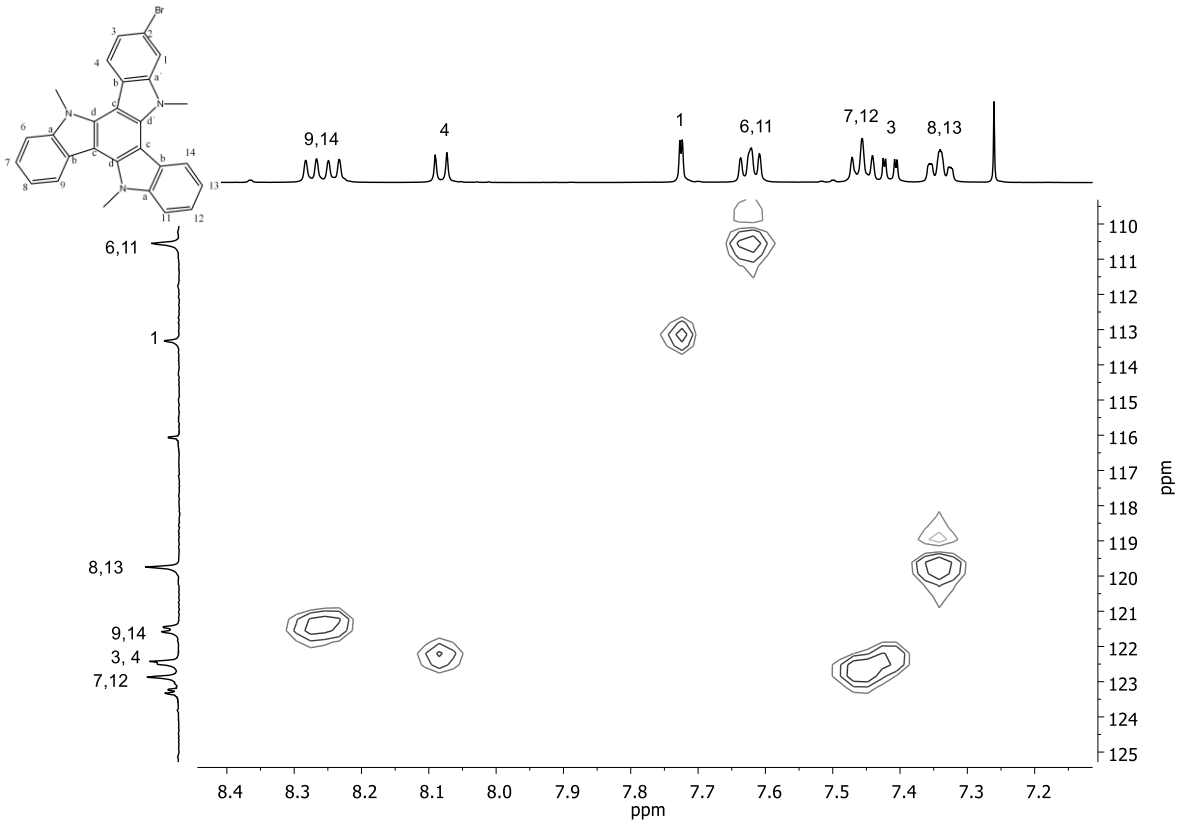

S.5.3. Copy of the ^{1}H NMR, ^{13}C NMR spectra of compounds 3-7

^{1}H NMR spectrum of compound **3**.

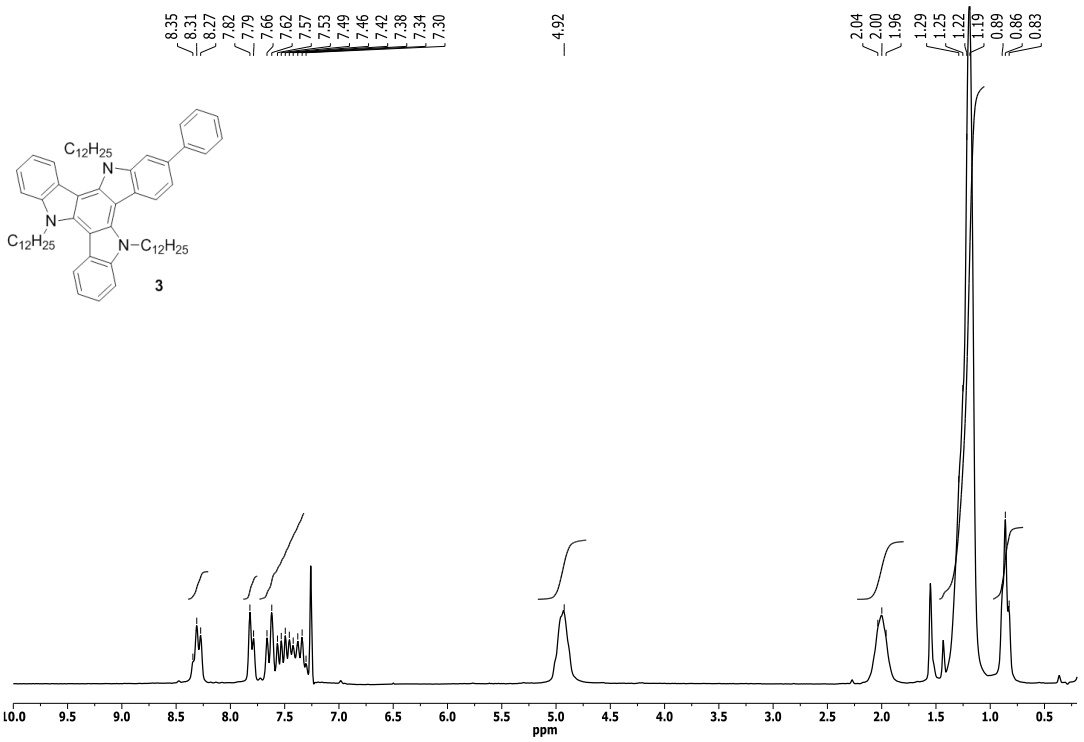

^{13}C NMR spectrum of compound **3**.

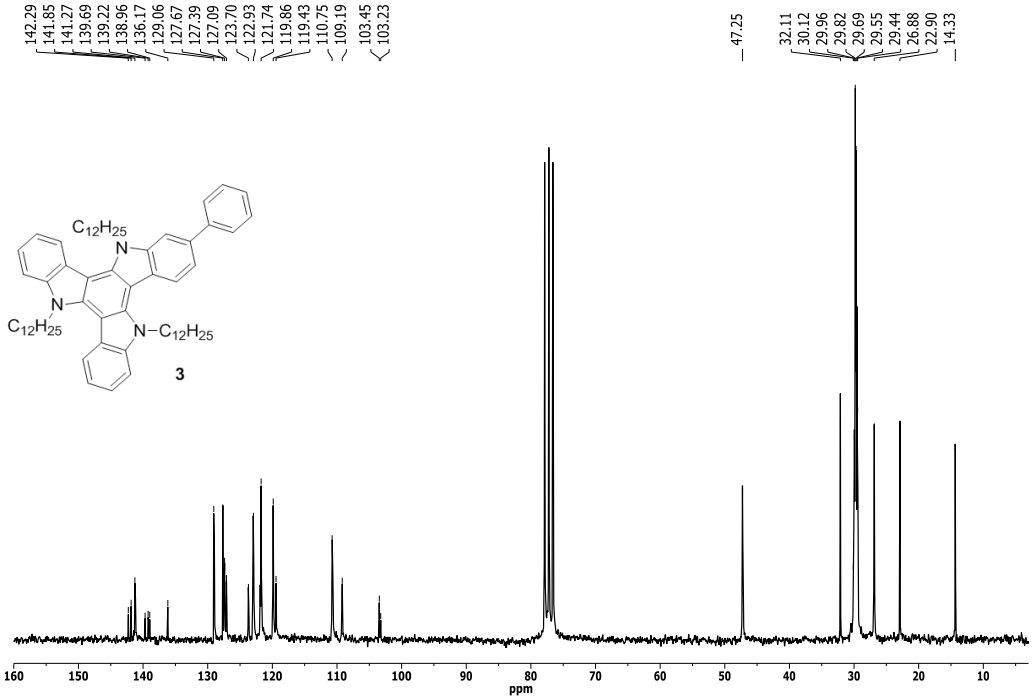

^{1}H NMR spectrum of compound **4**.

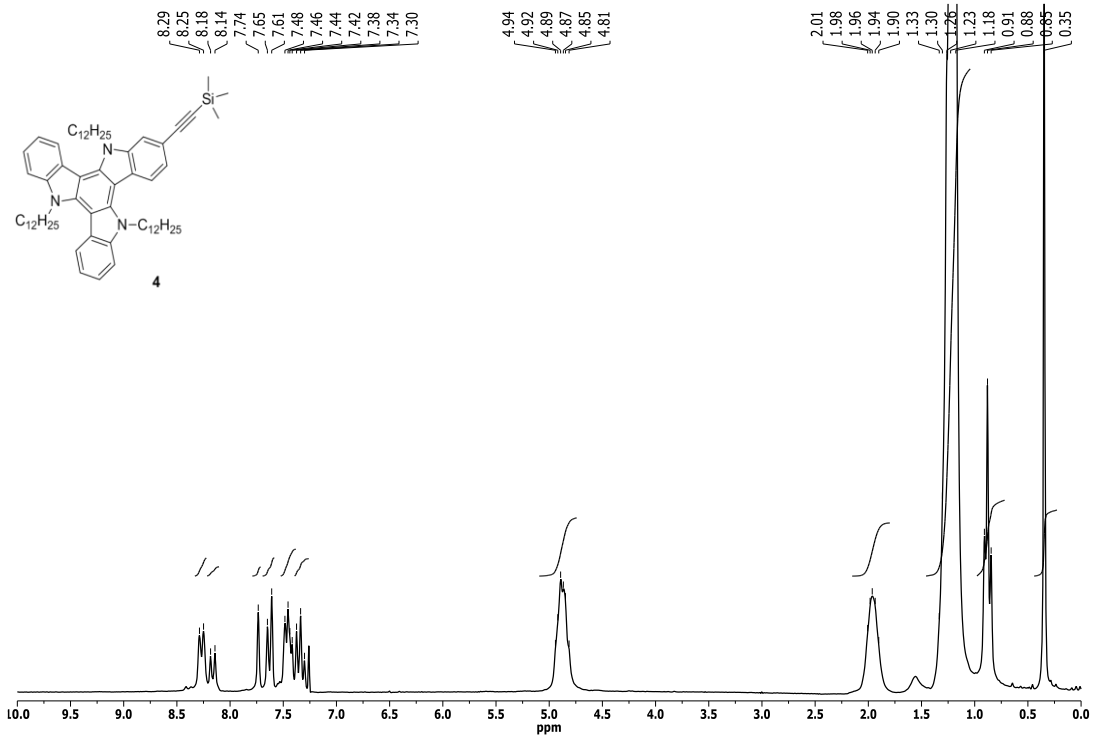

^{13}C NMR spectrum of compound **4**.

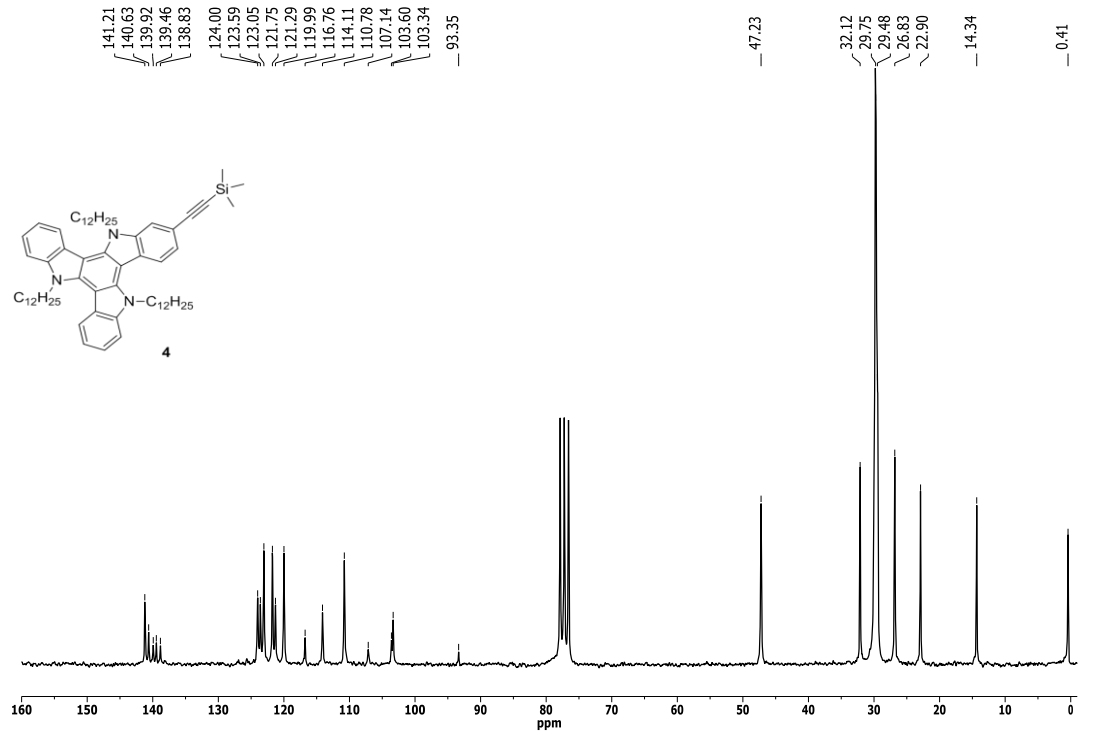

^{1}H NMR spectrum of compound **5**.

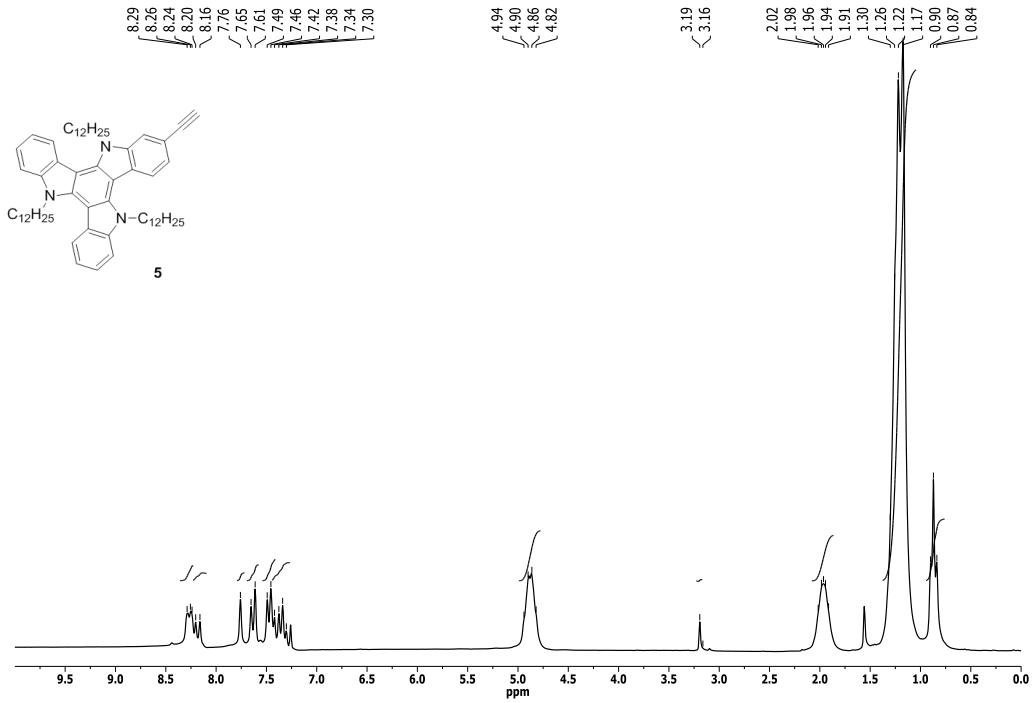

^{13}C NMR spectrum of compound **5**.

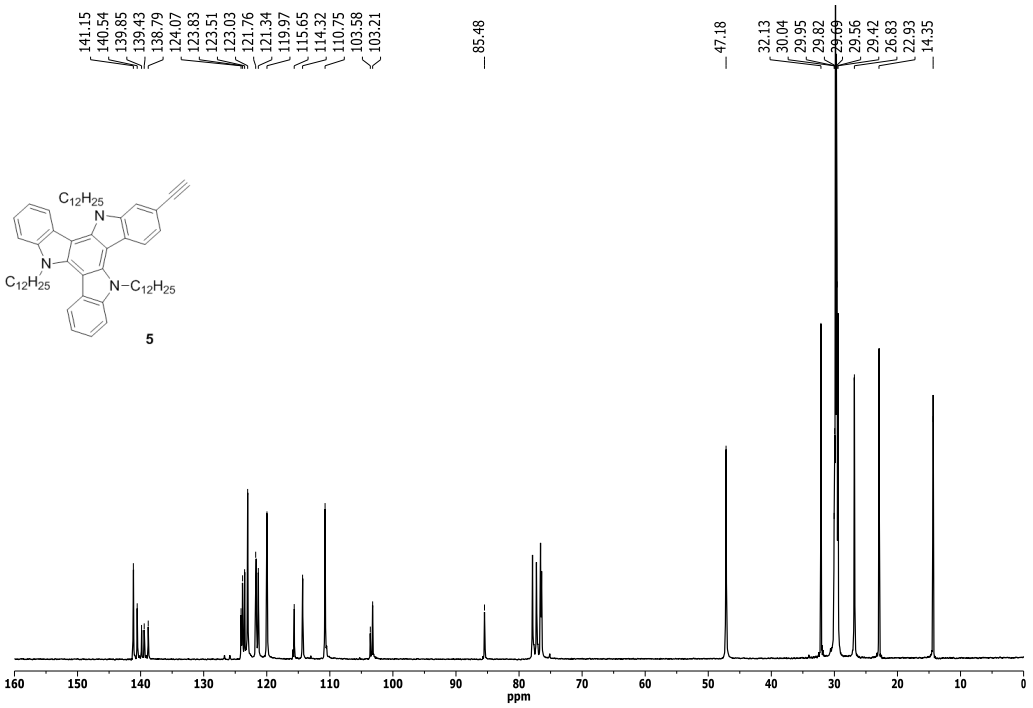

^{1}H NMR spectrum of compound **6**.

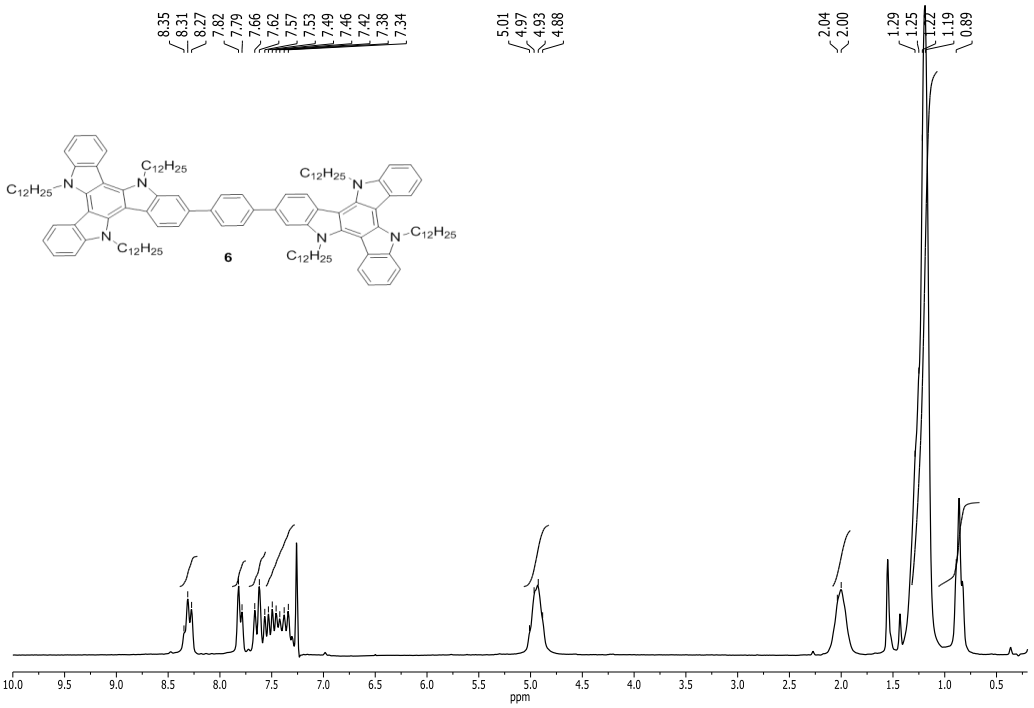

^{13}C NMR spectrum of compound **6**.

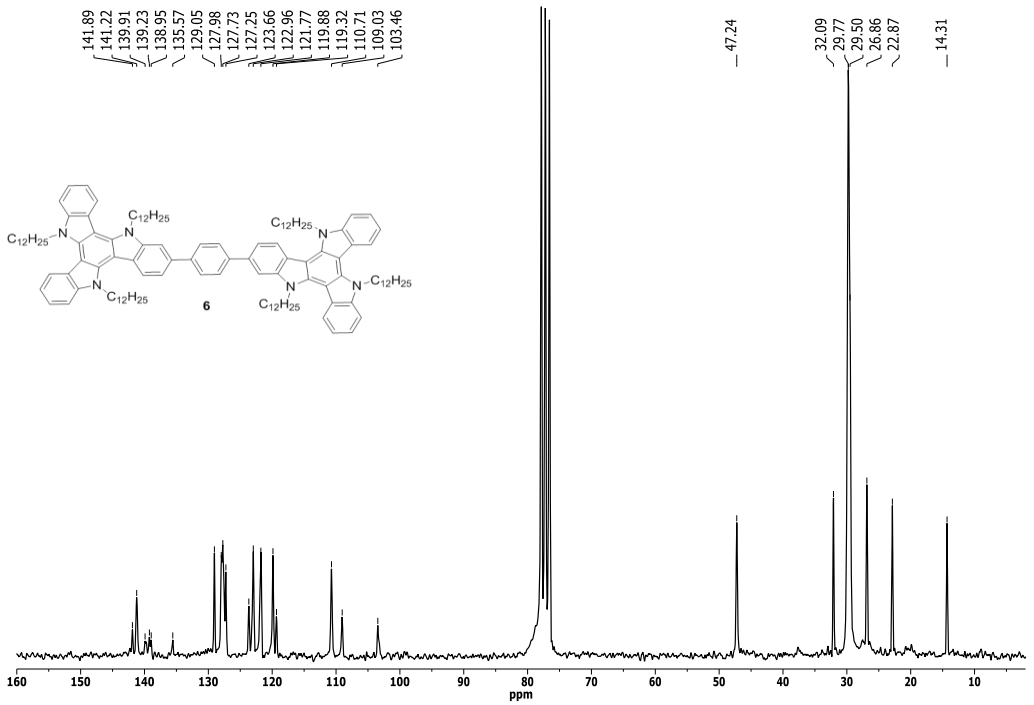

^{1}H NMR spectrum of compound **7**.

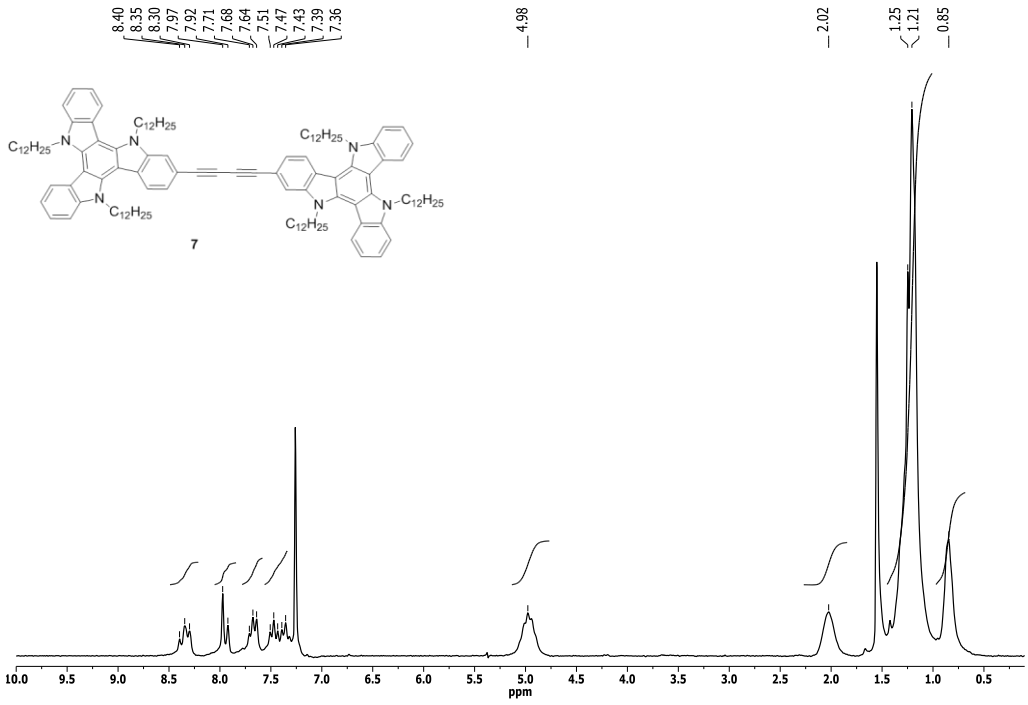

^{13}C NMR spectrum of compound **7**.

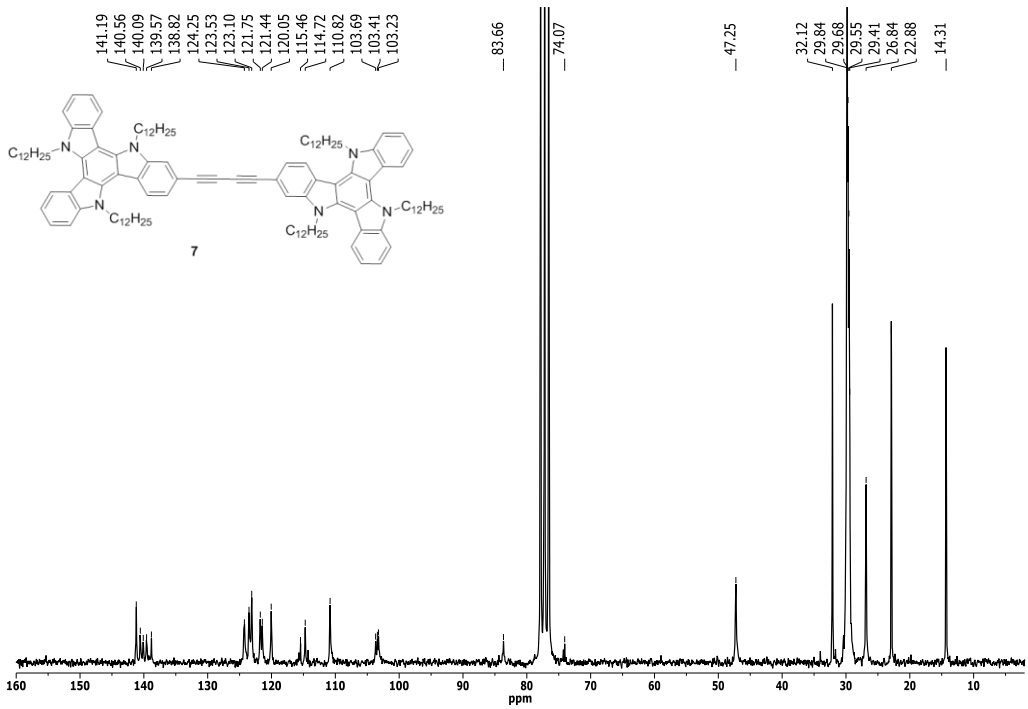

S.5.4. DFT calculations

- **Computational details**

The molecular geometries of neutral and radical-cation states of monomers **1**, **3**, **5** and dimers **6-8** were calculated at the Density Functional Theory (DFT) level using the hybrid, generalized gradient approximation (GGA) functional B3LYP[1, 2, 3, 4, 5] and a 6-31G** basis[6,7,8] set, as implemented in the GAUSSIAN09 program.[9] Note that the dodecyl chains attached to the nitrogen atoms have been replaced by octyl groups in order to reduce the computational cost. All geometrical parameters were allowed to vary independently apart from planarity of the rings and no symmetry constraints were imposed during the optimization process. On the resulting ground-state optimized geometries, harmonic frequencies calculations were performed to ensure we are in a global minimum. Vertical electronic excitation energies were computed by using the time-dependent DFT (TD-DFT) approach on the previously optimized molecular geometries. Absorption spectra were simulated through convolution of the vertical transition energies and oscillator strengths with Gaussian functions characterized by a half width at half-maximum (fwhm) of 0.3 eV. Molecular orbital contours were plotted using gausview 5.0. The reorganization energies associated with hole transfer were calculated directly from the relevant points on the potential energy surfaces using the standard procedure detailed in the literature.[10]

Figure S1. DFT-calculated molecular orbital energies (B3LYP/6-31G** level) for monomers **1**, **3** and **5**. The topologies of the frontier molecular orbitals are also shown.

[1] Smith, J. R.; Cox, P. A.; Campbell, S. A.; Ratcliffe, N. M.; *J. Chem. Soc., Faraday Trans.* **1985**, *19*, 2331. Ando, S.; Ueda, M. *Synth. Met.* **2002**, *129*, 207.
[2] Aperloo, J. J.; Groenendaal, L.; Verheyen, H.; Jayakanan, M.; Janssen, R.; Dhkissi, A.; Beljonne, D.; Lazzaroni R. and Brédas, J.-L. *Chem. Eur. J.*, **2002**, 8, 2384.
[3] Koopmans, T. *Physica* **1934**, *1*, 104-113.
[4] Becke, A. D. *J. Chem. Phys.* **1993**, *98*, 5648.
[5] Lee, C. T.; Yang, W. T.; Parr, R. G. *Phys. Rev. B* **1988**, *37*, 785.
[6] Harihara, P. C.; Pople, J. A. *Theor. Chim. Acta* **1973**, *28*, 213.
[7] Hehre, W. J.; Ditchfield, R.; Pople, J. A. *J. Chem. Phys.* **1972**, *56*, 2257.
[8] Francl, M. M.; Pietro, W. J.; Hehre, W. J.; Binkley, J. S.; Gordon, M. S.; Defrees, D. J.; Pople, J. A. *J. Chem. Phys.* **1982**, *77*, 3654.
[9] Frisch, M. J., et al.; Gaussian 09, revision B.01: Pittsburgh, PA, 2009.
[10] Bredas, J. L.; Beljonne, D.; Coropceanu, V.; Cornil, J. *Chem. Rev.* **2004**, *104*, 4971.

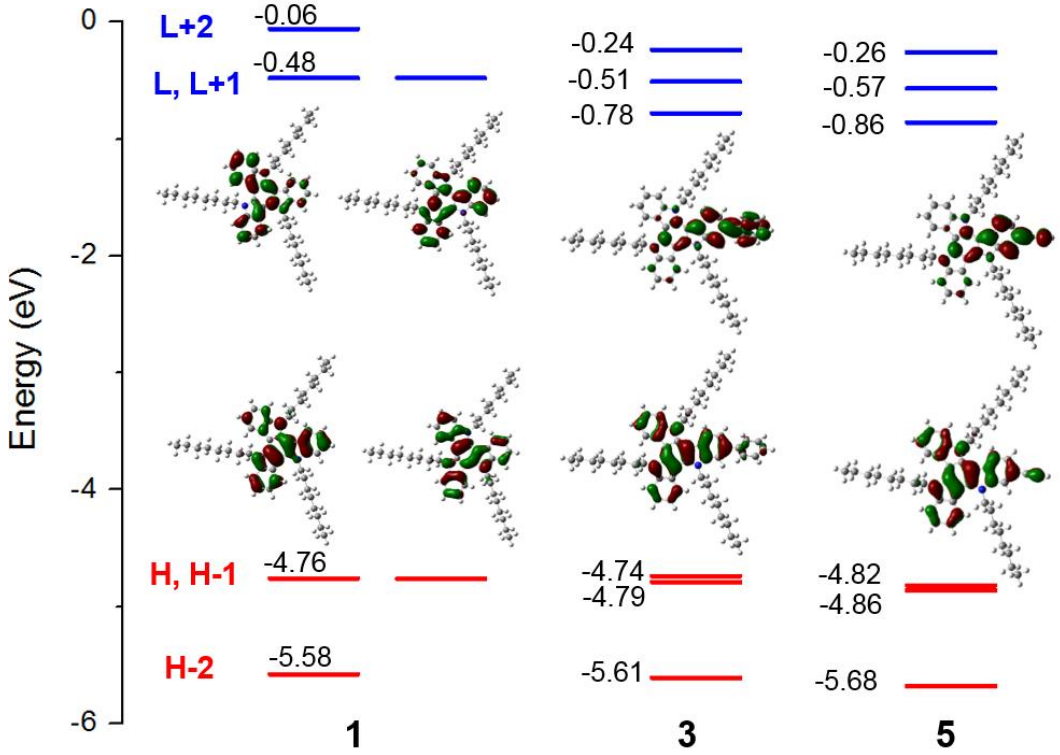

Figure S2. Simulated absorption spectra of monomers **3**, **5** and dimers **6**, **7** together with the excitations (wavelength vs. oscillator strength) shown as vertical bars as determined with TD-DFT.

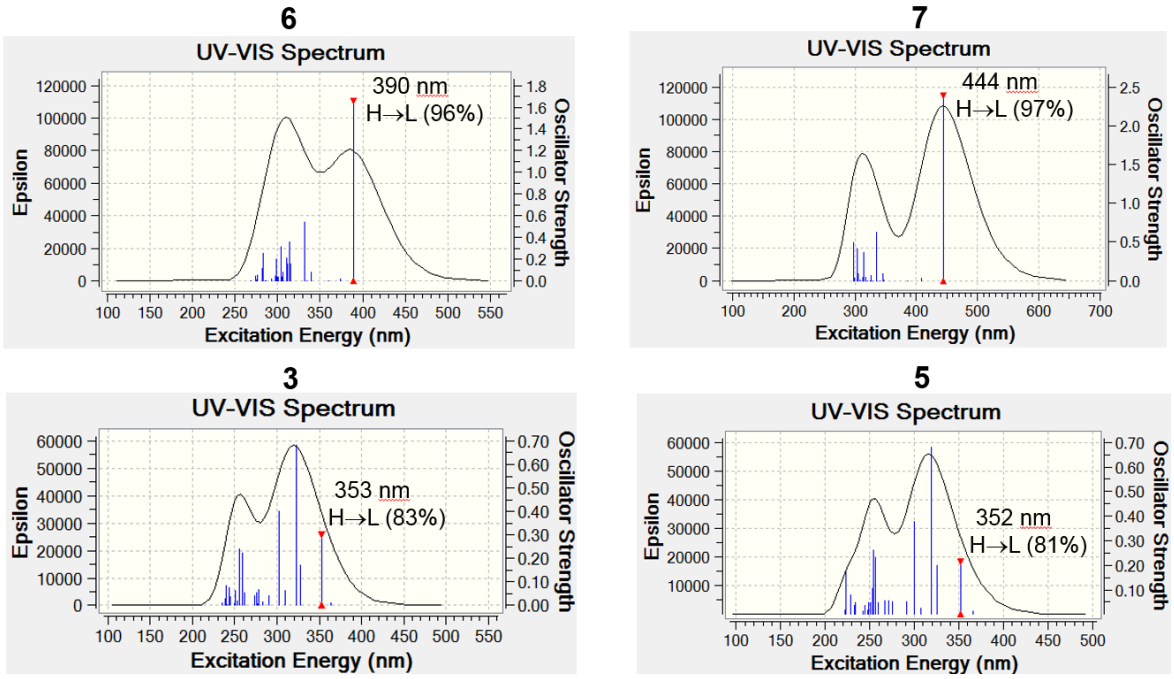

Figure S3. DFT rotational barriers for dimer **6** and **7** as a function of the inter-ring dihedral angle (θ) between central spacer (phenyl or diacetyl group) and the triindole unit. The structures of the less- and most-accessible conformers are also shown.

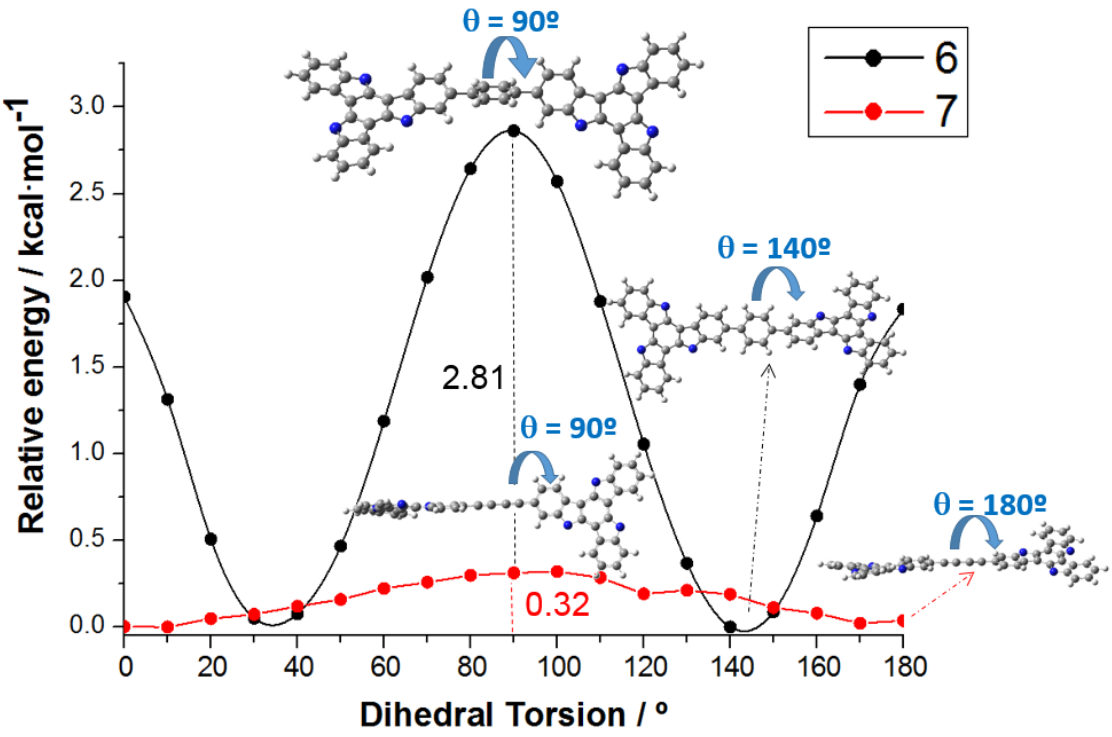

Figure S4. DFT-calculated bond lengths (B3LYP/6-31G** level) of: a) unsubstituted monomer **1** (blue) and phenyl-substituted monomer **3** (red) and dimer **6** (black), and b) unsubstituted monomer **1** (blue) and acetylene-substituted monomer 5 (red) and dimer **7** (black). For clarity reasons, only half of the molecule is shown in the case of the dimers.

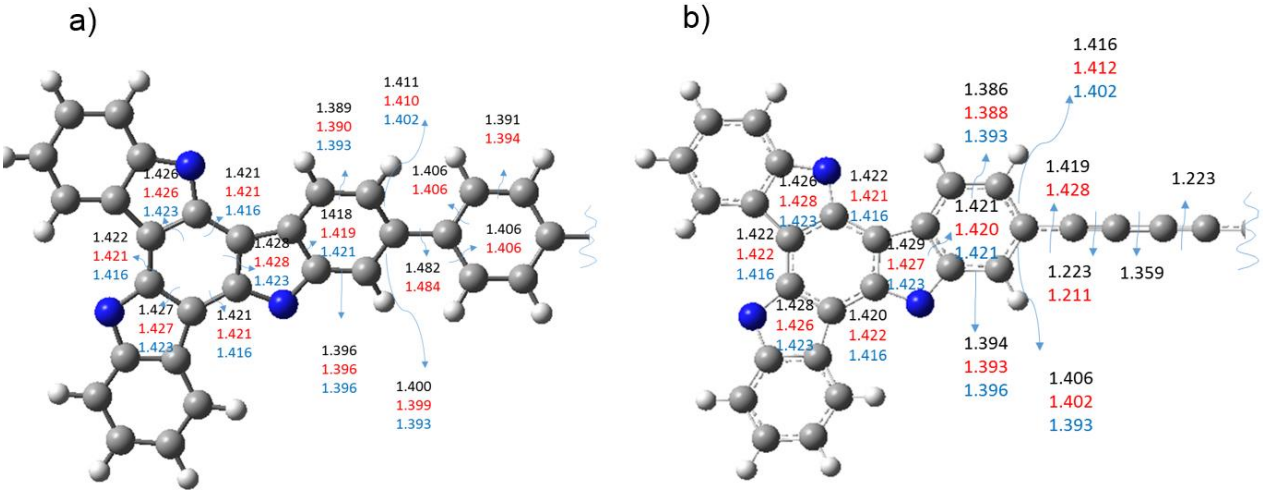

Figure S5. Theoretical Raman spectra of monomers **1**, **3**, **5** and dimers **6**, **7**. (p. S10)

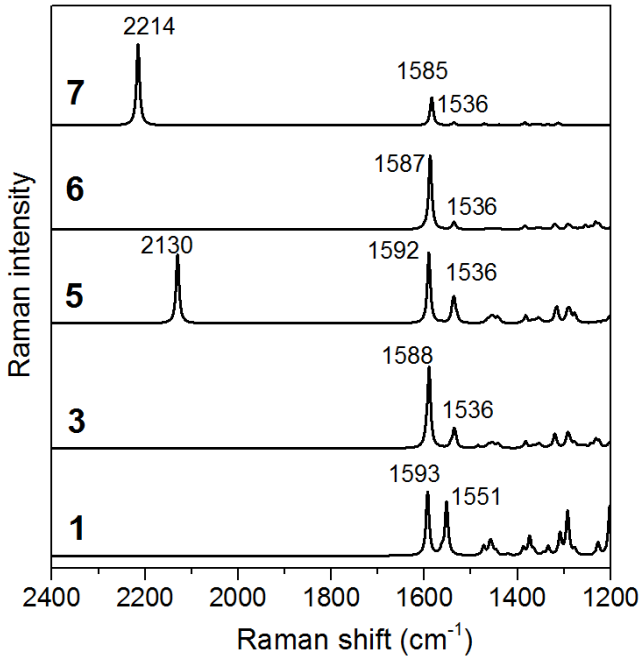

Figure S6. DFT-calculated inter-ring dihedral angle (θ) between central spacer (phenyl or diacetyl group) and the triindole unit in dimer **6** (a) and **7** (b). DFT-calculated bond lengths of dimer **6** (c) and dimer **7** (d) in the neutral (black), cation (red) and dication (blue) states.

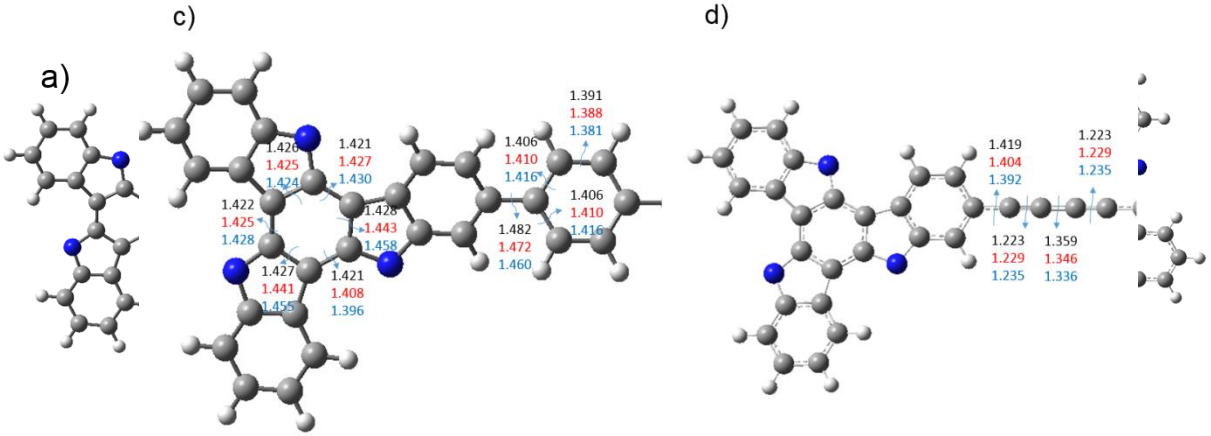

S.5.5. Temperature variable UV-Vis spectra experiments

Variable-temperature UV-vis absorption spectra of dimer **7** in CH_2Cl_2: a) High-temperature experiments and b) low-temperature experiments.

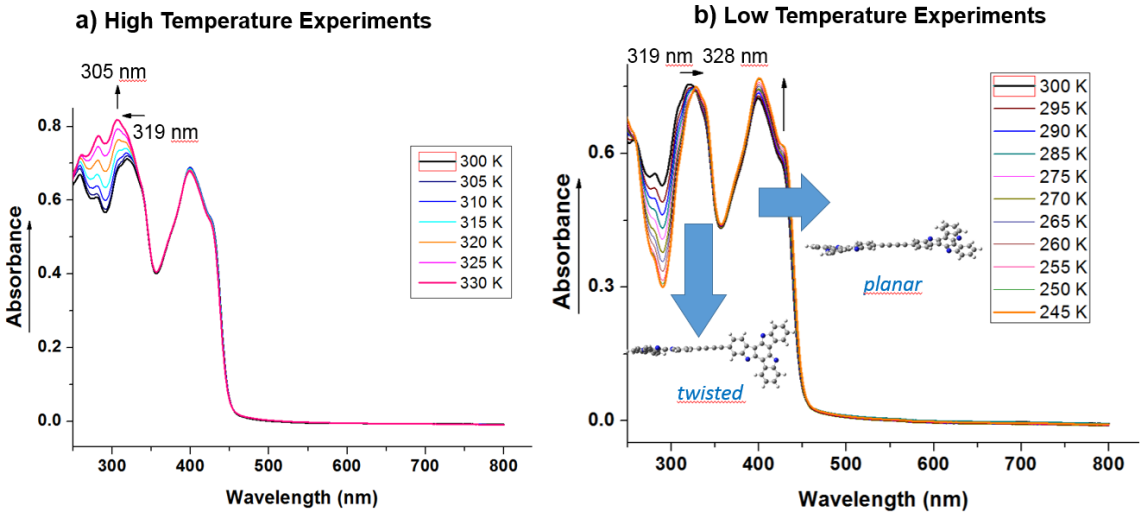

These experiments supports the hypotheses of the coexistence of two different conformers in equilibrium for the diacetylenic-bridged dimer **7**: the transplanar conformer and the slightly less stable twisted conformer (by 0.32 kcal/mol, as predicted by DFT calculations, see Figure S3). The band around 305-328 nm which is attributed to the twisted conformation increases in intensity and blue-shifts upon raising the temperature while the band at 400 nm due to the planar conformation increases in intensity when lowering the temperature.

S.6. SECTION 5.2. *"SYMMETRY LOWERING IN TRIINDOLES: IMPACT ON THE ELECTRONIC AND PHOTOPHYSICAL PROPERTIES."*

Constanza Ruiz, Eva M. Garcia-Frutos, Demetrio A. da Silva Filho, Juan T. López Navarrete,*
M. Carmen Ruiz Delgado* and Berta Gómez-Lor*
*E-mail: bgl@icmm.csic.es, teodomiro@uma.es; carmenrd@uma.es

S.6.1. Characterization of compound 2c

Characterization of 5,6,11-trioctyl-6,11-dihydro-5H-diindolo[2,3-a:2',3'-c]carbazole (2c). ^{1}H NMR (200 MHz, $CDCl_3$) δ 8.96 (d, J = 7.9Hz, 1 H; ArH), 8.90 (d, J = 7.7 Hz, 1 H; ArH), 8.41 (d, J = 8.1 Hz, 1 H; ArH), 7.70-7.63 (m; 3H, ArH), 7.57-7.33(m, 6 H; ArH), 4.95 (t, J = 7.9 Hz, 2 H; CH_2), 4.70 (t, J = 7.4 Hz, 2 H; CH_2), 4.58 (t, J = 7.5 Hz, 2 H; CH_2), 2.10 (m, 6 H; CH_2), 1.47-0.82 (m, 30 H; CH_2), 0.71 (m, 9 H; CH_3); ^{13}C NMR (50 MHz, $CDCl_3$, δ) 144.7, 143.3, 140.8, 133.8, 131.8, 127.0, 126.8, 125.2, 124.5, 124.1, 123.9, 123.5, 123.1, 122.7, 122.2, 120.3, 119.6, 119.0, 112.7, 112.5, 112.0, 109.8, 48.5, 48.0, 46.8, 31.7, 31.6, 31.5, 30.4, 29.7, 29.3, 29.2, 28.9, 28.8, 27.4, 27.0, 26.8, 26.6, 26.4, 22.6, 22.5, 14.1, 14.0; UV-vis (CH_2Cl_2, 25 ºC): λ_{max} (log ε) = 263 (7447), 309 (7674), 343 (3219), 357 (4092), 390 (1681), 408 (1844) nm; MALDI-TOF MS *m*/*z* 681 [M^+], HRMS (MALDI-TOF) calcd for $C_{48}H_{63}N_3$: 681.50165, found: 681.50189.

S.6.2. Absorption spectra

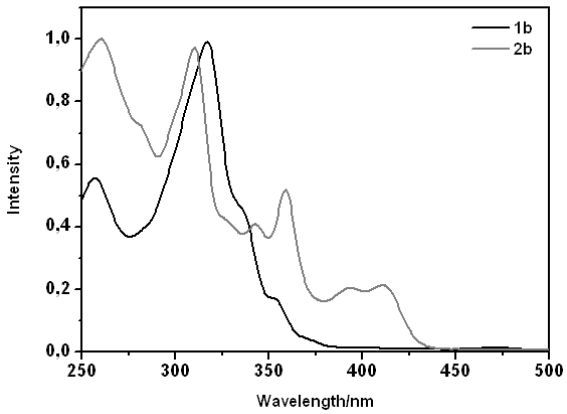

Figure S1. Experimental UV-Vis spectra of **1b** and **2b** in CH_2Cl_2 solutions.

S.6.3. Cyclic Voltammetry Measurements

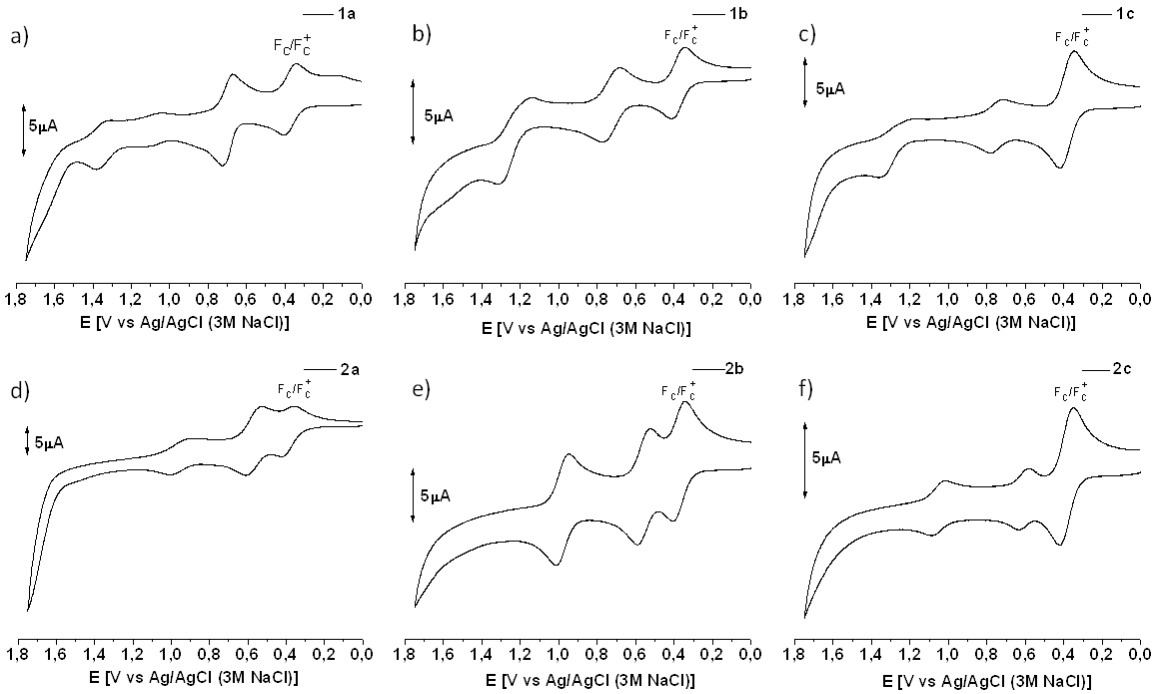

Figure S2. Cyclic voltammograms of **1a**, **1b**, **1c**, **2a**, **2b** and **2c** at c = $1x10^{-3}$ $molL^{-1}$ recorded in CH_3CN/ 0.1M tetra-*n*-butylammonium hexafluorophosphate ($TBAPF_6$) measured versus Ag/AgCl (3M NaCl) and containing ferrocene as internal standard. Measurements were performed at a scan rate 100mV/s using a Pt working electrode and a Pt wire auxiliary electrode.

S.6.4. Spectroelectrochemistry and chemical oxidation

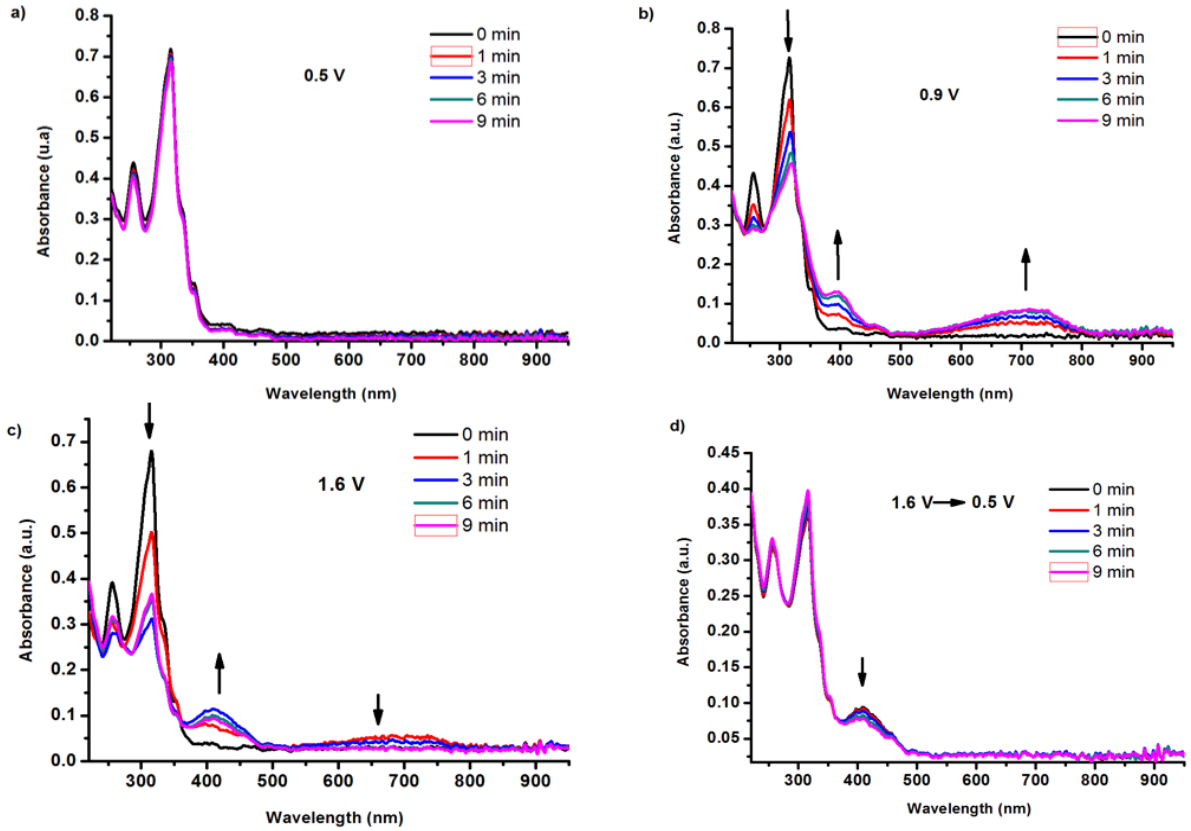

Figure S3: Spectroelectrochemistry of **1c** in acetonitrile solution containing 0.1 M Bu_4NPF_6 as supporting electrolyte at a) 0.5 V, b) 0.9 V c) 1.6 V and d) recovery of the compound from 1.6 to 0.5 V.

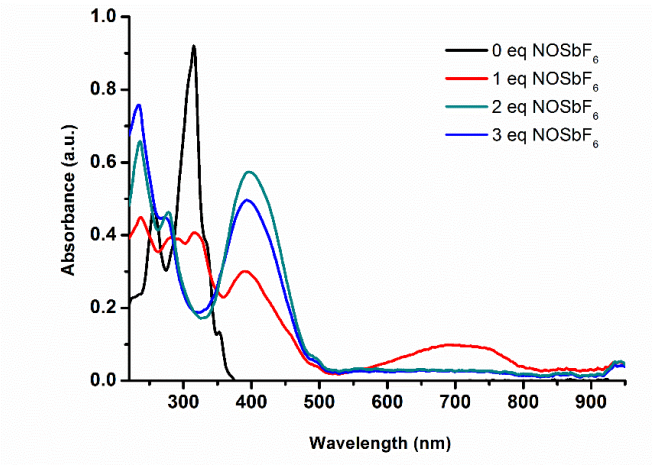

Figure S4: Chemical oxidation of **1c** in acetonitrile with different equivalent of $NOSbF_6$.

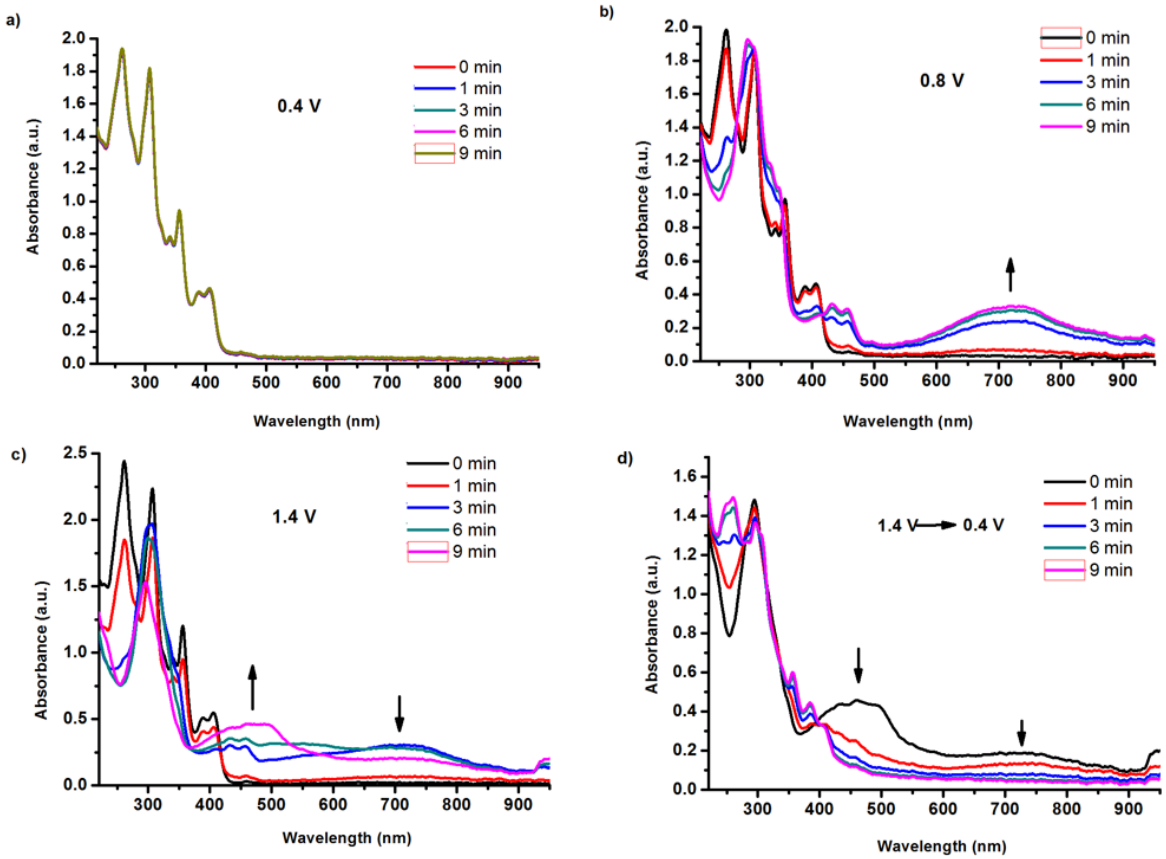

Figure S5: Spectroelectrochemistry of **2c** in acetonitrile solution containing 0.1 M Bu_4NPF_6 as supporting electrolyte at a) 0.4 V, b) 0.8 V c) 1.4 V and d) recovery of the compound from 1.4 to 0.4 V.

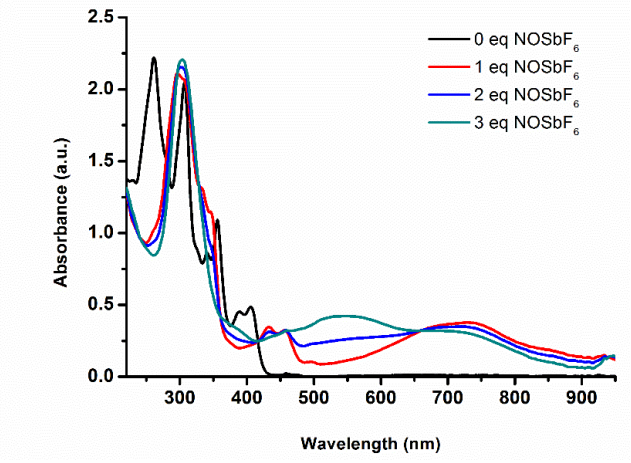

Figure S6 Chemical oxidation of **2c** in acetonitrile with different equivalent of $NOSbF_6$.

S.6.5. DFT calculations

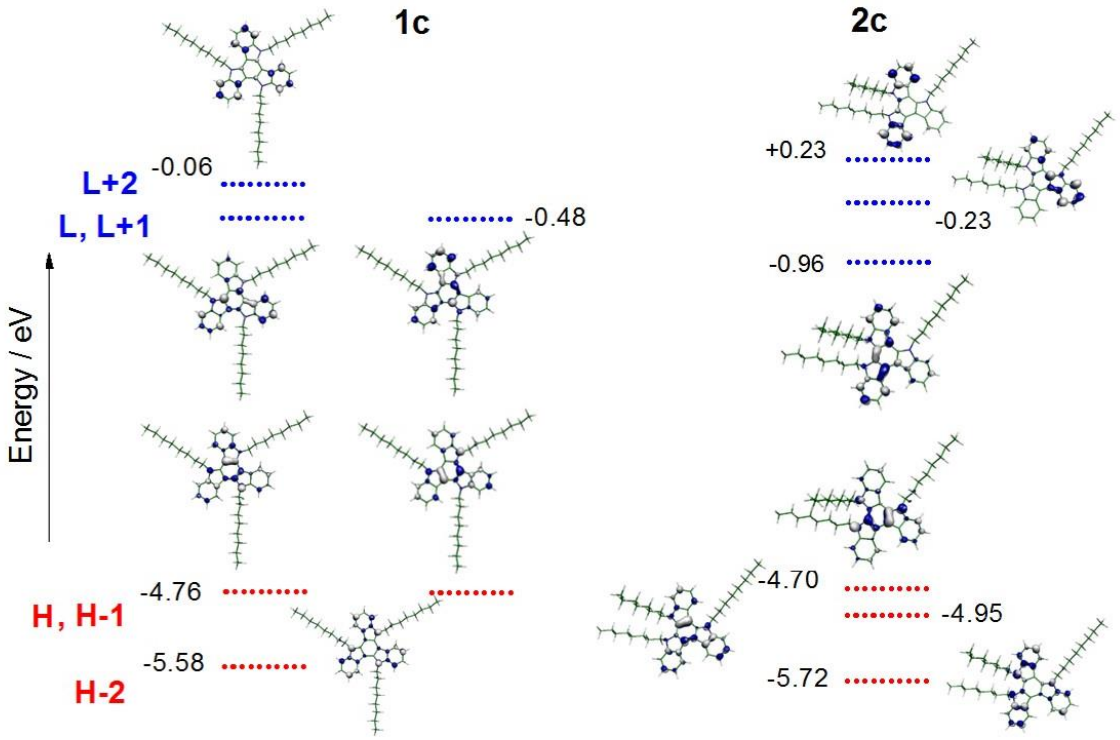

Figure S7. DFT//B3LYP/6-31G** molecular orbital energies and topologies for **1c** and **2c**.

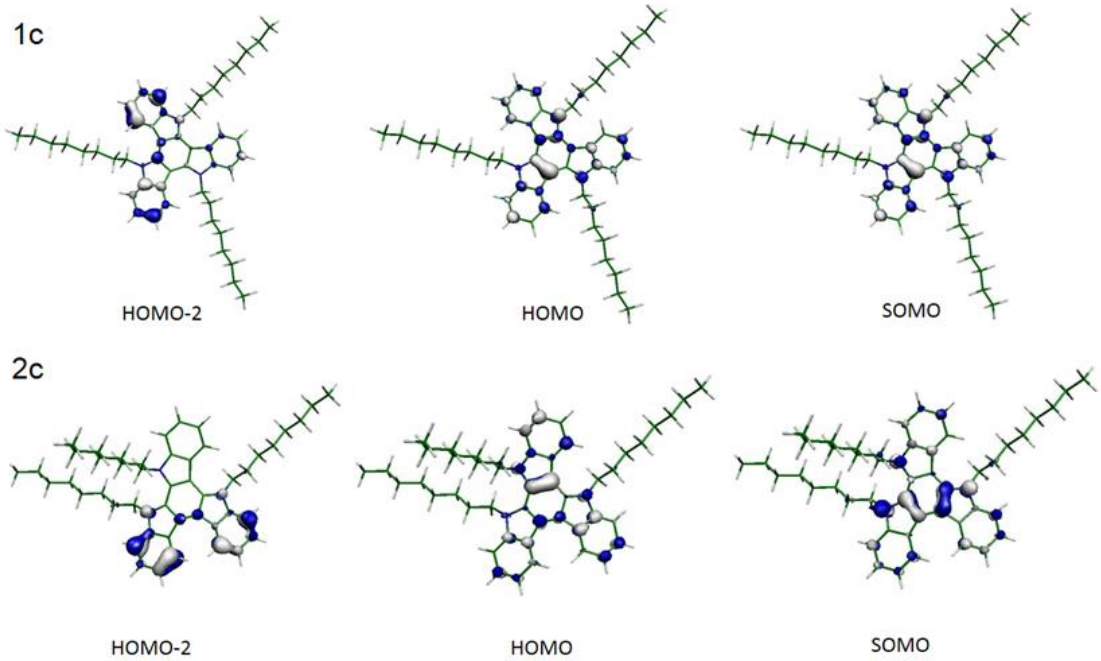

Figure S8. DFT// B3LYP/6-31G** molecular orbitals involved in the orbital transitions associated with the optical bands of radical cation species of **1c** (top) and **2c** (bottom).

Table S1. Vertical transition energies and oscillator strengths (f) calculated using TD-DFT//B3LYP/6-31G** for the **1b** and **2b** systems.

compound	TDDFT//B3LYP/6-31G** *Calculated Transition energy (eV)*	description
1b	4.02 (f=0.45)	**H →L, H-1→L +1**
	4.02 (f=0.45)	**H-1 →L,**
	4.23 (f=0.16)	**H →L+1**
	4.23 (f=0.16)	**H →L+2**
	4.89 (f=0.30)	**H-2 →L+2**
	4.89 (f=0.30)	**H →L+5**
		H-1 →L+5
1b$^{\bullet+}$	1.11 (f=0.05)	**H-1 →S**
	1.83 (f=0.14)	**H-2 →S**
	3.96 (f=0.16)	**H-1→L, H-9→S**
1b^{+}	1.29 (f=0.09)	**H-1→L**
	1.76 (f=0.10)	**H-3→L, H-2→L**
	2.17 (f=0.29)	**H-2→L, H-3→L**
2b^{+2}	3.21 (f=0.13)	**H →L**
	3.56 (f=0.21)	**H-1→L**
	3.99 (f=0.10)	**H →L+1**
	4.19 (f=0.10)	**H-2 →L**
	4.29 (f=0.27)	**H-2 →L, H-1→L+1**
	4.34 (f=0.28)	**H →L+2**
	4.79 (f=0.16)	**H →L+4**
	4.93 (f=0.40)	**H →L+5**
2b$^{\bullet+}$	1.42 (f=0.06)	**H-1 →S**
	1.73 (f=0.10)	**H-2 →S**
	3.85 (f=0.22)	**H→L**
2b^{+2}	1.57 (f=0.15)	**H-1→L**
	2.00 (f=0.17)	**H-2→L**
	2.16 (f=0.08)	**H-4→L**
	2.65 (f=0.05)	**H-5→L**

Figure S9. Simulated absorption spectra for **1b** (left) and **2b** (right) in the neutral, cation and dication states together with the TD-DFT//B3LYP/6-31G** excitations (wavelenght vs. oscillator strength) shown as vertical bars.

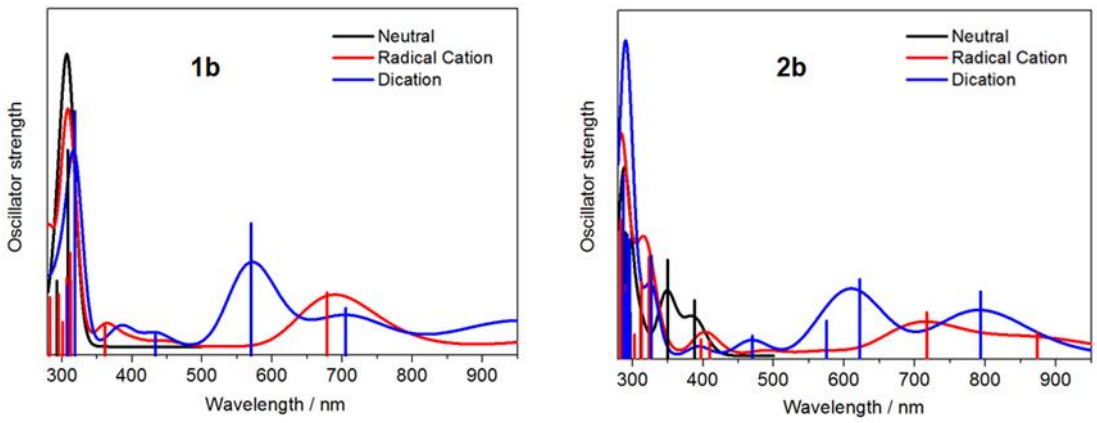

Figure S10. DFT-B3LYP/6-31G** calculated bond-length modifications (Å) for **1b** and **2b** molecules upon oxidation. The bond length modifications (Δx) larger than 0.010 Å are highlighted in red and those highlighted in blue corresponds to 0.005 Å <Δx > 0.010 Å.

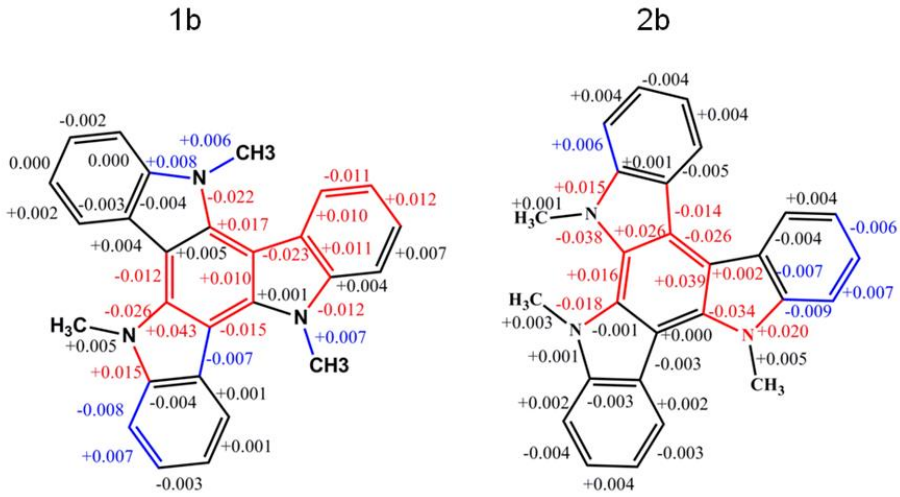

Figure S11. DFT-B3LYP/6-31G** calculated bond-length modifications (Å) for **1b** and **2b** molecules upon going from the S_0 ground state to the S_1 excited state. The bond length modifications (Δx) larger than 0.010 Å are highlighted in red.

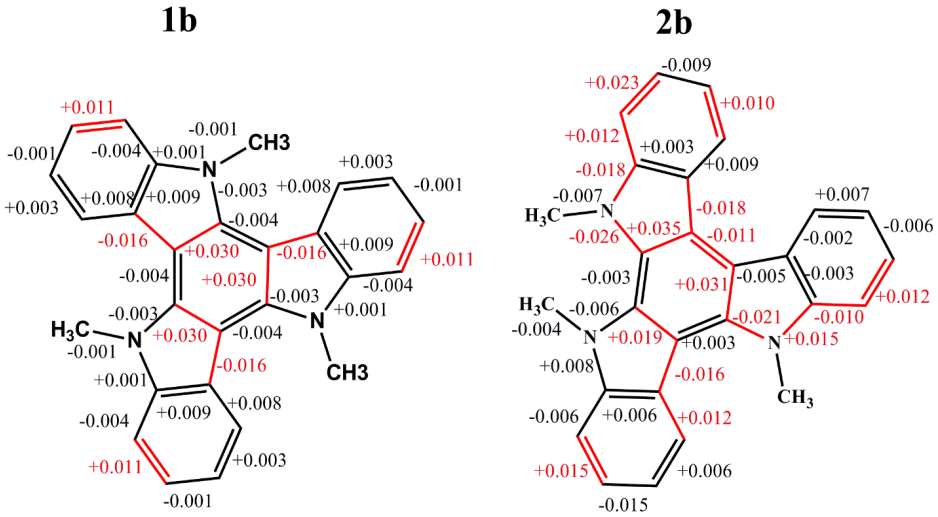

Figure S12. Representation of the **1a** 632 cm-1 (a) mode and 1330 cm-1 (b) S_1 modes presented on Table S3.

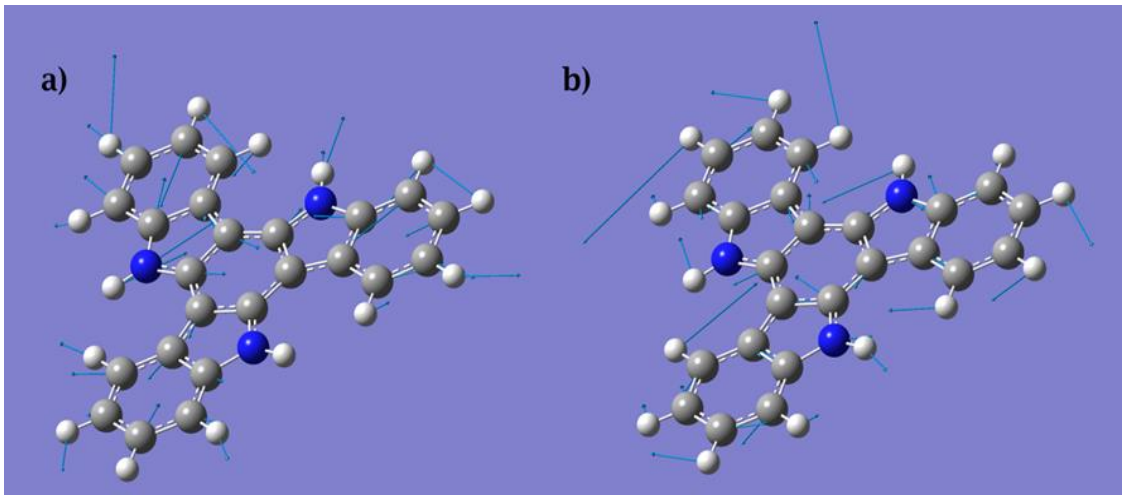

Figure S13. Representation of the **1b** 120 cm^{-1} (a), 333 cm^{-1} (b), 1243 cm^{-1} (c) and 1340 cm^{-1} (d) S_1 modes presented in table S4.

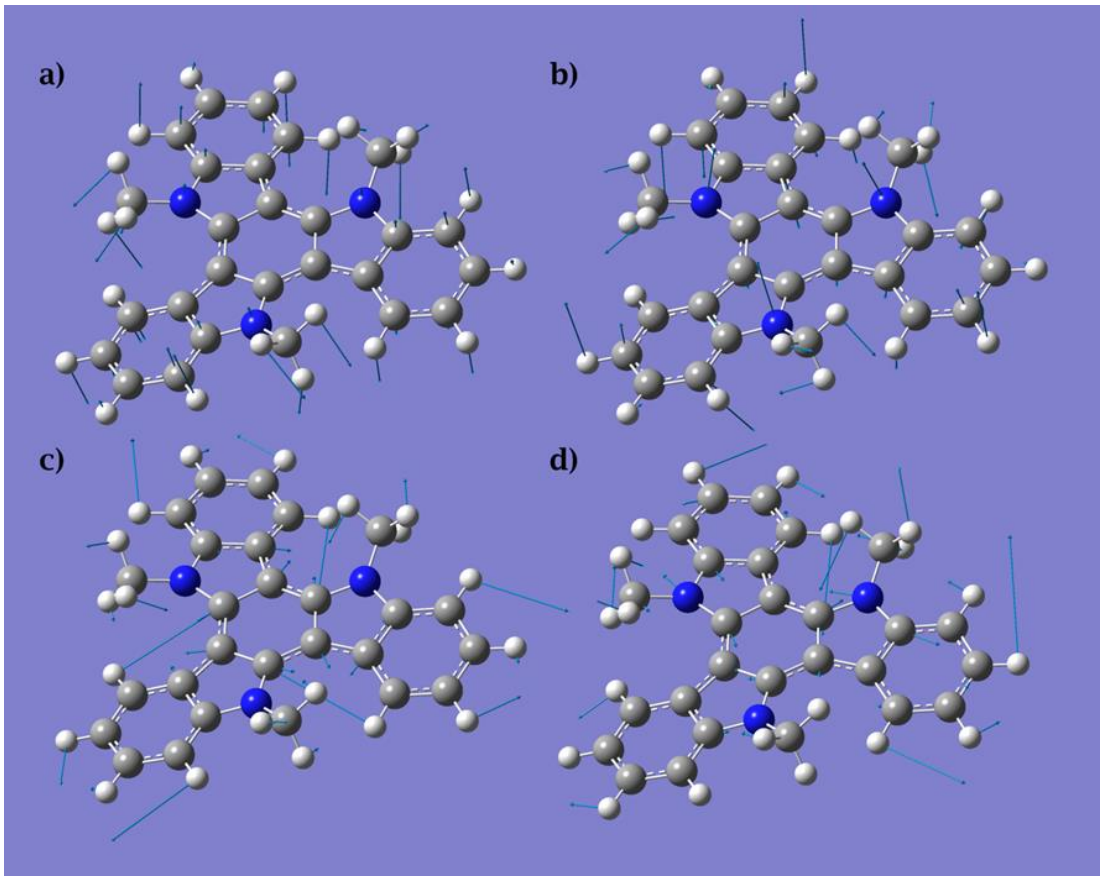

Figure S14. Representation of the **2a** 243 cm^{-1} (a), 293 cm^{-1} (b), 397 cm^{-1} (c) and 1329 cm^{-1} (d) S_1 modes presented in Table S5.

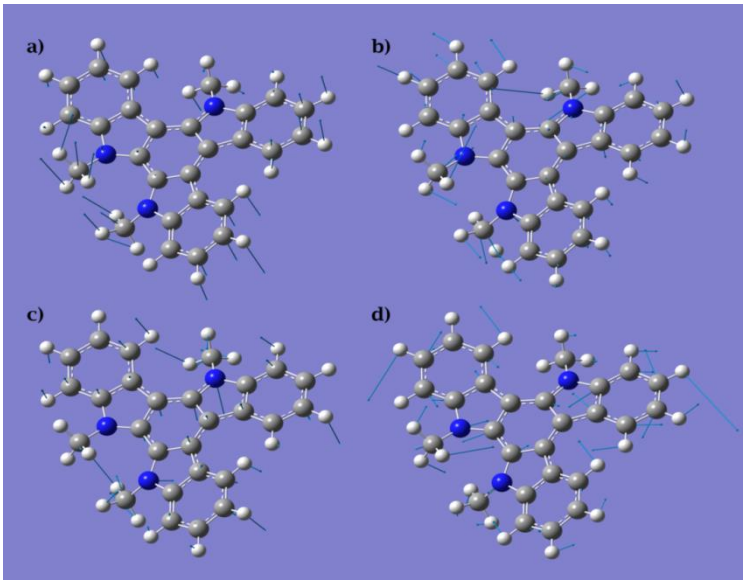

Figure S15. Representation of the **2b** 39 cm^{-1} (a), 262 cm^{-1} (b), 303 cm^{-1} (c) and 1394 cm^{-1} (d) S_1 modes presented in table S6

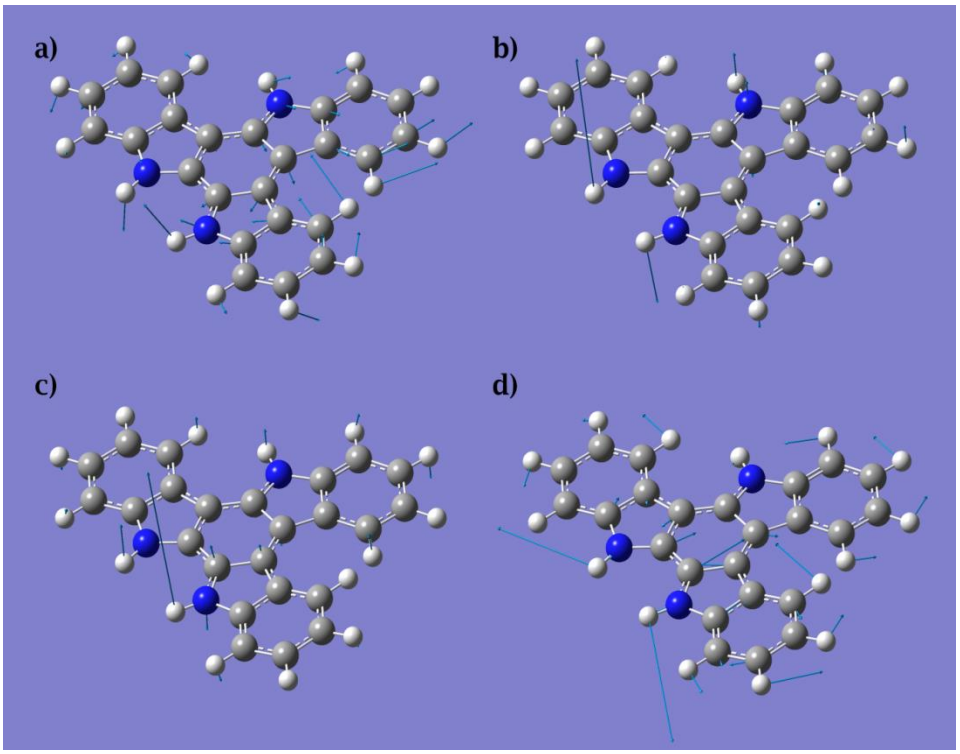

Figure S16. Emission ($S_1 \rightarrow S_0$) vibrational progression of **1a** together with the transitions with intensities larger than 1E-5.

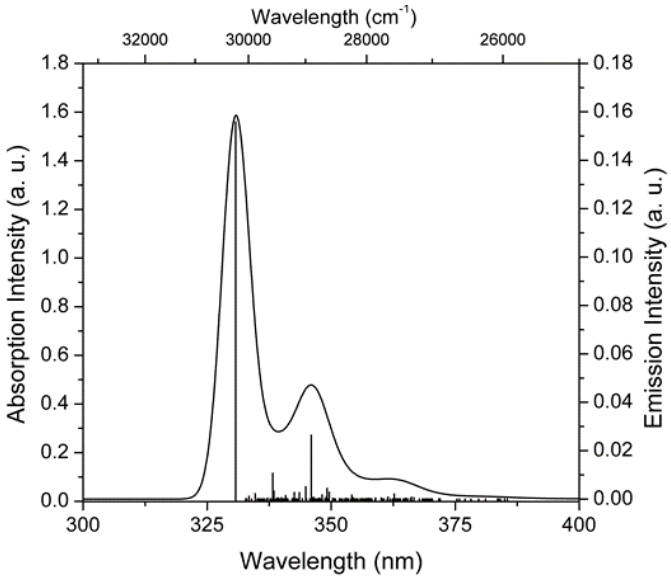

Figure S17. Emission ($S_1 \rightarrow S_0$) vibrational progression of **1b** together with the transitions with intensities larger than 1E-5

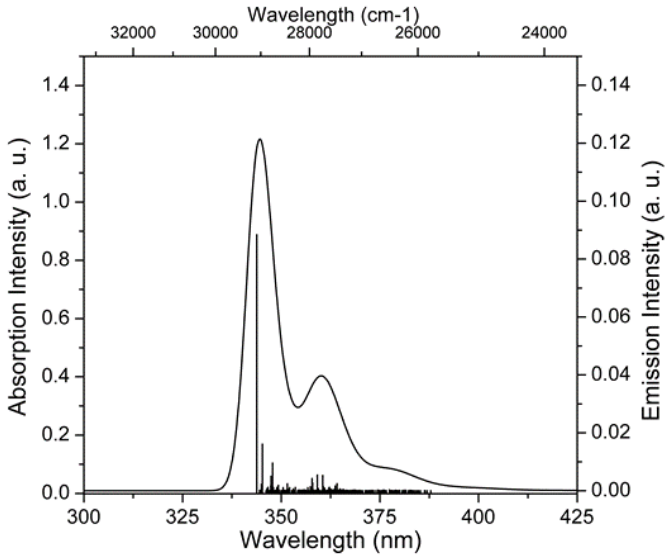

Figure S18. Absorption ($S_0 \rightarrow S_1$) (red) and emission ($S_1 \rightarrow S_0$) (black) vibrational progression of **2a** together with the transitions with intensities larger than 1E-5

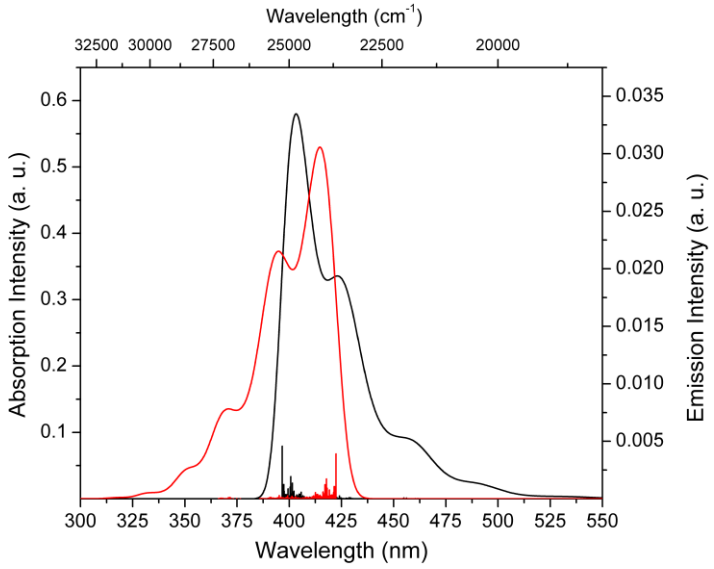

Figure S19. Absorption ($S_0 \rightarrow S_1$) (red) and emission ($S_1 \rightarrow S_0$) (black) vibrational progression of **2b** together with the transitions with intensities larger than 1E-5.

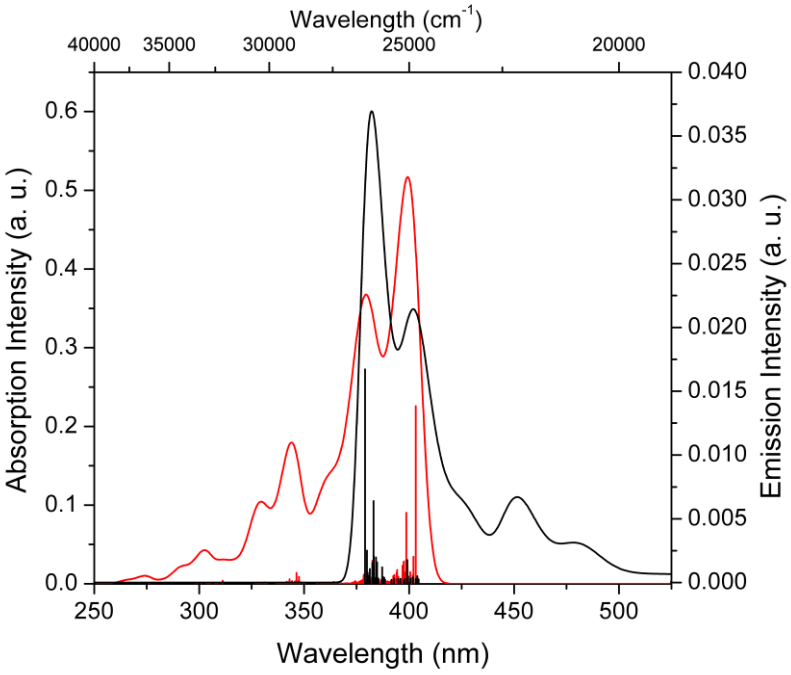

Table S2. $S_1 \rightarrow S_0$ relaxation energies computed by substracting the ground state energy at the S_1 geometry and the ground state energy at the optimized ground state geometry.

compound	DFT//B3LYP/6-31G**
	$\lambda^{S_1 \rightarrow S_0}$ (meV)
1a	67
1b	80
2a	143
2b	177

Table S3. Frequency, S (Huang-Rhys) factor and corresponding relaxation energy for **1a** emission. Only modes with S larger than 0.1 are presented.

Frequency (cm^{-1})	S	λ (meV)
632	0.1	5
1330	0.2	34

Table S4. Frequency, S (Huang-Rhys) factor and corresponding relaxation energy for **1b** emission. Only modes with S larger than 0.1 are presented.

Frequency (cm^{-1})	S	λ (meV)
120	0.2	3
303	0.1	2
333	0.1	5
1149	0.1	10
1243	0.1	15
1340	0.1	12

Table S5. Frequency, S (Huang-Rhys) factor and corresponding relaxation energy for **2a** emission. Only modes with S larger than 0.1 are presented.

Frequency (cm^{-1})	**S**	**λ (meV)**
69	0.1	1
89	0.1	1
139	0.1	1
162	0.1	1
243	0.3	8
264	0.1	4
293	0.2	7
397	0.2	8
1259	0.1	11
1329	0.2	29
1392	0.1	9
3667	0.1	27

Table S6. Frequency, S (Huang-Rhys) factor and corresponding relaxation energy for **2b** emission. Only modes with S larger than 0.1 are presented.

Frequency (cm^{-1})	**S**	**λ (meV)**
39	0.3	2
50	0.2	1
64	0.2	2
102	0.2	2
116	0.1	2
176	0.1	1
262	0.5	17
303	0.2	7
354	0.1	3
362	0.2	9
1145	0.1	10
1250	0.1	8
1394	0.1	15
1648	0.1	14

S.7. SECTION 5.3. *"SADDLE-SHAPED INDOLE CYCLIC TETRAMERS: 3D ELECTROACTIVE MOLECULES"*

Constanza Ruiz, Ángeles Monge, Enrique Gutiérrez-Puebla, Ibon Alkorta, José Elguero, Juan T. López Navarrete, M. Carmen Ruiz Delgado* and Berta Gómez-Lor*

*E-mail: carmenrd@uma.es, bgl@icmm.csic.es

S.7.1. Copy of ^{1}H NMR and ^{13}C NMR spectra of 1a-1d

Copy of ^{1}H NMR spectrum of compound **1a** ($C_2D_2Cl_4$, 500 MHz)

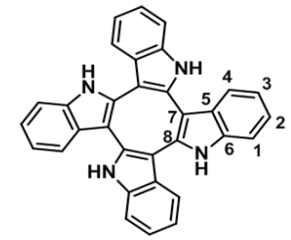

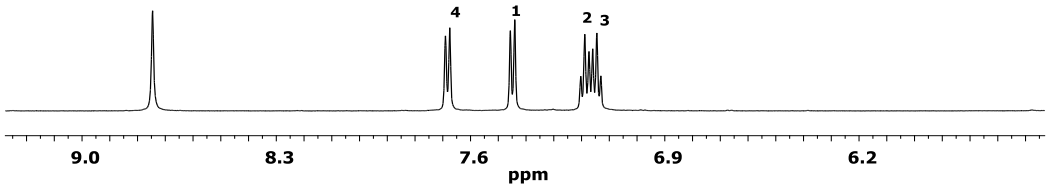

Copy of ^{13}C NMR spectrum of compound **1a** ($C_2D_2Cl_4$, 200 MHz)

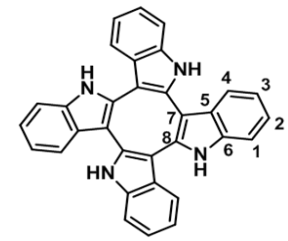

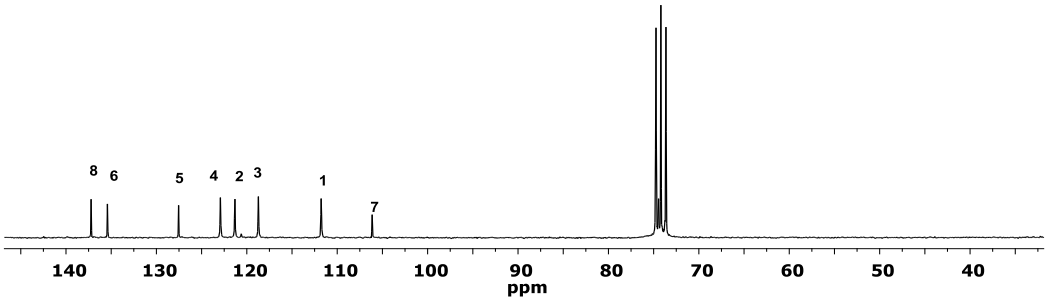

Copy of ^{1}H NMR spectrum of compound **1b** ($CDCl_3$, 200 MHz)

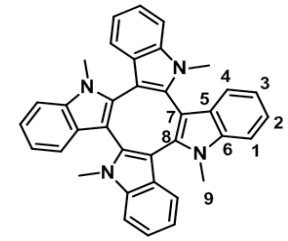

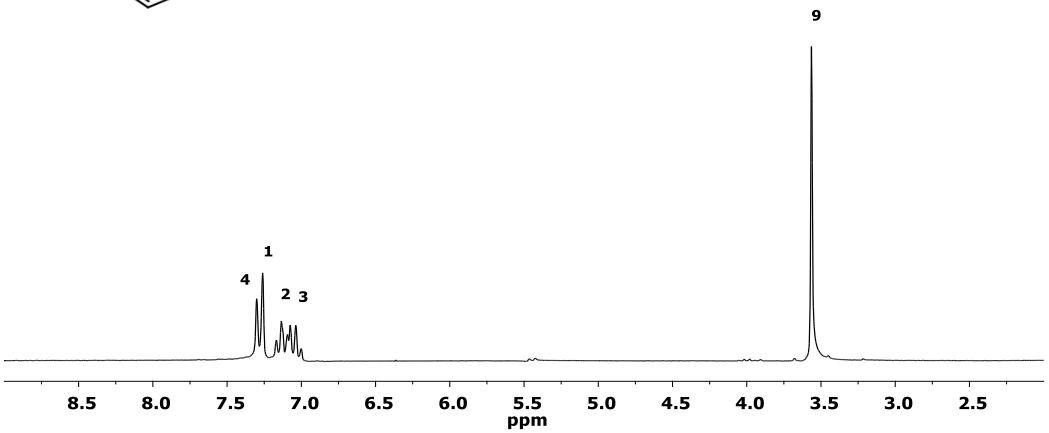

Copy of ^{13}C NMR spectrum of compound **1b** ($CDCl_3$, 50 MHz)

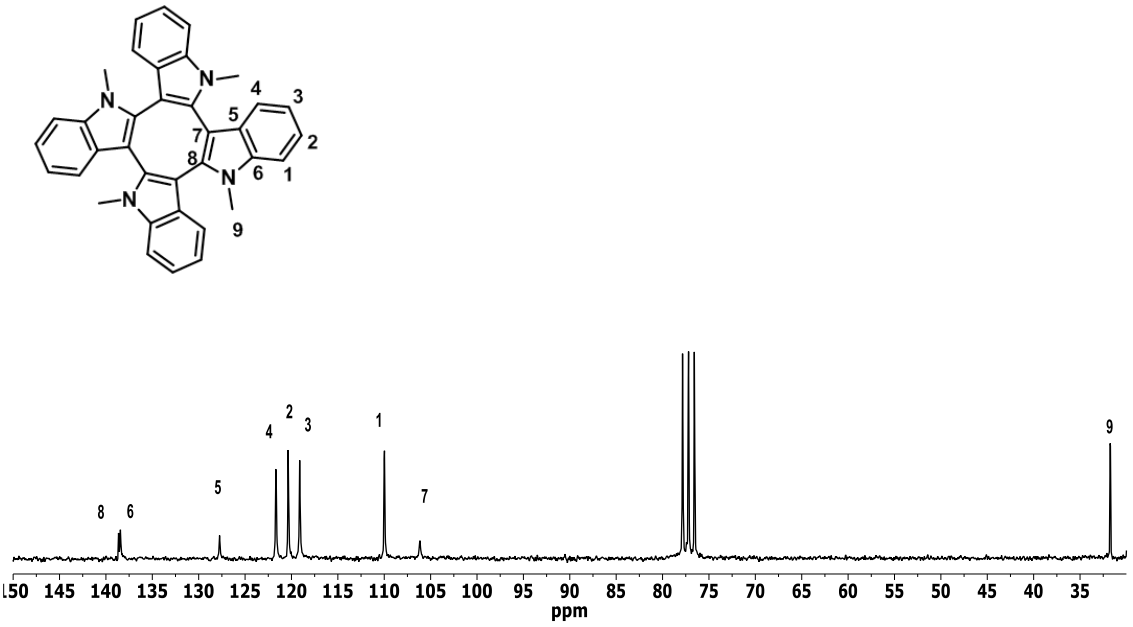

Copy of ^{1}H NMR spectrum of compound **1c** ($C_2D_2Cl_4$, 300 MHz)

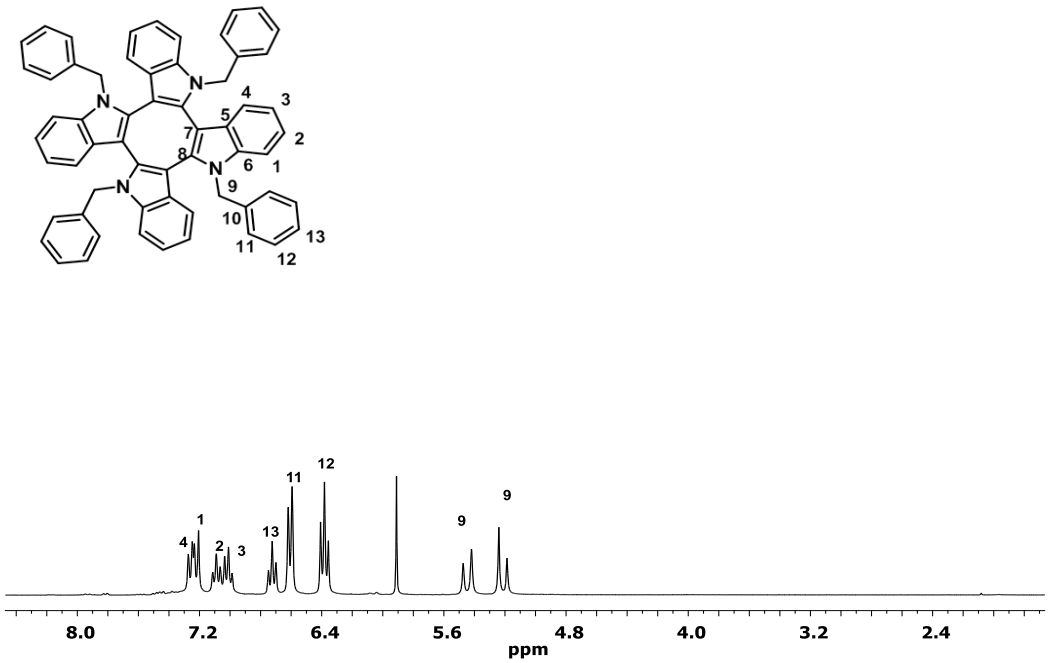

Copy of ^{13}C NMR spectrum of compound **1c** ($C_2D_2Cl_4$, 50 MHz)

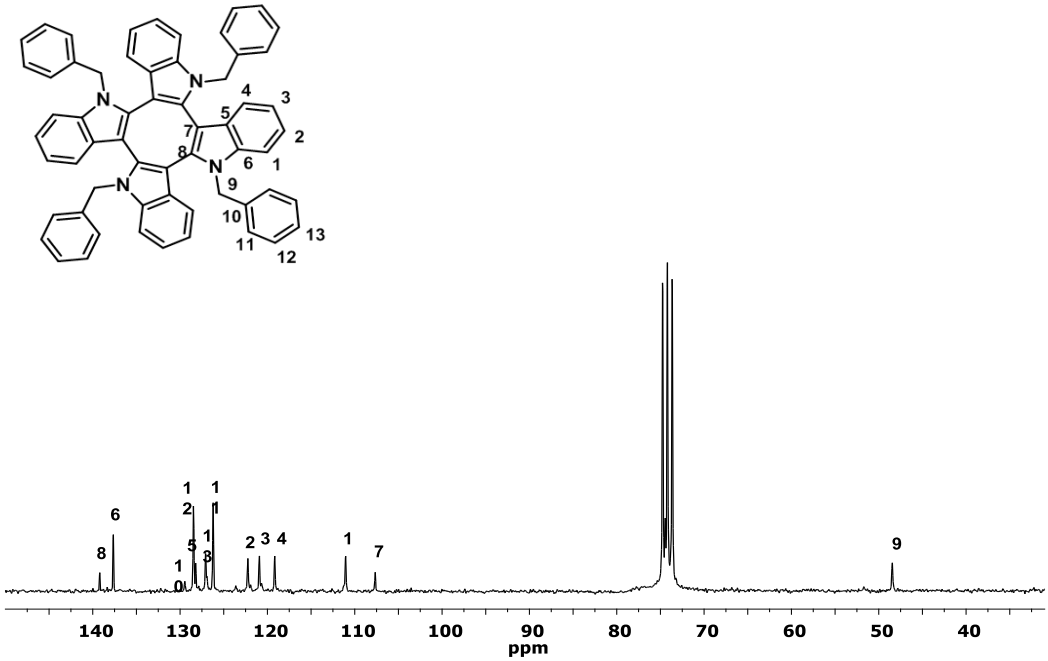

High temperature experiment of **1c** ($C_2D_2Cl_4$,500MHz)

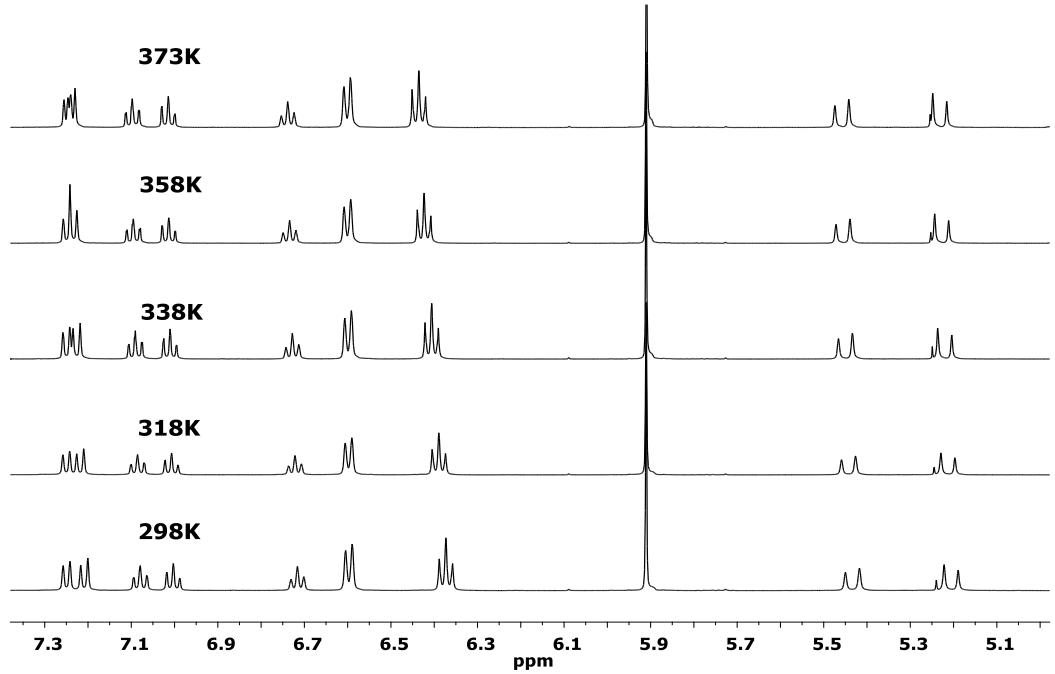

Low temperature experiment of **1c** (CD_2Cl_2, 500MHz)

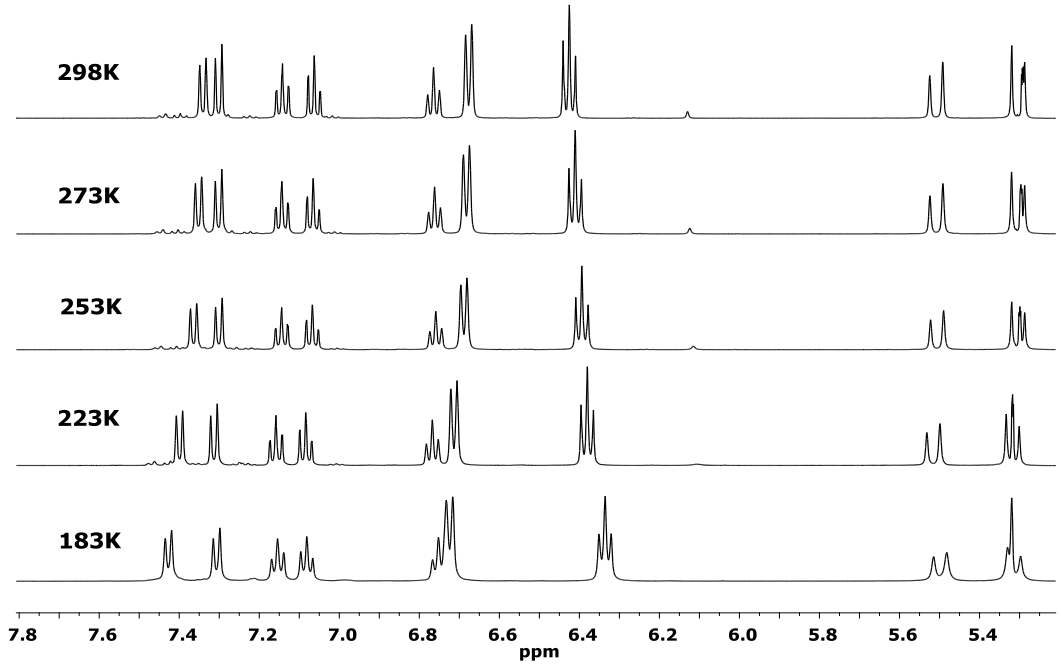

Copy of ^{1}H NMR spectrum of compound **1d** ($CDCl_3$, 300MHz)

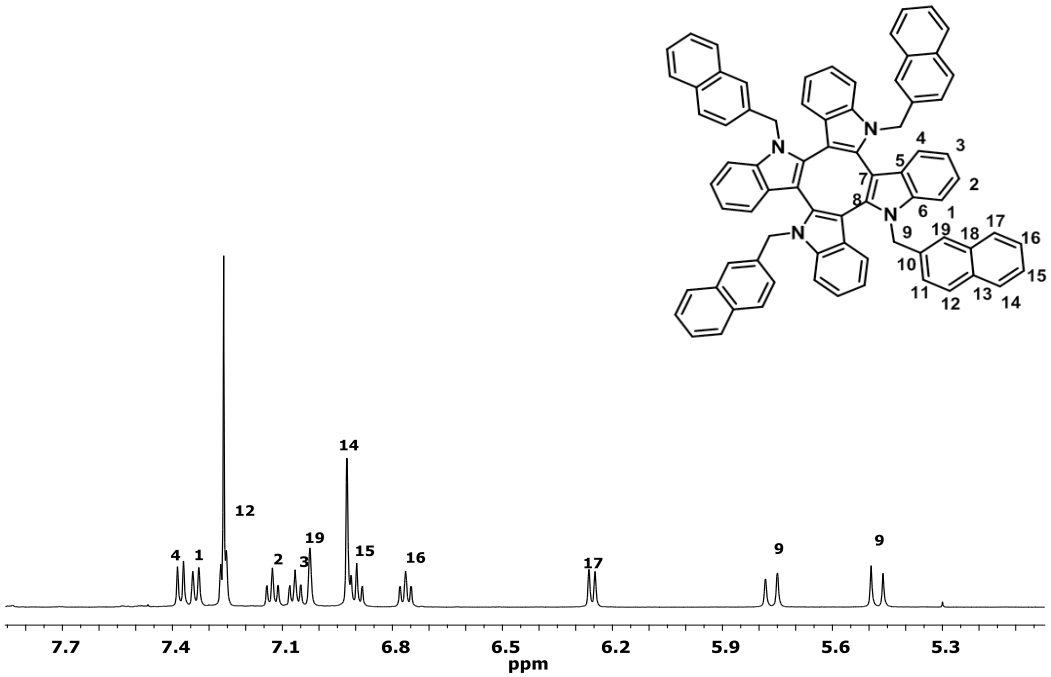

Copy of ^{13}C NMR spectrum of compound **1d** ($CDCl_3$, 50MHz)

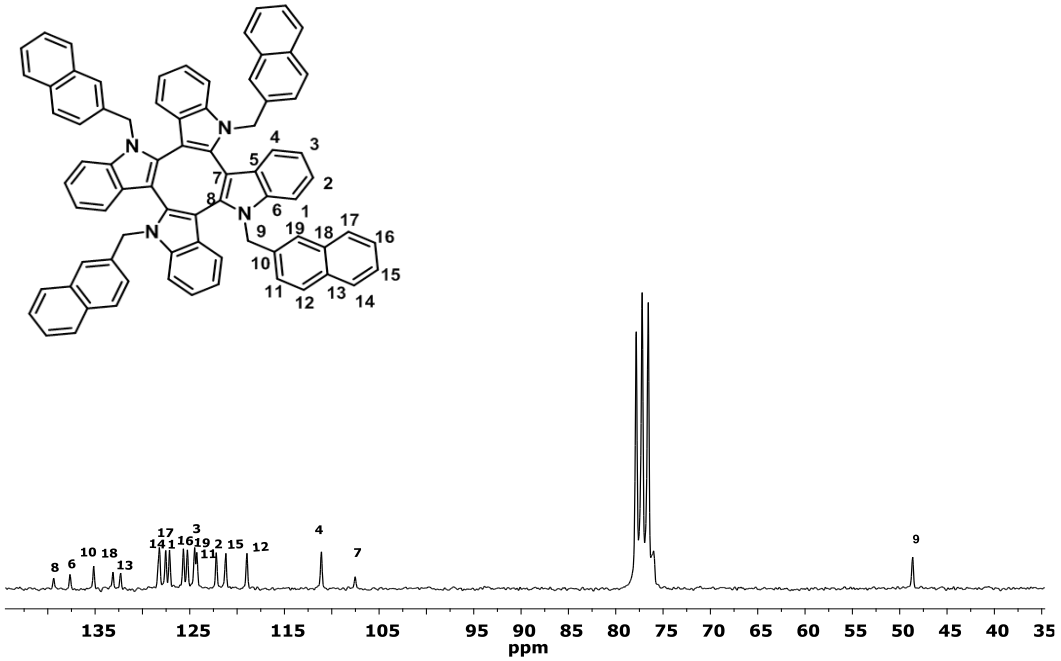

High temperature experiment of **1d** ($C_2D_2Cl_4$, 500MHz)

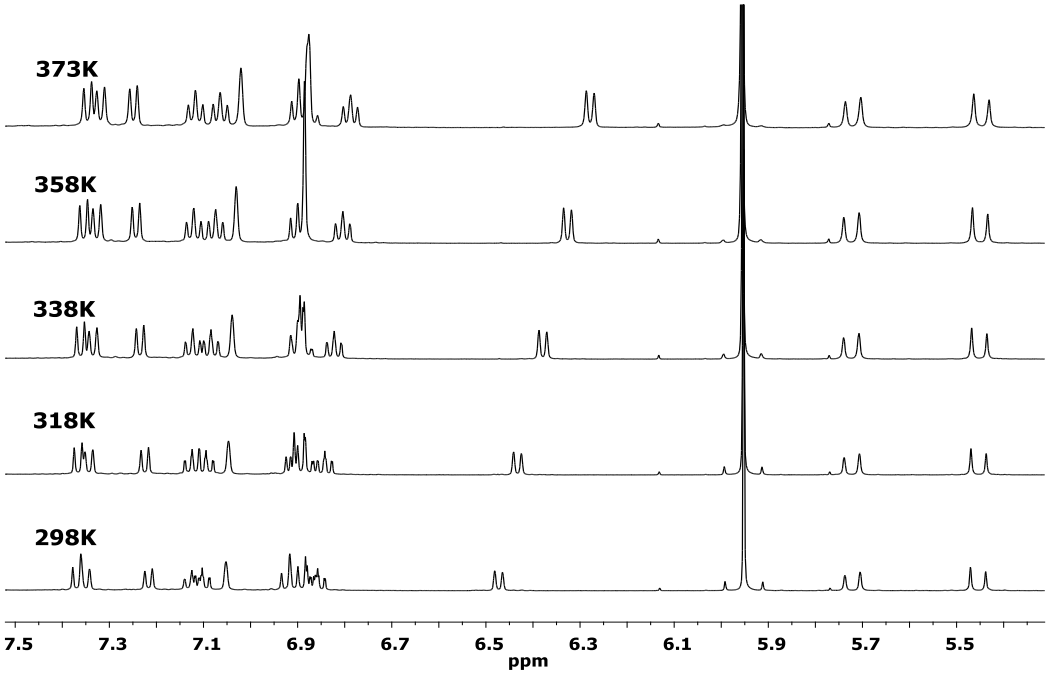

S.7.2. DFT calculations

Table S1. Calculated inversion barriers for **1b-1c** and other compounds containing the cyclooctatetraene ring previously reported.

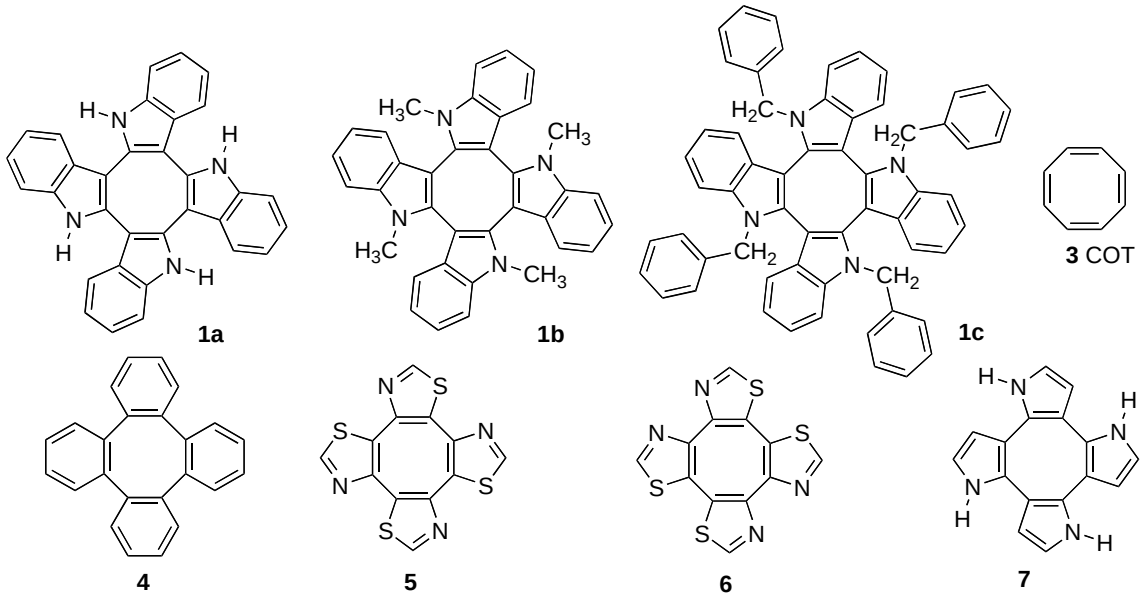

Compound	Barriers (kJ·mol^{-1})			
	B3LYP/ 6-31G(d)	B3LYP/ 6-31+G(d,p)	Literature	Literature
Tetraindole C_4 **6** (**1a**)	119.2	123.5	----	
Tetrametilindole C_4 **7** (**1b**)	279.0	280.1	----	
Tetrabenzylindole C_4 **8** (**1c**)	268.0	269.0	----	----
C_8H_8, COT, D_{4h} **3**	44.1	46.0	~43 (exp.)[1,2,3,4,5]	44.1[1-5]
Tetraphenylene, D_4 **4**	322.1	321.6	568.2*	320.0[7]
Tetrathiazole, C_{4h} **5**	19.9	29.5	28.4[6]	
Tetrathiazole, D_{2h} **6**	90.8	98.6	93.7	
Tetrapyrrole C_{4h} **7**	49.8	51.7	----	

* This value corresponds to a planar structure that it is not the TS.[7,8]

Table S2. Selected parameters (bond lengths and dihedral angle) for experimental and theoretical structures of **1a**-**1d**.

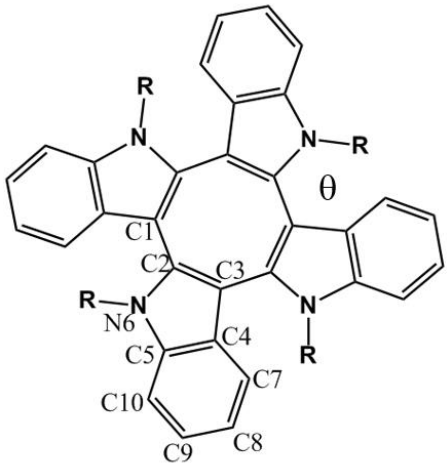

	1a		1b	1c		1d
	Experiment[a]	Calculation[b]	Calculation[b]	Experiment[a]	Calculation[b]	Calculation[b]
Bond Length/Å						
C1-C2	1.461	1.455	1.461	1.461	1.464	1.464
C2-C3	1.368	1.390	1.389	1.379	1.388	1.388
C2-C4	1.442	1.447	1.442	1.442	1.442	1.442
C4-C5	1.393	1.421	1.420	1.406	1.420	1.420
C5-N6	1.376	1.379	1.383	1.402	1.385	1.386
N6-C3	1.377	1.385	1.393	1.378	1.393	1.393
C4-C7	1.408	1.406	1.405	1.385	1.406	1.406
C7-C8	1.381	1.390	1.390	1.383	1.390	1.390
C8-C9	1.390	1.408	1.408	1.402	1.409	1.409
C9-C10	1.380	1.391	1.391	1.388	1.391	1.391
C10-C5	1.391	1.397	1.399	1.381	1.399	1.399
Avearage bend angle θ/°	36.6	34.3	41.5	43.4	43.2	43.3

[a]Experiment data from X-Rav structures. [b]DFT calculated bond lengths at the B3LYP/6-31G**.

Figure S1. DFT calculated bond lengths of triindole and cyclooctatetraene (COT) ring at the B3LYP/6-31G** level.

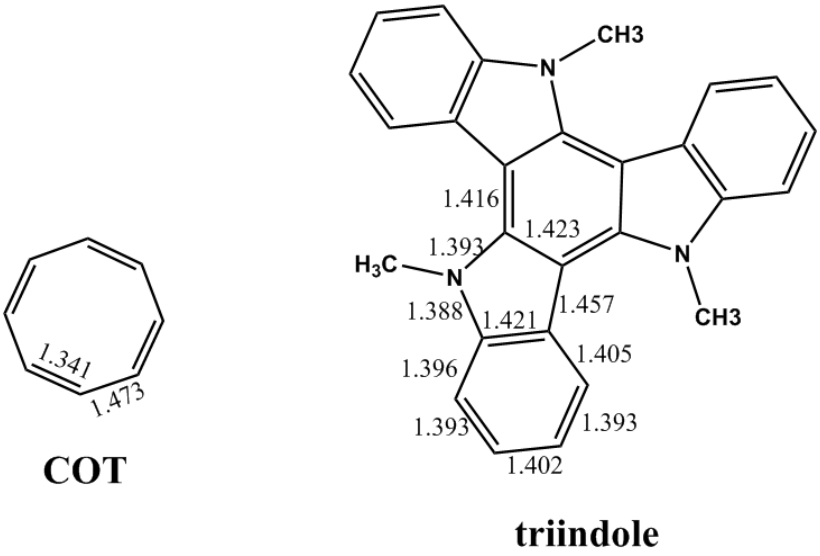

Table S3. Formal oxidation potentials, HOMO energies estimated from cyclic voltammetry data, HOMO energies calculated (B3LYP/6-31G** theoretical data), and DFT-calculated vertical (IEv) ionization energies.

Compound	$E^{o\prime}$ (V)	$HOMO_{exp}$(eV)	$HOMO_{calc}$ (eV)	IEv (eV)
1a	0.54	-4,85	-4.60	5.78
1b	0.72	-5,03	-4.75	5.89
1c	0.81	-5,12	-4.96	5.99
1d	0.86	-5,17	-4.98	5.95
triindole	0.69	-5.07	-4.96	6.27
***N*-trimethyltriindole**	0.73	-5.10	-4.83	6.09

[a] The HOMO energy values were estimated from the first oxidation potential with respect ferrocene/ferrocenium redox couple[9] and considering a value of - 4.8 eV for Fc with respect to zero vacuum level. This value is obtained from the calculated value of - 4.6 eV for the standard electrode potential (E) using a normal hydrogen electrode (NHE) on the zero vacuum level and the value of 0.2 V for Fc vs. NHE.[10,11]

Figure S2. Mülliken atomic charge increments (with respect to the optimized neutral system) of the thienyl rings for cyclic tetraiindole **1b** and triindole homologue as deduced from their DFT-optimized molecular geometries at the B3LYP/6-31G** level.

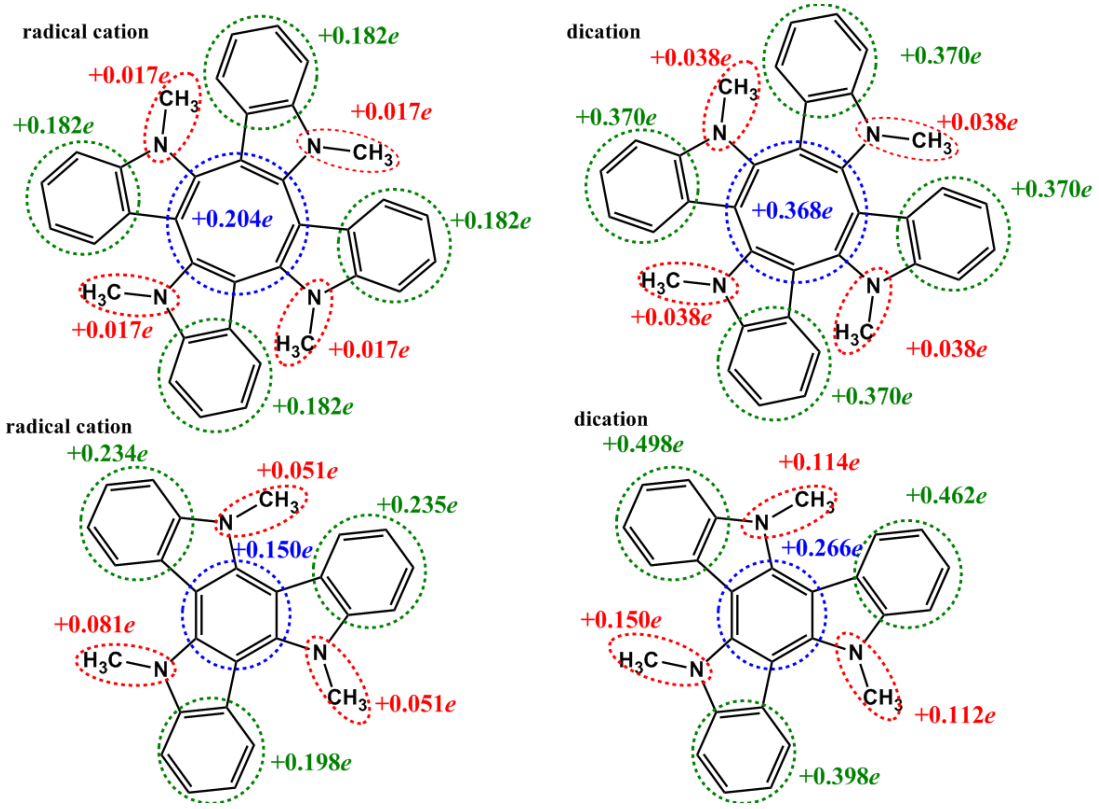

Figure S3. DFT-B3LYP/6-31G** calculated bond-length modifications (Å) for **1b** and **triindole** molecules upon oxidation. The bond length modifications (Δx) larger than 0.010 Å are highlighted in red.

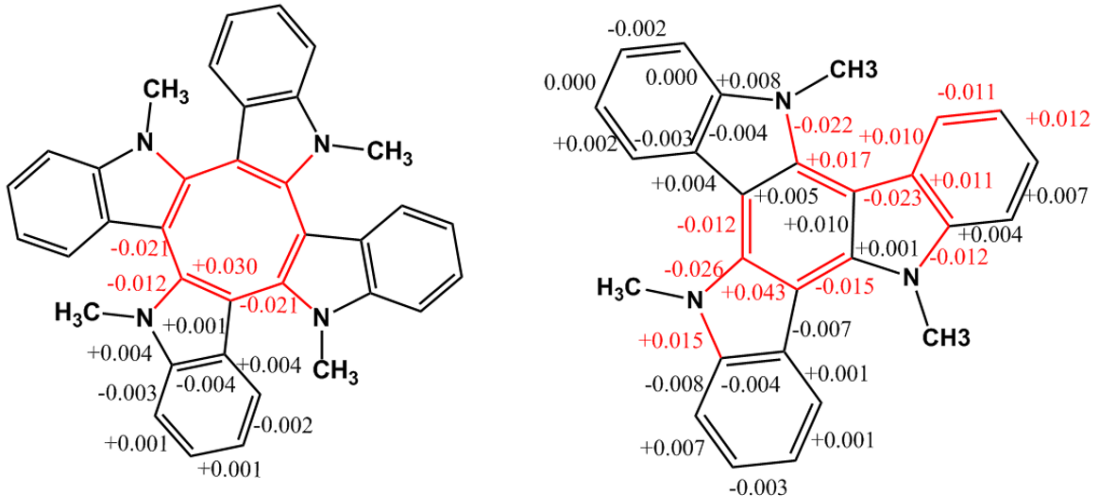

Figure S4. Simulated absorption spectra together with the excitations (wavelength *vs*. oscillator strength) shown as vertical bars as determined with TD-DFT at B3LYP/6-31G** level for tetraindoles **1a-1d** in the neutral state.

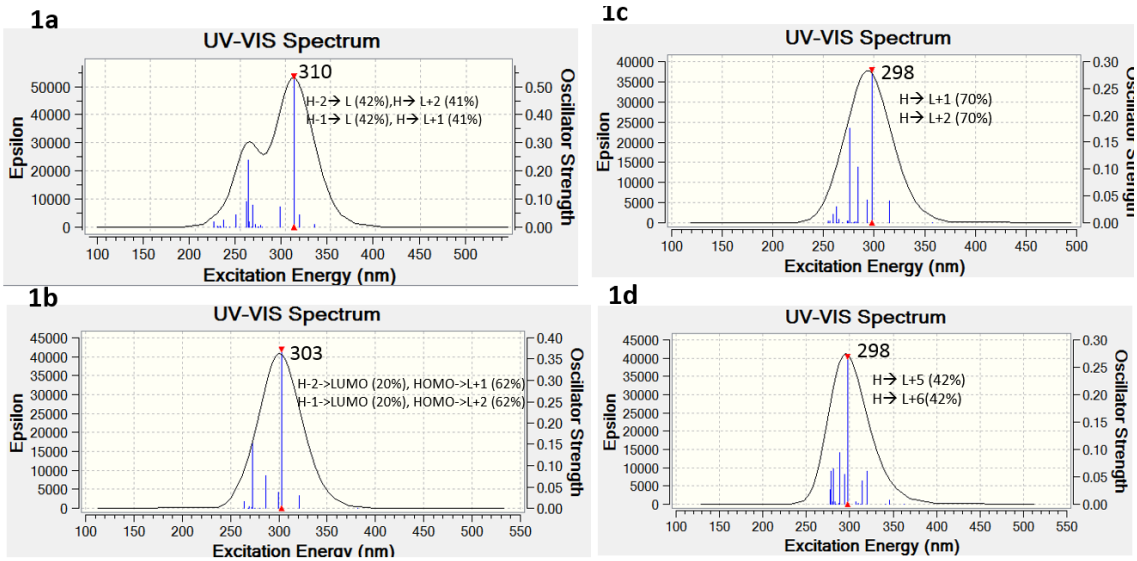

Figure S5. Simulated absorption spectra predicted for the neutral, radical cation and dication of **1b** together with the TD-DFT excitations at the B3LYP/6-31G** level (wavelength versus oscillator strength) shown as vertical bars.

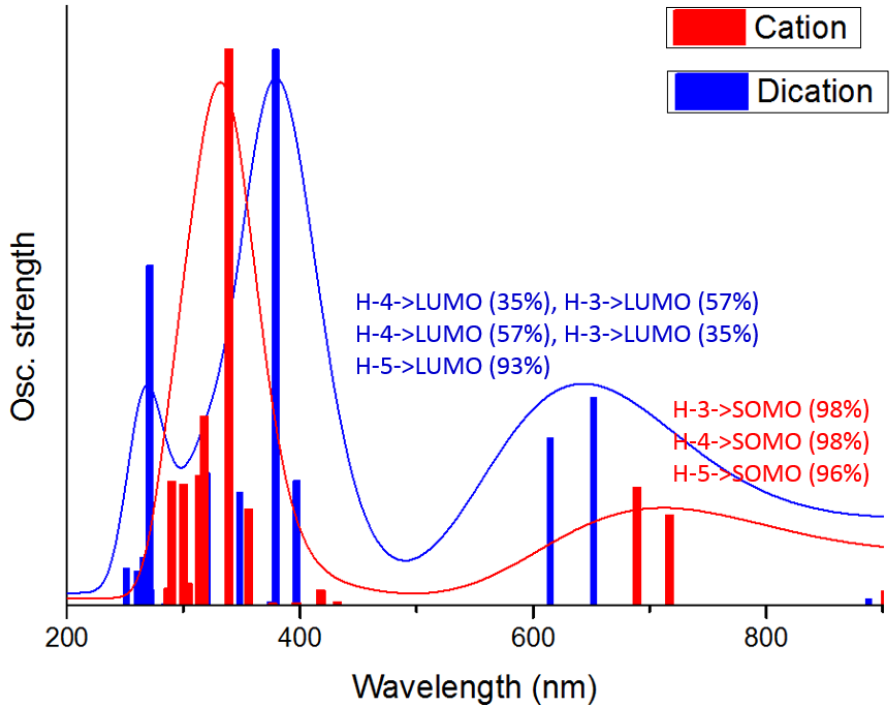

Figure S6. B3LYP/6-31G** molecular orbitals involved in the orbital transitions associated with the optical bands of radical cation (a) and dication (b) species of **1b**.

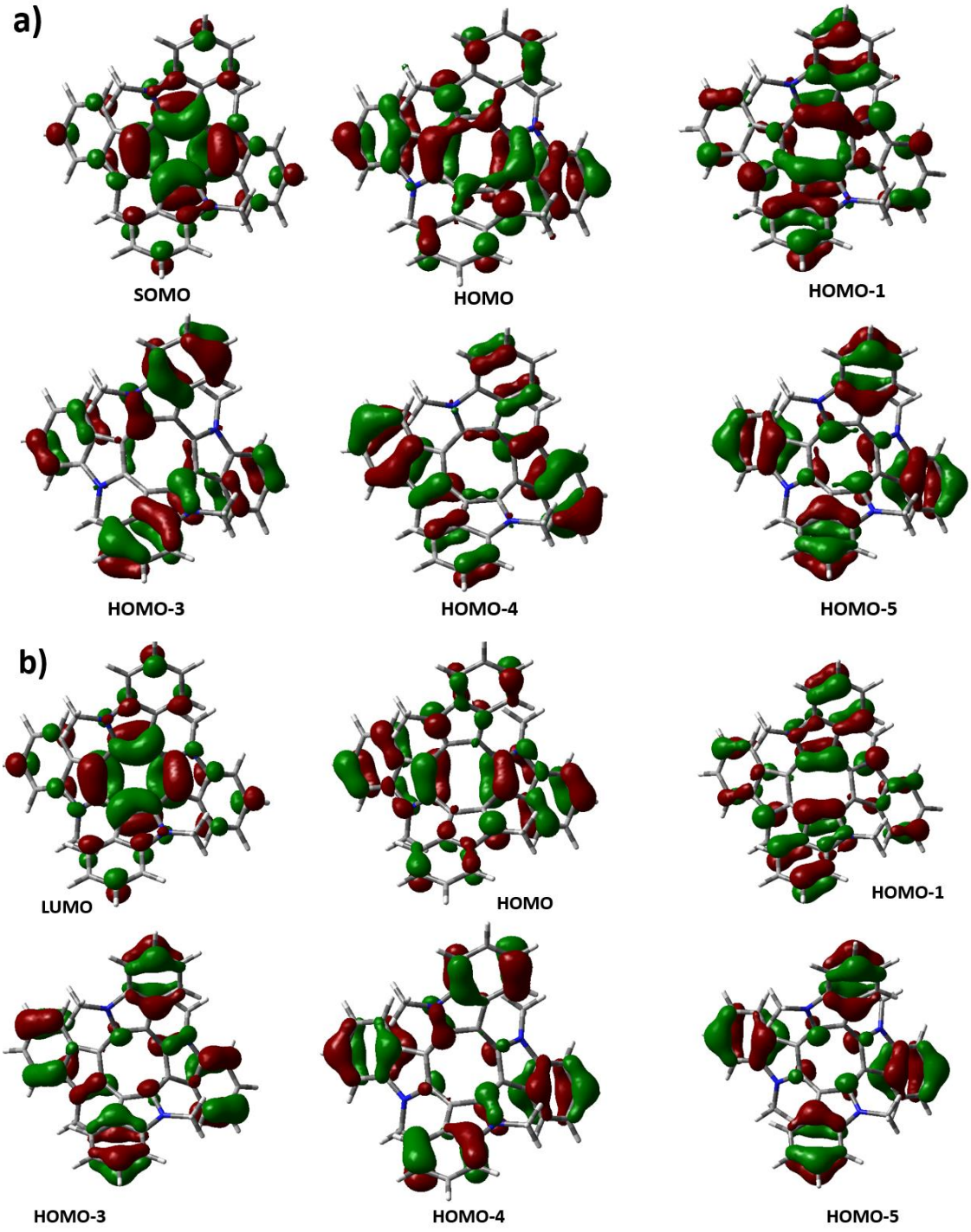

Figure S7. B3LYP/6-31G* vibrational eigenvectors associated with the most outstanding Raman features of **1a**. The measured and theoretical (in parentheses) wavenumbers are given in centimeters^{-1}.

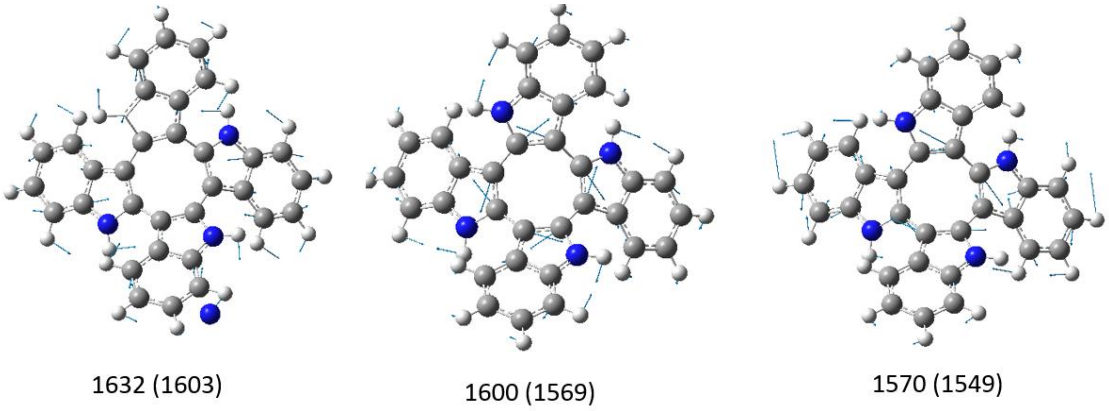

Figure S8. B3LYP/6-311++G(2d,f)//B3LYP/6-31G** NICS(0) values, computed at the geometrical center of the ring from the center of the ring for the individual rings of cyclic tetraiindole 1a, its triindole homologue and the unsubstituted COT ring. Values are given in ppm.

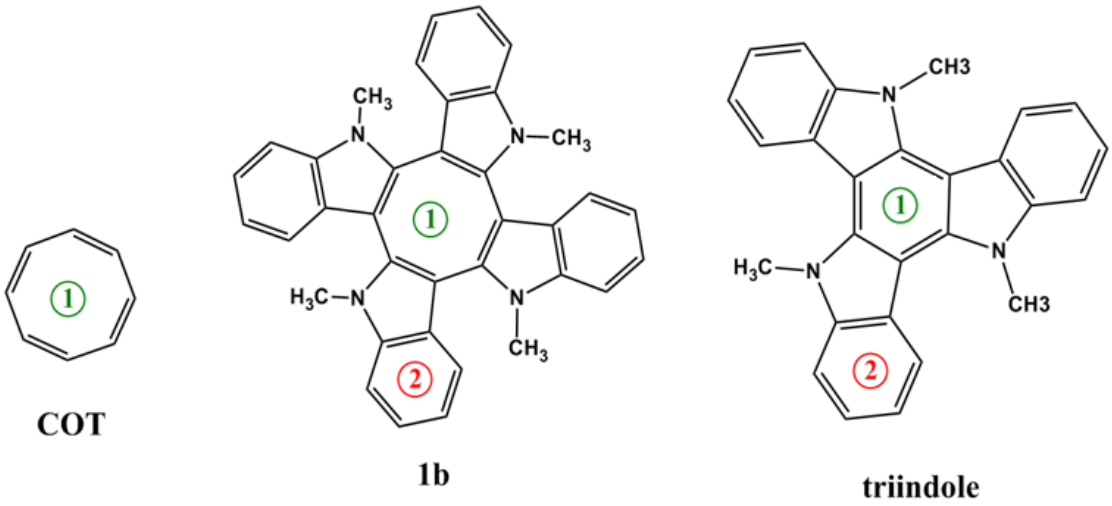

Ring	COT	NICS(0) 1b	triindole
①	+5.34	+3.98	-9.16
②		-8.98	-8.91

S.7.3. Spectroelectrochemical back reduction of 1a-1d

1a)

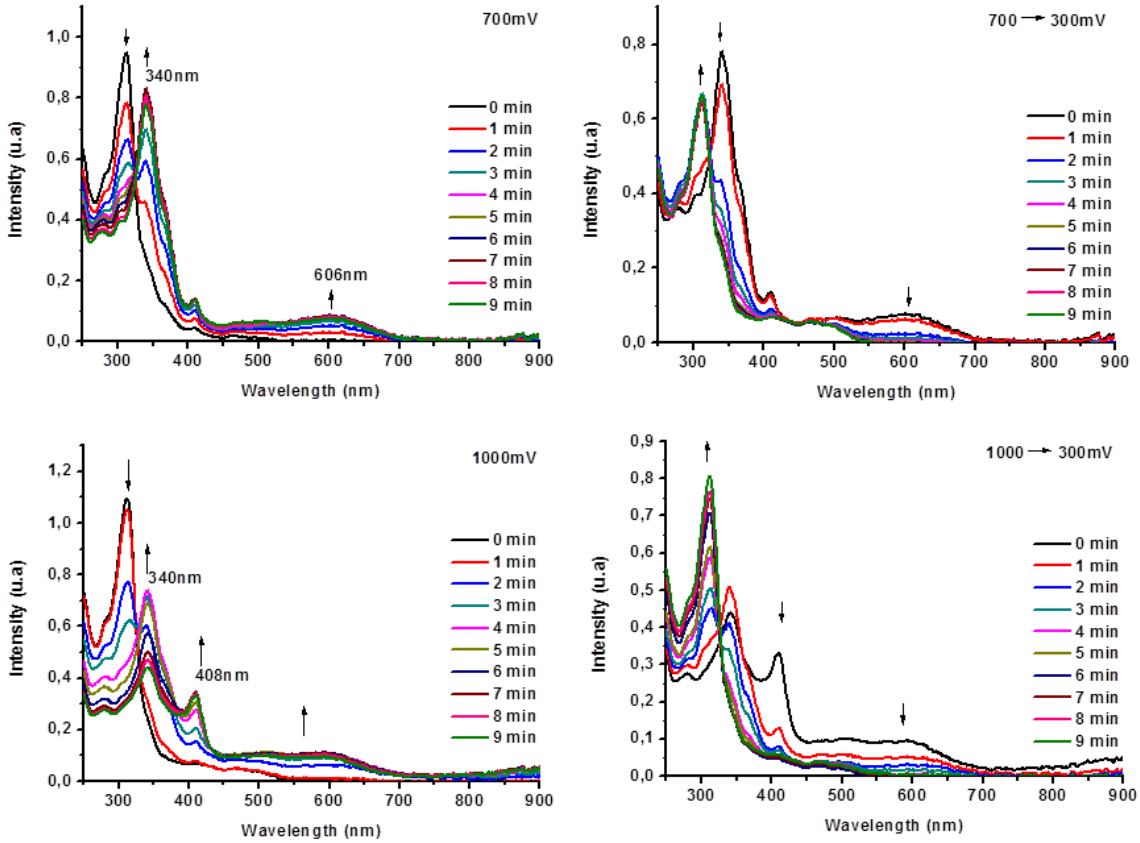

Figure S9: Spectroelectrochemistry of **1a** in CH_2Cl_2 solution containing 0.1 M Bu_4NPF_6 as supporting electrolyte at 700mV and 1000mV, and recovery of the compound 700→300mV and 1000→300mV.

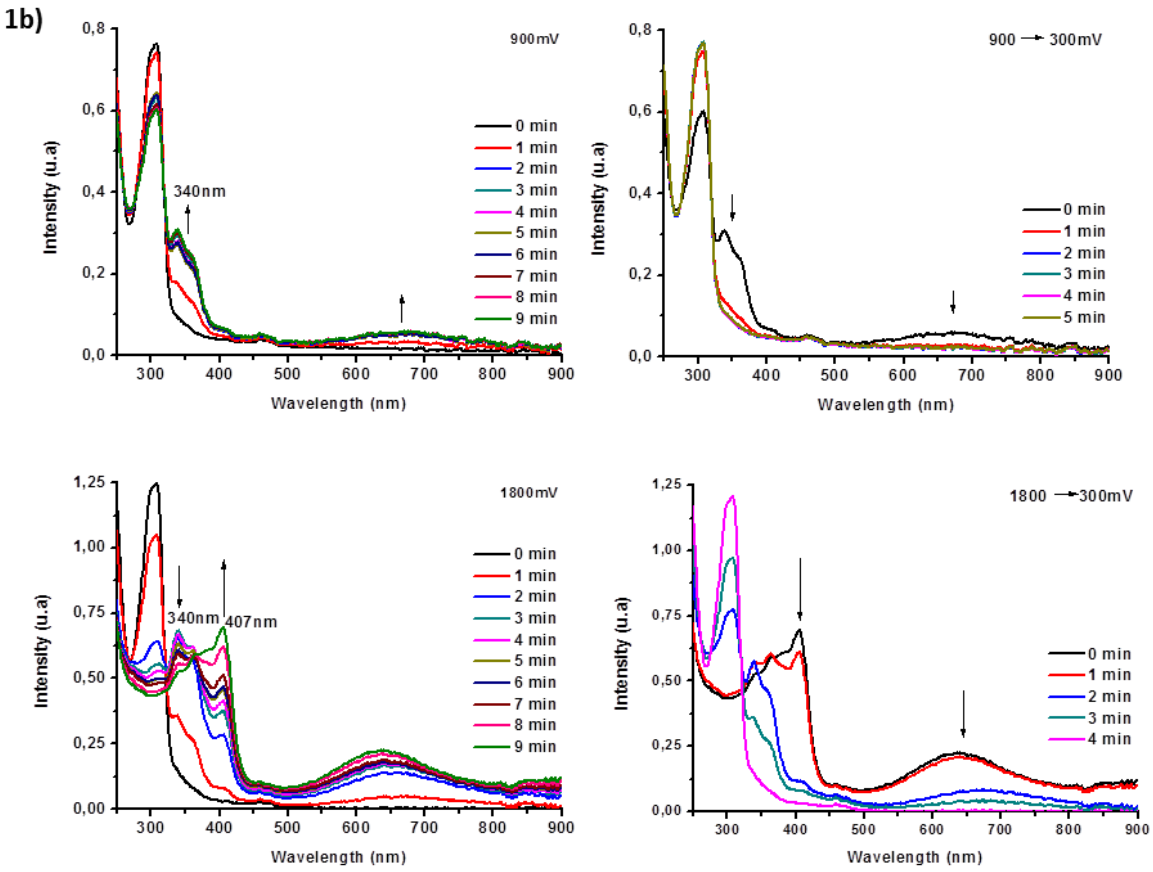

Figure S10: Spectroelectrochemistry of **1b** in CH_2Cl_2 solution containing 0.1 M Bu_4NPF_6 as supporting electrolyte at 900mV and 1800mV, and recovery of the compound 900→300mV and 1800→300mV.

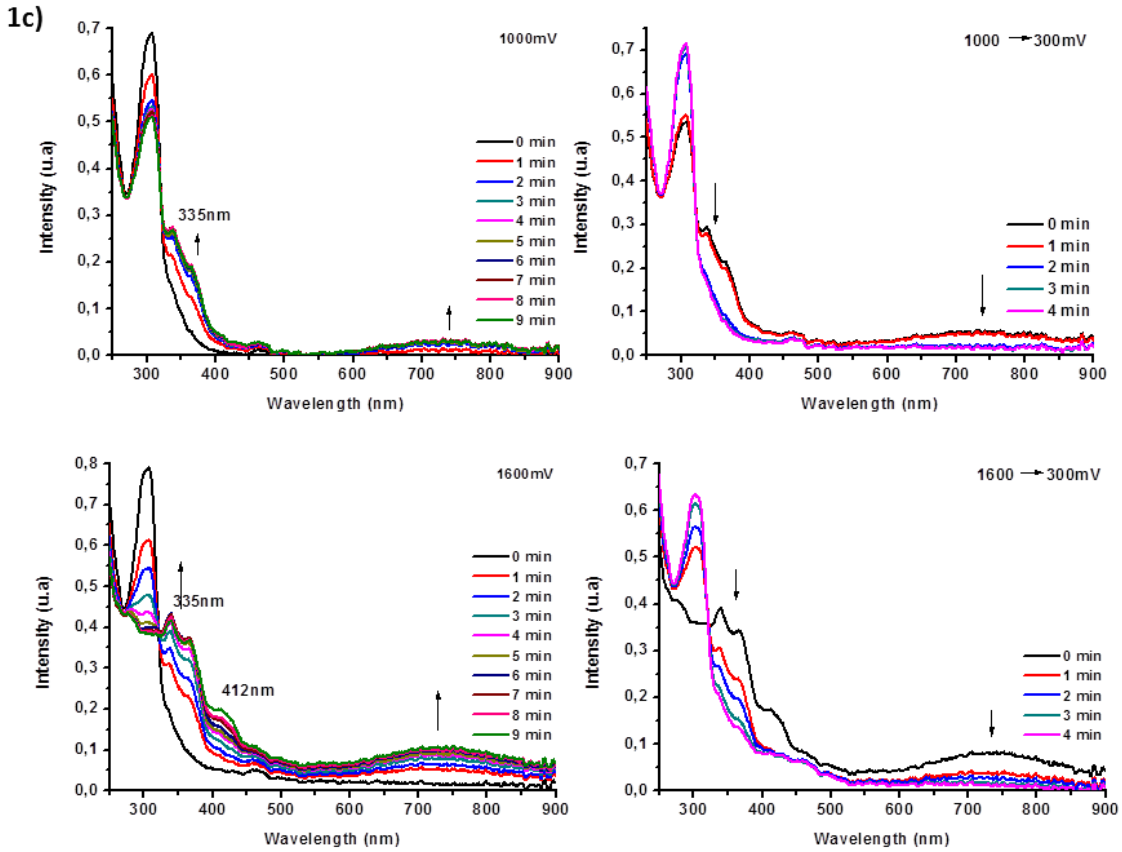

Figure S11: Spectroelectrochemistry of **1c** in CH_2Cl_2 solution containing 0.1 M Bu_4NPF_6 as supporting electrolyte at 1000mV and 1600mV, and recovery of the compound 1000→300mV and 1600→300mV.

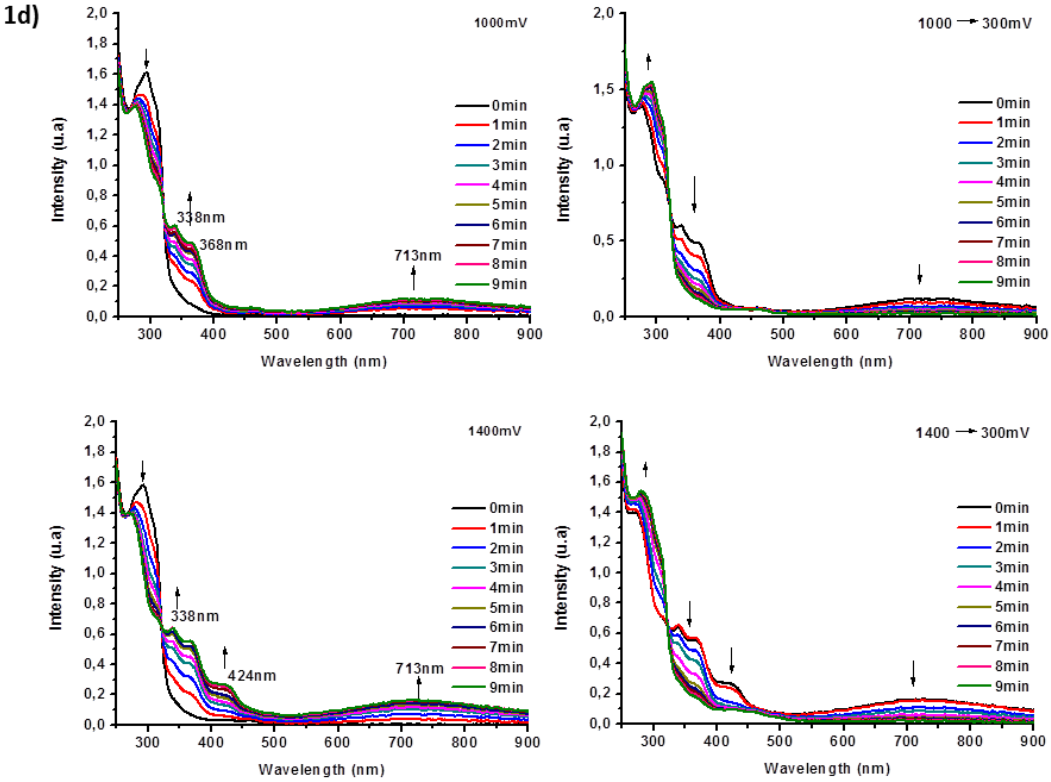

Figure S12: Spectroelectrochemistry of **1d** in CH_2Cl_2 solution containing 0.1 M Bu_4NPF_6 as supporting electrolyte at 1000mV and 1400mV, and recovery of the compound 1000→300mV and 1400→300mV.

REFERENCES

[1] Nishinaga, T.; Ohmae, T.; Iyoda, M.; *Symmetry* **2010**, 2, 76.
[2] Andrés, J. L.; Castaño, O.; Morreale, A.; Palmeiro, R.; Gomperts, R.; *J. Chem. Phys*. **1998**, 108, 203.
[3] Garavelli, M.; Bernardi, F.; Cembran, A.; Castaño, O.; Frutos, L. M.; Merchán, M.; Olivucci, M.; *J. Am. Chem. Soc*. **2002**, 124, 13770.
[4] Schild, A.; Paulus, B.; *J. Comput. Chem*. **2013**, 34, 1393.
[5] Wu, J. I.; Fernández, I.; Mo, Y.; Schleyer, P. v. R.; *J. Chem. Theor. Comput*. **2012**, 8, 1280.
[6] Mouri,K.; Saito,S.; Yamaguchi, S.; *Angew. Chem. Int. Ed*. **2012**, 51, 5971.
[7] Bachrach, S. M.; *J. Org. Chem*. **2009**, 74, 3609.
[8] Huang, H.; Stewart, T.; Gutmann, M.; Ohhara, T.; Niimura, N.; Li, Y. X.; Wen, J. F.; Bau, R.; Wong, H. N. C.; *J. Org. Chem*. **2009**, 74, 359.
[9] Gritzner, G.; Kuta, J.; Recommendations on Reporting Electrode-Potentials in Nonaqueous Solvents (Recommendations **1983**). *Pure Appl. Chem*. **1984**, 56, 461.
[10] Bard, A. J.; Faulkner, L. R.; Electrochemical Methods: Fundamentals and Applications; Wiley: New York, **2001**.
[11] Trassati, S.; *Pure Appl. Chem*. **1986**, *58*, 955.

Publications

- ***Star-shaped hexaaryltriindoles small molecules: Tuning molecular properties towards solution processed organic light emitting devices***
  Organic Electronics, **2012**, 13, 2138–2148. (Chapter 2 of this thesis)

- ***Organic Semiconductors toward Electronic Devices: High Mobility and Easy Processability***
  J. Phys. Chem. Lett, **2012**, 3, 1428−1436.

- ***Symmetry Lowering in Triindoles: Impact on the Electronic and Photophysical Properties***
  J. Phys. Chem. C, **2014**, 118, 5470−5477. (Chapter 5 of this thesis)

- ***Triindole-Bridge-Triindole Dimers as Models for Two Dimensional Microporous Polymers***
  Org. Lett. **2015**, 17, 2258−2261. (Chapter 4 of this thesis)

Submitted publications:

- ***The Role of CH-π Interactions in the Crystal Morphology and Packing of N-trialkylated Triindoles***
  Submitted to: *Crystal Growth & Design* **2016** (cg-2016-00144v) (Chapter 1 of this thesis)

- ***Saddle-shaped indole cyclic tetramers: 3D electroactive molecules***
  Submitted to: *Chemistry - A European Journal* **2016**, (chem.*201600932*) (Chapter 5 of this thesis)

Organic Electronics 13 (2012) 2138–2148

Contents lists available at SciVerse ScienceDirect

Organic Electronics

journal homepage: www.elsevier.com/locate/orgel

Star-shaped hexaaryltriindoles small molecules: Tuning molecular properties towards solution processed organic light emitting devices

Carmen Coya [a,*], Constanza Ruiz [b], Ángel Luis Álvarez [a], Susana Álvarez-García [a,c], Eva M. García-Frutos [b], Berta Gómez-Lor [b,*], Alicia de Andrés [b,*]

[a] Escuela Superior de Ciencias Experimentales y Tecnología, Electronic Technology Department, Universidad Rey Juan Carlos, 28933 Madrid, Spain
[b] Instituto de Ciencia de Materiales de Madrid, Cantoblanco, 28049 Madrid, Spain
[c] Instituto Química-Física Rocasolano, CSIC, C/Serrano 119, 28006 Madrid, Spain

ARTICLE INFO

Article history:
Received 20 February 2012
Received in revised form 14 June 2012
Accepted 15 June 2012
Available online 28 June 2012

Keywords:
Solution processing
Molecular OLED
Blue emitters

ABSTRACT

We present a series of differently substituted star-shaped hexaaryltriindoles with tunable light-emitting properties. The deep blue emission is unchanged by donor peripheral substituents while an increasing acceptor character produces a reduction of the optical gap, an increased Stokes shift and eventually leads to the appearance of a new electronic level and to the simultaneous deep blue (413 nm) and green (552 nm) emission in solution. Quenching by concentration increases with the acceptor character but is lower as the tendency of these compounds to aggregate is stronger. Solution processed thin films present optical and morphological qualities adequate for device fabrication and similar electronic structure compared to solutions with an emission range from 423 nm up to 657 nm (red), demonstrating the possibility of tuning the energy levels by chemical functionalization. We have fabricated and characterized single-layer solution processed organic light emitting diodes (OLED) to investigate the influence on transport and emission properties of the substituting species. We analyzed the *I–V* response using a single-carrier numerical model that includes injection barriers and non-uniform electric-field across the layer. As a result, we obtained the electric field dependence of the mobility for each device. Best results are obtained on the most electron rich derivative functionalized with six donor methoxy groups. This material shows the highest emission efficiency in solid state, due to aggregation-induced enhancement, and better transport properties with the highest mobility and a very low turn-on voltage of 2.8 V. The solution processed OLED devices produce stable deep blue (CIE coordinates (0.16,0.16)) to white (CIE coordinates (0.33,0.3)) emission with similar luminous efficiencies.

1. Introduction

In recent years an intense research effort has facilitated that a new generation of devices based on organic materials enters the market. Organic semiconductors offer great expectations in the development of low-cost, flexible and large-area devices (properties difficult to achieve with conventional electronics) but also the possibility of fine tuning key properties (luminescence, absorption, energy band gaps, and charge transport) through a convenient molecular design. A wide variety of polymers and small molecule organic semiconductors have been developed and investigated in devices such as organic thin-film transistors (OTFTs), organic photovoltaic cells (OPVs), and organic light-emitting diodes (OLEDs).

Amenability to solution or wet processing, is an inevitable prerequisite for large area, low cost mass production, and must be taken into consideration when designing mol-

* Corresponding authors.
E-mail address: ada@icmm.csic.es (A. de Andrés).

1566-1199/$ - see front matter © 2012 Elsevier B.V. All rights reserved.
http://dx.doi.org/10.1016/j.orgel.2012.06.018

ecules for organic active layers [1]. Conjugated polymers, usually amorphous materials can be easily processed from solution to yield homogeneous and uniform thin films, ideally suited for optoelectronics. However, small molecule semiconductors offer intrinsic advantages over polymeric materials in terms of ease of synthesis and purification. Owing to their monodisperse nature with well-defined chemical structure, they can be reproducibly prepared, functionalized and purified and batch-to batch variations common in polymeric materials are not a problem. These considerations make small molecules ideal candidates for structure-properties studies.

Incorporation of flexible alkyl chains is a useful strategy for enhancing the solubility of small molecules, facilitating wet processing. On the other hand, incorporation of bulky substituents able to promote various conformers, have successfully prevented easy packing of the molecules and hence ready crystallization resulting in excellent film-forming abilities and morphological stability in properly designed molecules. We have recently became interested in new organic semiconductor, the electron-rich 10,15-dihydro-5*H*-diindolo[3,2-a:3′,2′-c]carbazole (triindole). Triindole-based single crystalline [2] or liquid crystalline materials have been found to exhibit high hole mobilities [3,4] since they combine the good hole transport properties of carbazoles with a high tendency to form columnar supramolecular arrangements owing to their disk-like extended π-surface. Devices, such as OFETs [5] and OLEDs [6] have been fabricated using triindole-based semiconductors.

In addition, this platform provides two different locations for structural modification, essential to tailor electronic and self-assembling properties. Nitrogen can be easily *N*-substituted, while starting from known hexabromine triindol, the exploitation of cross-coupling methodologies opens flexible strategies to various functionalizations. Taking advantage of this chemical versatility we have introduced in this platform flexible *N*-alkyl chains intended to induce solubility (long alkylic chains) and peripheral bulky aryl groups that impede crystallization [7] to render a family of star-shaped hexaaryl triindoles that can be easily processed from solution to give good film-forming properties. A study of the electronic character of the peripheral substituents on the self-association behavior in these series indicates that the electron-donating character of the terminal substituents facilitates self-association while electron-withdrawing groups inhibit aggregation in agreement with important contributions of solvophobic and CH-π interactions in the self-assembly process. In fact attaching six strong donor methoxy groups result in a material that is liquid crystals in a broad range of temperature [8].

In this work, we show how the electronic communication of the external substituents with the central electron-rich triindole facilitates the tuning of the light-emitting properties and HOMO–LUMO levels. We study these small molecular materials in amorphous thin film morphology and we report emission and transport properties of solution processed OLEDs based on three representative triindole derivatives. The fabricated OLEDs have simple structure: glass/indium-tin oxide (ITO)/poly(3,4-ethylenedioxythiophene)-poly(styrenesulfonate) (PEDOT:PSS)/active layer/Ca/Al. The devices allow us to study the current–voltage (*I–V*) response using a numerical model that includes field-dependent carrier mobility under a single carrier approach. The mobility dependence with electric field and the electroluminescence (EL) performance is discussed.

2. Experimental

2.1. Synthesis and characterization of 2,3,7,8,12,13-Hexakis-(p-formylphenyl)-5,10,15-tris-(dodecyl)-10,15-dihydro-5H-diindolo[3,2-a:3′,2′-c]carbazole (1e)

A mixture of *N*-dodecylhexabromotriindole [9] (100 mg, 0.075 mmol), $Pd(PPh_3)_4$ (43 mg, 0.037 mmol), 4-formylphenyl boronic acid (136 mg, 0.907 mmol) in 0.5 mL of 2 M aqueous K_2CO_3 and 4 mL of THF was degassed. The mixture was heated at 90 °C for 4 days under nitrogen. The orange suspension was partitioned between H_2O and CH_2Cl_2, and the organic phase dried ($MgSO_4$). The solvent was evaporated and the residue was precipitated with acetone and acetonitrile to give **1e** as a yellow solid (78 mg, 70%): mp:173–176 °C, ^{1}H NMR (200 MHz, $CDCl_3$) δ 10.02 (s, 6H), 8.37 (s, 3H), 7.82 (d, J = 8.0, 12H), 7.68 (s, 3H), 7.46 (d, J = 8.0, 12H), 4.99 (m, 6H), 2.10 (m, 6H), 1.05 (m, 54H), 0.85 (t, J = 6.7, 9H); ^{13}C NMR (50 MHz, $CDCl_3$) δ 191.8, 191.7, 148.7, 148.10, 140.8, 140.0, 134.8, 134.6, 134.4, 132.0, 131.0, 130.8, 129.6, 123.6, 123.2, 112.2, 103.2, 47.4, 31.8, 30.3, 29.6, 29.5, 29.4, 29.3, 26.7, 22.6, 14.1; UV (CH_2Cl_2, 25 °C) λ_{max} (log ε) 361 (4.99); MALDI-TOF MS *m/z* 1475 (M^+); HRMS (MALDI-TOF) calcd. for $C_{102}H_{111}N_3O_6$: 1473.84674, found: 1473.84387.

2.2. Synthesis and characterization of 2,3,7,8,12,13-Hexakis-(p-dicyanomethyl)-5,10,15-tris-(dodecyl)-10,15-dihydro-5H-diindolo[3,2-a:3′,2′-c]carbazole(1f)

To a mixture of **1e** (100 mg, 0.067 mmol), malononitrile (53.5 mg, 0.435 mmol), pyridine (0.13 mL, 1.62 mmol) and CH_2Cl_2 (20 mL), titanium (IV) chloride (0.11 mL, 0.81 mmol) was added. The mixture reaction mixture was stirred overnight at room temperature. The suspension was partitioned between H_2O and CH_2Cl_2, and the organic phase dried ($MgSO_4$). The solvent was evaporated and the residue was washed with MeOH to yield **1f** as a red solid (87 mg, 74%): ^{1}H NMR (200 MHz, $CDCl_3$) δ 8.35 (s, 6H),7.89 (d, J = 7.5H, 12H,), 7.69 (s, 3H), 7.48 (s, 3H), 7.46 (d, J = 7.5H, 12H), 5.00 (m, 6H), 2,08 (m, 6H), 1,21(m, 54H)., ^{13}C NMR (50 MHz, $CDCl_3$) δ 158.9, 153.6, 148.8, 148.1, 141.0, 140.3, 134.3,131.38, 130.8, 129.5, 129.2, 123.9, 123.6, 113.7, 112.8, 112.5, 103.3, 82.5, 82.3,47.4, 31.9, 29.6, 29.3, 26.7, 22.6, 14.1, UV (CH_2Cl_2, 25 °C) λ_{max} (log ε) 230 (5.25), 338 (5.55), 434 (5.24); MALDI-TOF MS *m/z* 1763 (M^+); HRMS (MALDI-TOF) calcd. for $C_{102}H_{111}N_3O_6$: 1762.9173, found: 1762.9134.

2.3. Optical measurements

Optical absorption and photoluminescence (PL) spectra of the material in solution and in thin films on quartz substrates have been measured at room temperature. The absorption spectra were recorded with a Varian spectrophotometer

model Cary 4000. PL was excited with the 365 nm line of a Hg lamp, and analyzed with a Jobin-Yvon HR 460 monochromator coupled to a N_2 cooled charge coupled device. All the emission spectra have been corrected by the spectral response of the experimental setup. Emission lifetimes were recorder at room temperature exciting with an OPO laser from EKSPLA and an ultra-rapid intensified charge coupled device from Stanford Computer Optics. Spectral radiance and luminance from diodes was recorded with a Konica-Minolta CS-2000 spectroradiometer, in the same excitation conditions (duty cycle) as those used to measure *J–V* characteristics (duty cycle of 0.2%) using a TTi 40 MHz arbitrary waveform generator and a TREK-601C amplifier.

2.4. Device fabrication

The structure of the devices are ITO/PEDOT:PSS (50 nm)/Active layer/Cathode. Pre-patterned ITO glass plates with four circular diodes (1 mm and 1.5 mm radii) were extensively cleaned, using chemical and UV–ozone methods, just before the deposition of the organic layers. PEDOT:PSS (483095 from Aldrich) was deposited at 2000 rpm by spin-coating and then cured on a hot plate at 110 °C for 10–15 min. The active layers were deposited by spin coating from chloroform solutions and cured at 50 °C for 30 min on a hot plate. Precursor solutions (10 mg/mL) were kept in an ultrasonic bath for 10 min and filtered through a 0.2 μm polytetrafluoroethylene (PTFE) syringe filter, prior to be spin coated. We have found that heating the sample just below the solvent boiling point results in an improved film uniformity (highly reflecting surfaces) [10]. The thickness of the layers was measured using an Alpha step 200 profilomenter (Tenkor Instruments). The cathode was thermally evaporated in an atmosphere of 8×10^{-6} Torr on top of the organic layer surface and finally, the structure was encapsulated using a glass cover attached by a bead of epoxy adhesive [EPO-TEK(302-3M)]. All the process was carried out in an inert atmosphere glovebox (<0.1 ppm O_2 and H_2O).

2.5. Electrical measurements

The device current–voltage characteristics were measured using a semiconductor parameter analyzer Agilent 4155C and a SMU pulse generator Agilent 41501B. A pulse train was used as input signal. The duty cycle was set to be 0.2%, thus having a pulse width of 0.5 ms for a period of 100 ms. Refresh time between two consecutive pulses ensures long time operation without significant device degradation. Furthermore, the *I–V* curve stability was achieved by gradually increasing the pulse amplitude up to the point where reproducible measurements were observed. The voltage range was maintained below the onset for the electroluminescence (EL).

3. Results and discussion

3.1. Synthesis

The synthesis of the hexaaryl triindoles **1a**–**1d** Fig. 1 has been previously reported and was achieved using sixfold Suzuki coupling of known *N*-dodecylhexabromotriindole with commercially available boronic acids substituted in *para* with groups of different electronic character [7]. Using the same cross-coupling conditions **1e** was readily achieved by reaction of *N*-dodecylhexabromotriindole with (4-formylphenyl) boronic acid. Knoevenagel reaction of **1e** with malonitrile in the presence of $TiCl_4$ gave rise to compound **1f** as a deep red material in good yield.

3.2. Characterization of the electronic properties of solutions and thin films

The influence of the six peripheral groups, in the electronic properties of this family of compounds has been studied by cyclic voltammetry (Supporting information). All the compounds can be easily oxidized to stable radical cations and higher cationic charged species. The oxidazibility of these molecules varies in agreement with the nature of the peripheral substituents. Thus, attaching electron-donating groups results in an increase of the electron density in the π system and in consequence in a shift of the oxidation potentials to lower values. In contrast, upon attaching peripheral electron-withdrawing groups the oxidation potentials shifts anodically as increasing the acceptor character of the substituents. Compound **1f** show also a quasi reversible reduction wave in the accessible potential window of the solvent (CH_2Cl_2).

The HOMO energy values for these derivatives (Table 1) have been estimated from the first oxidation potential values with respect to ferrocene value of −4.8 eV with respect to zero vacuum level. This value is obtained from the calculated value of −4.6 eV for the standard electrode potential (E°) using a normal hydrogen electrode (NHE) on the zero vacuum level and the value of 0.2 V for Fc vs. NHE.

The influence of the peripheral groups on the electronic properties of the differently substituted hexaaryltriindoles is also clearly reflected in their absorption and emission spectra. Fig. 2(a) and (b) compare the absorption and the emission spectra obtained at 365 nm excitation of **1a, 1d, 1e** and **1f**. Compounds **1a**, **1b** and **1c** present almost identical absorption and emission spectra (shapes and intensities) while **1d** and **1e** show significant bathochromic shifts as the acceptor character of the peripheral groups increases. The emission of compound **1f** is very weak (note the factor ×20 in Fig. 2(b)) and presents two well separated

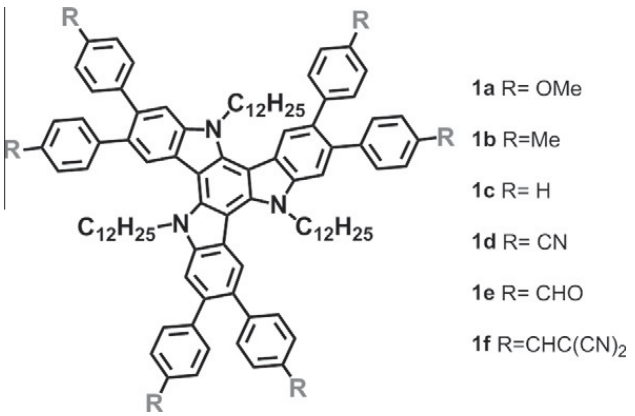

Fig. 1. Peripheral functionalization of triindoles.

Table 1
Values of HOMO, lowest transition and absorption onset E_g^{onset} (from absorbance) and main photoluminescence energies (E_{PL}) of compounds **1a–1f** in solution and in thin films. All data are in eV.

R	Solutions				Films		
	HOMO	Lowest trans.	E_g^{onset}	E_{PL}	Lowest trans.	E_g^{onset}	E_{PL}
1a	−5.07	3.17	3.0	3.08, 2.98	3.03	2.64	2.91
1b	−5.12	3.16	3.01	3.08, 2.98	3.07	2.66	2.91
1c	−5.12	3.17	3.03	3.08, 2.98	3.09	2.66	2.93
1d	−5.28	3.21	2.66	2.63	3.16	2.5	2.65
1e	−5.32	3.15	2.55	2.32	3.07	2.5	2.56
1f	−5.25	2.8	2.1	3.0, 2.25	2.66	1.96	1.89

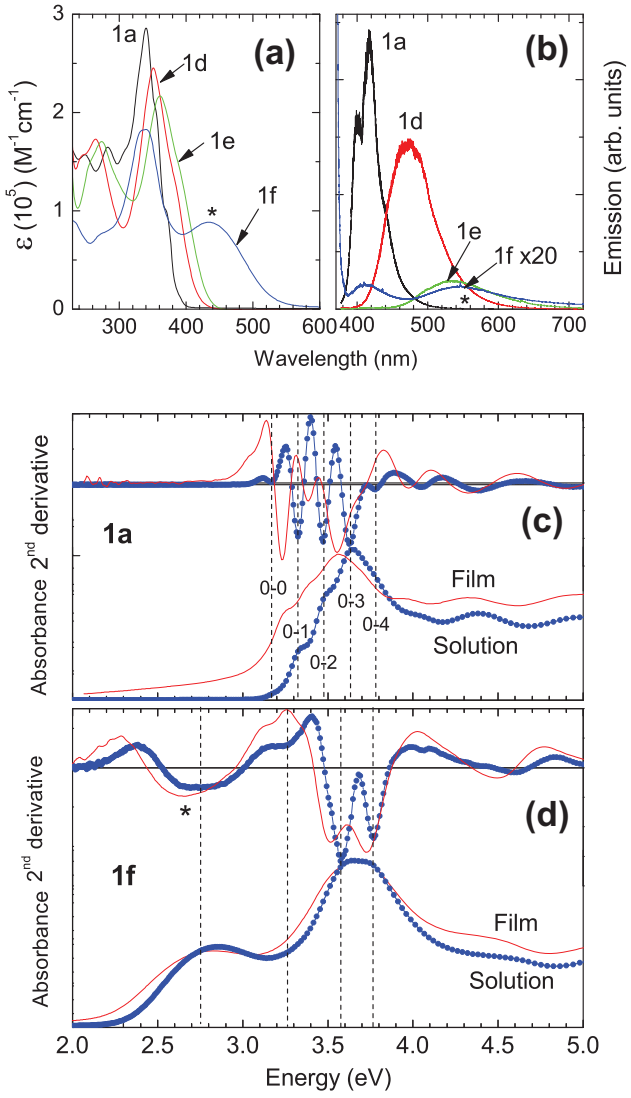

Fig. 2. (a) UV–vis spectra (molar absorption coefficients) and (b) photoluminescence spectra (excitation at 365 nm) in CH_2Cl_2 of **1a, 1d, 1e** and **1f** ($c = 10^{-5}$ M). (c) and (d) Comparison between absorption spectra and the second derivatives of **1a** (c) and **1f** (d) in solution and in thin film, respectively.

peaks at 413 and 552 nm (3.0 and 2.25 eV). The molar absorption coefficients are in the order of 10^5 ($M^{-1}cm^{-1}$) as it corresponds to π–π^* transitions [11]. In Fig. 2(c) and (d) we compare the absorption spectra and their second derivatives for **1a** and **1f** compounds in solution and as thin films.

Second derivatives of absorbance are useful to evidence the different components of the spectra [12] (minima correspond to absorption maxima and therefore to electronic transitions). In Fig. 2(c), the vertical dashed lines correspond to transitions of **1a** in solution. The five transitions (dashed vertical lines) of lower energy are equidistant in energy (around 151 meV = 1220 cm^{-1}) and correspond to transitions from the ground state (HOMO) to different vibrational states of the first excited state (LUMO) labeled with (0–*i*) with *i* = 0 to 4. The lowest transition (0–0) occurs at 3.17 eV while the main absorption peak is at 3.63 eV. This shift (0.46 eV) reveals that the atomic configuration of the excited state is different from that corresponding to the ground state of the molecule. The observation of the vibrational levels allows identifying the 0–0 transition.

The absorption onset (departure from zero in the second derivatives of the absorption spectra) is often used to define the optical gap (3 eV, in this compound) since it is the minimum energy where an optical absorption occurs and corresponds to the transition between the upper and lower edges of the HOMO and LUMO bands, respectively. Since HOMO and LUMO are bands whose width is related to homogeneous but also to inhomogeneous broadening which has different origins as different environments, stacking, inter-molecular coupling, defects, etc., the gap calculated from the absorption onset is not an intrinsic parameter. On the contrary, the energies of the absorption peaks are closer to an intrinsic description of the electronic structure. Strictly speaking, the LUMO should be obtained using the (0–0) transition. Table 1 collects the observed "lowest transition" values, that correspond to the (0–0) transition in **1a** to **1c**, and that we used to obtain an estimation of the LUMO levels shown in Fig. 3(b). Table 1 also collects the optical gap, E_g^{onset}, corresponding to the absorption onset.

The energy of the main peak (stars) as well as that of the lowest detected transition for the different compounds (rhombi) are plotted in Fig. 3(a). The figure evidences that the energy of the main peak is almost unvaried except for **1d** and **1e** where the coupling to the acceptor groups produces a lowering of the main peak energy and the loss of the vibronic structure. As a result the gap is shifted to lower energies. But only the $CHC(CN)_2$ groups, found in **1f**, which combine a strong acceptor character with an increase of the conjugation, lowers the gap down to about 2.1 eV by means of a new transition (at 2.8 eV, indicated with an asterisk in Fig. 2(a) and a circle in Fig. 3(a)). This new electronic state is most probably related to the electronic density transferred

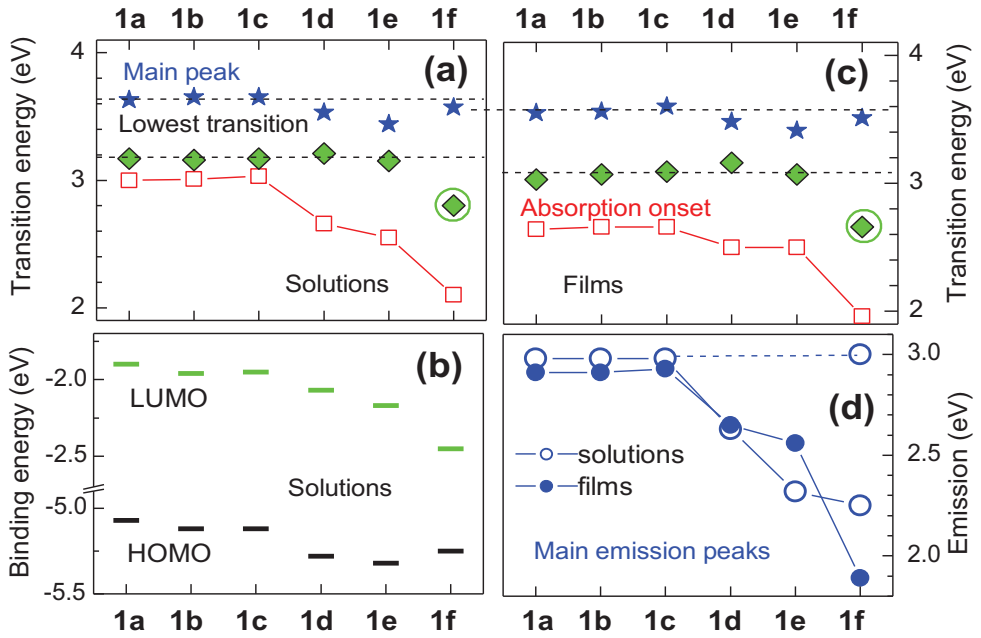

Fig. 3. Summary of relevant electronic transitions from absorption spectra in solution (a) and thin films (c), stars: main absorption peak, rhombi: lowest observed transition, open squares: absorption onset. (b) HOMO, from cyclic voltammetry, and LUMO, from the lowest detected transitions, for solutions. (d) Main emission energies in solutions and in thin films for all samples.

from the core to the peripheral groups giving rise to an octupolar character of the molecule. The progressive loss of the vibrational structure in **1d** and **1e** compounds prevents identifying the (0–0) transition so that the lowest observed transition in these compounds are most probably related to the (0–1) transition.

The dramatic influence that peripheral substituents of triindoles exert on the electronic properties of these derivatives offers a great opportunity to modulate their optical gap, again demonstrating the possibility of tuning the energy levels of these derivatives by chemical functionalization. Considering that organic electronic devices are usually constructed using multilayer architectures this possibility will be fundamental to facilitate charge injection from electrodes and minimize energy barriers between the different layers.

The emission spectra of **1a**, **1b** and **1c** compounds in solution are almost identical with two peaks at 403 and 418 nm (3.08 and 2.97 eV). In Fig. 2(b), the photoluminescence spectrum of **1a** is shown as well as those corresponding to **1d, 1e** and **1f**. The emission spectra are consistent with the changes in the electronic structure, previously deduced from the absorption data, related to the different character of the peripheral groups. Time resolved spectroscopy experiments performed for **1a** solution showed a lifetime of 3.0 ns for the 10^{-5} M solution which is consistent with fluorescence relaxation from singlet excited state (see Supplementary Information). The red shift of the emission peaks of solutions of **1d** and **1e** increases as the acceptor character of the peripheral groups increases (Fig. 3(d) and Table 1). **1f** emission in solution exhibits two distinct emission lines at 413 and 551 nm (3.0 and 2.25 eV, respectively). The highest energy peak, which coincides with that observed for **1a**–**1c**, corresponds to the relaxation from the excited state corresponding to the "main peak" in Fig. 3(a) while the lower energy one (2.25 eV) is the relaxation from the electronic level related to the charge transferred to the peripheral groups.

In order to select the best candidates for practical applications we have studied the film-forming properties of the new derivatives synthesized. Films of triindole derivatives were prepared by spin coating from 1 wt.% dichloromethane or chlorobenzene as precursor solutions on quartz. The obtained films were highly transparent and uniform to the eye and the optical microscope images reveal no inhomogeneities. Films thickness ranges from 20 to 100 nm.

The optical absorption spectra of the films, collected in Fig. 4(a), demonstrate their high optical quality and show almost identical features compared to the corresponding solution spectra with some differences in the peak energies (Table 1). The vibronic fine structure is also observed in thin films from **1a** to **1c** compounds maintaining the coupling of the excited state to the 150 meV vibration (see 2nd derivative in Fig. 2(c)). The main absorption peaks correspond, as in the solutions, to the (0–3) transitions.

Figs. 3b and c collect the energies of relevant electronic transitions from absorption and emission spectra of the thin films. A systematic shift to lower energies, in the range of 50–100 meV, is observed for the absorption bands of thin films compared to their dilute forms (Figs. 2 and 3). The lowering of the transition energies may be explained by the renormalization of the energy levels due to the close packing of the molecules. This energy shift is the only detected effect on the electronic structure related to the aggregation of the molecules in the thin films electronic transitions. The main emission of the thin films (Fig. 4(b)) ranges from the deep blue of the **1a**–**1c** compounds (426 nm) to the red for **1f** (656 nm). It is therefore

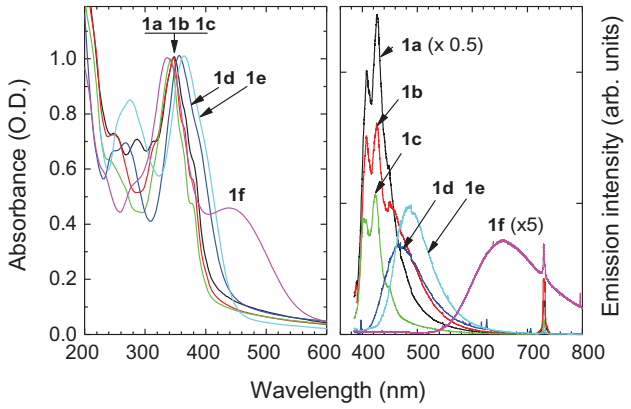

Fig. 4. Optical absorption spectra normalized to 1 at the main peak around 340 nm (left) and emission under 365 nm excitation (right) of **1a–1f** thin films. The emission intensities of the films have been corrected by the factor that normalizes their absorption to 1. Note that **1a** film emission intensity is divided by 2 and that of **1f** is multiplied by 5. (The narrow peak at 730 nm = 2 × 365 nm corresponds to the lamp).

possible to tune the emission in the whole visible range by chemical functionalization.

It is well known that whereas many organic molecules emit strongly in solution, they become weak fluorophores when increasing the concentration or when forming thin films due to non-radiative relaxation processes as energy transfer between neighboring molecules. This is a common problem found when looking for molecules that have to be incorporated in devices. However, in conveniently functionalized molecules emission may be enhanced when increasing the concentration owing to the restriction of intramolecular rotation processes upon aggregation or from the inhibition of geometry relaxation of the vertical excited state to a non-emitting state [13].

We have performed a study of the fluorescence of these compounds at different concentrations and found that two mechanisms are relevant for the resulting external quantum efficiency. On one hand, the quenching by concentration increases as the electron withdrawing character of the peripheral groups increases (Fig. 5). Note that because of the high molar absorption coefficients $\varepsilon(\lambda_{exc} = 365\ \text{nm})$ of these compounds, at concentrations of 10^{-5} M the absorbed intensity $(I_A/I_0 = 1 - \exp(-2.3\,\varepsilon(\lambda_{exc})l\,c) = 0.98 - 0.999$, where $l = 1$ cm and c is the concentration) is already almost saturated and, since the emission intensity is proportional to I_A, very weak or even no increase of the emission intensity is expected by increasing the concentration, as it occurs for **1b** and **1c** (Fig. 5). On the other hand, emission quenching by concentration is lower as the tendency of these compounds to aggregate is stronger, in particular an enhancement of the emission upon increasing the concentration is evident for **1a** (Fig. 5). Apparently, in these triindole derivatives functionalized with bulky peripheral groups, aggregation hinders rotation blocking non-radiative decay channels.

Similar trends can be observed in thin films. In Fig. 4, the emission intensities of the films have been corrected by the factor that normalizes their absorption to 1. It is therefore straightforward to compare the efficiencies of the different compounds as thin films and to detect that the efficiency of **1a** film is about 4 (3) times higher than that corresponding to the **1c** (**1b**) film while in solution their efficiencies are almost identical. It should be noted that this material has a strong tendency to self-assembly. In fact upon heating it enters a columnar hexagonal mesophase at 45 °C that extend in a broad range of temperatures [3]. Another interesting observation is the increase of the red emission efficiency of **1f** thin film compared to its solution (observe the factors applied to the spectra for the solution (×20) and for the film (×5) in Figs. 2 and 4, respectively). In this case the behavior of the two emission bands upon the solution concentration is different. While the 413 nm peak is rapidly quenched following the tendency of the whole series (in fact this emission is not observed in the film) the orange emission is not quenched. Moreover, this orange emission is significantly shifted to the red from the solution to the film (from 551 to 655 nm) probably indicating a different configuration of the peripheral groups in the solid state.

3.3. Fabrication and characterization of organic light emitting diodes

In order to analyze the semiconducting properties of these materials, solution-processed organic light emitting diodes (OLEDs) based on **1a**, **1d** and **1e** have been fabricated as described in the experimental section. These compounds have been selected considering their electronic properties, specifically their markedly different HOMO levels, band gaps and peak emissions (Table 1), as well as by their observed good film-forming properties. The structure of the fabricated OLED consists of: ITO (140 nm)/PEDOT:PSS (50 nm)/active layer/Ca/Al (200 nm). The thicknesses of the active layers are 85 nm, 110 nm and 116 nm for **1a**, **1d** and **1e**, respectively.

In Fig. 6 the energy level structure for materials **1a**, **1d** and **1e**, together with the work functions of anode and cathode, are shown. In this plot, we have used the HOMO levels of the solutions and the LUMO level energies calculated using the thin film absorption bandgaps, E_g^{onset} (Table 1) [14]. The work function for PEDOT:PSS thin films has been reported to range from 4.8 to 5.1 eV [15], depending on the PSS content in the top surface upon the addition of high-boiling solvents.

The electroluminescence (EL) spectra recorded from **1a**, **1d** and **1e**-based devices and their evolution with the driving current are plotted in Fig. 7. **1a**-based OLED exhibits a deep blue emission, CIE coordinates (0.16,0.16), with the maximum at 427 nm, and well resolved bands at 408 and 439 nm, similar to the thin film PL (Fig. 4). **1d** and **1e**-based OLED present broad emissions with white (CIE coordinates of (0.33,0.3)) and whitish green colour (CIE coordinates of (0.56,0.3)), respectively. The radiance, at 10 mA, is 0.14, 0.03 and 0.015 $\text{Wsr}^{-1}\,\text{m}^{-2}$ for **1a**, **1e** and **1d** respectively. The inferior EL performance of **1d** and **1e**-based OLEDs is consistent with their lower PL efficiencies. Nevertheless, the recorded luminance for **1a**, **1e** and **1d** are similar for the three devices (9, 11.2 and 3.6 $\text{Cd}\,\text{m}^{-2}$ respectively) because of the low efficiency of human eye response to the deep blue emission of **1a** (0.03 at 427 nm).

In devices **1a** and **1e** a very stable emission with increasing voltage is observed (see normalized spectra in

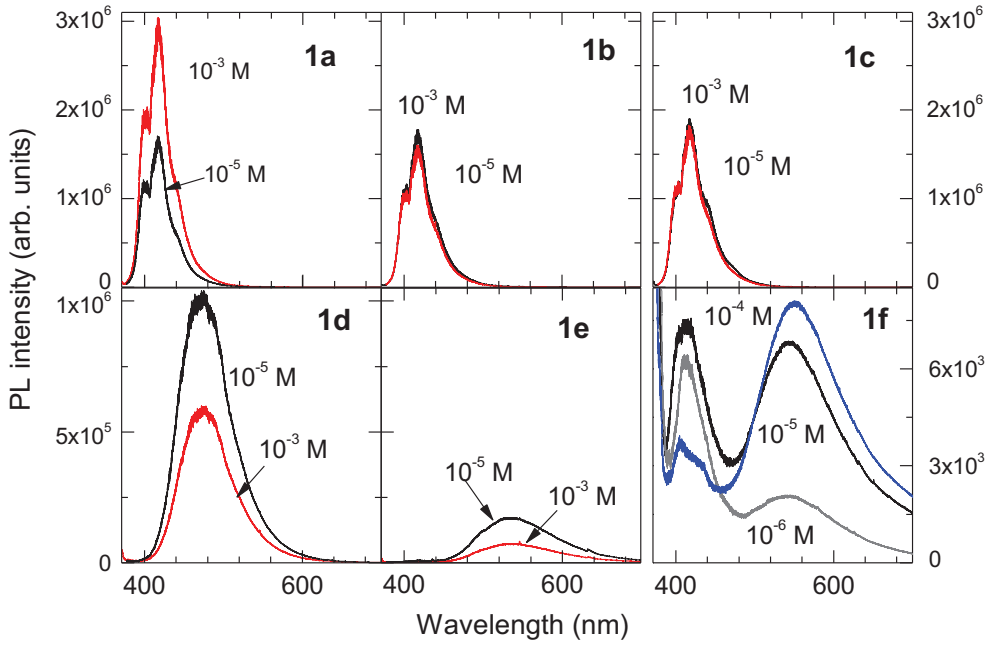

Fig. 5. Photoluminescence, under 365 nm excitation, of **1a**–**1f** in CH_2Cl_2 for different concentrations.

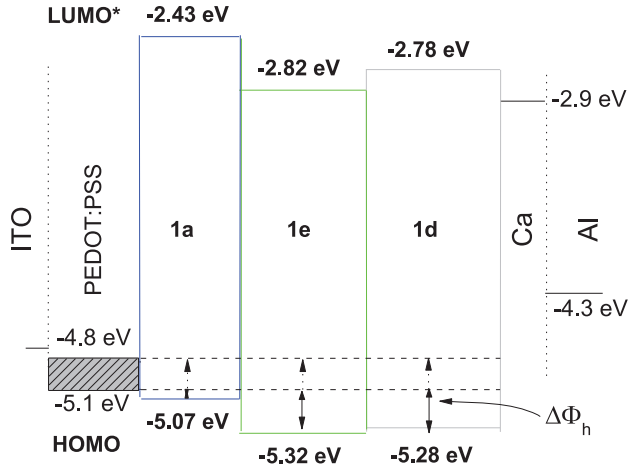

Fig. 6. Structure of solution processed OLEDs and energy levels of the electrodes and the materials. We use HOMO for solutions and LUMO levels are obtained from onset absorption energies of thin films.

Fig. 7 inset). However, in **1d**-based device, with very poor emissive efficiency the noticeable broadening of EL spectra compared to PL is attributed to a degradation which might be associated with an overheating by non radiative relaxation of injected carriers.

In Fig. 8, the experimental *I*–*V* responses (open symbols) of **1a**, **1d** and **1e**-based diodes are shown up to currents slightly above the onset for EL. We emphasize that minimizing turn-on voltages, V_T, and driving currents is an important issue in the organic electronics industry. In the present case, **1a**-based device exhibits a quite low threshold voltage (around 2.8 V) together with low driving currents. On the other hand, **1d** and **1e**-based devices show both higher turn-on voltages ($V_T > 11$ V) and driving currents, while their EL efficiencies are smaller.

The observed EL performance of the three devices may be qualitatively explained in terms of energy level alignment, electrical character (p or n) of the materials, and charge transport through the device. Using directly the HOMO and LUMO energies of isolated materials to determine the energy level alignment at interfaces is an assumption that may fail at organic-organic or metal–organic junctions, but it provides a reasonable approach for the energy barriers encountered by carriers during transport. On the other hand, in order to estimate the relevance of a barrier, one should keep in mind that for the usual low carrier mobilities in OLED active layers, it has been proven that an injection barrier below 0.3 eV does not limit current significantly [16] since transport turns to be bulk-limited instead of injection-limited. Our experience confirms this statement.

In Fig. 6, the alignment between PEDOT:PSS and **1a** levels suggests a negligible barrier for hole injection. According to this view, below V_T, conduction should be carried out by holes. For **1d** and **1e** materials, the energy level alignment is quite different presenting a noticeable *increment* of the barrier for hole injection together with a lowering of the electron injection barrier, (0.12 eV and 0.08 eV, respectively) and hence presumably an electron-driving conduction. Nevertheless electron mobility is usually lower than hole mobility in p-type materials. This could explain the higher threshold voltage and the poor EL performance of **1d** and **1e**-based OLEDs.

To get quantitative insight on the transport and EL mechanisms in the devices we have used a conduction model for voltages below the onset for EL, V_T, where single carrier transport is assumed [17,18] in order to fit the experimental *I*–*V* curves (Fig. 8) of **1a**, **1d** and **1e**-based diodes (open symbols). This model takes into account injection barriers, non-uniform electric-field across the layer thickness and field-dependent carrier mobility.

Active layer thickness is a relevant input of the model because it strongly affects the diodes threshold voltage not only in those of bulk-limited conduction but also in

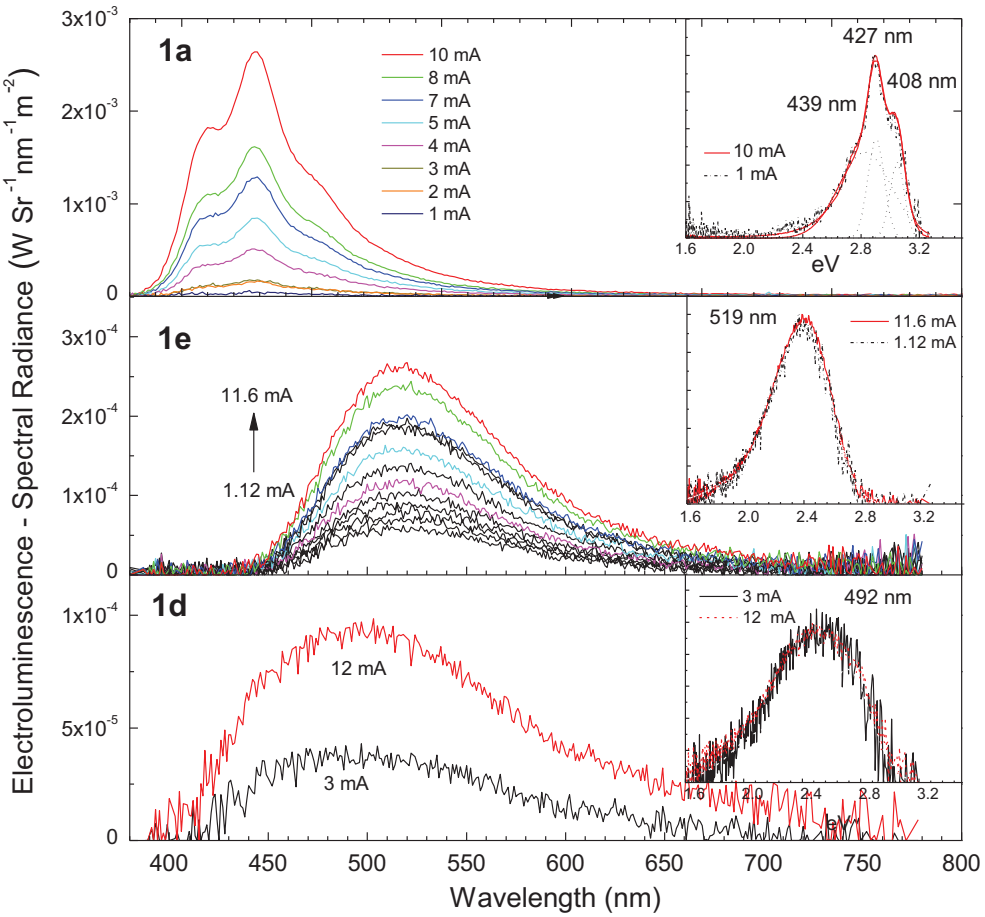

Fig. 7. EL spectral radiance for **1a**, **1d** and **1e** based OLEDs and their evolution with the driving current. The inset shows the normalized EL spectra for the maximum and minimum driving current fitted to a combination of Gaussian functions.

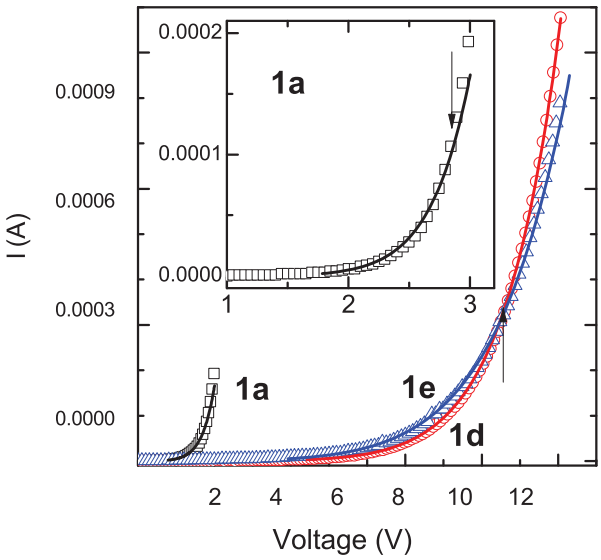

Fig. 8. Recorded *I–V* curves (open symbols) of diodes. The arrows mark the EL onset. Solid lines represent the fit using the model explained in the text. The inset shows an expansion of **1a** results.

those of injection-limited conduction. In the latter case this is due to the influence of the layer thickness on the interface field which drives the injection process [19]. It is therefore of major concern obtaining the electric field variation across the layer thickness $E(x)$. Moreover, in disordered organic materials carrier transport is usually accomplished by hopping between localized states and the mobility is a field-dependent function that can be approached to the expression [20,21]:

$$\mu(E) = \mu_0 \exp(k\sqrt{E}) \tag{1}$$

where E is the internal electric field, μ_0 is the so-called mobility at zero field [22] (i.e. at E not sufficiently high to enhance the conduction by reducing the effective barrier for trapped carriers) and k is a phenomenological factor related to the lowering of the effective trap depth or Frenkel effect [22]. The expression for the drift current density J_b Eq. (2), which includes the mobility Eq. (1), the one-dimensional Poisson Eq. (3) and the integral expression of voltage Eq. (4), are the fundamental equations of the model:

$$J_b = e\mu_0 \exp(k\sqrt{E})[p_n]E(x) = e\mu_0^* \exp(k\sqrt{E}[p]E(x)) \tag{2}$$

$$\frac{dE(x)}{dx} = \frac{e[p]}{\epsilon\epsilon_o} \tag{3}$$

$$V_b = \int_0^L E(x)dx \tag{4}$$

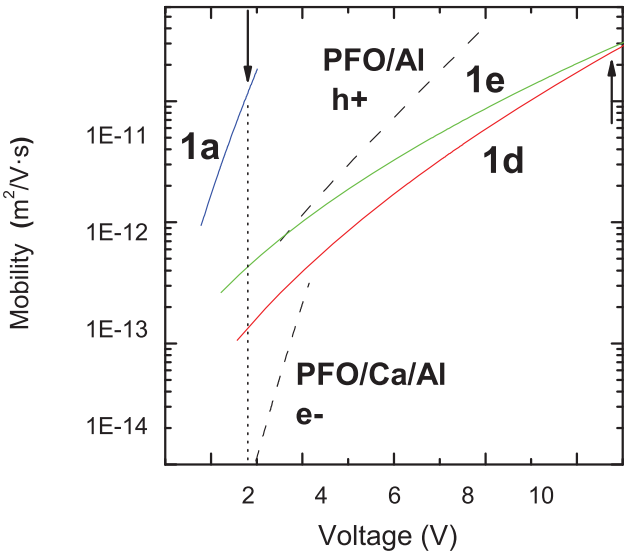

Fig. 9. Carrier mobility (μ^*)-applied voltage relationship derived from the model for **1a**, **1d** and **1e** based OLEDs (continuous lines) and for both PFO devices (dashed lines). The arrows mark the EL onsets.

where e the elementary charge, ε_o the vacuum permittivity, ε the material dielectric constant, L is the active layer thickness, V_b the external bias voltage and $[p]$ is the total carrier density. Finally $[p_n] = \theta\cdot[p]$ is the actual density of carriers contributing to transport. In disordered materials, only a small fraction, $\theta \ll 1$, of the injected carriers, those with energies close to the so-called transport level, contribute to the transport [23]. Since the determination of this parameter is usually difficult, from here on we use the effective mobility $\mu^*(E) = \mu(E)\cdot\theta$ and will extract the effective parameter $\mu_0^* = \mu_0 \cdot \theta$.

Integrating Eq. (3) using Eq. (2) it is possible to obtain the electric field dependence across the active layer $E(x, L, J_b)$. Further details of these calculations have been reported elsewhere [17,18]. A second integration of the electric field using Eq. (4) provides the electrical response of the diode $V_b(E_0, E_L, J_b)$ where E_0 and E_L are the values of the electric field at both interfaces: $E_0 = E(x = 0)$, $E_L = E(x = L)$. The determination of E_0 is obtained numerically via the continuity equation for the current density across the device: $J_{inj}(E_0) = J_b$, where J_{inj} is the injection current which is generally dependent on the electric field at the interface (E_0). In this work we have assumed the injection mechanism proposed by Arkhipov [19], in which the injection of carriers from the Fermi level of the electrode to the conduction level in the organic is not accomplished by conventional tunneling, but by incoherent hopping between localized states with an injection barrier Φ. The described model has been used to fit the experimental I–V curves using a standard quasi-Newton algorithm, where μ_0^*, k and Φ (in eV) are the output parameters.

The fits, shown as continuous lines in Fig. 8, reproduce very well the experimental data below the threshold voltage, V_T, in all cases while, in those devices with better EL performance (**1a** and **1e**) the agreement gets worse beyond the EL onset. This is attributed to the additional enhancement of conductivity associated with exciton recombination, which is a physical mechanism not included in the model. However, for the **1d**-based device, where the EL mediated carrier recombination is quite inefficient (with the worst EL performance), the model still fits nicely beyond this onset.

In order to validate the model and compare the output parameters (k, μ^* and Φ) to those of a commercial compound, we have fabricated OLEDs using blue emitting polyfluorene (PFO) with a multilayer structure identical to previous ones, being $L_{PFO} = 85$ nm. The PFO HOMO and LUMO levels were elsewhere determined by cyclo-voltammetry to be at −5.6 eV and −2.43 eV, respectively [24]. To promote an electron-based conduction, a Ca layer was inserted between PFO and Al at the cathode, whereas the removal of this layer should promote a hole-based conduction (as expected from the Al work function at −4.3 eV). The devices without Ca do not exhibit EL up to 12–15 V, and transport is expected to be driven by holes injected across a noticeable barrier. In the devices with Ca, the onset for EL drops significantly down to 3 V, and electron-driven conduction is assumed. Despite the low threshold voltage, the electron mobility resulting from the model is much lower than that for holes, as shown in Fig. 9. This is consistent with an electron-driven transport in a non-favorable p-type material as this type of polyfluorene [24]. We remark that hole mobility has been extracted in the presence of an injection barrier $\Phi = 0.51$ eV, in reasonable agreement with the energy level scheme.

Table 2 summarizes the obtained fitting parameters, μ_0^*, k, and Φ for **1a, 1d** and **1e** based devices and for both PFO OLEDs. Since the electric field $E(x)$ is not uniform, $\mu^*[E(x)]$ has been numerically averaged across the whole layer. The resulting average carrier mobility vs. applied voltage $\mu^*(V_b)$ is plotted in Fig. 9. We can observe that the carrier mobility in **1a** device (Fig. 9) is much higher in its operating range than that for devices **1d** and **1e** (Table 2 collects the average mobilities at 2.8 V for the all devices).

The present model for charge transport across this OLED structure has allowed us to obtain both electron and hole mobilities for these derivatives by fitting the I–V curves at low voltages ($<V_T$) where the transport is dominated by one carrier type. As explained previously, the alignment of the level energies of the successive layers favors hole

Table 2
Fitting parameters μ_0^*, k and Φ obtained for the active layer of each device. Average mobilities, μ^*, at the EL onset of **1a** based device (2.8 V). Results obtained for both holes (h^+) and electrons (e^-) from a commercial blue-emitting polyfluorene (PFO) based OLED are included for comparison.

	1a-h^+	1e-e^-	1d-e^-	PFO-h^+	PFO-e^-
μ_0^* ($\times 10^{-9}$) (m^2/V s)	5.2×10^{-2}	20.8	2.0	1.51×10^{-2}	1.91×10^{-7}
k ($\times 10^{-3}$) $(V/m)^{-1/2}$	2.84	1.02	1.33	1.49	3.84
Φ (eV)	<0.3	<0.3	0.38	0.51	<0.3
μ^* (at 2.8 V) ($\times 10^{-11}$) (m^2/Vs)	1.1	4.4×10^{-2}	1.3×10^{-2}	3.7×10^{-2}	9×10^{-4}

conduction for **1a** and PFO/Al devices while mainly electron conduction occurs in **1d**, **1e** and PFO without Al. The results indicate that hole mobility is more than two orders of magnitude higher compared to electron mobility, which is consistent with p-type materials. This factor is also observed comparing hole and electron mobilities in PFO (Fig. 9 and Table 2). Finally, we emphasize that hole-mobility of the solution processed **1a**-based device results significantly higher than that of PFO/Al. Regarding OLED performance, it is clear that increasing the luminance would require the optimization of the electron injection in 1a-based device and of hole injection in 1d and 1e devices. Nevertheless, we can conclude that these solution processed devices exhibited encouraging level of performance in terms of transport.

4. Conclusions

We have introduced peripheral groups in the electron-rich 10,15-dihydro-5*H*-diindolo[3,2-*a*:3′,2′-*c*]carbazole (triindole) platform that render solution processable and good film-forming compounds. The influence of the different peripheral groups on the electronic properties of solutions and films is evidenced in the tuning of the HOMO, LUMO, gap and emission energies which are discussed and correlated to the electronic communication of the external substituents with the central electron-rich triindole. The resulting films are amorphous, highly homogeneous and stable for months therefore suitable for device fabrication. The thin films emission ranges from deep blue (423 nm) to red (657 nm).

Single layer organic light emitting diodes (OLED) have been fabricated by solution processing methods with the structure: ITO/PEDOT:PSS/active layer/Ca/Al. Three compounds with different HOMO–LUMO alignment to the electrode work functions and different emission wavelengths were used to investigate the influence on transport and emission properties of the substituting species. A numerical model for conductivity that includes injection barriers and non-uniform electric-field across the layer as well as field dependent mobility has been used to analyze the OLEDs *I–V* response and to compare the results to devices fabricated with commercial PFO. Best results are obtained on the most electron rich derivative functionalized with six donor methoxy groups. This material shows the highest emission efficiency in solid state, due to aggregation-induced enhancement, and favors carrier transport with the highest mobility in the whole operating voltage range. We demonstrated encouraging performance in terms of very low turn-on voltage (2.8 V) and carrier mobility of a solution processed deep blue emitting molecular based OLED.

Acknowledgments

Support by Comunidad Autónoma de Madrid under project S2009/MAT-1756 and by Ministerio de Ciencia e Innovación (Spain) under projects MAT2009-08786, CTQ2010-18813, TEC2009-13991-C02-02 and TEC2011-13635-E are gratefully acknowledged.

Appendix A. Supplementary data

Supplementary data associated with this article can be found, in the online version, at http://dx.doi.org/10.1016/j.orgel.2012.06.018.

References

[1] L. Duan, L. Hou, T.W. Lee, J. Qiao, D. Zhang, G. Dong, L. Wang, Y.J. Qiu, Solution processable small molecules for organic light-emitting diodes, J. Mater. Chem. 20 (2010) 6392.
[2] E.M. García-Frutos, E. Gutierrez-Puebla, M.A. Monge, R. Ramírez, P. de Andrés, A. de Andrés, R. Ramírez, B. Gómez-Lor, Crystal structure and charge-transport properties of *N*-trimethyltriindole: a promising candidate as p-type organic semiconductor, Org. Electron. 10 (2009) 643.
[3] M. Talarico, R. Termine, E.M. García-Frutos, A. Omenat, J.L. Serrano, B. Gómez-Lor, A. Golemme, New electrode-friendly triindole columnar phases with high hole mobility, Chem. Mater. 20 (2008) 6589–6591.
[4] E.M. García-Frutos, U.K. Pandey, R. Termine, A. Omenat, J. Barberá, J.L. Serrano, A. Golemme, B. Gómez-Lor, High charge mobility in discotic liquid-crystalline triindoles: just a core business?, Angew Chem. Int. Ed. Engl. 50 (2011) 7399–7402.
[5] R.A. Valentine, A. Whyte, K. Awaga, N. Robertson, New indole trimers as precursors for molecular electronic materials, Tetrahedron Lett. 53 (2012) 657–660.
[6] W.Y. Lai, Q.Y. He, R. Zhu, Q.Q. Chen, W. Huang, Kinked star-shaped fluorene/triazatruxene co-oligomer hybrids with enhanced functional properties for high-performance, solution-processed, blue organic light-emitting diodes, Adv. Funct. Mater. 18 (2008) 265–276.
[7] E.M. García-Frutos, G. Hennrich, E. Gutierrez, A. Monge, B. Gómez-Lor, Self-assembly of C_3-symmetrical hexaaryltriindoles driven by solvophobic and CH–π interactions, J. Org. Chem. 75 (2010) 1070–1076.
[8] E.M. García-Frutos, A. Omenat, J. Barberá, J.L. Serrano, B. Gómez-Lor, Highly ordered p-extended discotic liquid-crystalline triindoles, J. Mater. Chem. 21 (2011) 6831–6836.
[9] E.M. García-Frutos, B. Gómez-Lor, Functionalized triindoles as a new class of p-type organic semiconductors, J. Am. Chem. Soc. 190 (2008) 9173–9177.
[10] C. Coya, A. de Andrés, R. Gómez, C. Seoane, J.L. Segura, On the blue emission of a novel solution-processed stilbenoid dendrimer thin film for OLED displays, J. Lumin. 128 (2008) 761.
[11] Bernard Valeur, Molecular Fluorescence: Principles and Applications, Wiley-VCH, 2001.
[12] The second derivative procedure searches for local minima within a smoothed second derivative data stream. These local minima often reveal hidden peaks. This procedure is often used in commercial software for spectroscopy and chromatography analysis.
[13] Z. Bian, A. Shakouri, Enhanced solid-state thermionic emission in nonplanar heterostructures, Appl. Phys. Lett. 88 (2006) 012102.
[14] For charge injection the relevant energy is the lower edge of the LUMO band which is obtained using the absorption onset.
[15] A.M. Nardes, M. Kemerink, M.M. de Kok, E. Vinken, K. Maturova, R.A.J. Janssen, Conductivity, work function, and environmental stability of PEDOT:PSS thin films treated with sorbitol, Org. Electron. 9 (2008) 727–734.
[16] V.I. Arkhipov, H. von Seggern, E.V. Emelianova, Charge injection versus space-charge-limited current in organic light-emitting diodes, Appl. Phys. Lett. 83 (2003) 5074.
[17] A.L. Alvarez, B. Romero, B. Arredondo, X. Quintana, R. Mallavia, J.M. Oton, Electrical model of organic diodes with field-dependent carrier mobility in the presence of an electric field at the injection interface, Int. J. Numer Model Electron. Networks Devices Fields 23 (2010) 332.
[18] C. Coya, A.L. Alvarez, W.S. Yoon, S.Y. Park, Influence of the 1,2,4-linking hyperbrancher poly(arylenevinylene) structure on organic light emitting diode performance as compared to convencional 1,3,5-linking one, J. Appl. Phys. 109 (2011) 094507.
[19] V.I. Arkhipov, E.V. Emelianova, Y.H. Tak, H. Bassler, Charge injection into light-emitting diodes: theory and experiment, J. Appl. Phys. 84 (1998) 848.
[20] H. Bässler, Charge transport in disordered organic photoconductors a Monte Carlo simulation study, Phys. Status. Solidi. B 13 (1993) 175.
[21] S. Baranosvski, Charge transport in disordered solids with application in electronics, in: S. Baranovski, O. Rubel (Eds.), Wiley, New York, 2006 (Chapter 6).

[22] P.N. Murgatroyd, Theory of space-charge-limited current enhanced by Frenkel effect, J. Phys. D: Appl. Phys. 3 (1970) 151.
[23] V.I. Arkhipov, E.V. Emelianova, H. Bässler, According to the model proposed inside, for a typical carrier localization radius of 2 Å, a width of the energetic level of 90 meV and a hopping site density of 1026 m^{-3}, θ amounts 2×10^{-7}, Philos. Mag. B. 81 (2001) 985.
[24]]R. Mallavia, F. Montilla, I. Pastor, P. Velasquez, B. Arredondo, A.L. Alvarez, C.R. Mateo, Characterization and side chain manipulation in violet–blue poly-[(9,9-dialkylfluoren-2,7-diyl)-alt-co-(benzen-1,4-diyl) backbones, Macromolecules 38 (2005) 3185.

THE JOURNAL OF PHYSICAL CHEMISTRY C

Article

pubs.acs.org/JPCC

Symmetry Lowering in Triindoles: Impact on the Electronic and Photophysical Properties

Constanza Ruiz,[†] Eva M. García-Frutos,[†] Demetrio A. da Silva Filho,[‡] Juan T. López Navarrete,*[,§] M. Carmen Ruiz Delgado,*[,§] and Berta Gómez-Lor*[,†]

[†]Instituto de Ciencia de Materiales de Madrid, CSIC, Cantoblanco 28049, Madrid, Spain

[‡]Institute of Physics, University of Brasilia, Brasilia 70.919-970, Brazil

[§]Department of Physical Chemistry, University of Málaga, 29071 Málaga, Spain

Supporting Information

ABSTRACT: The electronic and photophysical properties of 6,11-dihydro-5*H*-diindolo[2,3-*a*:2′,3′-*c*]carbazole, an asymmetric cyclic dehydrotrimer of indole, have been explored and compared to its symmetric analogue, 10,15-dihydro-5*H*-diindolo[3,2-*a*:3′,2′-*c*]carbazole (triindole), a well-known high hole mobility semiconductor. To this purpose, we use a joint experimental and theoretical approach that combines absorption and emission spectroscopies, cyclic voltammetry, and spectroelectrochemistry with DFT calculations. Lowering the symmetry of the triindole platform causes a red-shift of the absorption edge and emission maxima and improved the fluorescence quantum yield. Cyclic voltammetry and spectroelectrochemistry reveal the reversible nature of the two observable oxidation processes in the alkylated asymmetric triindoles together with an increase in the stabillity of their oxidized species. On the other hand, the insertion of alkyl groups on the nitrogen atoms results in a further fluorescence enhancement although larger reorganization energies are found. DFT and time-dependent (TD-DFT) calculations successfully support the experimental data and aid in the understanding of the tuning of the physicochemical properties of the triindole platform upon symmetry lowering toward their incorporation in electronic devices.

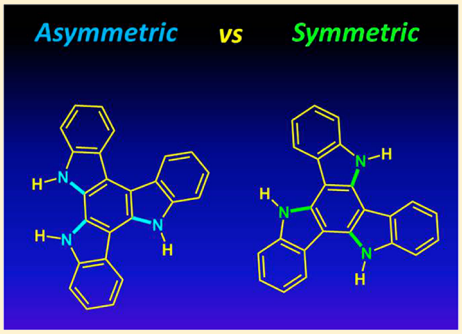

INTRODUCTION

The interest aroused by π-conjugated polymers after the discovery that their electrical conductivity increases substantially upon electrochemical doping paved the way to the emergence of the field of organic electronics. In only a few years, this area stimulated worldwide interest in the search for large area, flexible, lightweight, and cost-effective optoelectronics. Conjugated polymers, usually amorphous materials, can be easily processed from solution to yield homogeneous and uniform thin films ideally suited for optoelectronics.[1−5] Unfortunately, they pose problems of reproducibility due to variations in molecular weight, and polydispersity, from batch to batch. Low-molecular-weight π-conjugated oligomers have been identified as attractive targets to substitute the usual polymeric materials in electroactive devices. Although less appealing in terms of processability, they can be reproducibly prepared, functionalized, and purified, owing to their monodisperse nature with well-defined chemical structure.

In this context, we and others became interested in a C_3-symmetric dehydrotrimer of indole (triindole) readily available by cyclocondensation of either indolin-2-one[6] or indole itself through halogenation[7] followed by reductive dehydrohalogenation.[8] This novel molecule is highly stable and has intrinsic physical favorable properties such as attractive redox and linear and nonlinear optical properties. Despite the fact that this novel C_3-symmetric scaffold has only recently been investigated, it has already found applications in the development of bulk heterojunction solar cells,[9] organic light-emitting diodes,[10−12] and field effect transistors,[13] and it has been utilized as a central core in semiconducting discotic liquid crystals[14] showing record hole mobilities.[15−17]

In contrast to the well-documented C_3-symmetric dehydrotrimer of indole, its asymmetric analogue is much less explored.[18] Different substituted cyclic asymmetric trimers have been obtained during the electropolymerization of functionalized indoles.[19−23] In fact, it has been proposed that polyiindole is composed by linked redox-active asymmetric trimers initially formed upon electrooxidation and coupling.[20−23] Its formation has been explained by considering the greatest electron spin density distribution in indole monomer, dimer, and linear trimer radical cations.[24,25] Preparative synthesis of this scaffold by reaction of indole with nitrosobenzene[26] has also been reported; however, a deep study of its electronic properties is still lacking.

In the present study, we explore the electronic and photophysical properties of the asymmetric dehydrotrimer of

Received: December 11, 2013
Revised: February 10, 2014
Published: February 19, 2014

   dx.doi.org/10.1021/jp412129m | *J. Phys. Chem. C* 2014, 118, 5470−5477

indole in comparison with its symmetric analogue by using absorption and emission spectroscopies, cyclic voltammetry, and spectroelectrochemistry. The electronic structure differences between the symmetric and asymmetric platforms are investigated with the help of DFT and time-dependent (TD-DFT) calculations of the ground states (S_0), singlet excited states, and charged states. As it has been previously observed that insertion of alkyl groups on the nitrogen atoms benefits the redox and thermal stability of symmetric triindoles,[14−16] the influence of *N*-alkylation on the electronic properties of these compounds is also studied. This work aims to deepen the understanding of the structure−property relationships of triindoles and provide guidance for further development of these materials aiming potential applications in organic electronics. The results presented reveal that molecular engineering of this conjugated core via varying the symmetry as well as *N*-alkyl functionalization can be used to effectively tune their physicochemical (i.e., photophysical and electrochemical) properties.

EXPERIMENTAL SECTION

Materials Synthesis. The synthesis of unsubstituted **1a** and **2a** can be easily performed in just one step starting from indolin-2-one and indole, respectively, following previously reported procedures.[6,25] Simple alkylation under basic conditions and in the presence of a phase transfer catalyst can be easily achieved in quantitative yields allowing for the functionalization of the three indolic NH centers with alkyl groups (Scheme 1). Alkylated **1b**,[27] **1c**,[28] and **2b**[29] have been previously described; **2c** (see Supporting Information) is a new compound.

Scheme 1. Chemical Structure of Symmetric 1a−1c and Asymmetric 2a−2c Triindoles

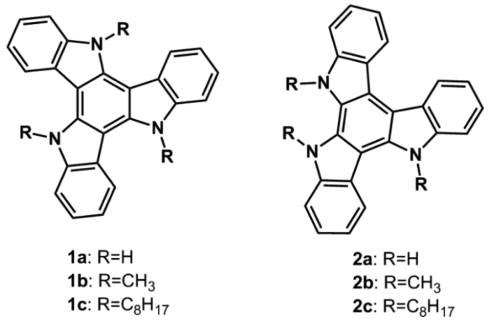

Linear Spectroscopy. UV−vis studies were carried out on a PerkinElmer Lambda XLS+ spectrometer. Fluorescence spectra were recorded on an Aminco SLM 8000 spectrophotometer.

Electrochemistry and Spectroelectrochemistry. Cyclic voltammetry (CV) experiments were performed on a Bioanalytical Systems Inc. (BASI) Epsilon electrochemical workstation in a three-electrode cell at room temperature under a nitrogen atmosphere. Electrochemical measurements were carried out in acetonitrile solution ($c = 1 \times 10^{-3}$ M) containing 0.1 M tetra-*n*-butylammonium hexafluorophosphate ($TBAPF_6$) of supporting electrolyte at a scan rate 100 mV/s. A three-electrode setup was used including a platinum working electrode, a Ag/AgCl (3 M NaCl) reference electrode, and a platinum wire auxiliary electrode. Ferrocene was used as an internal standard, and all potentials were referenced to the ferrocene/ferrocenium redox couple. Spectroelectrochemical experiments were performed using a BASI spectroelectrochemical cell kit, including a thin-layer quartz cuvette, a platinum minigrid working electrode, a platinum wire counter electrode, and a Ag/AgCl (3 M NaCl) reference electrode. The measurements were carried out in acetonitrile solution ($c = 1 \times 10^{-4}$ M) containing 0.1 M of supporting electrolyte tetra-*n*-butylammonium hexafluorophosphate ($TBAPF_6$). The voltage was held at different potential values during the measurements while the absorption spectra were monitored on a PerkinElmer Lambda XLS+ spectrometer.

Computational Details. The molecular geometries of the neutral and radical-ion states were calculated at the density functional theory (DFT) level using the B3LYP functional[30,31] and the 6-31G(d,p)[32,33] basis set, as implemented in the Gaussian 09 program.[34] The ionization energies (IEs) were calculated directly from the relevant points on the potential energy surfaces using the standard procedure detailed in the literature.[35] Specifically, vertical IEs were evaluated as the difference between the energy of the cation at the neutral geometry and that of the neutral species at the neutral geometry. Vertical one-electron excitations were computed using the time-dependent DFT (TD-DFT) method.[36,37] Absorption spectra were simulated through convolution of the vertical transition energies and oscillator strengths with Gaussian functions characterized by a full width at half-maximum (fwhm) of 0.3 eV.

The geometries of the first excited state (S_1) were optimized by the TD-DFT method. An algorithm included in this version of Gaussian 09[34] was used to generate a vibronically resolved absorption spectrum and emission to allow for a direct comparison with the experimental data.[38,39]

RESULTS AND DISCUSSION

Absorption Spectra and Orbital Topologies. Figure 1 displays the UV−vis absorption spectra of symmetric **1a**, **1c** and asymmetric **2a**, **2c** compounds (the spectra of **1b** and **2b** are shown in Figure S1). An examination of the electronic absorption spectra shows two clear effects: (i) lowering the symmetry of the platform leads to a more complex spectrum and considerably red-shifts the absorption edge (i.e., 375 nm in **1c** and 430 nm in **2c**),[40] and (ii) when going from the unsubstituted **1a**, **2a** to the octyl-substituted **1c**, **2c** systems, the overall shapes of the spectra remain unchanged but the position of their maxima and absorption edge are red-shifted by about 10−20 nm. However, completely superimposable absorption spectra are obtained when the octyl chains are replaced by the much shorter methyl groups (see Figure S1); this suggests that the geometrical effect (i.e., distortions from planarity upon *N*-alkyl substitution) seems to have a stronger impact than the larger inductive effect of the long alkyl chains.

As shown in Figure 1, the time-dependent DFT (TD-DFT) vertical excitation energies reproduce quite nicely (i) the higher complexity of the UV−vis spectra when the C_3-symmetry is broken (i.e., a large number of transitions with moderate intensity are predicted for **2a**, **2c** in comparison to **1a**, **1c**) and (ii) the red-shift of the absorption spectra when going from the symmetric to the asymmetric systems and upon *N*-alkylation. For example, in the symmetric systems, the strongest band at 306 (317) nm in **1a** (**1c**) corresponds to the degenerate $S_0 \rightarrow S_3/S_0 \rightarrow S_4$ electronic transitions calculated at 296 (312) nm, which is assigned to a combination of HOMO−1 → LUMO, HOMO → LUMO+1, HOMO−1 → LUMO+1, and HOMO

dx.doi.org/10.1021/jp412129m | J. Phys. Chem. C 2014, 118, 5470−5477

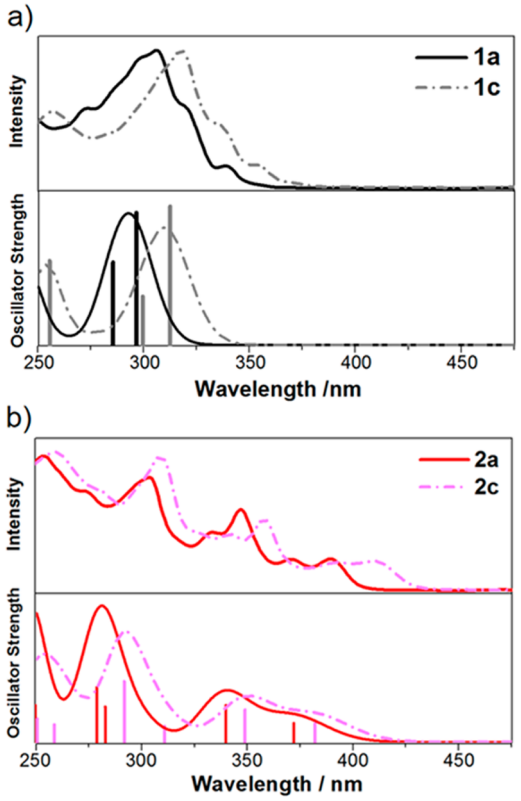

Figure 1. (a) Top: experimental UV−vis absorption spectra of **1a** and **1c** in CH_2Cl_2, $c = 5 \times 10^{-6}$ M. Bottom: simulated absorption spectra of **1a** and **1c** together with the TD-DFT//B3LYP/6-31G** level excitations (wavelength vs oscillator strength) shown as vertical bars. (b) Top: experimental UV−vis absorption spectra of **2a** and **2c** in CH_2Cl_2, $c = 5 \times 10^{-6}$ M. Bottom: simulated absorption spectra of **2a** and **2c** together with the TD-DFT//B3LYP/6-31G** level excitations (wavelength vs oscillator strength) shown as vertical bars.

→ LUMO one-electron excitations. Note that in the symmetric systems the $S_0 \rightarrow S_1$ transition is forbidden by symmetry with respect to dipole−dipole selection rules.[41] However, the $S_0 \rightarrow S_1$ transition becomes allowed in the asymmetric compounds; as seen in Figure 1, this band is calculated at 372 nm ($f = 0.13$) in **2a** and 382 nm ($f = 0.14$) in **2c**, and it is associated with a HOMO → LUMO transition.

Table 1. Formal Oxidation Potentials, HOMO Energies Estimated from Cyclic Voltammetry Data, HOMO Energies Calculated (B3LYP/6-31G Level Theoretical Data), and DFT-Calculated Vertical (IEv) Ionization Energies**

compd	$E^{\circ\prime}$ (V)	$HOMO_{exp}$ (eV)	$HOMO_{calc}$ (eV)	IEv (eV)
1a	0.69	−5.07	−4.96	6.27
1b	0.73	−5.10	−4.83	6.09
1c	0.75	−5.11	−4.76	5.94
2a	0.56	−4.94	−4.81	6.15
2b	0.56	−4.94	−4.71	5.99
2c	0.60	−4.97	−4.70	5.91

[a]The HOMO energy values for **1a−c** and **2a−c** were estimated from the first oxidation potential with respect ferrocene/ferrocenium redox couple[42] and considering a value of −4.8 eV for Fc with respect to zero vacuum level. This value is obtained from the calculated value of −4.6 eV for the standard electrode potential (E) using a normal hydrogen electrode (NHE) on the zero vacuum level and the value of 0.2 V for Fc vs NHE.[43,44]

Figure 2 shows the DFT//B3LYP/6-31G** frontier molecular orbitals of symmetric **1a**, **1c** and asymmetric **2a**, **2c**. Because of its C_3-symmetric structure, the HOMO and LUMO orbitals of **1a** and **1c** are doubly degenerated, whereas an energy gap of 0.25 (0.24) eV between HOMO and HOMO−1 and 0.78 (0.73) eV between LUMO and LUMO+1 is observed in the asymmetric **2a** (**2c**) analogues. In going from the symmetric to the asymmetric systems, LUMO is largely stabilized (by ∼0.50 eV) and HOMO is moderately destabilized (by ∼0.12 eV), thus decreasing the HOMO−LUMO gap. Upon *N*-alkylation, HOMO and LUMO are moderately destabilized with this effect being more pronounced for HOMO due to the inductive effect of the alkyl groups, thus resulting in a HOMO−LUMO gap decrease. These data are in good accordance with the experimental red-shift of the absorption edge when lowering the symmetry of the molecule

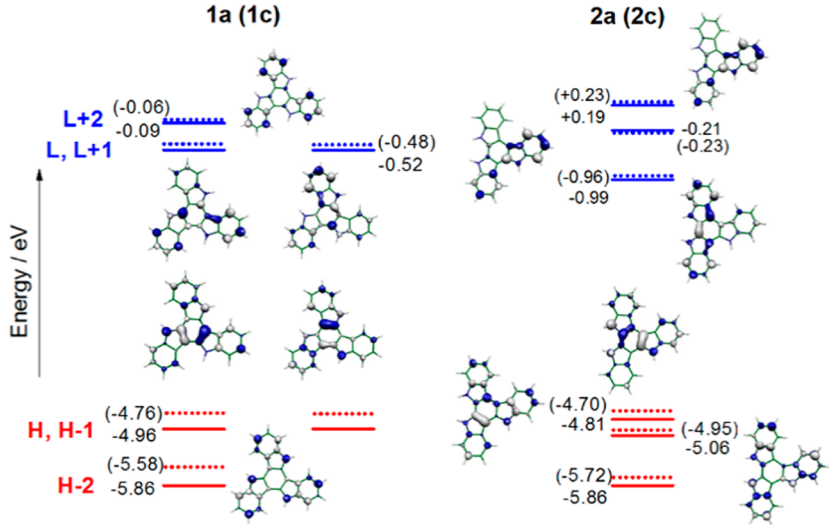

Figure 2. DFT-calculated molecular orbital energies (B3LYP/6-31G** level) for **1a**, **2a** (solid lines) and **1c**, **2c** (dotted lines, with the values shown in parentheses). The molecular orbital topologies for **1a** and **2a** are also shown (see the Supporting Information for the molecular orbital topologies of **1c** and **2c**).

dx.doi.org/10.1021/jp412129m | J. Phys. Chem. C 2014, 118, 5470−5477

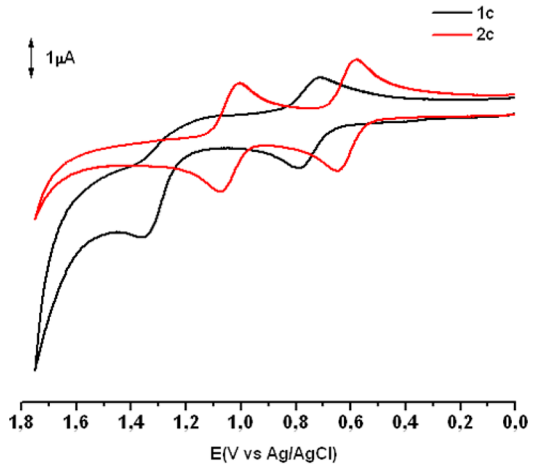

Figure 3. Cyclic voltammogram of **1c** and **2c** at $c = 1 \times 10^{-3}$ M recorded in CH_3CN/0.1 M tetra-*n*-butylammonium hexafluorophosphate ($TBAPF_6$) at a scan rate 100 mV/s using a Pt working electrode, a Ag/AgCl (3 M NaCl) reference electrode, and a Pt wire auxiliary electrode.

and upon *N*-alkylation, which is found to be more pronounced in the former than in the latter case in accordance with the DFT calculations.

Cyclic Voltammetry and UV/vis−NIR Spectroelectrochemistry. As determined by cyclic voltammetry, all six compounds exhibit a first oxidation reversible process as well as the formation of higher cationic charged species in the accessible potential window of the solvent. The first oxidation process which is associated with the easy generation of a cation radical in these electron-rich platforms allow us to estimate the value of the HOMO levels of these compounds (see Table 1, Figure 3, and Figure S2). The first oxidation potential shifts slightly anodically as decreasing the symmetry of the system. This trend is well captured by the DFT-calculated ionization energies (IE) as smaller IE values are found upon lowering the symmetry (i.e., 6.27/6.15, 6.09/5.99, and 5.94/5.91 eV for **1a**/**2a**, **1b**/**2b**, and **1c**/**2c** couples) and is consistent with the HOMO destabilization obtained when the symmetry is lowered (see Table 1). Conversely, the oxidation potentials are barely affected upon *N*-alkylation; this is not in consonance with the somewhat small destabilization of the calculated HOMO values upon *N*-alkylation. This disagreement, in turn, can be attributed

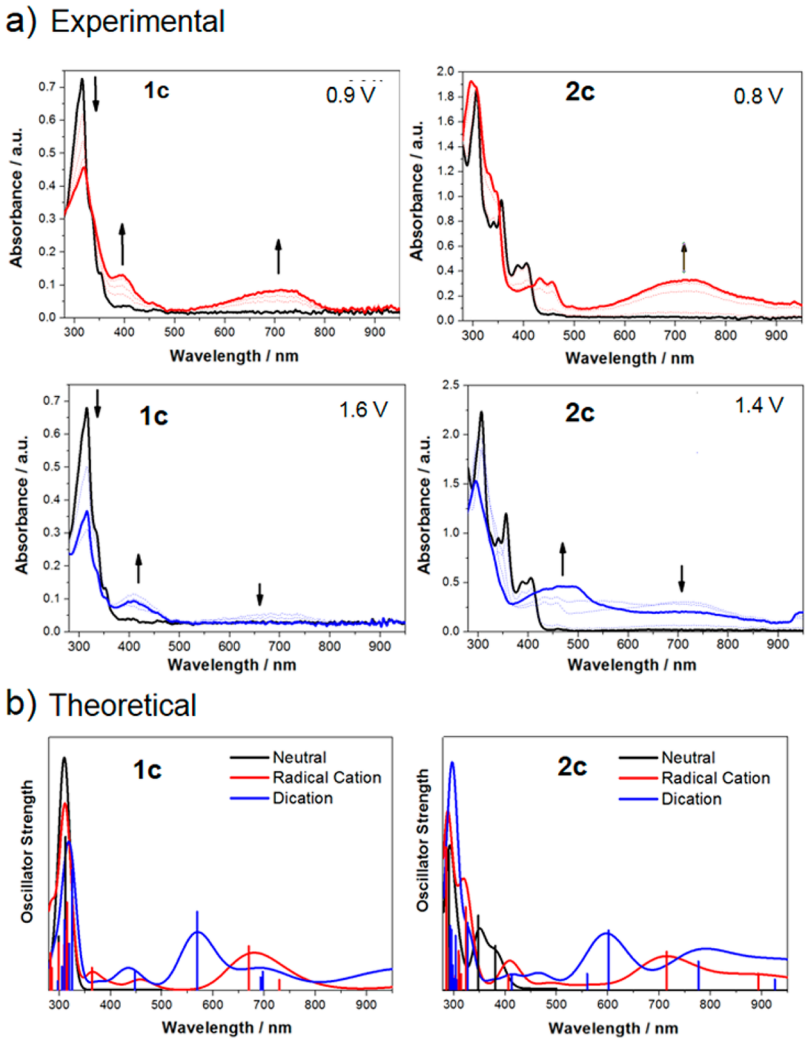

Figure 4. (a) UV/vis−NIR spectra of **1c** and **2c** obtained at different time intervals after applying a potential of 0.90−0.80 V (top) and 1.6−1.4 V (bottom) in CH_3CN. (b) Simulated absorption spectra predicted for the neutral, radical cation, and dication of **1c** and **2c** together with the TD-DFT (B3LYP/6-31G** level) excitations (wavelength versus oscillator strength) shown as vertical bars.

dx.doi.org/10.1021/jp412129m | *J. Phys. Chem. C* 2014, 118, 5470−5477

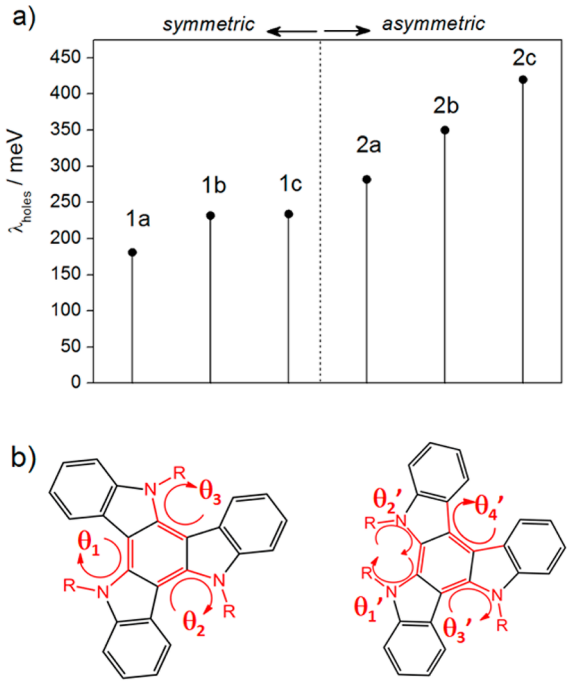

Symmetric Systems			
Compound	$\Delta\theta_1$	$\Delta\theta_2$	$\Delta\theta_3$
1a	0	0	0
1b	7	7	1
1c	8	8	1

Asymmetric Systems				
Compound	$\Delta\theta_1'$	$\Delta\theta_2'$	$\Delta\theta_3'$	$\Delta\theta_4'$
2a	14	18	3	2
2b	10	15	7	4
2c	7	23	7	7

Figure 5. (a) DFT-calculated reorganization energy values for holes (λ_h) for the symmetric and asymmetric triindole derivatives at the B3LYP/6-31G** level. (b) DFT-calculated dihedral changes (in absolute values) upon oxidation when going from the neutral to the cation states.

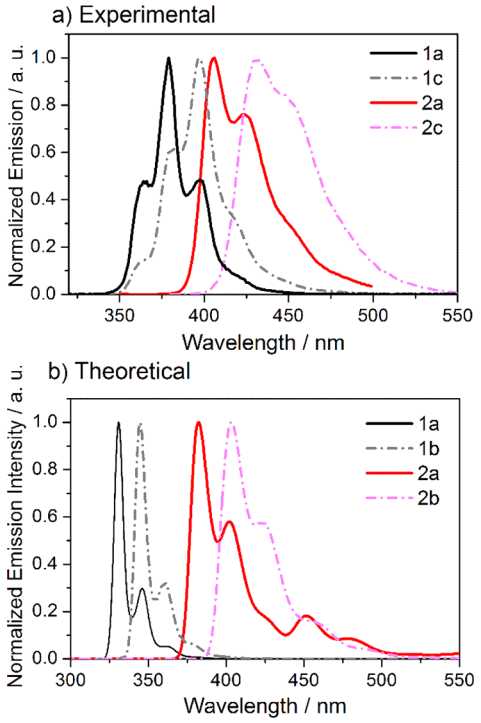

Figure 6. (a) Experimental emission spectra of the symmetric **1a**, **1c** and asymmetric **2a**, **2c** systems in CH_2Cl_2 solutions. (b) Vibronically resolved normalized emission of **1a**, **1b** and **2a**, **2b** systems. The methyl-susbtituted **1b** and **2b** are taken as models for the octyl-substituted **1c** and **2c** systems.

Table 2. Fluorescence Quantum Yields of 1a (λ_{exc} = 305 nm), 1c (λ_{exc} = 317 nm), 2a (λ_{exc} = 347 nm), and 2c (λ_{exc} = 357 nm) in CH_2Cl_2 ($c = 5 \times 10^{-6}$ M)

compound	$\lambda_{max,em}$/nm	Φ_f
1a	379	0.03
2a	405	0.42
1c	397	0.35
2c	431	0.75

to the fact that our calculations are in gas phase and do not account for geometrical distortions that are expected to occur in solution. It is interesting to note that the estimated HOMO levels from the first oxidation potentials of all the systems under study are adequate for the easy hole injection from gold electrode (Au work function 5.1 eV).

The influence of the platform symmetry on the electronic structure of the different oxidized species has been investigated by means of chemical oxidation, spectroelectrochemistry, and DFT calculations. Figure 4 shows the electronic spectra recorded during the electrochemical oxidation of **1c** and **2c** in CH_3CN. Upon oxidation at 0.90−0.80 V, the absorption of the neutral species disappears and a dominant broad band appears at 720 nm that can be ascribed to the formation of the radical cation species (Figure 4). This first process is found to be completely reversible for both systems as confirmed by back-reduction that recovers the neutral parent systems (Figures S3 and S5). TD-DFT calculations for the radical cation species allow the assignment of this experimental band to a HOMO−2 → SOMO transition predicted at 670 (715) nm for $\mathbf{1c}^{\bullet+}$ ($\mathbf{2c}^{\bullet+}$); the molecular orbital topologies are shown in the Figure S8. As observed in Figure 4, further increase of the potential up to 1.6−1.4 V drives to the disappearance of the band at 720 nm together with the emergence of new bands at 410 nm in **1c** and 480 nm in **2c**, presumably corresponding to the formation of the corresponding dications. Back-reduction from this second oxidation process leads to the recovery of the neutral compounds only in the case of **2c**, highlighting the higher stability of the cation in the asymmetric platform. Similar spectral changes evolution has been observed for the UV/vis−NIR spectra recorded upon in situ chemical doping with $NOSbF_6$ (see Figures S4 and S6). The blue-shift of the dication bands with respect to those of the parent radical cation is very well captured by TD-DFT calculations that predict a vertical transition at 568 (602) nm for the dication of **1c** (**2c**). Note that a similar electronic spectral evolution upon oxidation has been predicted for the methyl-substituted **1b** and **2b** compounds (Figure S9 and Table S2)

The easy one-electron reversible oxidations of these derivatives render them potential candidates as hole-transport materials. In fact, symmetric triindole have been found to be a high hole mobility semiconductor in both its crystalline[27] and liquid-crystalline state.[15,16] We now turn to a discussion of the intramolecular reorganization energies λ associated with hole

dx.doi.org/10.1021/jp412129m | J. Phys. Chem. C 2014, 118, 5470−5477

a)

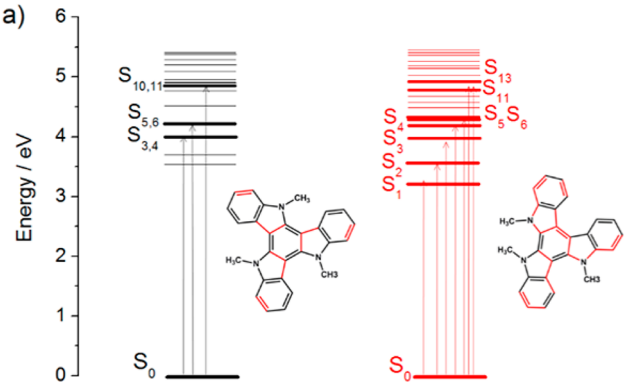

b)

Symmetric Systems			
Compound	$\Delta\theta_1$	$\Delta\theta_2$	$\Delta\theta_3$
1a	0	0	0
1b	2	2	2
Asymmetric Systems			
Compound	$\Delta\theta_1$'	$\Delta\theta_2$'	$\Delta\theta_3$'	$\Delta\theta_4$'
2a	15	21	4	1
2b	3	11	9	1

Figure 7. (a) TD-DFT excitation energies (B3LYP/6-31G** level) for **1b** and **2b** with the active transitions (allowed transitions) shown by arrows. The bonds highlighted in red are those related with the largest geometric changes along the $S_1 \rightarrow S_0$ transition. **1b** and **2b** systems are taken as model systems for the symmetric and asymmetric platforms, respectively. (b) DFT-calculated dihedral changes (in absolute values) upon when going from the S_1 excited state to the S_0 ground state. See Figure 5 for the dihedral captions.

transfer (λ_h), a molecular parameter which considers the structural reorganization needed to accommodate charge as a prerequisite for efficient transport. As see in Figure 5, larger λ_h values are found when the symmetry is lowered; this is in line with the larger geometrical relaxation found upon oxidation in the asymmetric platform, which mainly involves the central benzene ring and the C−N bonds connected to it, especially those facing in the same side (see the Supporting Information). However, it is important to note that the λ_h values for the asymmetric molecules (in the range of 282−420 meV) are in the same order than those calculated for many other organic systems considered as good hole-transport materials. For instance, values of 281 and 306 meV were obtained for phenyl-substituted tetrathienoacene (DP-TTA) and dithienoacene (DP-DTT) for which hole field-effect mobilities as high as 0.28[45] and 0.31[46] $cm^2/(V{\cdot}s)$, respectively, were reported.

On the other hand, *N*-alkylation increases the λ_h values (i.e., by 138 meV upon insertion of octyl groups from **2a** to **2c**). This is attributed to the larger distortions found upon oxidation when the nitrogen atoms are substituted with alkyl groups, especially in the case of the asymmetric platforms (see Figure 5b). In fact, the larger DFT dihedral changes are found in **2c** that exhibits the highest λ_h value (420 meV) within the series while the totally planar symmetric **1a** system displays the lowest λ_h value (181 meV).

Fluorescence Spectra. The fluorescent properties of the C_3-symmetric derivatives vary significantly when compared to their asymmetric analogues. Lowering the symmetry of the aromatic platform produces a red-shift of the emission maximum by about 30 nm and greatly enhances the quantum yield efficiency (see Figure 6 and Table 2).

The theoretical emission spectra of **1a** and **2a** including the vibronic progression for the $S_1 \rightarrow S_0$ transition reproduces quite well those experimentally observed (see Figure 6b). By comparing the shape of the emission spectra of **1a** and **2a** (or **1c** and **2c**), it is clear that the asymmetric derivative displays a larger electron−phonon coupling than its symmetric analogue; this is in consonance with the large relaxation energy of the $S_1 \rightarrow S_0$ transition obtained for the asymmetric platforms (see Table S2). By looking at the Huang−Rhys factors (dimensionless electron−vibration coupling constant) that provides a measure of the amount of energy contributed by a given mode to the overall relaxation energy (see Tables S3−S6), we observe that the vibronic progression in **1a** is mainly determined by the presence of two normal modes at 632 and 1330 cm^{-1}, while that in the less symmetric **2a** is mainly determined by the presence of several low-frequency modes associated with out-of-plane vibrations (an illustration of the main normal modes are displayed in the Supporting Information). On the other hand, *N*-alkylation results in a broader vibronic progression; this is associated with the larger contributions of the out-of-plane normal modes in the most distorted alkyl-substituted systems, in consonance with the larger distortion from coplanarity observed upon *N*-alkyl substitution (see Tables S4−S6).

Figure 7 displays the TD-DFT energies for the low-lying excitations together with the structural changes along the $S_1 \rightarrow S_0$ transition in **1b** and **2b** systems taken as model systems (the calculated bond length changes are displayed in the Supporting Information). The increase in the fluorescence efficiency in the asymmetric derivatives can be related to (i) the fact that the $S_0 \rightarrow S_1$ transition becomes allowed in the asymmetric systems while it is forbidden in the symmetric derivatives, and (ii) the larger structural changes upon $S_1 \rightarrow S_0$ transition observed in the asymmetric platforms in comparison to the symmetric derivatives which results in a less favorable coupling between the S_0 and S_1 states and thus favoring the fluorescence.

Interestingly, *N*-alkylation leads to stronger emission in both types of derivatives (see Table 1). This can be explained by the loss of planarity caused by the introduction of alkyl chains that could have a double effect: (1) increase of geometrical changes upon going from S_1 to S_0, thus reducing the coupling between the S_0 and S_1 states, and (2) mitigation of n−π^* character contributions imparted by the lone electron pairs of the nitrogen atoms, which is known to quench fluorescence emission.[47−49]

CONCLUSION

The optical and electronic features of the asymmetric triindole platform have been investigated by using a combined experimental and theoretical approach that links electronic spectroscopies (i.e., absorption, emission, spectroelectrochemistry) with DFT calculations. A comparison with the properties of the C_3-symmetric triindole homologue is proposed. Lowering the symmetry of the platform results in (i) slightly lower oxidation potential and red-shift of the absorption edge in agreement with the observed HOMO destabilization and LUMO stabilization; (ii) higher fluorescence quantum yield, which is related with the large geometrical differences between the S_0 and S_1 states and the allowed character of the $S_0 \rightarrow S_1$ transition; (iii) a broadening of the vibrational emission features that are mainly determined by the strong coupling

dx.doi.org/10.1021/jp412129m | J. Phys. Chem. C 2014, 118, 5470−5477

with the low-frequency modes; (iv) more stable cation and dication species as observed by inspection of the electronic absorption spectra evolution upon oxidation in combination with TD-DFT calculations; and (v) larger intramolecular reorganization energies for hole transfer, which is consistent with the observed significant geometrical relaxations upon oxidation.

The insertion of alkyl groups on the nitrogen atoms is found to further increase the fluorescence efficiencies and reorganization energies, especially in the asymmetric systems. This is explained in connection with the larger structural changes (distortions from coplanarity) observed upon *N*-alkylation when going from the S_1 excited states to the S_0 ground states and upon oxidation, respectively.

In summary, this detailed structure−property study reveals that the photophysical and electronic properties of triindoles can significantly be tuned via lowering the symmetry of the conjugated platform as well as *N*-alkyl functionalization. These intramolecular features together with the intermolecular effects are critical for their performance in organic electronics. Further studies of the symmetry lowering influence on the morphologies and charge-transport properties are currently under investigation. We believe that this work may provide guidance for further development of these materials with improved potential for electronic applications.

■ ASSOCIATED CONTENT

Supporting Information

Additional experimental data (characterization of **2c**, absorption spectra, cyclic voltammograms, and spectroelectrochemical measurements and chemical oxidation) as well as theoretical data (simulated absorption spectra of neutral, cation and dication species; calculated bond length modifications upon oxidation; $S_0 \rightarrow S_1$ relaxation energies; Huang−Rhys factors related with the $S_0 \rightarrow S_1$ transition; illustrations of the normal modes yielding the largest Huang−Rhys factors; absorption and emission vibrational progression of **2a** and **2b**). This material is available free of charge via the Internet at http://pubs.acs.org.

■ AUTHOR INFORMATION

Corresponding Authors

*E-mail bgl@icmm.csic.es (B.G.-L.).
*E-mail teodomiro@uma.es (J.T.L.N.).
*E-mail carmenrd@uma.es (M.C.R.D.).

Notes

The authors declare no competing financial interest.

■ ACKNOWLEDGMENTS

This work was financially supported by the MICINN of Spain (CTQ2010-18813) and the CAM (Project S2009/MAT-1756/CAM), MINECO of Spain (CTQ2012-33733), Junta de Andalucía (P09-FQM-4708). M.C.R.D. thanks the MICINN for a "Ramón y Cajal" Research contract. D.A.S.F. gratefully acknowledges the financial support from the Brazilian Research Councils CNPq CAPES, CNPq (grant 303084/2010-3) and FAP-DF (Fundaçâo de Apoio à Pesquisa do Distrito Federal).

■ REFERENCES

(1) Beaujuge, P. M.; Reynolds, J. R. Color Control in π-Conjugated Organic Polymers for Use in Electrochromic Devices. *Chem. Rev.* **2010**, *110*, 268−320.

(2) Burroughes, J. H.; Bradley, D. D. C.; Brown, A. R.; Marks, R. N.; Mackay, K.; Friend, R. H.; Burns, P. L.; Holmes, A. B. Light Emitting-Diodes Based on Conjugated Polymers. *Nature* **1990**, *347*, 539−541.

(3) Facchetti, A. π-Conjugated Polymers for Organic Electronics and Photovoltaic Cell Applications. *Chem. Mater.* **2011**, *23*, 733−758.

(4) Guenes, S.; Neugebauer, H.; Sariciftci, N. S. Conjugated Polymer-Based Organic Solar Cells. *Chem. Rev.* **2007**, *107*, 1324−1338.

(5) Gustafsson, G.; Cao, Y.; Treacy, G. M.; Klavetter, F.; Colaneri, N.; Heeger, A. J. Flexible Light-Emitting-Diodes Made From Soluble Conducting Polymers. *Nature* **1992**, *357*, 477−479.

(6) Franceschin, M.; Ginnari-Satriani, L.; Alvino, A.; Ortaggi, G.; Bianco, A. Study of a Convenient Method for the Preparation of Hydrosoluble Fluorescent Triazatruxene Derivatives. *Eur. J. Org. Chem.* **2010**, *2010*, 134−141.

(7) Robertson, N.; Parsons, S.; MacLean, E. J.; Coxall, R. A.; Mount, R. A. Preparation, X-Ray Structure and Properties of a Hexabrominated, Symmetric Indole Trimer and its TCNQ Adduct: a New Route to Functional Molecular Systems. *J. Mater. Chem.* **2000**, *10*, 2043−2047.

(8) Gómez-Lor, B.; Echavarren, A. M. Synthesis of a Triaza Analogue of Crushed-Fullerene by Intramolecular Palladium-Catalyzed Arylation. *Org. Lett.* **2004**, *6*, 2993−2996.

(9) Bura, T.; Leclerc, N.; Fall, S.; Lévêque, P.; Heiser, T.; Ziessel, R. Absorption Tuning of Monosubstituted Triazatruxenes for Bulk Heterojunction Solar Cells. *Org. Lett.* **2011**, *13*, 6030−6033.

(10) Coya, C.; Ruiz, C.; Álvarez, Á. L.; Álvarez-García, S.; García-Frutos, E. M.; Gómez-Lor, B.; de Andrés, A. Star-Shaped Hexaaryltriindoles Small Molecules: Tuning Molecular Properties Towards Solution Processed Organic Light Emitting Devices. *Org. Electron.* **2012**, *13*, 2138−2148.

(11) Lai, W. Y.; He, Q. Y.; Zhu, R.; Chen, Q. Q.; Huang, W. Kinked Star-Shaped Fluorene/ Triazatruxene Co-oligomer Hybrids with Enhanced Functional Properties for High-Performance, Solution-Processed, Blue Organic Light-Emitting Diodes. *Adv. Funct. Mater.* **2008**, *18*, 265−276.

(12) Levermore, P. A.; Xia, R.; Lai, W.; Wang, X. H.; Huang, W.; Bradley, D. D. C. Deep-blue Light Emitting Triazatruxene Core/ Oligo-fluorene Branch Dendrimers for Electroluminescence and Optical Gain Applications. *J. Phys. D: Appl. Phys.* **2007**, *40*, 1896−1901.

(13) Valentine, R. A.; Whyte, A.; Awaga, K.; Robertson, N. New Indole Trimers as Precursors for Molecular Electronic Materials. *Tetrahedron Lett.* **2012**, *53*, 657−660.

(14) Gomez-Lor, B.; Alonso, B.; Omenat, A.; Serrano, J. L. Electroactive C_3 Symmetric Discotic Liquid-Crystalline Triindoles. *Chem. Commun.* **2006**, 5012−5014.

(15) Benito-Hernández, A.; Pandey, U. K.; Cavero, E.; Termine, R.; García-Frutos, E. M.; Serrano, J. L.; Golemme, A.; Gómez-Lor, B. High Hole Mobility in Triindole-Based Columnar phases: Removing the Bottleneck of Homogeneous Macroscopic Orientation. *Chem. Mater.* **2013**, *25*, 117−121.

(16) García-Frutos, E. M.; Pandey, U. K.; Termine, R.; Omenat, A.; Barberá, J.; Serrano, J. L.; Golemme, A.; Gómez-Lor, B. High Charge Mobility in Discotic Liquid-Crystalline Triindoles: Just a Core Business? *Angew. Chem., Int. Ed.* **2011**, *50*, 7399−7402.

(17) Ye, Q.; Chang, J.; Shao, J.; Chi, C. Large Core-Expanded Triazatruxene-Based Discotic Liquid Crystals: Synthesis, Characterization and Physical Properties. *J. Mater. Chem.* **2012**, *22*, 13180−13186.

(18) Kaneko, T.; Matsuo, M.; Iitaka, Y. A Novel Indole Trimer; Diindolo[2,3-*a*:2′,3′-*c*]carbazole. *Heterocycles* **1979**, *12*, 471−474.

(19) Bocchi, V.; Colombo, A.; Porzio, W. The Synthesis and Structural Characterization of a Charge Transfer Complex of Iodine and Indole Trimer. *Synth. Met.* **1996**, *80*, 309−313.

(20) Jennings, P.; Jones, A. C.; Mount, A. R.; Thomson, A. D. Electrooxidation of 5-Substituted Indoles. *J. Chem. Soc., Faraday Trans.* **1997**, *93*, 3791−3797.

(21) Mackintosh, J. G.; Mount, A. R. Electropolymerisation of Indole-5-carboxylic Acid. *J. Chem. Soc., Faraday Trans.* **1994**, *90*, 1121−1125.
(22) Mackintosh, J. G.; Wright, S. J.; Langridge-Smith, P. R. R.; Mount, A. R. Electrochemical Copolymerisation of 5-substituted Indoles. *J. Chem. Soc., Faraday Trans.* **1996**, *92*, 4109−4114.
(23) Mount, A. R.; Thomson, A. D. Electrooxidation of N-methylindole. *J. Chem. Soc., Faraday Trans.* **1998**, *94*, 553−558.
(24) Henry, J. B.; Mount, A. R. Calculation of the Redox Properties of Aromatics and Prediction of Their Coupling Mechanism and Oligomer Redox Properties. *J. Phys. Chem. A* **2009**, *113*, 13023−13028.
(25) Kettle, L. J.; Bates, S. P.; Mount, A. R. Calculations of the Electronic Structure of Substituted Indoles and Prediction of Their Oxidation Potentials. *Phys. Chem. Chem. Phys.* **2000**, *2*, 195−201.
(26) Greci, L.; Tommasi, G.; Petrucci, R.; Marrosu, G.; Trazza, A.; Sgarabotto, P.; Righi, L.; Alberti, A. Oxidative Trimerization of Indole: on the Formation of Dications and Radical Cations by Reaction of Indole and Nitrosobenzene in the Presence of Acids. *J. Chem. Soc., Faraday Trans. 2* **2000**, 2337−2342.
(27) García-Frutos, E. M.; Gutierrez-Puebla, E.; Monge, M. A.; Ramírez, R.; de Andrés, P.; de Andrés, A.; Ramírez, R.; Gómez-Lor, B. Crystal Structure and Charge-Transport Properties of N-trimethyltriindole: Novel p-Type Organic Semiconductor Single Crystals. *Org. Electron.* **2009**, *10*, 643−652.
(28) Gallego-Gómez, F.; García-Frutos, E. M.; Villalvilla, J. M.; Quintana, J. A.; Gutierrez-Puebla, E.; Monge, A.; Díaz-García, M. A.; Gómez-Lor, B. Very Large Photoconduction Enhancement Upon Self-Assembly of a New Triindole Derivative in Solution-Processed Films. *Adv. Funct. Mater.* **2011**, *21*, 738−745.
(29) Bergman, J.; Eklund, N. Synthesis and Studies of Tris-Indolobenzenes and Related Compounds. *Tetrahedron* **1980**, *36*, 1445−1450.
(30) Becke, A. D. Density-Functional Thermochemistry. III. The Role of Exact Exchange. *J. Chem. Phys.* **1993**, *98*, 5648−5652.
(31) Lee, C. T.; Yang, W. T.; Parr, R. G. Development of the Colle-Salvetti Correlation-Energy Formula into a Functional of the Electron-Density. *Phys. Rev. B* **1988**, *37*, 785−789.
(32) Harihara, P. C.; Pople, J. A. Influence of Polarization Functions on Molecular-Orbital Hydrogenation Energies. *Theor. Chim. Acta* **1973**, *28*, 213−222.
(33) Hehre, W. J.; Ditchfield, R.; Pople, J. A. Self-Consistent Molecular-Orbital Methods. 12. Further Extensions of Gaussian-Type Basis Sets for Use in Molecular-Orbital Studies of Organic-Molecules. *J. Chem. Phys.* **1972**, *56*, 2257−2261.
(34) Frisch, M. J.; et al. *Gaussian 09, revision C.01*; Wallingford, CT, 2009.
(35) Bredas, J. L.; Beljonne, D.; Coropceanu, V.; Cornil, J. Charge-Transfer and Energy-Transfer Processes in π-Conjugated Oligomers and Polymers: A Molecular Picture. *Chem. Rev.* **2004**, *104*, 4971−5003.
(36) Gross, E. K. U.; Kohn, W. In *Advances in Quantum Chemistry*; Per-Olov, L., Ed.; Academic Press: New York, 1990; Vol. *21*, pp 255−291.
(37) Runge, E.; Gross, E. K. U. Density-Functional Theory for Time-Dependent Systems. *Phys. Rev. Lett.* **1984**, *52*, 997−1000.
(38) Barone, V.; Bloino, J.; Biczysko, M.; Santoro, F. Fully Integrated Approach to Compute Vibrationally Resolved Optical Spectra: From Small Molecules to Macrosystems. *J. Chem. Theory Comput.* **2009**, *5*, 540−554.
(39) Bloino, J.; Biczysko, M.; Crescenzi, O.; Barone, V. Integrated Computational Approach to Vibrationally Resolved Electronic Spectra: Anisole as a Test Case. *J. Chem. Phys.* **2008**, *128*, 244105.
(40) Please note that the absorption maximum is slightly blue-shifting by about 10 nm upon symmetry lowering; however, our TD-DFT calculations confirm that this band is associated to electronic transitions between excited states that have different nature in the symmetric and asymmetric systems. Therefore, the evolution of the absorption maximum upon symmetry lowering cannot be directly correlated.
(41) The discrepancy between the experimental and theoretical part of the spectrum in the region of 350 nm for the symmetric **1a** and **1c** systems can be related to the distortions from the C_3 geometry in solution that can contribute to the actication of the $S_0 \rightarrow S_1$ transition.
(42) Gritzner, G.; Kuta, J. Recommendations on Reporting Electrode-Potentials in Nonaqueous Solvents (Recommendations 1983). *Pure Appl. Chem.* **1984**, *56*, 461−466.
(43) Bard, A. J.; Faulkner, L. R. *Electrochemical Methods: Fundamentals and Applications*; Wiley: New York, 2001.
(44) Trassati, S. The Absolute Electrode Potential: An Explanatory Note. *Pure Appl. Chem.* **1986**, *58*, 955−966.
(45) Youn, J.; Huang, P.-Y.; Huang, Y.-W.; Chen, M.-C.; Lin, Y.-J.; Huang, H.; Ortiz, R. P.; Stern, C.; Chung, M.-C.; Feng, C.-Y.; Chen, L.-H.; Facchetti, A.; Marks, T. J. Versatile α,ω-Disubstituted Tetrathienoacene Semiconductors for High Performance Organic Thin-Film Transistors. *Adv. Funct. Mater.* **2012**, *22*, 48−60.
(46) Sun, Y. M.; Ma, Y. Q.; Liu, Y. Q.; Lin, Y. Y.; Wang, Z. Y.; Wang, Y.; Di, C. A.; Xiao, K.; Chen, X. M.; Qiu, W. F.; Zhang, B.; Yu, G.; Hu, W. P.; Zhu, D. B. High-Performance and Stable Organic Thin-Film Transistors Based on Fused Thiophenes. *Adv. Funct. Mater.* **2006**, *16*, 426−432.
(47) Chang, J. H.; Choi, Y. M.; Shin, Y. K. A Significant Fluorescence Quenching of Anthrylaminobenzocrown Ethers by Paramagnetic Metal Cations. *Bull. Korean Chem. Soc.* **2001**, *22*, 527−530.
(48) Juarez, R.; Moreno Oliva, M.; Ramos, M.; Segura, J. L.; Aleman, C.; Rodriguez-Ropero, F.; Curco, D.; Montilla, F.; Coropceanu, V.; Bredas, J. L.; Qi, Y.; Kahn, A.; Ruiz Delgado, M. C.; Casado, J.; Lopez Navarrete, J. T. Hexaazatriphenylene (HAT) versus tri-HAT: The Bigger the Better? *Chem.—Eur. J.* **2011**, *17*, 10312−10322.
(49) Mrozek, J.; Rzeska, A.; Guzow, K.; Karolczak, J.; Wiczk, W. Influence of Alkyl Group on Amide Nitrogen Atom on Fluorescence Quenching of Tyrosine Amide and N-Acetyltyrosine Amide. *Biophys. Chem.* **2004**, *111*, 105−113.

Organic LETTERS

Letter

pubs.acs.org/OrgLett

Triindole-Bridge-Triindole Dimers as Models for Two Dimensional Microporous Polymers

Constanza Ruiz,[†] Juan T. López Navarrete,[‡] M. Carmen Ruiz Delgado,*[,‡] and Berta Gómez-Lor*[,†]

[†]Instituto de Ciencia de Materiales de Madrid, CSIC, Cantoblanco 28049, Madrid, Spain

[‡]Department of Physical Chemistry, University of Málaga, 29071 Málaga, Spain

Supporting Information

ABSTRACT: New dimers with two triindole subunits bound together through different linkers (*p*-phenylene or diacetylene groups) have been synthesized and studied as model systems to determine the differences in the electron transfer ability of the two bridging units. Our results show that whereas a *p*-phenylene bridge nearly isolates the two subunits of the dimers a diacetylene bridge allows a high level of electronic connection between them.

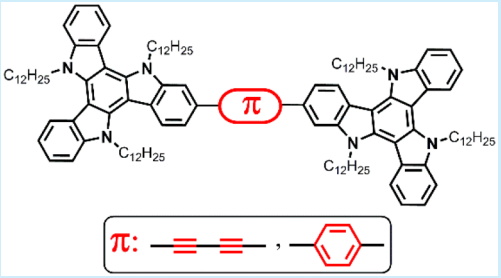

During the past decade, heptacyclic 10,15-dihydro-5*H*-diindolo[3,2-a:3′,2′-c]carbazole (triindole) has been extensively studied as a new π-conjugated platform in the construction of dendrimers and self-assembling materials for optoelectronics due to its strong light emission[1] and efficient charge transport properties.[2,3] Especially remarkable is the record hole mobility values determined on triindole-based semiconducting liquid crystals as a result of the favorable synergy between the intrinsic properties of the platform and its supramolecular arrangement.[3] This molecule has also recently been explored as the functional component in a microporous chemosensing polymer.[4]

Covalent microporous polymers constituted by π-conjugated building units have emerged as a new kind of organic material for electronic applications.[5] In this type of material, the covalent linkage of functional π-conjugated components gives rise to two-dimensional (2D) layers, among which π -π stacking interactions can induce additional order while their intrinsic porosity offers significant opportunities to incorporate guests/chemicals to tune their functionalities. Potential applications have been demonstrated, such as light harvesting,[6] luminescence,[7] sensing,[4] photochemical water splitting,[8] and charge transport.[9] For optoelectronic applications, it is highly desirable that the π-conjugation spans the 2D sheets; however, in covalent microporous polymers, electronic conjugation is often limited to the constituent building π-functional units. The degree of lateral conjugation and electronic coupling is highly dependent upon the nature of the bridge that connects the individual interacting components and has a profound effect on the behavior of excitons and charge carriers. In spite of the impressive progress that this field has experienced during the past few years, the insoluble character of covalent microporous polymers limits detailed postsynthetic studies to investigate how the structure will affect the desired properties and thus the design of optimal polymeric materials on a molecular basis. Note that examples of soluble conjugated microporous polymers reported to date are quite scarce.[10] Discrete low-molecular weight oligomers with well-defined chemical structures may represent invaluable models to establish clear structure−property relationships, therefore avoiding insolubility, irreproducibility issues, and variations from batch-to-batch, which are common drawbacks in polymeric materials.

To facilitate the design of new triindole-based polymeric materials on a molecular basis and establish clear guidelines to fine-tune parameters, such as energy gap, light absorption, and light emitting properties, we have synthesized two new dimers in which the two triindole molecules are linked by *p*-phenylene or diacetylene bridges. The present work aims to investigate the influence of the π-bridge in the electronic communication between the two triindole groups. To this end, we performed a detailed study of the electronic and photophysical properties of the new dimers and their monomeric analogues using absorption, emission, and Raman spectroscopies, cyclic voltammetry, and DFT calculations.

The synthesis of the two dimeric molecules has been performed starting from 2-monobromo-*N*-dodecyltriindole. This molecule has been obtained by bromination of *N*-dodecyltriindole **1** with 1 equiv of NBS under high-dilution conditions. Under these conditions, compound **2** is obtained along with some dibrominated derivatives. It should be noted that this molecule has been previously wrongly assigned as 3-monobromotriindole.[11] The unambiguous characterization of this molecule has been performed by MS, ^{1}H and ^{13}CNMR, as well as HMBC and HMQC 2D experiments (see Supporting Information).[12] Compound **6**, with two triindole units separated by a phenylene linker, was obtained by a

Received: March 27, 2015
Published: April 20, 2015

DOI: 10.1021/acs.orglett.5b00900
Org. Lett. 2015, 17, 2258−2261

palladium-catalyzed Suzuki cross-coupling reaction between 2 equiv of 2-bromotriindole **2** and 1 equiv of benzene 1,4-diboronic acid. Separately, compound **7** was obtained by Glaser homocoupling of 1-ethynyltrindol **5** (obtained by Sonogashira coupling of the monobrominated precursor with TMS acetylene to render **4**, followed by deprotection with NaOH).

Scheme 1. Synthesis of Dimeric Molecules 6 and 7 and Their Monomer Analogues 3 and 5, Respectively

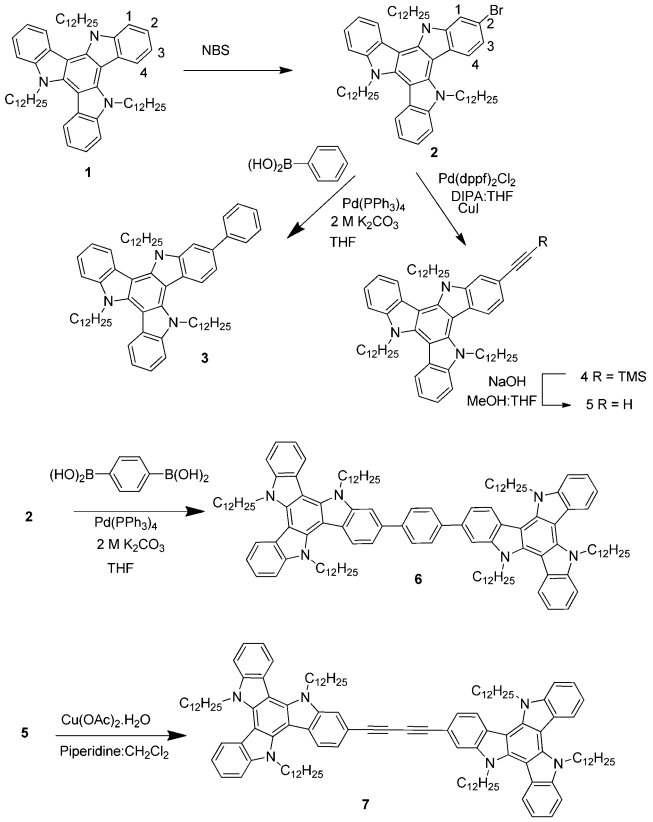

As shown in Figure 1 and Table 1, the electronic absorption maxima and the absorption edge of **3** and **5** monomers are slightly red-shifted when compared to the unsubstituted triindole **1** with both ethynyl and phenyl substituents exerting a very similar effect. This HOMO−LUMO gap decrease is associated with stabilization of the LUMO upon insertion of the ethynyl or phenyl groups, while the HOMO energies are slightly affected; note that the LUMOs of **3** and **5** are more localized at the external ethynyl or phenyl groups, whereas their HOMOs are delocalized over the entire molecular π-frameworks (see Figure S1, Supporting Information). However, when going from the monomers to the dimers, the overall shapes of the electronic spectra change with the appearance of a new band at a longer wavelength and a significant red-shift of the absorption edge with this effect being more significant in the diacetylene-bridged triindole dimer **7** (see Figure 1). Time-dependent DFT vertical excitation energies are in agreement with the experimental data and predict that this band is associated with a HOMO → LUMO one-electron excitation (see Table 1 and Figure S2, Supporting Information). As evidenced by the frontier molecular orbitals of dimers **6** and **7** shown in Figure 2, the lowest-energy electronic transition has a certain charge-transfer character (i.e., the HOMOs are delocalized over the entire molecular π-frameworks whereas the LUMOs are more localized at the central spacer) thus resulting in a HOMO−LUMO decrease. This effect is more pronounced in **7** due to the electron-accepting character and cylindrical symmetry of the diacetylenic spacer, which allows

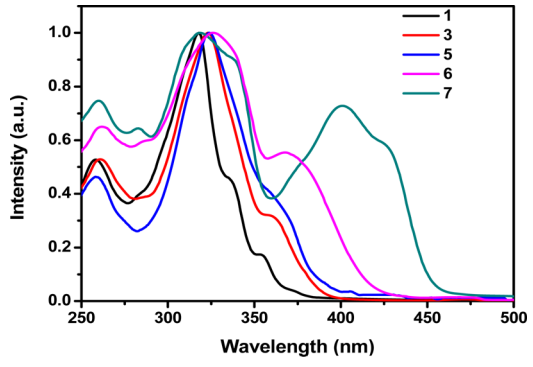

Figure 1. Experimental UV−vis spectra of unsubstituted **1**, monomers **3** and **5**, and dimers **6** and **7** in CH_2Cl_2, $c = 5 \times 10^{-6}$ M.

Table 1. Optical and Fluorescence Properties

	HOMO[a] (eV)	LUMO[a] (eV)	$\lambda_{(abs)}$[b] (nm)	$\lambda_{(abs,calc)}$[c] (nm)	$\lambda_{(em)}$ (nm)	Φ_{PL}[d] (%)
1	−5.05	−1.78	318 (4.19)	312 (f = 0.46)	397	0.23
3	−5.05	−1.93	320 (5.10)	353 (f = 0.30)	421	0.50
5	−5.13	−1.97	322 (4.90)	352 (f = 0.21)	427	0.47
6	−5.06	−2.07	326 (5.01)	390 (f = 1.66)	447	0.48
7	−5.08	−2.39	318 (5.23)	444 (f = 2.38)	468	0.42

[a]The HOMO energy values for **1** to **7** were estimated from the first oxidation potential with respect to the ferrocene/ferrocenium redox couple. The LUMO energy values were estimated by subtracting the energy of the optical band gap obtained by UV−vis from the HOMO values. [b]Absorbance (log ε) values are given in parentheses. [c]Absorption maxima calculated at the B3LYP/6-31G** level within the TD-DFT approach. Oscillator strengths (f) are given in parentheses. [d]Fluorescence quantum yields are relative to quinine hemisulfate.

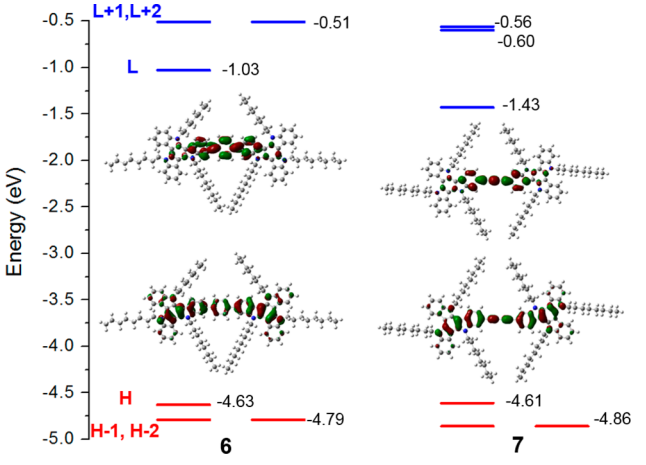

Figure 2. DFT-calculated molecular orbital energies (B3LYP/6-31G** level) for dimers **6** and **7**. The topologies of the frontier molecular orbitals are also shown.

DOI: 10.1021/acs.orglett.5b00900
Org. Lett. 2015, 17, 2258−2261

for better extension of π-conjugation.[13] In fact, the rotation around the triindole moieties and the central spacer has been explored by DFT calculations (see Figure S3, Supporting Information), and a rather flat torsional potential is found for the diacetylenic-bridged dimer **7** with a very small energy difference (0.32 kcal/mol) between the perpendicular conformation and the most stable *trans* coplanar conformer. The coexistence of these two conformers at room temperature has also been confirmed by temperature-dependent absorption spectra measurements (see Supporting Information). However, the most stable conformation of dimer **6** corresponds to a moderately distorted configuration, where the central phenyl ring is rotated by 36° with respect to the triindole moieties, which is thus less favorable toward π-electron delocalization than that of the diacetylenic spacer.

Next, the effective π-conjugation of the triindole dimers are investigated by Raman spectroscopy. As seen in Figure 3, the

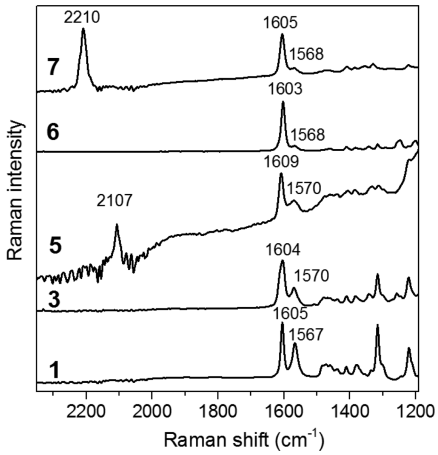

Figure 3. Experimental Raman spectra of unsubstituted **1**, monomers **3** and **5**, and dimers **6** and **7**.

strongest Raman band of triindole molecules is measured at ~1605 cm^{-1} and arises from a CC stretching mode (i.e., mode 8a of benzene[14]) involving the external benzene rings, whereas the Raman band at ~1567 cm^{-1} is due to the same CC stretching mode but located in the innermost benzene ring. Compared to unsubstituted triindole **1**, this doublet band increases in intensity in the monomers and dimers with respect to the rest of the bands recorded below 1500 cm^{-1}. A frequency downshift of this doublet and an increase in the I_{1605}/I_{1567} intensity ratio is also found in the following order: unsubstituted **1** < monofunctionalized monomers **3** and **5** < dimers **6** and **7**. This indicates more efficient π-conjugation in the dimers, which is in consonance with their larger geometrical relaxation when compared to the monomers (see Figure S4, Supporting Information). In diacetylenic-bridged dimer **7**, the most intense Raman band measured at 2210 cm^{-1} is described as fully in-phase C≡C stretching vibrations and evidences the strong participation of the diacetylenic bridge in the overall π-conjugation. The increase of the intensity of this band with respect to that associated with the central benzene rings (1605 cm^{-1}) in dimer **7** compared to monomer **5** is indicative that π-conjugation takes place more efficiently in the central part of the molecules and decreases toward the ends. The good agreement found between the theoretical and experimental Raman spectra gives support to the reliability of the structural information derived from this discussion (see Figure S5, Supporting Information).

Cyclic voltammetry analysis of these electron-rich triindole platforms shows that all compounds exhibit a first oxidation reversible process, which is associated with the easy generation of a cation radical as well as the formation of higher cationic charged species (see Figure 4 for **6** and **7** dimers and the

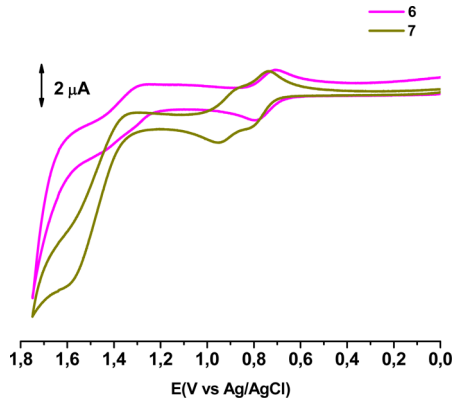

Figure 4. CV of dimers **6** and **7** at $c = 1 \times 10^{-3}$ M, recorded at a scan rate of 100 mV s^{-1} in CH_2Cl_2/0.1 M $TBAPF_6$ measured versus Ag/AgCl (3 M NaCl).

Supporting Information for the rest of the compounds). For the monomeric species, the first oxidation potential is found to slightly shift anodically on going from **3** to **5** as a consequence of the electron-withdrawing effect of the ethynyl group; this is in consonance with the small HOMO stabilization calculated for **5** (Table 1 displays the estimated HOMO levels from the first oxidation waves). For the dimers, the values of the first oxidation process are very similar and are in agreement with the low influence that the two different spacers have on the HOMO levels. However, whereas the cyclic voltammogram of dimer **6** is identical to that of its phenyltriindole monomer analogue **3**, indicating that the two triindole units are electronically isolated, the first oxidation wave of dimer **7** is split into two overlapping waves (Figure 4). This is evidence that, in the diacetylene-bridged system, the two triindole moieties are electronically coupled, allowing for their subsequent oxidation. This is consistent with the DFT calculations that show a larger charge delocalization in radical cation **7** than in **6**, and therefore better electronic conjugation across the diacetylenic group than over the phenyl spacer (see Figure S6, Supporting Information).

The easy one-electron reversible oxidation of the triindole dimers together with their moderate predicted values of hole intramolecular reorganization energy (λ_h) would render them as potential hole-transport material candidates, as previously found in unsubstituted triindoles.[15] Note that λ_h values of 149 and 163 meV are obtained for dimers **6** and **7**, respectively, which are on the same order as those calculated for many other organic systems considered to be good hole-transport materials (i.e., 306 meV was obtained for phenyl-susbtituted dithienoacene for which hole field-effect mobilities as high as 0.31 cm^2 V^{-1} s^{-1} were reported[16]).

An examination of the fluorescence properties (see Table 1) shows two clear effects: (i) a red-shift of the emission maxima is found when going from unsubstituted **1** to monofunctionalized monomers **3** and **5** and dimers **6** and **7** with this being more pronounced in the acetylenic-substituted systems compared to

DOI: 10.1021/acs.orglett.5b00900
Org. Lett. 2015, 17, 2258−2261

the phenyl-substituted analogues, and (ii) an increase in the fluorescence quantum yield is found upon insertion of the linkers with the four derivatives (**3**, **5**, **6**, and **7**) showing similar values.

In summary, we have presented the first systematic investigation focusing on the effects that π-spacers in triindole dimers exert on their fundamental properties, such as electronic, redox, and photophysical properties. Our study demonstrates that the optoelectronic properties of the triindole dimers are strongly influenced by the nature of the π-linkers; the diacetylenic bridge allows for better electronic delocalization. We hope that this study can not only advance useful structure−property relationships of conjugated triindole dimers but also guide the design of new polymeric microporous materials based on this interesting platform.

■ ASSOCIATED CONTENT

Supporting Information

Additional experimental (characterization of monomers **3** and **5** and dimers **6** and **7**, temperature variable absorption spectra of dimer **7**, emission spectra of **1** to **7** systems, cyclic voltammograms of **1**, **3**, and **5**) and theoretical data (molecular orbital energies and topologies of monomers **1**, **3**, and **5**; simulated absorption spectra of neutral species; DFT rotational barriers of dimers **6** and **7**; theoretical Raman spectra of monomers **1**, **3**, and **5** and dimers **6** and **7**; and calculated bond length modifications in the neutral species and upon oxidation). This material is available free of charge via the Internet at http://pubs.acs.org.

■ AUTHOR INFORMATION

Corresponding Authors

*E-mail: carmenrd@uma.es.

* E-mail: bgl@icmm.csic.es.

Notes

The authors declare no competing financial interest.

■ ACKNOWLEDGMENTS

This work was financially supported by the MINECO of Spain (CTQ2012-33733 and CTQ2013-40562-R) and the Comunidad de Madrid S2013/MIT-2740 and Junta de Andalucía (P09-FQM-4708). M.C.R.D. thanks the MICINN for a "Ramón y Cajal" Research contract.

■ REFERENCES

(1) (a) Lai, W. Y.; He, Q. Y.; Zhu, R.; Chen, Q. Q.; Huang, W. *Adv. Funct. Mater.* **2008**, *18*, 265−276. (b) Levermore, P. A.; Xia, R.; Lai, W.; Wang, X. H.; Huang, W.; Bradley, D. D. C. *J. Phys. D: Appl. Phys.* **2007**, *40*, 1896.

(2) (a) García-Frutos, E. M.; Gutierrez-Puebla, E.; Monge, M. A.; Ramírez, R.; Andrés, P. d.; Andrés, A. d.; Gómez-Lor, B. *Org. Electron.* **2009**, *10*, 643. (b) Reig, M.; Puigdollers, J.; Velasco, D. *J. Mater. Chem. C* **2015**, *3*, 506.

(3) (a) Ye, Q.; Chang, J.; Shao, J.; Chi, C. *J. Mater. Chem.* **2012**, *22*, 13180. (b) Benito-Hernández, A.; Pandey, U. K.; Cavero, E.; Termine, R.; García-Frutos, E. M.; Serrano, J. L.; Golemme, A.; Gómez-Lor, B. *Chem. Mater.* **2013**, *25*, 117. (c) García-Frutos, E. M.; Pandey, U. K.; Termine, R.; Omenat, A.; Barberá, J.; Serrano, J. L.; Golemme, A.; Gómez-Lor, B. *Angew. Chem., Int. Ed.* **2011**, *50*, 7399.

(4) Liu, X.; Xu, Y.; Jiang, D. *J. Am. Chem. Soc.* **2012**, *134*, 8738.

(5) (a) Xu, Y.; Jin, S.; Xu, H.; Nagai, A.; Jiang, D. *Chem. Soc. Rev.* **2013**, *42*, 8012−8031. (b) Thomas, H. *Angew. Chem., Int. Ed.* **2010**, *49*, 8328−8344.

(6) Chen, L.; Honsho, Y.; Seki, S.; Jiang, D. *J. Am. Chem. Soc.* **2010**, *132*, 6742−6748.

(7) (a) Jiang, J. X.; Trewin, A.; Adams, D. J.; Cooper, A. I. *Chem. Sci.* **2011**, *2*, 1777−1781. (b) Xu, Y.; Chen, L.; Guo, Z.; Nagai, A.; Jiang, D. *J. Am. Chem. Soc.* **2011**, *133*, 17622−17625.

(8) Sprick, R. S.; Jiang, J.-X.; Bonillo, B.; Ren, S.; Ratvijitvech, T.; Guiglion, P.; Zwijnenburg, M. A.; Adams, D. J.; Cooper, A. I. *J. Am. Chem. Soc.* **2015**, *137*, 3265.

(9) Ding, H.; Li, Y.; Hu, H.; Sun, Y.; Wang, J.; Wang, C.; Wang, C.; Zhang, G.; Wang, B.; Xu, W.; Zhang, D. *Chem.—Eur. J.* **2014**, *20*, 14614−14618. (c) Bildirir, H.; Paraknowitsch, J. P.; Thomas, A. *Chem.—Eur. J.* **2014**, *20*, 9543−9548.

(10) Cheng, G.; Hasell, T.; Trewin, A.; Adams, D. J.; Cooper, A. I. *Angew. Chem., Int. Ed.* **2012**, *51*, 12727.

(11) Bura, T.; Leclerc, N.; Fall, S.; Lévêque, P.; Heiser, T.; Ziessel, R. *Org. Lett.* **2011**, *13*, 6030.

(12) The regioselectivity of the reaction can be understood considering the radical character of the aromatic bromination exerted by NBS. The 2-position bears significantly higher electron density than the 3-position, as has been previously determined by Mulliken population analysis of the electron spin distribution of the triindole radical cation. See reference 2a.

(13) Ruiz Delgado, M. C.; Casado, J.; Hernández, V.; López Navarrete, J. T.; Fuhrmann, G.; Bäuerle, P. *J. Phys. Chem. B* **2004**, *108*, 3158−3167.

(14) Wilson, E. B.; Decius, J. C.; Cross, P. C. *Molecular Vibrations. The Theory of Infrared and Raman Vibrational Spectra*; McGraw-Hill: New York, Toronto, London, 1955.

(15) Ruiz, C.; García-Frutos, E. M.; da Silva Filho, D. A.; López Navarrete, J. T.; Ruiz Delgado, M. C.; Gómez-Lor, B. *J. Phys. Chem. C* **2014**, *118*, 5470−5477.

(16) Sun, Y. M.; Ma, Y. Q.; Liu, Y. Q.; Lin, Y. Y.; Wang, Z. Y.; Wang, Y.; Di, C. A.; Xiao, K.; Chen, X. M.; Qiu, W. F.; Zhang, B.; Yu, G.; Hu, W. P.; Zhu, D. B. *Adv. Funct. Mater.* **2006**, *16*, 426−432.

DOI: 10.1021/acs.orglett.5b00900
Org. Lett. 2015, 17, 2258−2261

The Role of CH-π Interactions in the Crystal Morphology and Packing of *N*-trialkylated Triindoles.

Constanza Ruiz,[†] Angela Benito-Hernández,[†] Enrique Gutierrez-Puebla,[†] Angeles Monge-Bravo,[†] and Berta Gómez-Lor[†]*

Instituto de Ciencia de Materiales de Madrid, CSIC, C/ Sor Juana Inés de la Cruz 3, 28049 Madrid, Spain

KEYWORDS: organic semiconductors, crystals packing, triindoles, CH-π interactions.

ABSTRACT. The self-assembling trends of a series of *N*-trialkyltriindoles in which the number of carbon atoms of the alkyl chains attached to the nitrogens was systematically varied have been investigated in the crystalline state. We have found that the length of the *N*-alkyl chains significantly impact on the position adopted in the crystal by each molecular component with respect to its neighbors and strongly influences the final morphology of the crystals which predominantly prefer to grow into one-dimensional shapes. Single crystal analysis demonstrate that this habit is determined by the highly anisotropic supramolecular bonding in the crystal packing and allows us to recognize the contribution of several cooperative CH-π interactions to

guide the self-assembly of this type of molecules. The results of this study represent a step forward towards the rational control of the supramolecular arrangement of this high performance semiconducting platform.

Introduction

The use of molecule-based semiconductors in the construction of electronic devices has expanded impressively in the last few years. Organic semiconductors arose great expectations in the development of low-cost, flexible and large-area devices [1,2] but also offer the possibility of fine tuning key properties through a convenient molecular design. Extended aromatic systems provide a high amount of ¨mobile¨ π-electrons and their electronic properties (luminescence, absorption, energy band gaps, charge transport…) can be readily modulated by introduction of functional groups in defined positions of the molecules.[2] However fundamental properties of molecular materials are not only governed by those of individual molecules but also by the way they are spatially ordered in the bulk.[3-5] Controlling the organization of the molecular building blocks at the nanometer level is therefore a main challenge in the field.

One-dimensional microstructures of π-extended molecules are gaining increasing attention in the development of next generation of organic devices. In these anisotropic structures, π-electron rich aromatic rings are usually arranged in stacks or slipped stacks providing an efficient pathway for charge migration owing to increased overlap between the electronic wavefunctions of neighbouring molecules. As a result 1D supramolecular structures have been extensively used as n or p-channel in field effect transistor devices.[6]

In order to be able to control the supramolecular organization of a particular building unit in a predefined manner, it is necessary to have a perfect knowledge of the non-covalent interactions acting among the molecules. This is usually a challenging task as intermolecular interactions involving π-conjugated systems are weak in nature and act in a cooperative way but often in opposite directions complicating their understanding.[7] Single crystal analysis provides invaluable information on the nature of intermolecular interactions among neighboring units and offers an excellent opportunity to investigate molecular arrangement dependent properties.

The presence of long alkyl side chains is a common structural feature to influence in the self-assembly of π-extended aromatics without significantly affecting the electronic properties of individual molecules: they increase the molecular solubility facilitating their processability and may induce their arrangement in highly anisotropic columnar mesophases.[8] The one–dimensional supramolecular organization found in columnar liquid crystals has aroused much interest in the search of efficient charge transporting systems.[9] In this context we became interested on electron-rich 10,15-dihydro-5*H*-diindolo[3,2-*a*:3',2'-*c*]carbazole (triindole) **1a** as new high performance π-extended semiconducting mesogen [10-12] Attachment of six long peripheral alkyl chains through bulky phenyl linkers to this disk-shape molecule, give rise to a columnar mesomorphism whose phase behavior can be further tuned by changing the substitution pattern on the nitrogen.[12] For example *N*-alkylation of this mesogen with 12, 8 or 6 carbon atoms chains give rise to hexagonal columnar mesophases in a broad temperature range. Curiously further reducing the length of the alkyl chains to 4 carbon atoms precludes mesomorphism, rendering a compound that melts into the isotropic liquid nearly at room temperature while reducing even more the length of the attached chains to three methyl groups result again in mesomorphic behavior. Interestingly in this case we observe a striking shortening

of the intrastack distance, providing the highest hole mobility discotic liquid crystalline semiconductor reported to date.[12]

In this manuscript we investigate the crystal structure of laterally unsubstituted parent *N*-trialkylated single crystalline triindoles finding that the size of the alkyl chains has also an important effect on the crystal packing and on their tendency to self-assemble into 1D-arrangements. Interesting parallelism can be driven between liquid crystals and non-mesogenic crystalline analogues as again only the butyl groups prevent the one-dimensional assembly of these molecules. In this particular case CH-π interactions have been identified as responsible of driving the different supramolecular organizations. It should be noted that although this type of interactions are individually quite weak, their effects are additive and therefore their influence can be really powerful.[13]

Materials and methods

SEM Characterization. Scanning electron microscopy (SEM) images were obtained on a Nova NanoSEM 230 FEI field-emission scanning electron microscope with a vCD detector operating at low presure with an accelerating voltage of 5 kV.

X-ray structure. A colorless crystal of **1c** showing well defined faces were mounted on a Bruker Smart CCD diffractometer equipped with a normal focus, 2.4 kW sealed-tube X-ray source (MoKα radiation, λ= 0.71067 Å) operating at 50 kV and 30 mA. Data were collected over a hemisphere of the reciprocal space by a combination of three exposure sets. Each exposure of 10 s covered 0.3º in ω over the range 2.5º <θ <28º. The first 100 frames were recollected at the end of the data collection to monitor crystal decay.

A colorless crystal of **1d** showing well defined faces was mounted on a Bruker four circle kappa-diffractometer equipped with a Cu INCOATED microsource, operated at 30 W power (45 kV, 0.60 mA) to generate CuKα radiation (λ = 1.54178 Å), and a Bruker VANTEC 500 area detector (microgap technology). Diffraction data were collected exploring over a hemisphere of the reciprocal space in a combination of φ and ω scans to reach a resolution of 0.86 Å, using a Bruker APEX2[14] software suite (each exposure of 40 s covered 1o in ω or φ).

Unit cell dimensions were determined for least-squares fit of reflections with $I > 20\sigma$.

A semi-empirical absorption and scale correction based on equivalent reflection was carried out using SADABS APEX[14]. The structures were solved by direct methods. The final cycles of refinement were carried out by full-matrix least-squares analyses with anisotropic thermal parameters of all non-hydrogen atoms. The hydrogen atoms were fixed at their calculated positions using distances and angle constraints. All calculations were performed using SMART[15] and APEX2[14] software for data collection and for data reduction; SHELXS[16] and SHELXL[17] to resolve and refine the structures using Olex2 GUI[18].

CCDC 1021612 and CCDC 1446933, contain the supplementary crystallographic data for **1c** and **1d** respectively. These data can be obtained free of charge at www.ccdc.cam.ac.uk/conts/retrieving.html [or from the Cambridge Crystallographic Data Centre, 12, Union Road, Cambridge CB2 1EZ, UK; fax: +44-1223/336-033; e-mail: deposit@ccdc.cam.ac.uk].

Results and discussion

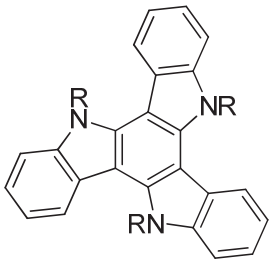

1a R=H
1b R=CH_3
1c R=C_4H_9
1d R=C_6H_{13}
1e R=C_8H_{17}

Figure 1. Chemical structure of the triindoles **1a**-**1e** under study

Compounds **1b**-**1e** can be readily obtained by alkylation of triindole **1a** in the presence of a charge transfer catalyst as it has been previously reported. [19-22] The length of the alkyl chains do not affect significantly their electronic properties (see SI), all of these derivatives oxidizes readily and reversibly which qualify them as promising candidates for hole injection and transport. However they influence strongly on how these molecules- which have a strong tendency to crystallize- interact with each other. The self-assembly tendencies of these molecules was initially investigated by scanning electron microscopy. Dip-coating of a substrate in a CH_2Cl_2:CH_3CN (1:1) solution of **1b** render highly aligned microwires that can reach a length up to some centimeters long and only a few micrometers of diameter (Figure 1a). As can be observed in the inset of Figure 1a, the wires show a perfect hexagonal cross-section. The formation of crystals of **1c**-**1e** can be readily accomplished by aging a CH_2Cl_2:CH_3CN (1:1) solution of each compound for a few minutes until a turbidity is clearly observed. The resulting aggregates were deposited on a silicon substrate and visualized by Field Emission Scanning Electron Microscopy (FE-SEM). As can be observed in the Figure 1, all the aggregates have perfectly delimited facets indicative of their crystalline character. X-Ray Powder diffraction experiments of the aggregates show in all cases sharp diffraction peaks confirming that these

supramolecular assemblies are crystalline (see Figures S3-S6). The images show that size of the alkyl chains has a dramatic influence in the crystal habit of these compounds: thus while most of these derivatives show a preference to grow into anisotropic shapes forming long crystalline wires (**1b**), microbelts (**1d**) or rods (**1e)**, the tributyl derivative (**1c**) grow as cubes. This trend is reminiscent of the mesomorphic behaviour observed in previously reported liquid crystalline triindoles in which only the tributyl chains prevent the one dimensional self-assembly[12]. Comparative studies between liquid crystals and non-mesogenic crystalline analogues have been previously found useful to shed light on the organizational preferences of mesogens and on the intermolecular forces that gives rise to mesomorphism. [23-25]

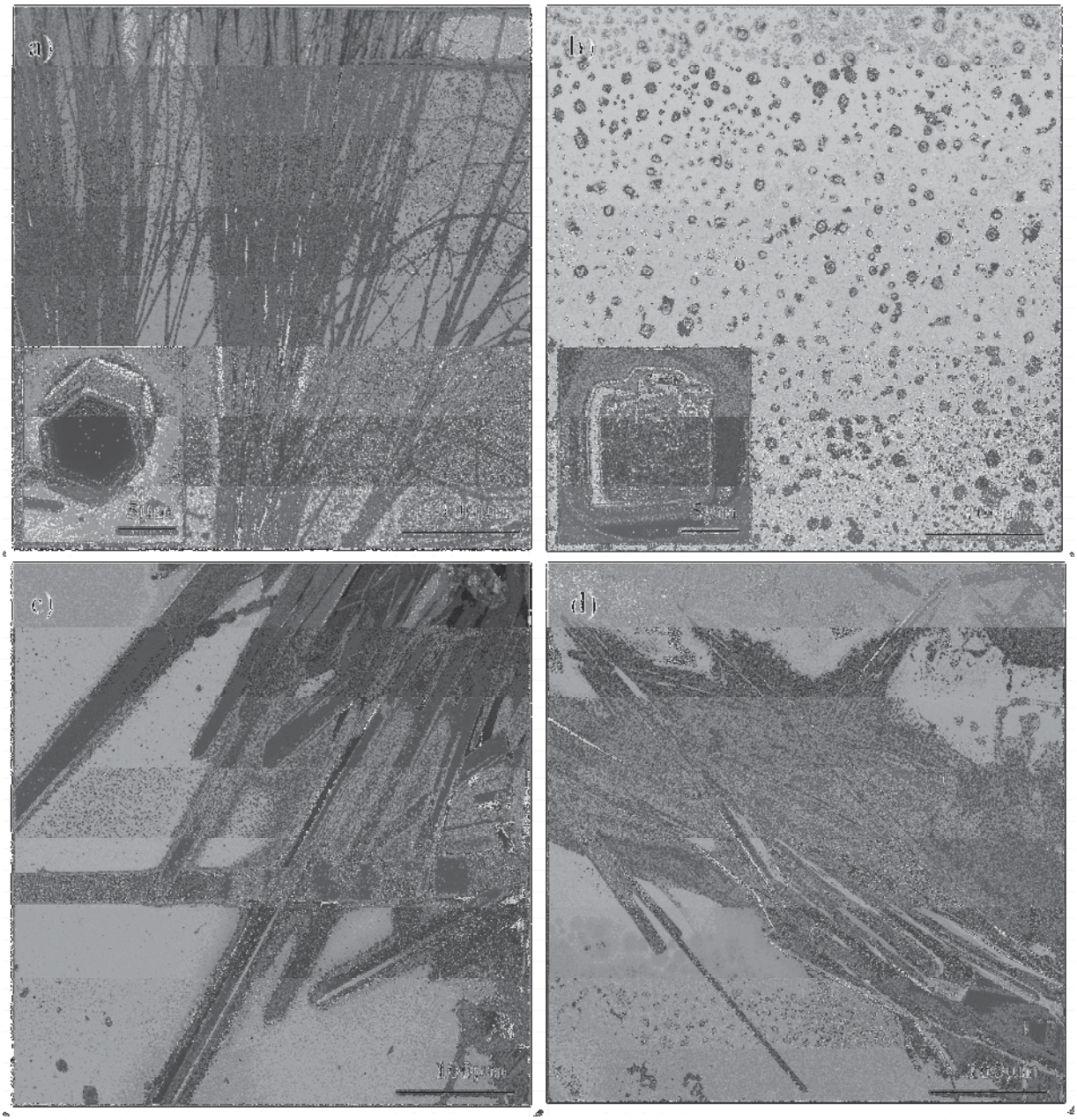

Figure 2. a) Images of the crystalline structures of **1b** (inset: view of the cross section) formed by dip-coating a silicon substrate on a concentrated 1:1 CH_2Cl_2:CH_3CN solution; b) c) and d) Images of the crystalline structures of **1c** (two different amplifications), **1d** and **1e** obtained by ageing a 1:1 CH_2Cl_2:CH_3CN solution of the corresponding compound and deposition of the crystalline material formed on silicon substrate.

In order to gain insight into the origin of these different crystalline habits and macroscopic morphologies, we have obtained crystals with sufficient size for X-ray single crystal analysis of **1c** and **1d** by slow evaporation of 1:1 CH_2Cl_2:CH_3CN solutions of the corresponding compounds and analysed how molecules pack in the crystals. The crystal structures of **1b**[19] and **1e**[22] have been previously reported by us. Simulated powder diffraction patterns of the bulk crystals of **1b**-**1d** match well with those obtained for the aggregates deposited on substrates confirming that they correspond to the same crystal phase. An analysis of the crystal packing shows that compounds **1a**, **1c** and **1d** crystallize as columnar assemblies, favoring the one-dimensional macroscopic growth; in contrast the tributyl derivative **1b** crystallizes as dimers that pack in a herringbone-like array resulting in no preferred growth direction. To understand the origin of these different packing tendencies we have traced how molecules interact with each other by establishing close contacts in the structures.

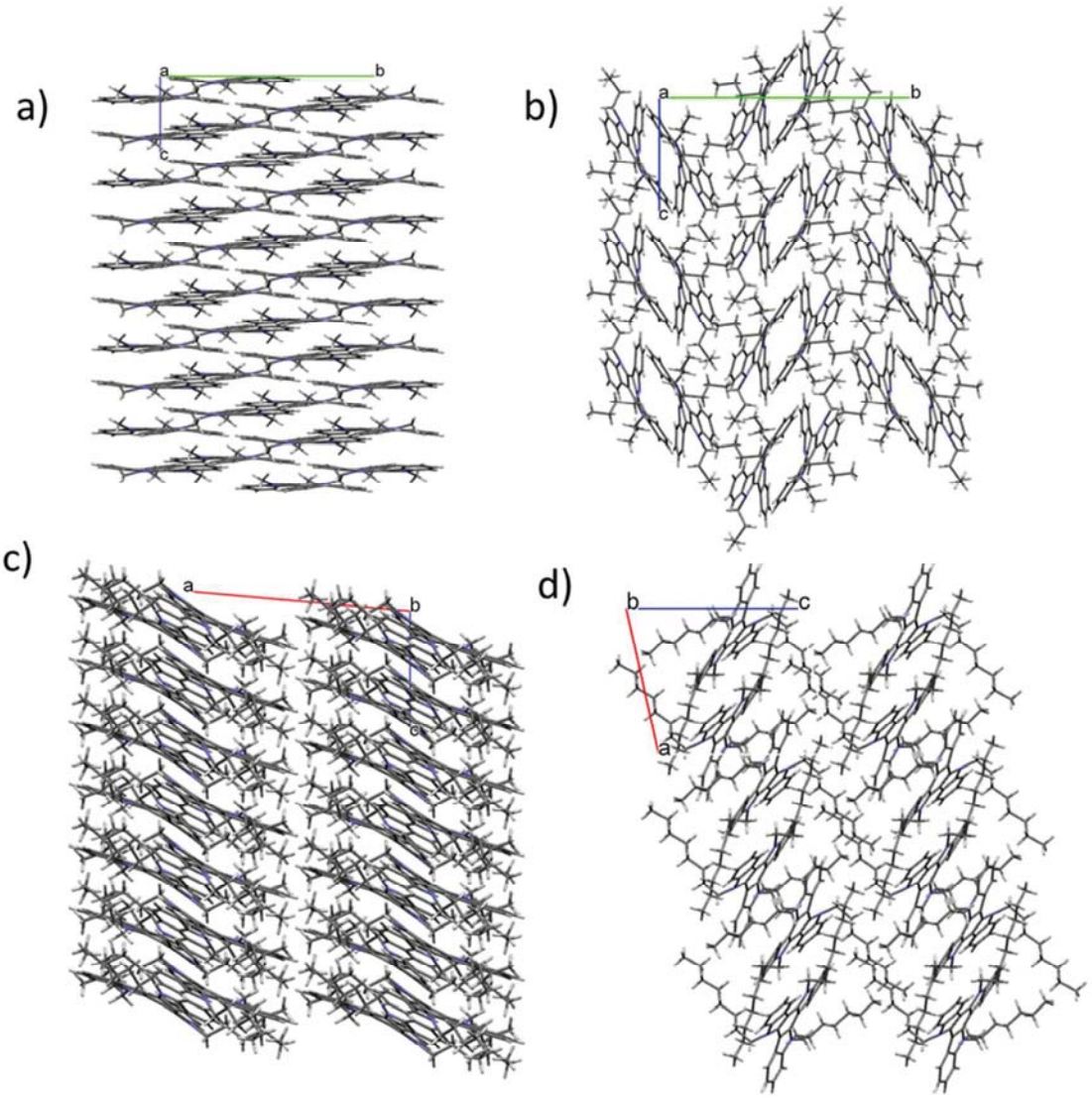

Figure 3. Different crystal packing shown by a) **1b** view along a, b) **1c** view along a, c) **1d** view along b and d) **1e** view along b .

Compound **1b** crystallizes in the $R\bar{3}$ space group with the hexagonal lattice parameters of a = 21.477(6) Å and c= 7.210(3) Å. In the crystals, molecules pack forming stacks along the crystallographic c-axis (Figure 1) which is coincident with the longest dimension of the crystal.

The molecules are oriented face-to-face in an alternate arrangement; one molecule rotated 60 degrees with respect to the next molecular unit, being the central aromatic rings perfectly superimposable. Due to this rotation each methyl group is involved in CH-π interactions with the aromatic rings that lie above and below it. Figure 3a depicts the unique interactions of **1b** (contact distances between the hydrogen of the methyl group and the centroid of the external ring: 2.935 Å and 2.985Å). As the molecule has C_3 symmetry with the centroid of the central aromatic ring situated in the threefold axis, all the methyl groups in the crystal are involved in CH-π interactions stabilizing the columnar arrangement. This network of interactions explains the high tendency of these molecules to crystallize in long wires. It has long been accepted that the growth rate of a facet is directly related to its attachment energy, which is considered as the energy necessary to split a slide of a facet. In this case cooperative interactions can be observed along the [001] direction crossing the most energetic plane.[26] No interaction can be observed which would justify the growth direction of other facets of the crystal.

Compounds **1d** and **1e** crystallize in the P-1 and P2(1)/c space group respectively. Both compounds crystallize also into columns that grow along a preferred direction. In this case molecules are not parallel but tilted with respect to the column axis (which coincide with the *c* and *a* axis respectively) and translated with respect to their neighbors in the column. An analysis of the close contacts in the crystal suggests that again multiple CH-π interactions are responsible of the packing and final morphology of the crystals as intermolecular interactions are only detected along the column while no interaction between the different stacks can be traced.

By elongating the chain, we increase the number of potential CH-π donors resulting in the observed columnar slipped arrangement. In the crystals of these two compounds, several CH hydrogen atoms of one alkyl chain of each molecular component are interacting with different 5

and 6 membered rings of the heptacyclic platform located below it, while several CH hydrogen atoms of other alkyl chain is involved in different CH-π interactions with the molecule placed above it (Figure 3b and 3c). Thus in the crystals of compound **1e**, each molecule is showing contact distances of 2.820 Å, 2.810 Å, 2.713 Å and 2.774Å with the molecule above and 2.599 Å and 3.049 Å with its next neighbor below, while compound **1d** each molecule show short contacts of 2.885Å and 2.899 Å with the molecule above and 2.837 Å and 2.796Å with its next neighbor below.

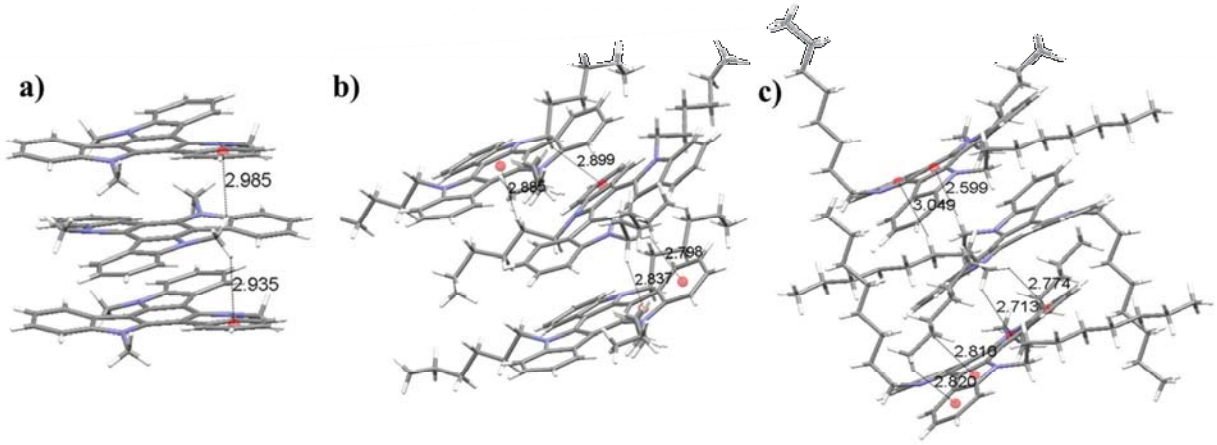

Figure 4. Depiction of the intermolecular CH-π interactions that stabilizes the arrangement into columns of (a) **1b**, (b) **1d** and (c) **1e**. Only unique interactions are shown, but the packing is stabilized by a number of additional interactions related by crystal symmetry. (Ring centroids are represented as red balls).

Parameters	1b	1c	1d	1e
Formula	$C_{27}H_{21}N_3$	$C_{36}H_{39}N_3$	$C_{42}H_{51}N_3$	$C_{48}H_{63}N_3$
Crystal System	Hexagonal	Monoclinic	Monoclinic	Triclinic
Space group	$R\bar{3}$	P2(1)/c	P2(1)/c	P-1

***a* (Å)**	21.477(6)	13.1045(14)	15.3638(19)	12.181(2)
***b* (Å)**	21.477(6)	21.445(2)	26.471(3)	12.617(3)
***c* (Å)**	7.210(3)	10.3406(11)	8.4581(8)	14.509(3)
***α* (deg)**	90.00	90.00	90.00	70.355(3)
***β* (deg)**	90.00	90.654(2)	94.961(7)	74.237(3)
***γ* (deg)**	120.00	90.00	90.00	77.492(3)
Volume (Å^3)	2879.9(17)	2905.8(5)	3427.0(7)	2001.7(7)
Z	6	4	4	2
ranges of *h*,*k*,*l*	$-21 \le h \le 9$ $-19 \le k \le 21$ $-6 \le l \le 7$	$-17 \le h \le 17$ $-27 \le k \le 27$ $-13 \le l \le 13$	$17 \le h \le 17$ $-29 \le k \le 29$ $-3 \le l \le 7$	$-16 \le h \le 16$ $-17 \le k \le 16$ $-19 \le l \le 19$
ranges of *θ*	$1.90 \le \theta \le$ 20.79	$2.45 \le \theta \le$ 28.00	$2.89 \le \theta \le$ 61.60	$1.73 \le \theta \le$ 29.04
Reflns total	656	5569	4731	7839
Reflns gt	452	2953	3015	4288
R factor all	0.1308	0.2420	0.2819	0.1450
R factor gt	0.0864	0.1192	0.0840	0.0762

Table 1. Selected crystallographic data of **1b-1d**.

Compound **1c** crystallize in space group P2(1)/c with the unit cell dimensions of *a* =13.1045(14) **Å**, *b* = 21.445(2) **Å**, *c* =10.3406(11) **Å**, *α* =90.00º, *β* =90.654(2)º, *γ* =90.00º.

In contrast to the other three derivatives this compound grows as cube-like crystalline prisms. Molecules arrange in the crystal as dimers that pack in a herringbone-like array. The different packing tendency exhibited by **1c**, can be also ascribed to the cooperation of a number of CH-π interactions. An analysis of the close contacts in its crystal packing evidences that each molecule is interacting with the other component of the dimer (contact distances: 2.621 Å and 2.981 Å) but is also with molecules of two adjacent dimers (contact distances: 2.714 Å) placed in planes above and below. These results in a 3D network of interactions which would explain the different morphologies observed (Figure 4).

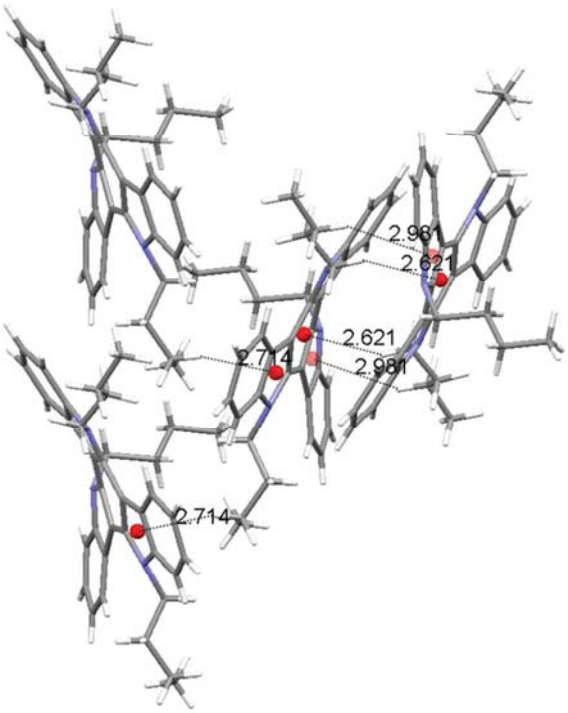

Figure 5. Depiction of the intermolecular CH-π interactions established between the molecules of **1c** within the dimers and among neighboring dimers (ring centroids are represented as red balls).

Conclusions

In conclusion, the relationship between the length of the *N*-alkyl chains and organization preferences of a series of *N*-trialkyl triindoles has been investigated. We have found that the size of the alkyl chains attached to the three nitrogens of this semiconducting platform, has a strong influence in the morphology of laterally unsubstituted crystalline *N*-trialkyl triindoles. A study of the crystalline packing of compounds **1b**-**1e**, allowed us to demonstrate that behind the different crystalline habits and macroscopic morphologies observed is the way in which molecules pack in the crystals and interacts with their nearest neighbors allowing us to establish interesting parallelism with triindole based liquid crystalline mesophases. The results of this study suggest that the influence of the length of the *N*-alkyl chains in the one dimensional assembly of triindoles is non-innocent and point towards cooperative CH-π interactions in the origin of the different superstructures observed. The recognition of such interactions is a prerequisite for obtaining well defined arrangements, relevant for their electronic applications.

AUTHOR INFORMATION

Corresponding Author

* E-mail: bgl@icmm.csic.es, Phone: (+34) 91-3349031, Fax: (+34) 91-3720623

Author Contributions

The manuscript was written through contributions of all authors. All authors have given approval to the final version of the manuscript.

Funding Sources

This work was partially funded by the Spanish Government MINECO CTQ2013-40562-R grants; and the Comunidad de Madrid S2013/MIT-2740 (PHAMA_2.0).

REFERENCES

(1) a) *Organic Electronics: Materials, Manufacturing and Applications*; Klauk, H., Ed.; Wiley- VCH: Weinheim, 2006. b) *Organic Electronics: More Materials and Applications*; Klauk, H., Ed.; Wiley- VCH: Weinheim, 2012.

(2) Special issue on π-functional materials for organic electronics: *Chem. Mater.* 2011, 23, 309–922.

(3) Liu, Z.; Zhang, G.; Zhang, D. *Chem. Eur. J.* 2016, *22*, 462 – 471.

(4) Modulation of optical properties of π-conjugated materials through a supramolecular approach: a) Varughese, S. *J. Mater. Chem. C* 2014, *2,* 3499-3516. b) Varughese, S.; Das, S. *J. Phys. Chem. Lett*. 2011, *2,* 863-873. c) Grepioni, F; D'Agostino, S.; Braga, D.; Bertocco, A.; Catalano, L.; Ventura, B. *J. Mater. Chem. C* 2015, *3*, 9425 – 9434. d) Nagarajan, K.; Rajagopal, S. K.; Hariharan M. *CrystEngComm*, 2014, *16*, 8946-8949.

(5) Modulation of semiconducting properties of π-conjugated materials through a supramolecular approach: a) Mas-Torrent, M.; Rovira C. *Chem. Rev.* 2011, *111*, 4833–4856. b) Mei, J.; Diao, Y.; Appleton, A. L.; Fang, L.; Bao, Z. *J. Am. Chem. Soc.* 2011, *133*, 6724-6746. c) Wang, C.; Dong, H.; Hu, W.; Liu, Y.; Zhu D. *Chem. Rev*. 2012, *112*, 2208–2267. d) Ruiz, C.; García-Frutos, E.; Hennrich, G.; Gómez-Lor, B: *J. Phys. Chem. Lett.* 2012, *3*, 1428.

(6) For some relevant reviews on one-dimensional materials able to transport charge carriers see: a) Briseno, A.L.; Mannsfeld S.C.B.; Jenekhe, S. A.; Bao, Z.; Xia, Y. *Materials Today* 2008, *11*, 38-48; b) Li, R.; Wu, H.; Liu, Y.; Zhu, D. *Acc. Chem. Res.* 2010, *43*, 529-540; c) Oh, J. H:, Lee, H. W.; Mannsfeld, S.; Stoltenberg, R.M.; Jung, E.; Jin, Y.W.; Kim, J.M.; Yoo, J.-B.; Bao, Z. *Proc. Mat. Acad. Sci.* 2009, 106, 6065-6070; d) Hasegawa, M.; Iyoda, M. *Chem. Soc. Rev.*, 2010, *39*, 2420-2427.

(7) a) *The Importance of Pi-Interactions in Crystal Engineering: Frontiers in Crystal Engineering*; Tiekink, E R.T., Zukerman-Schpector, J. Eds.; John Wiley & Sons, Ltd, Chichester, UK. b) Salonen, L.M.; Ellermann, M.; Diederich, F. *Angew. Chem. Int. Ed.* 2011, *50*, 4808-4842. c) Wheeler, S.E.; Bloom, J.W.G. *J. Phys. Chem. A*, 2014, *118*, 6133-6147. d) Desiraju, G.R. *J. Am. Chem. Soc.* 2013, *135*, 9952-9967.

(8) *Chemistry of Discotic Liquid Crystals: From Monomers to Polymers;* Kumar, S. Ed.; CRC Press, Taylor & Francis: Boca Raton, 2011.

(9) a) Pisula, W.; Zorn, M.; Chang, J. Y.; Müllen, Zentel, K. R.Macromol. *Rapid Commun.* 2009, 30, 1179. b) Kaafarani, B. R. *Chem. Mater*. 2011, *23*, 378; c) Sergeyev, S.; Pisula, W.; Geerts Y. H. *Chem. Soc. Rev*. 2007, *36*, 1902-1929 d) Wöhrle, T.; Wurzbach, I.; Kirres, J.;

Kostidou, A.; Kapernaum, N.; Litterscheidt, J.; Haenle, J. C.; Staffeld, P.; Baro, A.; Giesselmann, F.; Sabine Laschat *Chem. Reviews* 2016 DOI: 10.1021/acs.chemrev.5b00190.

(10) Talarico, M.; Termine, R.; García-Frutos, E. M.; Omenat, A.; Serrano, J. L.; Gómez-Lor, B.; Golemme, A. *Chem. Mater.* 2008, 20, 6589-6591.

(11) García-Frutos, E. M.; Pandey, U. K.; Termine, R.; Omenat, A.; Barberá, J.; Serrano, J. L.; Golemme, A.; Gómez-Lor, B. *Angew. Chem. Int. Ed.* 2011, 50, 7399-7402.

(12) Benito-Hernández, A.; Pandey, U. K.; Cavero, E.; Termine, R.; García-Frutos, E. M.; Serrano, J. L.; Golemme, A.; Gómez-Lor, B. *Chem. Mater*. 2012, 25, 117-121.

(13) A) The CH/π interaction. Evidence, Nature and Consequences, Nishio, M., Hirota, Y., Umezawa, Ed.; Wiley-VCH, New York, 1998. b) Nishio, M. *CrystEngComm*. 2004, 6, 130-158.

(14) APEX2; Bruker-AXS: Madison, WI, 2006.

(15) Software for the SMART system, V.5.04, Bruker-Siemens Analytical X-ray Instruments, Inc., Madison, WI, USA, 1998.

(16) Sheldrick, G. M. *Acta Cryst.* 2008, A64, 112-122.

(17) Sheldrick, G. M. *Acta Cryst*. 2015, C71, 3-8.

(18) Dolomanov, O.V., Bourhis, L.J., Gildea, R.J, Howard, J. A. K. & Puschmann, H.; *J. Appl. Cryst*. 2009, 42, 339-341.

(19) García-Frutos, E. M.; Gutierrez-Puebla, E.; Monge, M. A.; Ramírez, R.; Andrés, P. d.; Andrés, A. d.; Ramírez, R.; Gómez-Lor, B. *Org. Electron*. 2009, 10, 643-652.

(20) Yuan, M.-S.; Li, T.-B.; Wang, W.-J.; Du, Z.-T.; Wang, J.-R.; Fang, Q. *Spectrochim. Acta Mol. Biomol. Spectrosc.* 2012, *96*, 1020.

(21) Lai, W.-Y.; He, Qi-Y.; Zhu, R.; Chen, Q.-Q. Huang W. *Adv. Funct. Mater.* 2008, *18*, 265–276

(22) Gallego-Gómez, F.; García-Frutos, E. M.; Villalvilla, J. M.; Quintana, J. A.; Gutierrez-Puebla, E.; Monge, A.; Díaz-García, M. A.; Gómez-Lor, B. *Adv. Funct. Mater*. 2011, *21*, 738-745.

(23) Wu, D.; Pisula, W.; Enkelmann, V.; Feng, X. *J. Am. Chem. Soc.* 2009, 131, 9620-9621.

(24) Nguyen, H.L.; Horton, P.N.; Hursthouse, M.B.; Legon, A.C.; Bruce, D.W. *J. Am. Chem. Soc.* 2004, *126*, 16-17.

(25) Dai, C.; Nguyen, P.; Marder, T.B.; Scott, A.J.; Clegg, W. Viney, C. *Chem. Commun*. 1999, 2493-2494.

(26) a) Bacchi, A.; Cantoni, G.; Cremona, D.; Pelagatti, P.; Ugozzoli, F. *Angew. Chem. Int. Ed.* 2011, *50*, 3198-3201. b) Massaro, F.R.; Moret, M.; Bruno; M.; Aquilano, D. *Cryst. Growth Des.* 2013, *13*, 1334-1341. c) Hartman, P; Bennema, P. *J. Cryst. Growth* 1980, *49*, 145-156.

Saddle-shaped indole cyclic tetramers: 3D electroactive molecules

Constanza Ruiz,[a] Ángeles Monge,[a] Enrique Gutiérrez-Puebla,[a] Ibon Alkorta,[b] José Elguero[b] Juan T. López Navarrete,[c] M. Carmen Ruiz Delgado*[c] and Berta Gómez-Lor*[a]

Abstract: In this manuscript we present a joint theoretical and experimental study of a cyclic tetramer of indole with the aim of understanding the fundamental electronic properties of this three-dimensional (3D) platform and evaluate its potential in the construction of new semiconducting candidates. To this end, we combine absorption and emission spectroscopies, cyclic voltammetry, and spectroelectrochemistry with DFT calculations. Our results suggest that this platform can be easily and reversibly oxidized showing a HOMO level that matches very well with the work function of gold, therefore charge injection from this electrode is expected to occur without significant barriers. Interestingly, cyclic tetraindole allows for a good electron delocalization in spite of its saddle-shaped structure. The steric constrain introduced by N-substitution significantly inhibits ring inversion of the central cyclooctatetraene (COT) while it only barely affects its optical and electrochemical properties which show a slightly higher oxidation potential and blue-shift of the absorption edge upon alkylation.

Introduction

Flat π-extended electroactive molecules, with inherent 2D character have a strong tendency to stack into columns forming one dimensional superstructures. Such superstructures have been long considered to be among the best candidates to achieve high mobility semiconductors[1]. However due to their low dimensionality, these materials present anisotropic charge-transport properties which can pose specific problems for device fabrication and operation. The design of 3D electroactive systems allowing substantial electronic communication among conjugated segments in different directions may represent a potential answer to the problem of charge-transport anisotropy.[2] In this context several electroactive molecules containing silicon[3] or sp^3 carbon nodes[4] for connecting conjugated systems, have been reported. In these materials the central node interrupts electronic delocalization a factor that can be unfavorable for charge transport. Other approaches directed to obtain electroactive molecules with 3D architectures have made use of tetraphenyladamantane cores, [5] twisted bithiophenes, [6] or spirofluorenes[7] as connecting cores.

We have been long involved on the study a C_3-symmetrical cyclic dehydrotrimer of indole (triindole) a flat disk-like electroactive molecule, which can be easily obtained by $POCl_3$ mediated cyclocondensation of 2-indolinone.[8] This molecule has been extensively investigated in the area of organic electronics and has been successfully integrated as active layer in OLEDs,[9] solar cells[10] and OFEts.[11] Interestingly very high hole-mobility values have been obtained in triindole-based discotic liquid crystals which provide an active conducting core, surrounded by an isolating cover.[12,13] Unfortunately, as it is common in discotic mesogens, the high dependence of their electrical performance on the degree of columnar alignment represents an important drawback towards device application.

In this manuscript we propose the use of a highly strained saddle shape tetramer of indole (tetraindole) as a 3D rigid scaffold to obtain electroactive molecules with increased dimensionality. This tetramer, constituted by four indole molecules fused via a cyclotetraene (COT) core, is usually obtained as a side product during the synthesis of planar triindole by $POCl_3$ promoted cyclocondensation of 2-indolinone.[14,15] However in contrast to its trimeric counterpart, its electronic properties have been barely investigated probably due to difficulties to obtain it in large scale and pure form. Only recently this molecule has aroused interest in the synthesis on non-linear optical chromophores and electron donor moieties in D-π-A dyes for solar cells.[16,17] Although the formation of tetraindole can be favored by diluting the reaction mixture with chlorobenzene or $POCl_3$ although it is always obtained as a minor product together with the trimeric compound which complicates its purification.[18,19] Alternatively its synthesis through a multistep procedure has been also reported.[20] We have found that by performing the cyclotetramerization reaction in an autoclave we can favor the tetramerization *vs.* the trimerization rendering a much more easy to purify compound.

While fluxional dynamism characteristic of flexible cyclooctatetraenes has been long exploited in the development of molecule-based devices, such as electromechanical actuators [21] thermochromic [22] or environmental-dependent luminescent materials[23] the absence of flipping in rigid sterically hindered cyclooctatetraenes has been previously used to obtain molecular tweezers, optically active ligands [24] or chiral receptors [25] as high inversion barriers prevent racemization processes. In this manuscript we want instead to bring the attention to the potential of highly strained cyclooctatetraene as a scaffold to arrange electroactive moieties in three dimensions with potential applications in the field of organic electronics. It should be noted that while cyclooctatetraene planarization render it the prototype of 4n π antiaromatic system and twisting precludes effective π conjugation, it has been recently

[a] Dr. B. Gómez-Lor, Prof. Dr. A. Monge, Prof. Dr. E. Gutiérrez-Puebla, C. Ruiz
Instituto de Ciencia de Materiales de Madrid, CSIC
Cantoblanco, 28049 Madrid (Spain)
Fax: (+34) 91-3349031
E-mail: bgl@icmm.csic.es
[c] Prof. Dr. I. Alkorta, Prof. Dr. J. Elguero
Instituto de Química Médica, CSIC
Juan de la Cierva 3, E-28006 Madrid (Spain)
[c] Prof. J. T. López Navarrete, Dr. M. Carmen Ruiz Delgado
Department of Physical Chemistry, University of Málaga,
29071-Málaga, Spain
Supporting information for this article is given via a link at the end of the document.

recognized that strong stabilizing electron delocalization effects operates in tub-shaped cyclooctatetraenes, such as “two-fold” (double) hyperconjugative interactions across the twisted C–C bonds.[26]

Here, we perform a joint experimental and experimental study which combines absorption spectroscopy, cyclic voltammetry, and spectroelectrochemistry with DFT calculations, in order to understand the fundamental optical and electronic properties of the cyclic tetraiindole platform (1a in Scheme 1) and explore its potential in the development of new 3D semiconducting systems. The modulation of the photophysical and electrochemical properties of these cyclic tetramers upon *N*-alkylation (*i.e.*, methyl groups in **1b** or alkyl aryl groups in **1c**-**1d**, see Scheme 1) as well as a comparison with its trimeric counterpart, the high performance semiconductor triindole (**2** in Scheme 1), will be also presented. Interestingly, the X-ray crystal structures of tetraindole derivatives **1a** and **1c** are also successfully reported.

Results and Discussion

Compound **1a** was obtained by treating 2-indolinone with $POCl_3$ in an autoclave at 150ºC. Under these conditions **1a** is obtained together with a large amount of insoluble oligomers. Although the reaction yield is not improved compared to those based on classical heating, the absence of competing triindole **2** significantly facilitates the preparation of this material in pure form.[27] Akylation of this tetramer was achieved readily by treatment of **1a** with the corresponding alkyl halides in the presence of KOH as base and tetrabutylammonium hydrogensulfate as solid-liquid phase transfer catalyst in refluxing acetone in good yield.

.

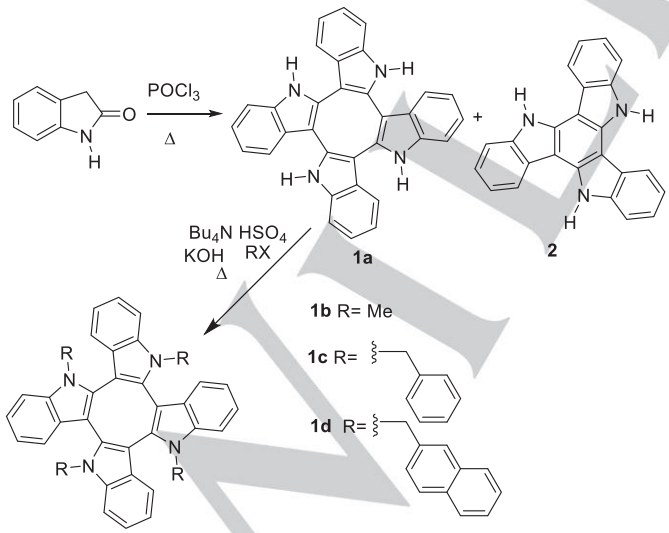

Scheme 1. Synthesis of cyclic tetraindoles **1a**−**1d** and its cyclic trimer triindole counterpart **2**.

Single crystal of **1a** suitable for crystallographic analysis was obtained by slow solvent evaporation from hexane: EtOAc. **1a** crystallize in the tetragonal system, in the I-4 spatial group. X-ray diffraction analysis confirm the saddle shape adopted by these molecules in which two opposite pairs of indole moieties are oriented above or below the average plane of the central eight membered ring presenting a bent angle of 36.6º showing a tub-to-tub inversion barrier of 123 $kJ \cdot mol^{-1}$ as has been calculated by DFT.

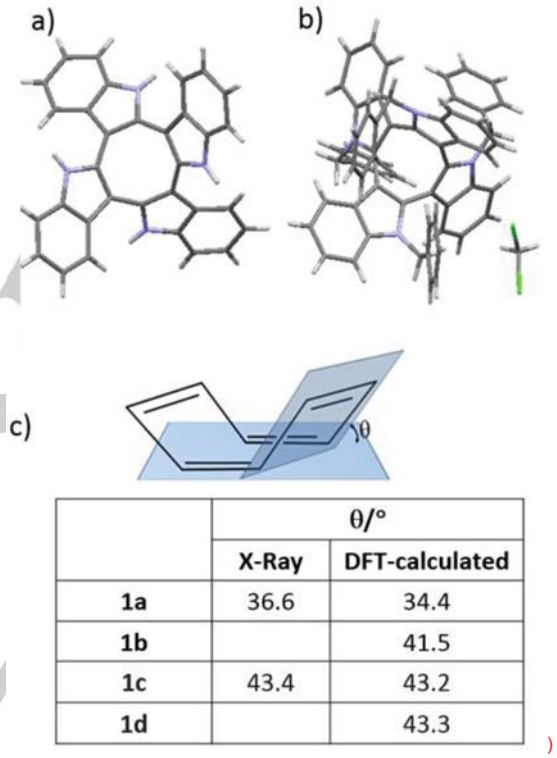

	θ/°	
	X-Ray	DFT-calculated
1a	36.6	34.4
1b		41.5
1c	43.4	43.2
1d		43.3

)

Figure 1. Crystal Structure of **1a** and **1c**, and comparisom of the theoretical and calculated bent angles.

The molecules crystallize forming columns that extend along the crystallographic *c* axis. Along the columns molecules are perfectly superimposed, stabilizing this arrangement by NH-π interactions that involve all the indole rings of the molecules. Indole rings situated below the average plane of the central eight membered rings are interacting with those situated in the upper wings of the neighboring molecule and vice versa.[28]

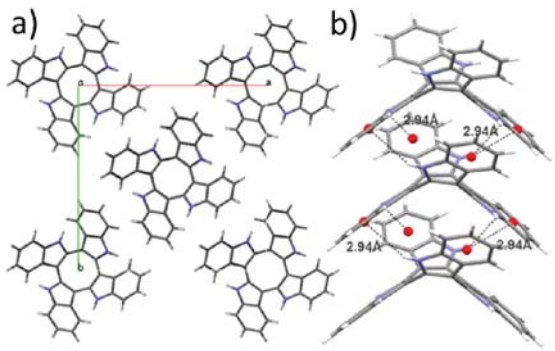

Figure 2. a) View of the packing of **1a** along the crystallographic c axis. b) Depiction of the intermolecular NH-π interactions that stabilizes the arrangement into columns of **1a**.

Single crystals of **1c** were obtained by slow solvent evaporation from CH_2Cl_2. Compound **1c** crystallizes in the tetragonal system, spatial group $P4_122$ with one CH_2Cl_2 molecule in the asymmetric unit. This compound crystallize forming orthogonal columns that extend along the perpendicular *a* and *b* axis. In contrast to the packing shown by **1a**, in this case no interaction are observed within the stacks. However each molecule is interacting with neighboring molecules of situated adjacent orthogonal columns through CH-π interactions resulting in a compact network that extends along the *a* and *b* axis. This arrangement leads to the formation of longitudinal channels along the c-axis which can be used to accommodate guest in these structures. The steric constrained introduced by alkylation is reflected in an enhanced bend angle that increases to 43.42º.

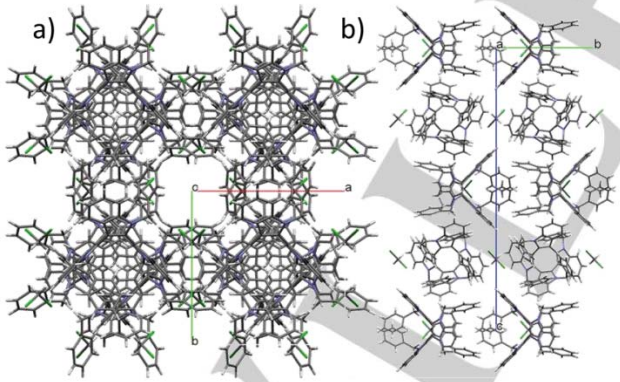

Figure 3. a) View of the packing of **1c** along the crystallographic c axis. b) View of the packing of **1c** along the crystallographic a axis. The stacks are aligned along the mutually orthogonal axis.

Alkylation has been also found to significantly inhibit ring inversion of the central COT ring, the estimated energy barrier increasing from 123 $kJ \cdot mol^{-1}$ up to 280 $kJ \cdot mol^{-1}$ upon methylation of **1a** to afford **1b** and up to 269 $kJ \cdot mol^{-1}$ upon benzylation to afford **1c**. We have calculated barriers for other compounds containing a cyclooctatetraene ring (see Supporting Information) obtaining correct values when experimental barriers were known. It is interesting to note that the ring inversion barrier of COT is strongly modulated by changing ring annulation on COT. (See table S1).

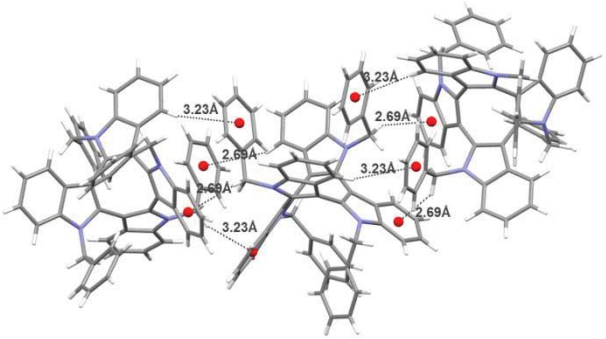

Figure 4. Depiction of the cooperative CH-π interactions among the perpendicular columns of **1c**.

Compounds **1a**-**1d** show one single set of signals, the chemical shifts of the indole moieties being slightly upfield shifted when compared with those of the triindole counterparts. Unequivocal assignment of the signals is performed on the basis of HMBC, HMQC and NOESY experiments. Methylene hydrogen atoms of **1c** and **1d** appear as AX systems with a coupling constant of J = 16.2 Hz highlighting the rigidity of this framework which is confirmed by performing NMR experiments at variable temperature. The absence of changes in the NMR signals upon heating indicates that neither COT inversion nor aryl rotation is taking place. The aromatic protons of the benzyl group are strongly magnetically shielded as they lie under the concave surface protons (see Supporting information).

The molecular geometries for the neutral state of **1a**-**1d** were optimized at the DFT level under S_4 symmetry. The agreement between the computed and experimental geometry of **1a** and **1c** is very good (see Table SI). Moderately large twisting of the saddle-shaped tetraindole core is obtained upon nitrogen substitution with methyl groups (**1b**) or methyl aryl groups (**1c** and **1d**) when compared to unsubstituted tetraindole **1a**, see Figure 1. Regarding the geometrical relaxation observed in the cyclic tetraindoles, it is interesting to highlight that the fusion of four indoles to the central COT ring results in a decreased degree of C-C bond-length alternation when compared to that in unsubstituted COT unit; for instance, C-C/C=C bond lengths in unsubstituted COT are 1.472/1.341 Å *vs.* 1.455/1.390 Å in **1a**. However, the bond length alternation pattern found for the phenyl rings of the indole moieties is very similar to that obtained for its indole cyclotrimer counterpart (see Figure S1).

We now used Raman spectroscopy in order to gain further insights into the structural and electronic properties of the cyclic tetraindoles. As seen in Figure 5a, the Raman spectra of the cyclic tetraindoles **1a**-**1d** are dominated by three strong Raman bands in the 1500-1700 cm^{-1} region. The band around 1620 cm^{-}

[1] corresponds to a C-C stretching mode (*i.e.*, mode 8a of benzene)[29] involving the external benzene rings, whereas the bands at 1600 (1570) cm^{-1} corresponds to symmetric (antisymmetric) C=C stretching modes localized in the central COT ring. These assignments are supported by the vibrational eigenvectors (see Figure S5). The good agreement between the experimental and theoretical Raman spectra of the cyclic tetraindoles confirms the good validity of our DFT approach (see Figure 7b). It is interesting to note that the C=C stretching modes associated to the COT ring (at 1651 and 1635 cm^{-1} in unsubstituted COT)[30] downshifts upon the fusion of four indoles (at around 1600 and 1570 cm^{-1} in **1a**-**1d**). This is in agreement with the decreased in bond length alternation of the central COT ring when compared to the cyclic tetraindoles as discussed above. Interestingly, *N*-substitution produces moderate changes in the relative position (slight frequency upshift) of the main Raman bands. This suggests that the geometrical effect (*i.e.*, *N*-substituted **1b**-**1d** display larger twisted structures than unsubstituted **1a**) seems to have a stronger impact than the larger inductive effect of the long alkyl aryl groups.

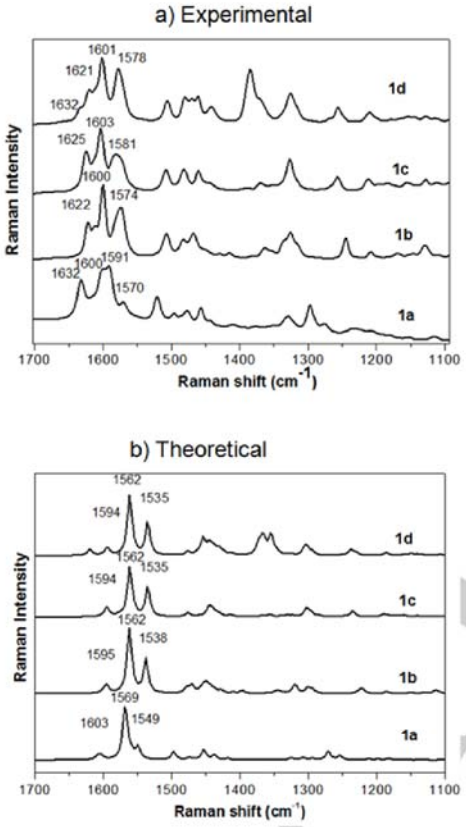

Figure 5. Comparison between the experimental (a) and theoretical (b) Raman spectra of cyclic tetraindoles **1a**-**1d**.

Furthermore, to complement the Raman analysis the nucleus-independent chemical shift (NICS) have been calculated (details of NICS calculations are provided in the SI). NICS methodology is one of the most widely employed indicators of aromaticity and is defined as the negative of the magnetic shielding at some selected point in space, *i.e.*, at a ring center.[31,32] Significant negative values imply aromaticity (diatropic ring current) and positive values correspond to antiaromaticity (paratropic ring current). The NICS value of the central COT ring in **1a** is estimated to be +3.98 ppm while for an unsubstituted COT ring this value is +5.34 ppm (see Figure S5); this indicates a smaller degree of antiaromatic character upon fusion of the indole units which is in consonance with lower bond length alternation and lower Raman frequencies in cyclic tetraindoles. The NICS values for the external benzenoid groups of **1a** exhibits negative values (–8.98 ppm) revealing the aromatic character; interestingly, these values are very similar to those obtained for triindole, thus suggesting similar electron delocalization in both cyclic trimer and tetramer systems. These results support the good electronic delocalization that is taking place in cyclic tetraindoles despite their twisted structures that would be expected to decrease the π-conjugation. This can be attributed to a double hyperconjugative effect between the CC and π orbitals across the twisted C-C bonds of the COT unit[26] which could enhance the electron delocalization in the cyclic tetraindole cores.

Next, in order to estimate the electron donor character of these cyclic tetramers we have investigated their electrochemical properties by cyclic voltammetry. These molecules oxidize readily. In anhydrous dichloromethane the cyclic voltammograms of these tetramer exhibited two subsequent reversible oxidation waves with half-wave potentials at 0.54 and 0.87 mV for **1a** and 0.72 and 1.09 mV for **1b** , 0.81 and 1.19 mV for **1c** and 0.86 and 1.25 mV for **1d** (see Figure 6). From the first oxidation process it is possible to estimate the HOMO level that is found to be very close to the work function of gold, and therefore hole injection from this electrode is expected to occur without significant barrier (see Table S2). As can be observed the first oxidation potential moderately shifts positively upon *N*-substitution (*i.e.*, 0.54 V in unsubstituted **1a** and 0.86 V in aryl-substituted **1d**). This experimental trend is well reproduced by the DFT calculations, which predicts larger ionization energies and stabilized HOMO levels (see Figure 7 and Table S2) upon *N*-substitution. Interestingly, the inclusion of an additional indole unit in the S_4-symmetric derivatives results in lower first oxidation potentials and then more easily oxidized systems when compared to the C_3-symmetric indole cyclotrimers (*i.e.*, 0.54 V in **1a** and 0.69 V in triindole analogue, see Table S2) [33]; this is in consonance with the HOMO destabilization in going from triindole to cyclic tetraindoles (*i.e.*, –4.96 eV in **2** and -4.60 eV in **1a**).

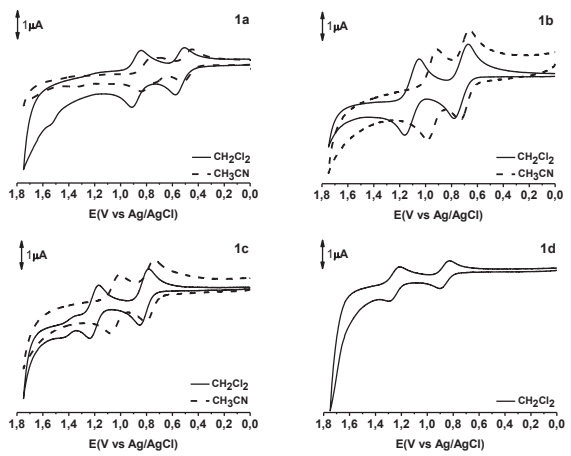

Figure 6. Cyclic voltammograms of **1a**–**1d** in $1x10^{-3}$ M solutions of CH_2Cl_2 (continuous line) and acetonitrile (dotted line) recorded at a scan rate 100mV/s using 0.1M tetra-*n*-butylammonium hexafluorophosphate ($TBAPF_6$) as supporting electrolyte, a Pt working electrode, a Ag/AgCl (3M NaCl) reference electrode and a Pt wire auxiliary electrode.

Interestingly, we have found that the redox processes of the cyclic tetraindoles are strongly influenced by the nature of the solvent being highly facilitated in CH_3CN *vs.* CH_2Cl_2 (see Figure 6). For instance, the second oxidation process is shifted anodically by 0.15 (0.08) for **1c** (**1b**) when the experiment is performed in CH_3CN. The stabilization of charged species gained in polar solvents point towards a more localized charge in the cyclic tetraindole species, and therefore a higher sensitivity to solvation in comparison with their trimer triindole analogues. This is in consonance with DFT-calculations that predicts large localization of the charge in the oxidized tetraindoles when compared to triindole derivatives (see Figure S2). For instance, 20% (18%) of the positive charge is located in the central COT ring in the radical (dication) states of tetramer **1a** while in the central phenyl ring of triindole radical (dication) the charge decreases to 15% (13%). In the same context, for cyclic tetraindoles the most significant geometrical changes upon ionization are localized in the central COT ring whereas in the case of triindoles significant bond length changes are also observed over the external phenyl rings (see Figure S3).

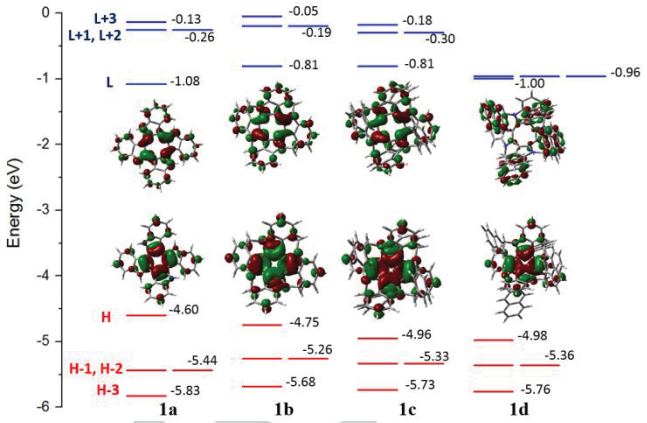

Figure 7. DFT-calculated molecular orbital energies (B3LYP/6-31G** level) for cyclic tetraindoles **1a**-**1d**. The molecular orbital topologies of the HOMO and LUMO orbitals are also shown.

The easy one-electron reversible oxidations of these derivatives render them potential candidates as hole-transport materials as occur with the triindole derivatives for which hole mobilities as high as 2.7 $cm^2/V^{-1}{\cdot}s^{-1}$ were reported. To evaluate that possibility we investigated the intramolecular reorganization energies λ associated with hole transfer (λ_h), a molecular parameter which considers the structural reorganization needed to accommodate charge as a prerequisite for efficient transport. The λ_h values for the unsubstituted **1a** and methyl substituted **1b** systems are 332 and 389 meV, respectively. These values are in the same order than those calculated for many other organic systems considered as good hole-transport materials (*i.e.*, values of 306 meV were obtained for dithienoacene for which hole field-effect mobilities of 0.31 $cm^2/V^{-1}{\cdot}s^{-1}$ were reported).[34]

The absorption spectra of cyclic tetraindoles **1a-1d** are characterized by a band at 290-320 nm, see Figure 8. *N*-substitution with methyl groups remains unchanged the position of the maxima but moderately blue-shits the absorption edge, whereas substitution with bulky alkyl aryl groups blue-shifts both the maxima and absorption edge. This is in consonance with the largest HOMO-LUMO gap predicted by DFT calculations upon *N*-alkylation as result of the HOMO (LUMO) stabilization (destabilization), see Figure 6.

TD-DFT calculations nicely predicts the experimentally observed blue-shift upon *N*-substitution (see Figure 8b). The strongest band at ≈ 300 nm in cyclic tetraindoles corresponds to the degenerate electronic transitions (*i.e.*, $S_0 \rightarrow S_5/S_0 \rightarrow S_6$ in **1a**); note that the $S_0 \rightarrow S_1$ transition is forbidden because of the S_4-symmetry of these systems. For instance, this band is calculated at 310 nm for **1a**, which is assigned to a combination of HOMO−2 → LUMO, HOMO → LUMO+2, HOMO−1 → LUMO, and HOMO→ LUMO+1 one-electron excitations (see Figure S4).

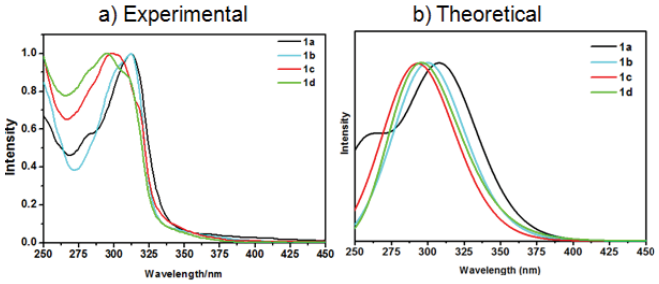

Figure 8. (a) Experimental UV/Vis spectra of **1a**–**1d** in 10^{-5}M CH_2Cl_2 solutions and (b) the corresponding simulated absorption spectra as determined with TD-DFT at the B3LYP76-31G** level.

In order to gain insight into the electronic structure of the oxidized species we perform spectroelectrochemical measurements by sequentially increasing the potential in order to stepwise oxidize them. Figure 7 shows the electronic spectra of **1a**-**1d** recorded during electrochemical oxidation. The electronic spectrum of the first oxidized species shows a dominant broad band around 700 nm which can be ascribed to the formation of a radical cation species. When the potential was increased up to 1000 mV and 1500 mV respectively, the broad bands increase in intensity and a new band around 400 nm emerges. These processes are reversible as confirmed by back-reduction which provides the starting neutral derivatives (see SI). The blue-shifting of the absorption band in going from the radical cation to the dication species is very well captured by TD-DFT calculations (see Figure S5).

It is interesting to note that cyclic tetraindoles show a very similar spectral evolution upon oxidation when compared to the cyclic triindole counterparts with a slight blue-shifting of the absorption maxima.[33] For instance, the band ascribed to the radical cation (dication) appears at 690 (440)nm in triindole **2** and at 600 (408)nm in tetraindole **1a**. This is in consonance with the larger charge localization found for both oxidized species in cyclic tetraindoles when compared to triindole (see figure S2-S3). Note also that the saddle-shaped (twisted) structure of tetraindoles is still maintained upon oxidation (*i.e.*, DFT-calculations predict that the bend angle slightly decreases from 34.3° to 32.0° and 30.8° in **1a** when going from the neutral, to the cation radical and dication species) whereas the oxidized triindole derivatives exhibit nearly planar conjugated cores.

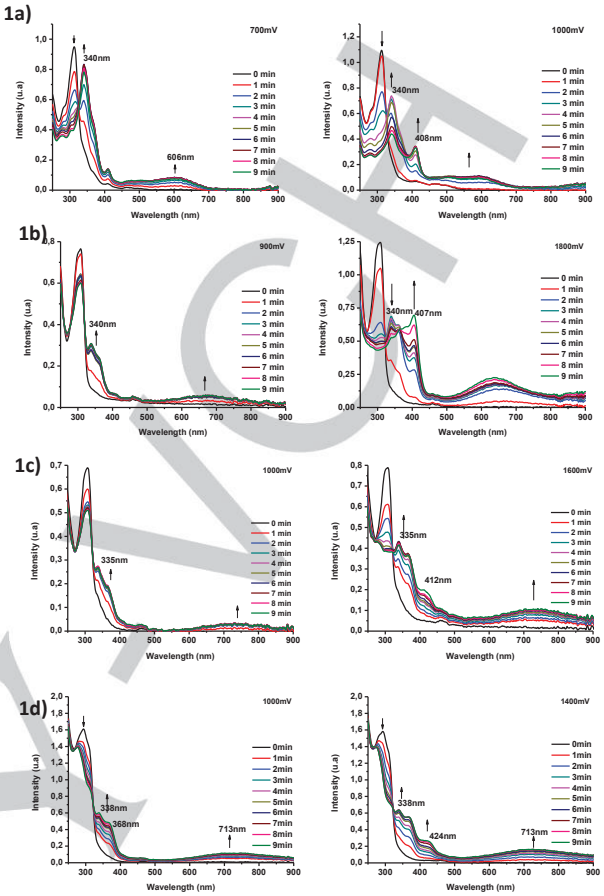

Figure 9. UV/Vis-NIR spectra of **1a**–**1d** obtained at different time intervals after applying a potential of 0.7-1.0 V (left) and 1.0-1.4 V (right) in CH_2Cl_2.

Conclusions

Here we explore the optical and electronic features of cyclic tetraindoles *N*-substituted with alkyl or alkyl aryl groups as interesting electroactive platforms with 3D architectures. The X-Ray crystal structures confirms their saddle-shaped structures which present moderately large tub-to-tub inversion barrier when compared to unsubstituted cyclooctatetraene (COT) rings. Interestingly, the steric constrain introduced by *N*-substitution results in more twisted structures and significantly inhibit ring inversion of the central COT unit but affect only slightly the optical and electrochemical properties. Raman spectroscopy suggests that cyclic tetraindoles allow for a good electron delocalization despite their twisted structures. The electronic absorption spectra evolution upon oxidation together with the DFT calculations evidences the formation of stable cation and dication species in cyclic tetramers with charge defects more localized in the central COT ring. In summary, we present cyclic tetraindole as an interesting electroactive scaffold to connect in three dimension functional moieties with potential applications in the field of organic electronics.

Experimental Section

Experimental Details Routine ^{1}H and ^{13}C NMR spectra were recorded on Bruker AMX 300 and Bruker AC-200 spectrometers. Solvents were purified and dried using standard procedures. Chromatography purifications were carried out using flash grade silica gel with distilled solvents. All reactions were carried out under Ar.

5,10,15,20-tetrahydrocycloocta[1,2-b:3,4-b':5,6-b'':7,8-b''']tetraindole,1a. A mixture of 2-Oxindole (2g, 15mmol) in 4 mL of toluene was stirred and 1mL of $POCl_3$ (10.71mmol) was slowly added. Then the mixture was heated at 150ºC in an autoclave overnight. To removal $POCl_3$ ice was added, and the mixture was neutralized with concentrated KOH to pH =7–8. The mixture was diluted with EtOAc, washed with water and then the organic phase dried ($MgSO_4$). The solvent was evaporated and the residue was purified by chromatography with EtOAc/hexane (1:3) to give a yellow solid crystalline **1a** (330mg, 19%). ^{1}H NMR (500 MHz, $C_2D_2Cl_4$) δ 8.75 (s, 4H), 7.68 (d, *J* = 7.7 Hz, 4H), 7.45 (d, *J* = 7.9 Hz, 4H), 7.17 (dt, *J* = 21.4, 7.2 Hz, 8H). 13C NMR (50 MHz, $C_2D_2Cl_4$) δ 137.2, 135.4, 127.5, 122.4, 121.3, 118.7, 111.2, 106,3. UV (CH2Cl2, 25 ºC) λ_{max} (log ε) 312 (4.40); MALDI-TOF MS m/z 460.2 (M+); HRMS (MALDI-TOF) calcd for $C_{32}H_{20}N_4$: 460.1682, found: 460.1701.

5,10,15,20-tetramethyl-5,10,15,20-tetrahydrocycloocta[1,2-b:3,4-b':5,6-b'':7,8-b''']tetraindole, 1b. A mixture of **1a** (40mg, 0.087 mmol), KOH (146mg, 2.1 mmol) and $[CH_3(CH_2)_3]_4N(HSO_4)]$ (5 mg, 0.03mmol) was heated to reflux in acetone (10mL). Metilsulfate (0,05ml, 0.522mmol) was added and the mixture was stirred for 12 h. The mixture was cooled to room temperature and the solvent was evapored. The mixture was diluted with CH_2Cl_2, washed with water, and dried ($MgSO_4$); the solvent was then evaported. The residue was triturated with CH_3CN to give a white solid **1b** (25mg, 54%). ^{1}H NMR (200 MHz, $CDCl_3$) δ 7.41 (dd, *J* = 6.9 Hz, 8H), 7.34 – 7.08 (m, 8H), 3.69 (s, 12H). ^{13}C NMR (50 MHz, $CDCl_3$) δ 138.6, 138.4, 127.7, 121.7, 120.3, 119.1, 109.9, 106.1, 31.7. UV (CH_2Cl_2, 25 ºC) λ_{max} (log ε) 312 (4.98); MALDI-TOF MS m/z 516.3(M+); HRMS (MALDI-TOF) calcd for $C_{36}H_{28}N_4$: 516.2308, found: 516.2323

5,10,15,20-tetrabenzyl-5,10,15,20-tetrahydrocycloocta[1,2-b:3,4-b':5,6-b'':7,8-b''']tetraindole, 1c. A mixture of **1a** (100 mg, 0.22 mmol), KOH (316 mg, 5.64 mmol) and $[CH_3(CH_2)_3]_4N(HSO_4)]$ (12 mg, 0.07 mmol) was heated to reflux in acetone (10 mL). Benzyl bromide (233 mL, 1.9 mmol) was added and the mixture was stirred for 12 h. The mixture was cooled to room temperature and the solvent was evaporated. The mixture was diluted with CH_2Cl_2, washed with water, and dried ($MgSO_4$); the solvent was then evaporated. The residue was triturated with CH_3CN to give a white solid **1c** (108mg, 60%). ^{1}H NMR (300 MHz, $C_2D_2Cl_4$) δ 7.24 (dd, *J* = 12.0, 7.9 Hz, 8H), 7.05 (dt, *J* = 14.7, 7.0 Hz, 8H), 6.72 (t, *J* = 7.4 Hz, 4H), 6.61 (d, *J* = 7.5 Hz, 8H), 6.38 (t, *J* = 7.7 Hz, 8H), 5.45 (d, *J* = 16.2 Hz, 4H), 5.21 (d, *J* = 16.1 Hz, 4H). ^{13}C NMR (50 MHz, $C_2D_2Cl_4$) δ 139.2, 137.6, 129.5, 128.4, 128.2, 127.1, 126.2, 122.2, 120.9, 119.2, 111.0, 107.6, 48.4. UV (CH_2Cl_2, 25 ºC) λ_{max} (log ε) 300 (3.88); MALDI-TOF MS m/z 820.4 (M+); HRMS (MALDI-TOF) calcd for $C_{60}H_{44}N_4$: 820.3560 found: 820.3579

5,10,15,20-tetrakis(naphthalen-2-ylmethyl)-5,10,15,20-tetrahydrocycloocta[1,2-b:3,4-b':5,6-b'':7,8-b''']tetraindole, 1d. A mixture of **1a** (45 mg, 0.10 mmol), KOH (146 mg, 2.6 mmol) and $[CH_3(CH_2)_3]_4N(HSO_4)]$ (5.6 mg, 0.03 mmol) was heated to reflux in acetone (2 mL). 2-(Bromomethyl)naphthalene (217 mg, 0.98 mmol) was added and the mixture was stirred for 12 h. The mixture was cooled to room temperature and the solvent was evaporated. The mixture was diluted with CH_2Cl_2, washed with water, and dried ($MgSO_4$); the solvent was then evaporated. The residue was triturated with CH_3CN to give a white solid **1d** (17mg, 41%). ^{1}H NMR (200 MHz, $CDCl_3$) δ 7.38 (d, *J* = 8.1 Hz, 4H), 7.30 (d, *J* = 6.1 Hz, 4H), 7.26 (d, 4H), 7.15 (t, *J* = 7.3 Hz, 4H), 7.08 (d, *J* = 6.3 Hz, 4H), 7.02 (s, 4H), 6.93 (d, 8H), 6.88 (t, *J* = 7.5 Hz, 4H), 6.76 (t, *J* = 7.5 Hz, 4H), 6.23 (d, *J* = 8.2 Hz, 4H), 5.77 (d, *J* = 16.3 Hz, 4H), 5.48 (d, *J* = 16.3 Hz, 4H). ^{13}C NMR (50 MHz, $CDCl_3$) δ 139.4, 137.6, 135.1, 133.1, 132.3, 128.3, 128.2, 127.5, 127.1, 125.7, 125.2, 125.5, 124.5, 122.2, 121.2, 119.0, 111.1, 107.5, 48.6. UV (CH2Cl2, 25 ºC) λ_{max} (log ε) 295 (4.12); MALDI-TOF MS m/z 1020.5 (M+); HRMS (MALDI-TOF) calcd for $C_{76}H_{52}N_4$: 1020.4186 found: 1020.4176

X-ray structure determinations

Colorless crystal of **1c** showing well defined faces were mounted Bruker four circle kappa-diffractometer equipped with a Cu INCOATED microsource, operated at 30 W power (45 kV, 0.60 mA) to generate CuKα radiation (λ = 1.54178 Å), and a Bruker VANTEC 500 area detector (microgap technology). Diffraction data were collected exploring over a hemisphere of the reciprocal space in a combination of φ and ω scans to reach a resolution of 0.86 Å, using a Bruker APEXII[35] software suite. The structure was solved by the Multan and Fourier methods. Crystal dimensions 0.20 x 0.20 x 0.20 mm3, unit cell dimensions **a** = 12.3240(5) , **b** = 12.3240(5), **c** = 35.3681(19) Å, monoclinic, $P4_122$ space group, **β** = 98.253 (1)° , **V**= 9144.9(3) Å3, **Z** = 8, ρ_{calcd} 1.12 Mg/m3. The structure was refined anisotropically R1(F) = 0.0768 for observed data (I>2σ(I)), R1(F) = 0.0893 for all data; GOF(F2) = 1.005.

Most of the calculations were carried out with APEXII[14] software for data collection and reduction, and OLEX2[15] for structure solution and refinements. CCDC 1455532 contain the supplementary crystallographic data for **1c** respectively. These data can be obtained free of charge via www.ccdc.cam.ac.uk/conts/retrieving.html (or from the Cambridge Crystallographic Data Centre, 12 Union Road, Cambridge CB21EZ, UK; (fax: (+44) 1223-336-033; or e-mail: deposit@ccdc.cam.ac.uk). P41 Some solvent molecules **1c** could not be modelled properly and have been disregarded. The Olex2[36]program was used to calculate the solvent disorder area and remove its contribution to the overall intensity data.

Computational details. The molecular geometries of neutral, radical-cation and dication states of tetraindoles **1a-1d** were calculated at the Density Functional Theory (DFT) level using the hybrid, generalized gradient approximation (GGA) functional B3LYP[37,38] and a 6-31G** basis[39,40,41] set, as implemented in the GAUSSIAN09 program.[42] For comparison purposes the molecular geometries of triindole and unsubstituted cyclooctatraene (COT) were calculated at the same level. For the neutral state of tetraindoles (triindole) S_4 (C_3) symmetry constraints were imposed during the optimization process. On the resulting ground-state optimized geometries, harmonic frequencies calculations were performed to ensure we are in a global minimum. Vertical electronic excitation energies were computed by using the time-dependent DFT (TD-DFT) approach on the previously optimized molecular geometries. Absorption spectra were simulated through convolution of the vertical transition energies and oscillator strengths with Gaussian functions characterized by a half width at half-maximum (fwhm) of 0.3 eV. Molecular orbital contours were plotted using GausView 5.0. The reorganization energies associated with hole transfer were calculated directly from the relevant points on the potential energy surfaces using the standard procedure detailed in the literature.[43] Using the B3LYP/6-31G** optimized structures, NICS[44] values were calculated at the B3LYP/6-11++G(2d,f) level using the GIAO[45] (gauge-independent atomic orbital) method. Inversion barriers were calculated at the B3LYP/6-31+G** computational level within the Gaussian-09 package. Frequencies calculations have been carried out to confirm that the

structures obtained correspond to energetic minima or true transition state.

Acknowledgements

This work was partially funded by the Spanish Government MINECO CTQ2013-40562-R grants; and the Comunidad de Madrid S2013/MIT-2740 (PHAMA_2.0)..

Keywords: tetraindole • organic semiconductors• spectroelectrochemistry • COT • hyperconjugation

[1] L. Zang, Y. Che, J. S. Moore, Acc. Chem. Res., 2008, 41, 1596.
[2] J. Roncali, P. Leriche, A. Cravino, A. *Adv. Mater*. **2007**, *19*, 2045. b) P. J. Skabara, J. B. Arlin, Y. H. Geerts, *Adv. Mater*. **2013**, *25*, 1948.
[3] S. Roquet, R. de Bettignies, P. Leriche, A. Cravino, J. Roncali, *J. Mater. Chem*. **2006**, *16*, 3040.
[4] W. Chen, X. Yang, G. Long, X. Wan, Y. Chen, Q. Zhang *J. Mater. Chem. C*, **2015**, *18*, 4698.
[5] S. Wang, W.-J. Oldham, Jr., R.-A. Hudack, Jr., G. Bazan, *J. Am. Chem. Soc*. **2000**, *122*, 5695.
[6] S. Karpe, A. Cravino, P. Frère, M. Allain, G. Mabon, J. Roncali, *Adv. Funct. Mater*. **2007**, *17*, 1163.
[7] C.-C. Wu, T.-L. Liu, W.-Y. Hung, Y.-T. Lin, K.-T. Wong, R.-T. Chen, Y.-M. Chien, Y.-Y. Chien, *J. Am. Chem. Soc*. **2003**, *125*, 3710.
[8] M. Franceschin, L. Ginnari-Satriani, A. Alvino, G. Ortaggi, A. Bianco, *Eur. J. Org. Chem*. **2010**, 134.
[9] a) W. Y. Lai, Q. Y. He, R. Zhu, Q. Q. Chem, W. Huang, *Adv. Funct. Mater*. **2008**, *18*, 265. b) C. Coya, C. Ruiz, L. Luis-Álvarez, S. Álvarez-García, E. García-Frutos, B. Gómez-Lor, A. Andrés, *Org. Electr.* **2012**, *13*, 2138.
[10] a) K. Rakstys, A. Abate, M. Ibrahim Dar, P. Gao, V. Jankauskas, G. Jacopin, E. Kamarauskas, S. Kazim, S. Ahmad, M. Grätzel, M. K. Nazeeruddin, *J. Am. Chem. Soc.* **2015**, 137, 16172. b) S. W. Shelton, T. L. Chen, D. E. Barclay, B. Ma, *ACS Appl. Mater. Interfaces* **2012**, 4, 2534.
[11] M. Reig, J. Puigdollers, D. Velasco, *J. Mater. Chem. C.,* **2015**, 3, 506.
[12] A. Benito-Hernández, U. K. Pandey, E. Cavero, R. Termine, E. M. García-Frutos, J. L. Serrano, A. Golemme, B. Gómez-Lor, *Chem. Mater.* **2013**, *25*, 117.
[13] E. M. García-Frutos, U. K. Pandey, TR. ermine, A. Omenat, J. Barberá, J. L. Serrano,A. Golemme, B. Gómez-Lor, *Angew. Chem. Int. Ed. Engl*. **2011**, *50*, 7399.
[14] The obtention of tetramers as side products in acid mediated trimerization of ketones has been reported for other moieties, see for example: a) M. M. Boorum, Y. V. Vasilév, T. Drewello, L. T. Scott, *Science*, **2001**, *294*, 828. b) Bergman, J.; Egestad, B. *Tetrahedron Lett*. **1978**, *19*, 3143.
[15] From all the possible coupling schemes for the polymerization of indole compound **2** and **3** have been predicted as the most stable cyclized oligomers: M. Yurtsever, E. Yurtsever, *Polymer* **2002**, *43*, 6019.
[16] X.Qian, H.-H. Gao, Y.-Z. Zhu, B. Pan, J.-Y. Zheng Dyes Pigm. **2015**, *121* 152.
[17] L. Wang, Q. Fang, Q. Lu, S.-J. Zhang, Y.-Y. Jin, Z.-Q. Liu, *Org. Lett*. **2015**, *17*, 4164.
[18] F. Wang, X. C. Li, W. Y. Lai, Y. Chen, W. Huang, F. Wudl, *Org. Lett*. **2014**, *16*, 2942.
[19] H. Hiyhoshi, T. Sonoda, S. Mataka, *Heterocyles* **2006**, *68*, 763.
[20] O. Talaz, N.Saracoglu Tetrahedron **2010**, *66*, 1902.
[21] M. J. Marsela, J. R. Rodney, S. Estassi, L.-S. Wang, *J. Am. Chem. Soc*. **2002**, *124*, 12507.
[22] T. Nishiuchi, Y. Kuwatani, T. Nishinaga, M. Iyoda, *Chem. Eur. J.* **2009**, *15*, 6838.
[23] a) T. Nishiuchi, K. Tanaka, Y. Kuwatani, J. Sung, T. Nishinaga, D. Kim, M. Iyoda, M. *Chem. Eur. J.* **2013**, *19*, 4110. b) C. Yuan, S. Saito, C. Camacho, S. Irle, I. Hisaki, S. Yamaguchi, *J. Am. Chem. Soc.* **2013**, *135*, 8842.
[24] a) A. Rajca, S. Rajca, *Angew. Chem. Int. Ed*. **2010**, *49*, 672. b) P. Wender, J. P. Christy, A. B. Lesser, M. T. Gieseler, *Angew. Chem. Int. Ed*. **2009**,*48*, 7687.
[25] a) C. Cheng, Z. Cai, X.-S. Peng, H. N. C. Wong, *J. Org. Chem*. **2013**, *78*, 8562-8573. b) J.-F. Cui, C. Chen, Z.-W. Cai, J.-W. Hang, H. N. C. Wong, *Helv Chim. Acta*, **2012**, *95*, 2604–2620.
[26] a) J. I. Wu, I. Fernández, Y. Mo, P. v. R. Schleyer, *J. Chem. Theory Comput*. **2012**, *8*, 1280. b) J. I. Wu, P. v. R. Schleyer, *Pure Appl. Chem*. **2013**, *85*, 921–940.
[27] At this stage it is not clear the reason for the preferred formation of the tetramer vs. the trimeric species. Probably it is just more stable under this harsh conditions.
[28] While this manuscript was on the preparation the structure of compound 1a was reported. See Reference 17.
[29] E. B. Wilson, J. C. Decius, P. C. Cross, Molecular Vibrations. The Theory of Infrared and Raman Vibrational Spectra; McGraw-Hill: New York, Toronto, London, 1955.
[30] a) X. Zhou, R. Liu, P. Pulay, Spectrochim. Acta 1993, 49A, 953. b) E. R. Lippincott, R. C. Lord, R. S. McDonald, J. Am. Chem. Soc. **1951**, *73*, 3370.
[31] a) P. v. R. Schleyer, C. Maerker, A. Dransfeld, H. Jiao, N. J. R. van Eikema Hommes, J. Am. Chem. Soc. **1996**, *118*, 6317. b) T. K. Zywietz, P. v. R. Schleyer, A. Meijere, *J. Org. Chem.* **1998**, *63*, 3417.
[32] NICS values have been calculated using the GIAO method (K. Wolinski, J. F. Hilton, P. Pulay, *J. Am. Chem. Soc.* **1990**, *112*, 8251) at the 6-311++G(2df,p) level. These data are considered only at the six(eight)-member ring centers which are determined by the nonweighted mean of the heavy atom coordinates.
[33] C. Ruiz, E. M. García-Frutos, D. A. Da Silva Filho, J. T. López Navarrete, M. C. Ruiz Delgado, B. Gómez-Lor, *J. Phys. Chem. C* **2014**, *118*, 5470.
[34] Y. M. Sun, Y. Q. Ma, Y. Q. Liu, Y. Y. Lin, Z. Y. Wang, Y. Wang, C. A. Di, K. Xiao, X. M. Chen, W. F. Qiu, B. Zhang, G. Yu, W. P. Hu, D. B. Zhu, *Adv. Funct. Mater*. **2006**, *16*, 426.
35 APEX2; Bruker-AXS: Madison, WI, 2006.
36 O. V. Dolomanov, L. J. Bourhis, R.J. Gildea, J.A.K. Howard, H. Puschmann, *J. Appl. Cryst*. **2009**, *42*, 339-341.
[37] A. D. Becke, *J. Chem. Phys.* **1993**, *98*, 5648.
[38] C. T. Lee, W. T. Yang, R. G. Parr, *Phys. Rev. B* **1988**, *37*, 785.
[39] P. C. Hariharan, J. A. Pople, *Theor. Chim. Acta* **1973**, *28*, 213.
[40] W. J. Hehre, R. Ditchfield, J. A. Pople, *J. Chem. Phys.* **1972**, *56*, 2257.
[41] M. M. Francl, W. J. Pietro, W. J. Hehre, J. S. Binkley, M. S. Gordon, D. J. Defrees, J. A. Pople, *J. Chem. Phys.* **1982**, *77*, 3654.
[42] M. J. Frisch, G. W. Trucks, H. B. Schlegel, G. E. Scuseria, M. A. Robb, J. R. Cheeseman, G. Scalmani, V. Barone, B. Mennucci, G. A. Petersson, H. Nakatsuji, M. Caricato, X. Li, H. P. Hratchian, A. F. Izmaylov, J. Bloino, G. Zheng, J. L. Sonnenberg, M. Hada, M. Ehara, K. Toyota, R. Fukuda, J. Hasegawa, M. Ishida, T. Nakajima, Y. Honda, O. Kitao, H. Nakai, T. Vreven, J. A. Montgomery, Jr., J. E. Peralta, F. Ogliaro, M. Bearpark, J. J. Heyd, E. Brothers, K. N. Kudin, V. N. Staroverov, R. Kobayashi, J. Normand, K. Raghavachari, A. Rendell, J. C. Burant, S. S. Iyengar, J. Tomasi, M. Cossi, N. Rega, J. M. Millam, M. Klene, J. E. Knox, J. B. Cross, V. Bakken, C. Adamo, J. Jaramillo, R. Gomperts, R. E. Stratmann, O. Yazyev, A. J. Austin, R. Cammi, C. Pomelli, J. W. Ochterski, R. L. Martin, K. Morokuma, V. G. Zakrzewski,

G. A. Voth, P. Salvador, J. J. Dannenberg, S. Dapprich, A. D. Daniels, Ö. Farkas, J. B. Foresman, J. V. Ortiz, J. Cioslowski and D. J. Fox, Gaussian 09, Revision D.01, Gaussian, Inc., Wallingford CT, **2009**.

[43] J. L. Bredas, D. Beljonne, V. Coropceanu, J. Cornil, *Chem. Rev.* **2004**, *104*, 4971.

[44] P. v. R. Schleyer, C. Maerker, A. Dransfeld, H. Jiao, H.; N. J. R. v. E. Hommes, *J. Am. Chem. Soc.* **1996**, *118*, 6317.

[45] K. Wolinski, J. F. Hilton, P. Pulay, *J. Am. Chem. Soc.* **1990**, *112*, 8251.